NASA/CP—2001-210747/REV1

16th Space Photovoltaic Research and Technology Conference

May 2005

The NASA STI Program Office . . . in Profile

Since its founding, NASA has been dedicated to the advancement of aeronautics and space science. The NASA Scientific and Technical Information (STI) Program Office plays a key part in helping NASA maintain this important role.

The NASA STI Program Office is operated by Langley Research Center, the Lead Center for NASA's scientific and technical information. The NASA STI Program Office provides access to the NASA STI Database, the largest collection of aeronautical and space science STI in the world. The Program Office is also NASA's institutional mechanism for disseminating the results of its research and development activities. These results are published by NASA in the NASA STI Report Series, which includes the following report types:

- TECHNICAL PUBLICATION. Reports of completed research or a major significant phase of research that present the results of NASA programs and include extensive data or theoretical analysis. Includes compilations of significant scientific and technical data and information deemed to be of continuing reference value. NASA's counterpart of peer-reviewed formal professional papers but has less stringent limitations on manuscript length and extent of graphic presentations.

- TECHNICAL MEMORANDUM. Scientific and technical findings that are preliminary or of specialized interest, e.g., quick release reports, working papers, and bibliographies that contain minimal annotation. Does not contain extensive analysis.

- CONTRACTOR REPORT. Scientific and technical findings by NASA-sponsored contractors and grantees.

- CONFERENCE PUBLICATION. Collected papers from scientific and technical conferences, symposia, seminars, or other meetings sponsored or cosponsored by NASA.

- SPECIAL PUBLICATION. Scientific, technical, or historical information from NASA programs, projects, and missions, often concerned with subjects having substantial public interest.

- TECHNICAL TRANSLATION. English-language translations of foreign scientific and technical material pertinent to NASA's mission.

Specialized services that complement the STI Program Office's diverse offerings include creating custom thesauri, building customized data bases, organizing and publishing research results . . . even providing videos.

For more information about the NASA STI Program Office, see the following:

- Access the NASA STI Program Home Page at ***http://www.sti.nasa.gov***

- E-mail your question via the Internet to help@sti.nasa.gov

- Fax your question to the NASA Access Help Desk at 301–621–0134

- Telephone the NASA Access Help Desk at 301–621–0390

- Write to:
  NASA Access Help Desk
  NASA Center for AeroSpace Information
  7121 Standard Drive
  Hanover, MD 21076

NASA/CP—2001-210747/REV1

16th Space Photovoltaic Research and Technology Conference

Proceedings of a conference
held at Ohio Aerospace Institute
and sponsored by NASA Glenn Research Center
Brook Park, Ohio, August 31–September 2, 1999

National Aeronautics and
Space Administration

Glenn Research Center

May 2005

Document Change History

This revised report, numbered as NASA/CP—2001-210747/REV1, May 2005, supersedes the previous version, NASA/CR—2001-210747, April 2001.

Pages 259 to 268: The attendee list has been removed.

Back of title page, Report Documentation Page, CD label, and CD insert: Non-Web statement has been removed.

Report Documentation Page, number 11, Supplementary Notes: The statement "This revised report supersedes the original report" has been inserted.

Trade names or manufacturers' names are used in this report for identification only. This usage does not constitute an official endorsement, either expressed or implied, by the National Aeronautics and Space Administration.

Contents were reproduced from the best available copy as provided by the authors.

Available from

NASA Center for Aerospace Information
7121 Standard Drive
Hanover, MD 21076

National Technical Information Service
5285 Port Royal Road
Springfield, VA 22100

Available electronically at http://gltrs.grc.nasa.gov

Foreword

The 16th Space Photovoltaic Research and Technology Conference, SPRAT–99, was held at the Ohio Aerospace Institute (OAI) from August 31 to September 2, 1999.

The SPRAT conference is scheduled on a sesquiennial, or every 18 months, convening roughly opposite to the IEEE Photovoltaic Specialists Conference. Once again, the workshop featured a meeting among representatives of industry, government, and universities to discuss the progress in the development of solar cells and arrays for space use, and brought together people from the research community, cell and array manufacturers, the space environmental effects community, and the end users.

The purpose of the SPRAT conference is to bring members of the space solar cell community together in a relatively informal conference setting to discuss the recent developments in solar cell technology and to discuss the future directions of the field. The conference is sponsored by the Photovoltaic and Space Environmental Effects Branch at the NASA Glenn Research Center. This is the first year in which the conference was held at OAI, just outside the gate of NASA Glenn, instead of onsite at NASA, and I think that the overall opinion of the participants was favorable.

This year's conference came at a time when the space photovoltaic business is in a state of change. New high-efficiency solar cell types are now seeing commercial use, and several new concepts for solar arrays, including flexible and concentrator arrays, are making their appearances in flight systems. Commercial communications satellites are reaching toward the unprecedented power levels of 30 kW and higher to feed a burgeoning broadcast and telecommunications market, while the International Space Station, which will feature the most powerful electrical power system ever flown in space, is approaching flight. All in all, it has been an extremely interesting 18 months.

At each SPRAT, the SPRAT Chairman has the privilege of awarding the Irving Weinberg Award to a researcher who has made significant contributions to space solar cell research and technology. Previous years' recipients have been Prof. Chandra Goradia and Dr. Masafumi Yamaguchi. This year I had the honor to give the Irving Weinberg Award to Dr. Dennis Flood, who has been for many years the chief of the Photovoltaic Branch at NASA Lewis (and later at NASA Glenn). Denny has been a great leader and a friend to the space photovoltaic community, and I do not think that we could have made a better choice.

In closing, I would like to give thanks to all the conference organizers, session chairs, and presenters for the hard work that they contributed toward making the conference a success. I hope to see you all in 2001 for the 17th sesquiennial SPRAT!

Geoffrey A. Landis,
Chairman

TABLE OF CONTENTS

FOREWORD iii

INVITED PAPERS

MODELING SOLAR CELL DEGRADATION IN SPACE: A COMPARISON OF THE JPL AND NRL METHODS
Geoffrey P. Summers, Scott R. Messenger, Robert J. Walters, and Edward A. Burke, Naval Research Laboratory 1

ESA SOLAR GENERATOR TECHNOLOGY PROGRAMME
C. Signorini, European Space Agency 13

SPACE RADIATION

EFFECT OF STOICHIOMETRY ON THE RADIATION RESPONSE OF $In_xGa_{1-x}As$ SOLAR CELLS
S.R. Messenger, SFA, Inc.; R.J. Walters and G.P. Summers, Naval Research Laboratory; and R.H. Hoffman, Jr., and M.A. Stan, Essential Research, Inc. 26

ANALYSIS OF THE ROLE OF DEEP LEVELS IN ANOMALOUS DEGRADATION OF Si SPACE SOLAR CELLS
Aurangzeb Khan, Masafumi Yamaguchi, and Stephen J. Taylor, Toyota Technological Institute 30

RADIATION HARD MULTI-QUANTUM WELL InP/InAsP SOLAR CELLS FOR SPACE APPLICATIONS
R.J. Walters and G.P. Summers, U.S. Naval Research Laboratory; A. Freundlich, C. Monier, and F. Newman, Space Vacuum Epitaxy Center; and S.R. Messenger, SFA, Inc. 31

USE OF DISPLACEMENT DAMAGE DOSE IN AN ENGINEERING MODEL OF GaAs SOLAR CELL RADIATION DAMAGE
T.L. Morton, Ohio Aerospace Institute; R. Chock and K.J. Long, NASA Glenn Research Center; S.R. Messenger, SFA, Inc.; R.J. Walters, Naval Research Laboratory; and G.P. Summers, Naval Research Laboratory and University of Maryland Baltimore County 35

DISPLACEMENT DAMAGE DOSE ANALYSIS OF NEUTRON IRRADIATED SINGLE AND DUAL JUNCTION GaAs-BASED SOLAR CELLS
R.J. Walters and G.P. Summers, Naval Research Laboratory; and S.R. Messenger and E.A. Burke, SFA, Inc. 39

SolaMax™ MICROSHEET SOLAR CELL COVERGLASS: SPACE RADIATION QUALIFICATION TEST RESULTS
Janeen A. Cooke, Mike Larro, and Mark Madigan, Optical Coating Laboratory, Inc. 44

SPACE ENVIRONMENT AND FLIGHT EXPERIENCE

COMBINED SILICON AND GALLIUM ARSENIDE SOLAR CELL UV TESTING
Douglas Willowby, NASA Marshall Space Flight Center 53

SOLAR ARRAY SAILS: POSSIBLE SPACE PLASMA ENVIRONMENTAL EFFECTS
Willie R. Mackey, NASA Glenn Research Center 54

OVERVIEW, TESTING, AND SOLUTIONS TO ESD-INDUCED, SOLAR-ARRAY-STRING, ON-ORBIT FAILURES
A. Meulenberg, Hi Pi Consulting 58

FLIGHT DATA OF GaAs SOLAR CELLS ON THE COMETS
Osamu Anzawa, Kazuhiro Aoyama, Takashi Aburaya, Koichi Shinozaki and Sumio Matsuda, National Space Development Agency of Japan; Takeshi Ohshima, Isamu Nashiyama, Hisayoshi Itoh, and Sohei Okada, JAERI, Tetsuya Nakao and Yusuke Matsumoto, AES Corporation 64

IN-ORBIT PERFORMANCE OF HUGHES HS601HP DUAL JUNCTION $GaInP_2$/GaAs/Ge SOLAR ARRAYS
Steven W. Gelb, Jay S. Fodor, and Joseph S. Powe, Hughes Space and Communications Company 74

MULTI-BANDGAP CELL DEVELOPMENT

TECSTAR'S NEXT GENERATION CASCADE® SOLAR CELL IMPROVEMENTS: A MONOLITHIC INTEGRAL DIODE AND NEW MIDDLE CELL FORMATION
Louis C. Kilmer, Charlie Chu, Milton Yeh, Peter Iles, P.K. Chiang, and Frank Ho, TECSTAR, Inc. 83

DEVELOPMENT, SPACE QUALIFICATION, AND PRODUCTION OF HIGH-EFFICIENCY LARGE-AREA InGaP/GaAs DUAL-JUNCTION SOLAR CELLS ON GE AT EMCORE PHOTOVOLTAICS (EPV)
Navid S. Fatemi, Hong Q. Hou, Paul R. Sharps, Paul M. Martin, B.E. Hammons, and Frank Spadafora, Emcore Photovoltaics 94

RECENT PROGRESS IN THE DEVELOPMENT OF HIGH-EFFICIENCY $Ga_{0.5}In_{0.5}P$/GaAs/Ge DUAL- AND TRIPLE-JUNCTION SOLAR CELLS
Nasser H. Karam, Richard R. King, Dimitri D. Krut, James H. Ermer, Moran Haddad, Hector Cotal, and Jack W. Eldredge, Spectrolab, Inc. 109

30% EFFICIENT INGaP/GaAs/GaSb CELL-INTERCONNECTED-CIRCUITS FOR LINE-FOCUS CONCENTRATOR ARRAYS
Lewis Fraas and James Avery, JX Crystals, Inc.; Peter Iles and Charlie Chu, TECSTAR, Inc.; and Mike Piszczor, NASA Glenn Research Center 110

HIGH GROWTH RATE METAL-ORGANIC MOLECULAR BEAM EPITAXY FOR THE FABRICATION OF GaAs SPACE SOLAR CELLS
A. Freundlich, F. Newman, C. Monier, and S. Street, Space Vacuum Epitaxy Center; and P. Dargan and M. Levy, Riber, Inc. 117

HIGH-EFFICIENCY MULTI-JUNCTION SPACE SOLAR DEVELOPMENT UTILIZING LATTICE GRADING
Mark A. Stan et al., Essential Research, Inc.; Richard W. Hoffman, Jr., Phillip P. Jenkins, and David A. Scheiman, The Ohio Aerospace Institute; and Navid S. Fatemi, Emcore Photovoltaics 122

ANTIREFLECTION COATING DESIGN FOR MULTI-JUNCTION, SERIES INTERCONNECTED SOLAR CELLS
Daniel J. Aiken, Sandia National Laboratories 129

INVITED PAPER

RECENT SPACE PHOTOVOLTAIC RESEARCH AND DEVELOPMENT IN JAPAN
Masafumi Yamaguchi, Toyota Tech. Inst., and Sumio Matsuda, National Space Development Agency of Japan . . . 135

THIN FILM CELL TECHNOLOGY

DEVELOPMENT OF A THIN FILM AMORPHOUS SILICON SPACE SOLAR CELL FOR THE POWERSPHERE CONCEPT
Edward J. Simburger, David Scott, Dennis Smith, David Gilmore, Mike Meshishnek, and Meg Abraham, The Aerospace Corporation, and Frank R. Jeffery, Iowa Thin Film Technologies, Inc. 143

TOWARDS A THIN FILM SILICON HETEROJUNCTION SOLAR CELL
Young Song, Elena Guliants, and Wayne Anderson, State University of New York at Buffalo 149

CHEMICALLY DEPOSITED THIN-FILM SOLAR CELL MATERIALS
R. Raffaelle and W. Junek, Rochester Institute of Technology; J. Gorse and T. Thompson, Baldwin-Wallace College; J. Harris and D. Hehemann, Kent State University; and A. Hepp and G. Rybicki, NASA Glenn Research Center 158

$Cu(In,Ga)S_2$, THIN-FILM SOLAR CELLS PREPARED BY H_2S SULFURIZATION OF CuGa-In PRECURSOR
Neelkanth G. Dhere, Shashank R. Kulkarni, Sanjay S. Chavan, and Shantinath R. Ghongadi, Florida Solar Energy Center 164

MEASUREMENTS

INVESTIGATION OF THE CARBON ARC SOURCE AS AN AMO SOLAR SIMULATOR FOR USE IN CHARACTERIZING MULTI-JUNCTION SOLAR CELLS
Jianzeng Xu and James R. Woodyard, Wayne State University 177

ELECTRICAL CHARACTERIZATION OF DEFECTS IN SiC SCHOTTKY BARRIERS
C.M. Schnabel and M. Tabib-Azar, Case Western Reserve University; R.P. Raffaelle, Rochester Institute of Technology; H.B. Su and M. Dudley, SUNY at Stony Brook, and P.G. Neudeck and S. Bailey, NASA Glenn Research Center 183

INVESTIGATIONS TO CHARACTERIZE MULTI-JUNCTION SOLAR CELLS IN THE STRATOSPHERE USING LOW-COST BALLOON AND COMMUNICATION TECHNOLOGIES
Glenroy A. Bowe, Qianghua Wang, and James R. Woodyard, Wayne State University; Richard R. Johnston, Lawrence Technological University; and William J. Brown, High Altitude Research Corporation 189

PHOTOVOLTAIC ENGINEERING TESTBED ON THE INTERNATIONAL SPACE STATION
Geoffrey A. Landis and David Scheiman, Ohio Aerospace Institute; and Andrew Sexton, Richard Abramczyk, Joseph Francz; D.B. Johnson; Liu Yang, Daniel Minjares, and James Myers, Dynacs, Inc. 195

ADVANCED CONCEPTS

SILICON CARBIDE RADIOISOTOPE BATTERIES
George C. Rybicki, NASA Glenn Research Center 199

HIGH QUALITY GaAs GROWTH BY MBE ON Si USING GeSi BUFFERS AND PROSPECTS FOR SPACE PHOTOVOLTAICS
J.A. Carlin and S.A. Ringel, The Ohio State University; E.A. Fitzgerald, Massachusetts Institute of Technology; and M. Bulsara, Amberwave, LLC 204

n/p/n TUNNEL JUNCTION InGaAs MONOLITHIC INTERCONNECTED MODULE (MIM)
David M. Wilt, NASA Glenn Research Center; Christopher S. Murray, Bechtel Bettis, Inc.; Navid S. Fatemi, Emcore, Inc.; and Victor Weizer, Essential Research, Inc. 211

NOVEL PASSIVATING/ANTIREFLECTIVE COATINGS FOR SPACE SOLAR CELLS
Mircea Faur, Maria Faur, H.M. Faur, and C.G. Mateescu, SPECMAT, Inc.; S.G. Bailey, D.J. Flood, S.A. Alterovitz, D.J. Brinker, J.D. Warner, and D.R. Wheeler, NASA Glenn Research Center; and D. Scheiman and P.P. Jenkins, Ohio Aerospace Institute 220

ADVANCED FLEXIBLE SOLAR ARRAY PROGRAM
Peter V. Meyers and Leon Fabick, ITN Energy Systems; Kitt C. Reinhardt, Air Force Research Laboratory; and William N. Shafarman, Institute of Energy Conversion 230

SOLAR POWER ON MARS

MARS ORBITER SAMPLE RETURN POWER DESIGN
N. Mardesich and S. Dawson, Jet Propulsion Laboratory 238

PROGRESS OF THE MARS ARRAY TECHNOLOGY EXPERIMENT (MATE) ON THE 2001 LANDER
David A. Scheiman, Phil Jenkins, and Geoff Landis, Ohio Aerospace Institute; Cosmo Baraona, Dave Wilt, Michael Krasowski, Lawrence Greer, John Lekki, and Daniel Spina, NASA Glenn Research Center 242

PROGRESS OF THE DUST ACCUMULATION AND REMOVAL TECHNOLOGY EXPERIMENT (DART) FOR THE MARS 2001 LANDER
Phillip Jenkins, Geoffrey A. Landis, and David Scheiman, Ohio Aerospace Institute; David Wilt, Michael Krasowski, Lawrence Greer, and Cosmo Baraona, NASA Glenn Research Center 248

WORKSHOPS

REPORT OF THE WORKSHOP ON NEXT-GENERATION SPACE PV: THIN FILMS 253

PREDICTING ENVIRONMENTAL INTERACTIONS 256

Modeling Solar Cell Degradation in Space: A Comparison of the JPL and NRL Methods

Geoffrey P. Summers

Scott R. Messenger (SFA)

Robert J. Walters

Edward A. Burke (SFA)

Naval Research Laboratory
Code 6825
Washington, DC 20375

16th Space Photovoltaic Research and Technology Conference
31 August 1999

OUTLINE

- The Problem
- The JPL Equivalent Fluence Method
- The NRL Displacement Damage Dose Method
- Comparison of Results
- Issues

Modeling Solar Cell Degradation in Space

The Problem

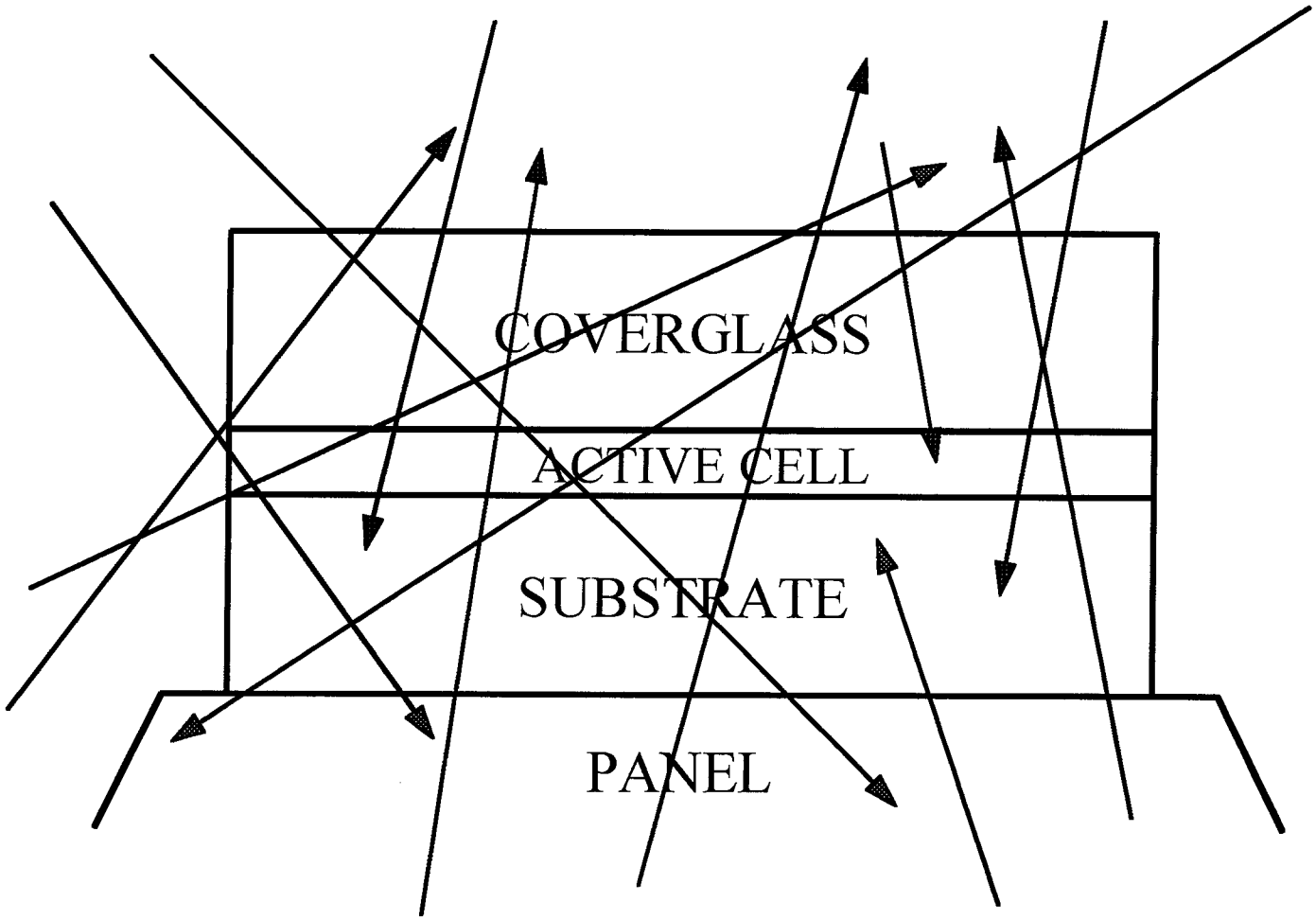

Issues to Consider

- **Incident radiation environment is complex**
  - **Isotropic protons and electrons 0<E<hundreds of MeV**
  - **Varies with orbit**
- **Cells are shielded**
  - **Incident spectrum is "slowed down"**
- **Cell degradation is particle and energy dependent**
- **Ground measurements use monoenergetic beams**

JPL and NRL Methods

- **JPL**
  - **Calculate equivalent 1 MeV electron fluence for mission**
  - **Read EOL power from measured 1 MeV electron curve**
- **NRL**
  - **Calculate displacement damage dose, D_d, for mission**
  - **Read EOL power from measured characteristic curve**

Modeling Solar Cell Degradation in Space

P_{max} Degradation Curves for GaAs/Ge Solar Cells

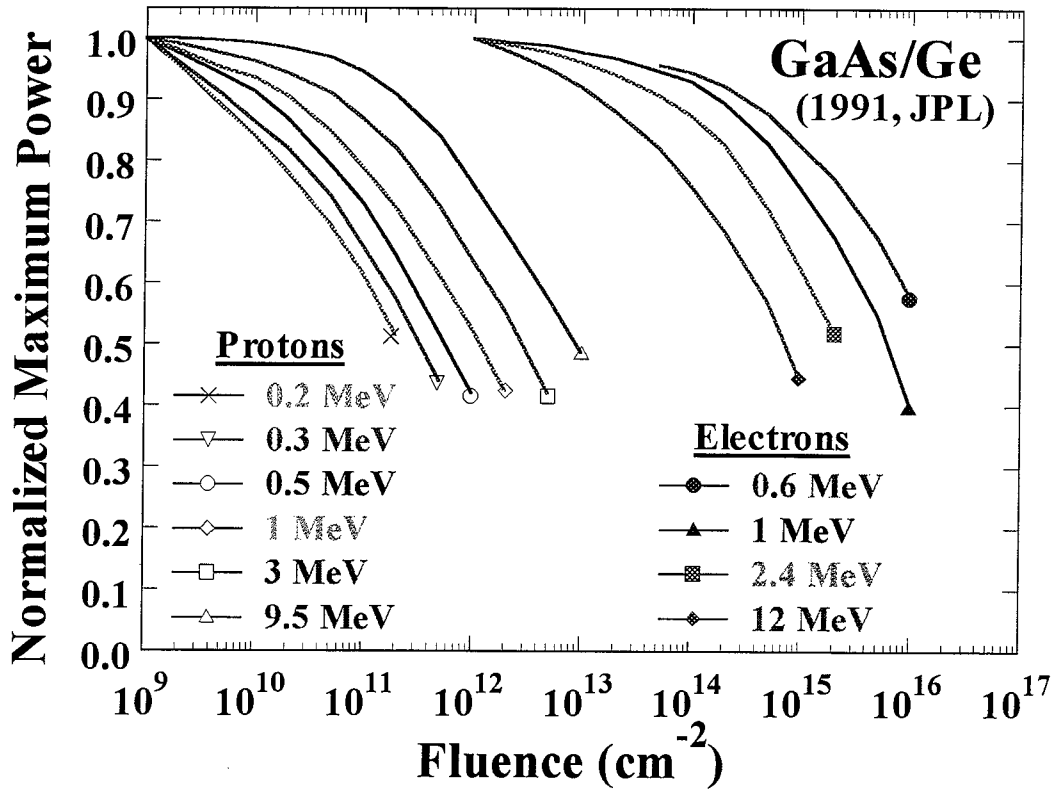

* B.E. Anspaugh, "Proton and Electron Damage Coefficients for GaAs/Ge Solar Cells", Proc. 22nd IEEE PVSC, 1593 (1991).

Modeling Solar Cell Degradation in Space

JPL Equivalent Fluence Method

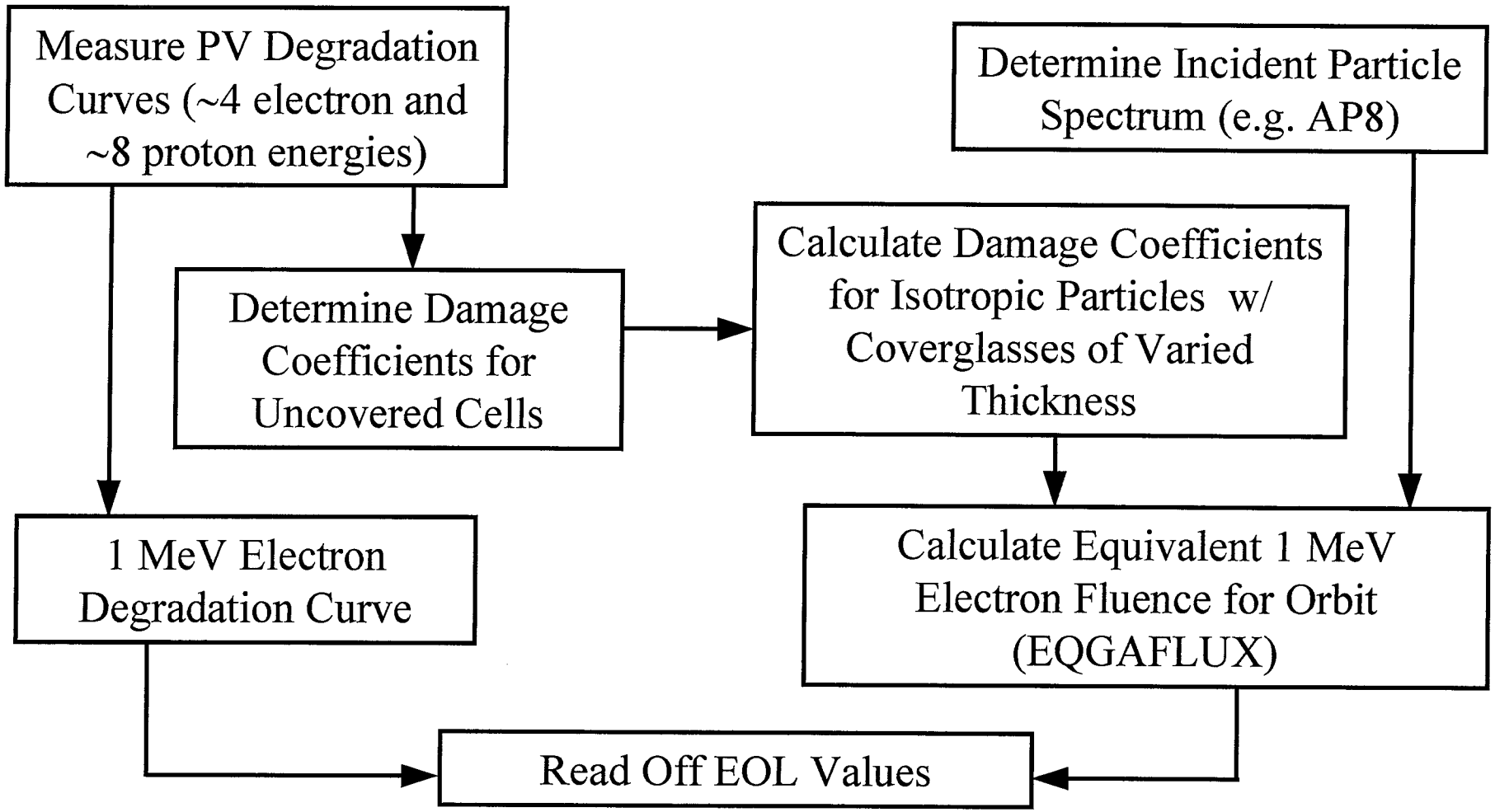

JPL Equivalent Fluence Method

Initial Isotropic Spectrum

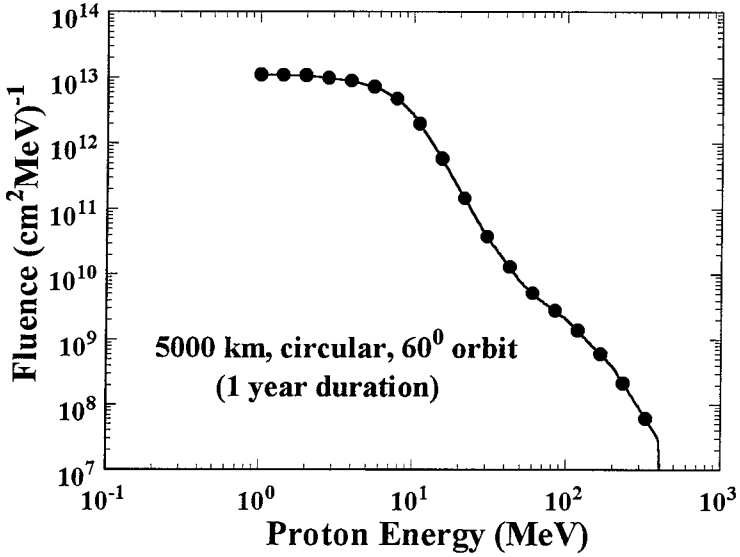

Proton Damage Coefficients

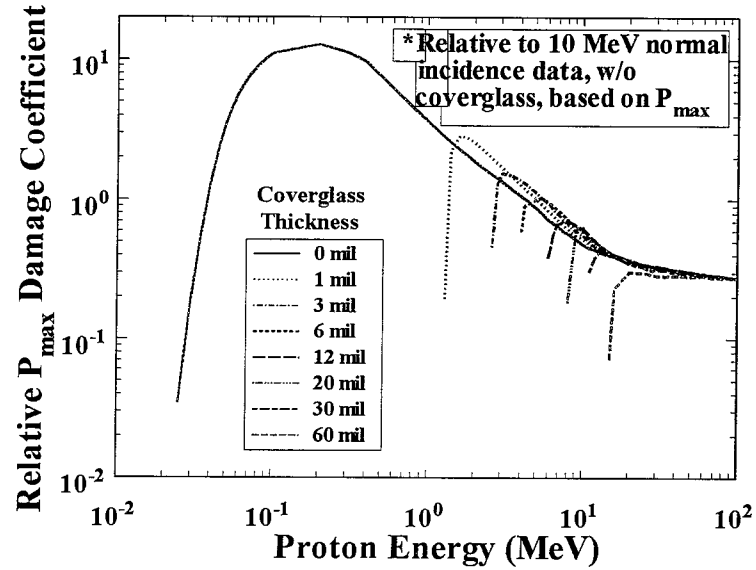

Equivalent 1 MeV Electron Fluence

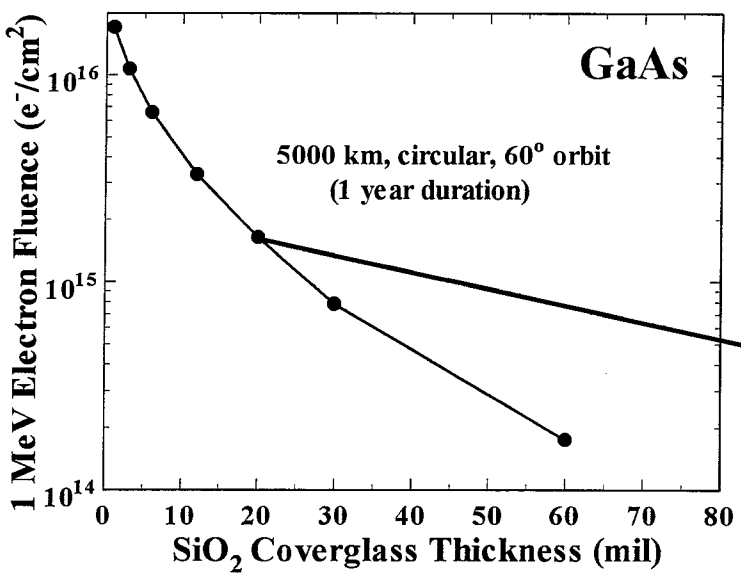

P_{max} Degradation

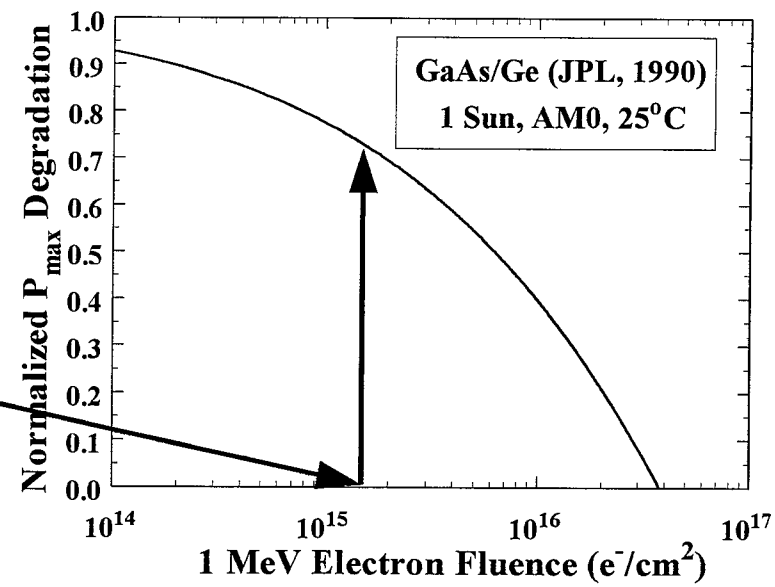

Modeling Solar Cell Degradation in Space

NRL Displacement Damage Dose Method

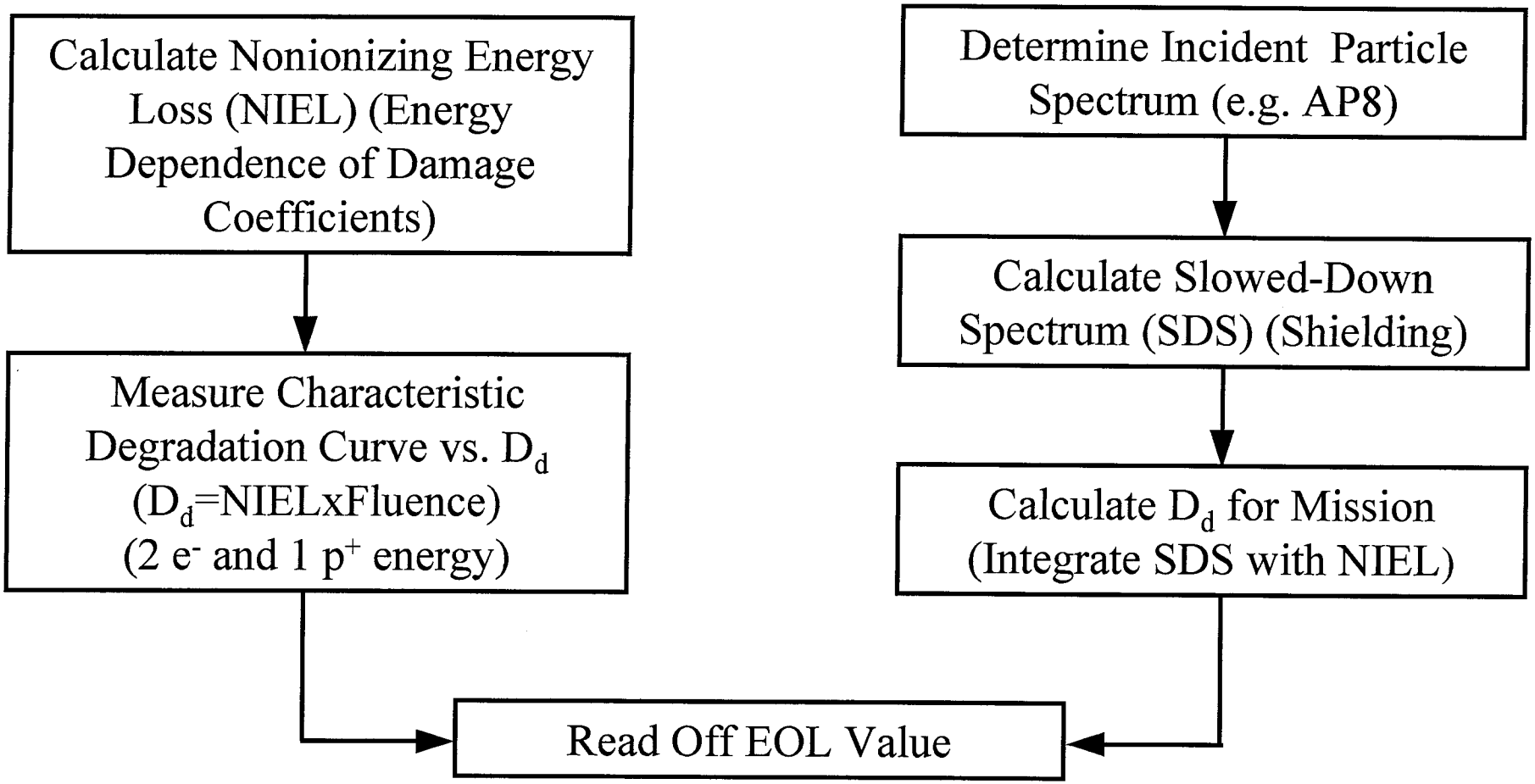

NRL Displacement Damage Dose Method

Incident and Slowed-Down Spectrum (Isotropic)

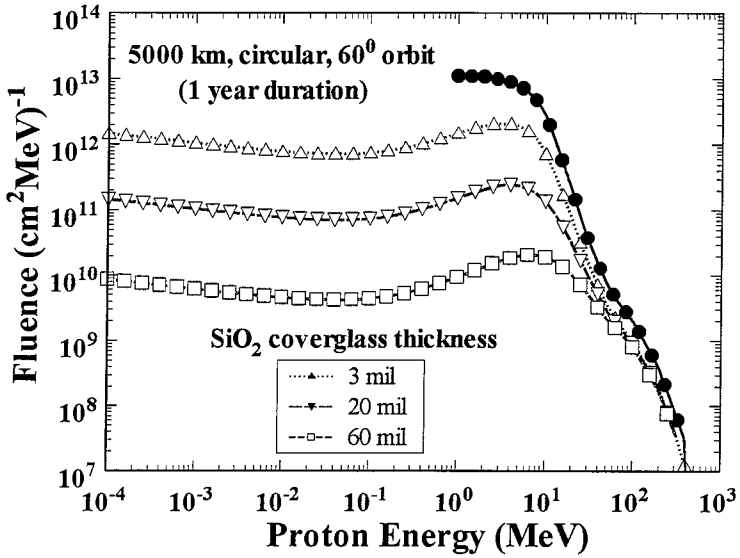

NonIonizing Energy Loss (Damage Coefficients)

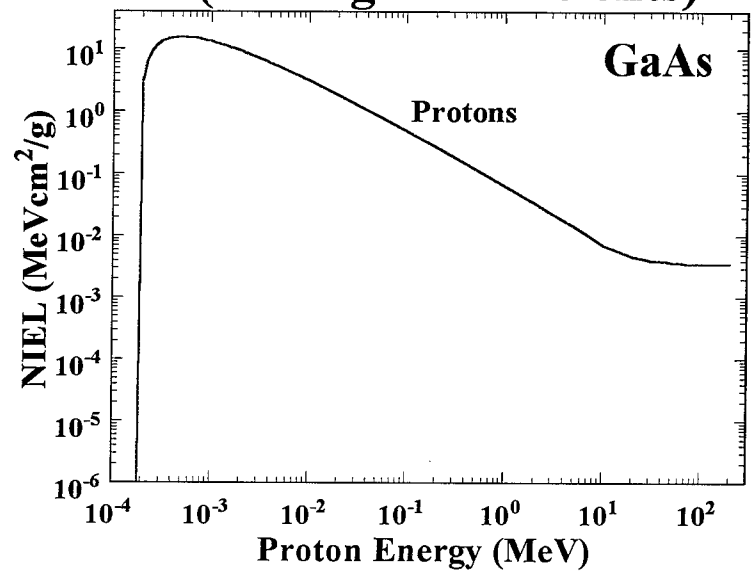

Total Mission Dose

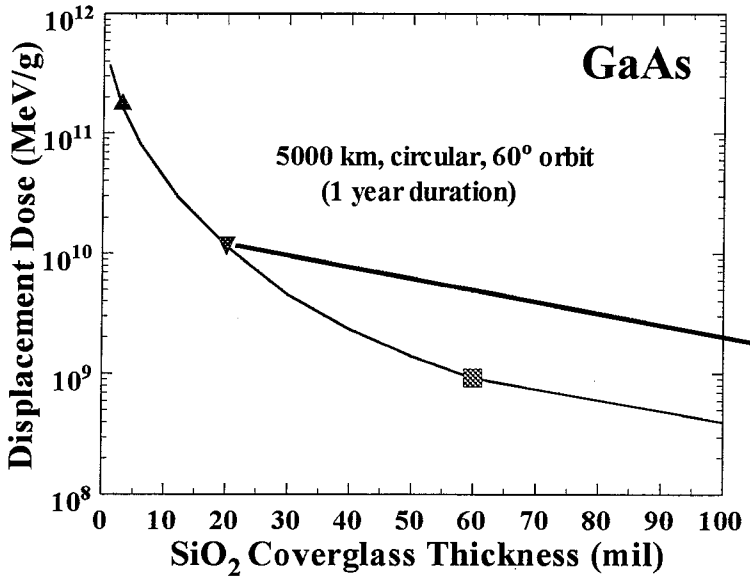

P_{max} Degradation

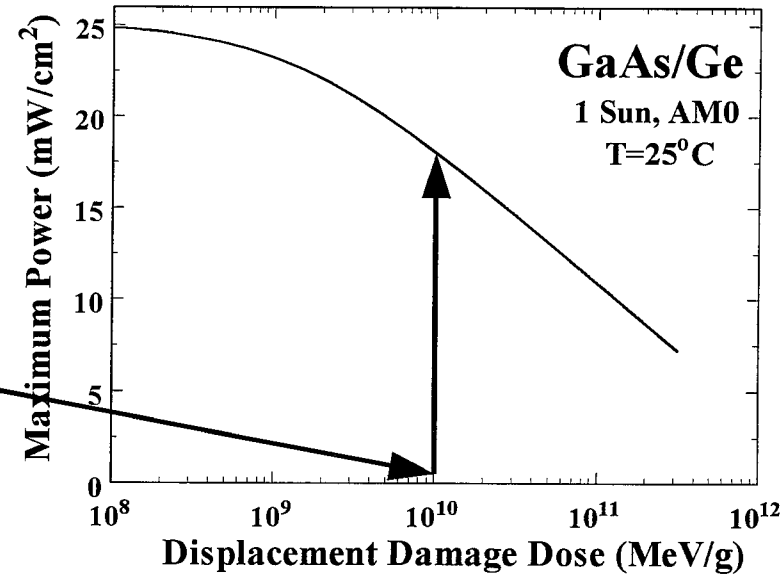

Modeling Solar Cell Degradation in Space

Comparison of Results

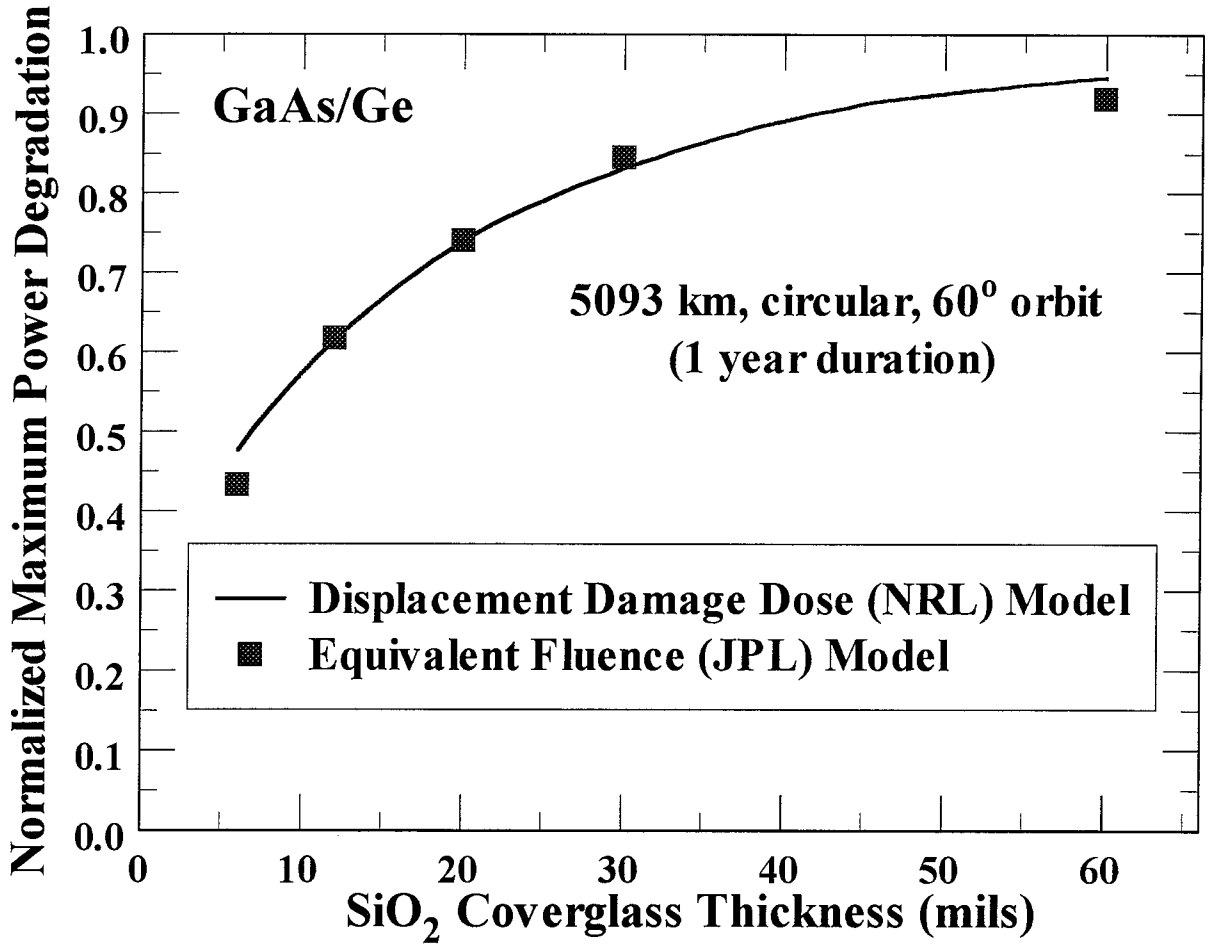

Modeling Solar Cell Degradation in Space

Issues

- **Electron transport through materials**
  - **Straggling**
  - **Backscatter**
- **Cells with thick active regions**
  - **Silicon**
- **Multi-junction cells**
  - **Calculation of damage coefficients**

C.Signorini

SPRAT 1999
Cleveland, Aug. 31 - Sept. 2

ESA
SOLAR GENERATOR TECHNOLOGY PROGRAMME

1 R. & D.

- Cell technology
- Assembly technology
- System studies & array development
- Testing & characterisation
- Flight experiments

2 Solar Arrays for ESA missions

R. & D. : Cell technology

Three main fields of activities:

- **High performances;**
- **Low cost;**
- **Qualification / pilot line / industrialisation**

R. & D. : CELL TECHNOLOGY / high performance

	Activity:	Status:	Details:
*	NEXT GENERATION GERMANIUM WAFERS	Running @ U.M.(B)	Advanced Substrates for Cascade Solar Cells
*	GaAs/Ge SOLAR CELLS BY MBE	Running @ TUT (Fin)	Pre-Development of MBE-based Cascade Cells on Ge
*	CASCADE SOLAR CELLS	Running @ OG(I)/ENEL(I)/ENE(B) and @ DSS(D)/ASE(D)/TUT(Fin)	MBE / MOCVD / on GE substrates
*	ULTRATHIN CASCADE CELLS	Running @ DSS (D)&ASE(D)	Superstrate Dual-junction cells without Substrate

esa European Space Agency	SOLAR GENERATOR TECHNOLOGY PROGRAMME	SPRAT 1999 # 4

R. & D. : CELL TECHNOLOGY / low cost

	Activity:	Status:	Details:
*	THIN FILMS & ULTRATHIN SOLAR CELLS	Running @ DSS(D) / IPE(D) / ASE (D)	Pre-development of Si-and CIS-Solar Cells for MEO

R. & D. : CELL TECHNOLOGY / industrialisation

	Activity:	Status:	Details:
*	PILOT LINE HI-ETA SILICON CELLS	Completed @DSS(D)/ASE(D)	EOL High Efficiency
*	PILOT LINE & QUALIFICATION OF CASCADE SOLAR CELLS	Start in 2000	

	SOLAR GENERATOR TECHNOLOGY PROGRAMME	SPRAT 1999 # 5

R. & D. : ASSEMBLY TECHNOLOGY

Activity:	Status:	Details:
* UV & IR REFLECTING COATING	Running @ PST(UK)	Reduction of operating temperature by reflector on cover-glass
* CMO-COVER GLASS	Running @ PST(UK)	Cover glass development for high radiation missions
* ASSEMBLY& INTEGR. OF ADVANCED GaAs CELLS	New proposals	
* HIHT SOLAR CELLS FOR MISSIONS NEAR THE SUN	Start in 2000	SCA's development for High Intensity High Temperature applications

	SOLAR GENERATOR TECHNOLOGY PROGRAMME	SPRAT 1999 # 6

R. & D. : SYSTEM STUDIES AND ARRAY DEVELOPMENT

	Activity:	Status:	Details:
*	CONCENTRATOR ARRAY EVALUATION	Running @ Joffe Inst. (Russia) and ISE (D)	Assess the current potential (small contracts)
*	ADVANCED RIGID PANEL ARRAYS	Running @ FSS(NL)	ARAFOM 5-panel / 15 kW array development
*	20 kW TELECOM. ARRAY	Running @ Alcatel (F)	Development of AS SOLARBUS 10-panel / 18-25 kW array development
*	FRED	Running @ FSS (NL)	Solar array generic design for ATV and Constellations

R. & D. : TESTING & CHARACTERISATION

- **Test methods and instruments**

Activity:	Status:	Details:
* LAPPS	New proposal	Flasher upgrading
* CASCADE CELL CHARACTERISATION	Running @ FHG-ISE(D)	New test methods

esa European Space Agency	SOLAR GENERATOR TECHNOLOGY PROGRAMME	SPRAT 1999 # 8

R. & D. : TESTING & CHARACTERISATION

- **Qualification and testing**

	Activity:	Status:	Details:
*	SPASOLAB	Running @ INTA(E)	Type approval tests (PSS-01-604)
*	p^+ AND e^- RADIATION	Running	p+ & e- tests of new cells
*	S-A ENVIRONMENTAL INTERACTIONS	Running @ DESP(F)	Failure Modes due to: micrometheorides/protons/atox/ESD
*	ADVANCED SOLAR CELLS ELECRICAL CHARACTERISATION	New proposal	Database: reverse characteristic and dynamic behaviour

R. & D. : FLIGHT EXPERIMENTS

	ACTIVITY:	Status:	Details:
*	EQUATOR -S SOLAR CELL EXPERIMENT	@ Max Plank Inst. (D)	Flight evaluation of new solar cells (CIS, UTGaAs, Cascade
*	IN-ORBIT DEMO CASCADE CELLS	Started @ TUT(Fin)	Supply of Cascade cells for flight experiment
*	HST SOLAR ARRAY POST FLIGHT INVESTIGATION	Future activity Start in 2001	

SOLAR ARRAYS FOR ESA MISSIONS

Mission	Solar Array
• ROSETTA Interplanetary mission 11 y. life time	ARAFOM, 10 panels, 64 sqm, HI-ETA LILT Si solar cells. EOL power at 5.2AU = 405 W
• CLUSTER II 4 satellites, 2.5 y. life time Highly eccentric polar orbit	6 curved body-mounted solar panels, BSR Si solar cells, EOL power = 240 W
• XMM & INTEGRAL Highly elliptical orbit, 10 y. life	Foldable rigid array, 6 panels, BSR Si cells, EOL power = 1.6 kW
• MARS EXPRESS Orbiter & Lander	TBD, possible use of LILT cells (Si or GaAs)
• SMART 1 Technology mission to Moon	TBD, GaAs SJ and MJ candidates.

SOLAR ARRAYS FOR ESA MISSIONS

Mission	Solar Array
• MERCURY	Tilted array, GaAs solar cells, 10kW at 1AU.
• ENVISAT Polar orbit, 4 y. life time	Deployable single wing, 14 panels, 70 sqm, BSR Si solar cells, EOL power = 6.4 kW
• METOP 5 y life time	Like ENVISAT, but 8 panels, EOL power = 3.9 kW
• MSG Spinning, 10 y. life time	8 rigid curved panels, HI-ETA Si solar cells, EOL power = 675W
• ATV	4 wings, 3 panels each, HI-ETA Si solar cells

CONCLUSIONS

- **The ESA solar generator R & D program, in spite of the modest funding (less than 3 M Euro / year, including applications and national support), meets the requirements of the European satellites.**

- **The need for new generation solar cells (both cascade and thin film) is not yet evident in the frame of the ESA operational programs.**

EFFECT OF STOICHIOMETRY ON THE RADIATION RESPONSE OF $In_xGa_{1-x}As$ SOLAR CELLS

S. R. Messenger
SFA, Inc, Largo, MD 20774, USA

R. J. Walters and G. P. Summers
Naval Research Laboratory, Washington, DC 20375, USA

R. H. Hoffman, Jr., and M. A. Stan
Essential Research Inc., Cleveland, OH 44122 USA

INTRODUCTION

Several types of multi-junction (MJ) solar cells contain subcells made from ternary materials produced by the addition of indium and/or phosphorus to GaAs. The addition of indium tends to reduce the radiation response of GaAs cells, whereas the converse is true for phosphorus. Since the softer subcell usually determines the overall response of an MJ cell, it is important to examine exactly how quickly the addition of indium reduces the response of GaAs cells. We are concerned here primarily with the effect of proton irradiation on the n/p $In_{0.22}Ga_{0.78}As$ (E_g=1.1 eV) solar cell fabricated by Essential Research, Inc. (ERI) [1]. This cell was designed to be the bottom cell of a high efficiency (>30%) InGaP(1.75eV)/InGaAs(1.1eV) MJ cell on a Ge substrate. We will compare these proton radiation results with those for an n/p $In_{0.53}Ga_{0.47}As$ (E_g=0.75 eV) solar cell fabricated by Research Triangle Institute (RTI), as well as with the single junction p/n GaAs/Ge solar cells. The RTI InGaAs cell, being lattice-matched with InP, was the choice for the bottom cell of an InP/InGaAs MJ combination.

CELL DESCRIPTIONS

Table 1 shows the relevant structural parameters of the three technologies considered. More detailed descriptions regarding the 0.75 eV InGaAs, the 1.1 eV InGaAs, and the GaAs cell technologies can be found in references [2], [1], and [3], respectively. Also, the AM0, 1 sun, solar cell efficiencies at 25°C of the three technologies prior to irradiation were 4.5%, 16%, and 18%, respectively. The reason for the differing efficiencies lies in the window layer. The 0.75 eV InGaAs cell had a 3 micron InP window layer to simulate the existence of the InP top cell in the MJ configuration. This InP window layer, having a very high absorption coefficient, filtered the light substantially, thereby reducing the amount of light with λ<900 nm incident on the InGaAs cell. An example calculation shows that, at 800 nm, only 2% of the light remains after 3 microns of InP. Window layer absorption was not a significant factor in the other two technologies considered.

Table 1. Relevant structures of $In_xGa_{1-x}As$ samples studied

	$In_{0.53}Ga_{0.47}As$(0.75 eV)	**$In_{0.22}Ga_{0.78}As$(1.1 eV)**	**GaAs(1.42 eV)**
Window Layer	**n-InP**	**n^+-$In_{0.68}Ga_{0.32}P$**	**P^+-$Al_{0.85}Ga_{0.15}As$**
Doping (cm^{-3})	10^{17}	$3x10^{18}$	$2x10^{18}$
Thickness (μm)	3	0.05	0.05
Emitter	**n^+**	**n^+**	**p^+**
Doping (cm^{-3})	10^{18}	$2x10^{18}$	$2\text{-}4x10^{18}$
Thickness (μm)	0.125	0.5	0.5
Base	**p**	**p**	**n**
Doping (cm^{-3})	$2x10^{17}$	$2x10^{17}$	$2x10^{17}$
Thickness (μm)	5	3	2-3

Another important consideration in these three samples is the fact that the base doping concentrations are all at the same level of $2x10^{17}$ cm^{-3}. It has been shown in other studies of many different technologies [4-6] that the radiation response is strongly controlled by the base dopant concentration. For $In_{0.53}Ga_{0.47}As$ [4], InP [5], and GaAs [6], similar trends exist in that the radiation degradation of the short circuit current increases with base dopant concentration, while the opposite

occurs for that of the open circuit voltage. The results for the solar cell efficiencies are approximately independent of the base doping concentration due to the above competing effects. These effects have also been observed in $In_{0.53}Ga_{0.47}As$. In addition, they have been shown to be independent of cell polarity [4].

RESULTS

Irradiations of the ERI $In_{0.22}Ga_{0.78}As$ cell using 2 and 4.5 MeV protons were performed at the Naval Surface Warfare Center in White Oak, MD. The dosimetry was accurate to within 15%. Figure 1 shows the proton degradation results for I_{sc}, V_{oc}, and P_{max} (AM0, 1 sun, 25°C solar illumination conditions) plotted as a function of displacement damage dose, D_d [8]. This kind of plot produces a single characteristic degradation curve for each parameter so that a comparison of the absolute radiation tolerance of the different cells can be made. The absolute values are plotted in Figure 1.

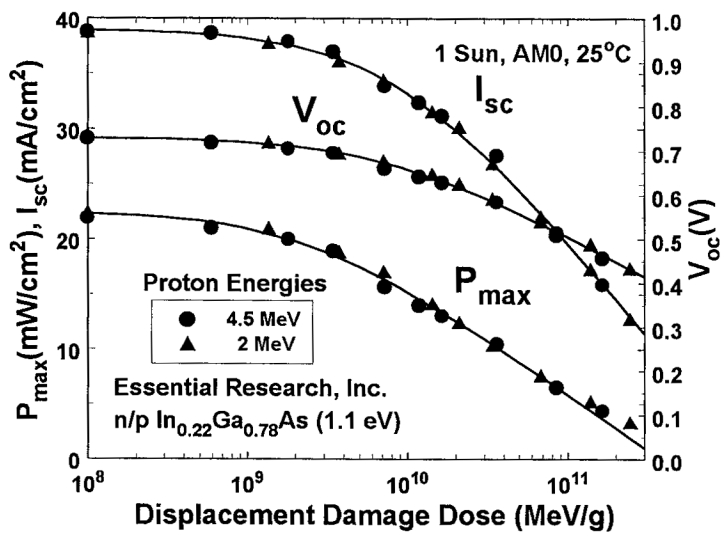

Figure 1. Radiation degradation of the photovoltaic parameters of the Essential Research, Inc. 1.1 eV n/p $In_{0.22}Ga_{0.78}As$ solar cell. The degradation is presented in terms of displacement damage dose. The lines are fits to the data.

Radiation results from the other cell technologies were presented elsewhere ([3], [7], and [8]). Figure 2 shows a comparison of the three technologies as a function of displacement damage dose, for the case of the solar cell maximum power. In this plot, normalized values are used in the comparison due to the large differences in starting efficiencies. The lines in Figure 2 were all determined from extensive data fits using several particle energies. As expected, there appears to be an overall trend in reduced radiation tolerance as the concentration of indium in the cell is increased, although the 1.1 eV InGaAs and the GaAs cell show a similar response over a significant range. For reference, the D_d equivalent to a one year mission in the heart of the earth's proton belts (5093 km, circular, 60°) is shown. The radiation response of both the $In_{0.22}Ga_{0.78}As$ and GaAs technologies are seen to be essentially equal up to that level.

Figures 3 and 4 show the same comparisons for the cases of I_{sc} and V_{oc}, respectively. Whereas no clear trend exists in the I_{sc} data, there is a reduction in the radiation tolerance in V_{oc} as the indium concentration is increased. The 1.1 eV cell is seen to give the best V_{oc} response out to a D_d value of 10^{10} MeV/g, after which the GaAs cell outperforms the rest.

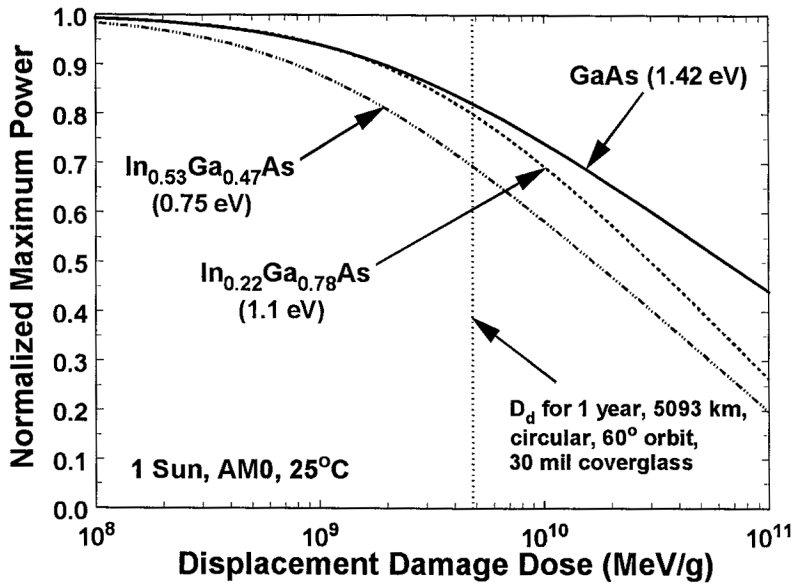

Figure 2. Comparison of the P_{max} (1 sun, AM0, 25°C) degradation curves for $In_xGa_{1-x}As$ solar cells, for x = 0, 0.22 and 0.53. Note that the initial efficiencies of the cells were ~18%, ~16% and ~4.5%, respectively (Table I). The effect of adding indium to GaAs is shown to decrease the overall radiation resistance of P_{max}. However, the response of the $In_{0.22}Ga_{0.78}As$ cell is seen to be equivalent to GaAs up to a relatively high D_d value, equivalent to a rather severe earth orbit.

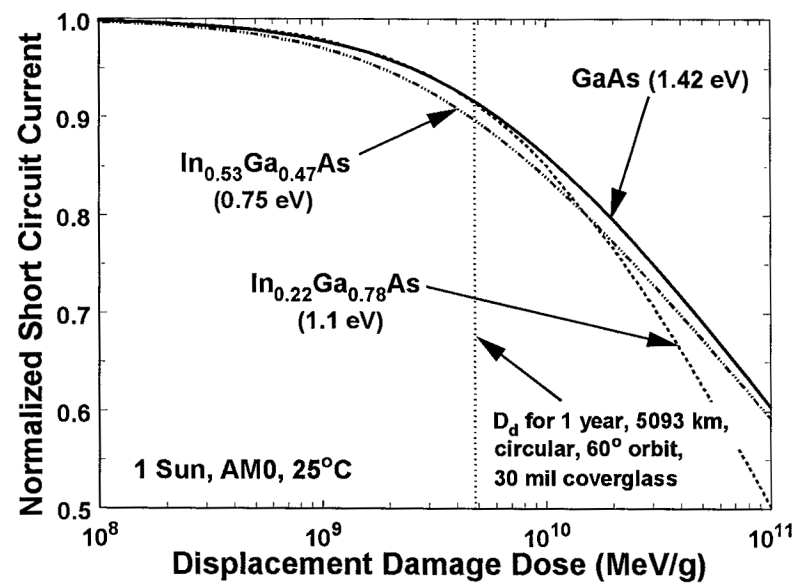

Figure 3. Comparison of the I_{sc} (1 sun, AM0, 25°C) degradation curves for $In_xGa_{1-x}As$ solar cells, for x = 0, 0.22 and 0.53.

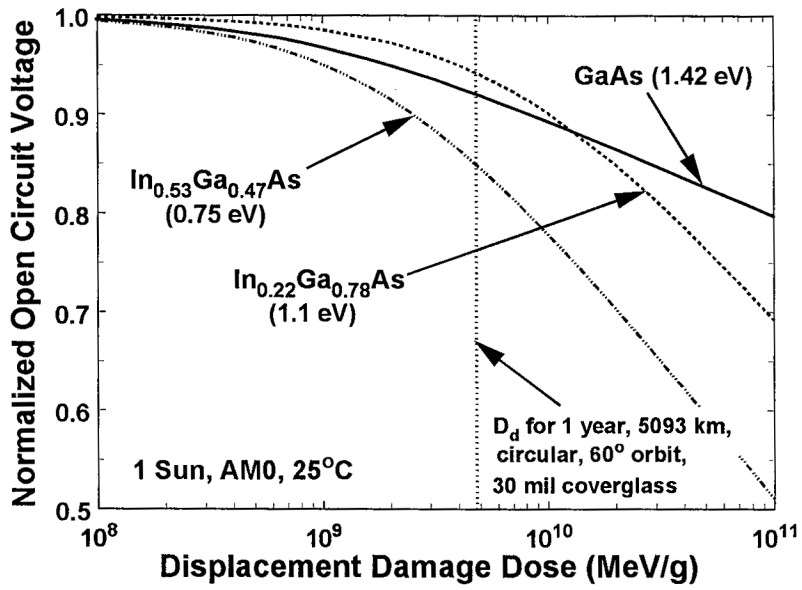

Figure 4. Comparison of the normalized V_{oc} (1 sun, AM0, 25°C) degradation curves for $In_xGa_{1-x}As$ solar cells, for x = 0, 0.22 and 0.53.

SUMMARY

The effect of adding increasing concentrations of indium to GaAs solar cells of has been shown to decrease the radiation tolerance of both P_{max} and V_{oc}. The case for I_{sc} is not as clear. The radiation response of the ERI $In_{0.22}Ga_{0.78}As$ (1.1 eV) cell has been presented here for the first time. The response of that cell, while suffering somewhat due to the higher indium content, was shown to be essentially equivalent to that of GaAs up to very high irradiation levels.

REFERENCES

[1] R.H. Hoffman, Jr. et al., 2nd IEEE World Conference and Exhibition on Photovoltaic Solar Energy Conversion, July, 1998, Vienna, Austria, p. 3604.

[2] R.J. Walters, G.J. Shaw, G.P. Summers, and S.R. Messenger, 5th IEEE International Conference on InP and Related Materials, April, 1993, Paris, France, p. 68.

[3] B.E. Anspaugh, 22nd IEEE Photovoltaic Specialists Conference, October, 1991, Las Vegas, NE, p.1593.

[4] S.R. Messenger, R.J. Walters, H.L. Cotal, and G.P. Summers, 6th IEEE International Conference on InP and Related Materials, March, 1994, Santa Barbara, CA, p. 504.

[5] C.J. Keavney, R.J. Walters, and P.J. Drevinsky, J. Appl. Physics 63, 5555 (1988).

[6] K.A. Bertness, B.T. Cavicchi, S.R. Kurtz, J.M. Olsen, A.E. Kibbler, and C. Kramer, 22nd IEEE Photovoltaic Specialists Conference, October, 1991, Las Vegas, NE, p.1582.

[7] S.R. Messenger, H.L. Cotal, R.J. Walters, and G.P. Summers, 14th Space Photovoltaic Research and Technology Conference, October, 1995, Cleveland, OH, p. 100.

[8] S.R. Messenger, H.L. Cotal, R.J. Walters, and G.P. Summers, 8th IEEE International Conference on InP and Related Materials, April, 1996, Schwäbisch Gmünd, Germany, p. 279.

Analysis of the role of deep levels in anomalous degradation of Si space solar cells

Aurangzeb Khan, Masafumi Yamaguchi and Stephen J. Taylor,

Toyota Technological Institute, 2-12-1 Hisakata, Tempaku, Nagoya 468-8511, Japan.

Correspondence to: Aurangzeb Khan Tel/Fax. +81-52-809-1877, **e-mail**: a.khan@toyota-ti.ac.jp

Over the past 30 years, many works have been done to investigate the origin of the radiation-induced defects in Si and space cells. However, anomalous degradation of Si space cells under high fluence irradiation stimulates further studies on radiation-induced defects that play the dominant role in type conversion (carrier removal) in Si as well as the origin of some major defects.

In this study, deep level transient spectroscopy (DLTS) analysis of defects in p-type Si has been carried out for n^+-p-p^+ Si space cells irradiated with heavy fluence of 1-MeV electrons and 10-MeV protons, in order to clarify mechanism on anomalous degradation of Si cells and origins of radiation-induced defects in Si.

We are able to correlate degradation of the minority carrier diffusion length L determined by solar cell properties and introduction of deep levels determined by DLTS. The E_V + 0.36eV majority carrier trap center correlates with degradation of minority-carrier diffusion length in p-Si base layer of the Si cells and thus is thought to act as a recombination center. Some of the interesting new information provided by our work is that type conversion of the base layer, is mainly due to a large concentration of a new electron trap (E_c - 0. 71eV) in type converted Si and a deep donor center (E_c – 0.2eV) in p-Si. The introduction rate of the (E_c - 0. 71eV) center is roughly consistent with the 0.36 eV center in the p type samples. The production of this level switch on the sample from p type to n-type and transformation/annealing of this level recovered the sample to p-type with the evolution of the E_V+0.36 eV level. These suggest that the (E_c - 0. 71eV) trap responsible might be related to interstitial-carbon and interstitial-oxygen complex. The recovery of the free carrier concentration after annealing occurs roughly also at the same temperature as disappearance of main defects (Ec-0.71eV) and (E_C-0.20eV). The significant recovery of power output of 2 x 2 cm^2 solar cell irradiated with 1 x 10^{14} protons/cm^2 at each step of the annealing also correlate the carrier removal and annealing of electrons traps. These results suggest that the minority carrier level (E_C-0.20eV) in p-type and majority level (E_C-0.71eV) in type-converted samples play a dominant role in carrier removal.

The radiation-induced traps, which play an important role regarding the carrier removal and conduction type conversion of the base region, are thought to be principally deep-level donors, which are positively charged before electron capture, leading to the compensation of the base layer of the cells. The irradiation not only changes the structure of the device (from p to n-type) but also makes the complex defect structure as compare to simple defect structure in low dose samples.

RADIATION HARD MULTI-QUANTUM WELL InP/InAsP SOLAR CELLS FOR SPACE APPLICATIONS

R.J. Walters and G.P. Summers
U.S. Naval Research Laboratory, Washington, DC 20375, USA

S.R. Messenger
SFA, Inc., Largo, MD , USA

A. Freundlich, C. Monier, F. Newman
University of Houston, Houston, TX , USA

INTRODUCTION

The U.S Naval Research Laboratory (NRL) and the University of Houston (UH) are conducting a collaborative research effort studying InP/InAsP multi-quantum well (MQW) solar cells [1]. The goal of this research is to demonstrate a high-efficiency InP solar cell, grown heteroepitaxially on a Si substrate. This technology is of interest because it is expected to show the extreme radiation resistance of InP combined with the durability and cost-effectiveness of Si. However, it is well known that a high-quality InP/Si device is difficult to realize due to the lattice mismatch between InP and Si. For this reason, MQW layers have been incorporated into the InP/Si cell. The MQW layers increase the spectral range of the cell response thereby increasing the photocurrent and allowing for a thinner cell. The MQW cell should, therefore, be able to operate efficiently despite the reduced minority carrier diffusion length of an InP/Si cell. Furthermore, a MQW cell should provide advantages in a multi-junction cell (i.e. InP/InGaAs/Si) in terms of overall efficiency and end-of-life current-matching.

While the MQW layers offer the potential for increased photocurrent, they also can lead to an increase in dark current and hence reduced operating voltage. The technical challenge is, then, to balance these effects to achieve a cell with improved efficiency. Furthermore, the radiation response mechanisms of the MQW cell must be understood in order to simultaneously optimize the beginning-of-life (BOL) and end-of-life (EOL) device performance.

In this paper, the latest results of this research are presented. MQW cells with varied structured have been fabricated and radiation tested to determine the effect of cell structure on the BOL and EOL performance and to determine the optimum structure for a MQW InP/Si cell for use in space.

CELL DESCRIPTION

The solar cells studied here are p^+-i-n structures where the i-region consists of a 10 period MQW structure fabricated with alternating layers of InP and $In_xAs_{1-x}P$ (Fig. 1). Details of the fabrication of these cells have been described previously [2]. Several cell structures were studied in which the thickness of the cell base and the QW region were varied. A control cell was included, in which no QWs were grown. In addition, the As concentration in the QW layers was varied in order to control the absorption edge of the QW region as characterized by the photoluminescence (PL) peak energy. The cell structures are summarized in Table I. The cells had no anti-reflective coatings, so the cell output was lower than would be measured in an optimized cell.

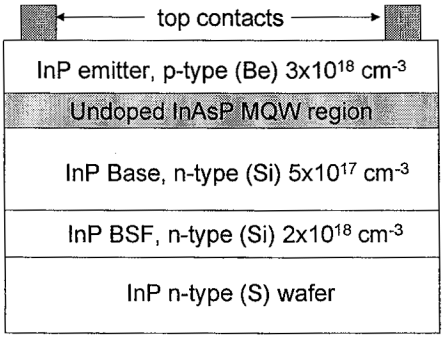

Fig. 1: Schematic drawing of the MQW cells. Details are given in Table I.

Table 1: Structure of the MQW solar cells. The QWs are a 10 period structure. The well and barrier thicknesses are given in monolayers equal to half of the InP lattice constant (ML ~ 3 Å). The As column gives the As atomic concentration in the well. The energy of the photoluminescence (PL) peak indicates the absorption edge of the well.

Cell ID#	Base Thickness (μm)	Emitter Thickness (μm)	As Atomic Fraction	Well Thickness (ML)	Barrier Thickness (ML)	(2K) PL (eV)
Control	1.56	0.114	0	0	0	-
680	0.23	0.107	0.44	6-7	75	1.17
711	1.00	0.080	0.65	3-4	106	1.21
712	1.00	0.080	0.44	8	106	1.15

AS GROWN CELL PERFORMANCE

The spectral response of a MQW cell (#712, Table I) is compared to the control cell in Fig. 2. The effects of the MQW region are clearly evident. The absorption edge of the MQW cell is extended beyond the InP band gap to nearly 1200 nm. In addition, the response of the MQW cell is better than the control cell at all wavelengths despite the significantly thinner base in the MQW cell (Table I).

Concentrating on the higher wavelength "tail" of the spectral response curves allows an investigation of the effect of varying the QW structure (Fig. 3). Comparison of the response of cell #680 with that of #711 shows that a thicker QW region results in a moderate increase in response. A more dramatic increase is observed with a decrease in the absorption edge as evidenced by the response of cell #712. These results suggest a thicker MQW region with a low absorption edge will provide maximum response at wavelengths above the InP band edge.

Analysis of the full spectral response of the MQW cells enables an investigation of the effect of varying the base thickness on the cell performance (Fig. 4). As noted above (Fig. 2), cell #712 shows the best response despite having a base only 1 μm thick. Given the absorption coefficient of InP, a 1 μm base is only expected to absorb about 95% of the incident light, but the increased absorption in the MQW layers offsets the reduced response. The response of cell #680 demonstrates the effect further reducing the base thickness. That cell clearly suffers from a poor red response which results in an overall reduction in photocurrent (Table II). The present data set suggests that the minimum base thickness for optimum photocurrent is ~ 1 μm [1].

The MQW layer, while enhancing the photocurrent, tends to increase the junction forward-bias dark current thereby reducing the photovoltage. The dark current of the MQW cells is shown in Fig. 5. As expected,

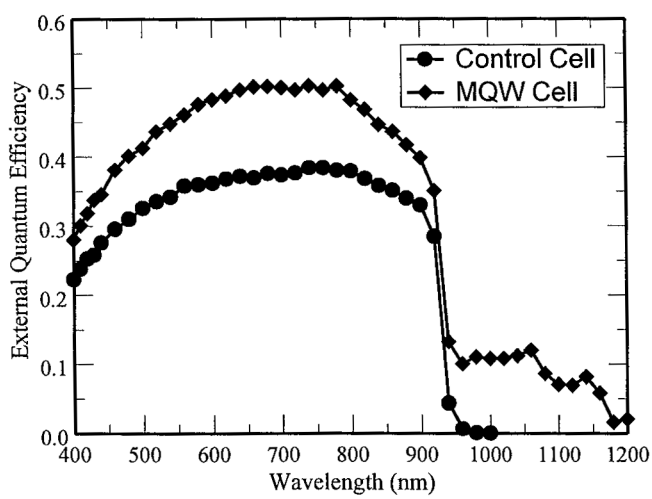

Fig. 2: Comparison of the spectral response of a MQW cell (#712, Table I) and a standard InP cell. The major effect of the QWs is to extend the cell response to wavelengths beyond the InP band gap.

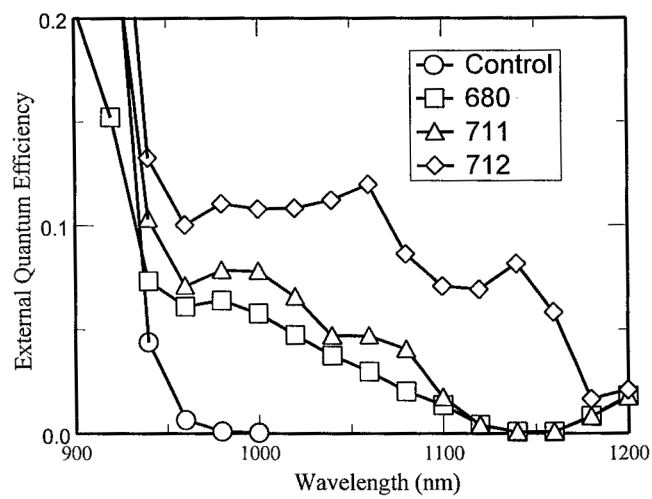

Fig. 3: Expansion of the spectral response curves to highlight the "tail" generated by the QWs. The realatively thicker well and lower absorption edge in cell #712 (Table I) result in the best response.

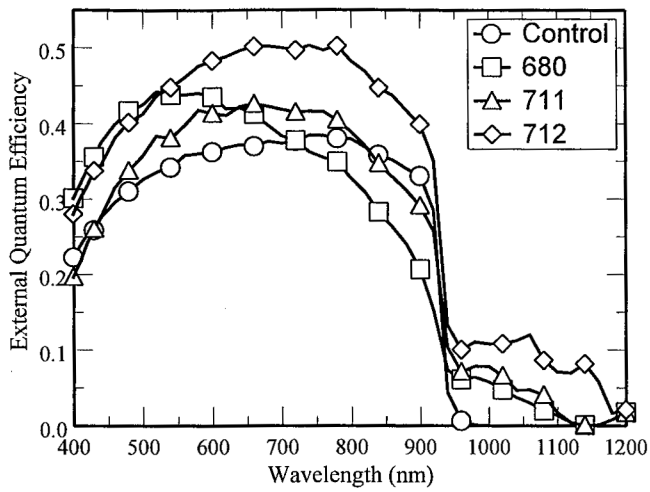

Fig: 4: Comparison of the spectral response of the MQW and the control cell (Table I). Cell #680 shows poor red response due to a very thin base. Both MQW cells #711 and 712 show improved response over the control cell.

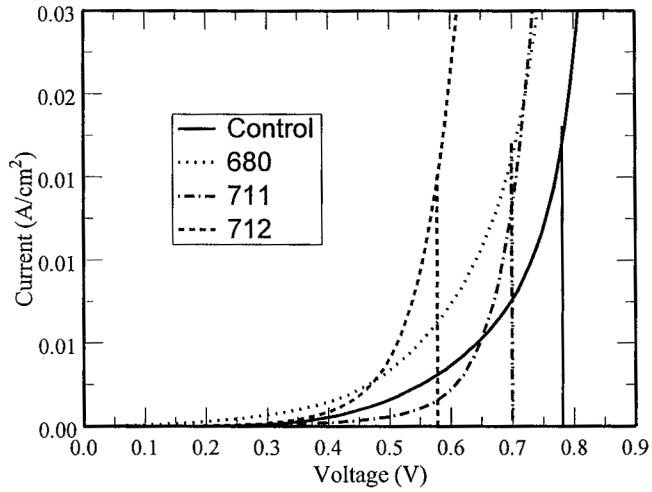

Fig. 5: Forward bias dark current curves measured before irradiation. The vertical lines indicate the open circuit voltage (V_{oc}) for each cell (Table II). The cells with more QW response have a larger dark current and lower V_{oc}.

the cell with the maximum QW response, i.e. #712, is seen to have the largest dark current, and, therefore, the lowest open circuit voltage (V_{oc}) (Table II). The control cell, with no QW region, cell displays the largest V_{oc}.

Considering the maximum power output (P_{max}) as a measure, the cell with the best overall performance is #711 (Table II). That cell combines a 1 μm thick base with a relatively thick QW region to achieve a good photocurrent (Fig. 4). At the same time, the somewhat higher QW band edge of 1.21 eV serves to somewhat mitigate the impact on V_{oc}. This results in a cell with a power output ~ 13% greater than the InP control cell.

Table 2: Photovoltaic parameters measured in the MQW and control cells prior to irradiation

Cell	I_{sc} (mA/cm^2)	V_{oc} (V)	P_{max} (mW/cm^2)
Control	18.0	0.781	8.58
680	18.4	0.700	7.40
711	***20.8***	***0.700***	***9.68***
712	22.0	0.578	8.04

MQW CELL RADIATION RESPONSE

The effects of 3 MeV proton irradiation on the long wavelength response of the MQW cells are shown in Fig. 6. The irradiation caused only minor degradation of the QW response. The effects of the proton irradiation on the photovoltaic response of the MQW cells are summarized in Fig. 7. In general, the MQW cells are seen to display good radiation tolerance so that increased photoresponse afforded by the QW region over that of the control cell is maintained throughout the fluence range studied.

The short circuit current (I_{sc}) degrades more rapidly in MQW cell #680 than in MQW cell #712, which is an unexpected result since cell #680 had the lowest BOL I_{sc} value, while cell #712 had the highest. Indeed, there appears to be a trend in the data such that the I_{sc} degradation rate increases as the BOL value decreases. Analysis of the spectral response curves, however, showed an opposite trend for the degradation of the base diffusion length (L_p). The L_p degradation rate

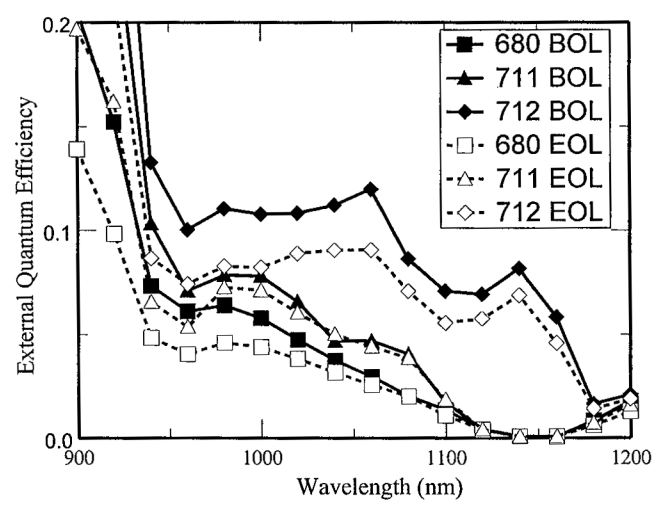

Fig. 6: Effect of 3 irradiation on the QW spectral response. EOL refers to measurements after 3 MeV proton irradiation up to 4×10^{13} cm^{-2}. The irradiation caused only a small amount of degradation to the cell response in this wavelength range.

increased as the BOL L_p (and, hence, I_{sc}) value increased. This can be partly explained by the fact that the QW response has been shown to be relatively immune to irradiation (Fig. 6), so the photocurrent of cells with larger QW response (like cell #712) should be less sensitive to base diffusion length degradation. In addition, a larger fraction of the photocurrent of cells with less QW response comes from the emitter, and the spectral response analysis showed the emitter diffusion length to degrade rapidly in those cells. This is especially true for cell #680 since the exceedingly thin base results in nearly 50% of the photocurrent being generated in the emitter.

In the case of V_{oc}, the rate of degradation with increasing fluence is nearly the same for all of the cells, including the control cell. The one exception is cell #712, where the degradation rate is less. This is the case because the dark current in that cell is already large before irradiation, so the irradiation has little effect on it. This lack of degradation in I_{sc} and V_{oc} helps to maintain the power output of cell #712 above the other cells after irradiation. However, the total fluence has to be rather high before this effect becomes evident.

SUMMARY

The present results demonstrate that the addition of MQWs to an InP solar cell can result in improved photovoltaic response. The results showed that the base could be as thin as 1 μm and still achieve good photocurrent provided the QW region is thick enough. Reducing the base thickness further results in a loss of red response and degradation of device performance. Furthermore, the absorption edge of the QWs must be maintained sufficiently high (~ 1.21 eV) in order to mitigate the effects of the dark current increase on V_{oc}. The radiation response of the MQW cells was shown to be equal to or greater than that of the control cell so that the enhanced response afforded by the QWs is maintained under irradiation. Preliminary analysis indicates that the response of the MQW cells is less sensitive to minority carrier diffusion length degradation than standard InP cells. This suggests that the incorporation of QWs into an InP/Si cell should result in improved performance both before and after irradiation.

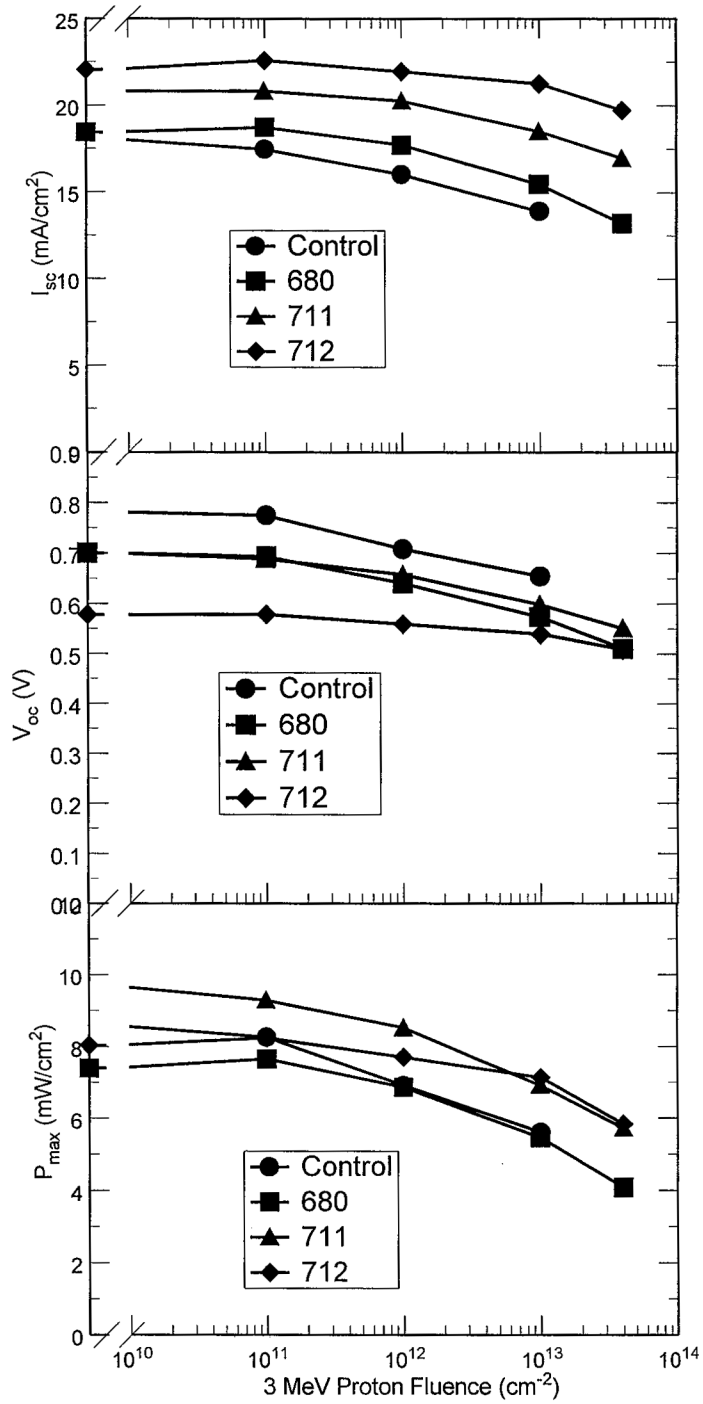

Fig. 7: Radiation-induced degradation of the PV response of the MQW and control cells. Even after irradiation, the MQW cells show improved performance over the control cell. The fact that I_{sc} degrades less rapidly in the cells with better QW response (cells #711 and 712) indicates that the MQW cells are less sensitive to diffusion length degradation.

REFERENCES

[1] R. J. Walters, G. P. Summers, S. R. Messenger, A. Freundlich, C. Monier, and M. Vilela, IEEE Second World Conference on Photovoltaic Energy Conversion, Vienna, Austria (1998), p. 1886.

[2] A. Freundlich, V. Rossignol, M.F. Vilela, P. Renaud, Proc. IEEE First World Conference on Photovoltaic Energy Conversion, Wiakola Hawaii (1994) 1886.

Use Of Displacement Damage Dose in an Engineering Model of GaAs Solar Cell Radiation Damage

T.L. Morton[1], R. Chock[2], K.J. Long[2], S. Bailey[2], S.R. Messenger[3], R.J. Walters[4], and G.P. Summers[4,5]

[1]Ohio Aerospace Institute, Brook Park, OH 44142, USA
[2]NASA Glenn Research Center, Cleveland, OH 44135, USA
[3]SFA Inc., Largo, MD 20774, USA
[4]Naval Research Laboratory, Washington, DC 20375, USA
[5]University of Maryland Baltimore County, Baltimore, MD 21250, USA

Introduction

Current methods for calculating damage to solar cells are well documented in the GaAs Solar Cell Radiation Handbook (JPL 96-9). An alternative, the displacement damage dose (D_d) method, has been developed by Summers, et al. This method is currently being implemented in the SAVANT computer program.

Description of Model

As illustrated in Figure 1, measured radiation damage when multiplied by non-ionizing energy loss (NIEL) leads to a single characteristic curve for all electron and proton energies.

Figure 1

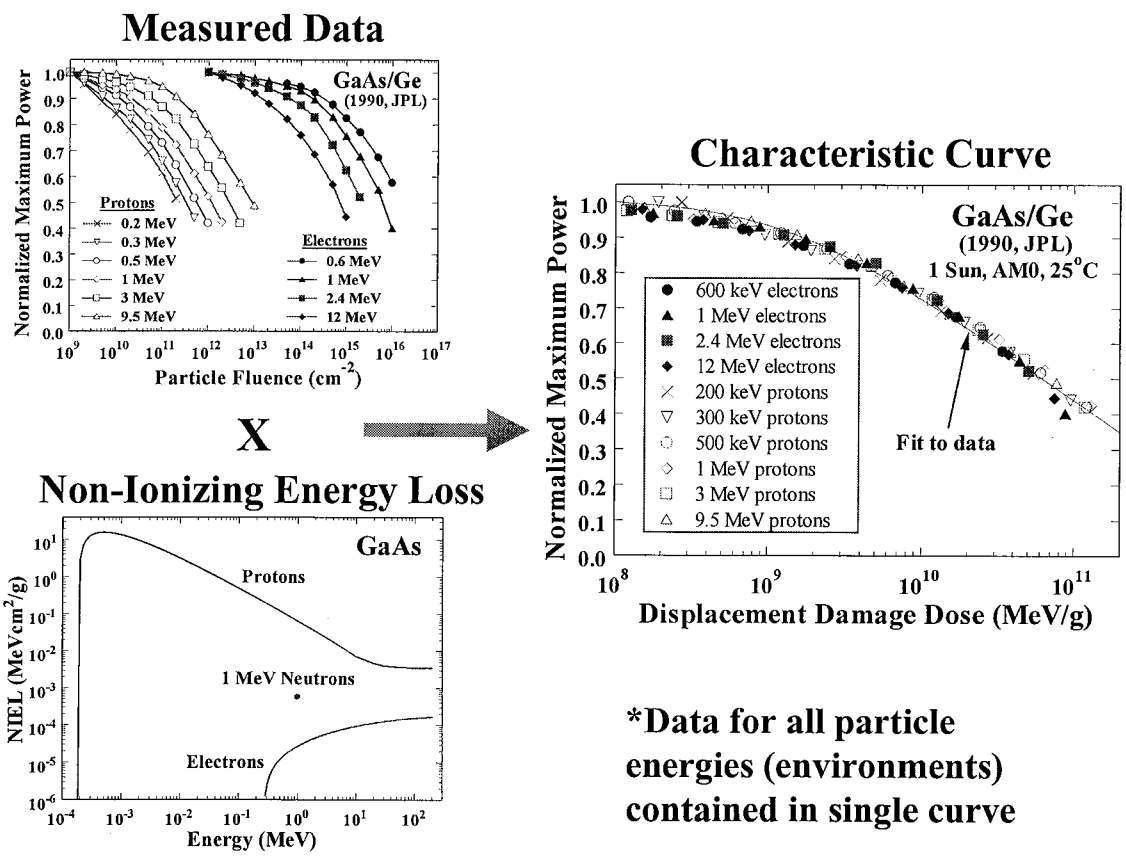

***Data for all particle energies (environments) contained in single curve**

The SAVANT program calculates differential fluence, transforms it to the slowed-down spectrum, and multiplies it by the appropriate NIEL factor to yield the displacement damage dose, D_d. The power loss is obtained from the characteristic curve, as shown in Figure 2.

Figure 2

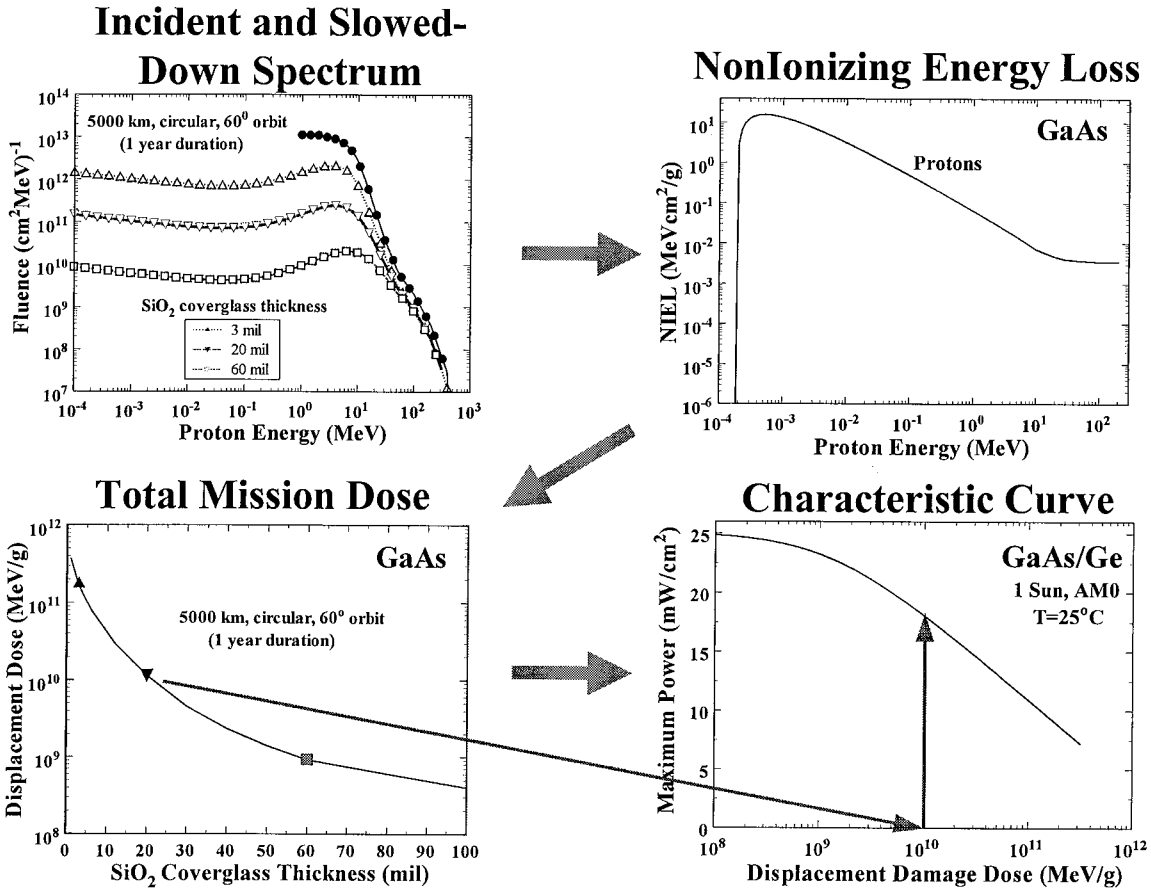

By comparison, the equivalent fluence method of the Radiation Handbook attempts to scale all the energies to 1 MeV electrons, in the form of damage coefficients. These are tabulated for specific thicknesses of coverglass. The algorithm is to multiply the incident differential fluence by the damage coefficient for the corresponding coverglass thickness to derive the equivalent 1 MeV electron fluence. The experimental curve tabulated for 1 MeV electrons is then used to determine the damage.

To date, damage coefficients have only been measured for Si and GaAs, limiting applicability of the equivalent fluence method to other cell materials. This equivalent fluence model requires measuring as many as thirteen discrete particle energies, whereas the displacement damage model requires only three, making it easier to extend to new materials.

Figure 3

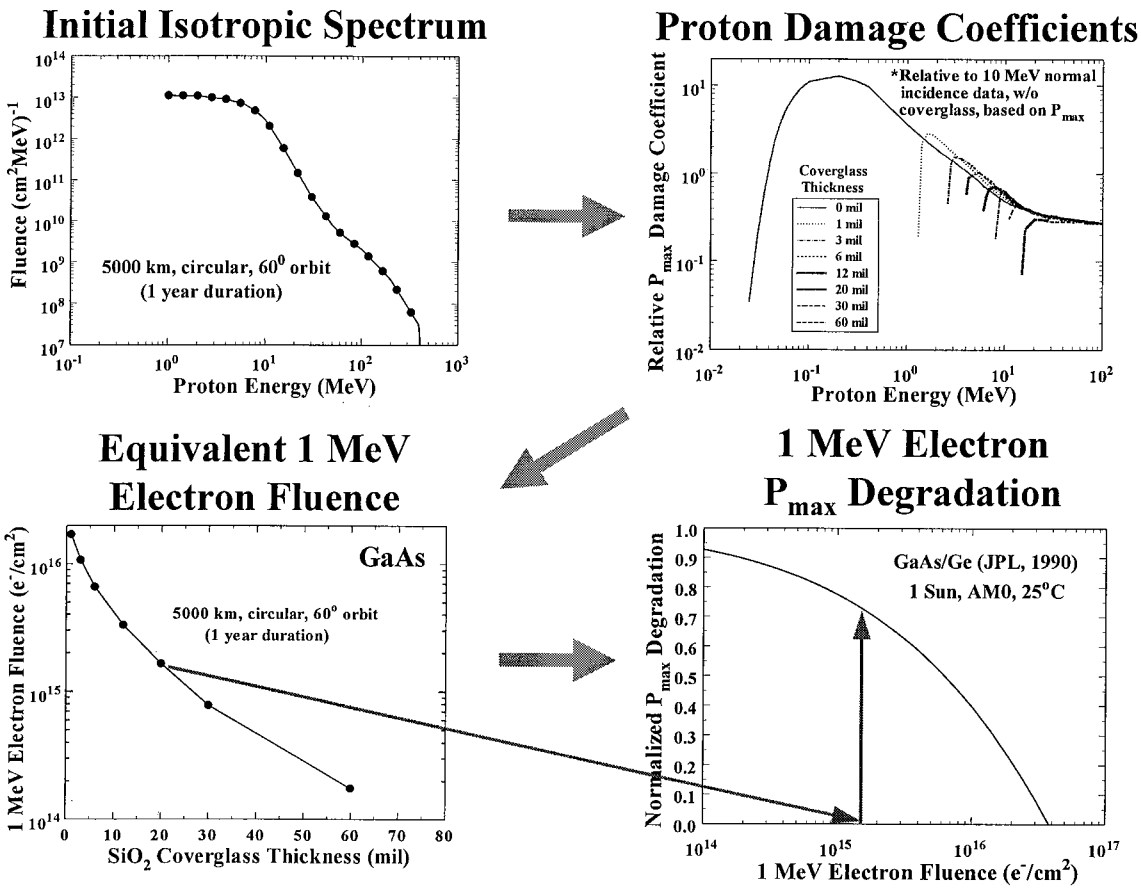

The SAVANT computer program combines an orbit generator with AE-8/AP-8 and IGRF-95 to calculate radiation fluence for a desired orbit. SAVANT applies the continuous slowing down approximation to calculate a slowed-down fluence. The user can enter a desired orbit, solar condition (MAX/MIN), mission duration, and coverglass thickness. The program currently is able to calculate D_d and power loss for GaAs cells. To perform trade studies, the user may enter a range of values for one of the input parameters, such as altitude, inclination, or coverglass thickness.

Figure 4 compares the two methods for a range of coverglass thickness from 6 to 60 mils. The equivalent fluence model shows only the results for five coverglass thicknesses, while the displacement damage dose modelling in SAVANT calculates damage for a range of thicknesses within the 6 to 60 mil interval.

Figure 4

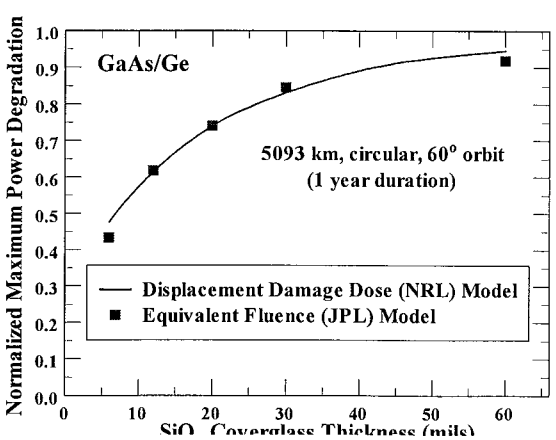

Figure 5

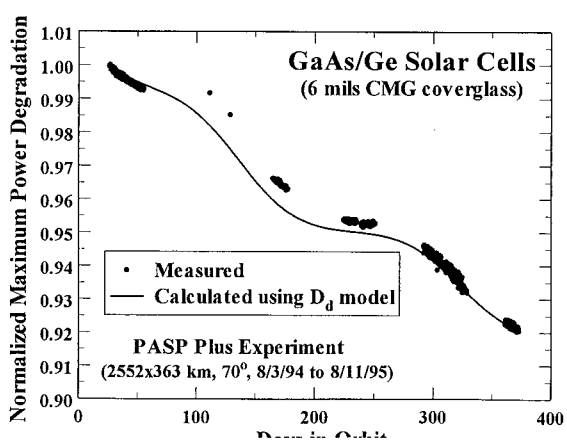

The SAVANT program is used to calculate damage to Module 11 (GaAs/Ge) of the PASP Plus experiment. Results, for albedo-free days only, are shown in Figure 5.

As a final example, Figure 6 illustrates a SAVANT calculation for a range of orbital altitudes. It can be readily observed that the proton radiation belt lies near 5000 km altitude.

Figure 6

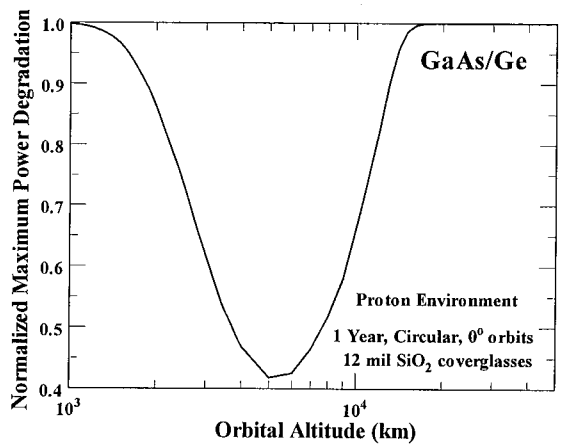

Conclusions

The displacement damage dose model, as incorporated in the SAVANT program, is a tool for rapid calculation of radiation damage. It accurately reproduces GaAs Radiation Handbook results, and agrees well with PASP Plus data for the GaAs/Ge test module. This model should lend itself to analysis of newly developed photovoltaic materials.

Future development of the displacement damage dose model will improve electron damage calculation, analyze cell geometry effects and end-of-life specific powers, and extend these calculations to new materials. A user-friendly interface is currently under development.

References

[1] G. P. Summers, R. J. Walters, M. A. Xapsos, E. A. Burke, S. R. Messenger, P. Shapiro, and R. L. Statler, Proc. 1st World Conference on Photovoltaic Energy Conversion, Waikiloa, HI (1994), p.2068

[2] M. Yamaguchi, T. Takamoto, S. J. Taylor, R. J. Walters, G. P. Summers, D. J. Flood, and M. Ohmori, J. Appl. Phys. **81**, 6013 (1997)

[3] G. P. Summers, S. R. Messenger, E. A. Burke, M. A. Xapsos, and R. J. Walters, Appl. Phys. Lett. **71**, 832 (1997)

[4] B. E. Anspaugh, "GaAs Solar Cell Radiation Handbook", JPL Publication 96-9 (1996)

[5] H. Curtis and D. Marvin, Proc. 25th IEEE Photovoltaic Specialist Conference, Washington, DC (1996), p. 195

[6] S. R. Messenger, M. A. Xapsos, E. A. Burke, R. J. Walters, and G. P. Summers, IEEE Trans. Nuc. Sci. **47**, 2169 (1997)

DISPLACEMENT DAMAGE DOSE ANALYSIS OF NEUTRON IRRADIATED SINGLE AND DUAL JUNCTION GaAs-BASED SOLAR CELLS

R. J. Walters and G. P. Summers
Naval Research Laboratory, Code 6825, Washington, DC 20375, USA

S. R. Messenger and E. A. Burke
SFA, Inc., Largo, MD 20774, USA

INTRODUCTION

The advantages of the Naval Research Laboratory (NRL) model in which the radiation response of space solar cells is analyzed in terms of displacement damage dose (D_d) are now well known. When analyzed in terms of D_d, degradation data due to irradiation by different particles at different energies can be described by a single, characteristic curve. The characteristic curve can then be used to describe the cell response to irradiation by any particle, or by a spectrum of particle energies, for which the NIEL is known, thereby simplifying predictions of on-orbit performance. Also, since the characteristic curve can typically be determined from only one or two sets of measurements, the NRL model greatly reduces the data required to characterize the radiation response of a new cell technology.

Application of the NRL model has been described for several solar cell technologies in the natural space radiation environment, i.e. for proton and electron irradiations [1,2]. However, there is little information in the literature about the response of cells to neutron irradiation. In this paper, the response of single-junction (SJ) GaAs/Ge and dual-junction (DJ) $InGaP_2$/GaAs/Ge solar cells to irradiation by a spectrum of neutrons produced by a fast burst reactor is presented. The solar cell degradation is compared to that measured under 1 MeV electron and 10 MeV proton irradiation. It is then shown how the neutron and natural environment data can be directly correlated the in terms of D_d.

NEUTRON IRRADIATION ENVIRONMENT

The solar cells studied here were irradiated with neutrons from the SPR-II fast burst reactor at Sandia National Laboratory. The SJ cell data were taken from Ref. 3. The DJ cell data were measured by NRL. Since the SPR-II reactor produces a spectrum of neutrons (Fig. 1), a methodology for characterizing the neutron spectra must be adopted. In this work, the standard methodology documented in the 1996 ASTM vol. 12.02 [4] was applied in which the neutron spectrum is reduced to an equivalent 1 MeV neutron fluence by means of the damage function for the material in question. For the SJ cells, the proper damage function should be that for GaAs, and the damage function employed in the present analysis is that given in the 1996 ASTM (Fig. 2).

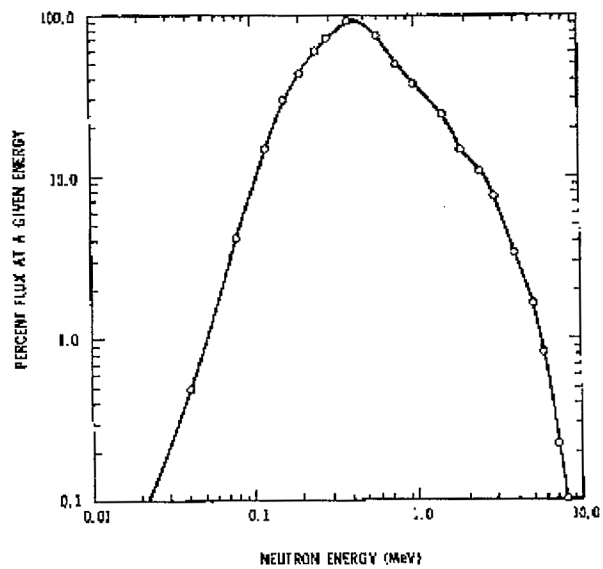

Fig. 1: The spectrum of neutrons produced by the SPR-II fast burst reactor at Sandia National Laboratory. The solar cells in this study were exposed to this neutron spectrum.

The proper damage function for the DJ cells is more complicated since there are active photovoltaic junctions in two different materials, i.e. InGaP and GaAs. The proper damage function for InGaP has not yet been established. However, studies of the response of these DJ cells to electron and proton irradiation suggest that the radiation response is controlled mainly by the GaAs sub-cell [5,6]. Therefore, in the present analysis, the GaAs damage function (Fig. 2) was also used in the analysis of the DJ neutron data.

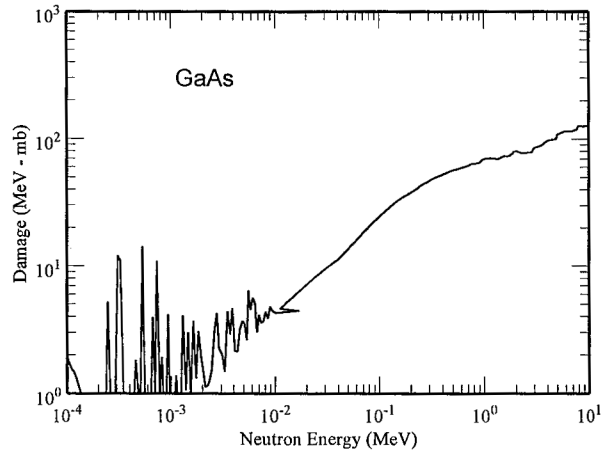

Fig. 2: Neutron damage function for GaAs from the 1996 ASTM Standard.

NONIONIZING ENERGY LOSS VALUES

NIEL values for proton and electron irradiation of GaAs have been published previously [7]. For the DJ cells, on the other hand, the proper NIEL value to use is more complicated since, again, the device consists of active junctions in two different materials. As noted above, most analyses of this DJ cell have shown the GaAs bottom cell to be the more radiation sensitive sub-cell, so that the overall DJ cell radiation response is generally controlled by the GaAs bottom cell. Therefore, as a first approximation, the NIEL for GaAs was used for the DJ cells.

The NIEL for 1 MeV neutrons was determined from the 1 MeV neutron displacement kerma, which for GaAs has been calculated to be 70 MeV-mb [8]. This value can be converted to a NIEL by multiplying by the numbers of atoms per gram and converting mb to cm^2. The resultant NIEL for 1 MeV neutrons in GaAs is 5.910×10^{-4} MeV-cm^2/g. The D_d for 1 MeV neutrons was calculated by multiplying the equivalent 1 MeV neutron fluence by this value of NIEL.

RESULTS FOR SJ GaAs/Ge CELLS

The response of SJ GaAs/Ge solar cells to a range of electron and proton energies has been measured by Anspaugh [9]. The response of SJ GaAs/Ge solar cells to neutron irradiation has been measured by Flock [3]. The data for cell maximum power (P_{max}) degradation due to electron, proton, and neutron irradiation are plotted as a function of particle fluence in Fig. 3. For the proton and neutron data, D_d is given by the product of the particle

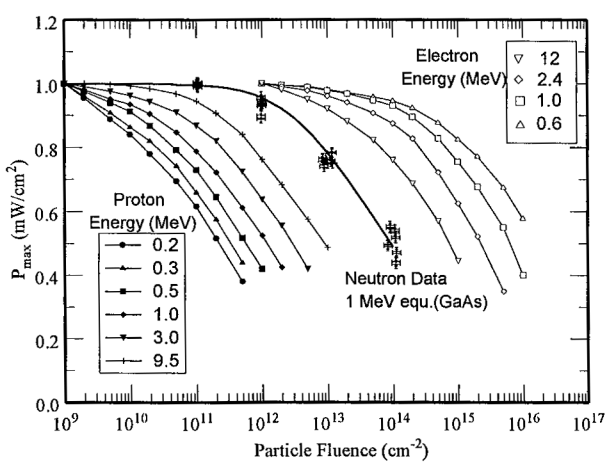

Fig. 3: Degradation of SJ GaAs cells plotted as a function of particle fluence. The electron and proton data are from [9] and the neutron data are from [3].

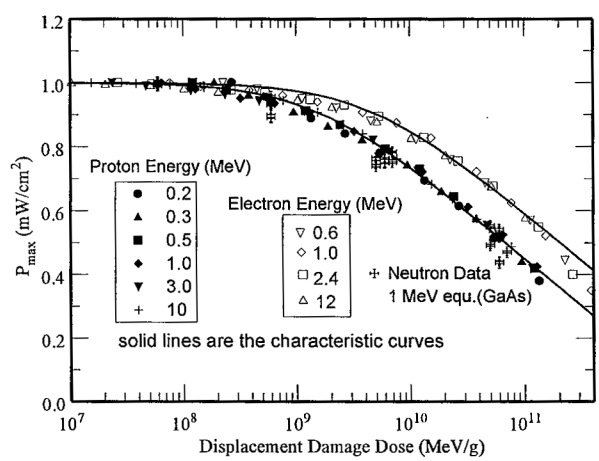

Fig. 4: Degradation of SJ GaAs cells plotted as a function of D_d (electron data as a function of equivalent 1 MeV D_d). All of the electron and proton data are described by the characteristic curves, and the proton characteristic curve is seen to accurately describe the neutron data.

fluence and the appropriate value of NIEL. However, the electron damage coefficients for GaAs/Ge cells are not directly proportional to NIEL, so for the electron data, a 1 MeV equivalent D_d is calculated from the product of the particle fluence and the NIEL raised to the 1.7 power and normalized to the NIEL at 1 MeV. The justification for this procedure is described in Ref. [10]. As demonstrated previously [10], the electron and proton data then collapse to single curves, which are referred to as the characteristic curves. What is remarkable is that the neutron data fall directly on the proton characteristic curve. This result confirms that the damage coefficients for heavy particles in GaAs are directly proportional to NIEL, as previously suspected.

RESULTS FOR DJ InGaP/GaAs/Ge CELLS

In Fig. 5, the degradation of the DJ cells due to neutron irradiation is plotted as a function of particle fluence. Also shown are data measured by Brown et al. after 1 MeV electron and 10 MeV proton irradiation [5]. The particle fluence data are then converted to D_d by multiplying by the NIEL where the appropriate NIEL for the DJ technology is taken to be that for GaAs. It can be seen in Fig. 6 that for D_d <~ $1x10^{10}$ MeV/g, the neutron data coincide with the proton data, as found above for the SJ cells.

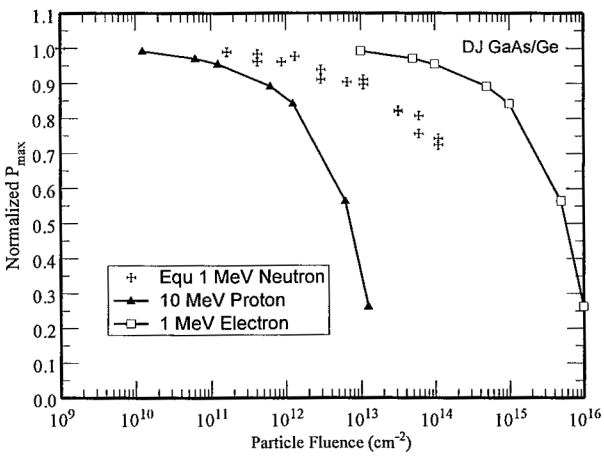

Fig. 5: Degradation of DJ InGaP/GaAs/Ge solar cells under electron and proton [5] and neutron irradiation as a function of fluence.

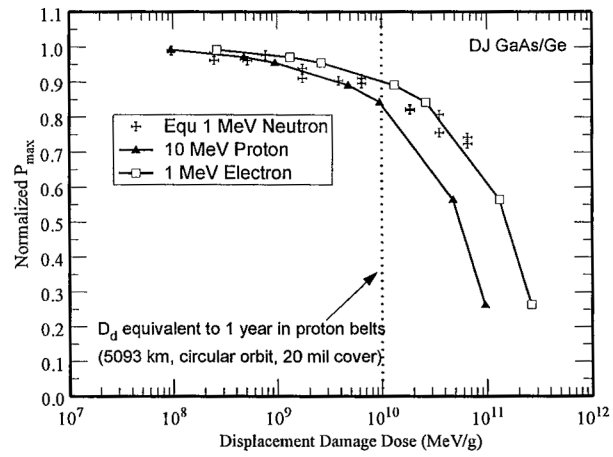

Fig. 6: DJ cell degradation as a function of D_d. Below $1x10^{10}$ MeV/g, the neutron and proton data coincide. The level of $1x10^{10}$ MeV/g is seen to be equivalent to a harsh earth orbit.

Figure 6 shows that the neutron and proton P_{max} data for the DJ cells diverge for values of D_d >$1x10^{10}$ MeV/g, with the neutrons having less effect than expected. This occurs because the short circuit current (I_{sc}) of the DJ cells degraded very little under neutron irradiation (Fig. 7). This was very unexpected behavior given that I_{sc} of the SJ cells, which are representative of the bottom cell of the DJ devices, degraded under electron, proton and neutron irradiations (Fig. 8) [9]. Also shown in Fig. 8 are I_{sc} data for a SJ InGaP solar cell measured after proton irradiation [6], which gives an indication of the response of the top cell of the DJ device, and again, degradation of I_{sc} is observed. The reasons for the unusual behavior of DJ cells under neutron irradiation are not yet understood and are currently under investigation.

It should be noted that a D_d level of $1x10^{10}$ MeV/g is equivalent to about one year in the heart of the proton belts with a 20 mil coverglass (Fig. 6) and therefore represents a high level of displacement damage to a cell. Therefore, while the present analysis is restricted in its application to levels of D_d less than $1x10^{10}$ MeV/g, in practice this will not impose much of a limitation in terms of most earth orbit missions.

DISCUSSION

Analysis of the response of a solar cell to a particular neutron radiation environment is typically performed by relating the equivalent 1 MeV neutron fluence for the neutron environment to an equivalent 1 MeV electron using an empirically determined equivalency factor. This value was determined for Si many years ago to be 2400 [11]. No value for such a parameter has yet been published for GaAs cells. Thus, the results and analysis

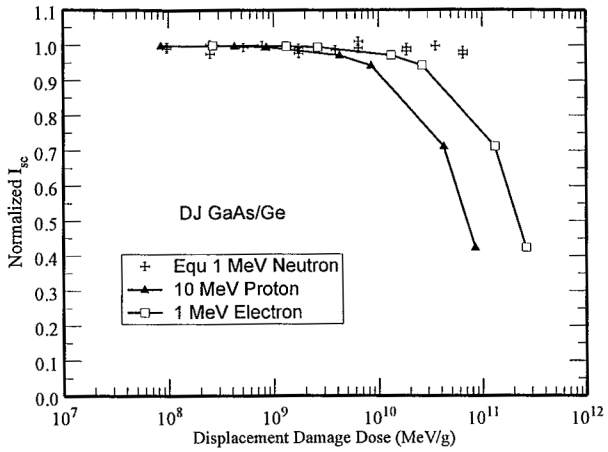

Fig. 7: The degradation of I_{sc} in the DJ cells. No degradation was observed under neutron irradiation. The electron and proton data are from [5].

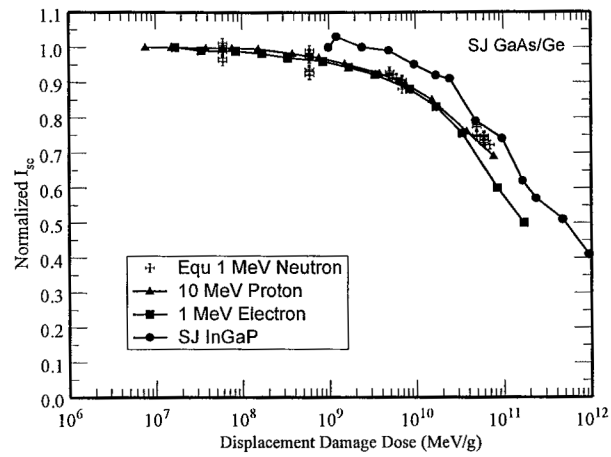

Fig. 8: Degradation of I_{sc} in SJ GaAs after electron and proton [9] and neutron irradiations and in InGaP cells after 3 MeV proton irradiations [6]. Degradation is observed in all cases.

presented here represent an important addition to the solar cell radiation data base by providing a methodology for relating proton, neutron, and electron degradation data for the SJ and DJ GaAs technologies. For the SJ cells, the ratio is found to be 66.8, i.e. a 1 MeV neutron is 66.8 times more damaging than a 1 MeV electron, thus a 1 MeV electron fluence can be converted to an equivalent 1 MeV neutron fluence by dividing the electron fluences by 66.8. For the DJ cells, the equivalent ratio is 74.

While the data presented here has enabled the determination of the 1 MeV electron/1 MeV neutron equivalency ratio for GaAs technologies, the present analysis has established a superior methodology for characterizing neutron radiation damage. When analyzed in terms of D_d, the neutron data were seen to coincide with the proton data, so the proton characteristic curve (determined for the SJ GaAs/Ge cells in [7] (Fig. 4)) can now be applied to neutron irradiation as well. Thus, the expected degradation of a solar cell due to neutron irradiation can be determined in the same way and with the same accuracy as for natural environment radiation.

The analysis of the DJ cell degradation presented here is the first application of the NRL model to a multijunction device, and the results suggest that the model should accurately describe the radiation response of DJ as well as SJ solar cells, once the appropriate NIEL has been determined. This is a key result considering that most of the advanced solar cell technologies now under development are high-efficiency, multijunction technologies. In addition, the present analysis has provided an accurate method for predicting the DJ cell response to neutron irradiation and for correlating electron, proton and neutron irradiation data.

SUMMARY

The response of SJ GaAs/Ge and DJ InGaP/GaAs solar cells to electron, proton, and neutron irradiation has been presented and analyzed in terms of D_d. The data presented here have enabled, for the first time, the determination of the 1 MeV electron/1 MeV neutron equivalency ratio for these two technologies. Moreover, the present analysis has shown that the neutron data correlate directly with the proton data in terms of D_d up to very high damage levels for SJ cells so that the proton characteristic curve will also accurately describe the neutron response. For DJ cells the proton and neutron correlation is close for $D_d <\sim 1\times10^{10}$ MeV/g. These results provide another example of the power of the displacement damage dose model for accurately describing solar cell radiation response in a complex radiation environment.

REFERENCES

[1] M. Yamaguchi, T. Takamoto, S. J. Taylor, R. J. Walters, G. P. Summers, D. J. Flood, and M. Ohmori, J. Appl. Phys. **81**, 6013 (1997).

[2] G. P. Summers, S. R. Messenger, E. A. Burke, M. A. Xapsos, and R. J. Walters, Appl. Phys. Lett. **71**, 832 (1997).

[3] R. A. Flock, Final Report for AF Wright Patterson Contract# F33615-88-C-2815, January 1991.

[4] ASTM Standard E722-94, Vol 12.02, Annual Book of ASTM Standards (1996), American Society for Testing Materials

[5] M. R. Brown, L. J. Goldhammer, G. S Goudelle, C. U. Lortz, J. N. Perron, J. S. Powe, J. A. Schwartz, B. T. Cavicchi, M. S. Gillanders, and D. Krut "Characterization Testing of Dual Junction GaInP/GaAs/Ge Solar Cell Assemblies", Proc. 26th IEEE Photovoltaic Specialist Conference, Anaheim, CA, Sept 30th 1996, p. 805.

[6] R. J. Walters, M. A. Xapsos, H. L. Cotal, S. R. Messenger, G. P. Summers, P. R. Sharps, and M. L. Timmons, "Radiation Response and Injection Annealing of p^+n InGaP Solar Cells", Solid State Elec. **42**, 1747 (1998).

[7] G. P. Summers, E. A. Burke, P. Shapiro, S. R. Messenger, and R. J. Walters, "Damage Correlation in Semiconductors Exposed to Gamma, Electron, and Proton Radiations", IEEE Trans. Nuc. Sci. **40**, 1300 (1993).

[8] A. M. Ougouag, J. G. Kelly, H. J. Stein, M. S. Lazo, C. E. Lee, and L. R. Dawson, "Differential Displacement Kerma Cross Sections for Neutron Interactions in Si and GaAs", IEEE Trans. Nuc. Sci., **37**, 1937 (1990).

[9] B.E. Anspaugh, "Proton and Electron Damage Coefficients for GaAs/Ge Solar cells", Proc. 22nd IEEE Photovoltaic Specialist Conference, 1991, pp. 1593-1598.

[10] G. P. Summers, R. J. Walters, M. A. Xapsos, E. A. Burke, S. R. Messenger, P. Shapiro, and R. L. Statler, "A New Approach to Damage Prediction for Solar Cells Exposed to Different Radiations", Proc. 1st IEEE World Conf. On Photovoltaic Energy Conversion, Dec 5-9, 1994, Wakiloa, HI, p. 2068.

[11] H. Y. Tada, J. R. Carter, B. E. Anspaugh, and R. G. Downing, "The Solar Cell Radiation Handbook", JPL Publication 82-69, 1982.

SolaMax™ MICROSHEET SOLAR CELL COVERGLASS: SPACE RADIATION QUALIFICATION TEST RESULTS

Janeen A. Cooke, Mike Larro, and Mark Madigan

Optical Coating Laboratory, Inc.
Santa Rosa, CA 95407

ABSTRACT

For more than 15 years, coated ceria-doped borosilicate microsheet solar cell coverglass, like Corning 0213, has provided maximum power output when bonded to space solar cells. However, during the past several years, space photovoltaic manufacturers have made numerous improvements in cell designs to significantly increase efficiency. Such improvements include front-surface etching of silicon solar cells and adding multiple junctions to III-V solar cells. The effect of these changes has been the broadening of the bandwidth response of the improved cells, to the point where the coverglass limits the solar cell response, particularly in the UV region of the spectrum. To solve this inefficiency in existing solar cell coverglass, OCLI has developed SolaMax™, a new generation of high performance microsheet.

A standard suite of simulated space radiation tests of SolaMax™ microsheet glass has been completed, and herein, we present the BOL/EOL results. In-process data analysis indicates that SolaMax™ undergoes minimal changes in performance after exposure to space radiation environments. The space effects test matrix included 300 equivalent sun days in vacuum UV, high-energy electron radiation of 1.0 MeV to a fluence of 1.0E+15/cm^2, high-energy proton radiation at 0.5 MeV to 5.0E+14/cm^2, and low-energy proton radiation at 30 keV to 7.4E+15/cm^2. Results of standard manufacturing qualification tests are also described.

Keywords: Coverglass, **microsheet**, and **space solar cells**

1.0 INTRODUCTION

Optical Coating Laboratory, Inc. (OCLI) has been a part of the space power industry for more than 35 years, primarily as a supplier of solar cell coverglass. For more than fifteen years, OCLI has manufactured covers using Corning 0213 microsheet. Corning 0213 is a drawn borosilicate glass that protects space solar cells from the damaging effects of radiation found in orbital environments. Radiation stability in 0213 is achieved with the addition of cerium oxide to the glass melt. The presence of cerium ions in the microsheet also gives rise to a broad UV absorption band that cuts off in the blue region of the visible spectrum. This absorption edge is centered near 350 nm in 0213; thus, it also protects the silicone coverglass adhesive, which is susceptible to UV degradation. The application of 0213 coverglass to Si and GaAs space solar cells has long provided the required radiation protection with the additional benefit of maximizing cell power output. However, of late, progress in solar cell designs has challenged the performance of the coverglass, and inadequacies have been identified in microsheets.

Recent years have seen extreme increases in the power output requirements of satellite solar arrays. To meet the power demands of current and future satellite bus designs, space solar cell manufacturers have developed high-performance x-Si and III-V cells with conversion efficiencies rapidly approaching 30%. Solar cell performance has been improved with modifications such as front-surface etching of silicon solar cells and adding multiple junctions to GaAs-based solar cells. Such cell advances have resulted in broader response bandwidths, with increases in both the blue and the infrared regions of the solar spectrum. The performance of the latest space cells has been improved to the point where the coverglass absorption edge now limits the cell's UV response. As solar cells evolve, so must the coverglass. To this end, OCLI has developed SolaMax™, the next generation of high performance microsheet.

SolaMax™ is a reformulated borosilicate drawn glass, developed to meet the requirements of advanced space photovoltaics, particularly multijunction GaAs cells. It has been designed to have much higher transparency and a significantly lower UV cut-on wavelength than 0213, while being stable to space radiation effects. SolaMax™ also has a sharper UV absorption edge/shoulder than 0213 (350-450 nm) and higher broadband transparency from 400-1800 nm. Improved spectral performance allows SolaMax™ to maximize the power output and efficiency of all space solar cells, with additional coverglass gain of up to 3%. Yet, it still provides the UV protection that is necessary to prevent darkening of the cover/cell adhesive. Evaluation of this new microsheet has shown that SolaMax™ is compatible with the entire range of OCLI's coverglass coatings.

The SolaMax™ glass development was done in conjunction with Corning, Inc in Corning, NY and Schott-Desag Deutsche Spezialglas in Grünenplan, Germany. Applying the same objectives, OCLI worked with two vendors in order to obtain the best possible space glass. During its genesis, forty-four different patty melt compositions were evaluated for spectral performance and space radiation stability by OCLI. The different melts were successively formulated to identify the minimum level of cerium required to maintain stability towards UV and high-energy charged particle radiation, and also protect the silicone cement. Radiation stability was then balanced with transparency improvements. Maintaining a bulk resistivity as low as that of Corning 0213 was also a factor in the formulation of the new solar glass. This required multiple iterations to balance the alkali metal oxide ratio in the patty melts. The results of developmental test data led to the selection of two new glass types for pilot draw production. Once produced, each glass underwent full space and manufacturing qualification. The glasses are herein identified as SolaMax™ A and SolaMax™ B, respectively.

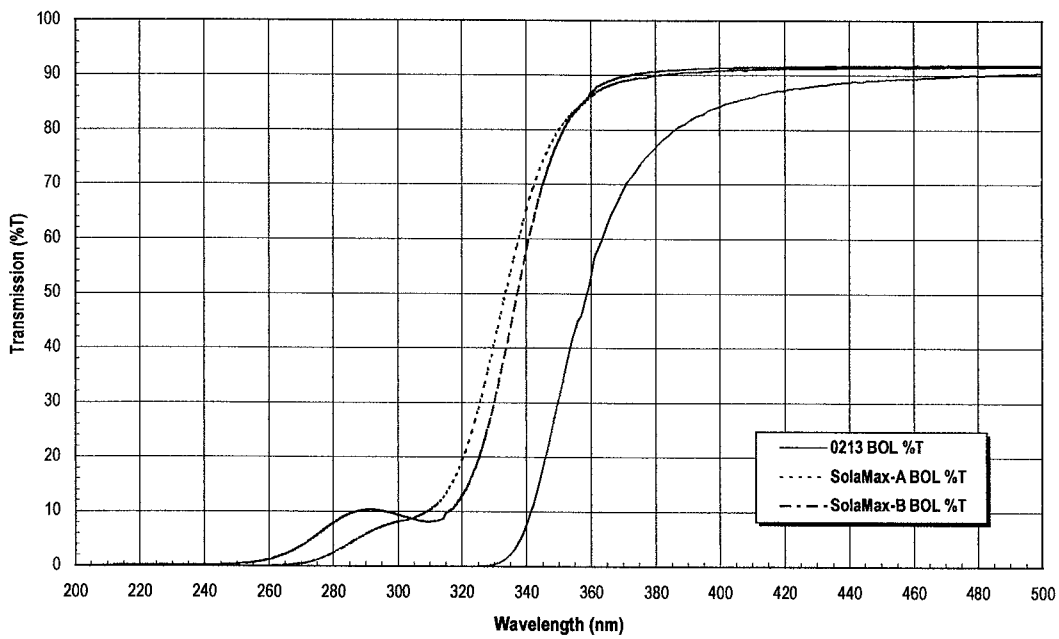

Figure 1. BOL UV Transmission of SolaMax™ A and B vs. Corning 0213 (150 μm/0.006 in.)

Both SolaMax™ A and B were manufactured in volume, at a variety of thicknesses, ranging from 75 μm (0.003 in.) to 500 μm (0.020 in.). Each glass has undergone thorough spectral analysis (as received), and is compared with 0213 in Figure 1. Table I lists selected properties of both SolaMax A and B in three different thicknesses, as compared to Corning 0213.

A standard full-qualification suite of simulated space radiation tests of both SolaMax™ A and B microsheet glasses has been completed, and herein, we present the BOL/EOL results. In-process data analysis indicates that SolaMax™ A and B microsheets undergo minimal changes in performance after exposure to space radiation environments. The space effects test matrix included 300+ equivalent sun days in vacuum UV, high-energy electron radiation of 1.0 MeV to a fluence of 1.0E+15/cm^2, high-energy proton radiation at 0.5 MeV to 5.0E+14/cm^2, and low-energy proton radiation at 30 keV to 7.4E+15/cm^2. All radiation exposures were conducted at Boeing facilities. Results of standard manufacturing qualification tests are also described.

Table I. Selected BOL properties of uncoated Corning 0213, SolaMax™ A, and SolaMax™ B.

Coverglass Type	Thickness		50% Cut-On Wavelength (nm)	Average %T (400-1200 nm)	Average %T (350-400 nm)	Emittance (ε_N)	Bulk Resistivity (Ωcm^2) 25°C
	μm	inches					
Corning 0213	100	0.004	350 ± 5	>91.5	>65.0	>0.85	1.8E+15
	150	0.006	355 ± 5	≥91.5	≥65.0	>0.85	1.8E+15
	500	0.020	375 ± 5	≥90.0	≥35.0	>0.85	1.8E+15
SolaMax™ A	100	0.004	328 ± 5	≥92.5	>85.0	>0.87	≤1.8E+15
	150	0.006	333 ± 5	≥92.5	≥85.0	>0.87	≤1.8E+15
	500	0.020	346 ± 5	>92.0	>82.0	>0.87	≤1.8E+15
SolaMax™ B	100	0.004	332 ± 5	≥92.5	>85.0	>0.87	≤1.0E+15
	150	0.006	337 ± 5	≥92.5	≥85.0	>0.87	≤1.0E+15
	500	0.020	348 ± 5	>92.0	>82.0	>0.87	≤1.0E+15

2.0 EXPERIMENTAL

SolaMax™ glass was developed by OCLI in an effort to create a new coverglass that maximizes the performance of enhanced silicon and multijunction GaAs space solar cells. Developmental test samples with thicknesses of 150 μm (0.006 in.) and 500 μm (0.020 in.) were fabricated from each of 44 separate patty melts, and exposed to high-energy charged particle radiation and an vacuum UV radiation. Samples of candidate glasses cemented with Dow Corning DC 93-500™ adhesive were also included in the abbreviated UV test to evaluate the ability of these glass types to prevent darkening of the silicone. Pre and post-radiation spectral analysis was performed on the melt samples. Based upon the performance of these developmental formulations, two glass types were down-selected and simultaneously produced as drawn microsheet, at different thicknesses. They are identified as *SolaMax-A* and *SolaMax-B*. OCLI employed a standard matrix of qualification tests for the evaluation of the spectral and environmental stability of SolaMax™ microsheet coverglass. Both SolaMax A and B were fully qualified concurrently to allow for side-by-side comparison, and were handled under identical conditions.

For the purposes of this product qualification, samples with a thickness of 150 μm (0.006 in.) were used for all tests. The qualification testing included both uncoated and coated SolaMax™ A and B samples, taken from production coating lots. The coated samples included the following standard types of OCLI coatings:

- Evaporative antireflection coating (AR)
- Evaporative conductive antireflection coating (ARC)
- MetaMode™ UV reflection coating (MMUVR)
- MetaMode™ blue/red reflection coating (MMBRR)

Glass samples for space radiation tests were sized to 0.59 in. x 0.59 in. (1.50 cm x 1.50 cm), in order to fit the test fixtures, using scribe and break technique. The UV, high-energy electron/proton, and low-energy proton radiation experiments were performed simultaneously using separate sample test plates for each radiation experiment. The parts were rigorously cleaned, then the spectral performance of each sample was measured before radiation exposure (BOL.) Performance was evaluated by transmission (%T), reflection (%R), and normal emittance (ε_N). Spectral measurements were made on a Shimadzu 3101 spectrophotometer. A fused silica transmission reference was used to ensure stability of the spectral measurements. Normal spectral emittance was calculated for all samples based on spectral reflection measurements over the range of 5μm to 50 μm, at 300 K. Fused silica references were included in all radiation test sample sets. Upon the return of each test plate to OCLI, parts were unloaded, then re-cleaned in a sonic line to remove any trace of contamination due to handling during testing. Post-radiation (EOL) spectral performance was then determined.

2.1 Vacuum UV Radiation Testing

Vacuum ultraviolet (VUV) exposure of SolaMax™ was performed at the Boeing Environmental Test Laboratory in the Boeing Kent Space Center using a Spectrolab X200 Xenon UV source. OCLI provided Boeing with a custom fixture containing 68 uncoated and coated glass samples. Coated samples were fixed with the exterior coating facing the incident radiation. The sample plate was mounted to a heat sink in the test chamber and maintained near room temperature (30-35°C) during the exposure by active cooling. Four thermocouples were attached to the plate to continuously monitor its temperature. A cold plane

was established on a sheath around the chamber perimeter to trap any contaminants. High vacuum pumping was accomplished with an ion pump to a level below 1.0E-07 Torr. The total UV exposure consisted of 7503 equivalent UV sun hours (EUVSH) at an average of 6.8 suns.

2.2 High-Energy Charged Particle Radiation Testing

The high-energy charged particle radiation exposures of SolaMax™ coverglass were performed using the Dynamitron Accelerator at the Boeing Radiation Effects Laboratory in Seattle, WA. OCLI provided two sample plates for the high-energy irradiations, with each plate containing twenty-six uncoated and coated glass samples. Coated samples were mounted with the exterior coating facing the incident radiation. Each high-energy particle radiation test consisted of both a 1.0 MeV electron exposure to a fluence of 1.0E+15 e/cm^2 and a 0.5 MeV proton exposure to a fluence of 5.0E+14 p/cm^2 (fluence measurement accuracy of ±15%). The irradiations were performed sequentially, beginning with the electrons. The particle beam was scattered over the exposure area by an aluminum foil mounted 120 inches from the sample fixture, and the beam flux was measured using a calibrated Faraday cup. Beam uniformity was determined to be 3% and 8% for the electron and proton radiation, respectively. The vacuum pressure in the chamber was maintained below 1.0E-06 Torr at all times, and the temperature was 20°C.

2.3 Low-Energy Proton Radiation Testing

The low-energy proton radiation testing of SolaMax™ was done in the Combined Radiation Effects Test Chamber (CRETC) located at the Boeing Radiation Effects Laboratory in Seattle, WA. Three test plates of 16 samples each were exposed to 30 keV protons to a fluence of 7.4E+15 p/cm^2. The 48 samples consisted of standard OCLI coverglass coatings on SolaMax™ A and B, with the exterior coatings facing the incident proton beam. The sample fixture was mounted to a water-cooled thermal control plate in the test chamber, and plate temperatures varied from 22 to 24°C. Chamber pressure was held at or below 1.0E-06 Torr at all times using both an ion pump and a cryopump.

2.4 Manufacturing Qualification Testing

An internal manufacturing qualification test matrix was employed to evaluate SolaMax™ A and B for compatibility with the OCLI Space Solar Products production platform. In-house Quality Assurance personnel conducted all testing at OCLI in accordance with MIL standards, where applicable. Coated samples were taken from two production runs of each type, then sized to 3.30 cm X 7.11 cm (1.3 in X 2.8 in) by scribe and break method. Table II describes the individual tests that were performed on the uncoated and coated SolaMax sample groups, and the results of manufacturing qualification for SolaMax™ A and SolaMax™ B.

Table II. OCLI manufacturing qualification tests for SolaMax™ A and SolaMax™ B.

Test Requirement	SolaMax™ A	SolaMax™ B
Test Group Sample Quantity*	8+8 for all	8+8 for all
Dimensions	3.30 cm x 7.11 cm (1.3" x 2.8")	3.30 cm x 7.11 cm (1.3" x 2.8")
Surface Quality, Workmanship	Pass	Pass
Transmission Measurements, Pre-test	Pass	Pass
Reflection Measurements, Pre-test	Pass	Pass
Normal Emittance	Pass	Pass
Cleaning, Surface Quality	Pass	Pass
Residual Stress	Pass	Pass
Bend Strength, Scribe & Break	Pass	Pass
Edge Quality, Scribe & Break	Pass	Pass
Coating Orientation	Pass	Pass
Humidity A, 72 hours	Pass	Pass
Humidity B, 10 day cycling	Pass	Pass
Salt Fog, 48 hours	Pass	Pass
Thermal Shock, 77K to 450K	Pass	Pass
Temperature Cycle, 1000, -180C to 195C	Pass	Pass
15 min. Boil	Pass	Pass
Abrasion Resistance, 20 Rub Eraser	Pass	Pass
Adhesion, Slow Tape	Pass	Pass
Transmission Measurements, Post-Test	Pass	Pass
Reflection Measurements, Post-Test	Pass	Pass

3.0 RESULTS

The results of the space radiation qualification testing of SolaMax™ A and SolaMax™ B are summarized in Tables III-VI. In all of the irradiation experiments, transmission losses in the fused silica references (FS7940) are consistent with historical qualification data. Reported BOL and EOL data are averaged for the respective population of each sample type. The pre- and post-radiation transmission measurements included for AR, ARC, and UVR SolaMax™ coating samples were performed in air. Measurements made with the back surface immersed in n=1.43 oil typically result in gains of 3-4%T. The BOL and EOL normal emittance values for SolaMax™ A and SolaMax™ B are summarized in Table V, and are consistent with the ε_N performance of Corning 0213.

3.1 Vacuum UV Radiation Test Results

After exposure to 7503 EUVSH (or 312 EUVSD) of UV radiation, SolaMax™ A and SolaMax™ B experienced minimal degradation, as shown by the transmission data in Table III. Both uncoated glass types lose less than 1% in broadband transmission, and exhibit similar stability to the fused silica references. Although SolaMax™ A and B show a higher transmission loss than Corning 0213, their EOL UV absorption edges are still 20 nm lower than the EOL edge position of 0213. As shown in Figures 2 and 3, the UV shoulders of A and B, respectively, also remain quite sharp after UV exposure. The slight increase in the glass absorption below 350 nm in each glass results is a flattening of the base of the UV edge. AR, ARC, and UVR-coated samples of SolaMax™ A and B demonstrated comparable UV stability to the uncoated glass. Samples of A and B coated with the MetaMode™ Blue Red Reflector (MMBRR) were also found to be as stable to UV radiation as 0213 BRR samples tested in previous qualification programs at OCLI.

Table III. Results of 7503 EUVSH irradiation of uncoated and coated SolaMax™ A and SolaMax™ B.

Glass	Coating	BOL Ave. %T (400-1200 nm)	EOL Ave. %T (400-1200 nm)	Change Ave. %T (400-1200 nm)	BOL 50%T UV Cut-on	EOL 50%T UV Cut-on	Change 50%T UV Cut-on
FS7940	none	93.87	93.62	0.25			
0213**	none	91.71	91.62	0.09	355	≥356	≥1
SolaMax A	none	92.55	92.29	0.26	333.34	338.29	4.95
SolaMax B	none	92.68	92.31	0.38	337.08	339.51	2.42
SolaMax A	AR*	94.03	93.86	0.17	332.32	337.15	4.83
SolaMax B	AR*	94.10	93.78	0.32	336.11	338.54	2.43
SolaMax A	ARC*	94.57	94.12	0.44	333.50	338.18	4.69
SolaMax B	ARC*	94.37	94.22	0.15	337.33	339.52	2.19
SolaMax A	MMUVR*	94.36	94.06	0.30	343.44	345.89	2.45
SolaMax B	MMUVR*	94.44	93.95	0.49	343.84	345.81	1.97
Glass	**Coating**	**BOL Ave. %T (400-450 nm)**	**EOL Ave. %T (400-450 nm)**	**Change Ave. %T (400-450 nm)**	**BOL Ave. %T (450-1100 nm)**	**EOL Ave. %T (450-1100 nm)**	**Change Ave. %T (450-1100 nm)**
0213**	MMBRR	90.55	85.18	5.37	97.06	96.58	0.48
SolaMax A	MMBRR	95.61	92.71	2.90	97.82	97.09	0.73
SolaMax B	MMBRR	95.42	92.62	2.80	97.41	96.97	0.44

* BOL and EOL transmission measurements were made in air. Measurements made in 1.43 index matching oil result in a 3-4% gain in %T.

** Corning 0213 data taken from a previous 7200 EUVSH qualification test, and are included for comparative purposes.

3.2 High-Energy Charged Particle Radiation Test Results

SolaMax™ A and B samples were irradiated with simulated geosynchronous orbit (GEO) dosages of 1.0 MeV electrons and 0.5 MeV protons. This space radiation is known to be the most damaging to bare glass substrate, as the bulk or the particle energy is imparted into the bulk of the glass thickness. Therefore, the high-energy e-/p+ test is the most rigorous measure of the performance of a new coverglass type. The results of these radiation exposures of SolaMax™ A and B are shown in Table IV.

Because the cerium level in SolaMax™ is significantly lower than that of 0213, A and B were more susceptible to degradation than the 0213 references on the test plate. When the samples were returned to OCLI, a slight darkening of the uncoated

SolaMax™ parts was observed, consistent with the measured absorption increase in the blue region of the solar spectrum. The change in the UV absorption edge position of SolaMax™ B was nearly two times greater than that of bare 0213, while the edge shift in SolaMax™ A was more than three times more. However, the EOL UV cut-on performances of both A and B are still 20 nm better than Corning 0213. Both SolaMax™ candidates have such improved transparency over 0213, that they can afford to change more in high-energy particle radiation and retain their advantage. The change in the broad-band transparency of bare SolaMax™ A and B was quite similar to that of fused silica and 0213, as were those of the various coated SolaMax™ samples included in these tests. The high-energy e-/p+ BOL and EOL spectral performances of A and B are compared in Figures 4 and 5.

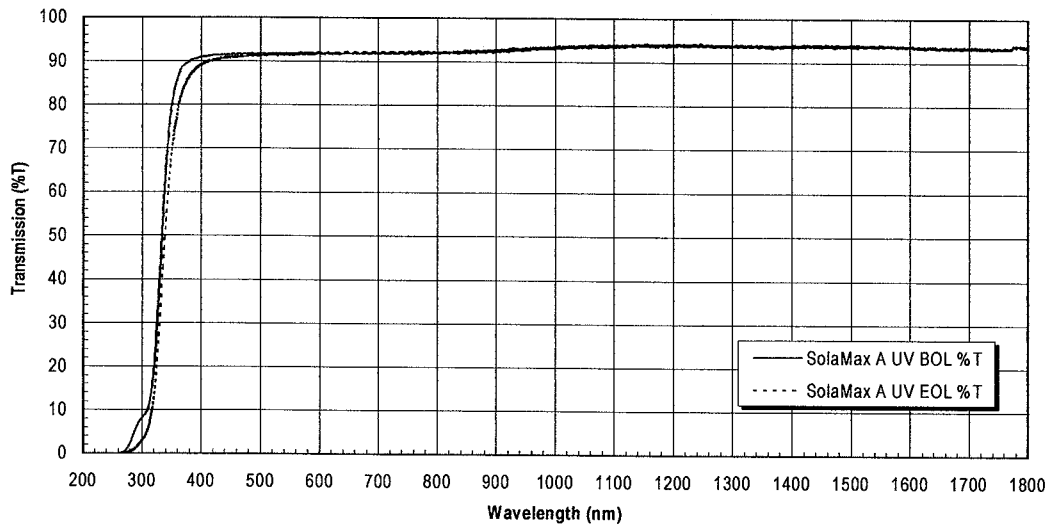

Figure 2. 7503 EUVSH BOL and EOL spectral performance of SolaMax™ A

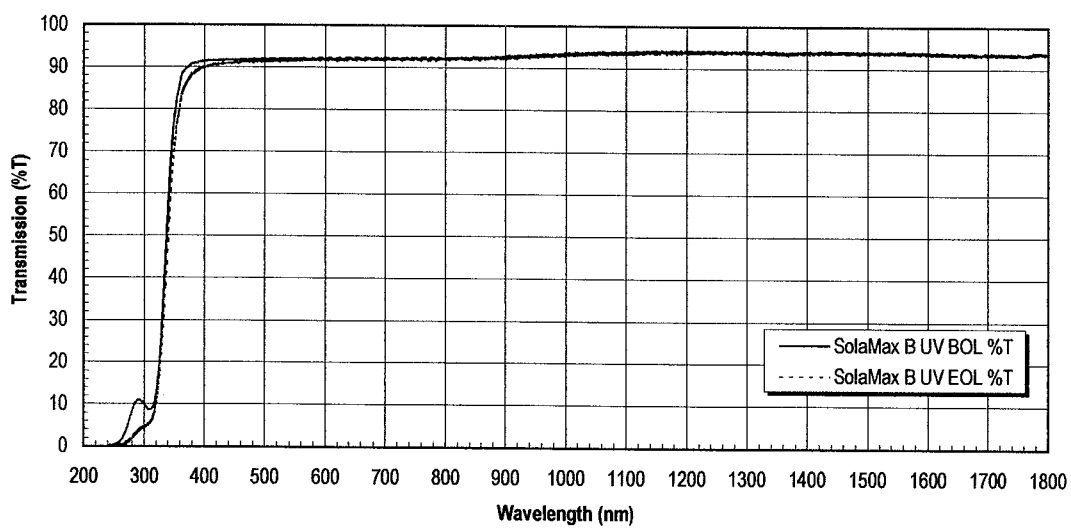

Figure 3. 7503 EUVSH BOL and EOL spectral performance of SolaMax™ B

3.3 Low-Energy Proton Radiation Test Results

A series of 30 keV low-energy proton radiation tests were performed on a coated SolaMax™ A and SolaMax™ B samples to verify the stability of OCLI's standard solar cell coverglass coating when applied to the new glass. This radiation environment is typically more damaging to thin film coatings because the energy of keV particles is only deposited into the first few microns of surface thickness upon bombardment. To this end, bare glass samples were not included in the 30 keV p+ tests. The results of the low-energy proton exposures are summarized in Table VI.

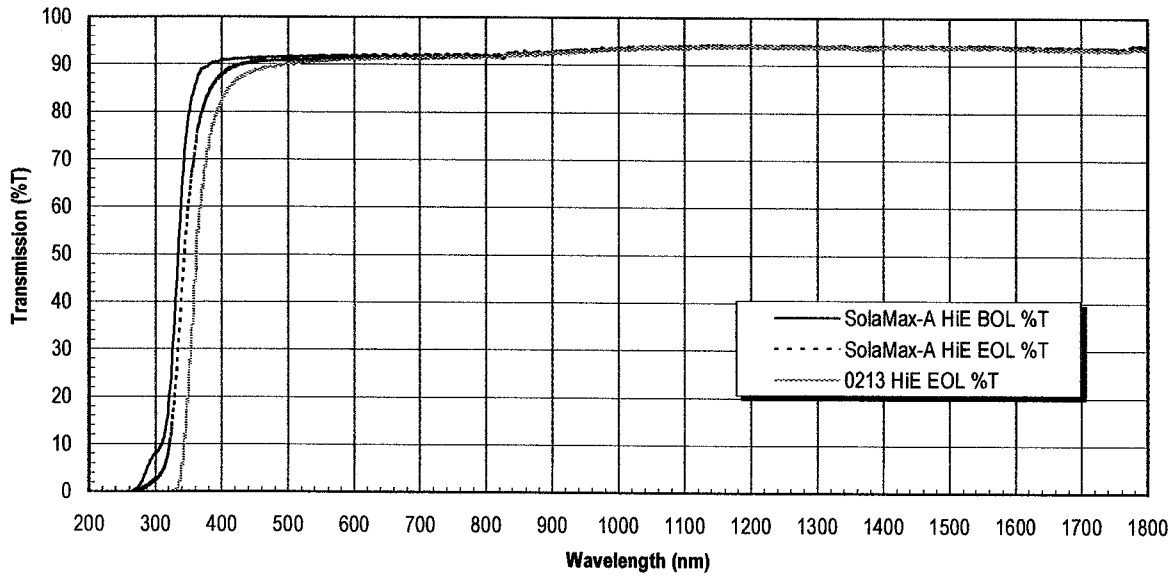

Figure 4. 1.0 MeV e- and 0.5 MeV p+ radiation BOL and EOL spectral performance of SolaMax™ A

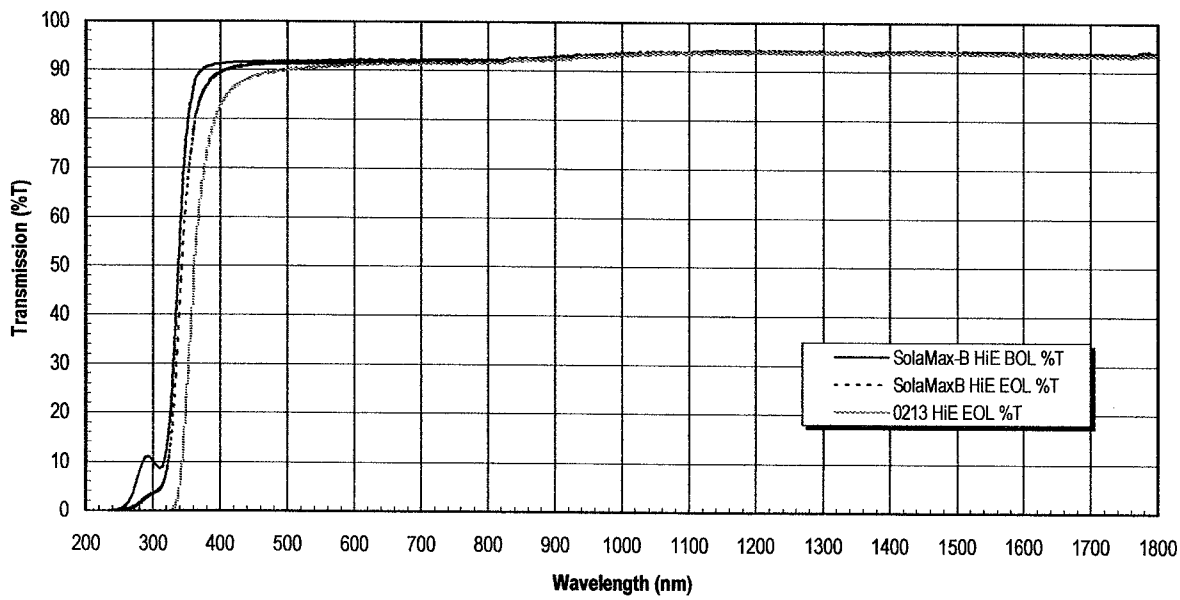

Figure 5. 1.0 MeV e- and 0.5 MeV p+ radiation BOL and EOL spectral performance of SolaMax™ B

Upon receiving of the irradiated samples from BREL, they were examined and unloaded from the sample tray. Sight darkening of the exposed front surface of each coated part was observed. The parts were cleaned using ultrasonics before EOL spectral analysis to ensure no discoloration was due to contamination. Spectral data for coated SolaMax™ A and B show a minimal broad-band transmission loss for the AR samples, a MgF_2 is quite stable to low-energy particle radiation. The ARC samples exhibit a larger absorption change to the darkening of the conductive indium tin oxide layer within the coating stack. There is relatively little shift in the UV cut-on for the coated samples, as compared with those irradiated with high-energy electrons and protons. This is also indicative of the low-energy proton radiation stability of SolaMax™ glass. As with the UV, 1.0 MeV e-, and 0.5 MeV p+ exposures, the 30 keV p+ EOL performance of A and B is significantly better than that of Corning 0213.

Table IV. Results of 1.0 MeV electron and 0.5 MeV proton irradiation of uncoated and coated SolaMax™ A and SolaMax™ B.

		BOL Ave. %T	EOL Ave. %T	Change Ave. %T	BOL 50%T	EOL 50%T	Change 50%T
Glass	**Coating**	**(400-1200 nm)**	**(400-1200 nm)**	**(400-1200 nm)**	**UV Cut-on**	**UV Cut-on**	**UV Cut-on**
FS7940	none	93.75	93.78	0.23			
0213	none	91.99	91.74	0.26	358.74	361.61	2.87
SolaMax A	none	92.45	92.19	0.26	333.41	342.77	9.36
SolaMax B	none	92.57	92.39	0.19	337.12	342.08	4.96
SolaMax A	AR*	93.98	93.84	0.14	332.35	341.15	8.80
SolaMax B	AR*	93.97	93.74	0.24	336.17	340.62	4.46
SolaMax A	ARC*	94.35	94.21	0.13	334.96	342.50	7.54
SolaMax B	ARC*	94.52	94.16	0.36	337.31	341.65	4.34
		BOL Ave. %T	**EOL Ave. %T**	**Change Ave. %T**	**BOL Ave. %T**	**EOL Ave. %T**	**Change Ave. %T**
Glass	**Coating**	**(400-450 nm)**	**(400-450 nm)**	**(400-450 nm)**	**(450-1100 nm)**	**(450-1100 nm)**	**(450-1100 nm)**
0213**	MMBRR	90.66	89.95	0.71	97.15	97.14	0.01
SolaMax A	MMBRR	95.15	93.36	1.79	97.38	97.08	0.30
SolaMax B	MMBRR	95.20	93.93	1.28	97.12	96.69	0.44

* BOL and EOL transmission measurements were made in air. Measurements made in 1.43 index matching oil result in a 3-4% gain in %T.

** Corning 0213 data taken from previous high-energy e-/p+ radiation qualification tests, and are included for comparative purposes.

Table V. BOL and EOL Emittance of SolaMax™ A and SolaMax™ B for UV and High-Energy Particle radiation tests.

Glass	UV BOL ε_N	UV EOL ε_N	Change in UV ε_N	Hi-E BOL ε_N	Hi-E EOL ε_N	Change in Hi-E ε_N
0213*	0.883	0.885	0.002	0.885	0.886	0.001
SolaMax A	0.886	0.885	0.001	0.884	0.884	0.000
SolaMax B	0.887	0.884	0.003	0.887	0.886	0.001

* Corning 0213 data taken from previous high-energy e-/p+ radiation qualification tests, and are included for comparative purposes.

Table V. Results of 30 keV proton irradiation of coated SolaMax™ A and SolaMax™ B.

		BOL Ave. %T	EOL Ave. %T	Change Ave. %T	BOL 50%T	EOL 50%T	Change 50%T
Glass	**Coating**	**(400-1200 nm)**	**(400-1200 nm)**	**(400-1200 nm)**	**UV Cut-on**	**UV Cut-on**	**UV Cut-on**
FS7940	none	93.71	93.56	0.15			
0213	AR*	93.38	93.29	0.09	355.24	356.58	1.34
SolaMax A	AR*	94.10	93.81	0.29	332.19	333.34	1.15
SolaMax B	AR*	94.10	93.86	0.24	335.99	337.04	1.05
SolaMax A	ARC*	94.53	92.86	1.67	333.52	335.45	1.93
SolaMax B	ARC*	94.45	92.80	1.66	337.18	338.85	1.67
SolaMax A	MMUVR*	94.45	93.90	0.55	341.66	343.44	1.78
SolaMax B	MMUVR*	94.47	93.84	0.62	343.17	345.13	1.96
		BOL Ave. %T	**EOL Ave. %T**	**Change Ave. %T**	**BOL Ave. %T**	**EOL Ave. %T**	**Change Ave. %T**
Glass	**Coating**	**(400-450 nm)**	**(400-450 nm)**	**(400-450 nm)**	**(450-1100 nm)**	**(450-1100 nm)**	**(450-1100 nm)**
0213	MMBRR	91.00	89.52	1.48	97.28	97.25	0.03
SolaMax A	MMBRR	94.73	92.19	2.54	97.12	96.45	0.67
SolaMax B	MMBRR	94.62	92.29	2.32	96.82	96.42	0.40

* BOL and EOL transmission measurements were made in air. Measurements made in 1.43 index matching oil result in a 3-3.5% gain in %T.

4.0 CONCLUSIONS

The data presented in this paper demonstrate the stability of OCLI SolaMax™ microsheet solar cell coverglass against space radiation effects. The uncoated and coated SolaMax™ samples included in the qualification tests experienced minimal changes in their optical properties after being exposed to simulated GEO dosages of UV, 1.0 MeV electron, 0.5 MeV proton, and 30 keV proton radiation. In each of these tests, the BOL-EOL change for SolaMax™ was less than 0.3% in broadband transmission. Although SolaMax™ samples degraded slightly more than Corning 0213 standards, the BOL and EOL spectral performance of this new glass is significantly higher than that of 0213. The stability of SolaMax™ makes it extremely well suited for use as a space glass.

In addition to providing the required level of space environmental protection for both solar cells and the adhesive, SolaMax™ demonstrates the desired transparency improvements for enhanced silicon and multijunction III-V solar cells. OCLI used modeling to predict performance gain for various coverglass-integrated-cell (CIC) arrangements with both 0213 and SolaMax™ microsheets. Our modeling predicts that the BOL transparency of uncoated SolaMax™ affords an additional coverglass gain of 2% for enhanced Si and 1% to 2.5% for multijunction GaAs cells over 0213 microsheet. When a MgF_2 AR coating is applied to SolaMax™, the added gain for Si cells is predicted to be more than 3.5% over a comparable 0213 coverglass. In the case of multijunction III-V cells, the models show the expected gain for a SolaMax™ AR to be approximately 2.5% more than an 0213 AR coverglass. Such improvements to coverglass gain will allow SolaMax™ to maximize the output of space photovoltaics in order to meet the power demands of evolving satellite systems. Additionally, the low bulk resistivity in SolaMax™ covers ($\leq$1.8E+15 Ω-cm^2) allows this new microsheet to meet the ESD requirements for solar panel designers.

The qualification of SolaMax™ glass has shown it to be compatible with all the steps of OCLI's coverglass manufacturing facility. SolaMax™ A and B samples passed all of the internal environmental and mechanical tests, and no significant performance differences were observed. Full qualification of both SolaMax™ A and SolaMax™ B is near completion at this time, and reports will soon be issued for both glass types.

SPRAT XVI
John Glenn Research Center
August 31 through September 2, 1999

ABSTRACT FOR SPRAT:

COMBINED SILICON AND GALLIUM ARSENIDE SOLAR CELL UV TESTING

Douglas Willowby
Electrical Power Group
NASA Marshall Space Flight Center
Huntsville, AL 35812

The near and long-term effect of UV on silicon solar cells is relatively understood. In an effort to learn more about the effects of UV radiation on the performance of GaAs/Ge solar cells, silicon and gallium arsenide on germanium (GaAs/Ge) solar cells were placed in a vacuum chamber and irradiated with ultraviolet light by a Spectrolab XT 10 solar simulator. Seventeen GaAs/Ge and 8 silicon solar cells were mounted on an 8 inch by 8 inch copper block. By having all the cells on the same test plate we were able to do direct comparison of silicon and GaAs/Ge solar cell degradation. The test article was attached to a cold plate in the vacuum chamber to maintain the cells at 25 degrees Celsius. A silicon solar cell standard was used to measure beam uniformity and any degradation of the ST-10 beam.

The solar cell coverings tested included cells with AR-0213 coverglass, fused silica coverglass, BRR-0213 coverglass and cells without coverglass. Of interest in the test is the BRR-0213 coverglass material manufactured by OCLI. It has an added Infrared rejection coating to help reduce the solar cell operating temperature. This coverglass is relatively new and of interest to several current and future programs at Marshall.

Due to moves of the laboratory equipment and location only 350 hours of UV degradation have been completed. During this testing a significant leveling off in the rate of degradation was reached. Data from the test and comparisons of the UV effect on the bare cells and cells with coverglass material will be presented.

SOLAR ARRAY SAILS: POSSIBLE SPACE PLASMA ENVIRONMENTAL EFFECTS

Willie R. Mackey
NASA Glenn Research Center at Lewis Field, Cleveland, OH 44135

An examination of the interactions between proposed "solar sail" propulsion systems with photovoltaic energy generation capabilities and the space plasma environments. Major areas of interactions are: Arcing from high voltage arrays, ram and wake effects, V x B current loops and EMI. Preliminary analysis indicates that arcing will be a major risk factor for voltages > 300V. Electron temperature enhancement in the wake will produce noise that can be transmitted via the wake echo process. In addition, V x B induced potential will generate sheath voltages with potential tether like breakage effects in the thin film sails. Advocacy of further attention to these processes is emphasized so that plasma environmental mitigation will be instituted in photovoltaic sail design.

INTRODUCTION:

NASA New Millenium Program has promoted the development of advanced propulsion technologies to enable less expensive future space exploration (1). Solar sailing as a mean of space propulsion is one system under consideration. The range of potential missions with this technology is only limited by the solar flux.

ENVIRONMENTS	FLUX
LEO/MEO/GEO	1368 $Js^{-1}m^{-2}$
JUPITER	55 $Js^{-1}m^{-2}$

Solar sailing essentially involves utilizing the radiation pressure of the sun to accelerate a spacecraft to its desired mission. There are however several variant of the sail concepts under consideration by NASA (2). The variations differ primary in the source of the propulsive power.

PROPULSIVE SOURCES
Solar Photons
Solar Wind
Lasers
Microwaves

The major design considerations for all sail types are mass, stability of the sail, temperature control and optimizing reflectivity (3). Possible plasma interactions with sail technologies are usually given secondary consideration in the quest for peak sail accelerations. However, experience with spacecraft charging in LEO and GEO and the projected increase particle and UV radiation due to Solar Cycle 23 warrants investigation of environmental compatibility as an ongoing design factor.

SAIL ACCELERATION:

A solar sail of area A, a few micron thick and mass m will in the near earth environment experienced an acceleration of

$$a_s = \frac{2A_s P}{m_s}\eta \approx few\ mm\,s^{-2}$$

where η is the efficiency factor due to the sail imperfect optical properties, structural billowing and P is the local solar radiation pressure (4). Sail area, mass and optical attributes are the key design elements. Mass reduction as in all spacecraft design is the major cost driver. In the case of solar sails, the mass reduction is critical to achieving the highest possible accelerations. Mass reduction in sail design is achieved by the use of polymer such as Kapton®, a mainstay substrate of solar array power systems. Environmental mitigation is well established for array substrates and may readily transfer to sail technologies (5). Lets examine some possible environmental effects associated with the design factors unique to sail technologies.

SAIL AREA

In order to achieve significant accelerations, sail lengths will be .1-10km. Sail area then becomes the dominant region of environmental interactions. Three environmental effects must be considered in the design: V x B, wake and ram effects.

V x B

An electric field will be induced along the sail as it crosses planetary, galactic and solar magnetic fields. In LEO orbits this induced field has a value of E = .22 V/m. This induced field will effect the dynamics of plasma currents to the sail and consequently sheath formation. For this case, a key intrinsic environmental design consideration is that the sail is restricted to a diameter of less than a km since the plasma environment will induce voltage breakdown near 200 volts on exposed conductors at attitudes less than 1000 km.(Fig 1). Alven wave generation in the kHz region will be transmitted if the induced field supports a current through the sail (6). Radiation induced drag will then represent a loss mechanism to the sail acceleration (7).

If the induced current within the sail structures form a loop then a magnetic dipole moment given by M = IA will be produced. For a current loop in the plane of the sail, the magnet dipole moment will be perpendicular to the sail area normal. The magnetic dipole moment will tend to orient itself parallel to the ambient B field in the position of minimum potential energy. Mission specifics will determine whether this torque is a source of drag and station keeping power loss. However it does point to a possible interesting application in solar cycle trapped radiation physics as a means of measuring particle flux coupled with secular variations in the ambient magnetic field.

WAKE AND RAM

The front and rear surfaces of the sail will experience different particle and radiation flux. Photoelectron generation from solar UV and space plasma absorption will produce differential voltages between the ram and wake surfaces. The required micron thinness of the sail material and substrate may be subject to up to kilo voltage stress which will lead to arcing (8). Arcing can then lead to tearing of the sail materials and ultimately failure. This differential-charging problem is not restricted to the LEO-GEO environments. The solar wind is a plasma and the sunspot maximum for solar cycle 23 will mean an increase in solar wind density and solar UV throughout the solar – interplanetary region. Models of the 11-year solar cycle lack real time density capabilities thereby elevating differential charging as a critical sail design factor. Mitigation of the

potential threat of differential charging can be achieved by grounding all conductive surfaces to the same potential thereby severely complicating the sail design. However sail designs that include solar arrays as an additional power source either within the sail or on the spacecraft body will increase the possibility of differential charging and thereby the potential for arcing.

OPTICAL PROPERTIES

Solar sails require a reflective surface in order to achieve optimal accelerations. A metallic coating which is vapor deposited on a Kapton[R] substrate is the typical sail design (9). Reflectivity across the entire solar spectrum is desired. In practice, UV transparency and thermal absorption are key design boundaries. Research at the NASA Glenn Research Center has indicated that whenever there is a conductor–dielectric junction in a plasma there exist a potential arc site (10). The metallic reflective coating and dielectric design of solar sails is a conductor dielectric junction and therefore arcing mitigation should then be a initial design priority.

Combining the reflective and photovoltaic potential of the sail coating may optimize the optical properties of the sail. Terrestrial photovoltaic manufacturers are experimenting with spray deposition of photovoltaic material. Given the size of sail structures the low efficiency spray deposition array may enable sail designs with smaller diameters thereby reducing area related environmental effects. Grounding and arc mitigation would still be the major plasma environmental consideration.

SUMMARY

Solar sails can provide an alternate means of increasing access to space. The size and power requirement of sail technologies will require consideration of environmental effects such as arcing and radiation drag in order to optimize sail design. Sail area is a major benefit and detriment to sail technologies. A combined reflective and photovoltaic sail coating may reduce the negative environmental impacts of sail area.

REFERENCES

1) NASA New Millennium Program http://nmp.jpl.nasa.gov

2.) Ibid.

3.) McInnes, Colin., Solar Sailing, Springer-Praxis Publishing, p. 14, 1999

4.) Ibid., p. 39

5.) Spacecraft Design Guidelines, http://powerweb.lerc.nasa.gov/psvee/publications

6.) Hasting, D.E., & Wang, J., Induced Emission of Radiation from Large Space Station Like Structures in the Ionosphere, AIAA Journal, April, 1989

7.) Drell, S.D., Foley, H.M., & Ruderman, M. A., "Drag and propulsion of Large Satellites in the Ionosphere", J. Geophysical research., p.3131, July, 1965.

8.) Ferguson, D.C., Synder, D. B., Vayner, B.V., & Galafaro, J.T., Array Arcing in Orbit – From LEO to GEO, 37th AIAA Aerospace Science Meeting, Reno, Nevada, Jan. 11-14, 1999.

9.) McInnes, Colin., Solar Sailing, Springer-Praxis Publishing, 1999

10.) Vayner, B., Galofaro, J., Ferguson, D., & De Groot, W., "Conductor-Dielectric Junction in Low Density Plasma" 38th AIAA Aerospace Science Meeting, Reno, Nevada, Jan. 10-13, 2000.

Figures From Space Power Design Course, LaunchSpace, M. Patel. 1999

MAXIMUM VOLTAGE Vs. ORBIT ALTITUDE

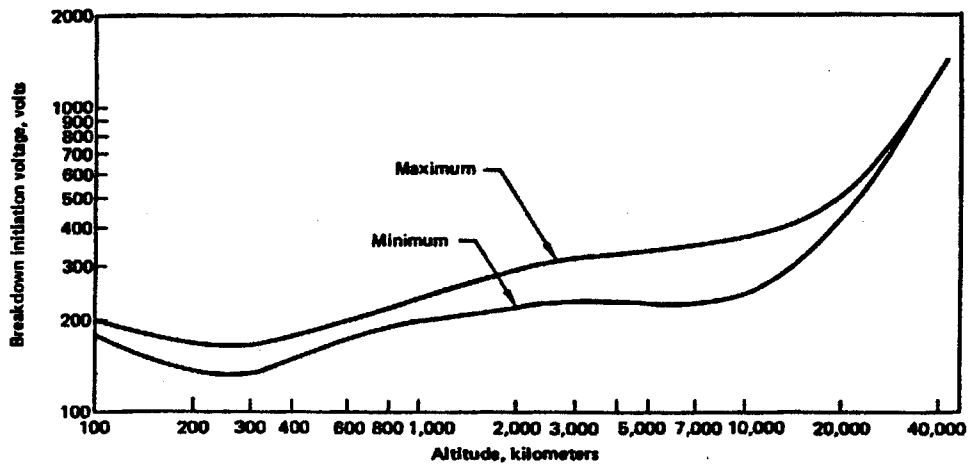

Effects of Plasma on Exposed Bare Conductors

ORBIT PARAMETERS INFLUENCING THE VOLTAGE SELECTION

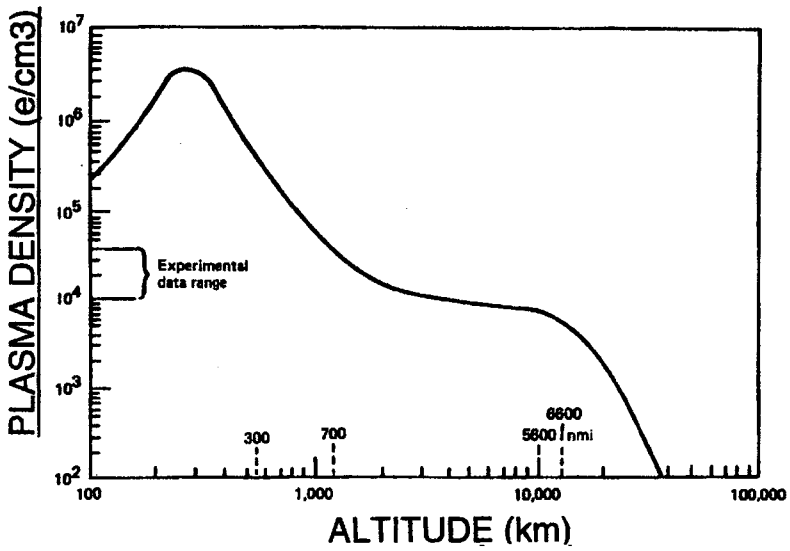

OVERVIEW, TESTING, AND SOLUTIONS TO ESD-INDUCED, SOLAR-ARRAY-STRING, ON-ORBIT FAILURES

A. Meulenberg
Hi Pi Consulting
Gaitherburg, MD

Abstract

Geostationary satellites have had sections of their high-voltage GaAs (and perhaps silicon) solar arrays fail abruptly on orbit. The recent (1997/8) occurrence of the problem was shown to correlate highly with active Geomagnetic-substorm activity (of the type that can result in spacecraft charging events) and thus was attributed to electrostatic discharge (ESD). A review of the cause and damage mechanisms of the effect is provided, along with the array requirements for this type of damage and the solutions to the problem. A comparison is made between several aspects of silicon and GaAs cells and how these could affect the probability of such damage. An extended discussion of the various points includes speculation about earlier solar-cell-string failures on silicon arrays.

Introduction

LORAL and Matra Marconi Space (MMS) separately funded in-house and outside experimental efforts, e.g., at LeRC and ONERA (in Toulouse, France) respectively, to determine the possibility and boundaries of ESD-induced problems in GaAs solar arrays. LORAL pushed such efforts because its spacecraft had displayed the problem on orbit [1, 2]. MMS supported their effort because it was planning to launch spacecraft with GaAs solar arrays in 1998 (and their customers were understandably nervous). Despite the different facilities, approaches, and techniques, the main conclusions and common solutions were reached independently. [Separate papers on the respective efforts were presented by Ira Katz and Leon Levy at the 6th Spacecraft Charging Technology Conference, 2-6 November 1998, Air Force Research Laboratory, Hanscom AFB, Bedford, MA, USA. Proceedings will be available on compact disk and, perhaps, the internet]

ESD-Induced Failure Mechanisms

The cause of a major loss in spacecraft power capability has been demonstrated (in the laboratory). It results from ESD-triggered, secondary discharges powered by the solar array section itself. The primary discharge is a high-voltage, fast, breakdown of charge on the solar-cell-coverslide surfaces to the differentially charged spacecraft ground (near which potential the solar cells reside). Once the initial arc is created, the string voltage (and section current) may be sufficient to maintain a secondary discharge. The high power, but low voltage (less than 100V), available in a solar-cell section can cause the secondary discharge to burn a conductive path between adjacent cells or strings, or between cells and the solar-panel substrate (spacecraft ground potential).

In the initial studies at LeRC and ONERA, two different discharge mechanisms were employed to trigger the main (secondary) discharge. Plasma-induced surface charging was used at LeRC and electron-beam surface charging was used at ONERA. (At that time, there was no agreement as to the on-orbit conditions that would result in the surface discharge of a solar array.) Both sources were able to generate primary discharges (albeit at different voltage levels). When the simulated solar-array voltage was high enough, both primary discharges could trigger the secondary discharges required to damage a solar array.

Each experiment had a fortuitous (and different) test-circuit-design "error" that greatly clarified the results. The LORAL design at LeRC used a capacitor in the primary discharge circuit that would simulate the total area of a

panel discharging through the single discharge point. For an array with no dielectrics between the solar cells, such a single-point discharge of the full panel would be an exceedingly unlikely event. Nevertheless, the result was a "smoothed" primary discharge trace which permitted an easy identification of the transition into the secondary discharge. The MMS design at ONERA used a capacitor in the secondary discharge circuit that would have simulated the capacitance of the array cells in parallel, not in series. This "mistake" permitted an analysis of the secondary discharge which identified the critical voltages and currents for sustaining such a discharge. A preliminary LORAL experiment, an electron-beam test at SRI, had neither error. It was not able to distinguish or identify the two-stage damage mechanism in the observed discharges. However, because its circuit simulated a string, not the full section, it was also unable to reproduce the destruction experienced on orbit or in the other two experiments.

The destruction observed in the course of the experiments ranged from reduced solar-cell fill factor (minor junction damage) to centimeter-size holes burned through the cells and/or the Kapton substrate. This range of negligible to total shorting of a string (in the laboratory) reproduced very well the on-orbit loss of solar-array sections (3 to 5 strings).

Solar Cell Charging in an Energetic Plasma Environment

Spacecraft charging (during solar-activity-induced terrestrial magnetic substorms) has caused problems for many years. Solar flares interacted with the Earth's magnetic field lines and raised the average temperature of the low-energy (in the eV range) trapped electrons and protons by several orders-of-magnitude. This now-energetic plasma would charge dielectrics negatively (into the multi-kiloVolt range relative to S/C ground). Early on, in laboratory investigations of the problem, a bilayer model of charge-buildup in dielectrics [3] was identified as the most likely trigger for discharges of the charge stored in a dielectric. Conclusions, based on later theoretical and experimental studies of conductivity in dielectrics[4], indicated that, given the electron-energy distribution in near-earth orbits, solar-cell coverslides were unlikely to accumulate the high voltages and voltage gradients needed to precipitate a discharge. This predicted immunity was based on the photo- and radiation-induced-conductivity of the coverslides in sunlight and an energetic-plasma environment. Net electron migration (from point of deposit) to local ground, is enhanced by the presence of photo- and radiation-generated electrons within the dielectric. Concern about discharges on the solar cell coverslides (the largest area of dielectric on most spacecraft) was further reduced as the coverslides were made thinner to save mass. This raised the average dielectric conductivity and lowered the breakdown potential (and thus the ESD energy available). While the evidence for solar array immunity was compelling, spacecraft were still experiencing ESD from some source and suspicion of the coverslides was not completely removed [5].

As solar arrays became larger relative to external spacecraft conductors, a new dielectric-charging mechanism was proposed. The source of the charge bilayer, secondary emission, would now hold the coverslides at a smaller negative potential than the S/C as a hot plasma drove the S/C (ground) potential negative. Since the surface breakdown potential of a dielectric, positive relative to ground, is smaller than that of a dielectric, negative relative to ground, less energetic and less dense (and more common) hot-plasma events could cause surface discharges on dielectrics. The lower temperatures (particle energies) of these discharge-producing events meant that there was less radiation-induced conductivity in the dielectrics and the lower surface voltages meant that there was a higher probability and less time required to reach breakdown potentials. Thus, once again, we have a possible mechanism for ESD on solar arrays.

Solar Array Requirements for a Destructive Secondary Discharge

In the past, when solar-array ESD events were considered, they were thought to be dangerous only to the S/C electronics - not to the cells. (Any discharge went from the coverslides directly, or through the low-impedance path of the forward-biased cells, to S/C ground.) However, with the use of high-voltage arrays (> 50V), the possibility of self damage becomes real. The primary discharge is generally across the surface between the coverslide edge and the solar cell contacts or interconnect. The intense discharge dislodges surface atoms and ionizes them. This plasma spreads and can create a conductive path between adjacent cells. If the voltage between the two cells is sufficient, current flows between the cells through this plasma.

In experimental tests, **the threshold for ion multiplication, necessary for a secondary discharge, seems to be about 50V**. (Above this voltage, an increase-of-gap width increases the secondary breakdown threshold.) While the threshold is on the order of 50V, the probability of secondary-discharge initiation is very low at this voltage. As the voltage increases, the probability increases rapidly until at some higher voltage (e.g., 75V, but dependent on gap width, etc.,) 100% of the primary discharges within the gap will initiate secondary discharges. With this model, it is clear that there will be preferred locations for damaging discharges. While the cell voltage will have little effect on primary discharge location (less than 100 Volts out of the kiloVolts needed for a primary discharge), it is crucial to the initiation of a secondary discharge. Unless the string voltage is very high, only the voltage in the gaps between cells at the extreme ends of a folded string are likely to initiate a secondary discharge. As one moves in from the folded-string ends, the voltage difference between adjacent cells diminishes. Thus only a small portion of the array is actually susceptible to secondary discharges.

It is not sufficient that a secondary discharge be initiated; to be damaging, it must be sustained. To sustain the discharge (in vacuum), it is necessary to generate ions and atoms (that can be ionized) at a rate higher than their dispersal. Thus, if the voltage between two adjacent cells (e.g., at opposite ends of a folded string) is high enough, the current within the plasma will grow. As the current grows, neutral atoms blown off by the primary discharge are ionized. In addition, more electrons, atoms, and ions are knocked off the electrodes by the electrons and ions accelerated by the field in the gap.

The conductive-plasma path, generated by the secondary discharge, has a resistance which provides a variable "load" for the solar cell string. This resistance decreases as the current increases. If the string voltage is inadequate, if the primary discharge is too small, or **if the cell gap is too wide (or filled with dielectric), the secondary-arc-path resistance is high and the arc is never established**. If the string voltage is sufficient, the arc current increases rapidly and approaches short-circuit current (at which point the string voltage falls and equilibrium is established between the arc resistance, the string current, and the arc voltage). If the string short-circuit current is inadequate to sustain the arc, the string voltage falls too far and the arc current drops. As the current decreases, the arc resistance and arc voltage increase. The arc extinguishes abruptly when (if) the string voltage exceeds the string maximum-power point. If, however, the current capacity is close to the critical value, the arc may re-ignite as the gap voltage jumps up when the current ceases to flow. This phenomenon (repetitive discharges) has been observed in the laboratory (at ONERA) and is just as destructive as a continuous arc.

Circuit-current availability is critical to the secondary-arc damage mechanism. For most solar arrays, operating at a voltage adequate for secondary-arc breakdown, the current available from a single string is not adequate to sustain an arc. In the on-orbit string failures, there were no blocking diodes to prevent the other strings in the section from contributing to the arc current. Thus, not only was the damage mechanism enabled, when it occurred, it shorted the whole section.

Circuit resistance reduces the voltage available at the arc gap when current is flowing. Therefore, the voltage across the gap between cells could be significantly higher before the arc begins than after. If the gap voltage is not high enough, a primary discharge will only act to discharge the capacitance between the two cells. The result is a harmless secondary transient, not a damaging arc. Circuit resistance must include the diode characteristics of the cells through which the current flows.

GaAs vs Silicon Cells

This ESD-caused solar array damage was first identified in GaAs arrays. Silicon arrays on the same design S/C did not exhibit the problem (at that time). However, over the years ESD had been investigated as the cause of silicon-string failures and electrical transients [e.g., Reference 5]. Furthermore, silicon strings on the LORAL panels have subsequently failed with a similar signature. What are the differences between the two cell types that could alter their susceptibility to this type of damage? This problem has not yet been conclusively resolved or even pursued. (Why spend money on the details, if the general problem has been solved?) However, there are several differences (identifiable to a solar-cell expert) that could contribute to the different performance on-orbit and in the laboratory. The first difference has to do with the reverse-bias characteristics of the two cell types. If the discharge occurs at any location other than the last cell of a string, the cell(s) between the discharge site and the section harness will act as blocking diodes. Since the breakdown voltage of a silicon cell is generally >20V (versus >5V for GaAs), this drop in the available string voltage can easily prevent most secondary

discharges from being sustained in a silicon array. Thus, damaging secondary discharge only occurs at a single location (near the last cell) on each silicon string, dramatically lowering the probability of such events.

The second difference has to do with the material properties. GaAs decomposes at a much lower temperature than that at which silicon evaporates. Thus, a surface arc can drive off arsenic ions which readily contribute to the plasma. The residual gallium would be sputtered across the Kapton in a gap and, thus, provide a conductive path that could sustain an arc even at lower current densities. (This statement of the idea begs the question of melting versus arc sputtering. The melting is affected by the greater thermal conductivity of the silicon and the sputtering is affected by the greater atomic mass of the Ga and As.} This hypothesis has not yet been tested.

The third difference also has to do with the material properties. GaAs substrates are very low resistivity; silicon substrates are much higher (typically 2 to 10 Ohm-cm). While primary discharges are most likely to be at the interconnects, the secondary discharges must take place at the sides of the cells where the large cell-to-cell potential differences exist. Since neither the cell grids nor the backside metallization extend to the edge of a cell, the arc will be from semiconductor-to-semiconductor. The arc is generally a point event and therefore creates a high current density in the local region. The high resistivity of the silicon cells thus results in a voltage drop, within the semiconductor, that adds to the circuit resistance. (Again, this effect has not been confirmed.)

One difference actually favors damaging discharges on silicon arrays. For a given cell size, the silicon cells produce more short-circuit current than do GaAs cells. Furthermore, silicon cells are presently, and into the future, likely to be larger in size than GaAs. Thus, for the same bus voltage and circuit resistance, an arc is more likely to be sustained in a silicon string - if the above effects do not dominate the situation.

Solutions to the Problem

Based on the experimental work and analyses, generalized solutions can now be presented. (These go beyond the quick fixes that had to be implemented on arrays that were already manufactured, or in process.) One solution to the problem is to prevent ESD or, at least, prevent it from occurring in locations where secondary discharges can be initiated. Another solution is to limit the ability of the secondary discharge to be initiated. The last solution is to make certain that the secondary discharge cannot be maintained. Unsustained discharges from present solar array sections do not have sufficient energy (integrated power) to short the strings.

The first solution can be implemented in the design stage by incorporation of grounded conductive coatings on the coverslides. As a quick-fix, use of solar cell adhesive inserted between cells where the potential difference can exceed 50V (maybe 70V for silicon arrays) can push any potential ESD sites away from hazardous regions.

The second solution can be implemented in the design stage by proper layout of the solar cell strings so that no potential differences between adjacent cells or wiring of the same or different strings can exceed 50V (under any operational circumstances). As a quick-fix, rewiring of the strings can be implemented. However, use of solar cell adhesive in the critical areas also raises the onset-voltage for initiation of secondary discharge (increasing the gap between cells will also increase this onset voltage).

The third solution is actually the simplest, but for some reason has never seemed convincing to non-solar-cell people and so has not been implemented alone. A secondary discharge will quench when the secondary-arc power drops below a critical value. The arc acts as a variable load for the solar array string (section). Thus quenching occurs if there is not enough current or voltage in the circuit. (The shape of the solar cell I-V curve allows the use of or rather than and in the previous sentence.) The simple addition of a blocking diode on each string would have been adequate to solve LORAL's problem. They did that and then added 2 other fixes. MMS already had the blocking diodes on a lower-voltage bus and needed no fixes for their arrays. They added an additional fix anyhow. Such is life in the fast lane.

Being aware of the problem and planning ahead solves any future problems of this type. However, not having a complete understanding of the problem can cause the imposition of unnecessary constraints and "fixes." On the other hand, lack of understanding can also cause a false sense of security which allows technological "refinements" to be made without demanding a quantifiable margin analysis.

Discussion

With this background, it is possible to identify the critical features required for a destructive secondary discharge:

- String voltage must exceed the secondary-discharge threshold (> 50V).
- String layout must allow some adjacent cells (in the same or another string) to exceed the discharge threshold voltage across the gap (at least under some conditions).
- The string voltage must be high enough to overcome the circuit resistance and still maintain enough arc voltage to support a sustaining current.
- The string/section current must be sufficient to maintain an arc without significantly reducing the available string voltage.

This section seeks to generalize the discussion about these features.

While the secondary-discharge threshold is >50V, no damaging arcs will occur while an array is only at that voltage. However, a 50V bus can have array voltages which exceed this level, particularly when the S/C is coming out of eclipse and the array is cold. This period is only a small percentage of the S/C life and therefore coincidence with the occasional hot-plasma period is statistically improbable. Nevertheless, eclipse exit is the location in a GEO orbit where hot-electron activity often peaks. Furthermore, if the S/C encounters a hot plasma while in eclipse, the whole S/C may become charged negatively during that dark period. Upon exposure to sunlight, the coverslides would become positively charged, relative to S/C ground, by losing negative charge faster (from photoemission) than the S/C ground. This danger would occur if the primary-discharge probability grows faster with time than the rate at which secondary-discharge probability decays. Calculation would be needed to identify the true threat level (and the required material parameters for such a calculation are not well known). However, to my knowledge, no solar-cell strings have yet been lost during this brief period.

Few environments, other than GEO, are likely to produce ESD on the arrays. However, high-voltage arrays may be susceptible to secondary discharge resulting from the plasma generated by voltage transients from ESD elsewhere on/within the spacecraft or even by a micrometeoroid impact [6]. In the laboratory, an ESD event located several inches from a high-voltage solar-cell gap could precipitate a secondary discharge, if the voltage between the cells exceeded 125V. Therefore, thermal blankets and OSRs, which are much more susceptible to ESD than are solar cells, could trigger secondary discharges on the array. Low earth orbit, with its higher levels of manmade space debris, could also be a hazardous region for high-voltage arrays.

Early in solar array development, parallel/series cell arrangements were produced to improve redundancy in string interconnections. Based on our present understanding of the ESD problem, it has been suggested (Francois Serre, of Matra Marconi Space) that some European array problems in the 1980's were a result of this configuration. It would lower the circuit resistance and inductance and provide adequate current without introducing silicon cells as "blocking " diodes for a discharge at locations a few cells away from the string ends. This problem in the European arrays has never been convincingly solved. However, subsequent design changes appeared to have prevented its future occurrence. These changes were: paralleling strings (rather than cells) and including blocking diodes on the strings; introduction of an additional Kapton layer to reduce the probability of cell shorting to the conductive graphite fiber substrate; and electrical isolation of the panels (typically through 100 kΩ resistors) to eliminate single point failures if such a short did occur. In each case the solution would have helped to reduce the problem addressed here.

The first design change would have reduced the current available to below the critical level. The last two changes addressed a point not mentioned above. In the LORAL/LeRC experiment, a hole was burned through the Kapton to the substrate and aluminum honeycomb. It was clear that, even if the cells were not shorted together, the string would have been shorted to S/C ground. It was felt that the pyrolyzed Kapton (burnt by the plasma) would have provided a sufficiently conductive path between cells to short the section. However, burning through the Kapton would have provided a shorter path to ground. The second Kapton layer would have increased the arc time required to burn through to the conductive panel substrate. The electrical isolation of that substrate would have meant that a single burn-through would not cause a problem and even multiple burn-throughs might only cost the array a few volts (depending upon how close the arc occurred to the string ends and if no surface short occurred between cells)

While blocking diodes would prevent this secondary-arc damage on all present solar arrays, they may not be adequate for some future arrays. As solar cells get larger, their short-circuit current gets larger and single strings may be able to supply more than the critical current. As higher voltage arrays are produced, the critical current goes down. Remember that, to first order, arc resistance varies inversely with power dissipated in the arc. (Data now exists to better determine this dependence, but such information is a "science" project and is not required to solve the present problem.)

Not yet addressed in this paper are the effects of spacecraft and solar array characteristics, time in orbit, and repetitive ESD events. Spacecraft cleanliness affects the plasma density created by ESD and, thus, the probability and severity of secondary discharge. A S/C which vents or outgasses a lot of material onto the solar arrays will be more vulnerable to this problem. On the other hand, much accumulated material will tend to dissipate over time in the thermal and vacuum environment of the solar array in space. Thus, over time the S/C becomes less susceptible to damaging secondary discharge. In fact, a launch after the equinox seasons may provide an opportunity for sufficient outgassing and removal of adhered gases to significantly reduce the chance of such damage when the high-ESD-density equinox season returns.

Solar array design and manufacture can affect the probability of ESD-induced damage in several ways. As mentioned before, residual contamination (on and between cells) can reduce the damage probability and a laydown procedure which allows adhesive to "well-up" between the cells can prevent this type of damage. However, if the adhesive gets too close to the top surface of the coverslides, then the possibility exists for ESD-induced redistribution of minute quantities of the adhesive over the coverslide surfaces. Future ESD events then can contribute this material to the "blow-off" plasma which could trigger secondary discharges elsewhere. This effect also falls into the time-on-orbit and repetitive event categories. Other repetitive event effects include: reverse-bias junction damage from primary discharges (the transient suppression methods used to protect internal electronics actually aggravate this problem); arc erosion of field-emission "points" on cells (this can increase or decrease the possibility of damaging secondary emission); and clean-up of surface adherents that contribute to plasma density.

References

1. I. Katz, V. A. Davis and D. B. Snyder, "Mechanism for Spacecraft Charging Initiated Destruction of Solar Arrays in GEO," 36th Aerospace Sciences Meeting & Exhibit, January 12-15, 1998/Reno, NV
2. C.F. Hoeber, E. A. Robertson, I. Katz, V. A. Davis and D. B. Snyder, "Solar Array Augmented Electrostatic Discharge in GEO," AIAA Paper 98-1401 (A98-19062), International Communications Satellite Systems Conference and Exhibit, 17th, Yokohama, Japan, Feb. 23-27, 1998;
3. A. Meulenberg, "Evidence for a New Discharge Mechanism for Dielectrics in a Plasma," in Spacecraft Charging by Magnetospheric Plasmas, A. Rose, Ed., AIAA, MIT Press, 1976, pp. 237 - 246.
4. A. Meulenberg, L. W. Parker, E. J. Yadlowski, and R. C. Hazelton, "Investigation of Radiation-Induced and Carrier-Enhanced Conductivity," Proceedings of the Spacecraft Environmental Interactions Technology Conference, U. S. Air Force Academy, Colorado Springs, CO, 4-6 October 1983, pp. 571 - 590
5. L. Levy, R. Reulet, D. Sarrail, J. M. Siguier and A. Robben, "Investigations of transients on the solar array bus caused by electrostatic discharges," European space power conference, ESA SP--320, August 1991b
6. L. Levy, J. C. Mandeville, J. M. Siguier, R. Reulet, D. Sarrail, J. P. Catani, and L. Gerlach : "Simulation of in-flight ESD anomalies triggered by photoemission, micrometeoroid impact and pressure pulse," IEEE Trans. Nucl. Sci. 43, 416, 1996

Flight Data of GaAs solar cells on the COMETS

Osamu Anzawa, Kazuhiro Aoyama, Takashi Aburaya,Koichi Shinozaki, Sumio Matsuda,
Takeshi Ohshima*, Isamu Nashiyama*, Hisayoshi Itoh*, Sohei Okada*,
Tetsuya Nakao**, and Yusuke Matsumoto**
National Space Development Agency of Japan (NASDA)
2-1-1, Sengen, Tsukuba-shi, Ibaraki 305-8505, Japan
Department of Material Development, JAERI*
1-6-1, Takezono, Tsukuba-shi, Ibaraki 305-0032, Japan
Advanced Engineering Service(AES) corporation**
1233, Watanuki, Takasaki-shi, Gunma 370-1292, Japan

ABSTRACT

Communication and Broadcasting Engineering Test Satellite (COMETS), which was not put into the scheduled geostationary orbit by the failure of H-Ⅱ rocket, became a result of flying in the more severe radiation environment than predicted. By this result, the necessity of re-prediction of the degradation of solar array paddle performance occurred. In order to predict again we carried out the irradiation tests of solar cells on the earth. In this paper this irradiation tests results are shown. And this results were examined based on simulation results using the TRIM code. Then the results of re-prediction of solar array paddle performance and actual flight data are shown.

INTRODUCTION

On February 21st, 1998, Communication and Broadcasting Engineering Test Satellite (COMETS) was launched by the H-Ⅱ rocket. In this satellite, the experiments in the geostationary orbit would be carried out. Because combustion time of the second engine of the rocket were shorter than the scheduled time, it failed in applying this satellite to the geostationary orbit. As the result, this satellite became that the orbiting of the elliptical orbit (perigees about 500km, apogee about 17,700km) which passes Van Allen belts[1] was done. In geostationary orbit which has scheduled at the beginning, the degradation of the solar cell by electron is dominant except for Solar Flare. But in the elliptical orbit which the COMETS does the orbiting, the degradation by the low energy proton becomes dominant[2], because Van Allen belts are passed. Hence it becomes necessary for urgently doing the degradation prediction of solar array paddle which is power source of the satellite. From such fact, proton irradiation tests of the GaAs solar cell of the structure equal to mounted solar cell on COMETS were carried out for the purpose of degradation prediction. By present irradiation tests, it was possible to carry out the lifetime prediction of solar array paddle in elliptical orbit which the COMETS does the orbiting. And it was possible to acquire the data necessary for the reexamination of the operation plan. Then various experiments scheduled in the COMETS were carried out. We finished operation of COMET. And we will stop the operation in the Autumn of 1999.

ABOUT COMETS

Figure1 shows the COMETS. The purpose of the COMETS is mainly to carried out the sophisticated satellite communication experiment and the satellite-broadcasting experiment and the inter-satellite communication experiment. The COMETS is 3[m] tall,2[m] wide and 2.8[m] long. Two flexible solar array paddles were mounted on the COMETS. The size of this solar array paddle is 14.5×3[m^2]. GaAs solar cells in the 7 parallel×74serial×60string were mounted on main solar array paddle. And GaAs solar cells in the 3 parallel×82serial×4string were mounted on charge array paddle. The COMETS change the orbit 7 times in total in order to carry out many planned experiments. Figure2 shows the aspect of this orbit change of 7 times. As the result, this satellite became that the orbiting of the elliptical orbit which passes Van Allen belts was done.

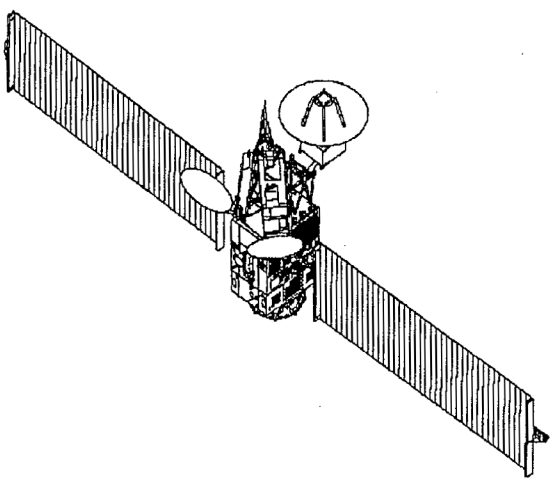

Figure1. The appearance of COMETS

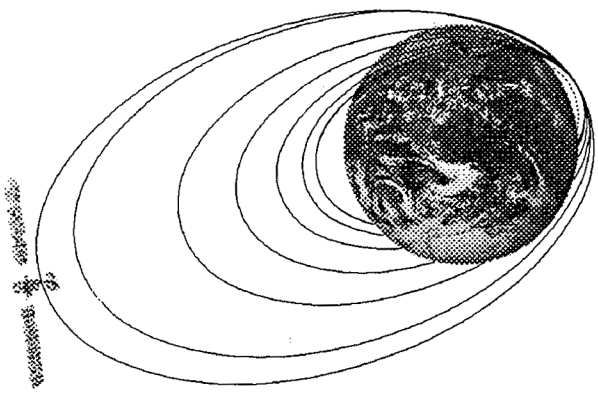

Figure2. The aspect of orbit change

EXPERIMENTAL NOTES

Structure and Fabrication of GaAs solar cells

In this study, GaAs solar cells of the structure equal to mounted solar cell except for cell size were used. The size of solar cell mounted on COMETS is 21×42[mm^2] for main solar array paddle and 20×40[mm^2] for charge array paddle. The Figure3 shows the photograph of the solar cell mounted on COMETS. Figure4 shows the schematic cross section of this solar cell. N type single crystal GaAs substrate (orientation: <100>, dope impurity: Sn and Zn) was used for this solar cell fabrication. Zn doped P-type AlGaAs layer are grown on the N-type GaAs buffer layer on the substrate by using the Liquid Phase Epitaxy(LPE) technique. By diffusing of doped Zn into the N-type GaAs, P-type GaAs layer was formed. And, Si_3N_4 layer is deposited by Chemical Vapor Deposition(CVD) method as an antireflection layer. The thickness of this layer is 750[Å]. The electrode is produced by sputter and vapor deposition. The N-electrode is Au/Ge/Ni/Ag. The thickness is 5 [μ m] in total. The P-electrode is Ti/Ag. The thickness is 5[μ m] in total. The size of the solar cell for

irradiation tests is 20×20[mm²] and 20×40[mm²]. Thickness of the GaAs layer is 200[μ m]. The interconnector is welded to the solar cell. The cover glass of 100[μ m] thickness is stuck on the surface of this solar cell. The efficiency is about 17～18%.

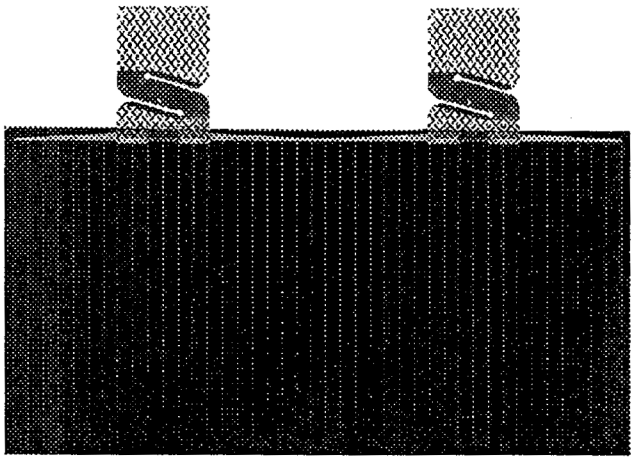

Figure3. The GaAs solar cell

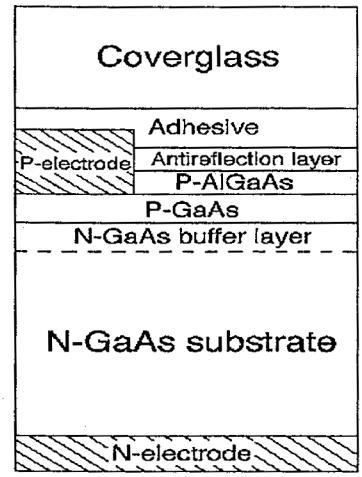

Figure4. Schematic cross section of GaAs solar cell

Irradiation tests

The irradiation tests were carried out in Takasaki Ion Accelerators for Advanced Radiation Application(TIARA) in collaboration with Japan Atomic Energy Research Institute(JAERI). The solar cells were irradiated by electron and proton from front surface and back surface of the cells perpendicularly. Irradiation energy of proton is 3,4,5,6 and 10[MeV] . And the cell was irradiated by electron of 1[MeV] energy. For the irradiation of 3,4,5 and 6[MeV] protons, the tandem accelerator was used. For the irradiation of 10[MeV] protons, the cyclotron accelerator was used. The characteristics were immediately measured using portability solar-simulator after the irradiation. The measurements were carried out at the condition of 28[℃] and A.M.0.

RESULTS AND DISCUSSION

irradiation test results

Figure5 shows the degradation characteristics of normalized maximum power at the irradiation of 3,4,5,6 and 10[MeV] protons from front surface of the cell. And this figure also shows degradation characteristics at irradiation of 1[MeV] electrons for the reference. The quadrature axis shows the fluence of proton or electron. The vertical axis shows the normalized maximum power of the cell. The figure shows that the solar cell dose not degrade, when the 3[MeV] protons are irradiated. And regardless of the fluence of the proton, the degradation has not completely been done. When the 4[MeV] protons are irradiated, the maximum power of cell is most degraded in the irradiation of other energy protons. The proton of 4[MeV] energy causes the rapid characteristic degradation. The degradation rate gradually decreases in order of 5,6 and 10[MeV] protons irradiation results following 4[MeV] proton results.

Figure6 shows the degradation characteristics of normalized maximum power at the irradiation of 3,4,5,6 and 10[MeV] protons from back surface of the cell. The maximum power seldom degrades, when the 3[MeV]

and 4[MeV] protons are irradiated. In comparison with this result, it is proven to intensely degrade than other energy protons irradiation, when 6[MeV] protons are irradiated. When the cell was irradiated the 5[MeV] and 6[MeV] protons, though there is the part inversion at 10^{12} [p/cm^2] fluence, the degradation rate gradually decreases in order of 6,10 and 5 [MeV] protons irradiation results.

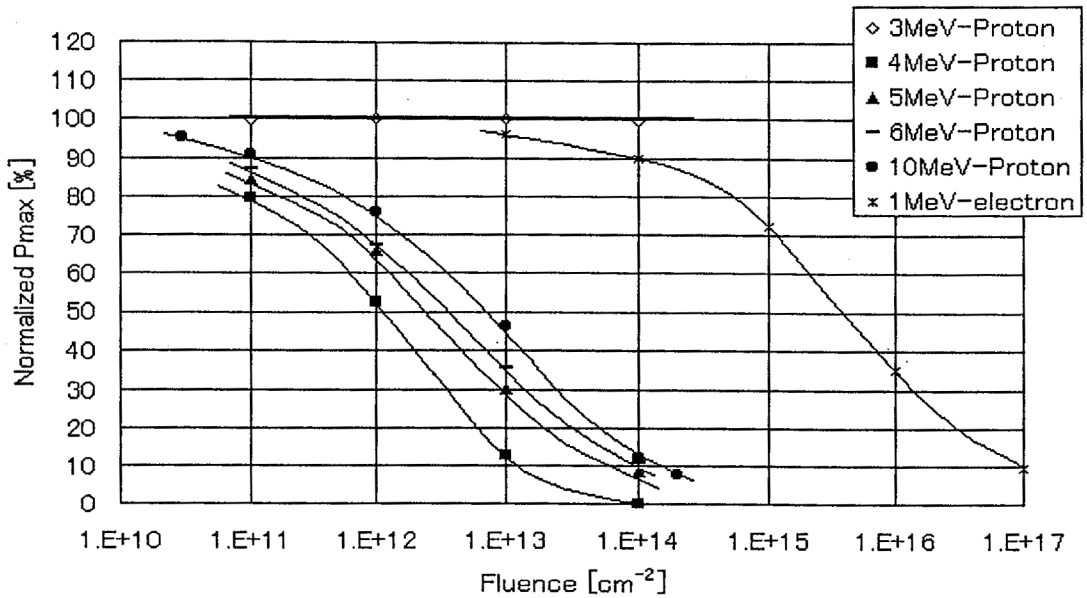

Figure5. Degradation characteristics of normalized Pmax by irradiation from front surface

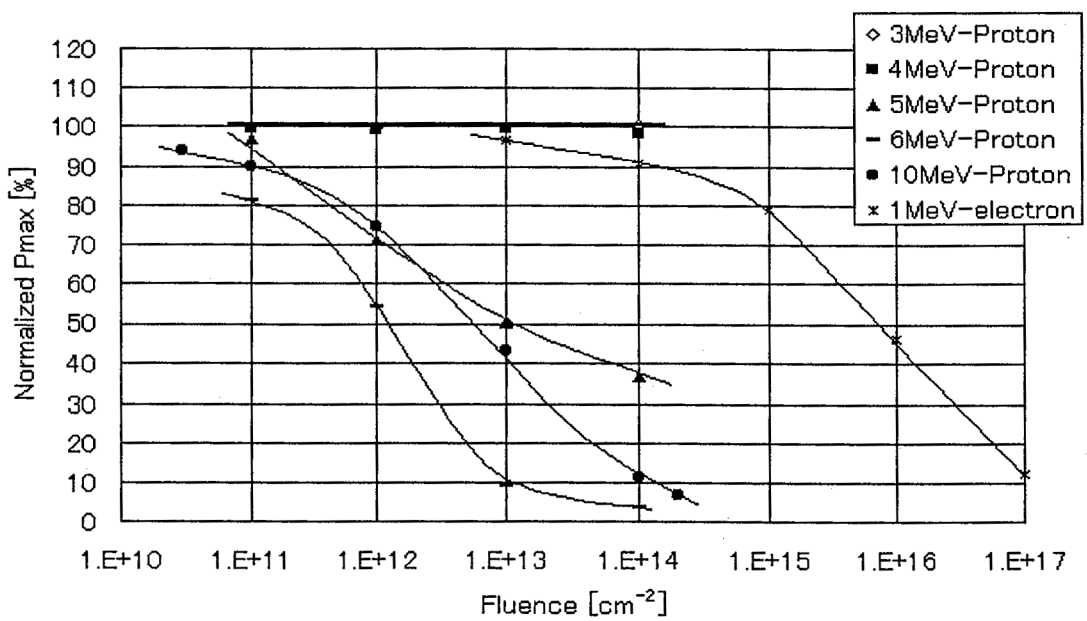

Figure6. Degradation characteristics of normalized Pmax by irradiation from back surface

Figure7,8 and 9 shows the degradation characteristics of Isc,Voc and FF by irradiation from front surface of the cell respectively. These figures show the degradation characteristic equal to the figure5. That is to say, it does not degrade in the case of 3[MeV] protons irradiation. And it degraded largest, when the 4[MeV] protons were irradiated.

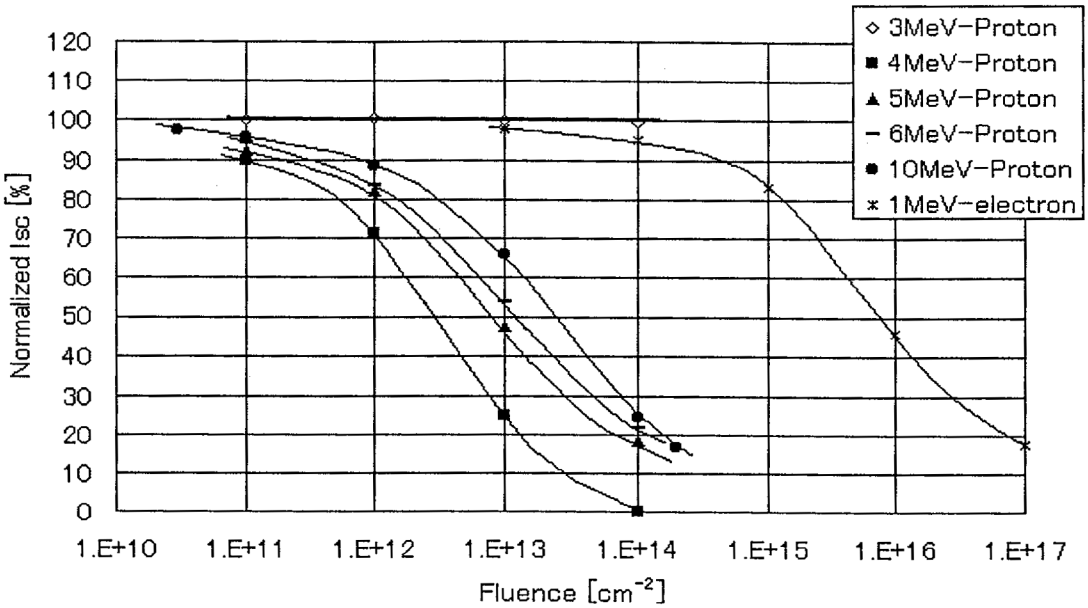

Figure7. Degradation characteristics of normalized Isc by irradiation from front surface

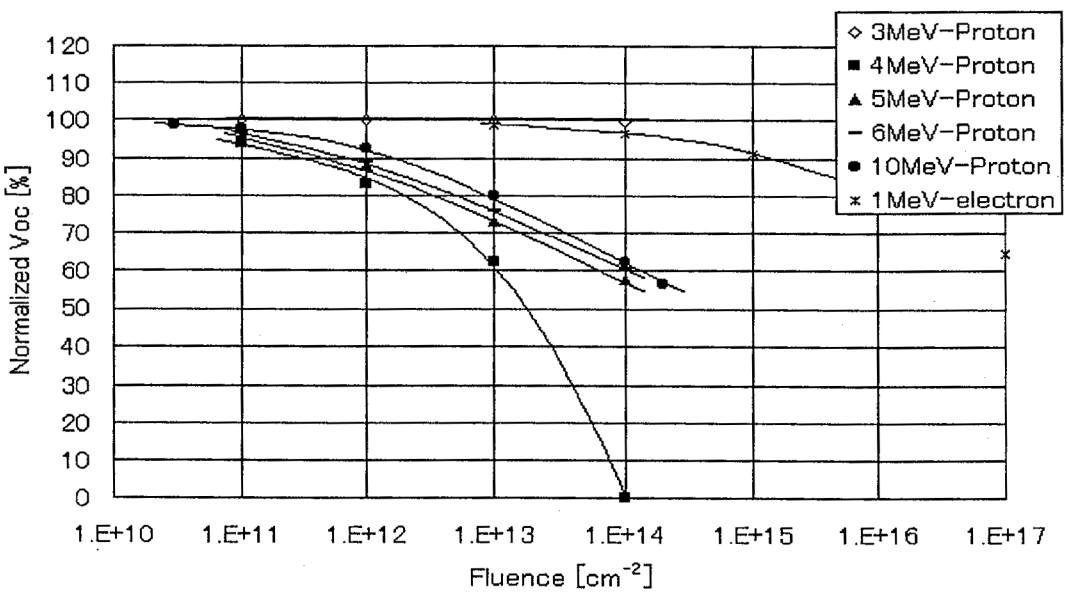

Figure8. Degradation characteristics of normalized Voc by irradiation from front surface

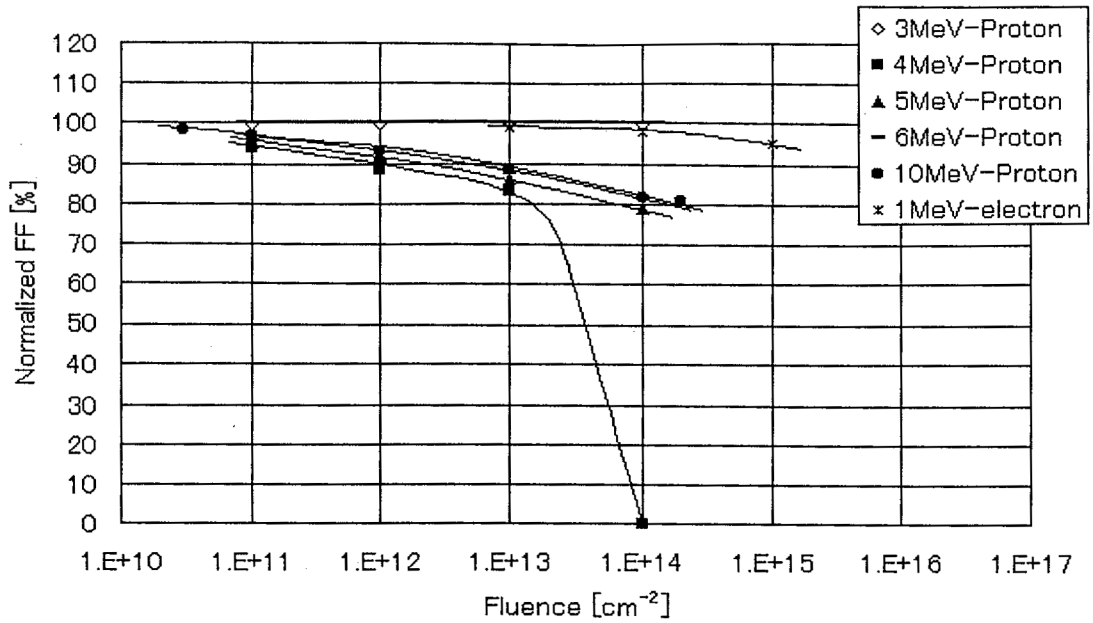

Figure9. Degradation characteristics of normalized FF by irradiation from front surface

In general, electron radiation damage is produced uniformly throughout the cell volume and the cell performance is strongly related with average diffusion length of the minority carriers[3,4,5]. But, the low energy proton damage is not uniformly throughout the cell volume. Thus, in order to analyze the cell degradation characteristics, it is necessary to examine the distribution of low energy proton damage in the cell. Thus, the TRIM code[6] was used in order to examine this distribution of the damage. Using the TRIM code, the production rate of Vacancy which was caused by proton irradiation were calculated. Figure10 shows this results in the case of irradiation from front surface of the cell. The vertical axis shows the production rate of Vacancy which was caused by the proton irradiation after it passed cover glass. That is to say, It shows that it puts on the value of vertical axis with irradiation proton fuluence for vacancy concentration. The quadrature axis shows the depth from the surface of cover glass. In this calculation, the cover glass thickness is 100[μ m]. And it was assumed that GaAs existed on the back of cover glass directly. It is not the accurate production rate, because the existence of the adhesive and the electrode are not considered in this calculation. However, it is able to think as a relative production rate at any point. In the 3[MeV] proton irradiation result in this figure we are able to observe the peak of production rate of vacancy in 80[μ m] from the surface of the cover glass. In short, it is not possible that all protons pass the cover glass of the 100[μ m] thickness, when the protons of under 3[MeV] energy were irradiated. Therefore, the characteristics were not degrade, when the protons of under 3[MeV] energy were irradiated. We are able to observe the peak of production rate at 120[μ m] from the surface of the cover glass, when the 4[MeV] protons were irradiated.

P-N junction of this GaAs solar cell exists in about 0.5 [μ m] from the surface of the GaAs layer. And the useful-light is absorbed effectively within about 5[μ m] from the surface of GaAs layer[7]. In short, the power is generated by electron-hole pare which created in less than 5[μ m] active region from the surface of the GaAs layer. In Figure5, the degradation by 4[MeV] protons irradiation is biggest, because the vacancy which the 4[MeV] proton makes concentrate in the active region of solar cell and the total of the vacancy in the active region was relatively largest in other energy.

Figure11 shows the distribution of production rate of vacancy which was caused by proton irradiation from the back surface of the cell. It is shown that the proton of 4[MeV] energy or less can seldom reach at the active region of solar cell. This result agrees with the result of the figure6.

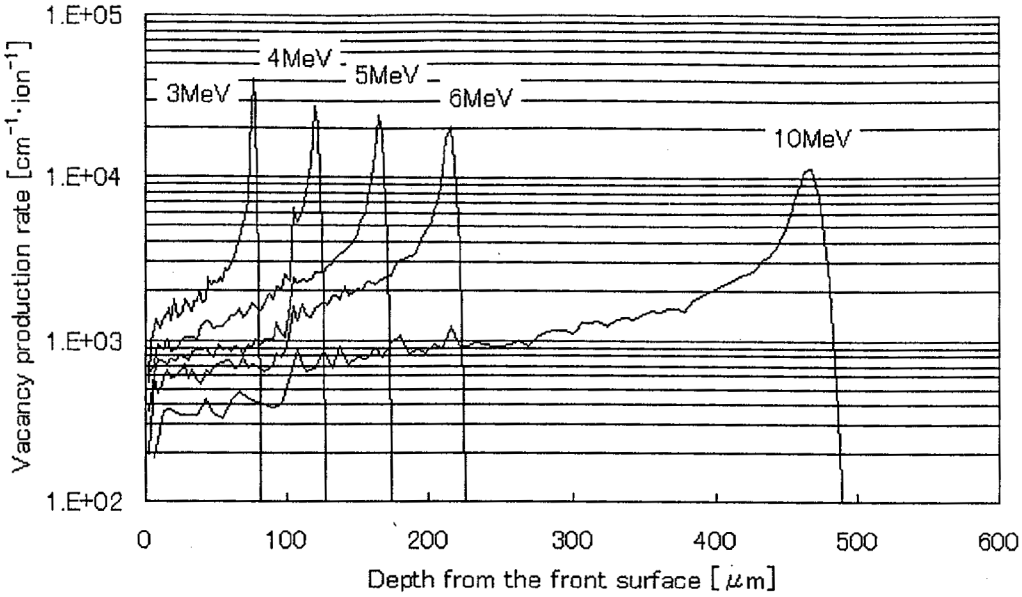

Figure10. The calculation results of vacancy conduction rate in the cell using TRIM.

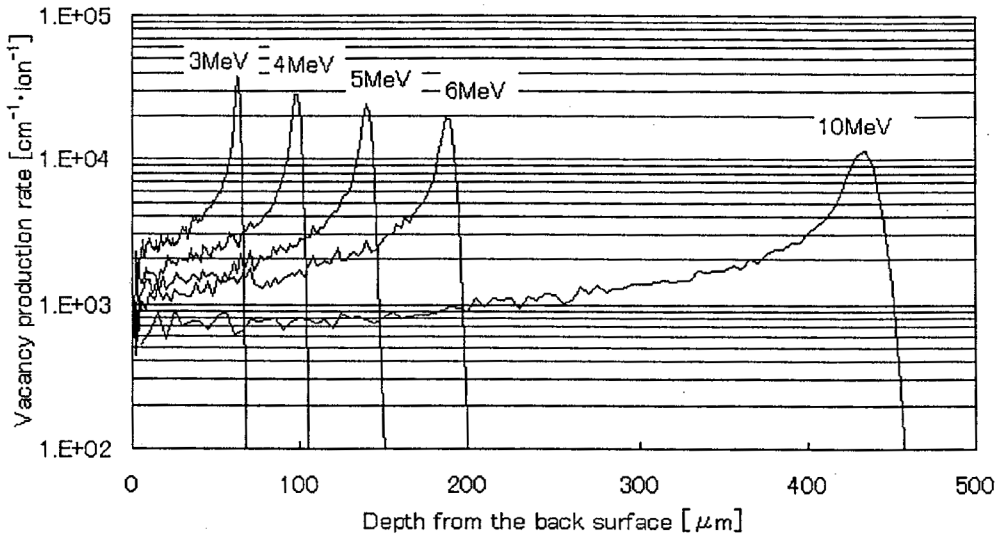

Figure11. The calculation results of vacancy conduction rate in the cell using TRIM.

It is difficult to compare the results of TRIM and experimental results, because the accurate position of p-n junction and the width of active region is not actually proven and because there is actually the electrode and the adhesive. However, it is proven that there is strongly correlation with the amount of vacancy in the active region and degradation characteristics of the cell.

When the region which contributes to the power generation is assumed 5[μ m] and it is assumed that the p-n junction exists in 110[μ m] from the cover glass surface, Figure12 shows the correlation between the amount of total vacancy in this region and the degradation of short circuit current. Though there is a

difference of gradient between each fluence, and it is shown that the good correlation exists in each fluence. In short, with the increase of the total number of calculated vacancy in this region, the short circuit current decreases. And this tendency is not dependent on the fluence. Figure13 shows the correlation between the amount of total vacancy and the degradation of maximum power. This figure shows the similar results.

In actual inside of the solar cell, generated defects move, and it were compounded, it is complicated. In present experiments, generation amount of actual vacancy and the defect type are not examined. And how generated defect functions as carrier traps or recombination center, is not examined. Further investigations are necessary to clarify this points. As actual defect four electron traps, Ec-0.24[eV], Ec-0.41[eV], Ec-0.51[eV], Ec-0.59[eV],caused by electron irradiation are reported[8].

By present experiments, it is proven that the degradation of the solar cell performance is explained by the amount of the calculated vacancy in the active region at vicinity of p-n junction.

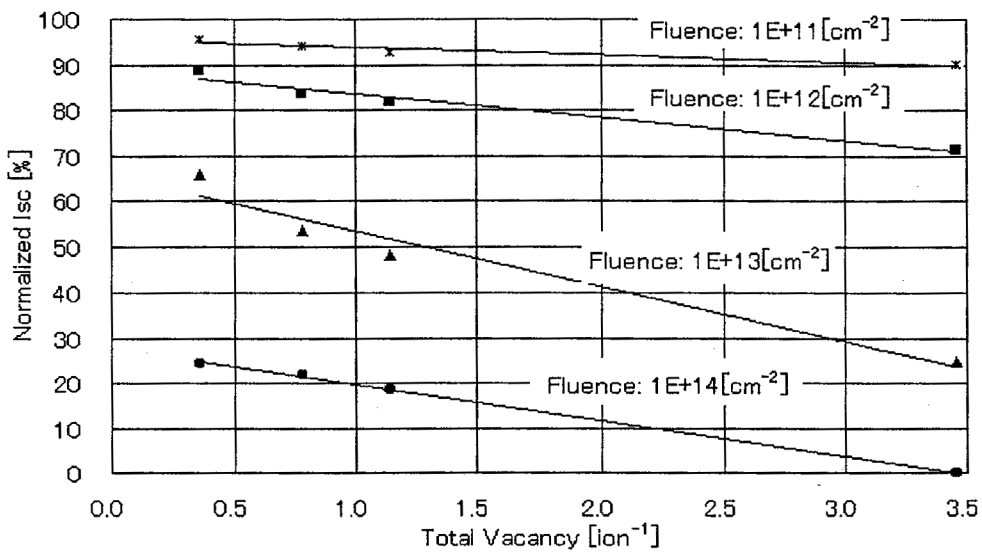

Figure12. The correlation between the total vacancy and the degradation of Isc.

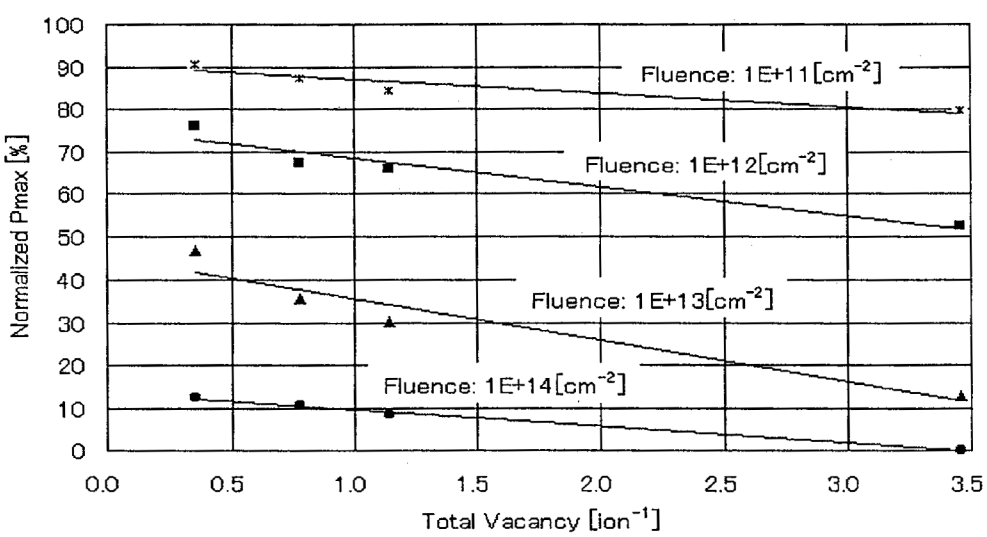

Figure13. The correlation between the total vacancy and the degradation of Pmax.

FLIGHT DATA

Figure14 shows the flight data of charge array. The vertical axis shows the generation current of this array. The continuous line is prediction of the current which the charge array generate in space on the basis of the superscription irradiation test results. And each point is the generation current of this array measured in space actually. This predictive current has not revised the temperature. The figure shows that the measured current agrees well with predictive current. Since the gradient of the satellite too increase, the disagreement between the predictive current and measured current of November 1998 occurred. Since the satellite severely inclined, a part of this charge array came to be in shadow. So the total generation current is reduced and this disagreement occurred.

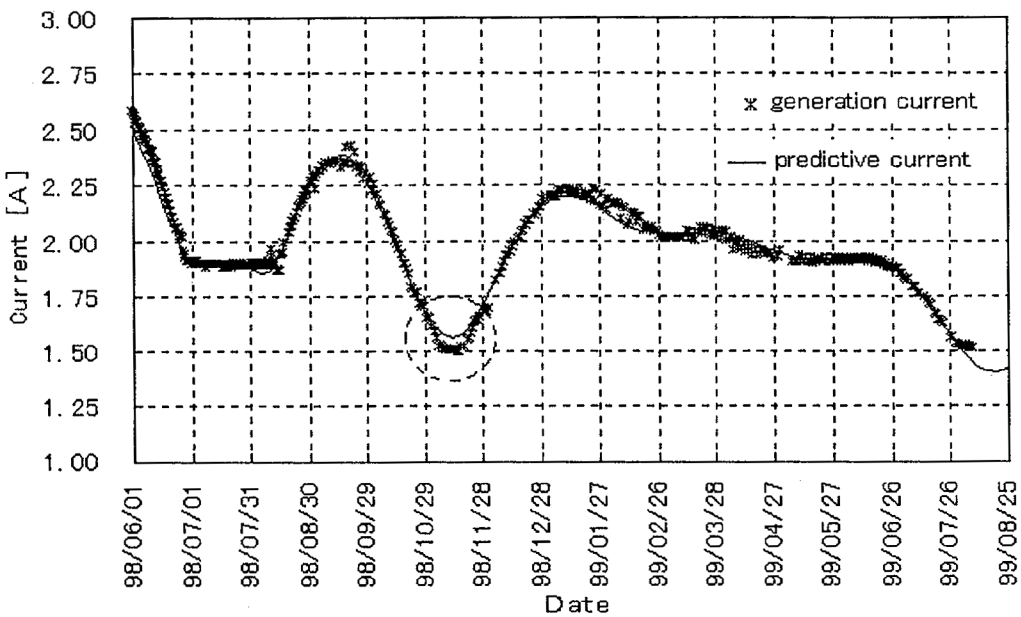

Figure14. Flight data of charge array.

CONCLUSIONS

By present experiment, next facts are clarified. By using the TRIM code, the degradation characteristics of the solar cell which is irradiated the proton of the various energy can be aptly explained. And there is strongly correlation with the amount of vacancy in the active region and degradation characteristics of the cell. Then proton irradiation test of the energy which makes the defect near the p-n junction are necessary in order to predict the degradation of solar cell in space. Especially, this examination is important, when the satellite which passes Van Allen belts is designed.

REFERENCES

[1] J. A. Van Allen, Geomagnetically Trapped Radiation, Space Science, J. Wiley & Sons, Inc., New York-London, (1963)

[2] Henry B. Garrett, Space Radiation Environment, 3rd International Workshop on Radiation Effects in Semiconductor Devices for Space Applications, p.82-88, (1998)

[3] Walker Gilbert H., Conway Edmund J., Short Circuit Current Changes in Electron Irradiated GaAlAs/GaAs Solar Cells, 13 IEEE Photovoltaic Specialists Conference, p.575-579, (1978)

[4] Walker Gilbert H., Conway Edmund J., Recovery of Shallow Junction GaAs Solar Cells Damaged by Electron Irradiation, J. Electrochem. Soc., Vol.125, no.10, p.1726-1727, (1978)

[5] Heinbockel J. H., Conway E. J., Walker G. H., Simultaneous Radiation Damage and Annealing of GaAs Solar Cells, 14 IEEE Photovoltaic Specialists Conference, p.1085-1089, (1980)

[6] J. F. Ziegler, Handbook of Ion Implantation Technology, Elsevier,Amsterdam, p.1-6, (1992)

[7] C. Hardingham, S. P. Wood, High Efficiency GaAs Solar Arrays in Space, GEC REVIEW, Vol.13, No.3, 163-171, (1998)

[8] Xiang Xianbi, Du Wenhui, Chang Xiulan, Lial Xianbo, Electron Irradiation and Thermal Annealing Effect on GaAs Solar Cells, Sol. Energy Mater. Sol. Cells,Vol.55, p.313-322, (1998)

IN-ORBIT PERFORMANCE OF HUGHES HS601HP DUAL JUNCTION $GaInP_2/GaAs/Ge$ SOLAR ARRAYS

Steven W. Gelb, Jay S. Fodor and Joseph S. Powe
Hughes Space and Communications Company
El Segundo, CA 90245

Abstract

Hughes Space and Communication Company's body-stabilized HS601HP communications satellites represent the first commercial spacecraft to utilize dual junction $GaInP_2/GaAs/Ge$ solar cells as their primary power source. The in-orbit electrical performance of four of these spacecraft has been monitored and compared to ground-based predictions. The predictions employ the as-built solar array configuration and electrical performance, the actual in-orbit radiation environment, and additional predicted environmental factors. Hughes' manufacturing and prediction methodology has led to agreement between the average telemetered and predicted power of ± two percent for these spacecraft.

Introduction

The Hughes HS601 class of satellites is one of the most popular commercial communications satellite series ever produced, with more than 70 spacecraft sold. The body-stabilized HS601HP ("high power") satellites discussed herein utilize solar arrays with dual junction $GaInP_2/GaAs/Ge$ solar cells as the primary power source. These solar arrays provide up to 10 kW of power in geosynchronous orbit. To date, Hughes has 9 HS601HP satellites in orbit, with a backlog of 6 satellites.

Hughes' ability to accurately predict the orbital performance of solar arrays combines four areas of solar array technology:

1) Standardized designs and fabrication practices
2) Accurate, controlled solar array performance testing on the ground
3) Accurate solar array modeling techniques and software
4) In-depth understanding of the space environment and its effects on solar cell performance

The purpose of this paper is to review the Hughes solar array prediction methodology and to summarize the utilization of this methodology in predicting the actual flight performance of HS601HP spacecraft. These ground-based predictions compare within ± two percent to the solar array telemetry data obtained from spacecraft in orbit. An overview of the HS601HP solar array design will also be presented.

HS601HP Solar Array Description

The HS601HP solar array is composed of two deployable wings (each with four rigid solar panels), a yoke and deployment mechanisms (Figure 1). The solar wings are stowed against the spacecraft bus during launch and

transfer orbit. During transfer orbit, power is supplied to the spacecraft from the exposed outer solar panels of each wing.

The solar array is designed for fifteen years of geosynchronous orbit operation and is customized for a 50-volt bus. The solar arrays described herein are populated with dual junction $GaInP_2$/GaAs/Ge solar cells, which provide primary power to the spacecraft. The solar cell characteristics are summarized in Table I. Reverse-bias damage of the GaAs solar cells due to potential on-station shadowing is prevented by integral bypass diodes mounted to the backside of every solar cell (1). Particulate radiation protection is provided by a ceria-doped microsheet coverglass with an antireflective coating on each of the solar cell assemblies. Conventional wire harnesses are used between the solar panels and from the inboard panel to the bus voltage limiter. The harnesses are configured to minimize resistive torques during solar wing deployments.

All solar cells and solar panels for the HS601HP solar arrays were manufactured by Spectrolab, Inc., a unit of Hughes Electronics Corporation. The solar arrays were designed, assembled, and tested at Hughes Space and Communications Company (HSC).

Prediction Methodology

Solar array performance predictions were generated using the HSC solar array prediction model (Figure 2). The model incorporates a large number of input variables to determine the electrical performance over the course of the mission life (2). These factors include the solar array circuit design, the array temperature, and the space radiation environment. Also used in the analysis are the detailed solar cell characterization data generated by Hughes. These data include the effects of radiation exposure, temperature, and angle of incident light on the solar cell current-voltage (I-V) curves.

The detailed design data for the solar arrays are used to generate predictions for the HS 601HP spacecraft. These data include the layout of the solar cell circuits on the panels, I-V curves for isolation diodes, and the estimated voltage drops due to the wiring on each panel and in the interpanel harnesses. The design data also include the predicted temperatures for each panel. Included in the analysis is the effect of shadows from other objects on the spacecraft that can degrade the performance of the solar array. For example, several of the HS 601HP spacecraft have antennas that shadow the inner solar panel during winter and summer solstice seasons. The prediction model includes the predicted nominal losses due to these shadows as a function of time.

Inputs to the power prediction model also include the space radiation environment. For the predicted pre-launch performance, the model uses the AE8 and AP8 trapped radiation environments (3), (4) and the 22nd solar cycle environment for solar flare protons. All radiation environments are reduced to a single equivalent 1 MeV electron fluence for each time in the mission. The fluxes from the trapped environments are assumed constant over time and are determined by the operational longitude of the spacecraft in geosynchronous orbit. After the spacecraft is in orbit, the actually experienced solar flare data (provided by the National Oceanic and Atmospheric Administration Space Environment Laboratory) are used to assess the model's accuracy.

A complete understanding of the effects of the space environment on the performance of the solar cells is critical to the accuracy of the Hughes prediction model. The details of the Hughes test methodology and the data accumulated are described in (5). The test program includes complete electrical characterization testing of the devices, radiation testing (including electrons, protons, and ultraviolet radiation), the radiometric properties that are used for temperature predictions, and mechanical testing, including thermal cycle testing and reverse-bias data.

The output of the prediction model is the solar array power as a function of time in orbit. The model determines the beginning-of-life (BOL) power from the LAPSS solar simulator electrical data. It then corrects the data for the predicted operating temperatures and sun angles using the characterization and design information. Characterization data and the radiation environment are then used to generate power predictions throughout the life of the spacecraft.

Comparison of Predicted and Telemetered Performance

The in-orbit telemetry data for the dual junction $GaInP_2$/GaAs/Ge HS601HP spacecraft were compared to telemetry-based power predictions. This comparison was performed to assess the accuracy of the prediction methodology using completely nominal inputs and excluding fluctuations in solar activity and any deviation from the expected spacecraft attitude.

The predicted power was determined using the Hughes prediction model and the actual solar flare data for the spacecraft being monitored. The telemetered power is determined by multiplying the telemetered solar array current and bus voltage. The solar array current is the sum of the bus current and the shunt current. The telemetered shunt current is corrected to the expected current at the bus voltage.

Solar Array Comparisons

Detailed comparisons of solar array telemetry and prediction have been performed on four HS601HP spacecraft employing dual junction $GaInP_2$/GaAs/Ge solar cells. Table II gives a summary of the HS601HP spacecraft designations, launch years, and average percentage deviations between telemetry and prediction. Also shown in the table is the average percentage deviation between telemetry and prediction for the group of four spacecraft.

Figure 3 shows the comparison data for HS601HP C1, which has been in orbit since 1997. In this case, the telemetered power is below the predicted power. The average difference between telemetry and prediction is -1.40 percent. The agreement between telemetry and prediction is closer early in life. After about one year in orbit, the two quantities differ more greatly. Figure 4 presents a plot of the percentage deviation between telemetry and prediction for HS601HP C1. The percentage deviation is always negative (i. e. telemetry is lower than prediction). The deviation becomes increasingly negative from launch through 1.5 years in orbit. Thereafter, it increases to a stable range.

Figure 5 details a cross-plot of telemetered and predicted power versus time in orbit for HS601HP K1. This spacecraft was launched in 1998. During the first half of the given time period, the telemetered power lies slightly above or nearly equal to the predicted power. After this point, the relationship between telemetry and prediction is reversed. The average deviation between telemetry and prediction is close to zero percent.

Figure 6 presents a comparison plot of telemetered and predicted power as a function of years in orbit for HS601HP F1. This spacecraft has been in orbit since 1998. The telemetered power begins higher than prediction, tracks prediction closely midway through the time interval, and falls below prediction at the very end of the interval. The average deviation between telemetry and prediction for this spacecraft is 0.40 percent.

Figure 7 details a cross-plot of telemetered and predicted power as a function of time in orbit for HS601HP D2. This spacecraft was launched in 1999. The telemetered power lies above the predicted power for the entire time interval. The average deviation between telemetry and prediction is 1.4 percent.

Uncertainty Analysis

The uncertainties in the in-orbit performance analysis are summarized in Table III. These uncertainties can introduce errors both in the predicted performance of the arrays and in the telemetered data. These errors have been categorized as either systematic or random. The systematic errors will affect the average values in the comparison study. The random errors, though important on a panel-by-panel basis, will not affect the average comparison results when a large number of spacecraft is analyzed (2).

The major systematic errors associated with the in-orbit predictions are found in the large area pulse xenon testing of each completed solar panel. The primary error sources are the balloon flight standards used to calibrate

the system and the calibration of the test equipment. The uncertainty due to the balloon standards is greater than ± 1% for GaAs solar cells, based on the available data. The other systematic error is associated with the calibration of the LAPSS solar simulator equipment for each panel measurement. This error is estimated to be ± 1%. The error applies to the individual panels being tested and should become a random error after many solar panels have been measured. This error still may be an influence in the dual junction cell panel data due to the relatively small measurement database that is presently available.

The systematic errors in the telemetry are found in the solar array voltages. The telemetered bus voltage of the spacecraft is used to determine the operating voltage of the solar array. This telemetry error is ± 0.02 percent. In addition, early in the mission life, significant power from the solar array is shunted through the bus voltage limiter electronics. There is an error of ± 0.2 percent associated with the conversion of this shunted current to the expected current at the bus voltage.

Based on the above uncertainties, the HS601HP solar array predictions are expected to agree with the telemetered data within ± 2 percent. To date, the agreement between telemetry and prediction for the HS601HP solar arrays falls within these limits.

Summary

The Hughes Space and Communications Company's manufacturing and prediction methodology has resulted in solar arrays which are performing as predicted for every HS601HP dual junction $GaInP_2$/GaAs/Ge cell spacecraft that was monitored. The average deviation between telemetry and prediction for these four spacecraft is 0.10 percent. This result is comparable to previous studies on Hughes satellites, which indicate an agreement within ± 2 percent between telemetry and prediction.

REFERENCES

(1) R. B. Dally, et al. "The Design, Qualification and Use of Bypass Diode Integration onto GaAs/Ge Solar Cells" Proceedings of the 25th IEEE Photovoltaic Specialists Conference (1996) 333-335.

(2) R. E. Daniel, et al. "In-Orbit Performance of HS376HP GaAs/Ge Solar Arrays", Proceedings of the 15th SPRAT Conference, NASA (1997) 154-161.

(3) J. I. Vette "The AE8 Trapped Electron Model Environment" NSSDC/WDC-A-R&S 91-24 (1991).

(4) D. M. Sawyer and J. I. Vette "AP8 Trapped Proton Environment for Solar Maximum and Solar Minimum" NSSDC/WDC-A-R&S 76-06 (1976).

(5) M. R. Brown, et al. "Characterization Testing of Dual Junction $GaInP_2$/GaAs/Ge Solar Cell Assemblies", Proceedings of the 26th IEEE Photovoltaic Specialists Conference (1997), 805-810.

Table I. HS601HP Solar Cell Description

Cover material	CMG
Shadow Protection	Integral bypass diodes

Table II. HS601HP Spacecraft Summary

S/C NAME	LAUNCH YEAR	% DIFFERENCE, TELEMETRY VS PREDICT
HS601HP C1	1997	-1.40
HS601HP K1	1998	0.01
HS601HP F1	1998	0.40
HS601HP D2	1999	1.40
AVERAGE DEVIATION		**0.10**

Table III. Uncertainty Analysis

Uncertainty in Telemetered Power		
Uncertainty	**Random/ Systematic**	**Estimated Error**
Bus voltage telemetry	Random	±0.02%
Bus current telemetry	Random	±0.50%
Shunt current telemetry	Random	±0.20%
Solar array voltage	Systematic	> -0.20%
Sun angle telemetry	Random	Negligible

Uncertainty in Predicted Power		
Uncertainty	**Random/ Systematic**	**Estimated Error**
LAPSS fluctuation	Random	±1%
LAPSS calibration	Systematic (per panel)	±1%
Balloon std accuracy	Systematic	±1%
Shadow pattern (21 June)	Systematic (per S/C)	±1%

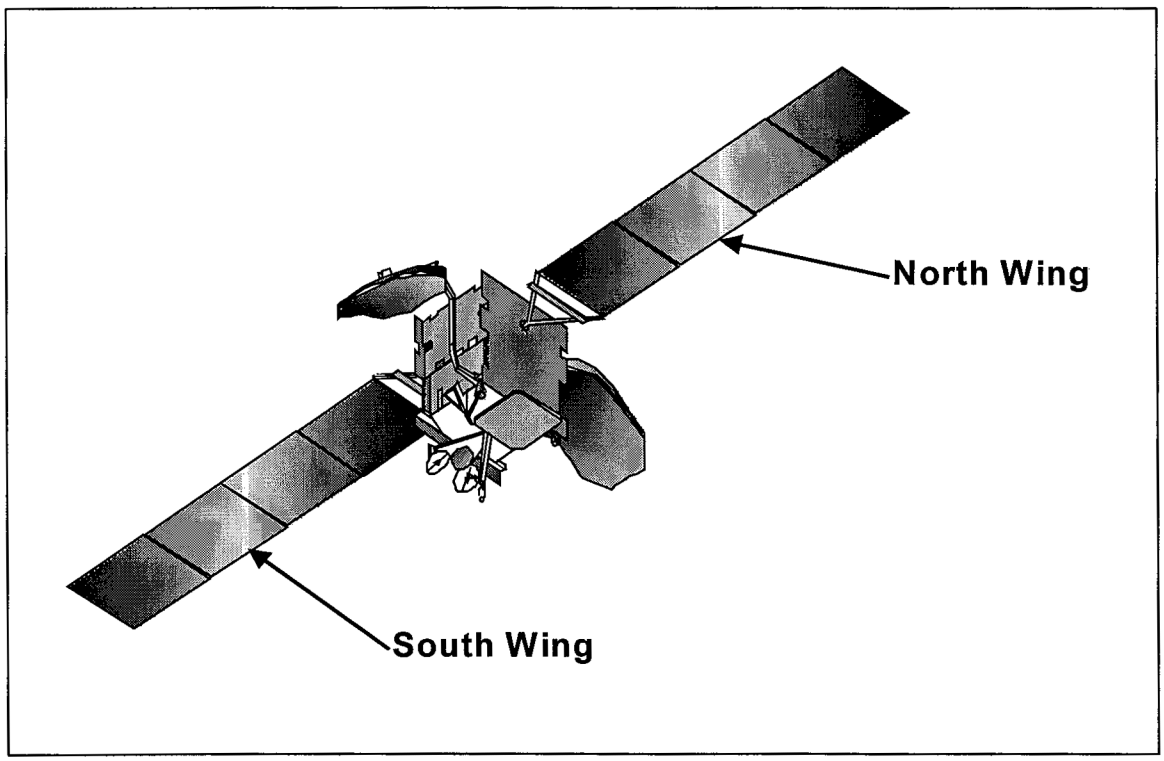

Figure 1. HS601HP Spacecraft Configuration

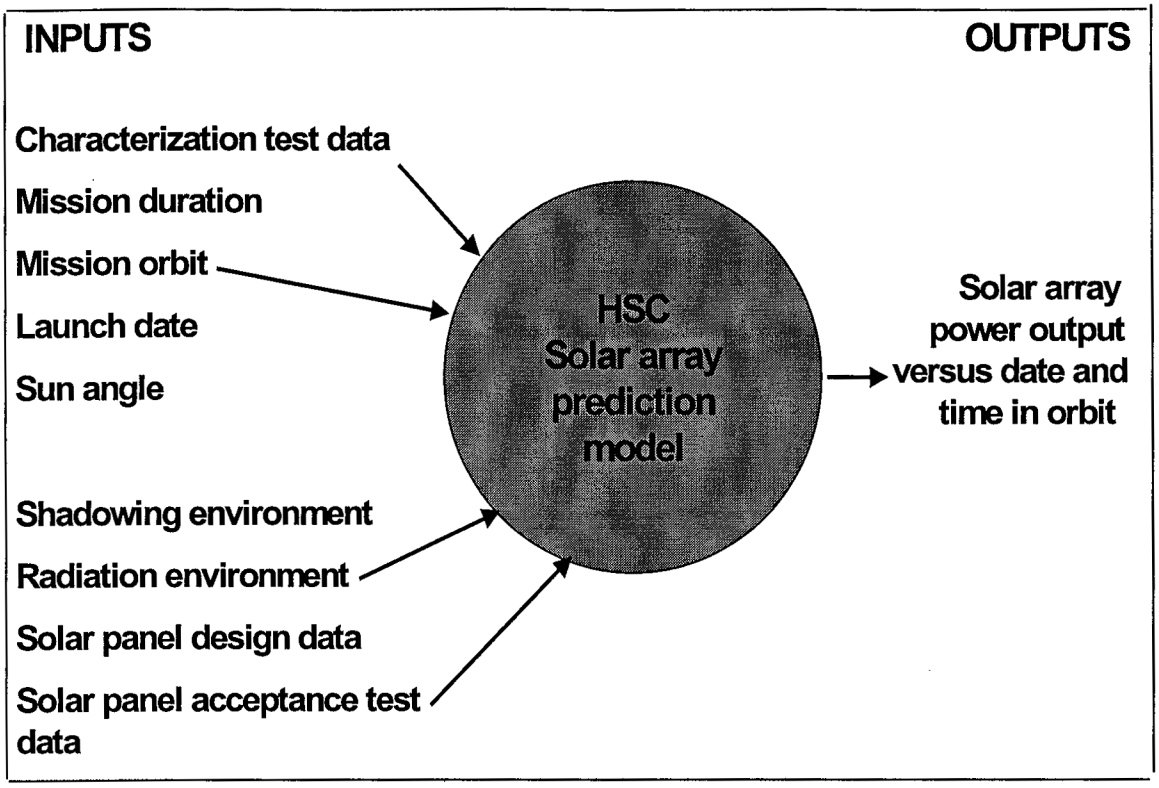

Figure 2. Hughes Solar Array Performance Prediction Methodology

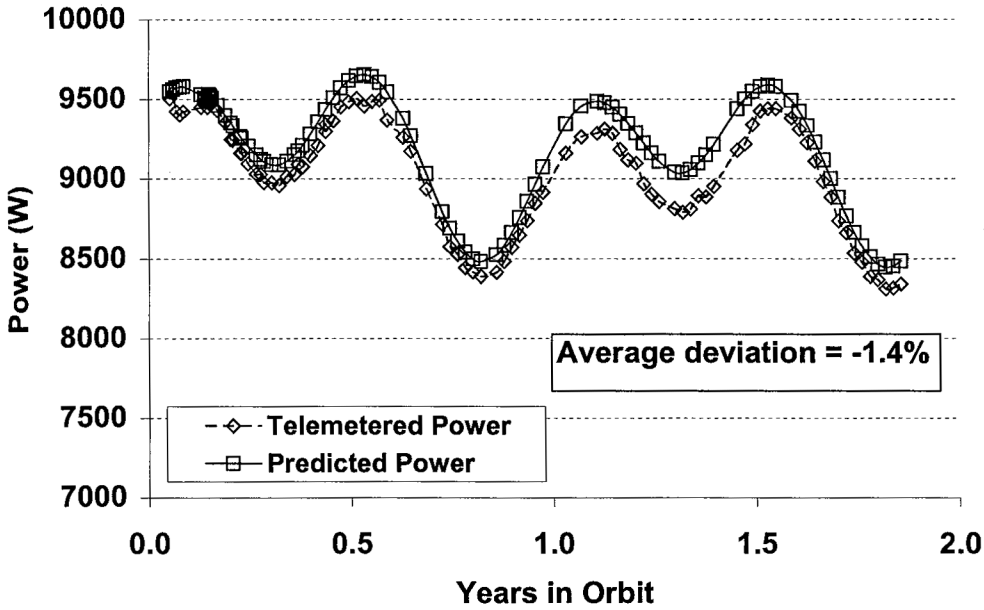

Figure 3. HS601HP C1 Solar Array Comparison

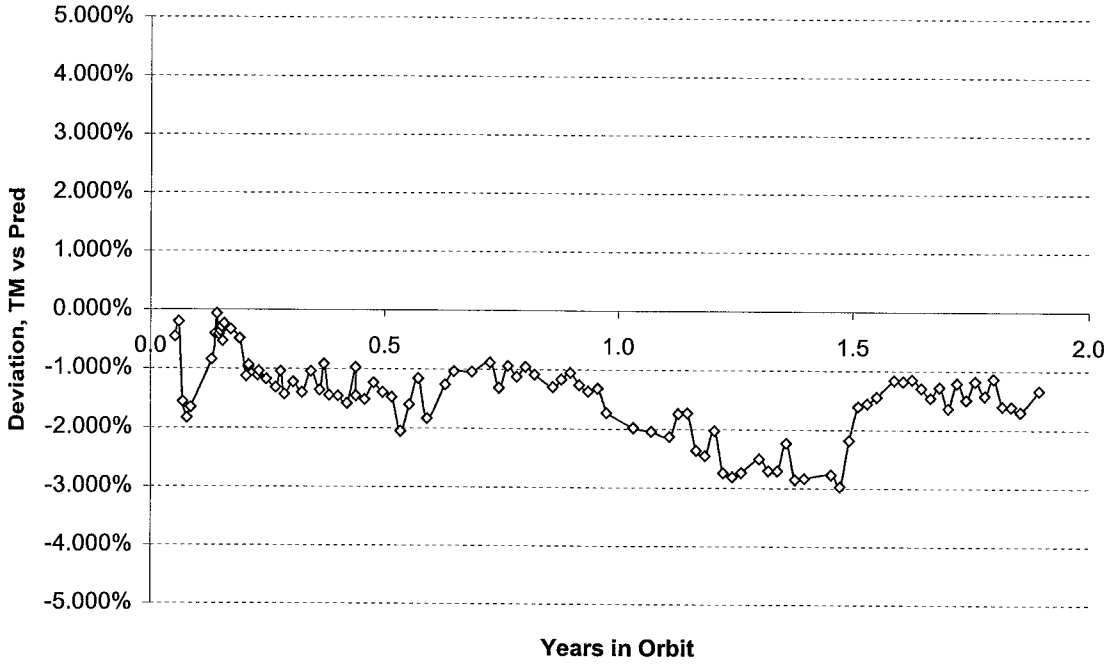

Fig 4. HS601HP C1 Telemetry vs. Prediction Deviation Plot

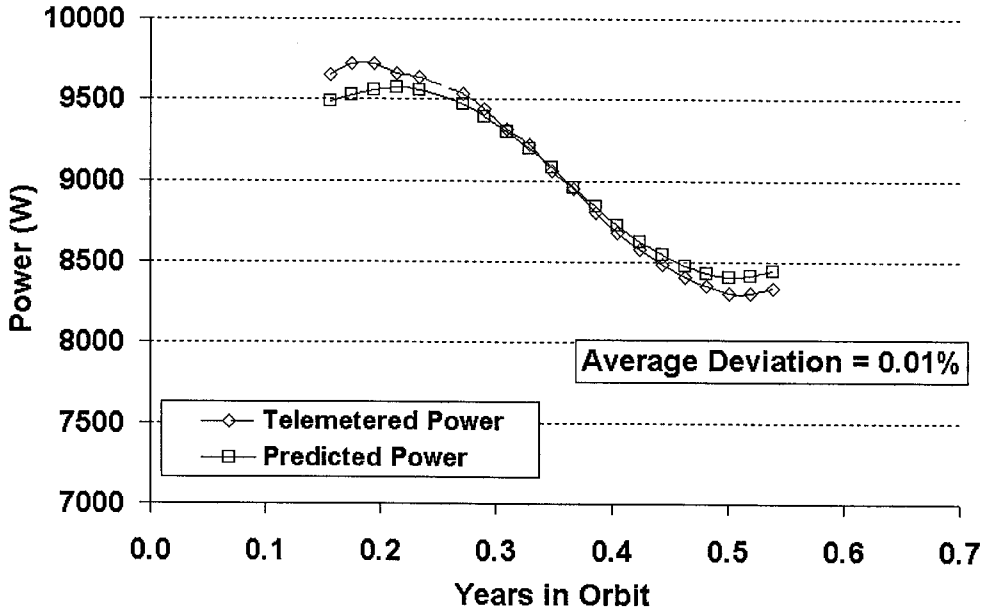

Figure 5. HS601HP K1 Solar Array Comparison

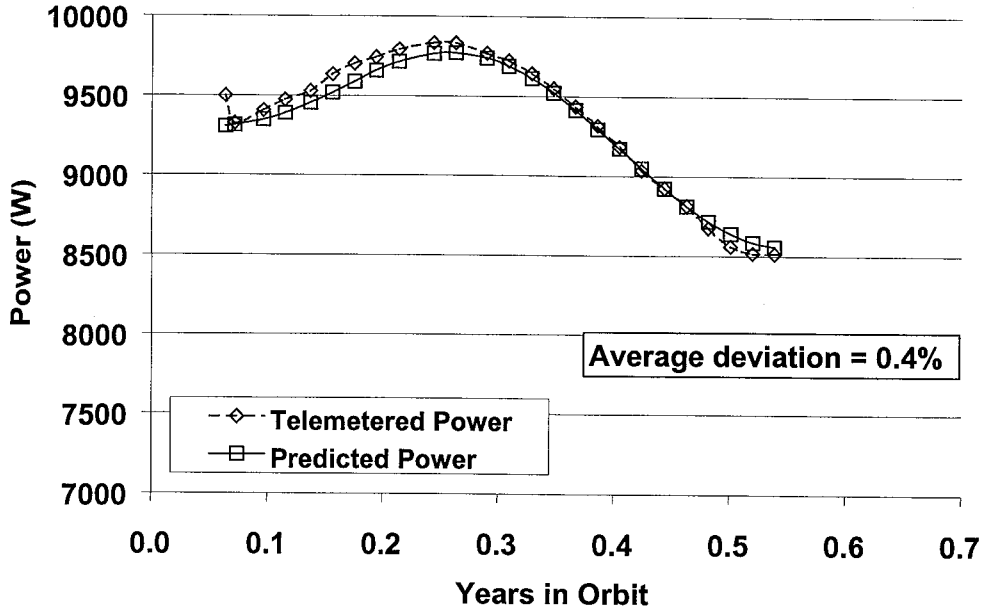

Figure 6. HS601HP F1 Solar Array Comparison

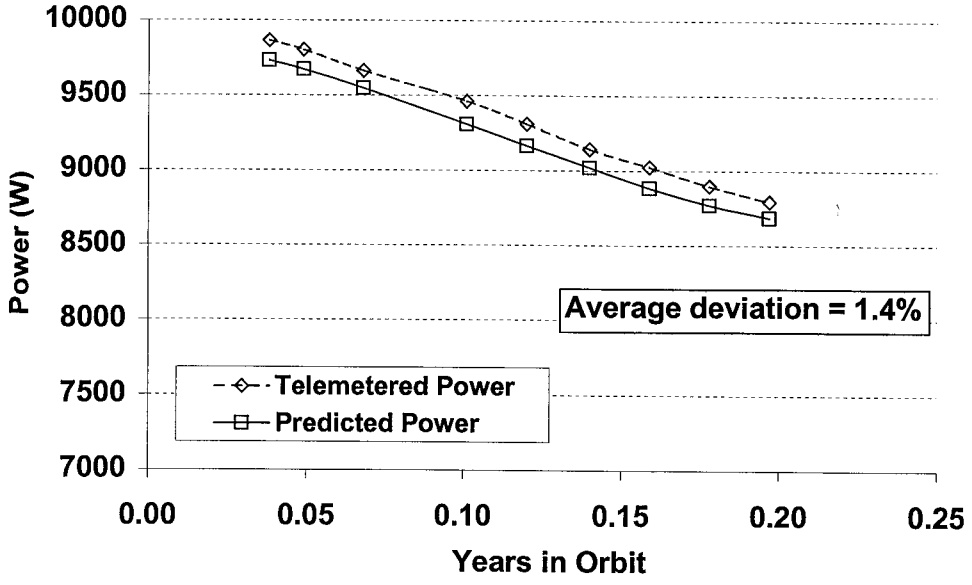

Figure 7. HS601HP D2 Solar Array Comparison

TECSTAR'S NEXT GENERATION CASCADE®® SOLAR CELL IMPROVEMENTS: A MONOLITHIC INTEGRAL DIODE AND NEW MIDDLE CELL FORMATION

Louis C. Kilmer, Charlie Chu, Milton Yeh, Peter Iles, P. K. Chiang, and Frank Ho
TECSTAR Inc.
City of Industry, CA 91745

Abstract

TECSTAR has developed several major improvements to its Commercial Cascade® multijunction solar cell throughout the early part of 1999, that when combined, increase the efficiency of the solar cells by 4.3% at beginning-of-life (BOL) and 10.4% at end-of-life (EOL). TECSTAR fully qualified and began production of its standard Commercial Cascade® multijunction solar cell in mid-1998 and early production achieved average efficiencies around 21.9%. By the end of 1998, this was improved to 23.0% and the path to even higher efficiencies was established and was aggressively pursued such that 24.0% fully reverse bias protected, radiation hard solar cells will be space qualified and available by the end of 1999.

Background

In 1992, TECSTAR began developing dual junction $GaInP_2$/GaAs/Ge solar cells. This was a direct extension of the patented single junction GaAs/Ge solar cell technology based on a common MOCVD structure in which the same manufacturing processes and procedures are applied to the higher efficiency cells. After successful space qualification testing, TECSTAR transitioned the dual junction solar cell from development to production in 1995. Early production average efficiencies were around 20.5% and through an improved wide bandgap tunnel junction, production average efficiencies increased to 21.5%.

Concurrently, TECSTAR began improving upon the dual junction solar cell performance by photovoltaically activating the GaAs/Ge bottom cell-to-substrate interface to create a third junction. These solar cells are grown and processed identically to the dual junction solar cells, producing higher efficiencies due to the contribution of the active Ge interface. The triple junction cell has now been standardized for low-cost, high-volume production and has supported significant customers and programs as shown in Table 1. Again, early development cells had an average efficiency of around 20.5%, early large volume production average efficiencies were around 21.9%, and more recent production average efficiencies are around 23.0%.

TECSTAR triple junction Cascade® solar cells leverage the experience and flight heritage of previously space qualified dual and single junction GaAs based solar cells. The design of the current production solar cell has been previously reported.[1] Solar cell, CIC, and GEO coupon space qualification testing was successfully completed (LEO coupon testing is continuing). Table 2 summarizes the qualification test program and limits.[2] Qualification of the mechanical properties of the solar cells (humidity, weldability, contact pull test, optical properties, and angle of incidence) was low risk through similarity to previous space qualification testing and on-orbit flight operation. However, due to the added active interface third junction, electron and proton radiation tests were repeated to provide accurate data. In addition, a reverse bias protection bypass diode was implemented at the CIC level. The present $GaInP_2$/GaAs/Ge solar cells require a bypass diode to protect the cell during reverse bias conditions (such as solar array shadowing). Without the bypass diode, even small amounts of reverse bias can catastrophically degrade the performance of the cell by creating shunt paths through the active junctions.

[1] F. Ho et. al., "Production Experience with 3rd Generation Space Solar Cells/Arrays", IEEE Photovoltaic Specialist Conference, 1998.
[2] E.B. Linder and L. C. Kilmer, "Cascade Solar Power System Benefits, Heritage, Status and Plans", AIAA Space Technology Conference and Exposition, 28-30 September 1999.

TECSTAR's patented triple junction Cascade® cells are protected by a discrete silicon bypass diode that is mounted on the front surface of the solar cell in a novel way (patent pending). Although putting the diode on the front of the solar cell reduces the light active area, and therefore the solar cell efficiency by 1.8%, the higher yield, improved CIC manufacturing approach increases the overall value of the cell in terms of dollars per watt. By placing both of the diode connections on the top of the cell, the entire diode mounting, interconnecting, and coverglass application can be easily automated for low cost, high volume manufacturing. The solar cell does not need to be flipped to attach any leads to the back of the solar cell. Figure 1 shows the top view of TECSTAR's standard triple junction Cascade® CIC (coverglassed-interconnected-cell). This diode configuration enabled thermal soaking and cycling to be successfully performed as part of the qualification program. The CIC drawing provided in Figure 1 shows the location of the interconnects and bypass diode assembly. The diode is bonded to the solar cell for efficient thermal transfer and is sized to operate reliably under all expected environmental conditions.

TECSTAR currently manufactures 24.5% peak efficiency Cascade® solar cells using a standard 24.3 cm^2 area cell configuration with over 150,000 solar cells produced since 4Q98. This performance would increase to 24.9% if the area set aside for the bypass diode was replaced with active cell layers (an option if external bypass diodes are utilized). A 23.1% minimum average efficiency was attained for 80,000 of these standard production cells and represents current capability. All work is performed within a 150,000 ft^2 factory in Southern California featuring state-of-the-art, high-throughput semiconductor manufacturing equipment. Present TECSTAR capacity is 380 kW annually. Cell and CIC electrical and mechanical characteristics are provided in Table 3. Table 4 provides the electrical data on a representative sample of present technology standard CICs. Standardizing the solar cell configuration minimizes cost and several qualified coverglass thickness (100-500 μm) and coating (AR, AR/UVR, AR/ITO) options are available.

Table 1: *TECSTAR Cascade® Solar Cells Were Flown in 1998*

Customer/ Program	Delivery	Status	# Cells Produced	Cell Size (cm x cm)	Junction Topology	Ave. Cell Eff. @ AM0
NASA MSFC	Jun-95	Ground Test Coupon	20	2 x 4	2J	20.5%
NASA SSTI Clark	Sep-95	Program On-Hold	~100	4.8 x 4 / 2 x 4	2J/3J	20.6%
NASA TRACE	Dec-95	On-Orbit (4/98)	4	2 x 2	3J	22.4%
NASA LEWIS	Dec-95	Failed to Reach Orbit	6	2 x 2	3J	21.9%
USAF Mightysat 1	Mar-96	On-Orbit (12/98)	~100	2 x 2	3J	21.8%
NASA Deep Space 1	Jan-98	On-Orbit (10/98)	3,900	1 x 4 (conc.)	2J/3J	21.8%
NASA SMEX (Wire)	Jan-98	On-Orbit (3/99)	120	2 x 4	3J	22.6%
Classified	Various	Classified	Classified	4.8 x 4	2J	20.5-21.5%
NASA EO-1	Dec-98	Will Launch Late 1999	100	4 x 6	3J	22.0%
Telecomm Sat's	On-Go Prod	First Launch End 1999	>100,000	4 x 6	3J	23-24%
NASA NANOSAT	Dec-98	Program On-Hold	60	4 x 6	3J	22.5%
NASA STRV	Jun-99	Panels Delivered	200	4 x 6	3J	22.0%
DERA STRV	Jun-99	Panels Delivered	900	4 x 6	3J	22.0%
ORBVIEW 3	4Q99	In Process	1,300	4 x 6	3J	23.0%
ORBVIEW 4	4Q99	In Process	1,250	4 x 6	3J	23.0%

Table 2: TECSTAR Cascade® Solar Cells, CICs and Panels are Space Qualified

Test	Condition
Electron Radiation/ Temperature Coefficient	1 MeV, $5x10^{13}$ to $1x10^{16}$ e/cm^2, 28 °C to 95 °C
Proton Radiation	200 keV to 10 MeV, $3x10^{10}$ to $1x10^{13}$ p/cm^2
Relative Humidity (Cell and CIC)	95% at 45 °C for 30 Days
Weldability (pre and post-RH)	<2% I_{load} Loss
Contact Pull (Cell and CIC)	>150 gram @ 45° Pull, >300 gram @ 0° Pull
Cell Solar Absorptance	<0.91 over 0.28 to 2.5 mm
Bypass Diode	Electron/Proton, Contact Pull, Humidity, Thermal Cycling
CIC Optical Properties	for UVR/AR, AR and ITO/AR Coverglass
CIC Angle of Incidence	0° to 80° Sun Angle
CIC UV Radiation	550 Sun-Hours at 1-Sun AM0
CIC Thermal Cycle and Soak	3,000 Cycles, -175°C to +100°C, +150 °C Soak
CIC Shadow Tolerance	1.22 x Isc @ 100°C, 20 minutes
CIC Reverse Bias Voltage	3,000 RBV Cycles @ 10^{-5} Torr, 80 °C
String Reverse Bias Voltage	3,000 RBV Cycles @ 10^{-5} Torr, 135 °C
GEO Coupon	3,000 Thermal Cycles -175°C to +150°C
LEO Coupon (in process)	20,000 Thermal Cycles -100°C to +110°C

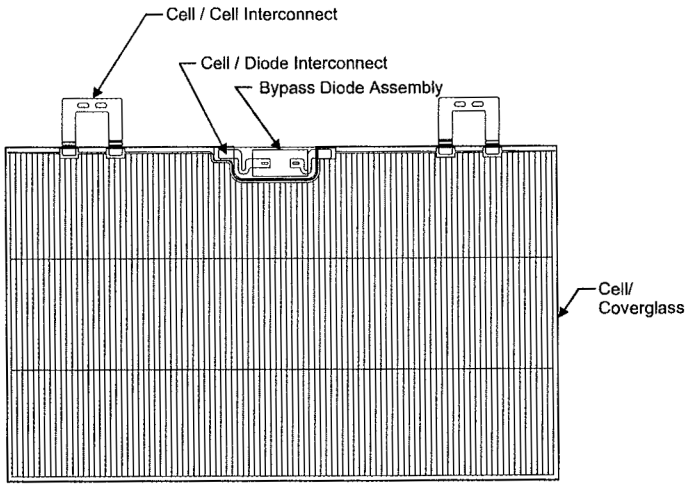

Figure 1: *3.85 cm x 6.32 cm Area Cascade® Cover-Interconnect-Cell (CIC) with Bypass Diode Protection*

Table 3: *Performance Characteristics of Current TECSTAR Cascade® Production Solar Cells*

Cover Interconnect Cell (CIC)		
Area (defined by coverglass) cm^2		3.85 x 6.32 or 24.33
CIC (gms)		3.06
Bypass diode		yes
Interconnects		2/CIC, horseshoe, Ag-Invar, welded
Coverglass adhesive		DC-93500
CIC efficiency @ BOL, 28°C (w/diode)		24.1%
electrical parameters, BOL		
	Voc (V)	2.515
	Isc (A)	0.382
	Vmp (V)	2.183
	Imp (A)	0.363
	Cff (%)	82.5
	Pmp (W)	0.792
CIC Efficiency after 1.0E15 1MeV e-/cm^2		18%
Coverglass		
Thickness (μm)		152
Coating/material		AR/ITO
Bypass diode assembly		
Diode type		p-n silicon
Interconnects		Ag-Invar, welded
Solar cell		
Cell thickness (μm)		140
Cell area (cm^2)		24.3
Temperature coefficients, BOL		
	Voc (%/C)	-0.213
	Isc (%/C)	0.052
	Vmp (%/C)	-0.241
	Imp (%/C)	0.037
	Pmp (%/C)	-0.208

Table 4: *A Representative Sample of Present Technology Cascade® CICs*

TEC1 Cascade Solar Cell CIC With 6 Mil AR/ITO Glass(24.3 cm^2)								
Fab. Lot	Cell ID	Voc (mV)	Isc (mA)	I2.12 (mA)	Vmp (mV)	Imp (mA)	CFF (%)	AMO Eff (%)
1182	2	2511.8	378.3	368.8	2167.0	363.3	82.9	24.0
1182	6	2518.9	384.9	370.6	2175.0	362.8	81.4	24.0
1182	9	2518.2	384.2	369.9	2174.0	362.9	81.5	24.0
1182	11	2514.4	382.1	368.4	2149.0	365.0	81.6	23.8
1182	13	2508.9	384.0	368.2	2166.0	362.0	81.4	23.8
1182	14	2521.8	381.3	371.2	2177.0	364.5	82.5	24.1
1182	15	2511.5	383.2	368.0	2168.0	362.0	81.5	23.9
1182	16	2524.6	384.2	372.3	2180.0	365.0	82.0	24.2
1182	20	2519.5	382.3	368.4	2175.0	361.8	81.7	23.9
1183	1	2510.0	377.6	369.5	2188.0	361.5	83.5	24.0
1183	4	2520.1	381.9	371.0	2175.3	364.9	82.5	24.1
1183	6	2518.0	380.4	369.5	2195.0	360.7	82.7	24.1
1183	9	2516.5	381.7	371.3	2214.6	359.0	82.8	24.2
1183	10	2525.6	382.9	374.9	2202.0	365.5	83.5	24.5
1183	11	2518.7	381.9	370.8	2196.0	361.0	82.4	24.1
1183	12	2521.3	381.3	372.0	2177.0	366.0	82.9	24.2
1183	13	2513.6	380.0	371.5	2191.0	363.4	83.4	24.2
1183	14	2508.2	379.9	370.0	2187.0	361.2	82.9	24.0
1183	15	2502.2	380.1	370.4	2181.0	363.1	83.3	24.1
1183	16	2508.5	379.6	370.7	2187.0	362.6	83.3	24.1
1183	17	2510.6	379.5	370.2	2189.0	361.4	83.0	24.1
1183	20	2515.9	381.1	371.5	2193.0	362.6	82.9	24.2
1183	21	2503.8	382.3	369.4	2183.0	360.0	82.1	23.9
1183	22	2520.6	381.3	372.1	2197.0	362.7	82.9	24.2
1183	24	2520.9	383.0	372.9	2176.0	366.3	82.6	24.2
	Average	2515.4	381.6	370.5	2182.5	362.8	82.5	24.1

Solar Cell Improvements: A Monolithic Integral Diode

To improve upon the performance and cost of the Cascade CIC manufacturing, TECSTAR has developed a monolithic integral bypass diode that is formed by growing additional InGaAs layers during the MOCVD process and subsequent photolithography patterning, and reduces the overall area required for the diode by 56%. This novel approach (patent pending) offers a very high reliability, lower cost method of diode protection while increasing the solar cell efficiency by 1.0% (0.25% absolute).

Figure 2 shows the top view of the monolithic integral diode and the overall CIC configuration. The top contact to the bypass diode is connected to the bottom contact of the solar cell by using a silver plated Invar jumper welded to a metalized pad on an exposed area of Ge (a via is etched through the MOCVD grown layers identically to the patent pending method created for discrete bypass diode configuration as shown in Figure 1). Figure 3 shows a cross sectional view of the same device.

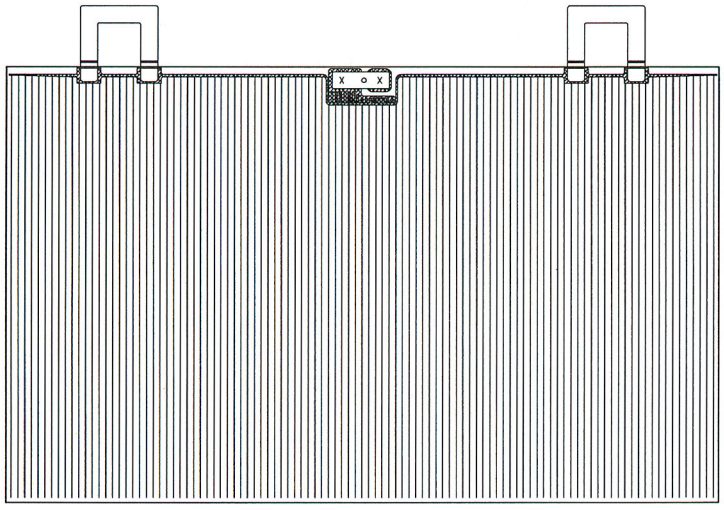

Figure 2: *Top View of the Monolithic Integral Diode Cascade® CIC*

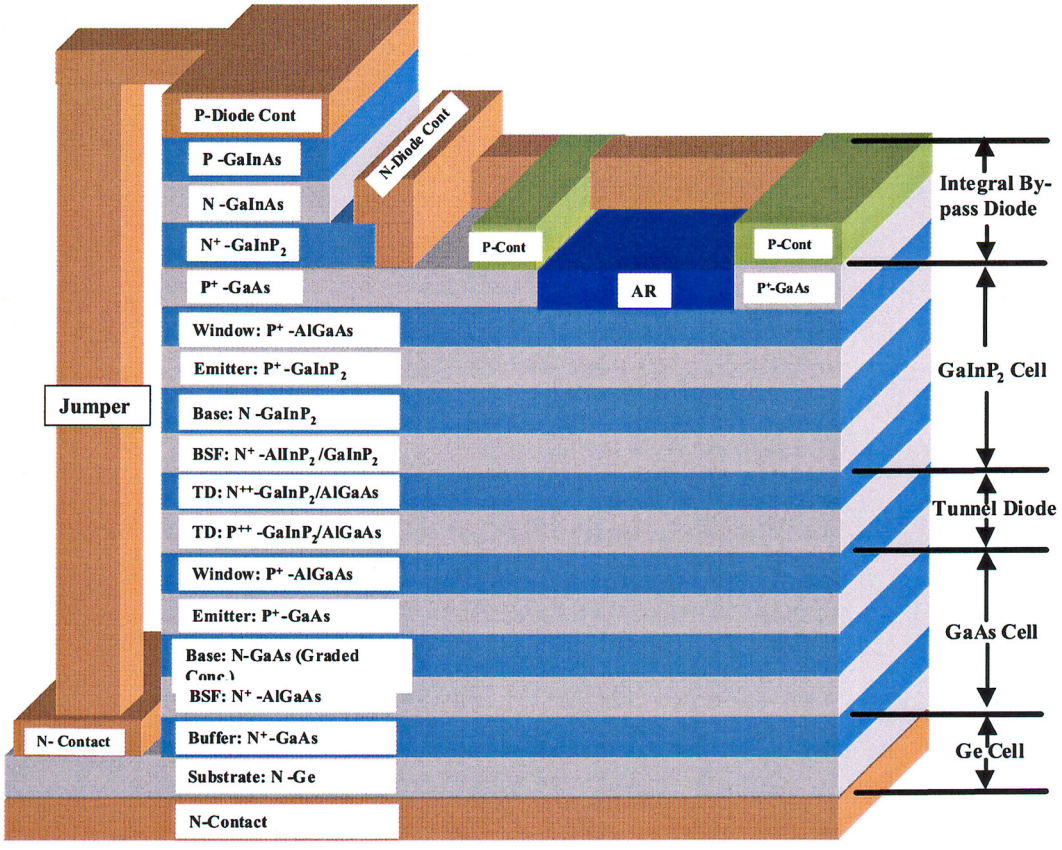

Figure 3: *Side View of the Monolithic Integral Diode Cascade® CIC*

The monolithic integral diode protected Cascade® cell is now undergoing full space qualification testing (same tests as those listed in Table 2). However, the monolithic integral diode successfully completed all preliminary

tests prior to initiating the qualification testing. These preliminary tests showed a comparable (to the discrete Si bypass diode) temperature increase in the diode at 400 mA (1.1 times Isc) dark reverse current. This test was performed in both ambient and vacuum conditions. In addition, no electrical performance degradation was observed in the diode after 1E15 1 MeV e^-/cm^2. Also, no degradation in cell performance was observed after a 3,000 dark reverse cycle test at a current of –1.1 times the short circuit current at 80 °C in vacuum.

TECSTAR expects that the monolithic integral diode will pass all space qualification tests, after which the design will be transitioned to large volume production. This diode configuration is expected to become TECSTAR's standard Cascade® cell/CIC configuration for all applications.

Solar Cell Improvements: New Middle Cell Formation

Higher BOL Efficiency

The present solar cell design was frozen back in April of 1998 and therefore represents about 2 year old technology. Since the technology was frozen, a continuous research and development program investigated improved cell designs to increase the overall efficiency. This program resulted in several world record setting efficiency milestones including 25.8% in May 1998, 26.1% in August 1998, 26.4% in June 1999, and 27.0% in July 1999. Figure 4 shows the I-V curve for the best cell efficiency to date. This cell performance was achieved in a small production lot that had several cells with efficiencies at the 27% level and an average of near 26.5%.

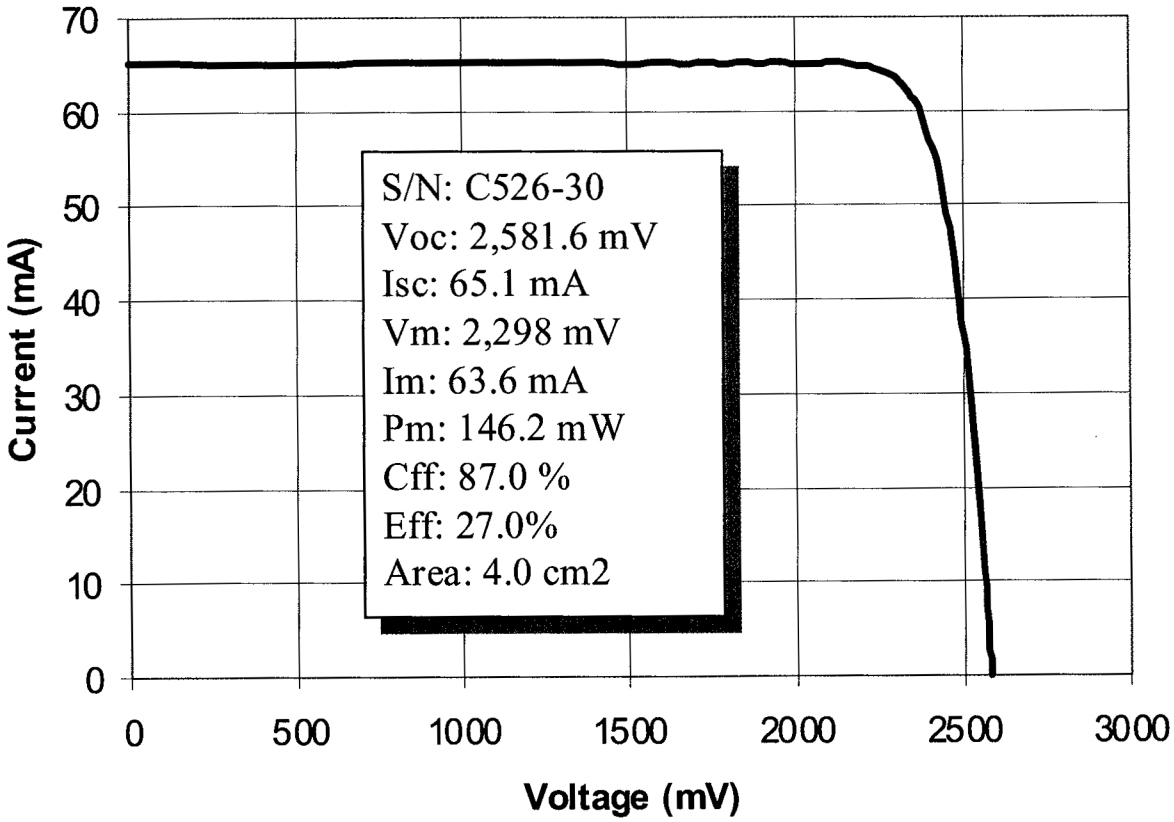

Figure 4: *Best Cell Performance to Date*

The solar cell performance increase is a result of a higher current from the GaAs subcell, a higher voltage from the Ge heterojunction subcell, and a higher overall fill factor. The higher current from the GaAs subcell results from the drift field created in the base layer and the back surface field (BSF) at the bottom of the cell. The higher voltage from the Ge heterojunction subcell was achieved by optimizing the initial growth conditions inside the MOCVD reactor and the quality of the initial GaAs layers. The higher fill factor is a result of reduced series resistance and the overall quality improvement of all grown layers. These cell design changes have undergone small production validation tests to insure that the cell efficiency improvements will be realized in large volume, multiple reactor production, and do not simply represent the upper spectrum of a production yield curve. These cell design changes have been implemented in our standard, full size Cascade® cell design and are presently going through full space qualification testing. Table 5 shows the overall performance achieved on multiple small production lots of 2 cm x 2 cm solar cells using the improved cell structure.

Table 5: *Production Lot Data Using the New Cell Structure*

Cell ID	Voc (mV)	Isc (mA)	IL (mA)	Vm (mV)	Im (mA)	Cff (%)	Eff (%)
27	2579.1	63.0	62.6	2295.0	61.2	86.4%	26.0%
29	2565.6	62.3	62.1	2263.0	60.7	85.9%	25.4%
9	2560.2	63.4	63.3	2278.6	61.3	86.1%	25.8%
16	2573.3	63.5	62.6	2290.0	60.5	84.8%	25.6%
28	2575.8	63.8	63.2	2292.0	61.3	85.5%	26.0%
26	2571.1	63.9	63.4	2288.0	61.6	85.8%	26.0%
11	2563.4	64.1	63.7	2281.0	61.9	85.9%	26.1%
37	2563.2	63.9	63.4	2281.0	61.7	85.9%	26.0%
7	2562.9	64.2	64.2	2281.0	62.1	86.1%	26.2%
15	2577.4	64.1	63.6	2314.0	61.2	85.7%	26.2%
21	2557.4	64.3	63.9	2256.0	62.0	85.1%	25.8%
35	2550.0	64.0	63.7	2228.0	61.9	84.5%	25.5%
36	2558.5	64.2	64.0	2277.0	62.1	86.1%	26.1%
12	2558.6	64.4	63.9	2277.0	61.6	85.1%	25.9%
4	2567.5	65.6	65.4	2243.0	63.9	85.1%	26.5%
22	2542.9	64.6	63.7	2263.0	61.2	84.3%	25.6%
8	2564.5	64.8	64.8	2283.0	62.2	85.5%	26.2%
18	2568.8	65.0	65.0	2266.0	63.3	85.9%	26.5%
39	2541.6	64.6	64.4	2242.0	61.7	84.3%	25.6%
17	2574.1	65.4	65.3	2270.0	63.6	85.8%	26.7%
38	2561.3	65.1	64.8	2279.6	62.2	85.0%	26.2%
24	2550.7	65.5	63.7	2250.0	61.1	82.3%	25.4%
1	2568.2	66.0	65.1	2265.0	63.3	84.6%	26.5%
20	2563.4	65.8	64.7	2281.0	62.0	83.8%	26.1%
3	2547.5	65.9	65.2	2226.0	62.7	83.1%	25.8%
AVG	**2562.7**	**64.5**	**64.0**	**2270.8**	**61.9**	**85.1%**	**26.0%**

Higher Radiation Tolerance/Increased Radiation Resistance

As mentioned above, the improved solar cell structure incorporates a drift field in the GaAs base layer and a back surface field at the back of the GaAs cell. These cell design features not only increase the BOL efficiency of the cell, but they increase the EOL performance as well. Figure 5 shows a cross section view of the present cell structure and Figure 6 shows the cross section view of the improved performance cell structure that highlights the drift field and BSF.

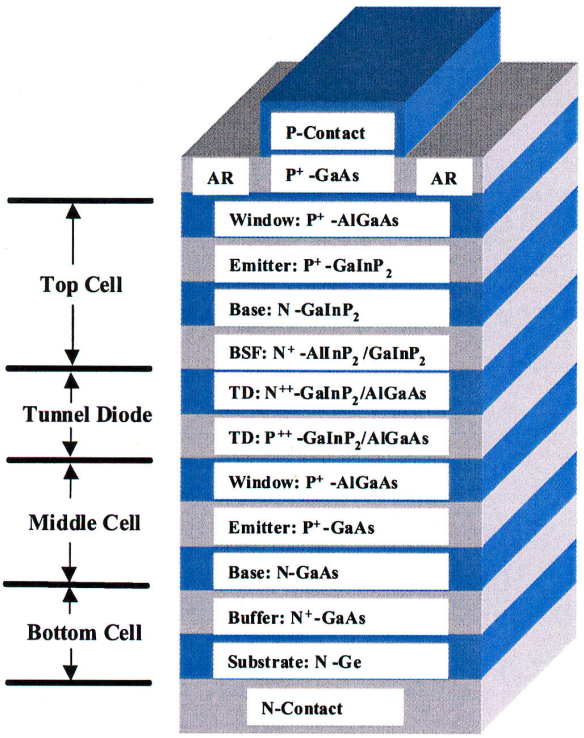

Figure 5: *Present Cascade® Cell Structure*

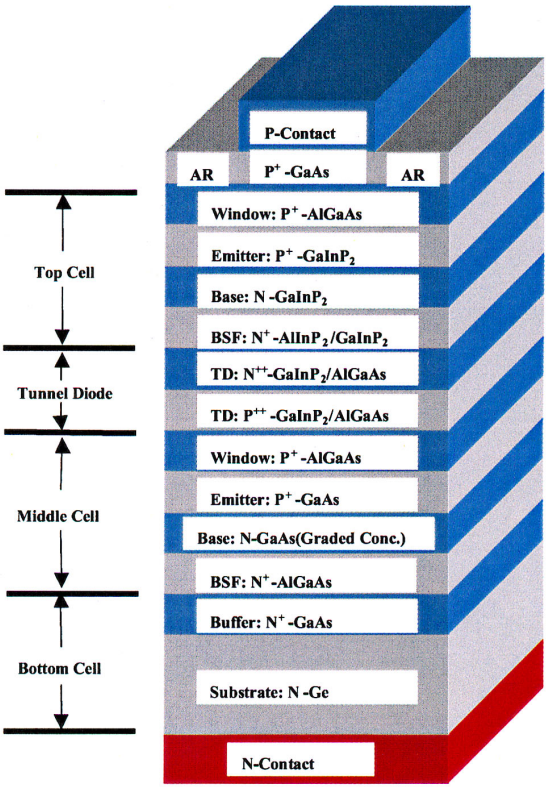

Figure 6: *Improved Cascade® Cell Structure with Drift Field and BSF*

The combined effects of the drift field and the back surface field on EOL performance are shown in Figure 7. The higher EOL performance of the improved cell structure (TEC2) results in over 10.4% more power at EOL (defined as 1E15 1 MeV electrons per cm^2).

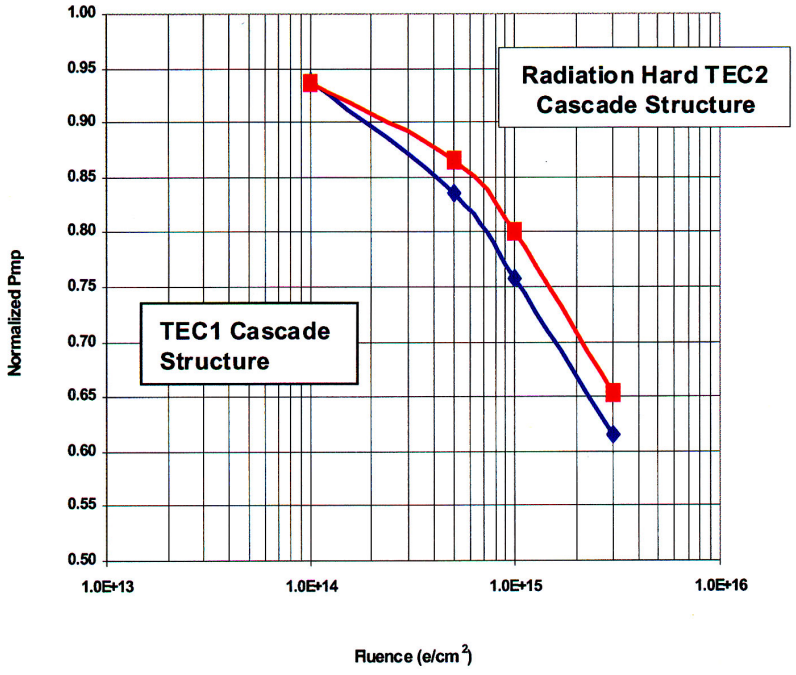

Figure 7: *1 MeV Electron Degradation for both the TEC1 (Present Technology) and TEC2 (Improved Performance) Cascade® Solar Cells*

To better illustrate the impact and improved performance of the new cell structure, Figures 8-10 shows the external quantum efficiency of the top two junctions, both before and after 1E15 1MeV electron irradiation. Figure 8 shows the external quantum efficiency of the current production (older) cell structure, called TEC1. Figure 9 shows the external quantum efficiency of the new cell structure, called TEC2. Figure 10 shows the relative degradation in external quantum efficiency (after electron irradiation) for the GaAs middle cell and directly shows the performance enhancements of the new cell structure.

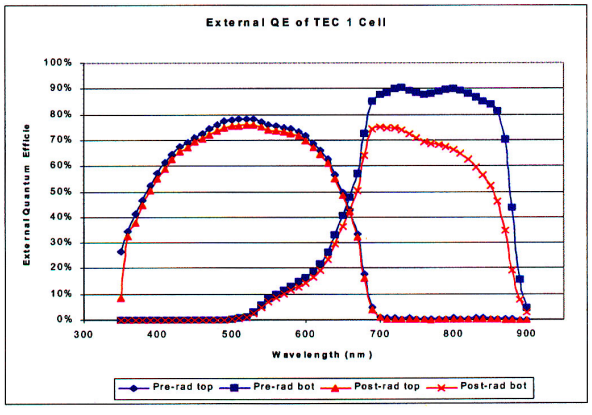

Figure 8: *External Quantum Efficiency of the Current (TEC1) Cell Structure*

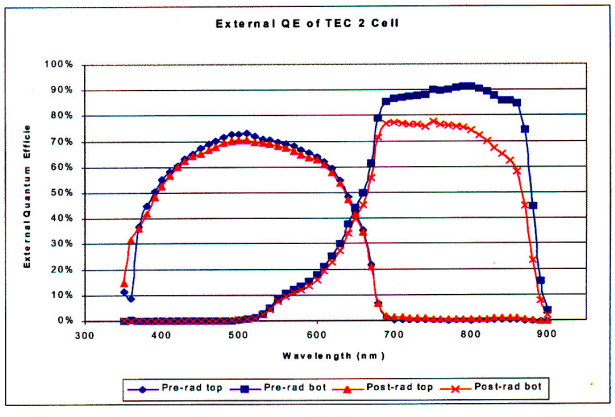

Figure 9: *External Quantum Efficiency of the New (TEC2) Cell Structure*

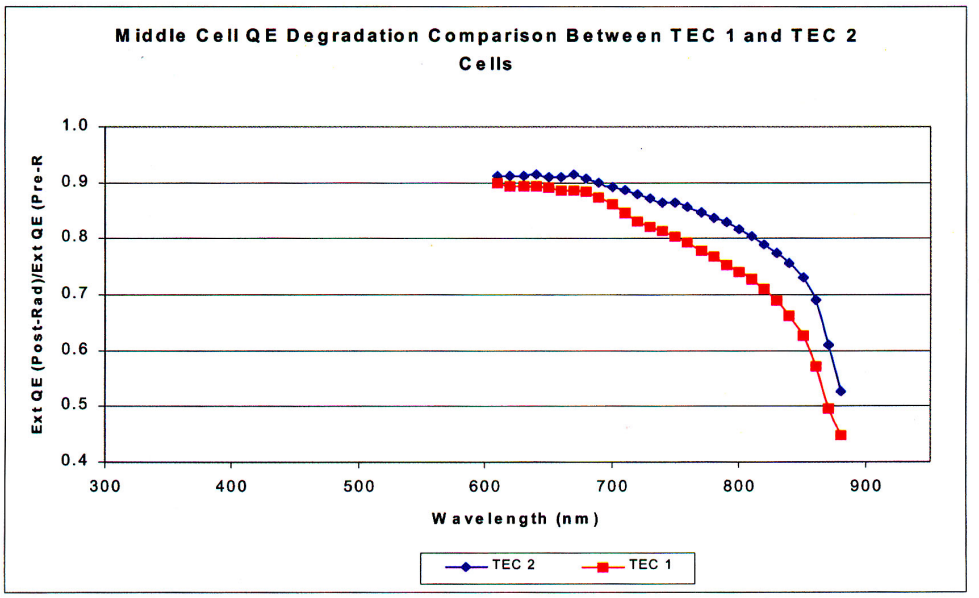

Figure 10: *Relative Change in External Quantum Efficiency for Both the Current (TEC1) And New (TEC2) Cell Structure*

Summary

TECSTAR has developed and is fully space qualifying several major improvements to its Cascade ® triple junction solar cell technology. These improvements will increase the average cell production efficiencies from around 23.0% to over 24.0%, while also increasing the radiation resistance of the cells. The average cell efficiencies after 1E15 1 MeV electron irradiation will increase from around 17.4% to over 19.2%. The data presented supports the higher efficiencies and all developmental testing to date leads confidence to successfully completing all space qualification testing and transition to production by the end of 1999.

The technology developments and solar cell optimizations have also identified several other areas for improvement, such that TECSTAR expects to achieve over 26.0% average cell efficiencies in production in 2000. These cells will perform at over 20.8% average efficiency at EOL, which represents over 19.6% more power to the satellite compared with the present technology.

DEVELOPMENT, SPACE QUALIFICATION, AND PRODUCTION OF HIGH-EFFICIENCY LARGE-AREA InGaP/GaAs DUAL-JUNCTION SOLAR CELLS ON Ge AT EMCORE PHOTOVOLTAICS (EPV)

Navid S. Fatemi, Hong Q. Hou, Paul R. Sharps, Paul M. Martin, B. E. Hammons, and Frank Spadafora

Emcore Photovoltaics (EPV),
10420 Research Rd., SE
Albuquerque, NM 87123
e-mail: navid_fatemi@emcore.com

ABSTRACT

This paper describes the development, space qualification, and production of high-efficiency dual-junction InGaP/GaAs solar cells grown on Ge substrates, at Emcore Photovoltaics (EPV). The fully automated EPV manufacturing facility in Albuquerque, New Mexico was built in late 1998 from ground up for volume production of multi-junction solar cells for space power. High-efficiency InGaP/GaAs dual-junction solar cells, with n-on-p polarity, were space qualified and in volume production in the middle of 1999. All the solar cells were designed for the best end-of-life (EOL) performance. The power remaining factor after irradiation with 1-MeV electrons at a fluence of 1E15 e/cm^2 is 0.83. The minimum average conversion efficiency of the large-area (27.5 cm^2) solar cells currently in production is 23.0% (AM0, 135.3 mW/cm^2, 28°C), producing about 0.86 watts of power per cell. The highest efficiency from this dual-junction solar cell (on Ge) measured to date is 24.1%. We will also present a product roadmap for the development of ultra-high-efficiency (>30%) solar cells.

INTRODUCTION

Multi-junction InGaP/GaAs-on-Ge solar cells have been manufactured in large volume for the past several years [1, 2]. They have proven to be an attractive alternative to the conventional silicon solar cells for many space applications. Multi-junction solar cells are not only more efficient than Si, they also have better radiation hardness. The main obstacle to the wider use of these cells in place of Si, however, has been the cost of the material growth and device fabrication and the cost of the Ge substrate. The cost figure of merit for space solar cells is dollar per watt ($/W). There are several factors that can desirably reduce this figure. Increasing the cell efficiency and cell size (for the same size Ge substrate), for example, can directly increase power per cell, and consequently lead to a lower $/W value. The cell efficiency is dependent on many factors, including the material quality and uniformity. The cell size is limited by the size of the starting Ge substrate, as well as, the area uniformity of the material grown on the wafer. Growth uniformity will determine how far the cell boundaries can approach the edge of the Ge wafer and still maintain their high performance.

To address the above issues, a proprietary epitaxial growth technique was developed at Emcore Photovoltaics (EPV) to enable the production of very large-area solar cells on 100-mm diameter Ge substrates. The high degree of the epitaxial material quality and uniformity has allowed the boundaries of the solar cell to be only 2 mm away from the edge of the Ge wafer, yielding a large cell area of 27.5 cm^2. To utilize the maximum

available area of the round Ge wafer, the top corners of cells were cropped. A photograph of two cells on a 100-mm diameter wafer is shown in Figure 1. The cell area of 27.5 cm^2 is 14-27% greater than the conventional industry solar cell areas of 24.0 and 21.65 cm^2 [1, 2]. Even though our n/p InGaP/GaAs-on-Ge dual-junction cells have the largest commercially available cell area, they have exhibited the highest performance level in a production environment: minimum lot average AM0 efficiency of 23.0%.

Implementing automated manufacturing practices is another factor that can lead to lower cost by reducing labor requirements and improving mechanical and electrical yields of fabricating solar cells. Traditionally, however, unlike the silicon semiconductor device manufacturing, the production of compound semiconductor solar cells has not involved a great deal of automation. To address this issue, a cleanroom facility was erected at EPV that contains highly automated tools and equipment. Minimizing the operator manual handling of the wafers has the advantages of better mechanical yield and process repeatability, as well as, greater processing speed and reduced labor hours.

In this paper we will describe the results for the development and manufacturing of high-efficiency dual-junction solar cells at EPV, as well as the results for the space qualification tests. In addition, we will present a product roadmap for the development of ultra-high-efficiency (>30%) triple- and quadruple-junction solar cells.

EXPERIMENT

The semiconductor layers for all the solar cells described in this paper were epitaxially grown on high-throughput metalorganic chemical vapor deposition (MOCVD) reactor platforms made by Emcore (Enterprise E400) on 100-mm diameter Ge wafers [3]. The rotating disc reactor technology can produce epitaxial materials with extremely uniform structural (better than 1%), electrical, and optical properties across the platter that houses twelve 100-mm diameter wafers. All reactors were equipped with in situ reflectometers for accurate determination of thickness and alloy composition, and also for monitoring the growth process and comparing with the fingerprint traces from known-to-be-good epitaxial growth runs. TruTemp pyrometer probes, which incorporate the correction for the change of emissivity during heterostructure growth, are also mounted on the top viewport of the growth chamber for accurate determination of the process temperature. The Ge substrate used in epitaxial growth process is 140 μm (5.5 mils.) thick with zero etch-pit defect density (EPD). The n-type Ge wafers were used for the growth of the dual-junction n/p InGaP/GaAs cells. The schematic structure of the cells is shown in Figure 2. Two large-area cells were fabricated on each wafer (see Figure 1). The nominal cell dimensions were 37.2x76.1 mm^2 with the top corners cropped at a 45° angle. The cropped space in the upper left-hand corner of the cell was allocated to house a co-planar (140 μm thick) triangularly-shaped silicon by-pass diode. A photograph of a cell with a Si by-pass diode is shown in Figure 3. The total area for each cell was 27.55 cm^2.

A dual-source solar simulator, made by TS Space, was used to measure the current-voltage (I-V) output of the cells. InGaP top single-junction cells (grown on an inactive GaAs layer) and GaAs bottom single-junction cells (with an inactive InGaP layer on top), as well as, InGaP/GaAs dual-junction standard cells were used to calibrate the solar simulator measurements. The standard cells were calibrated by the NASA Glen learjet [4] and the Jet Propulsion Laboratory (JPL) balloon [5] flights. All air-mass zero (AM0) measurements were taken at a temperature of 28°C, except for the temperature coefficient measurements which were performed in the temperature range of 28 to 80°C.

The space qualification tests were performed in several categories. The radiation tests were carried out at Jet Propulsion Laboratory by irradiating the cells with 1-MeV electrons in the fluence range of 5E13 to 3E15 e/cm^2. The electrical performance of the cells was fully characterized before and after irradiation. This also included the spectral response (SR) and quantum efficiency (QE) measurements. The temperature coefficient

measurements were also performed before and after the radiation exposure. The thermal cycling and humidity tests were performed at Garwood Laboratories. The test conditions are to simulate the operating condition in GEO orbit. Welded contact integrity tests were carried out before and after the thermal cycling and humidity tests. Solar cell emissivity and absorptance measurements, and contact and anti-reflection coating (ARC) adhesion pull tests were also carried out. The dual-layer TiO_x/Al_2O_3 AR-coating on the cells was designed to have an optimal transmission characteristics when coupled to a Pilkington CMG 100 or an OCLI 0213 coverglass with a MgF_2 coating layer.

RESULTS

In the following sections, the results for the electrical characterization, radiation tests, space qualification tests, and temperature coefficient measurements for the dual-junction InGaP/GaAs-on-Ge solar cells will be presented.

Electrical Characterization

The current-voltage (I-V) measurements were performed for every fabricated solar cell under AM0 illumination conditions. For selected cells, spectral response (SR) and quantum efficiency (QE) measurements were also performed. As mentioned earlier, the cells were designed for the best end-of-life (EOL) performance, where the thickness of the top InGaP cell is intentionally reduced from optimum. The thinner-than-optimum InGaP cell results in approximately a 7% current mismatch between the top and the bottom cells at beginning-of-life (BOL). This is illustrated in Figure 4, where a typical QE plot for a dual-junction cell is shown. As seen in the figure, the top InGaP cell produced less current than the bottom GaAs cell at BOL. Since the InGaP cell electron radiation damage degradation rate is slower than the GaAs cell, the two subcells are expected to be current-matched at EOL (i.e., 1-MeV electron irradiation at a fluence of 1E15 e/cm^2).

The minimum lot average conversion efficiency for the dual-junction cells was 23.0% under AM0, 135.3 mW/cm^2 illumination condition, and 28°C constant cell temperature. A typical I-V plot for a dual-junction solar cell is shown in Figure 5. The average values for the open-circuit voltage (V_{oc}), voltage at maximum power point (V_{mp}), short-circuit current (I_{sc}), current at maximum power point (I_{mp}), maximum power point (P_{mp}), fill factor (FF), and efficiency (η) for the cells are given in Table I. As shown in the table, the average J_{sc} value was about 16.2 mA/cm^2. The top tunnel-junction diode is composed of III-V materials with higher energy bandgaps (Eg) than GaAs which, unlike the conventional GaAs TJ diode, allows for a greater "red" portion of the AM0 spectrum to reach the bottom cell, resulting in a greater output current.

The highest measured efficiency for the large-area (27.5 cm^2) solar cell was 24.1% (AM0, 135.3 mW/cm^2, 28°C). To the best of our knowledge, this is the highest measured efficiency for a large-area InGaP/GaAs dual-junction solar cell grown on a Ge substrate. The I-V plot for this cell is shown in Figure 6. This cell had an excellent diode ideality factor of 2.5 and a reverse saturation current density (J_o) of 3.6E-18 A/cm^2.

A typical yielded efficiency distribution curve for 450 large-area dual-junction cells is shown in Figure 7. As seen in the figure, a relatively narrow distribution of performance is observed with these cells. This narrow distribution is very desirable for the purpose of selecting cells for panel and array fabrication, where balance of output power is critical in the panel circuit strings. The high BOL efficiency values and tight performance distribution observed with these cells are mainly due to the high degree of epitaxial growth material quality and uniformity across the wafer, as well as, across the wafer platter which accommodates twelve 100-mm diameter Ge wafers. An area of 2 mm from the edge of each wafer was found to have large non-uniformity in material

growth, and was therefore excluded from the above uniformity measurements. The outer boundaries of the solar cells were designed to fall just outside of this exclusion zone (see Figure 1).

Electron Irradiation Tests

From the satellite power systems point of view, the usable solar array power (performance) is defined under the EOL conditions. This performance is dependent on many factors. The most important factors are the BOL cell performance, cell design and structure and material quality (i.e., cell polarity, epitaxial layer thickness, doping levels, diffusion lengths, etc.), and the electron and proton irradiation energy and fluence levels impinging on the solar cell. The latter is a function of the spacecraft's orbital altitude and inclination, the expected life-span, and the solar cell coverglass thickness.

The solar cells reported here were designed to exhibit optimum performance in the 1-MeV electron irradiation fluence range of 1E14 to 1E15 e/cm^2. This included optimization of the BOL current mismatch between the top InGaP and the bottom GaAs cells by controlling the base thickness of the InGaP top cell. An investigation of the effects of the top and bottom cell base layer doping concentration levels on the cell radiation hardness was also carried out. The observed degradation rates due to irradiation for these cells were in general agreement with what other manufacturers of dual- and triple-junction solar cells have observed [1,6]. Although, irradiation tests were only carried out for dual-junction cells, little variation is expected in the radiation degradation behavior for the triple-junction cells in comparison to the dual-junction cells. It should also be mentioned that as a rule, the n-on-p polarity cells show better radiation hardness characteristics than do the p/n polarity cells [1,6]. This is mainly due to the fact that the base layer of the GaAs bottom cell, where the minority-carrier diffusion length is reduced by irradiation, controls the radiation behavior of the dual-junction cell. Since the minority-carrier diffusion length values in p-type GaAs (i.e., electrons) are far greater than in n-type GaAs (i.e., holes), the remaining diffusion length value after irradiation is also greater in p-GaAs than it is in n-GaAs.

To characterize the performance of the cells under various EOL conditions, a set of dual-junction cells were irradiated with 1-MeV electrons at the Jet Propulsion laboratory. The fluence values were: 5E13, 1E14, 5E14, 1E15, and 3E15 e/cm^2. The I-V characteristics and QE data were measured for every cell before and after irradiation. The average remaining factors for the V_{mp}, I_{mp}, and P_{mp} after irradiation for each fluence is given in Table II. A plot of the remaining power factor (P_{mp}/P_{mpo}) as a function of 1-MeV fluence level is also shown in Figure 8. The average measured P_{mp}/P_{mpo} values were 0.97, 0.95, 0.88, 0.83, and 0.67 for 5E13, 1E14, 5E14, 1E15, and 3E15 e/cm^2 fluences, respectively.

Temperature Coefficient Measurements

The solar cell BOL and EOL electrical measurement results are normally reported at an ambient temperature of 28°C. The actual operating temperature of the cells in an array in space is usually greater than the room temperature on earth. Solar arrays in space normally operate in the approximate temperature range of 50-70°C in the geosynchronous orbit (GEO) and 70-90°C in the low-earth orbit (LEO). Hence, the electrical characterization of the cells as a function of temperature were also carried out. From the measured solar cell power output as a function of temperature, a linear degradation rate is extracted. This degradation rate is a figure of merit for a cell, and it is referred to as the temperature coefficient. The temperature coefficient measurements were performed both before and after the electron irradiation tests.

The temperature coefficient measurements were performed in the temperature range of 28-80°C in 10°C increments. Under the BOL conditions, a coefficient of -0.033 absolute percentage per degree Celsius (abs.%/°C) was measured. The BOL temperature coefficient measurement results for the V_{mp}, I_{mp}, P_{mp}, and η are

presented in Table III. These results are comparable to what has been measured previously for the dual-junction InGaP/GaAs-on-Ge solar cells [6].

To determine the EOL temperature coefficients, the performance of the cells was measured as a function of temperature after they were irradiated with 1-MeV electrons in the fluence range of 5E13 to 3E15 e/cm^2. The solar cell efficiency temperature coefficients for the 5E13, 1E14, 5E14, 1E15, and 3E15 e/cm^2 fluences were measured to be -0.031, -0.030, -0.031, -0.028, and -0.021 abs.%/°C, respectively. This result is illustrated in Figure 9. The EOL temperature coefficient measurement results for the V_{mp}, I_{mp}, P_{mp}, and η for the fluence range of 5E13 to 3E15 e/cm^2 are presented in Table IV.

Temperature Cycling and Humidity Exposure Tests

As part of a satellite, solar cells in space experience many temperature cycles while orbiting the earth. The cells must retain a great deal of their electrical performance and mechanical robustness in the course of this temperature cycling. Accelerated testing is normally performed on earth to characterize the electrical and mechanical performance of the cells. Fifteen thermal cycles were performed in the temperature range of -180 to +140°C, followed by 2000 cycles in the temperature range of -180 to +90°C to simulate the GEO thermal conditions. The following tests were performed before and after temperature cycling: electrical I-V measurements, welded interconnect adhesion pull strength measurements, and anti-reflection coating (ARC)/cell surface adhesion strength test.

The widely accepted criterion for the performance of the solar cells after temperature cycling is that the cells must not degrade in efficiency by more than 2% (relative). Twelve dual-junction solar cells were subjected to the temperature cycling schedule described above. The average degradation in efficiency was measured to be less than 1.4% (relative). For the interconnect pull strength test, the interconnects (usually silver tabs) that are welded to the cell metal contact pads were pulled, at an angle of 45°, until the weld integrity was compromised. The three possible failure mechanisms for welded contact pull test were: metal contact delamination, interconnect tab breakage, or cell breakage. The pull-strength force values for front and back metal contacts were 698 and 669 gram-force, respectively. These values exceeded the traditional requirement for the pull strength force of ≥500 gram-force. The pull-strength force values were measured when either the silver tab tore or the cell broke, i.e., no front or back metal contact delamination was observed.

Fifteen solar cells were also subjected to a relative humidity (RH) atmosphere of 95% for 30 days at an ambient temperature of 45°C. The average degradation in efficiency was measured to be less than 1.35% (relative). Welded contact integrity test was also carried out after the humidity test. The pull-strength force values for front and back metal contacts were 605 and 740 gram-force, respectively. These values again exceeded the traditional requirement for the pull strength force of ≥500 gram-force. As before, the front and back metal contacts never delaminated during the pull-strength tests. A summary of the test results for electrical degradation and pull-strength tests after temperature cycling and humidity exposure are given in Table V.

Finally, the adhesion of the AR-coating to the solar cell surface was tested by two traditional methods: the eraser rub and 3M adhesive tape pull tests. The structural integrity and adhesion of the AR-coating was maintained after these tests. The surface appearance of the coating also remained unaffected. In addition, the average solar cell absorptance and emittance were measured to be 0.90 and 0.87, respectively.

ULTRA-HIGH-EFFICIENCY SOLAR CELLS

To meet the increasing demand for higher power by satellite manufacturers, EPV is aggressively developing higher efficiency solar cells beyond the 23% dual-junction cells currently in production. In the near term (by the end of 1999), a conventional triple-junction InGaP/GaAs/Ge solar cell will be introduced into the market with an expected BOL minimum average efficiency of 26.0%. An advanced version of this cell-type will soon follow with an expected efficiency of 28.0%. These solar cells are also expected to be significantly more radiation-hard than the conventional dual-junction cells. The expected remaining power fraction (P/P_o), after 1-MeV electron irradiation at a fluence of 1E15 e/cm^2, for these advanced cells is 0.87.

The next class of ultra-high efficiency solar cells will include novel quaternary low-bandgap InGaAsN and high-bandgap materials [7]. The energy bandgaps of InGaAsN and InGaAlP are expected be about 1.05 and 2.0 eV, respectively. With the introduction of these compounds, the optimization of bandgap-matching with the AM0 solar spectrum for the solar cells in a multi-junction stack will improve significantly. This is expected to enable, for the first time, the production of triple- and quadruple-junction solar cells with efficiencies in the range of 33-35%. A schematic drawing showing the cell structure, expected practical efficiency, and the timeline for the development of these solar cells is given in Figure 10.

The development of the ultra-high-efficiency solar cells will have a significant beneficial impact on the mass and area requirements of solar arrays. The expected BOL and EOL efficiencies, specific area (W/m^2), specific weight (W/Kg), and power per cell (W/Cell) for the on-orbit operating temperatures of 28°C (base-line), 55°C (i.e., GEO conditions), and 85°C (i.e., LEO conditions) for the dual-junction cell, as well as, the above-mentioned advanced solar cells are summarized in Table VI.

SUMMARY

The main topics and results illustrated in this paper are summarized below:

1. High-volume manufacturing of large-area (27.5 cm^2) dual-junction n/p InGaP/GaAs solar cells, grown on 100-mm diameter Ge substrates, has been established at Emcore Photovoltaics (EPV). The minimum lot average conversion efficiency was measured to be 23.0% (AM0, 135.3 mW/cm^2, 28°C).

2. Record BOL efficiencies as high as 24.1% were measured for the large-area solar cells. Very low reverse saturation current density (J_o) of 3.6E-18 A/cm^2 and excellent diode ideality factor of 2.5 were also measured. The cell structure was optimized for the best EOL performance.

3. As part of the space qualification program, irradiation tests with 1-MeV electrons were conducted under several fluence levels. The average measured remaining power fraction (P/P_o) after irradiation were 0.97, 0.94, 0.88, 0.83, and 0.67 for 5E13, 1E14, 5E14, 1E15, and 3E15 e/cm^2 fluences, respectively.

4. Temperature coefficient measurements were performed in the temperature range of 28-80°C in 10°C increments. The solar cell efficiency temperature coefficients for the 1-MeV 5E13, 1E14, 5E14, 1E15, and 3E15 electrons/cm^2 fluences were measured to be -0.031, -0.030, -0.031, -0.028, and -0.021 absolute percent per °C, respectively.

5. The dual-junction solar cells were subjected to fifteen thermal cycles in the temperature range of -180 to +140°C, followed by 2000 cycles in the temperature range of -180 to +90°C to simulate the GEO thermal conditions. The average degradation in cell efficiency was measured to be less than 1.4% (relative). The cells were also tested for mechanical metal contact weld integrity. The pull-strength force values for front and back metal contacts were measured to be 698 and 669 gram-force, respectively. These values exceeded the traditional requirement for the pull strength force of ≥500 gram-force.

6. The solar cells were subjected to a relative humidity (RH) atmosphere of 95% for 30 days at an ambient temperature of 45°C. The average degradation in cell efficiency was measured to be less than 1.35% (relative). Welded contact integrity test was also carried out after the humidity test. The pull-strength force values for front and back metal contacts were measured to be 605 and 740 gram-force, respectively.

7. The adhesion of the AR-coating to the solar cell surface was tested by the eraser rub and 3M adhesive tape pull tests. The structural integrity and adhesion of the AR-coating, as well as, the surface appearance of the coating were maintained after these tests. The average solar cell absorptance and emittance were measured to be 0.90 and 0.87, respectively.

8. Several very-high and ultra-high efficiency solar cell technologies are currently being developed at EPV. Near-term (by the end of 1999) very-high efficiency triple-junction solar cells based on InGaP/GaAs/Ge are expected to show minimum average AM0 efficiency of 26%. Longer-term ultra-high efficiency solar cells based on InGaAlP/GaAs/InGaAsN/Ge cells are expected to show minimum average efficiencies of 33-35%. They are also expected to be significantly more radiation-hard than the dual-junction solar cells currently in production.

REFERENCES

[1] N.H. Karam, J.E. Ermer, R.R. King, M. Haddad, L. Cai, D.E. Joslin, D.D. Kurt, M. Takahashi, J.W. Eldredge, W. Nishikawa, B.T. Cavicchi, and D.R. Lillington, "High Efficiency $GaInP_2$/GaAs/Ge Dual and Triple Junction Solar Cells for Space Applications," proc. 27th IEEE Photovoltaic Specialists Conference (PVSC), Vienna, Austria, 6-10 July 1998, p. 3534.

[2] Y.C.M. Yeh, F.F. Ho, C.L. Chu, and P.K. Chang, "Advances in Production of Cascade Solar Cells for Space," proc. 26th IEEE Photovoltaic Specialists Conference (PVSC), Anaheim, CA, 29 September - 3 October 1997, p. 827.

[3] W.J. Kroll, A.G. Thompson, E. Armour, R.A. Stall, T. Brennan, and H.Q. Hou, "MOCVD Technology for Advanced Space Solar Cell Production," proc. 27th IEEE Photovoltaic Specialists Conference (PVSC), Vienna, Austria, 6-10 July 1998, p. 3753.

[4] Learjet flight AM0 calibration measurements performed at NASA Glenn Research Center (GRC) in Cleveland, OH by D. Brinker, March 1999.

[5] Balloon flight AM0 calibration measurements performed by the Jet Propulsion Laboratory by B. Anspaugh, July 1999.

[6] Y.C.M. Yeh, C.L. Chu, J. Krogen, and F.F. Ho, "Production Experience with Large Area, Dual Junction Space Cells," proc. 25th IEEE Photovoltaic Specialists Conference (PVSC), Washington, DC, 13-17 May 1996, p. 187.

[7] H.Q. Hou, K.C. Reinhardt, S.R. Kurtz, J.M. Gee, A.A. Allerman, B.E. Hammons, P.C. Chang, and E.D. Jones, "Novel InGaAsN pn Junction for High-Efficiency Multi-Junction Solar Cells," proc. 27th IEEE Photovoltaic Specialists Conference (PVSC), Vienna, Austria, 6-10 July 1998, p. 3600.

Table I. — Minimum average electrical performance of InGaP/GaAs-on-Ge dual-junction solar cells under 28°C, AM0, 135.3 mW/cm^2 solar constant (Cell Area=27.5 cm^2)

Isc (A)	Jsc (mA/cm^2)	Imp (A)	Jmp (mA/cm^2)	Voc (V)	Vmp (V)
0.445	16.2	0.407	14.8	2.35	2.10

Fill Factor (%)	Pmp (W)	Efficiency (%)
82.0	0.856	23.0

Table II. — The average remaining factors for the Vmp, Imp, and Pmp as a function of radiation dose (1-MeV electrons) for InGaP/GaAs-on-Ge dual-junction solar cells.

Radiation Dose (e/cm^2)	I_{mp}/I_{mpo}	V_{mp}/V_{mpo}	P_{mp}/P_{mpo}
5×10^{13}	1.00	0.97	0.97
1×10^{14}	0.97	0.98	0.95
5×10^{14}	0.92	0.95	0.88
1×10^{15}	0.89	0.93	0.83
3×10^{15}	0.75	0.90	0.67

Table III. — BOL Temperature Coefficients for InGaP/GaAs-on-Ge dual-junction solar cells.

Δ Imp (μA/°C-cm^2)	Δ Vmp (mV/°C)	Δ Pmax (μW/°C-cm^2)	Δ Efficiency (abs.%/°C)
9.5	-4.4	-44	-0.033

Table IV. — EOL Temperature Coefficients as a function of radiation dose (1-MeV electrons) for InGaP/GaAs-on-Ge dual-junction solar cells.

Radiation Dose (e/cm^2)	**Δ Imp ($\mu A/°C\text{-}cm^2$)**	**Δ Vmp (mV/°C)**	**Δ Pmax ($\mu W/°C\text{-}cm^2$)**	**Δ Efficiency (abs.%/°C)**
5×10^{13}	10.2	-4.2	-42	-0.031
1×10^{14}	10.8	-4.2	-40	-0.030
5×10^{14}	11.6	-4.5	-42	-0.031
1×10^{15}	11.2	-4.4	-38	-0.028
3×10^{15}	13.0	-4.5	-28	-0.021

Table V. — Summary of the results for electrical performance degradation and pull-strength force tests after temperature cycling and humidity exposure for InGaP/GaAs-on-Ge dual-junction solar cells.

Qualification Test	**Δ Efficiency (%) (Relative)**	**Weld Metal Pull-Strength (gram-force)**	
		Front	**Back**
Temperature Cycle	-1.40%	698	669
95% Humidity, 30 days @45°C	-1.34%	605	740

Table VI. — Summary of the expected BOL and EOL performance for current and advanced solar cells under LEO and GEO conditions (1-MeV, 1E15 e/cm^2)

	BOL (28°C)				EOL (28°C)				
Cell Technology	η (%)	W/m^2	W/Kg	W/ Cell	P/P$_0$	η (%)	W/m^2	W/Kg	W/ Cell
Dual-Junction	23.0	311	370	0.85	0.83	19.1	258	307	0.71
Triple-Junction	26.0	352	418	0.97	0.87	22.6	306	364	0.84
Advanced Triple-Junction	28.0	379	450	1.04	0.87	24.4	330	392	0.90
InGaAlP/GaAs/ InGaAsN Triple-Junction	33.0	447	530	1.23	0.87	28.7	389	461	1.07
InGaAlP/GaAs/ InGaAsN/Ge Quad-Junction	35.0	474	562	1.30	0.87	30.5	412	489	1.13

	EOL (GEO, 58°C)					EOL (LEO, 85°C)			
Cell Technology	%Abs. η/°C	η (%)	W/m^2	W/Kg	W/ Cell	η (%)	W/m^2	W/Kg	W/ Cell
Dual-Junction	-0.028	18.3	248	295	0.68	17.5	236	281	0.65
Triple-Junction	-0.044	21.3	288	342	0.80	20.1	272	323	0.76
Advanced Triple-Junction	-0.044	23.1	312	371	0.87	21.9	296	352	0.82
InGaAlP/GaAs/ InGaAsN Triple-Junction	-0.036*	27.6	373	443	1.04	26.7	361	429	1.00
InGaAlP/GaAs/ InGaAsN/Ge Quad-Junction	-0.044*	29.2	395	469	1.10	28.0	379	450	1.05

*Estimated Temperature Coefficients

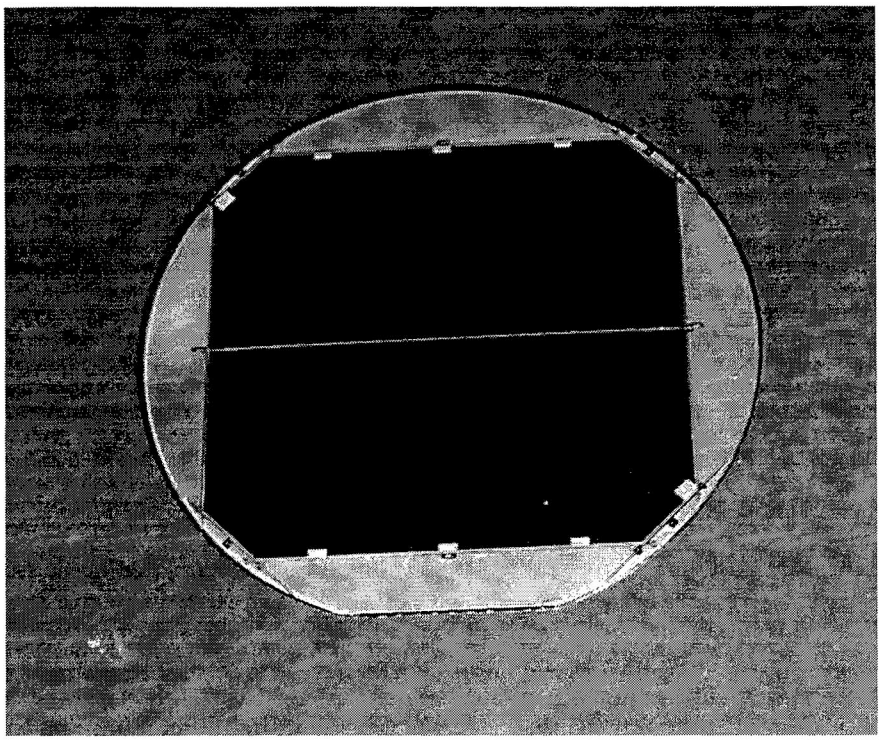

Fig.1 — Photograph of two InGaP/GaAs solar cells on a 100-mm diameter Ge wafer.

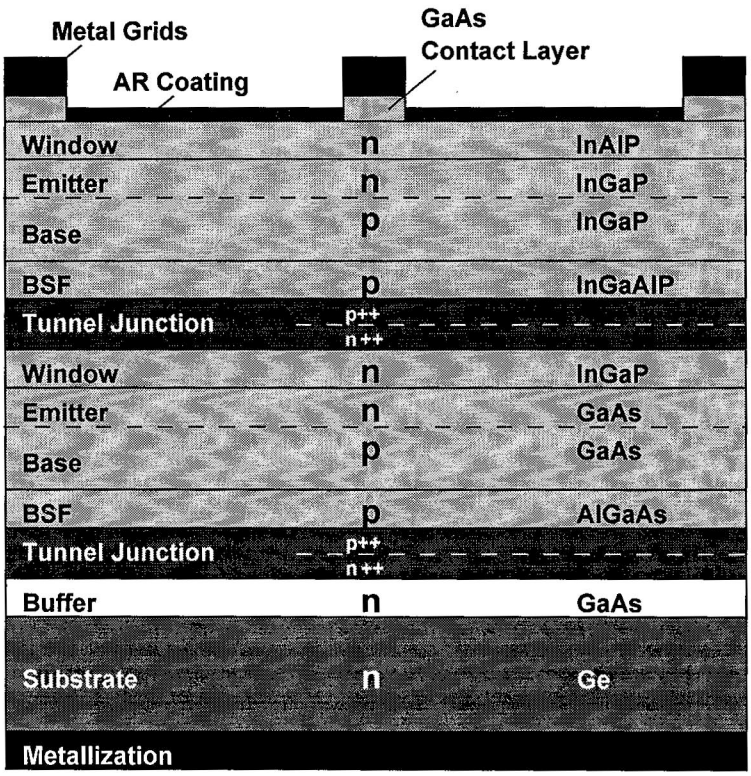

Fig.2 — Schematic structure for an InGaP/GaAs-on-Ge dual-junction solar cell.

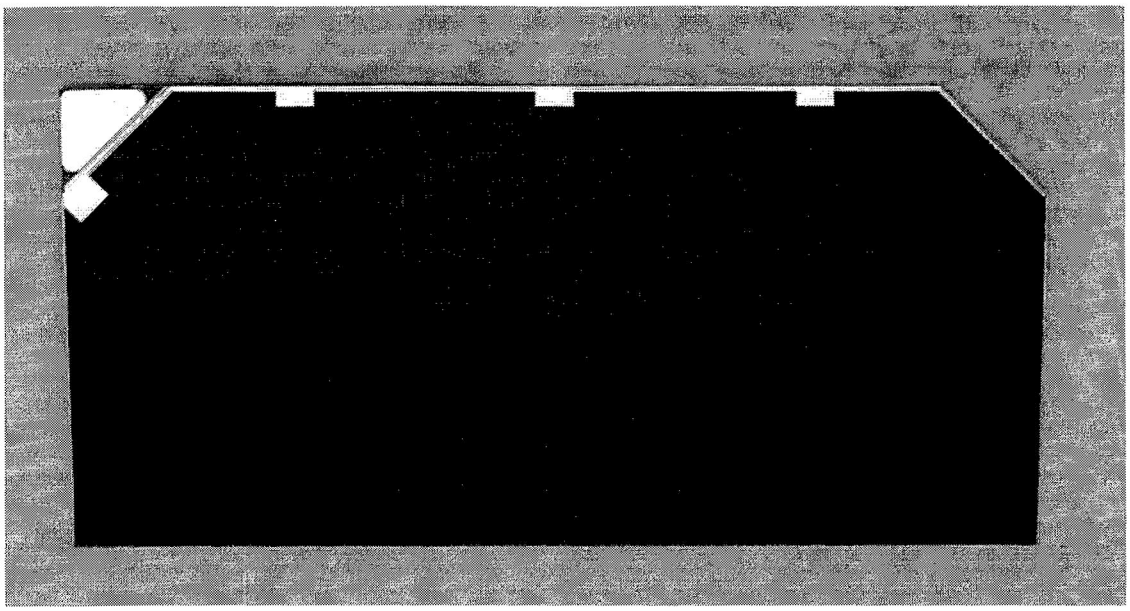

Fig.3 — Photograph of an InGaP/GaAs-on-Ge dual-junction solar cell with a Si bypass diode.

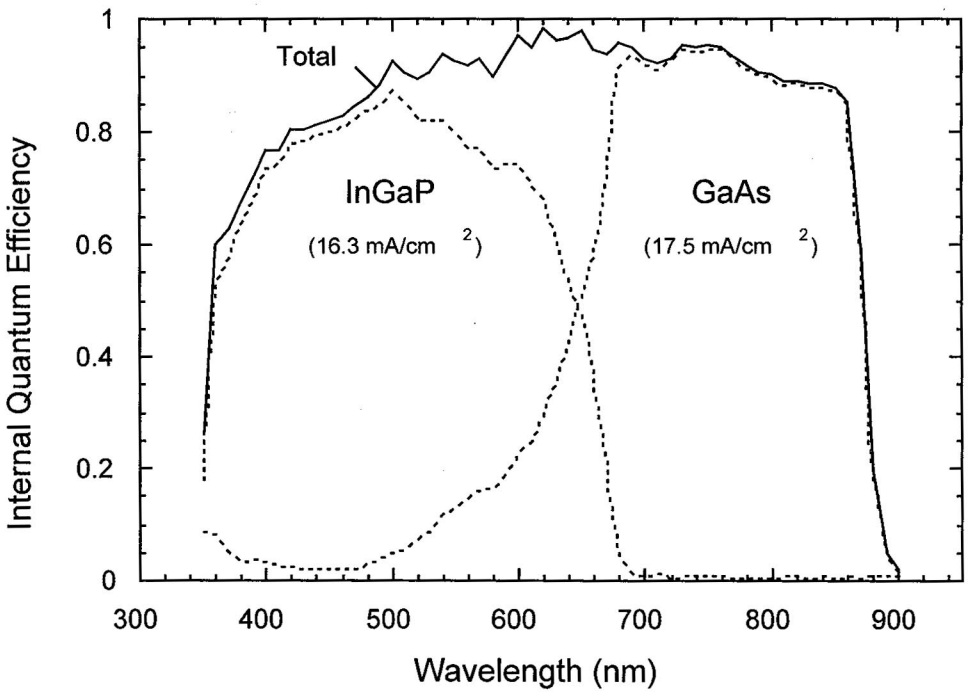

Fig.4 — A typical quantum efficiency plot of an InGaP/GaAs-on-Ge dual-junction solar cell, optimized for the highest end-of-life (EOL) performance (1-MeV, 1E15 e/cm^2).

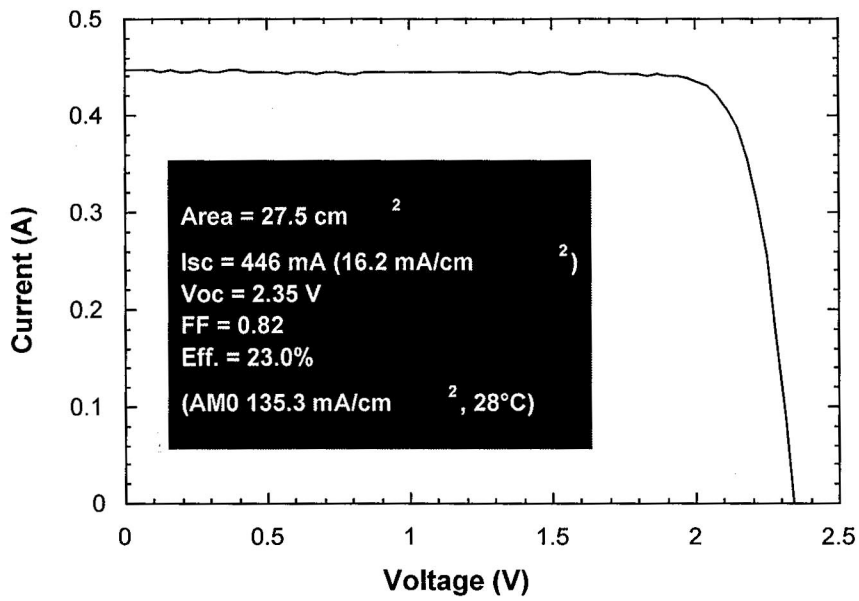

Fig.5 — A typical current-voltage (I-V) plot of an InGaP/GaAs-on-Ge dual-junction solar cell with a total area of 27.5 cm^2.

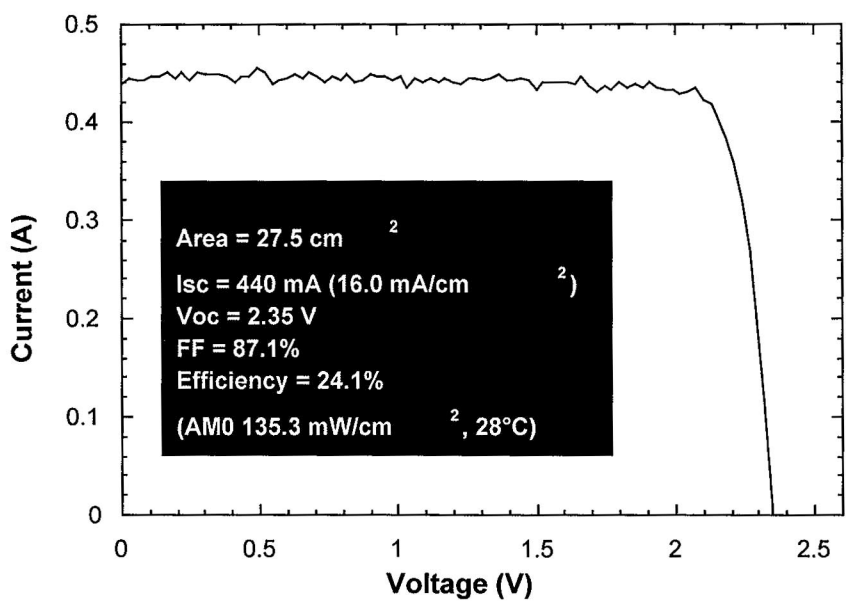

Fig.6 — A current-voltage (I-V) plot of a record efficiency InGaP/GaAs-on-Ge dual-junction solar cell with a total area of 27.5 cm^2.

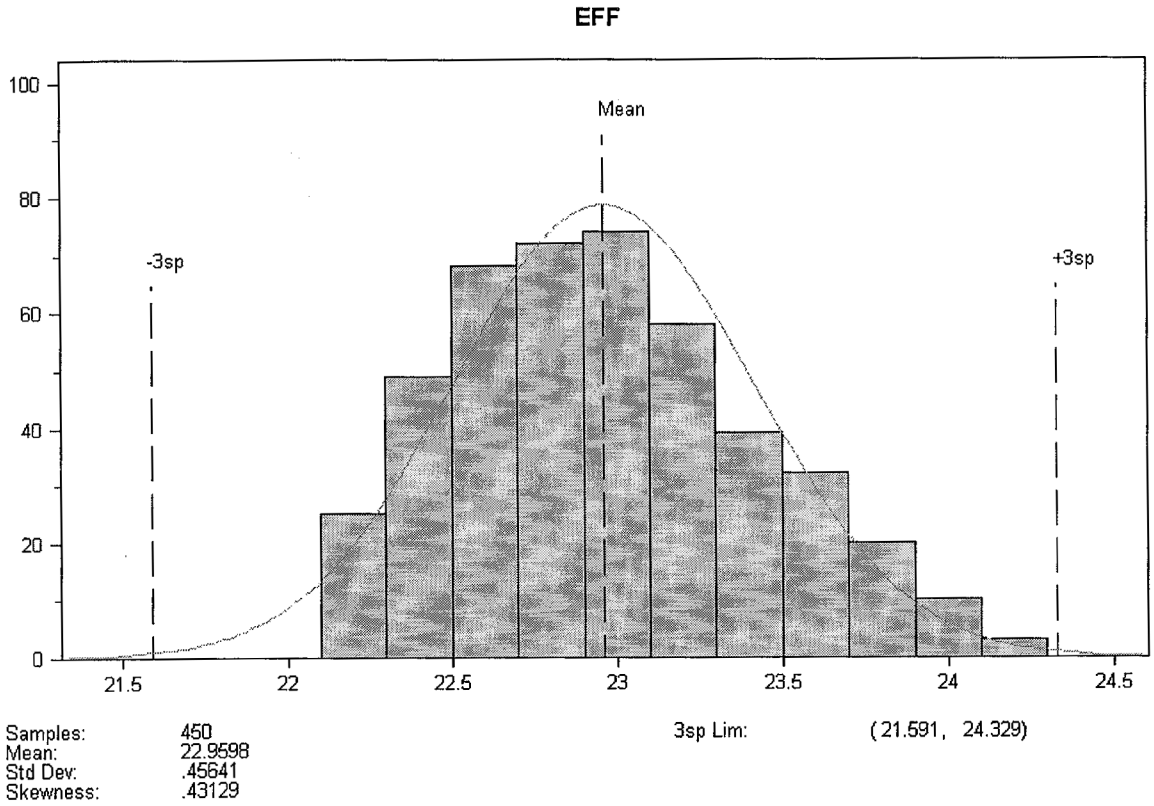

Fig.7 — A typical yielded efficiency distribution curve for a batch of 450 large-area dual-junction cells.

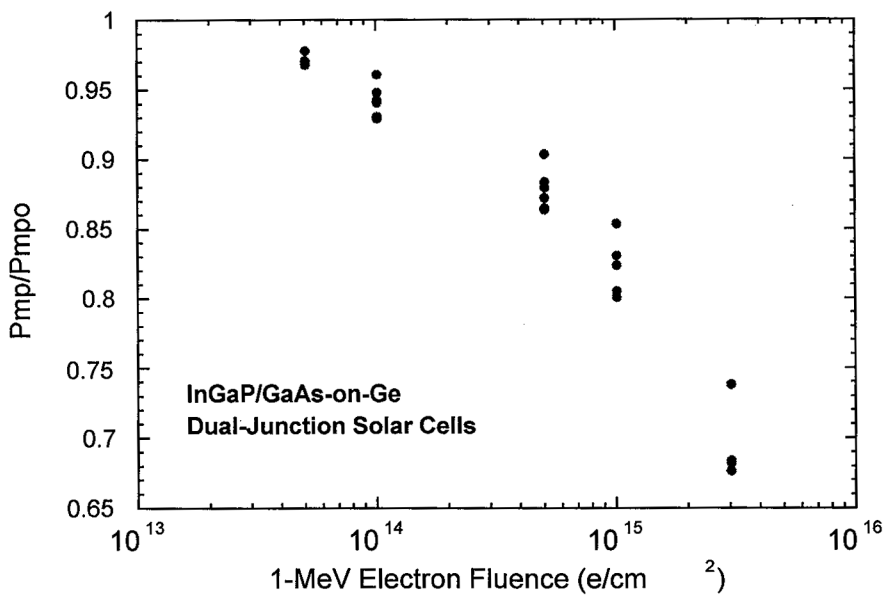

Fig.8 — Remaining power factor (P/Po) as a function of radiation dose plot of the InGaP/GaAs-on-Ge dual-junction solar cells.

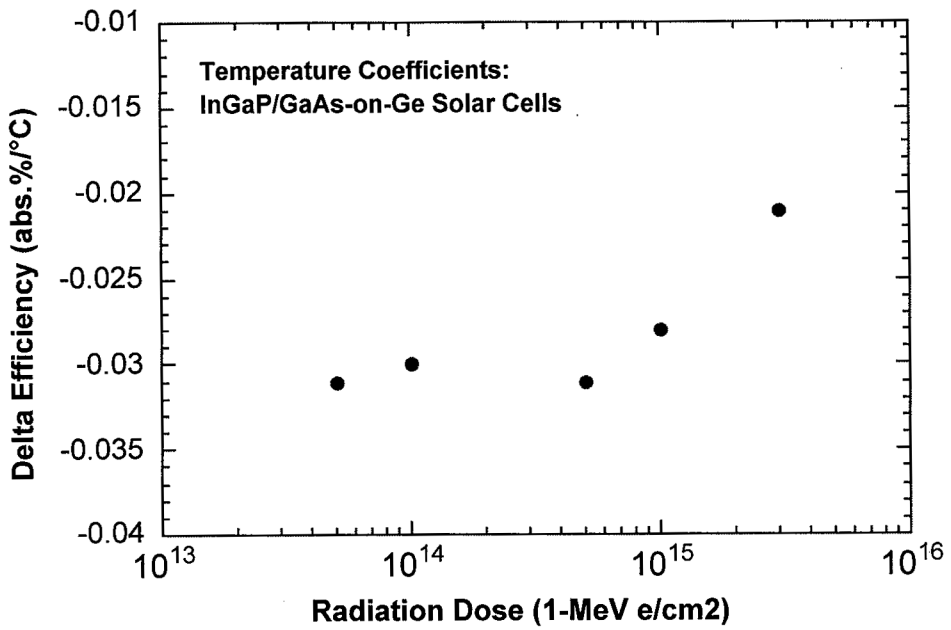

Fig.9 — EOL temperature coefficients as a function of radiation dose for the InGaP/GaAs-on-Ge dual-junction solar cells.

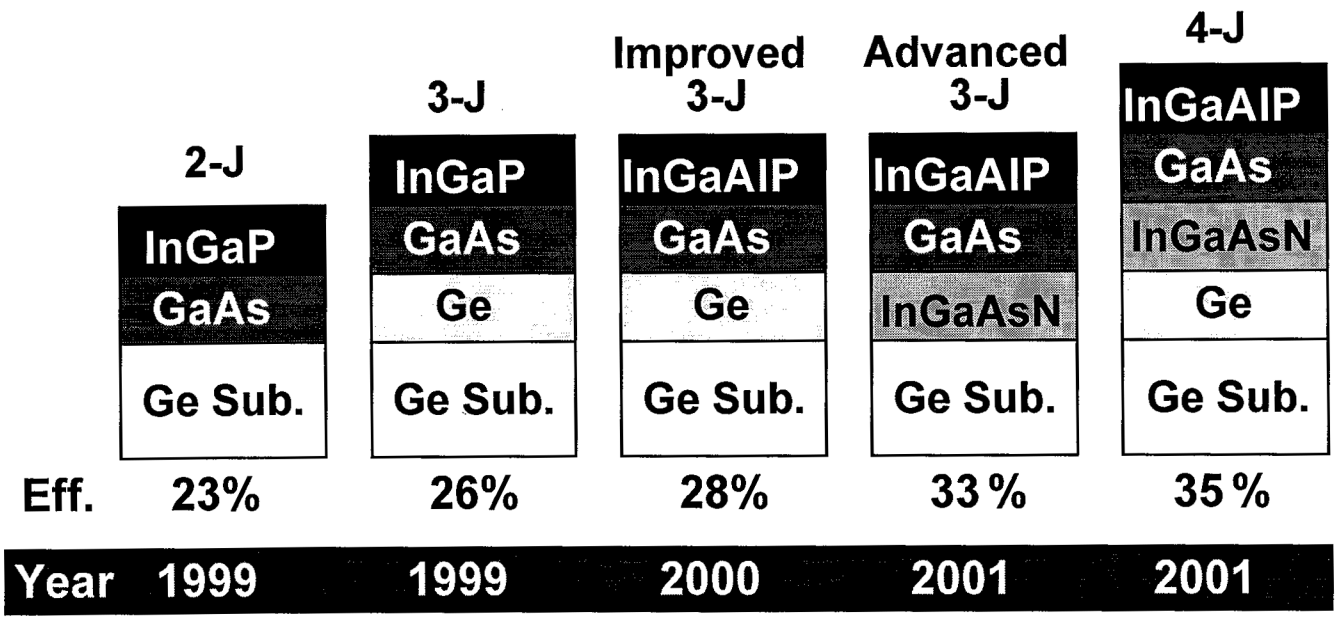

Fig.10 — The roadmap for the production of ultra-high-efficiency solar cells at Emcore Photovoltaics (EPV).

Recent Progress in the Development of High-Efficiency $Ga_{0.5}In_{0.5}P/GaAs/Ge$ Dual- and Triple-Junction Solar Cells

Nasser H. Karam, Richard R. King, Dimitri D. Krut, James H. Ermer, Moran Haddad, Hector Cotal, and Jack W. Eldredge

Spectrolab, Inc., 12500 Gladstone Ave., Sylmar, CA 91342 U.S.A.

This paper describes recent progress in the development and characterization of high-efficiency, radiation-resistant $Ga_{0.5}In_{0.5}P/GaAs/Ge$ dual-junction (DJ) and triple-junction (TJ) solar cells developed under the Manufacturing Technology phase II program. DJ cells have rapidly transitioned from the laboratory to full-scale production at Spectrolab in 1997. Advances in next-generation triple-junction $Ga_{0.5}In_{0.5}P/GaAs/Ge$ cells with an active Ge component cell are discussed, giving efficiencies up to 26.7% (21.65-cm^2 area), AM0, at 28°C. Over 1580 triple-junction solar cells have been fabricated during the cell development stages of this program with an average efficiency of 24.7% AM0, at 28°C. Final-to-initial power ratios P/P_0 of 0.83 were measured for these n-on-p DJ and TJ cells after irradiation with 10^{15} 1-MeV electrons/cm^2. Dual- and triple-junction $Ga_{0.5}In_{0.5}P/GaAs/Ge$ cells are compared to competing space photovoltaic technologies, and found to offer 60-75% more end-of-life power than high-efficiency Si cells at a nominal array temperature of 60°C. We will report on the recent advances in the miltijunction solar cell technology at Spectrolab.

30% EFFICIENT InGaP/GaAs/GaSb CELL-INTERCONNECTED-CIRCUITS FOR LINE-FOCUS CONCENTRATOR ARRAYS

Lewis Fraas[1], James Avery[1], Peter Iles[2], Charlie Chu[2], and Mike Piszczor[3]
JX Crystals Inc[1], Issaquah, WA 98027
Tecstar[2], Industry, CA 91745
NASA Glenn[3], Cleveland, OH 44135

Introduction

In 1989, Fraas and Avery demonstrated a world-record 31% efficient AM0 GaAs/GaSb tandem solar cell (1-5). This record efficiency still holds today. However, the GaAs/GaSb mechanical-stacked cell was designed to work with concentrated sunlight and at that time, the space community had no experience with concentrated sunlight solar arrays. So the photovoltaic community continued to work on improving flat plate cell efficiencies for satellite power systems. This work led to the adoption of the InGaP/GaAs/Ge monolithic tandem cell with an efficiency of 23%. Meanwhile in 1992, Fraas and Avery fabricated GaAs/GaSb cells and Entech supplied lenses for a concentrator min-module that was flown on the Photovoltaic Advanced Space Power (PASP) satellite. This mini-module performed well with high power density, excellent radiation resistance, and absolutely no problems with sun tracking. The success of the PASP module then led to the successful use of a 2.5 kW line-focus concentrator array as the main power source on Deep Space 1. Deep Space 1 was launched in 1998.

So now ten years later, concentrating solar photovoltaic arrays are proven. It is now time to bring a 30% efficient concentrator cell into production. We plan to do this by combining the InGaP/GaAs cell with the GaSb cell in a two-terminal triple-junction mechanical-stacked configuration. Herein, we describe a 30% efficient, lightweight, affordable cell-interconnected-circuit for line-focus concentrator systems. These two-terminal triple-junction mechanical-stacked cell-interconnected-circuits (TJ-MS-CICs) can be fitted into the concentrator panels of the type used on the Deep Space 1 (DS1) mission.

Over the past ten years, monolithic tandem cells have been used exclusively because they are preferred over stacked cells for flat plate arrays. However, it is noteworthy that stacked cells still out-perform the monolithic cells by a substantial margin. The reason why both the GaAs/GaSb stacked cell and the InGaP/GaAs/GaSb stacked cell out-perform the InGaP/GaAs/Ge monolithic dual junction (DJ) cell is really quite straight-forward. The monolithic DJ cell only uses the energy in the sun's spectrum between 0.4 and 0.9 microns while the GaAs/GaSb DJ cell and the InGaP/GaAs/GaSb TJ cell both use the much larger spectral range between 0.4 and 1.8 microns. Recently, there has been an attempt to close this performance gap by making the Ge junction active (6). However, the 26% efficiency recently demonstrated for the InGaP/GaAs/Ge monolithic triple-junction (TJ) cell still falls short of the 30% mark. There is a good reason for this as well. The problem with the monolithic TJ cell is that the Ge cell is automatically series connected with the DJ cell. However while the DJ cell only produces a 1 sun current of 16 mA/cm^2, both the GaSb and Ge cells are capable of producing 33 mA/cm^2. In the series connected configuration, the current in excess of 16 mA/cm^2 cannot be used. However, this is not a problem in the voltage-matched configuration used in mechanical-stacked circuits.

Even more recently, attempts have been made to close the performance gap by adding a fourth junction in the monolithic configuration. This has led to the InGaP/GaAs/GaInAsN/Ge cell. However to date, the quantum yields in the new GaInAsN cell have been poor (7).

This paper is divided into two sections. In the first section, we present data showing that 30% is real for the InGaP/GaAs/GaSb stacked cell. Then in the second section, we describe a simple two terminal circuit (TJ-MS-CIC) that mounts into line-focus arrays of the type used on Deep Space 1. In our view, a TJ-MS-CIC is actually much easier to produce than a InGaP/GaAs/GaInAsN/Ge cell.

Stacked Cell Performance

The original GaAs/GaSb mechanically stacked tandem cell was developed for point-focus systems. At 100 suns concentration, the GaAs cell converted 24% of the sun's energy to electric power while the GaSb cell boosted this efficiency by seven percentage points. However, the subsequently developed concentrator systems used line-focus optics operating in the 5 to 15 sun concentration range. The cells in DS1 operate at 7.5 suns. Since conversion efficiencies fall off at lower concentration ratios, we decided to build four terminal InGaP/GaAs/GaSb stacks and measure the performance of these stacks in the 5 to 15 suns range. We anticipated that the InGaP/GaAs DJ cell efficiency would be at least 25% with the GaSb cell providing a five percentage point boost. In a Phase I BMDO SBIR contract effort, Tecstar provided InGaP/GaAs cells to JX Crystals and JX Crystals fabricated the GaSb booster cells and the stacks. An efficiency of 29.6% was demonstrated during this phase I activity.

While our efficiency goal was achieved, there still were some surprises. The good news was that the GaSb cell boost efficiency of 6.3% at 15 suns was higher than anticipated as can be seen in table I. Furthermore, the GaSb cell performances were very tightly grouped.

However, this good news was compensated by a lower than expected performance from the InGaP/GaAs DJ cells. While the DJ cell efficiencies were tightly grouped around 22.7% at 1 sun (table II), the performances at 15 suns varied significantly as can be seen in table III.

While the best DJ cell had an efficiency of 23.3% at 15 suns, the efficiency for the worst cell was only 14.9% and the best cell efficiency was well below the 25% efficiency anticipated. Still from a global perspective, the lower than expected performance for the InGaP/GaAs cell was compensated for by the higher than anticipated performance from the GaSb cell such that the overall performance anticipated was achieved.

The scatter in the performances associated with the DJ cell can be attributed to the tunnel junction between the InGaP and the GaAs cells as can be seen in the current vs. voltage curves shown in figure 1. However, the cells we received predated DS1. We have been assured that this problem has now been solved.

Using the cells available to us in the Phase I effort, three stack assemblies were fabricated as shown in the photograph in figure 2. The performances for these three stacks are summarized in table IV.

Practical Two-Terminal Circuits

In our phase I effort, we demonstrated that 30% efficiency can be achieved at the cell level. Stated differently, given the highest performance DJ cells available commercially, we demonstrated that the GaSb cell can boost performance by 6.3 percentage points. This means that the Deep Space 1 array type output of 2.5 kW can be increased to 2.5kW x (23.3+6.3) / 23.3 = 3.2 kW. This is a very substantial improvement. However in order to realize this gain, we first need to describe how these cells can be successfully integrated into circuits and modules.

The InGaP/GaAs/GaSb articles tested in phase I were four terminal devices. The solar power community is accustomed to two terminal structures. Figure 3 shows a drawing of a simple two-terminal triple-junction mechanical-stacked cell-interconnected-circuit (TJ-MS-CIC) that can be used as an array building block. The TJ-MS-CIC shown is simply a 1.8 cm by 6.1 cm two-terminal 30% efficient circuit. It consists of an alumina substrate with seven GaSb cells wired in series and two InGaP/GaAs cells wired in parallel. It also contains a bypass diode to protect the DJ cells. The series and parallel cell interconnect scheme used is called a "voltage matching" configuration. It is based on the fact that seven times the maximum power voltage for a GaSb cell (7x0.34 V=2.38 V) is equal to or slightly larger than the maximum power voltage of the InGaP/GaAs cell (2.27 V).

The InGaP/GaAs cells are similar in size (1.2 cm by 3.0 cm) to the cells used in the receiver circuits on DS1. However, the InGaP/GaAs cells used here are made transparent in the infrared by growing the active layers on a thin GaAs substrate.

TJ-MS-CICs are made simply as follows. First thin GaSb cells (0.85 cm x 1.2 cm) are solder bonded to the alumina substrate. This is done rapidly with an automated pick-and-place machine. Then these cells are connected to the circuit traces shown at the right of the circuit in figure 3. This is done with an automated ribbon bonder. The DJ cells are supplied with leads already attached. These cells are then adhesive-bonded on top of the GaSb cells with silicone adhesive and the leads are then welded to the circuit traces shown to the left on the circuit in figure 3. The DJ cell lead welding is done with the same automated ribbon bonder that was used previously for the GaSb cell ribbon bonding. While the TJ-MS-CICs shown here in figure 3 is novel, this assembly procedure is similar to that used in fabricating the first concentrator PASP module flown in space in 1994. So the materials and procedures are already proven.

So far in this discussion, we have focused on a primary goal: to provide for increased energy conversion efficiency. This goal translates to a higher power per unit area for the array. However, there are additional goals. We want light weight for more Watts per kg. We also want to know that the TJ-MS-CICs can be produced in quantity at a reasonable cost. In the following, we address each of these additional goals.

The TJ-MS-CIC is attractive because it is lightweight. Table V summarizes the weight contributions to these CICs. Two alternate cell thicknesses are presented based on 4 mil or 8 mil thick component cells. In the lighter DJ configuration, the 8 mil thick GaAs substrate used during epitaxy will be thinned to 4 mils at some point during subsequent processing prior to being bonded to a glass superstrate. Similarly, 4 and 8 mil thick GaSb cells are possible with the base line being the 8 mil thick cell. The TJ-MS-CIC weight in the light configuration corresponds to 0.34 kg/m^2 (aperature). The alternate heavier but more conservative configuration assumes 8 mil thick substrates. In this configuration the TJ-MS-CIC weight is 0.51 kg/m^2. In either case our TJ-MS-CICs are lighter than the receiver used in DS1.

The impact of these circuit weights at the array level can be inferred from the following comparisons. If the 30% TJ-MS-CICs were to have been used on DS1, the panel power density would have increased from 200 W/m^2 to 260 W/m^2. With the lighter CICs (heavier CICs), the power to weight density would have increased from 47 W/kg to 64 W/kg (62 W/kg). Given a 260 W/m^2 panel, the panel weight would have to decrease to 2.6 kg/m^2 in order to achieve 100 W/kg. If 100 W/kg were required, the CIC weights would still be small compared to this required panel weight.

In order to address the cost issue, note that the industry array cost target is $200 per Watt. Also note that a TJ-MS-CIC will generate approximately 1.25 W of which the GaSb cell contributes about 0.25 W. If a 1 W DJ cell plus lens and support structure cost $200, then a TJ-MS-CIC plus lens and support structure would be competitive at a cost of $250. This means that all else being equal, the 7 GaSb cells and circuit assembly cost allowance is $50 per TJ-MS-CIC. This gives us a target of $5 per GaSb cell and $15 for assembly per CIC.

We begin by noting that the additional cell, the GaSb cell, is easy and inexpensive to fabricate. Its fabrication process is similar to the silicon cell manufacturing process. We use converted silicon crystal pullers for the GaSb crystal growth and diffusions for junction formation. In contract to the InGaP/GaAs/Ge cell, no epitaxy is required and no toxic gases are required. The materials cost of the Ga and Sb in a GaSb cell add up to only 14 cents / cm^2. So in high volume production, the GaSb cell should be inexpensive compared to the InGaP/GaAs/Ge cell. JX Crystals already makes thousands of GaSb cells per year for TPV applications.

Besides the additional cost of the GaSb cell, there will also be the costs associated with circuit assembly. As previously pointed out the circuit assembly tasks can be automated. The TJ-MS-CIC die bonding step can be done with an automated pick-and-place machine. JX Crystals already has such a pick-and-place machine operating at its facility for the fabrication of TPV circuits. A photograph of this machine is shown in figure 4.

The remaining circuit assembly task is lead bonding. This task can also be automated using the ribbon bonder shown in figure 5. The microscope shown in the photo of this machine is for initial alignment only. After initial setup and part loading, both the pick-and-place and the ribbon bonder have vision recognition systems enabling automated operation.

Summary

In summary, the time is now right to bring the 30% mechanical-stacked concentrator cell described here into the main stream. The component technologies for this approach are already in place and in any case, there is no other near term approach that can rival the performance of this approach. The fact that 30% stacks have once again been demonstrated combined with the recent success of Deep Space 1 implies that this approach represents a minimal risk path to dramatically improved performance.

References

1. "III-V Materials for Photovoltaic Applications", Materials Research Society Bulletin, XVIII #10, p. 48 (1993).
2. "Design and Development of a Line-Focus Refractive Concentrator Array for Space", Space PV Research and Technology, NASA SPRAT XIII (1994).
3. "A Novel Space PV Module Using a Linear Fresnel Lens and a Line-Focus Tandem Cell Receiver", 23rd IEEE PV Specialist Conference, p. 1386 (1993).
4. "GaSb Booster Cells for 30% Efficient Solar Cell Stacks", Journal of Applied Physics, 66(8) p. 3866 (1989).
5. 2nd World Conference On Photovoltaic Solar Energy Conversion, p. 268, 1998.
6. 2nd World Conference On Photovoltaic Solar Energy Conversion, p. 3534, 1998.
7. 2nd World Conference On Photovoltaic Solar Energy Conversion, p. 3, 1998.

Table I: JXC GaSb Booster Cell Performance Near 15 Suns AM0.

	FF	Voc (volts)	Isc (amps)	Imax (amps)	Vmax (volts)	Pmax (watts)	Eff (%)
	0.722	0.426	0.477	0.419	0.350	0.147	6.32
	0.711	0.428	0.478	0.415	0.351	0.146	6.28
	0.712	0.428	0.485	0.433	0.341	0.148	6.36
	0.716	0.429	0.476	0.425	0.344	0.146	6.28
	0.714	0.430	0.474	0.417	0.350	0.146	6.28
	0.713	0.430	0.484	0.427	0.348	0.149	6.41
	0.719	0.430	0.472	0.422	0.346	0.146	6.28
	0.724	0.431	0.471	0.425	0.346	0.147	6.32
average	0.716	0.429	0.477	0.423	0.347	0.147	6.32
%stdev	0.67	0.37	1.08	1.39	0.99	0.77	0.77

Table II: Tecstar Cell IV Data at 1 Sun AM0

Cell#	Voc (volts)	Isc (amps)	FF	Eff (%)
34	2.36	17.2	0.85	23.1
37	2.36	17.4	0.82	22.7
38	2.36	17.1	0.85	22.9
41	2.36	17.5	0.82	22.7
42	2.36	17.5	0.81	22.4
43	2.37	17.3	0.83	22.7
47	2.37	17.3	0.84	22.9
48	2.36	17.5	0.82	22.7
62	2.35	17.7	0.82	22.9
67	2.35	17.6	0.82	22.7

Table III: Tecstar Cell IV Data Flash Tested Near 15 Suns AM)

Cell#	FF	Voc (volts)	Isc (amps)	Imax (amps)	Vmax (volts)	Pmax (watts)	Eff (%)
34	0.781	2.53	0.267	0.240	2.20	0.528	22.7
37	0.684	2.53	0.264	0.216	2.11	0.457	19.6
38	0.559	2.52	0.247	0.178	1.96	0.348	14.9
41	0.754	2.52	0.271	0.244	2.11	0.514	22.1
42	0.618	2.51	0.266	0.217	1.90	0.411	17.6
43	0.761	2.55	0.265	0.233	2.20	0.513	22.0
47	0.798	2.53	0.269	0.238	2.29	0.543	23.3
48	0.716	2.53	0.233	0.191	2.22	0.423	18.2
62	0.713	2.52	0.272	0.228	2.15	0.490	21.0
67	0.710	2.54	0.276	0.228	2.18	0.496	21.3

Table IV: Stacked Cell Flash Test Data at 15 Suns AM0

Type	FF	Voc (volts)	Isc (amps)	Imax (amps)	Vmax (volts)	Pmax (watts)	Eff (%)
GaInP/GaAs	0.749	2.50	0.257	0.232	2.08	0.481	21.2
GaSb	0.706	0.429	0.497	0.444	0.339	0.150	6.56
			Combined Efficiency of Stack # 3				**27.8**
GaInP/GaAs	0.803	2.54	0.264	0.237	2.27	0.538	23.3
GaSb	0.687	0.427	0.501	0.437	0.336	0.147	6.26
			Combined Efficiency of Stack # 4				**29.6**
GaInP/GaAs	0.774	2.54	0.259	0.232	2.20	0.510	22.3
GaSb	0.715	0.431	0.500	0.445	0.347	0.154	6.62
			Combined Efficiency of Stack # 5				**28.9**

Table V: Receiver weight parameters

Part	Density G/cc	Area cm^2	Thickness cm	Mass/Lens kg/m^2
Cover	2.6	1.2x21	0.01	0.039
Adhesive	1.0	1.2x21	0.005	0.007
Top Cell	5.4	1.2x21	0.01	0.080
Adhesive	1.0	1.2x21	0.005	0.007
Bottom Cell	5.6	1.2x20	0.01	0.084
Solder	8.8	1.2x20	0.005	0.006
Base	4.0	1.8x21	0.012	0.108
Adhesive	1.0	1.8x21	0.005	0.010
		Total (light)		**0.341**
Top Cell	5.4	1.2x21	0.02	0.162
Bottom Cell (alternate)	5.6	1.2x21	0.02	0.168
		Total (heavier)		**0.515**

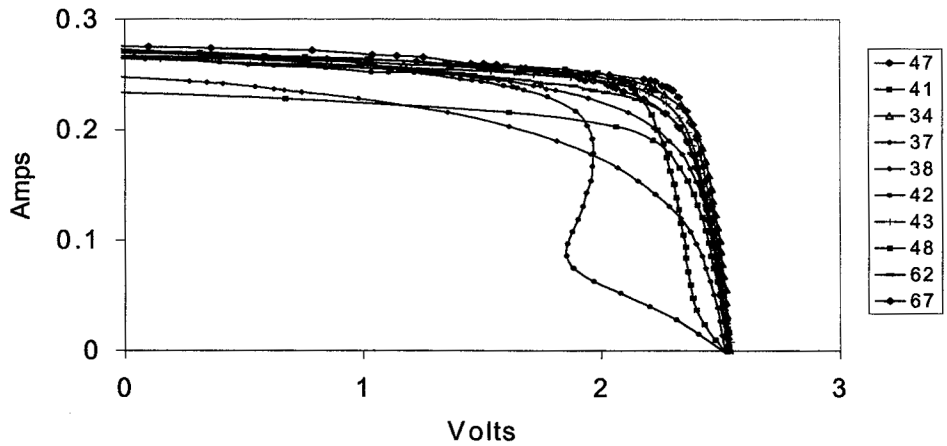

Figure 1. Dual Junction IV Curves Near 15 Suns AM0

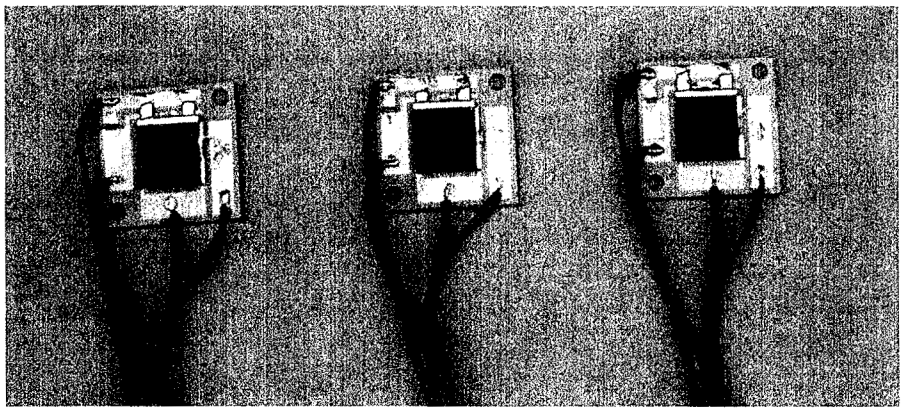

Figure 2. Dual Junction $GaInP_2$/GaAs on GaSb Mechanically Stacked Test Articles

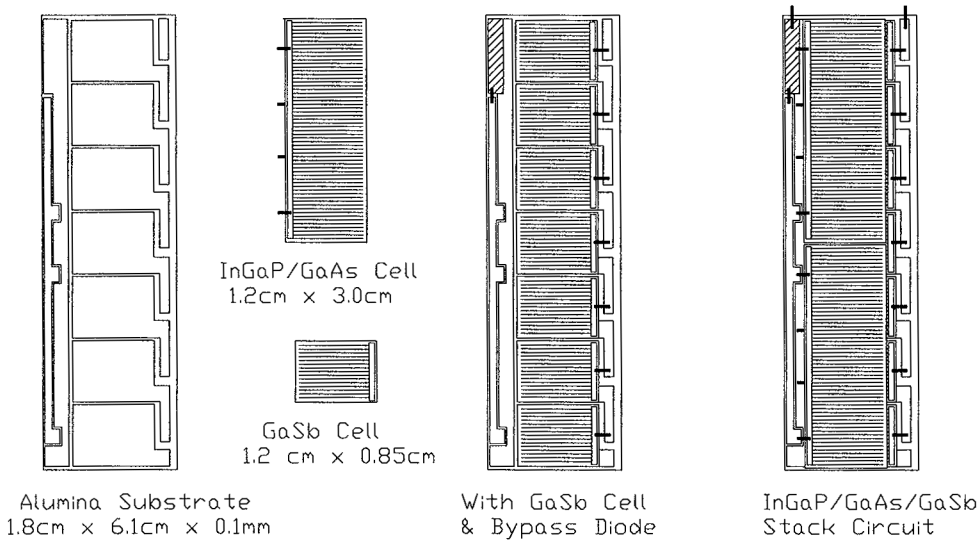

Figure 3: Triple-Junction Mechanical-Stacked Cell-Interconnected-Circuit (TJ-MS-CIC)

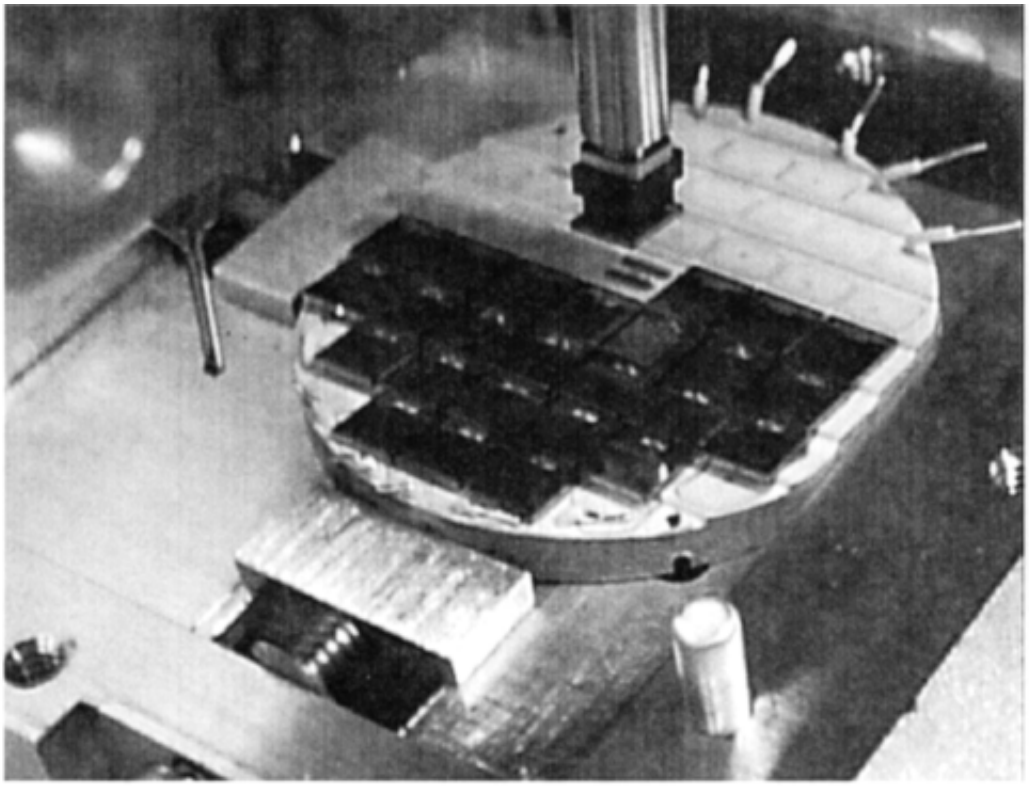

Figure 4: Automated Pick and Place machine for circuit assembly at JX Crystals

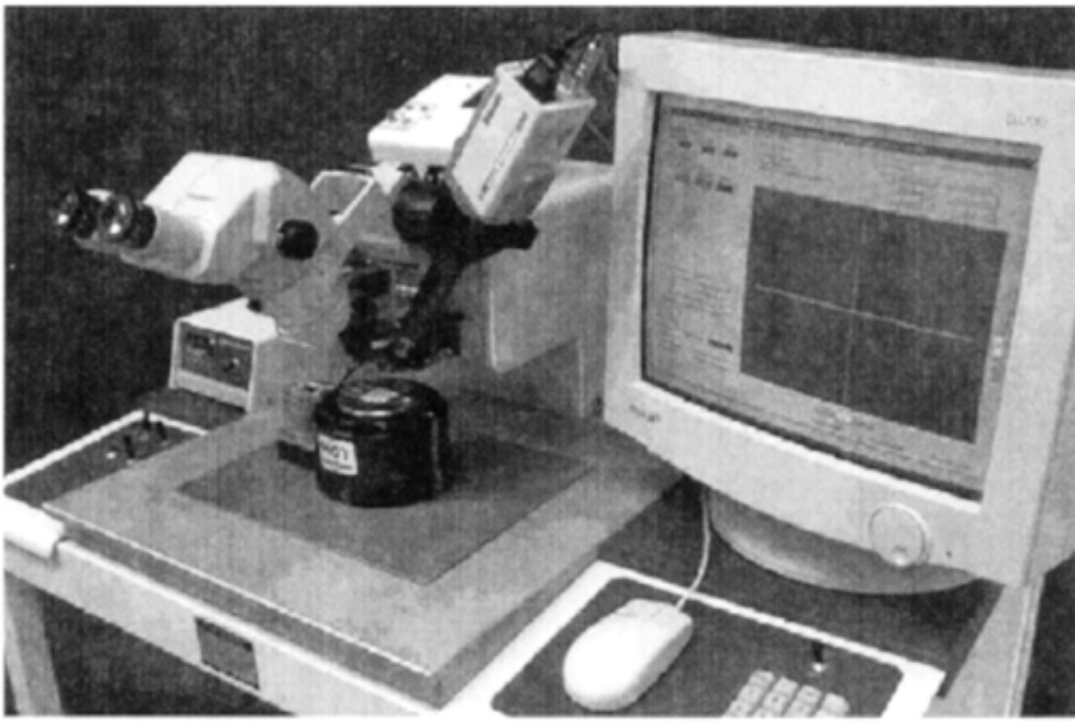

Figure 5: Automated wire bonder to be purchased by JX Crystals

HIGH GROWTH RATE METAL-ORGANIC MOLECULAR BEAM EPITAXY FOR THE FABRICATION OF GaAs SPACE SOLAR CELLS.

A. Freundlich, F. Newman, C. Monier, S. Street
Space Vacuum Epitaxy Center, University of Houston, Houston TX 77204-5507,

P. Dargan, M. Levy
Riber Inc.3880 Park Avenue, Edison NJ 08820

INTRODUCTION

The demand for satellite with increased power capabilities has promoted the development and use of high efficiency GaAs-based single junction and multijunction solar cells. Major photovoltaic manufacturers are already producing these devices [1,2] and the technology has captured a large share of the space solar cell market.

Currently high efficiency single junction and multijunction III-V space solar cells are produced by metal-organic chemical vapor deposition (MOCVD). MOCVD requires the use of large quantities of group V hydrides such as arsine and phosphine which raises serious safety and environmental concerns, and also affects the final solar cell cost. Production of such solar cells by Molecular Beam Epitaxy (MBE), which uses solid arsenic and phosphorus species and provides access to a large variety of in situ diagnosis tools, has been proposed to minimize toxicity issues and improve yields [4,5]. MBE and related techniques have been shown as being capable of producing very high quality epilayers and devices, including solar cells [5-6]. Recent development of MBE multi-wafers systems capable of MOCVD production throughputs is also an attractive feature. Figure 1 provides a photograph of an MBE Riber 6000 system, the 16" wafer holder in this system could allow the simultaneous growth of III-V on four six inch wafers or 34 (6cm x 4 cm) solar cell wafers per run (Fig.1). Nevertheless, MBE growth rates generally in 1 to1.5 microns per hours range (Growth rates in MOCVD systems ranges from 2-10 μm/h) have generated skepticism about the ability of MBE and related techniques as a production tool for thick (>4 μm) devices such as solar cells.

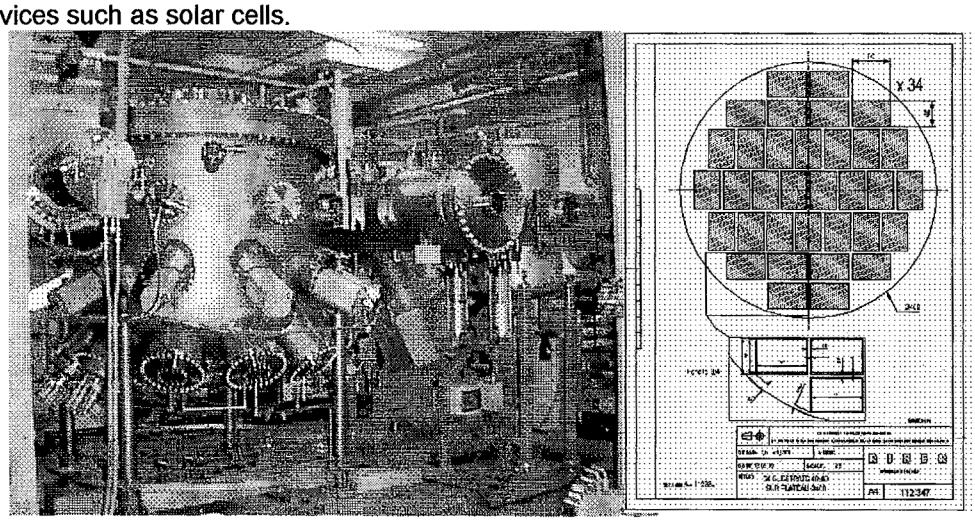

Figure 1: Photograph of a Riber 6000™ MBE production system. Up to 34 (40mmx60 mm) solar cell wafers can be processed per run.

In this work it is shown that high quality GaAs photovoltaic devices can be produced by MBE with growth rates comparable to MOCVD through the substitution of group III solid sources by metal-organic compounds. The influence the III/V flux-ratio and growth temperatures in maintaining a two dimensional layer by layer growth mode and achieving high growth rates with low residual background impurities is investigated. Finally subsequent to the study of the optimization of n- and p doping of such high growth rate epilayers, results from a preliminary attempt in the fabrication of GaAs photovoltaic devices such as tunnel diodes and solar cells using the proposed high growth rate approach are reported.

GROWTH AND CHARACTERIZATION

All growth runs are performed in Riber CBE32 reactor. Tri-ethyl-gallium (TEG) and tri-methyl-indium (TMI) are used as group III precursors. The organometallics(OM) are maintained at 40C and introduced mixed with hydrogen through a low temperature (80C) injector. The OM flux is adjusted using mass flow controllers. To allow an optimum operation of the flow controller the down-stream pressure of the OM/H_2 mixture is maintained at 40 torr using pressure controllers. The group V element flux was provided by a tetrameric arsenic (As_4) source. The Arsenic flux at the substrate was between 1-4 x 10^{-5} torr. Si and Be solid sources are used as n-type and p-type dopants respectively.

GaAs layers are grown with growth rates ranging from 0.5 to 3 monolayers (ML) per second (0.5-3.2 microns per hour) on nominal (100) highly Si doped GaAs wafers. The GaAs surface reconstruction and growth mode is monitored real- time using reflection high-energy electron diffraction (RHEED). Substrate temperatures are measured using an IR sensitive pyrometer. The precursor decomposition and species partial pressures (flux) in the reactor were monitored using mass spectrometry.

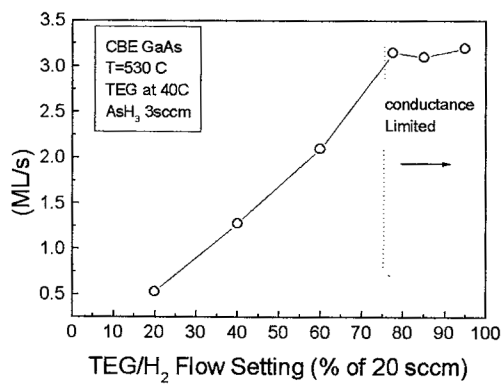

Figure 2: Growth rate as a function of TEG/H2 flux setting.

The GaAs growth rate as determined through the intensity oscillations of the specular beam in the (2x4) reconstruction RHEED diagram is found to increase linearly with the increasing TEG flux. However the growth rate saturates for fluxes exceeding 16sccm of TEG/H_2 mixture to slightly above 3 ML/sec. It is worth noting that beyond this threshold partial and total pressure analysis indicated that the OM pressure in the chamber remained unchanged. The latest suggests that the growth rate is most likely limited by the conductance of our TEG/H_2 $^1/_8$ inch-diameter lines.

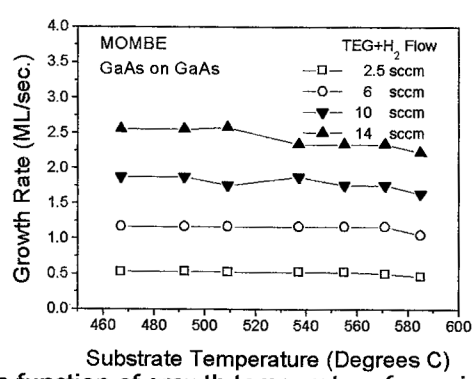

Figure 3: GaAs growth rate (a) as a function of growth temperature for various TEG fluxes 14 sccm (solid up triangle) 10 sccm (solid down triangle) 6 sccm (open circle) and 2.5 sccm (open square).

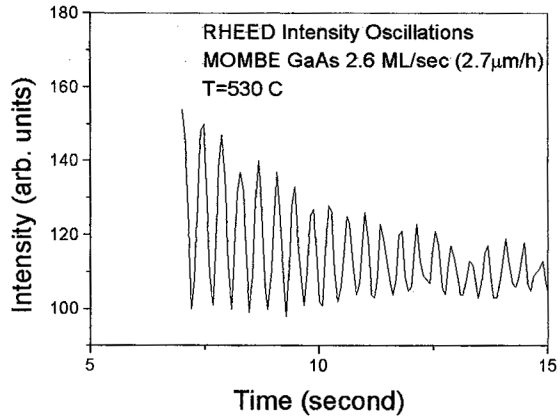

Figure 4: RHEED specular beam intensity oscillations recorded during the growth of GaAs (growth rate 2.62 ML/sec, temperature 530 C)

The MOMBE growth of GaAs is investigated over a wide range of temperature. A 2x4 RHEED diagram and a nearly constant growth rate are obtained within a range of 460-560 C (Figure 3). A slight drop in the growth rate is noticed for temperatures exceeding 570C suggesting a reduction in the Ga sticking coefficient. A fuzzy RHEED diagram suggesting the epilayer surface roughening characterized growths performed at substrate temperatures below 500C or/and with high arsenic partial pressures. Strong RHEED intensity oscillations demonstrating a layer by layer growth mode are observed in the range of 520-580C. In optimum growth conditions even at growth rates exceeding 3 monolayer/sec distinct RHEED intensity oscillations are observed (Figure 4).

GaAs layers grown under optimum conditions (520-590C) exhibit a specular morphology. Background carrier concentrations determined using C-V electrochemical profilometry indicate the possibility of obtaining high growth rate GaAs layers with residual active impurity levels in low $10^{16}cm^{-3}$ range. The bound excitonic transitions at 1.512 eV and Carbon neutral acceptor-band (e-C0) at 1.494 eV dominate the 10K-photoluminescence spectra of these samples. As for conventional MBE/CBE samples, these photoluminescence analyses suggests carbon as the main residual acceptor impurity in our high growth rate not intentionally doped epilayers.

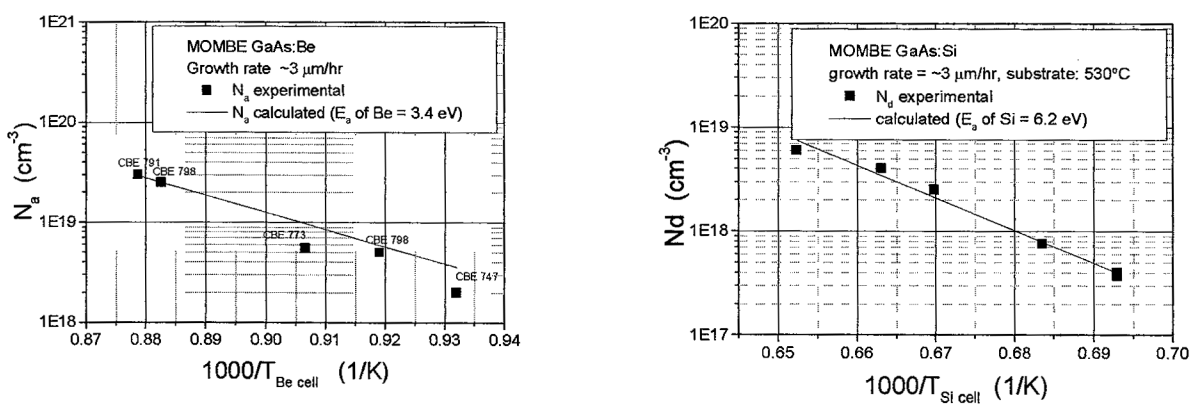

Figure 5: N and P type doping of GaAs grown at 3 microns/hour

n and p type intentional doping of GaAs layers grown at 3 micrometer/hour was performed using Be and Si respectively. Intentional beryllium p-type doping ranging from $5x10^{17}$ cm^{-3} to $2x10^{20}$ cm^{-3} and silicon n-type doping ranging from $3x10^{17}$ cm^{-3} to $8x^{18}$ m^{-3} were obtained reproducibly. Doping

concentrations are compatible with the development of photovoltaic devices such as solar cells and tunnel diodes. The activation energies associated with dopant incorporation in the solid phase are in agreement with those observed for materials grown with lower growth rates and are in the order of 3.4 eV and 6.2 eV for Be and Si respectively (Fig.5).

PRELIMINARY PHOTOVOLTAIC DEVICE PERFORMANCE

Finally in order to validate the compatibility of the developed high growth rate epilayers for the fabrication of GaAs based advanced solar cells a preliminary attempt is made to fabricate a GaAs p/n solar cell and a tunnel diode.

Device structures are grown at rates of about 3 microns /hour on a highly n-doped 3 inch diameter (100) GaAs wafer at a temperature of 530-560 C. Following the growth process non-alloyed Au metallic layers, deposited by vacuum evaporation, are used as n-type (on substrate) and p-type ohmic contacts. The Au-top contact grid is obtained using a lift off technique.

For the solar cell devices an intermediate highly p-doped GaAs layer is introduced to lower the top contact resistivity. A mesa etching of the structure provides a total area per cell of 5 x 5 mm^2. The top-grid shadowing is estimated to be about 7.5%. The GaAs contact layer was removed from the cell active area using a selective etching and the $Al_{0.8}Ga_{0.2}As$ window layer as an etch stop. Following this step a two layer MgF_2/ZnS anti-reflection coating is implemented to minimize the solar cell reflective losses. Concerning the tunnel diode device processing a mesa is etched directly using the top contact dots as a mask The latest provides a set of devices with mesa diameters of 100 and 200 microns.

GaAs p/n Tunnel diodes

Figure 6 shows the C-V profile of the fabricated tunnel diode stressing the high dopant incorporation and the sharpness of the p/n interface. All diodes exhibit high peak current densities in excess of 150Acm^{-2}, a good peak to valley ratio and a specific resistivity of less than 0.5 $m\Omega cm^2$ (at 30 A/cm^2). Current- voltage characteristic of such device are reported in Figure 7. It is worth nothing that this preliminary tunnel diode device outperforms best MBE-grown GaAs devices[5] (Jp=46A/cm^{-2}) and has a performance comparable to best results achieved by carbon-doped MOCVD tunnel diodes [7]. The associated voltage drop in a tandem device operating using such tunnel diodes even under moderate concentration (x20-x50) is expected to be below few mV and therefore negligible.

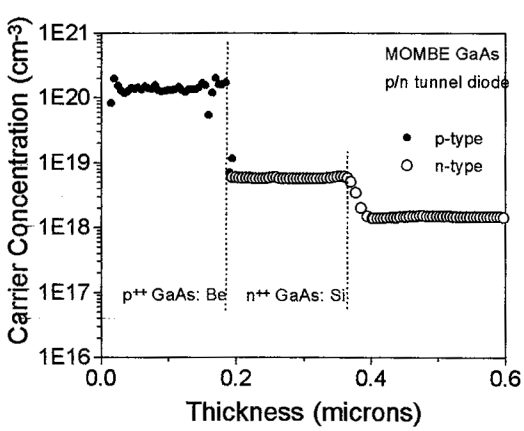

Figure 6: Carrier concentration profile of MOMBE grown GaAs tunnel diode.

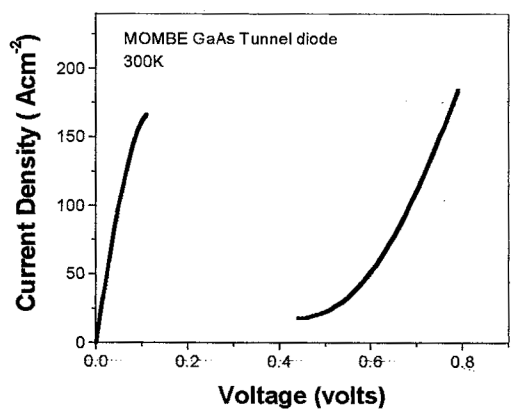

Figure 7: I-V characteristics of a 100 microns diameter MOMBE GaAs tunnel diode. Jp= 162 A/cm^{-2}

GaAs p/n Solar cell

All solar devices exhibit good PV characteristics. Room temperature spectral response of this preliminary device is provided in Figure 8 and compares well with data reported in the literature for high quality GaAs MOCVD grown solar cells [1,2,8]. The typical device short circuit current exceed 32 mA cm^{-2}

under one sun AM0 simulation with the best device on the wafer reaching 32.5 $mAcm^{-2}$ (comparable to the highest current densities reported for GaAs solar cells). Devices exhibit an open circuit voltage in excess of 950 mV, about 5% below the state of the art GaAs solar cells. Despite poor fill factor 74-78 % (compared to 86-88% for best GaAs solar cell), probably associated with a non optimized GaAs solar cell design/processing, all cells exhibit AM0 efficiencies in excess of 16 %. We believe that through the optimization of cell design and processing, cells with efficiencies in excess of 20% efficient cell would be easily achieved with high growth rate Metal-organic MBE.

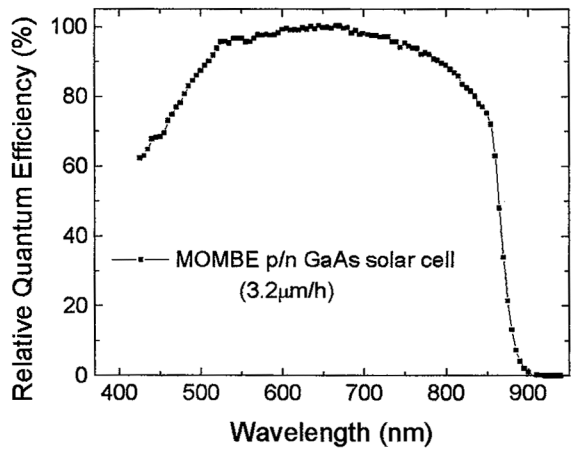

Figure 8: External quantum efficiency of high growth rate MOMBE GaAs p/n solar cell.

CONCLUSION

In this work we have shown that high quality GaAs epilayers can be produced by MOMBE at growth rates exceeding 3 μm/h. Despite high growth rates, the optimization of III/V flux-ratio and growth temperatures leads to a two dimensional layer by layer growth mode characterized by a (2x4) RHEED diagrams and strong intensity oscillations. The material characteristics are shown to be compatible with the fabrication of high efficiency space-photovoltaic devices. As mentioned earlier the growth rates here seems to be limited by the conductance of the TEG delivery line rather than by the growth kinetics. One then may speculate that substantially higher growth rates would be attainable using standard larger diameter OM delivery line. Preliminary high growth rate GaAs photovoltaic device fabrication has yielded to the realization of record breaking tunnel diodes and encouraging solar cell performance. These results demonstrate the potential of MOMBE as reduced toxicity alternative for the production III-V space photovoltaics. It is worth noting that even at a rate of 3 microns per hour an existing MBE production system would be capable of producing over 100,000 solar cell epi-wafer per year.

AKNOWLEDGEMNET

The work at University of Houston was partially supported through the NASA Cooperative agreement NCC8-127 and AFRL research grant.

REFERENCES

1. Y.C.M. Yeh, C.L. Chu, J. Kinger, F.F. Ho, J.M. Olson, M. Timmons, in Proc.25th *IEEE Photovoltaic Specialist Conference*, (1996) p187.
2. E.B. Linder, J.P. Hanley in *Proc. 25th IEEE Photovoltaic Specialist Conference*(1996), p267
3. M. Meyer, R. E. Metzger, Compound Semiconductors (Special Issue), pp 40-41(1997).
4. S. Ringel, R.M. Sieg, S.M. Ting and E. Fitzgerald, Proc. 26th *IEEE Photovoltaic Specialist Conference*, 1997, p793-799
5. J. Lammasniemi, K. Tappura, R. Jaakola, A. Kazantev, K. Rakennus P.Uusimaa, M. Pessa, in Proc.25th *IEEE Photovoltaic Specialist Conference*, 1996 , p97-100
6. A. Freundlich, M. Vilela, A. Bensaoula and N. Medelci, Proc. 23 IEEE PVSC (1993) p 685
7. K.A. Bertness, S.R. Kurtz, D.J. Friedman and J. M. Olson, *in Conference records of 1st World Conference on Photovoltaic Energy Conversion (*1994) p1859-1862
8. K.A. Bertness, S.R. Kurtz, D.J. Friedman A.E. Kibbler, C. Kramer and J. M. Olson *in Conference records of 1st World Conference on Photovoltaic Energy Conversion* (1994) pp 1671-1675. *ibid* Appl. Phys. Lett. 65, (1994) p989

HIGH EFFICIENCY MULTI-JUNCTION SPACE SOLAR DEVELOPMENT UTILIZING LATTICE GRADING

Mark A. Stan, Victor G. Weizer, AnnaMaria Pal, Linda M. Garverick, Osman Khan, and Samar Sinharoy
Essential Research, Inc., Cleveland, OH 44135

Richard W. Hoffman, Jr., Phillip P. Jenkins, and David A. Scheiman
The Ohio Aerospace Institute, Cleveland, OH 44135

Navid S. Fatemi
EMCORE PhotoVoltaics
Albuquerque, NM 87123

Abstract

Progress towards achieving a high one-sun air mass 0 (AM0) efficiency in a monolithic dual junction solar cell comprised of a 1.62 eV InGaP top cell and a 1.1 eV InGaAs bottom cell grown on buffered GaAs is reported. The performance of stand-alone 1.62 eV InGaP and 1.1 eV InGaAs cells is compared to that of the dual junction cell. Projected AM0 efficiencies of 15.7 % and 16.5 % are expected for the 1.62 eV InGaP and 1.1 eV InGaAs cells grown on buffered GaAs. The dual junction cell has a projected one-sun AM0 conversion efficiency of 17 %. The projected efficiencies are based upon the application of an optimized anti-reflective coating (ARC) to the as-grown cells. Quantum efficiency (QE) data obtained from the dual junction cell indicate that it is bottom cell current limited with the top cell generating 50 % more current than the bottom cell. A comparison of the QE data for the stand-alone 1.1 eV InGaAs cell to that of the 1.1 eV InGaAs bottom cell in the tandem configuration indicates a degradation of the bottom cell conversion efficiency in the tandem configuration. The origin of this performance degradation is at present unknown. If the present limitation can be overcome, then a one-sun AM0 efficiency of 26 % is achievable with the 1.62 eV/1.1 eV dual junction cell grown lattice-mismatched to GaAs.

Introduction

Theoretical predictions of the solar conversion efficiency of multi-junction solar cells show that the maximum conversion efficiency occurs for devices whose bandgaps are such that they are not lattice-matched to substrates of binary III-V compounds. Consequently, a trade-off between choosing compounds with optimized bandgaps or compounds that lattice match to binary III-V substrates must be made. The traditional approach has been to utilize compounds that are lattice-matched to the underlying substrate. [1] In this approach one avoids misfit and threading dislocation formation. Such defects have been shown to introduce trapping centers. [2]

The dual junction monolithic space solar cell presently used in production consists of an $InGaP_2$ top cell lattice-matched to a GaAs bottom cell. Modeling shows that this design will yield a one-sun air mass 0 (AM0) efficiency of 28.6%. [3] The highest efficiency reported to date with this archetypal cell design is 26.9%. If, however, one relaxes the constraint of lattice matching, then an upper limit efficiency of nearly 32.5% is possible in a dual junction configuration. This efficiency is theoretically possible in a tandem design that utilizes a 1.75 eV top cell and a 1.1 eV bottom cell. Recently, a one-sun AM0 efficiency of 21.6% has been reported in a design that uses a 1.65 eV InGaP top cell and a 1.18 eV InGaAs bottom cell grown lattice-mismatched to GaAs. [4] Further improvements in the efficiency are possible by thinning the top cell. Quantum efficiency measurements indicate that the top cell generated 24% more current than did the bottom cell under one-sun AM0 illumination.

Our approach to space solar cell design is based upon optimizing the dual junction cell in terms of bandgap. [5] This method allows one to achieve current matching of the top and bottom cells without resorting to thinning of the top cell. The 1.75 eV bandgap top cell lattice-matched to the underlying 1.1 eV InGaAs bottom cell requires the quaternary compound InGaAlP. As a first step in our process development we have chosen to grow a tandem cell using a 1.62 eV InGaP ternary top cell latttice-matched to a 1.1 eV InGaAs bottom cell. In this paper we present performance data for the dual junction components: a 1.1 eV n/p InGaAs cell, a 1.62 eV n/p InGaP cell, a 1.1 eV p++/n++ tunnel junction interconnect, and the complete 1.62 eV/1.1 eV n/p dual junction cell.

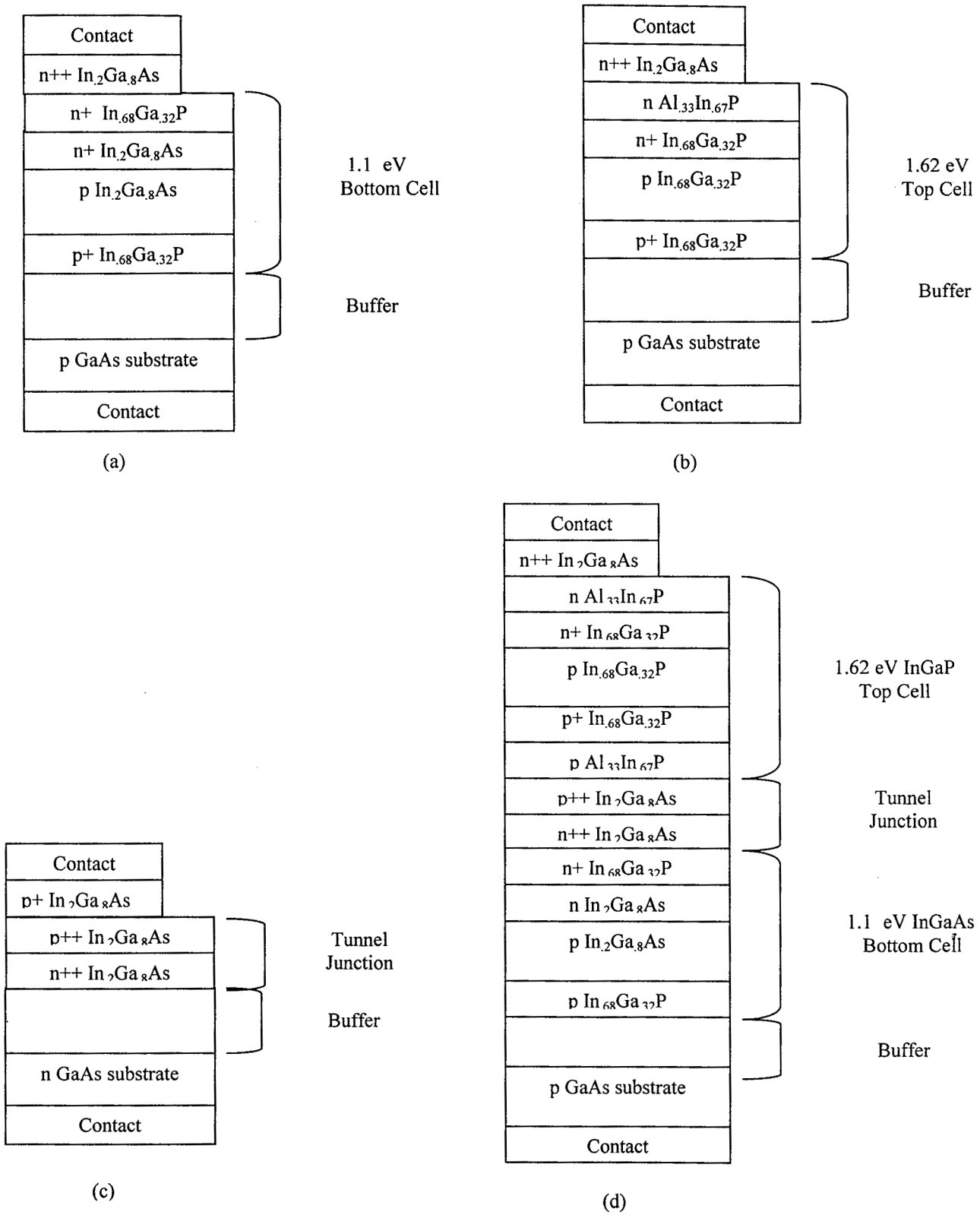

Figure 1. Epilayer structures for the 1.1 eV n/p InGaAs, 1.62 eV n/p InGaP, 1.1 eV p++/n++ InGaAs tunnel junction test structure, and the 1.62 eV InGaP/ 1.1 eV InGaAs dual junction cells are shown in (a), (b), (c), and (d) respectively.

Device Fabrication and Evaluation

The device epilayers were grown using low pressure organometallic vapor phase epitaxy (LP-OMVPE) in a horizontal reactor. All layers were grown at 150 torr on (100) GaAs substrates with 2° off cut to the nearest <110> direction or a 6° off cut to the <111>B direction. The growth rate was 7 um/hr and 4.4 um/hr for the InGaAs and InGaP cells, respectively. Precursors used for the growth were trimethylgallium (TMGa), trimethylindium (TMIn), pure arsine, pure phosphine, diethylzinc (DEZn), and diluted silane in hydrogen. Each of the devices is fabricated with a proprietary buffer layer structure whose purpose is to grade the lattice parameter from GaAs (5.6532 Å) to that of $In_{.2}Ga_{.8}As$ (5.736 Å). The buffer layer structure is designed to prevent threading dislocations from reaching the active area of the solar cells. Transmission electron microscopy (TEM) was used to determine defect structure related to lattice mismatch and to estimate the dislocation defect densities. Typically, if one defect is observed in the TEM field of view, then the defect density is above $1x10^7$ cm^{-2}. No dislocation defects were observed in the active area of any of the solar cell structures. High-resolution x-ray diffraction (HRXRD) was used to determine composition and lattice matching of the InGaAs and InGaP alloys. The InGaAs and InGaP epilayers have [004] reflection full width at half maximum (FWHM) values of approximately 250 arc-sec. In addition, all epilayers above the buffer structure are lattice-matched to one another to within 100 arc-sec.

Fig. 1 contains a schematic diagram of each of the devices discussed in this paper. The 1.1 eV bottom cell shown in Fig. 1 (a) is comprised of a 0.5 um n+ $In_{.2}Ga_{.8}As$ emitter, a 3.0 um p $In_{.2}Ga_{.8}As$ base and a 0.05 um $In_{.68}Ga_{.32}P$ window layer. The 1.62 eV bottom cell shown in Fig. 1 (b) is comprised of a 0.05 um n+ $In_{.68}Ga_{.32}P$ emitter, a 1.5 um p $In_{.68}Ga_{.32}P$ base, a 0.05 um p+ $In_{.68}Ga_{.32}P$ back surface field, and a 0.05 um n $Al_{.33}In_{.67}P$ window layer. A p++/n++ $In_{.2}Ga_{.8}As$ tunnel junction test structure, shown in Fig. 1 (c), with the same thickness (0.05 um) and doping levels ($1x\ 10^{19}$ /cm^3) used in the dual junction was evaluated prior to it's incorporation in the dual junction. The dual junction cell shown in Fig 1 (d) combines the components of each of the subcells and connects them together with the $In_{.2}Ga_{.8}As$ tunnel junction. We have chosen to use InGaAs as the tunnel junction interconnect compound since it is easily degenerately doped. The use of InGaAs as the subcell interconnect results in some absorption of red light that the bottom cell is designed to convert. As such, we plan to use a higher bandgap compound as the tunnel junction interconnect material in future designs.

Vacuum evaporated gold-based metallization was used for front and rear contacts. The front grid was fabricated using reverse image photolithography and lift off techniques. Individual cells were isolated by mesa etching into cell areas of 1 cm^2 with a grid shadow of 5%. AM0 conversion efficiencies were measured at 25°C using a single source, Spectrolab X25 solar simulator at the NASA Glenn Research Center in Cleveland, OH. Spectral response measurements as well as reflectance measurements were performed on each of the cells in order that the internal quantum efficiency could be determined.

The light current-voltage (I-V) of a 1.1 eV InGaAs bottom cell is show in Fig. 2. The one-sun AM0 efficiency of 12.56%, open circuit voltage V_{oc} = 764 mV, short circuit current density J_{sc} = 26.8 mA/cm^2, and fill factor FF= 78.6% indicate the high quality of this InGaAs cell grown mismatched to GaAs. We expect that this cell would have a one-sun AM0 efficiency of 16.5% with an optimized anti-reflective coating (ARC).

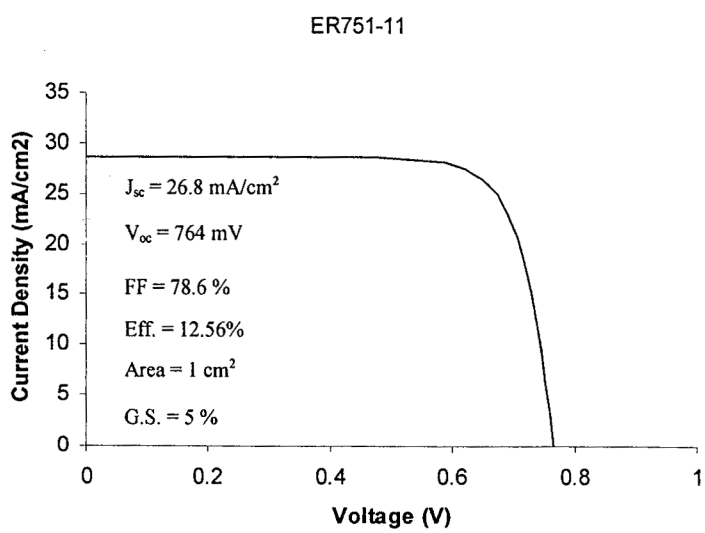

Figure 2. Current-voltage characteristic of a 1 sq. cm. 1.1 eV n/p InGaAs/ GaAs solar cell under AM0, one-sun illumination.

To put this performance into perspective, one need only to compare these data to that of a planar Si solar cell. The one-sun AM0 efficiency, open circuit voltage, and fill factor for high quality Si are 15%, 615 mV, and 81% respectively. [6] Our 1.1 eV cell performance indicates the effectiveness of the proprietary buffer in localizing the dislocation defects away from the active area of the cell.

The internal quantum efficiency of the 1.1 eV n/p InGaAs solar cell is shown in Fig.3. This data was obtained from the measured external quantum efficiency (EQE) and the optical reflectance in same wavelength interval. The optical reflectance measurements were performed on the fully processed cell and the data were not corrected for additional reflection

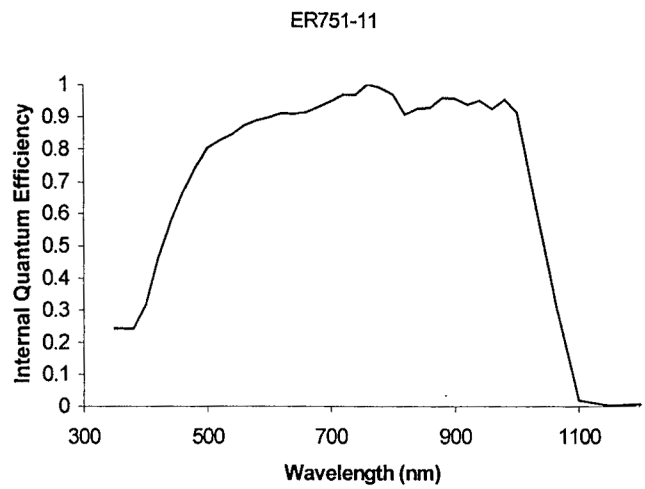

Figure 3. Internal quantum efficiency of a 1 sq. cm. 1.1 eV n/p InGaAs/ GaAs solar cell.

from the Au contact metallization. The most important portion of the IQE characteristic of the InGaAs cell lies between the 1100 nm absorption edge of the InGaAs and the 765 nm absorption edge of the InGaP. Within that wavelength band the IQE magnitude is $\geqslant$ 0.9. This cell performance is typical of the best 50% of the devices on a 2" diameter wafer.

The light I-V of a 1.62 eV n/p $In_{.68}Ga_{.32}P$ solar cell is shown in Fig. 4. The one-sun AM0 efficiency of 11.56%, V_{oc} = 1.13 V, J_{sc} = 17.0 mA/cm^2, and FF= 82.4% represents the best cell performance on this particular wafer. However 50 % of the devices had one-sun AM0 efficiencies in excess of 11%. We expect that this cell will demonstrate a one-sun AM0 efficiency of 15.7% and a J_{sc} = 22.4 mA/cm^2 with an optimized ARC.

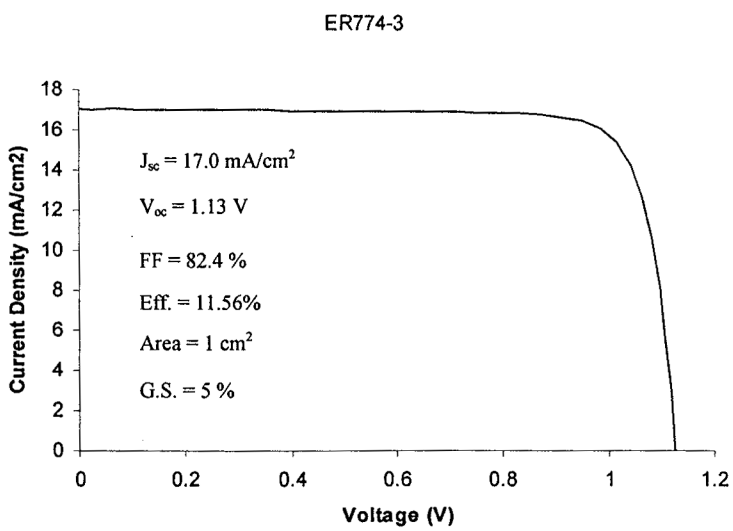

Figure 4. Current-voltage characteristic of a 1 sq. cm. 1.62 eV n/p InGaP solar cell under AM0, one-sun illumination.

The internal quantum efficiency of this cell shown in Fig. 5 is quite good, however there is a rather abrupt fall off in the IQE below 590 nm. Reflectance of this material has been performed and it is essentially flat in the wavelength region about 590 nm. The position of the transition in the IQE at 590 nm correlates well with the absorption edge of the $Al_{.33}In_{.67}P$ surface passsivation layer. In fact, this feature can be seen in the QE data of the dual junction cell grown by the Fraunhofer group. [4]

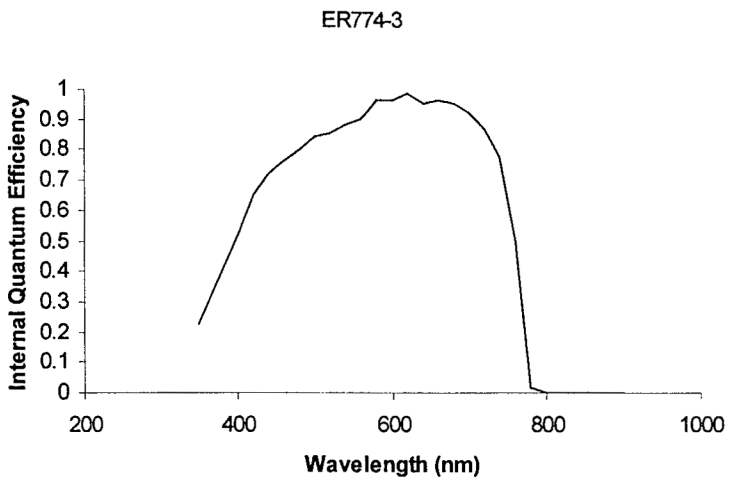

Figure 5. Quantum efficiency of a 1 sq. cm. 1.62 eV n/p InGaP solar cell.

They use a 0.03 um thick AlInP as the front surface passivation layer. This suggests that our $Al_{.33}In_{.67}P$ passivation layer thickness should be decreased from the present value of 0.05 um. Further improvements in the InGaP top cell may be realized by thinning the top cell such that the open circuit voltage may increase as a consequence of reducing the bulk recombination currents.

The structure shown in Fig. 1 (c) was processed into 150 um dia. circular diodes to evaluate the p++/n++ $In_{.2}Ga_{.8}As$ compound as a tunnel junction interconnect. Junction thicknesses of 0.1um and 0.05 um were evaluated. The peak-to-valley currents were found to be independent of the junction thickness whereas the peak voltage increased with decreasing junction thickness. A typical I-V characteristic of a 0.05 um thick tunnel junction is shown in Fig. 6. The junction was grown on the proprietary buffer layer to roughly simulate the conditions in a dual junction configuration. The device is characterized by a peak tunneling current density of 750 mA/cm^2 and a series resistivity of .1 $ohm\text{-}cm^2$ at the expected operating current density of 20 mA/cm^2. This tunnel junction series resistance will result in a negligible voltage drop at the dual junction operating current.

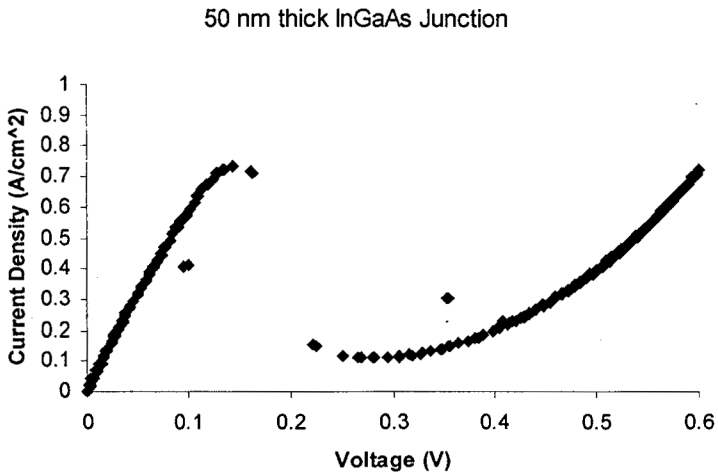

Figure 6. Current-voltage characteristic of a 150 um dia. 1.1 eV p++/n++ $In_{.2}Ga_{.8}As$ tunnel diode.

Shown in Fig. 7 is the light I-V characteristic of a 1.62 eV/1.1 eV n/p dual junction cell. The cell is characterized by a V_{oc} = 1.77 V, a J_{sc} = 11.9 mA/cm^2, a FF = 84.1%, and a one-sun AM0 efficiency of 12.9%. The AM0 efficiency of our dual junction cell would be 17% with an optimized ARC. The predicted efficiency of a 1.62 eV/1.1 eV n/p dual junction cell is 27.0 %. The short fall in the AM0 efficiency is a consequence of lower than expected V_{oc} and J_{sc} values. The dual junction V_{oc} is ≅100 mV less than the sum of the V_{oc} 's of the best 1.1 eV InGaAs and 1.62 eV InGaP cells. The origin of this voltage difference may be due to a degradation of the InGaP top cell base layer as a result of Zn out diffusion from the InGaAs tunnel junction. Secondary ion mass spectroscopy (SIMS) analysis of the cell is required to confirm this. Similar observations have been made in the lattice-matched

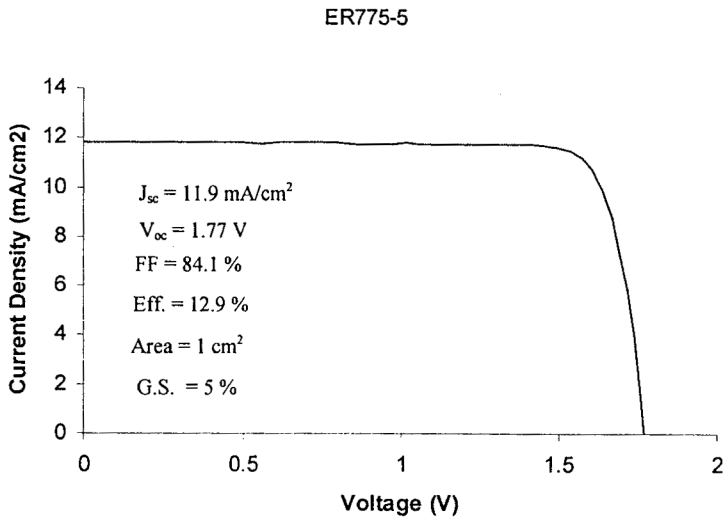

Figure 7. Current-voltage characteristic of a 1 sq. cm. 1.62 eVn/p $In_{.68}Ga_{.32}P$/ 1.1 eV $In_{.2}Ga_{.8}As$ dual junction cell.

$InGaP_2$/GaAs dual junction cell. [7] In that case the problem was solved with the use of C doping instead of Zn doping. In fact, the Fraunhofer group [4] uses C doped AlGaAs in their InGaP/InGaAs design and they report a V_{oc} /E_g ratio of 0.69 where E_g is the sum of the bandgaps of the dual junction subcells. The V_{oc} /E_g ratio for our dual junction cell is 0.65. These facts are consistent with the hypothesis of Zn dopant diffusion into the InGaP cell base acting to increase the dark current in our dual junction cell. If we are able to design a dual junction cell with no V_{oc} loss i.e. V_{oc} = 1.89 V then we would have a dual junction cell with an 18.5 % one-sun AM0 efficiency.

In addition to a lower than expected V_{oc}, the dual junction J_{sc} is only 70% of the value of the stand-alone 1.62 eV top cell. As such, the dual junction device is bottom cell current limited. The IQE for the 1.62 eV n/p InGaP/ 1.1 eV n/p InGaAs dual junction is shown in Fig. 8 along with the IQE data of the 1.1 n/p $In_{.2}Ga_{.8}As$ cell from Fig. 3 and the IQE data of the 1.62 eV n/p $In_{.68}Ga_{.32}P$ cell from Fig. 5. Integration of the QE data of the top and bottom subcells indicates that the top cell is generating 50% more current than the bottom cell. The bottom cell IQE data in Fig. 8 indicates that for this subcell the performance is not the same in the stand-alone and dual junction configurations. In particular, the magnitude of the bottom cell QE is 15% lower in the dual junction configuration. As mentioned previously, we expected some absorption of the light for wavelengths beyond 765nm. Computer modeling of absorption due to the presence of a lightly doped 0.05 um thick InGaAs layer indicates that a 7% reduction of the bottom cell J_{sc} would result. This reduction is far short of the measured 50 % reduction. Possible explanations for the reduced QE in the bottom cell could be a high interface recombination velocity at the InGaP window/ InGaAs emitter interface or a short diffusion length in the InGaAs emitter. Perhaps these effects are due to the presence of the tunnel junction. An experiment in which the QE of the tandem cells is measured after the InGaP top cell and InGaAs tunnel junction are removed via wet etching should allow one to determine if the reduced QE observed in the InGaAs bottom cell is a result of absorption in the InGaAs tunnel junction or a defective InGaAs bottom cell. Computer modeling indicates that the InGaAs bottom cell should produce 22 mA/cm^2 under one-sum AM0 illumination in the dual junction configuration. As such, the bottom cell is generating only 75 % of the current that it is predicted to produce.

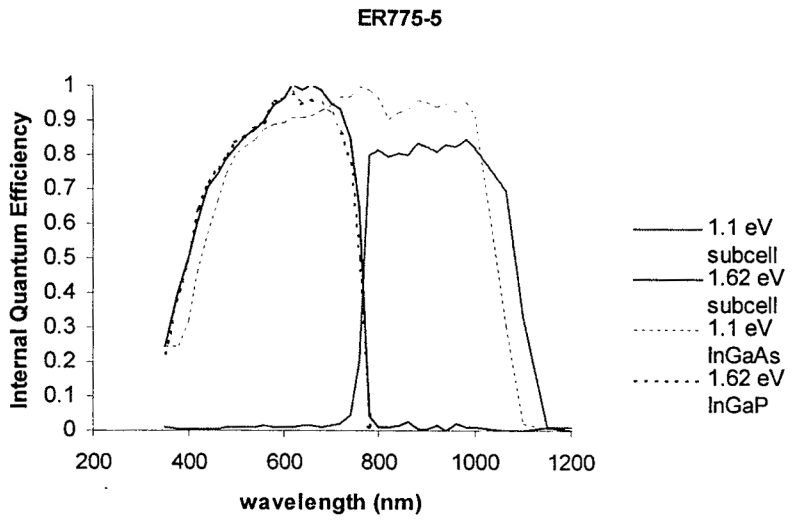

Figure 8. Internal quantum efficiency of a 1 sq. cm. 1.62 eV n/p InGaP/ 1.1 eV InGaAs dual junction cell, a 1 sq. cm. 1.62 eV n/p InGaP single junction cell, and a 1 sq. cm. 1.1 eV InGaAs single junction cell.

If a dual junction cell can be fabricated with a thinned top cell having the same quality top cell characteristics as those shown in Fig. 4 one can expect a dual junction efficiency as high as 26 %. A possible low absorption structure for the tunnel junction may be a C doped AlGaAs emitter and a Si doped InGaP base. Finally, the use of the InGaAlP quaternary for a 1.75 eV top cell in the dual junction design is necessary in order to achieve the highest conversion efficiency in the mismatched solar cell structure.

Summary

We have grown 1.1 eV n/p InGaAs cells, 1.62 eV n/p InGaP cells, and 1.62 eV n/p InGaP / 1.1 eV n/p InGaAs dual junction cells. Given an optimized ARC, the projected one-sun AM0 efficiencies of those cells are 16.5 %, 15.7 %, and 17.0 % respectively. A comparison of the dual junction V_{oc} with that of the individual 1.62 eV InGaP and 1.1 eV InGaAs cells indicates that the present dual junction design has an enhanced dark current leading to a V_{oc} loss. A similar comparison of the J_{sc} data indicates a loss of conversion efficiency in the InGaAs bottom cell. Additional experiments are necessary to determine the origin of the InGaAs bottom cell degredation in the dual junction configuration. Despite these difficulties, our results indicate that a 26 % one-sun AM0 efficiency can be obtained by controlling the dual junction dark currents, the tunnel junction optical losses, and employing top cell thinning.

This work was supported by the NASA Glenn Research Center under SBIR contract NAS3-98026.

References

[1] J.M. Olson, S.R. Kurtz, A.E. Kibbler, and P. Faine, Appl. Phys. Lett., 56, 623 (1990).
[2] D. Pal, E. Gombia, R. Mosca, A. Bosacchi, and S. Franchi, J. Appl. Phys., 84, 2965 (1998).
[3] J.C.C. Fan, B-Y. Tsaur, and B.J. Palm, Proc. 16th IEEE Photovoltaic Specialists Conf., 692 (1982).
[4] F. Dimroth, U. Schubert, and A.W. Bett, preprint submitted to the J. Appl. Phys. (1999).
[5] R.W. Hoffman, N.S. Fatemi, M.A. Stan, P. Jenkins, V.G. Weizer, D.A. Scheiman, and D.J. Brinker, Proc. of the Fall Meeting of the Materials Research Society, Boston MA, Nov. 30-Dec. 4, 1998.
[6] *Solar Cells and their Applications,* edited by L. D. Partain, (John Wiley and Sons, New York 1995), p. 25.
[7] K.A. Bertness, S. R. Kurtz, D.J. Friedman, A.E. Kibbler, C. Kramer, J.M. Olson, Appl. Phys. Lett., 65, 989 (1994).

ANTIREFLECTION COATING DESIGN FOR MULTI-JUNCTION, SERIES INTERCONNECTED SOLAR CELLS

Daniel J. Aiken
Sandia National Laboratories*
Albuquerque, NM, 87185

ABSTRACT

Analytical expressions used to optimize AR coatings for single junction solar cells are extended for use in monolithic, series interconnnected multi-junction solar cell AR coating design. The result is an analytical expression which relates the solar cell performance (through J_{SC}) directly to the AR coating design through the device reflectance. It is also illustrated how AR coating design be used to provide an additional degree of freedom for current matching multi-junction devices.

INTRODUCTION

Proper antireflection (AR) coating design for monolithic series interconnected solar cells will become more important and challenging as the number of junctions increases. These devices will require an increasingly broad spectrum AR coating while also maintaining current matching for all subcells. The goal in designing antireflection coatings for series interconnected multi-junction solar cells is not only to couple the maximum amount of light into the device, but also to distribute that light to each subcell such that the device is as closely current matched as possible. . A formal procedure for designing AR coatings for these multi-junctions is necessary. This can be accomplished by extending the analytical expressions often used in single junction AR coating design to be applicable to multi-junction design. Antireflection coating design can then be used in conjunction with subcell thickness adjustments to provide a greater flexibility for achieving current matching.

SINGLE JUNCTION AR COATING DESIGN

The goal in developing high performance antireflection (AR) coatings for solar cells is to maximize the light generated current. An expression coupling the short circuit current of a single junction solar cell to the total device reflectance $R(\lambda)$ is given by

$$J_{SC} = q \int_{\lambda} F(\lambda) \cdot EQE(\lambda) d\lambda = q \int_{\lambda} F(\lambda) \cdot IQE(\lambda) \cdot [1 - R(\lambda)] d\lambda, \tag{1}$$

where $F(\lambda)$ is the photon flux. This is the expression often used to calculate an integrated current in terms of the measurable parameters on the right side of Equation 1. Equation 1 can also be used to design an optimum AR coating because it directly relates J_{SC} to the AR coating design through the parameter $R(\lambda)$.

Another convenient parameter used in AR coating design is the solar weighted reflectance (SWR) [1], defined as

* Sandia is a multi-program laboratory operated by Sandia Corporation, a Lockheed Martin Company, for the U.S. Department of Energy under contract DE-AC04-94AL85000.

$$SWR = \frac{\text{useable photons reflected}}{\text{total useable photons}} = \frac{\int F(\lambda)\cdot IQE(\lambda)\cdot R(\lambda)\cdot d\lambda}{\int F(\lambda)\cdot IQE(\lambda)\cdot d\lambda}. \tag{2}$$

Equation 1 can be manipulated and inserted into Equation 2, resulting in an alternative expression for SWR given by [2]

$$SWR = 1 - \left(\frac{J_{sc}}{J_{sc}\big|_{R(\lambda)=0}} \right) \tag{3}$$

Minimizing the SWR will minimize the number of reflected photons that would otherwise generate electrons which are then also collected. Minimizing SWR therefore couples the maximum amount of useable light into the solar cell and maximizes the short circuit current, as suggested by Equation 3. These equations assume negligible parasitic absorption in the antireflection coating.

MULTI-JUNCTION AR COATING DESIGN

Maximizing the light generated current in series interconnected multi-junction solar cells places an additional design requirement on AR coatings. In this case the goal is not only to couple the maximum amount of light into the device, but also to distribute that light to each subcell such that the device is as closely current matched as possible. Stated alternatively, the goal is to maximize the light generated current of the current-limiting subcell.

Equations 1 or 2 could also be used to design AR coatings for series connected multi-junction solar cells, provided that the term IQE(λ) is replaced with $IQE_x(\lambda)$. Here $IQE_x(\lambda)$ is the internal quantum efficiency of the current limiting subcell as measured using the spectrally selective light biasing technique described by Burdick and Glatfelter [3]. The problem in doing this is that, in searching for an AR coating design that minimizes the SWR, R(λ) will change which may also result in a different subcell limiting the current, especially if the subcells are already closely current matched before AR coating deposition. To eliminate this difficulty, Equation 1 can be modified to accommodate multi-junction AR coating design such that the correct current limiting subcell for any given AR coating design does not have to be explicitly known. A more general form of Equation 1 which is applicable to multijunction AR coating design is then given by

$$J_{sc} = \mathrm{MIN}\left[J_{sc1}, J_{sc2}, etc.\right] = \mathrm{MIN}\left[q \int_{\lambda} F(\lambda)\cdot IQE_1(\lambda)\cdot[1-R(\lambda)]d\lambda \;,\; q \int_{\lambda} F(\lambda)\cdot IQE_2(\lambda)\cdot[1-R(\lambda)]d\lambda \;,\; \text{etc.} \right], \tag{4}$$

where J_{SC1} and J_{SC2} are the short circuit currents that subcells 1 and 2 are capable of generating, respectively. Although the solar weighted reflectance is a useful parameter for designing and comparing AR coatings for single junction solar cells, this parameter loses its physical significance for multi-junction solar cells and is therefore not defined here. The difficulty is that a different subcell may be limiting the device in the two cases R(λ) = 0 and R(λ) ≠ 0, resulting in a SWR greater than unity.

Equation 4 is employed in practice by using optical theory [4] to model and calculate R(λ) as a function of the thicknesses and optical properties of the materials used in a given AR coating structure. These equations will accurately optimize the AR coating as long as the reflectance of the multi-junction cell structure can be accurately modeled. This requires knowledge of the index of refraction and absorption coefficients for all relevant cell materials. Additionally, because multi-junction cell structures are optically very complicated, analytic expressions for R(λ) quickly become unmanageable and computer simulation must be used. For example, all

AR coating optimization reported here was done using FILM-STAR DESIGN optical thin film software from FTG Associates [5].

AR COATING DESIGN AS A CURRENT MATCHING TECHNIQUE

Multi-junction subcells that are already well current matched before AR coating deposition require a reflectance that is as low and flat as possible across the spectral range of interest such that current matching is maintained. The primary technique for current matching a multi-junction solar cell is by adjusting the individual subcell thicknesses. This technique is not infinitely flexible because the absorption in any subcell is dependent not only on its own thickness but also on the thickness of all subcells above it. Furthermore, increasing a subcells thickness to values significantly greater than the base diffusion length will not enhance that subcell's current generating capability. This imposes an upper limit on the useful thickness of any subcell in terms of current matching.

Proper AR coating design can provide an additional degree of freedom for current matching multi-junction devices by minimizing the reflectance in spectral regions where the corresponding subcells are current limiting the device, and trading that for higher reflectivity where other subcells have current to spare. Equation 4 will automatically perform this task by optimizing the AR coating design so as to maximize the current generating capability of the current limiting subcell.

This technique is illustrated with Figures 1 and 2. Shown in Figure 1 are the individual IQE curves of a typical 2-junction InGaP/GaAs multi-junction that is well current matched. Also shown is the modeled reflectance of a simplified cell structure with double layer AR coating that was optimized using Equation 4. It is apparent that the AR coating has been properly optimized such that reflectance loss is divided equally between both subcells, thereby keeping the multi-junction current matched.

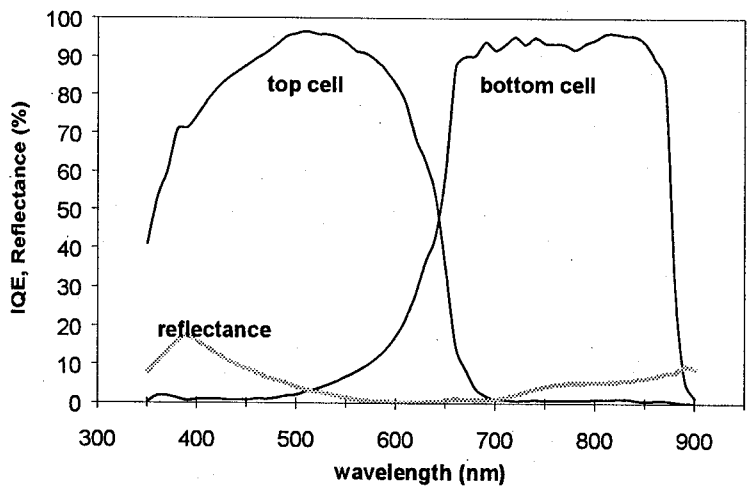

Figure 1 Reflectance of a 2-junction solar cell with an AR coating optimized for current matched subcells.

In Figure 2 a current mismatch scenario has been modeled by lowering the IQE of the top subcell. The AR coating optimized for this case has traded higher reflectance in the bottom cell spectral region for lower reflectance in the top cell region, thereby assisting in current matching this multi-junction. Table 1 lists the simulated short circuit current densities for the devices in Figures 1 and 2. The optimized AR coating for the current matched subcells of Figure 1 has resulted in both subcells possessing equal current loss due to reflection. This results in a maximum Jsc for the multi-junction. The optimized AR coating for the top subcell limited multi-junction of Figure 2 has traded higher reflectivity for the bottom subcell in exchange for low reflectivity for the current limiting top subcell. This results in a lower current lost due to reflection for the top subcell (0.48 mA/cm^2) and maximizes the multi-junction Jsc.

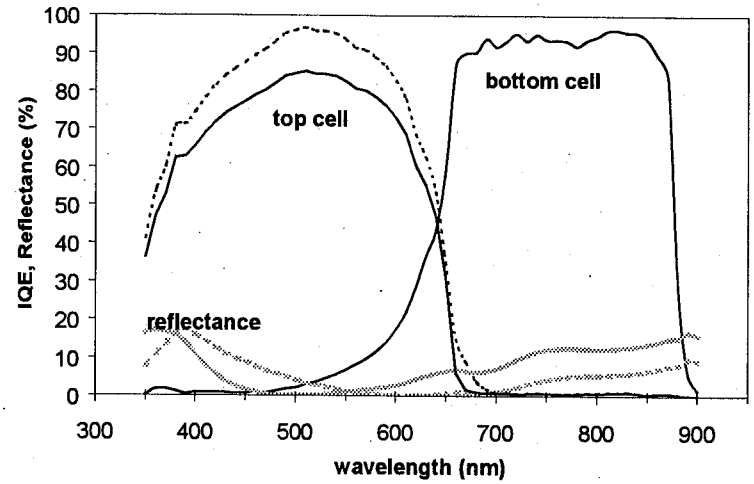

Figure 2 Reflectance of a 2-junction solar cell with an AR coating optimized for a current limiting top subcell. The top cell IQE and optimized reflectance from Figure 1 are shown as dashed lines for comparison.

Table I Simulated short circuit current densities for the 2-junction solar cells in Figures 1 and 2.

	Current matched (Figure 1)		Current mismatched (Figure 2)	
	Top cell	Bottom cell	Top cell	Bottom cell
Jsc (R(λ)=0), (mA/cm^2)	17.95	18.05	15.68	18.05
Jsc, (mA/cm^2)	17.22	17.22	15.20	16.39
Jsc lost to reflectance, (mA/cm^2)	0.73	0.83	0.48	1.66

Figure 3 illustrates the current matching technique for a hypothetical 4-junction solar cell with bandgaps chosen such that the multi-junction is nearly current matched. Shown in Figure 3 is the portion of the AM0 spectrum that each subcell could convert to current. The area under each curve is the current available to each subcell. In the limiting case of no reflectance loss this multi-junction is current limited by subcell 3, as suggested by Table II. This multi-junction is likely to be more difficult to current match by adjusting subcell thicknesses due to the larger number of subcells and the limited flexibility afforded by changing subcell thicknesses as discussed previously. The AR coating which optimizes this multi-junction performance is also shown in Figure 3. Current matching has been assisted by minimizing the current that subcell 3 has lost to reflection, as shown in Table II.

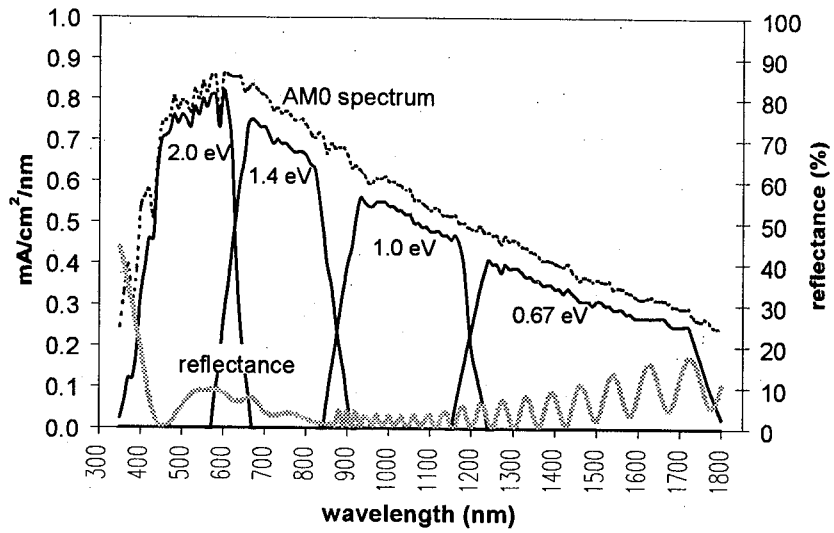

Figure 3 Reflectance of a simulated future 4-junction solar cell with an AR coating optimized for a current limiting third subcell.

Table II Simulated short circuit current densities for the 4-junction solar cell simulated in Figure 3.

	Top cell	2nd cell	3rd cell	Bottom cell
Jsc (R(λ)=0), (mA/cm^2)	17.31	17.34	16.30	18.29
Jsc, (mA/cm^2)	16.03	16.64	15.97	17.09
Jsc lost to reflectance, (mA/cm^2)	1.28	0.70	0.33	1.20

CONCLUSIONS

Analytical expressions exist for designing and optimizing AR coatings for single junction solar cells. In the single junction case the goal is to couple the maximum amount of light into the cell. For series connected multi-junction devices current matching is also a critical design goal. The goal in designing antireflection (AR) coatings for series interconnected multi-junction solar cells is therefore not only to couple the maximum amount of light into the device, but also to distribute that light to each subcell such that the device is as closely current matched as possible. Analytical expressions used to optimize AR coatings for single junction solar cells have been extended for use in monolithic, series interconnnected multi-junction solar cell AR coating design. The result is an analytical expression which couples the solar cell performance (through J_{SC}) directly to the AR coating design through the device reflectance. This expression assumes that the reflectance of a multi-junction device structure can be accurately modeled and therefore requires knowledge of optical constants for all relevant materials in the multi-junction. It was also illustrated how this expression can be employed such that AR coating design can be used to provide an additional degree of freedom for current matching multi-junction devices.

REFERENCES

[1] P. Doshi, G.E. Jellison, and A. Rohatgi, "Characterization and Optimization of Absorbing Plasma-Enhanced Chemical Vapor Deposition Deposited Antireflection Coatings for Silicon Photovoltaics", *Applied Optics*, vol 36, no. 30, p. 7826, 1997.

[2] J. Zhao and M.A. Green, "Optimized Antireflection Coatings for High Efficiency Silicon Solar Cells", *IEEE Transactions on Electron Devices*, vol. 38, no. 8, p.1925, 1991.

[3] J. Burdick and T. Glatfelter, "Spectral Response and I-V Measurements of Tandem Amorphous Silicon Alloy Solar Cells", *Solar Cells*, vol. 18, p. 301, 1986.

[4] H.A. MacLeod, *Thin Film Optical Filters*, McGraw-Hill, 1989.

[5] version 2.0 from FTG Software Associates, P.O. Box 579, Princeton, N.J. 08542.

RECENT SPACE PHOTOVOLTAIC RESEARCH AND DEVELOPMENT IN JAPAN

Masafumi Yamaguchi and Sumio Matsuda*

Toyota Tech. Inst., Tempaku, Nagoya 468-8511, Japan
** National Space Development Agency of Japan, Tsukuba, Ibaraki 305-8505, Japan*

This paper reviews recent space solar cell R&D activities in Japan. R&D of super-high efficiency multi-junction cells are carried out in the New Sunshine Project. Up to now, the InGaP/GaAs 2-junction cells fabricated on Ge substrates have reached 30.9% at AM1.5, and high-efficiency of 26.9% at AM0 has also been attained with the InGaP/GaAs 2-junction cells on GaAs substrates. As by-product of high-efficiency cells, the same cells are thought to have the potential for space applications.

By using a small satellite MDS-1 with a solar cell monitor board, Japanese solar cells developed for terrestrial use such as poly-Si, a-Si/n-Si hetero-junction, $CuInGaSe_2$ and InGaP/GaAs 2-junction cells will be evaluated in space. For this end, such cells have been evaluated on the ground.

In the field of Si space solar cells, the accident of the Engineering Test Satellite-VI has provided an opportunity to clarify the mechanism on the anomalous degradation of Si space cells under high fluence irradiation. As previously reported by the authors, the anomalous degradation of Si space cells under high fluence irradiation is explained by carrier removal effect and type conversion caused by radiation-induced defects in p-type base layer. According to the DLTS analysis, carrier removal and type conversion in p-Si are found to be caused by generation of E_v+0.36eV (C_i-O_i), E_v+0.18eV (V-V) and E_c-0.18eV (B_i-O_i). A new project to improve the end-of-life efficiency of Si space cells has also been started.

I. R&D Activities of III-V Compound Solar Cells in Japan [1]

The super-high efficiency solar cell project for terrestrial use started under the New Sunshine program of MITI (Ministry of International Trade and Industry) and NEDO (New Energy and Industrial Technology Development Organization) in fiscal year 1990. The challenging objectives of the projects are to obtain twice conversion efficiencies of the 90-year values at the laboratory level by the beginning of the 21st century and to produce such efficiency cells by 2010. Although some subprograms for super-high efficiency solar cells have been conducted, only R&D subprogram for the multi-junction solar cells are remained.

High-efficiency InGaP/GaAs 2-junction cells with efficiencies of 30.6% at AM1.5 and 26.9% at AM0 were fabricated on GaAs substrates by the metal-organic chemical vapor deposition (MOCVD) method by Japan Energy Co. The mechanically stacked 3-junction cells of monolithically grown InGaP/GaAs 2-junction cells and InGaAs bottom cells have reached the highest efficiency of 33.3% at 1-sun AM1.5 following joint work by Japan Energy Co. and Sumitomo Electric Co.

Selection of top cell materials is also important for high-efficiency tandem cells. As a top cell material latticed matched to GaAs or Ge substrates, InGaP has some advantages [2] such as lower interface recombination velocity, less oxygen problem and good window layer material compared to AlGaAs. The top cell characteristics depend on the minority carrier lifetime in the top cell layers.

Figure 1 shows changes in photoluminescence (PL) intensity of the solar cell active layer as a function of the minority carrier lifetime (τ) of the p-InGaP base layer grown by MOCVD and surface recombination velocity (S). The lowest S was obtained by introducing the AlInP window layer and the highest τ was obtained by introducing buffer layer and optimizing the growth temperature. The best conversion efficiency of the InGaP single junction cell was 18.5 %.

Another important issue for realizing high-efficiency monolithic-cascade type tandem cells is the achievement of optically and electrically low-loss interconnection of two or more cells. A degenerately doped tunnel junction is attractive because it only involves one extra step in the growth process. To minimize optical absorption, formation of thin and wide-bandgap tunnel junctions is necessary. However, the formation of a wide-bandgap tunnel junction is very difficult, because the tunneling current decreases exponentially with increase in bandgap energy.

In addition, impurity diffusion from a highly doped tunnel junction during overgrowth of the top cell increases the resistivity of the tunnel junction. A double hetero (DH) structure was found to be useful for preventing diffusion by the authors [3]. Figure 2 shows formation and migration enthalpy of group III-vacancy versus bond-gap energy of the materials. Effective suppression of the Zn diffusion from tunnel junction by the InGaP tunnel junction with the AlInP-DH structure is thought to be attributed to the lower diffusion coefficient for Zn in the wider bandgap energy materials such as the AlInP barrier layer and InGaP tunnel junction layer.

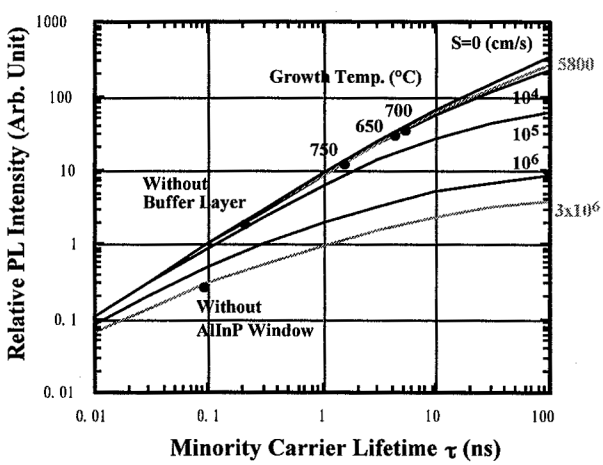

Fig. 1. Changes in PL intensity of the solar cell active layer as a function of the minority carrier lifetime (τ) of the p-InGaP base layer and surface recombination velocity (S).

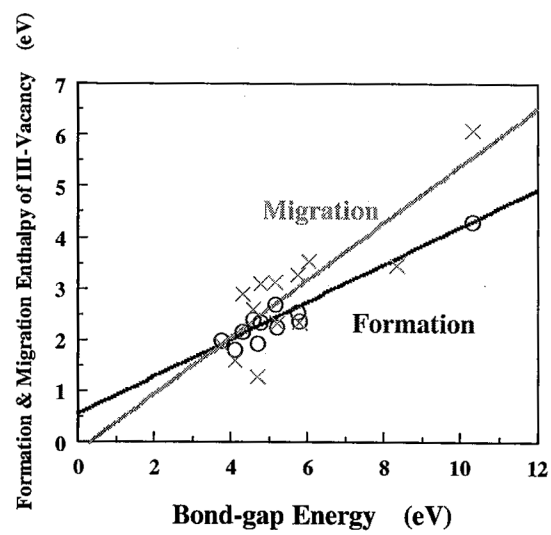

Fig. 2. Changes in formation and migration energies of III-group element vacancies as a function of bond-gap energy of III-V compound materials.

More recently, monolithically grown InGaP/InGaAs 2-junction cells with a 1-sun AM1.5 efficiency of 30.9% have been successively fabricated on Ge substrates by Japan Energy Co. [4] as results of lattice-match improvement between bottoms cells and Ge substrates and introduction of the C-doped AlGaAs/Si-doped InGaP hetero-structure tunnel junction with AlInP barriers. This value is the highest ever reported for the 2-junction cells under 1-sun illumination. Figures 3 and 4 show a schematic structure of an InGaP/InGaAs 2-junction fabricated on a Ge substrate and its light-illuminated I-V

curve and spectral response. Lattice matching is also one of the most important issues for achieving high minority-carrier lifetime and high-efficiency cells.

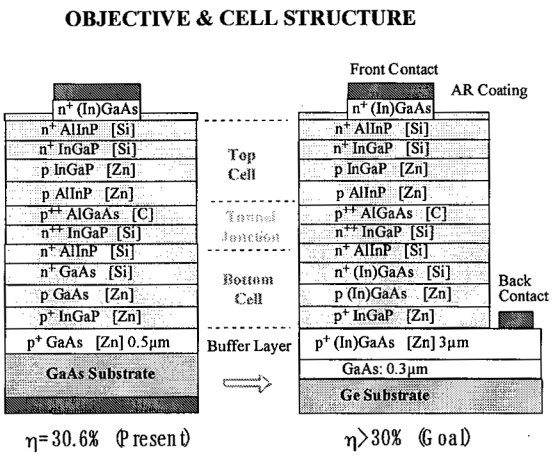

Fig. 3. A schematic structure of an InGaP/InGaAs 2-junction fabricated on a Ge.

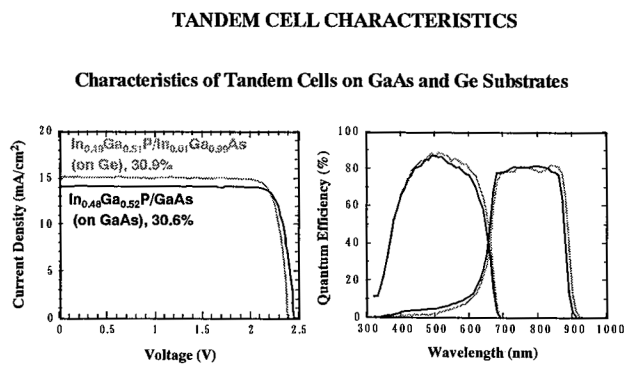

Fig. 4. Light-illuminated I-V curve and spectral response of an InGaP/InGaAs 2-junction fabricated on a Ge substrate.

Table I summarizes research activities of III-V compound solar cells in Japan.

Table I. Summary of research activities of III-V compound solar cells in Japan.

Solar Cells		Area (cm^2)	AM	Efficiency (%)	Organization	Year
Bulk	GaAs bulk	0.25	AM1.5	25.4	Hitachi Cable	1996
		4	AM0	22.5	Mitsubishi Electric	1987
	InP bulk	0.25	AM1.5	22.0*	NTT	1986
Thin-film	InGaP/InGaAs 2-junction-on-Ge	1	AM1.5	30.9	Japan Energy	1999
	GaAs-on-Si	1	AM1.5	20.0	NTT	1989
Tandem	InGaP/GaAs 2-Junction	4	AM1.5	30.3	Japan Energy	1996
		9	AM1.5	30.6	Japan Energy	1998
		4	AM0	26.9	Japan Energy Toyota Tech. Inst.	1997
	AlGaAs/GaAs2-Junction	0.25	AM1.5	20.2	NTT	1987
		0.25	AM1.5	27.6	Hitachi Cable	1999
	GaAs/InGaAs Mechanically Stacked	1	AM1.5	28.8	Sumitomo Electric	1996
	AlGaAs/Si 2-Junction	0.25	AM0	21.2*	Nagoya Inst. Tech.	1996
	InGaP/GaAs/InGaAs MS 3-Junction	1	AM1.5	33.3	Japan Energy Sumitomo Electric	1997
Concen. Tandem	InGaP/GaAs 2-Junction	1	AM1.5 (x 20)	31.5	Toyota Tech. Inst. Japan Energy	1999

* active-area efficiency

Some effort has been made to put this type cells into commercial production for space applications by TECSTAR and Spectrolab. based on the Multi-junction Solar Cell Manufacturing Technology Program [5]. In fact, the commercial satellite with 2-junction GaInP/GaAs-on Ge solar arrays was launched in August 1997 [6]. Therefore, tandem solar cells will be widely used in space. In order to apply super high-efficiency cells widely, it is necessary to improve their conversion efficiency and reduce their cost.

II. Evaluation Program of Terrestrial Solar Cells in Space by MDS-1

NASDA plans to launch a small satellite MDS-1 (Mission Demonstration-test Satellite-1) and put into the geostationary-transfer-orbit (apogee 500km, perigee 36,000km, inclination 28.50) in the summer of 2000. The objectives of this project are to test the function of commercial-off-the-shelf (COTS) devices in orbit, to test the minimization technology for components, and to measure space environment data. Although the satellite mission period is one year, the devices will be exposed under 10 times accelerated-radiation conditions. As a part of this project, Japanese solar cells developed for terrestrial use such as poly-Si, a-Si/n-Si hetero-junction, $CuInGaSe_2$ and InGaP/GaAs 2-junction cells will be installed on a solar cell monitor board and will be evaluated in space. The purposes of this experiment are to study the feasibility of using the cells in space and to utilize the obtained data to the development of future space solar cells. Tabel II lists the state-of-the-art Japanese six solar cells developed for terrestrial use [7].

Table II. Performance of evaluated terrestrial solar cells.

Cell Symbol	Voc (mV)	Isc (mA/cm²)	FF	Pmax (mW/cm²)	Eff. (%)	Φ_{CE} (e/cm²)	Φ_{CP} (p/cm²)	Φ_{CPL} (p/cm²)	Comment
A	586	33.1	0.75	14.5	10.7	4.2×10^{15}	1.2×10^{12}	2.7×10^{11}*	Poly-Si Cell
B	589	36.1	0.73	15.5	11.5	3.5×10^{15}	1.5×10^{12}	3.0×10^{11}*	Poly-Si Cell
C	552	40.9	0.69	18.3	13.5	2.3×10^{13}	1.7×10^{11}	3.2×10^{9}*	n-Type Base Si Cell
D	2362	15.9	0.88	33.2	24.5	2.5×10^{13}	3.7×10^{12}	1.3×10^{12}*	InGaP/GaAs Cell
E	540	37.8	0.61	12.4	9.2	------ ***	9.5×10^{13}	4.1×10^{12}**	CIS Cell
F	599	31.5	0.66	12.5	9.2	------ ***	1.7×10^{14}	1.6×10^{13}**	CIS Cell

Listed Output is at Before Irradiation
AM0, 135.3mW/cm², 28°C
Φ_{CE} : 1MeV electron fluence at 60% of initial Pmax.
Φ_{CP} : 10MeV proton fluence at 60% of initial Pmax.
Φ_{CPL}: Low energy (* 3MeV, ** 380KeV) proton fluence at 60% of initial Pmax.
*** : Too Large

For this end, such cells have been evaluated on the ground. Figure 5 shows the results of 1-MeV electron irradiation tests and 10-MeV proton irradiation tests for two poly-Si cells, a-Si/n-Si hetero-junction cell, InGaP/GaAs 2-junction cell, and two $CuInGaSe_2$ (CIGS) cells.

Radiation tolerance of the polycrystalline Si cells with initial AM0 conversion efficiencies of 10.7-11.5% is found to be similar to that of single-crystalline Si cells.

Although the a-Si/n-Si hetero-junction cell has shown an initial efficiency of 13.5% at AM0, large radiation degradation is observed. This is because n-Si base layer is substantially not radiation tolerant than p-Si base layer due to larger damage coefficient of n-Si.

The InGaP/GaAs tandem cell has shown the highest initial AM0 conversion efficiency of 24.5% and better radiation resistance to 1-MeV electron and 10-MeV proton irradiations. Slightly higher radiation degradation of our InGaP/GaAs tandem cell compared to those of GaAs-on-Ge and InGaP/GaAs space cells seems to be due to deeper junction depth of the GaAs bottom cell.

Although CIGS cells have shown low initial efficiency of 9.2% at AM0, excellent radiation resistance to 1-MeV electron irradiation has been observed. The CIGS cells are also found to be not so resistant to proton irradiation, especially for low-energy (380keV) protons.

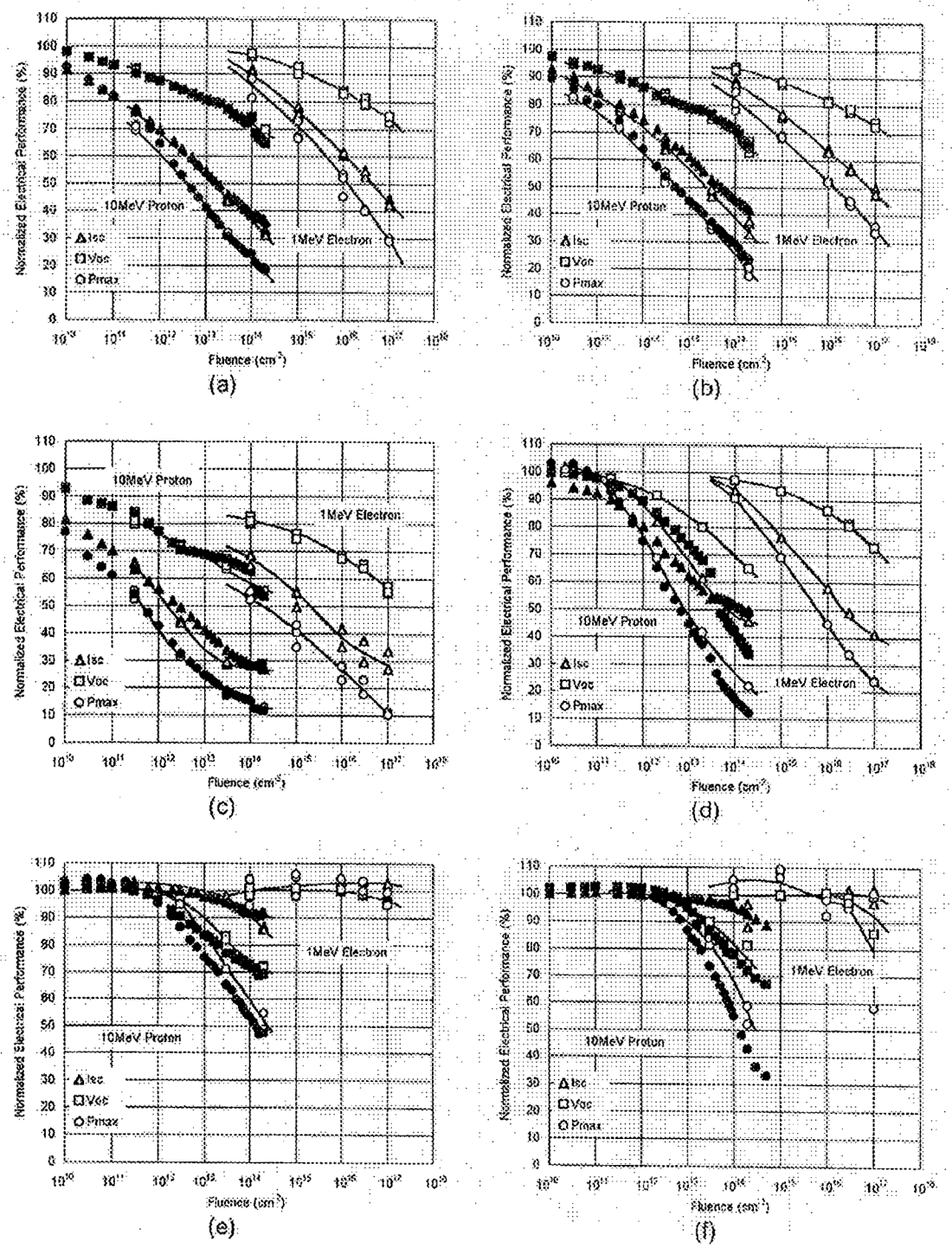

Fig. 5. The results of 1-MeV electron irradiation tests and 10-MeV proton irradiation tests for (a), (b) two poly-Si cells, (c) a-Si/n-Si hetero-junction cell, (d) InGaP/GaAs 2-junction cell, and (e), (f) two $CuInGaSe_2$ (CIGS) cells.

III. Fundamental Researches on Radiation Damages to Space Solar Cells and Materials

In the field of Si space solar cells, the accident [8] of the Engineering Test Satellite-VI (ETS-VI) has provided an opportunity to clarify the mechanism on the anomalous degradation of Si space cells under high fluence irradiation. NASDA (National Space Development Agency of Japan) has organized "the Committee for the Study of Radiation Damage Mechanism of Solar Cells" and some professionals have analyzed the radiation damages to Si and solar cells by deep-level transient spectroscopy (DLTS), photoluminescence, electron spin resonance measurements, and so forth.

The samples were BSFR (Back-Surface Field and Reflector) structure n^+-p-p^+ Si space solar cells and diodes with p-base layer resistivity of around 10Ωcm (base doping concentration of 1-2 x 10^{15} cm^{-3}) and junction depth of 0.15μm. In the cell and diode fabrication, B-doped Si single crystals grown by the Czochralski method were used and n^+-p-p^+-BSF (Back-Surface Field) layers were made by thermal diffusion of P and B. Cell and diode thickness was 50 μ m.

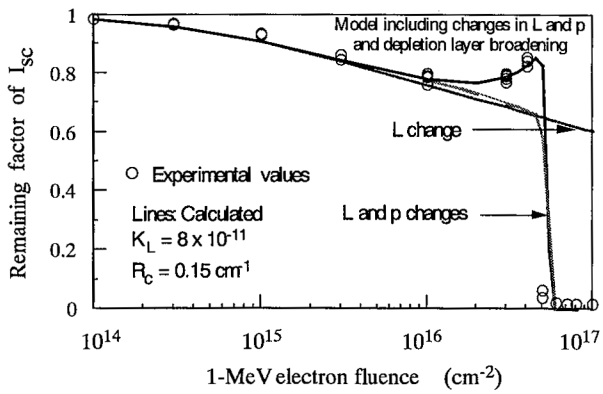

Fig. 6. Comparison of experimental results for short-circuit current degradation of Si cells with 1-MeV electron irradiation and analytical results calculated by considering mechanisms; (1) minority-carrier diffusion length decrease, (2) depletion layer broadening, and (3) carrier concentration decrease with irradiation.

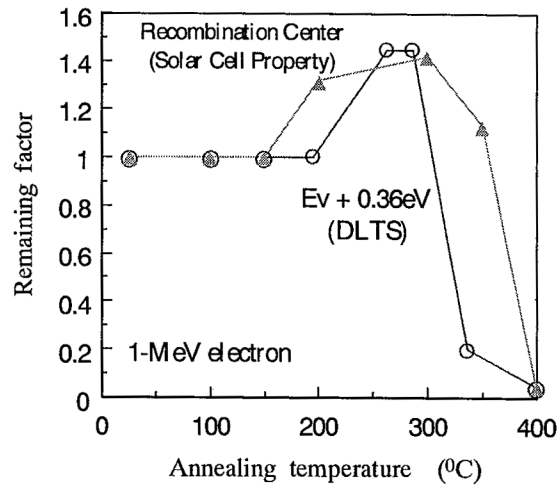

Fig. 7. Comparison of isochronal (10 minutes) annealing of density of the majority-carrier trap at E_v+0.36eV measured by DLTS with that of recombination center determined by solar cell properties in p-type Si irradiated with 1-MeV electrons.

As previously reported by the authors [9], the anomalous degradation of Si space cells under high fluence irradiation is explained by carrier removal effect (including depletion layer broadening) and type conversion caused by radiation-induced defects in p-type base layer. Figure 6 shows comparison of experimental results for short-circuit current degradation of Si space cells with 1-MeV electron irradiation and analytical results calculated by the model proposed. Moreover, type conversion of p-type Si from p-type to n-type has also been observed under the higher fluence irradiation above 5 x 10^{16} cm^{-2}, by using electron beam-induced current (EBIC) and Hall effect measurements. Change from n^+-p-p^+ structure to n^+-n-p^+ structure due to type conversion of p-Si layer in Si solar cells under high fluence irradiation has also been confirmed using the EBIC method.

Deep level transient spectroscopy (DLTS) analysis [10-12] of radiation-induced defects in p-type Si crystals and solar cells has been carried out to clarify the mechanism on an anomalous degradation of Si n^+-p-p^+ structure space cells induced by high-energy, high-fluence electron/proton irradiations. A large concentration of a minority carrier trap with an activation energy of about 0.18eV has been observed in irradiated p-Si using DLTS measurements, as well as the

majority carrier traps at around E_v+0.18eV and E_v+0.36eV. Correlation between DLTS data and solar cell properties for irradiated and annealed Si diodes and solar cells have shown that type conversion of p-Si base layer from p-type to n-type is found to be mainly caused by introduction of the 0.18eV minority-carrier trap center, that is, this center acts as a deep donor center. [13]. The E_v+0.36eV majority-carrier trap center is thought to also act as a recombination center [14] that decreases minority-carrier lifetime (diffusion length). Figure 7 compares isochronal (10 minutes) annealing of density of the majority-carrier trap at E_v+0.36eV measured by DLTS and recombination center determined by solar cell properties in p-type Si irradiated with 1-MeV electrons.

Moreover, origins of radiation-induced defects in heavily irradiated p-Si and generation of deep donor defect have also been examined.

In order to clarify the origins of radiation-induced defects in Si and correlation between their behavior and Si solar cell properties, DLTS analysis has been carried out. Table III summarizes trap levels, introduction rates, cross sections and possible identifications of defects in p-type Si induced by 1-MeV electrons. The possible identifications of the E_v+0.18eV, E_v+0.36eV and. E_c-0.18eV are the di-vacancy V-V^+, C_i-O_i and B_i-O_i, respectively.

Table III. Trap levels E_a, introduction rates I_t, cross sections σ and possible identifications of defects induced by 1-MeV electrons

E_a (eV)	I_t (cm^{-1})	σ (cm^2)	possible identification
E_v + 0.18	0.003	8.9×10^{-17}	V-V^+ +?
E_v + 0.36	0.007	7.2×10^{-16}	C_I-O_I +? (V-O-B / V-C-O)
E_c - 0.18	0.013	1.8×10^{-16}	B_I-O_I+?

However, the microscopic origins of the above defects are still unclear at present. Further study is necessary.

IV SUMMARY

This paper reviewed recent space solar cell R&D activities in Japan. Up to now, the InGaP/GaAs 2-junction cells fabricated on Ge substrates have reached 30.9% at AM1.5, and high-efficiency of 26.9% at AM0 has also been attained with the InGaP/GaAs 2-junction cells on GaAs substrates. By using a small satellite MDS-1 with a solar cell monitor board, Japanese solar cells developed for terrestrial use such as poly-Si, a-Si/n-Si hetero-junction, $CuInGaSe_2$ and InGaP/GaAs 2-junction cells will be evaluated in space. For this end, such cells have been evaluated on the ground. In the field of Si space solar cells, the accident of the Engineering Test Satellite-VI has provided an opportunity to clarify the mechanism on the anomalous degradation of Si space cells under high fluence irradiation. As previously reported by the authors, the anomalous degradation of Si space cells under high fluence irradiation is explained by carrier removal effect and type conversion caused by radiation-induced defects in p-type base layer. According to the DLTS analysis, carrier removal and type conversion in p-Si are found to be caused by generation of E_v+0.36eV (C_i-O_i), E_v+0.18eV (V-V) and E_c-0.18eV (B_i-O_i).

REFERENCES

[1] M. Yamaguchi, to be presented at PVSEC-11, Sapporo, Japan, (1999).

[2] J.M. Olson, S.R. Kurtz and K.E. Kibbler, Appl. Phys. Lett. **56**, 623 (1990).

[3] C. Amano, H. Sugiura, A. Yamamoto and M. Yamaguchi, Appl. Phys. Lett. **51**, 1998 (1987).

[4] T. Takamoto, E. Ikeda, T. Agui, and H. Kurita, to be presented at PVSEC-11, Sapporo, Japan, (1999).

[5] D.N. Keener, D.C. Marvin, D.J. Brinker, H.B. Curtis and P.M. Price, Proc. 26th IEEE Photovoltaic Specialists Conf., (IEEE, New York, 1997) p.787.

[6] M.R. Brown, L.J. Goldhammer, G.S. Goodelle, C.U. Lortz, J.N. Perron, J.S. Powe, J.A. Schwartz, B.T. Cavicchi, M.S. Gillanders and D.D. Krut, Proc. 26th IEEE Photovoltaic Specialists Conf., (IEEE, New York, 1997) p.805.

[7] T. Hisamatsu, T. Aburaya and S. Matsuda, Proc. 2nd World Conference on Photovoltaic Solar Energy Conversion (WIP, 198) p.3568.

[8] Y. Yamamoto, O. Kawasaki, S. Matsuda and Y. Morita, *Proc. of European Space Power Conference*, (ESA, 1995) p.573.

[9] M.Yamaguchi, S.J. Taylor, S. Matsuda and O. Kawasaki, Appl. Phys. Lett. **68**, 3141 (1996).

[10] S.J. Taylor, M. Yamaguchi, S. Matsuda, T. Hisamatsu and O. Kawasaki, J. Appl. Phys. **82**, 3239 (1997).

[11] M. Yamaguchi, A. Kahn, S.J. Taylor, K. Ando, T. Yamaguchi, S. Matsuda and T. Aburaya, J. Appl. Phts. **86**, 217 (1999).

[12] A. Kahn, M. Yamaguchi, S.J. Taylor, T. Hisamatsu and S. Matsuda , Jpn. J. Appl. Phts. **38**, 2679 (1999).

[13] T. Yamaguchi, S.J. Taylor, S. Watanabe, K. Ando, M. Yamaguchi, T. Hisamatsu and S. Matsuda, Appl. Phys.Lett. **72**, 1226 (1998).

[14] I. Weinberg and C.K. Swartz, Appl. Phys. Lett. 36, 693 (1980).

Development of a Thin Film Amorphous Silicon Space Solar Cell For the PowerSphere Concept

Edward J. Simburger, David Scott, Dennis Smith, David Gilmore, Mike Meshishnek and Meg Abraham
The Aerospace Corporation
Los Angeles, Ca. 90009

Frank R. Jeffery
Iowa Thin Film Technologies, Inc.
Boone, IA 50036

Abstract

The Aerospace Corporation has independently developed conceptual designs for microsatellites and nanosatellites. This development of microsatellites and nanosatellites for low earth orbits requires the collection of sufficient power for onboard instruments with a low weight, low volume spacecraft. Because the overall surface area of a microsatellite or nanosatellite is small, body-mounted solar cells are incapable of providing enough power. Deployment of traditional, rigid, solar arrays necessitates larger satellite volumes and weights, and also requires extra apparatus needed for pointing. One potential solution to this "power choke" problem is the deployment of a large, spherical, inflatable power system. This power system, termed the "PowerSphere", would offer a high collection area, low weight, and low stowage volume, and eliminate the need for a pointing mechanism.[1][2]

Development of the PowerSphere concept in FY 99 focused on the design and fabrication of Amorphous Silicon Solar Cells that would meet the space thermal requirements identified in work completed in FY 98.[3] This effort was carried out in cooperation with Iowa Thin Films where minor modifications to the terrestrial product line were identified and implemented in producing a first generation thin film amorphous silicon solar cell deposited on a polyimide substrate for space applications. The up to date results of this effort will be reported on in this paper.

Thin Film Amorphous Silicon Solar Cell Products

Thin film amorphous silicon solar cells are presently produced by a number of different solar cell companies for the terrestrial market. United Solar has been producing an amorphous silicon product deposited on a stainless steel substrate for a number of years. Recently United Solar Systems Corp. has been exploring the space market and has a flight experiment on the Mir space station.[4] Solarex produces amorphous silicon on a 1/4" plate glass substrate for the terrestrial market. TRW in cooperation with Solarex has been working on adapting the Solarex process to use very thin (3 to 8 mil thick) glass substrates.[5][6] Both the United Solar Systems Corp. and TRW processes produce solar cells with efficiencies greater than 8%. Iowa Thin Films produces an amorphous silicon product for the terrestrial market, which uses a 2-mil thick polyimide substrate.[7] The Iowa Thin Films Solar Cell product has an efficiency of approximately 5%.

Thin Film Space Solar Cell Design Requirements

The PowerSphere concept has been under development by the Aerospace Corporation since FY 98. The work completed in FY 1998 identified the following requirements for the amorphous silicon solar array, which would

Copyright August 1999 The Aerospace Corporation

be integrated into a PowerSphere. The requirements identified are as follows:

1. The solar array shall be flexible.

2. The solar array shall be designed to maximize the specific power per unit of mass.

3. The materials used in fabricating the solar array shall be space qualified.

4. The front and back surfaces shall have a thermal emittance approaching 0.8.

5. The solar cell shall be capable of operating at temperatures of approximately 80 ^{O}C.

6. The array shall be capable of surviving at least 5000 thermal cycles between –100 ^{O}C and +100 ^{O}C.

7. The solar array shall be rugged and capable of surviving launch environments with a minimum of special handling and/or stowage and deployment fixtures.

8. The solar array shall be capable of being stowed in a minimum volume during launch.

9. The solar array shall be capable of being integrated with both inflatable and mechanical deployment structures.

10. The solar cell shall be capable of producing approximately 1.0 volts at peak power point.

11. The solar cells shall be capable of being fabricated in any geometric shape required for the specific application.

Thin Film Space Solar Cell Design Features Necessary to Meet Design Requirements

Presently Iowa Thin Films is the only domestic U.S. commercial producer of Amorphous Silicon Solar Cells, which use a polyimide web for the substrate.

In FY 99 Aerospace and Iowa Thin Films entered into a joint development of a Thin Film Space Solar Cell, which would be capable of meeting all of the requirements, identified in the previous section. Specific design features of the Space Solar Cell are listed in Table 1.

Process Changes Implemented in the Standard Terrestrial Iowa Thin Film Manufacturing Process

The standard manufacturing process used by Iowa Thin Films was modified as follows:

1. The standard Iowa Thin Film product has stainless steel deposited on the back surface to bleed off static charge during the vacuum deposition of the amorphous silicon solar cells. The stainless steel has a thermal emittance of 0.3. However, the 2 mil base polyimide has a thermal emittance of 0.8, which is the desired value of this property. Thus, Aerospace performed some experiments to identify a material which could be used on the back surface of the polyimide to provide the conductive path to bleed off static charge during the vacuum deposition of the solar array material and would either have the proper thermal properties or could be easily removed after the cells were fabricated. Samples of the polyimide were e-beam vapor coated with silicon, germanium and aluminum. The silicon and germanium samples retained a thermal emittance of 0.8. The aluminum-coated sample was subsequently etched to remove the aluminum. The polyimide did not exhibit any swelling or effects from the exposure to the etchant. Since Iowa Thin Films was using aluminum on the front side of the polyimide it was determined that the use of aluminum on the back of the polyimide would have the smallest impact upon their standard manufacturing process.

Table 1. List Of Design Features Implemented in the Fabrication of the Prototype Space Solar Cells

Requirement	Design Feature Necessary to Meet Requirement
1	Use of Polymide
2	2 Mil Polyimide provides material capable of having a specific power of 75 W/Kg with a cell efficiency of only 5%
3	The Polyimide Substrate (Kapton), and Tefzel Top cover have been used in space applications in the past
4	The base Polyimide has a thermal emmitance of 0.8, 1.5 mil Tefzel has a thermal emmitance of 0.7
5	The Iowa Thin Film Solar Cell can operate at 80 ^{O}C and has demonstrated annealing of the Staebler-Wronski effect at this temperature
6	The use of vapor deposited/plated top contacts to replace printed ink contacts used for the terrestrial product
7	The Polyimide Substrate provides for a extremely flexible and rugged finished solar array
8	Very large areas can be stowed in a extremely small volume because the finished solar array is approximately 4.0 mil thick
9	The thin film solar array can be integrated into a wide variety of inflatable or mechanical deployment structures. For inflatable structures the solar array can be the inflatable web material
10	The use of a dual junction solar cell
11	Prototype cells produced in the shape of rectangles, hexagons, and pentagons

2. The implementation of large area single cell devices required the production of special masks and screens for the screen printing processes of insulating inks and printed silver inks. This also required special software for the laser scribing and welding processes.

3. The off line vapor deposition/plating of the silver top contacts will require manual welding of the back contacts after the plating process is completed.

Lessons Learned Process Changes Implemented in the Standard Terrestrial Iowa Thin Film Manufacturing Process

1. The substitution of aluminum for stainless steel did produce a material, which would bleed off the static charge during the vacuum deposition process. However, the web did not spread the same way that the material with stainless steel does. This caused a longitudinal wrinkle to form in the web as it entered the deposition area within the roll to roll process.

   To solve this problem in future prototype production runs, the back metalization of the web could be a thin layer of stainless steel, which would be etched off after processing. The downside to this solution is that a fairly strong etchant will be required which would attack the aluminum back contact along the edges of the web. The application of Photoresist to the front of the web would protect the cell material from the etchant.

2. The large area pentagons, hexagons and rectangles did not introduce any problems in the laser scribing or printing processes, which were performed after deposition of the cell material.

3. There were no problems encountered during the final processing of the web where the Zinc Oxide and Indium Tin Oxide were deposited as the top contact for the finished cells.

4. The cells fabricated with printed silver ink, top contacts exhibited a relatively high series resistance as

expected during initial I-V characterization of the cells. It is expected that the plated silver top contacts that will be deposited on some of the cells from this run will overcome this issue. The series resistance of the back aluminum layer is also affecting performance. Thus, for large area cells, a thicker layer of aluminum will be required. This modification will be implemented on a second prototype

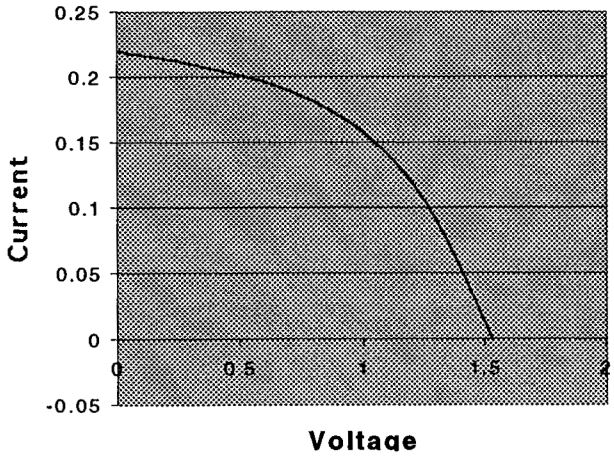

Figure 1 I-V Curve of Rectangular Cell

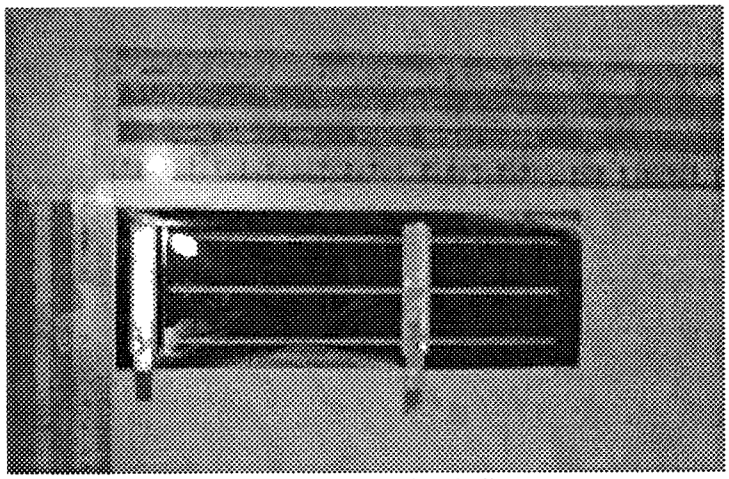
Figure 2 Photograph of Rectangular Cell

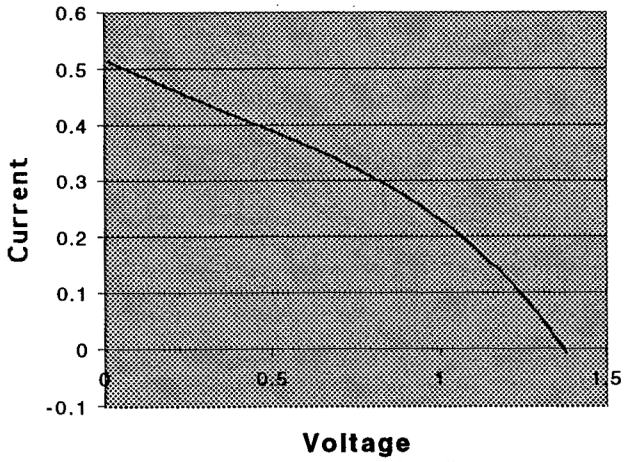

Figure 3 I-V Curve of Pentagonal Cell

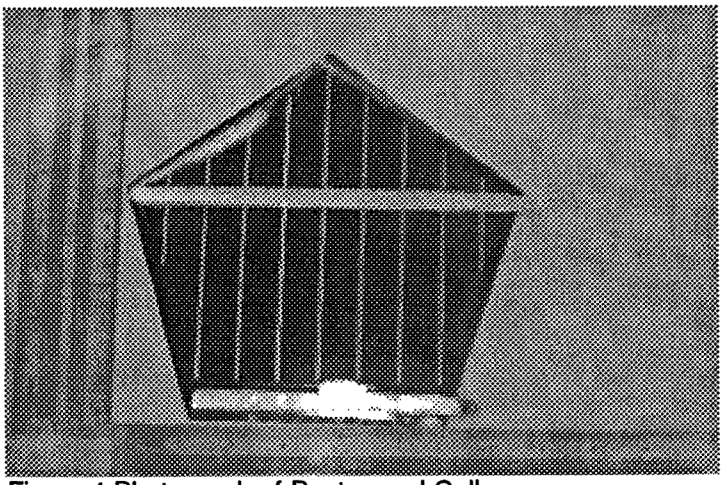
Figure 4 Photograph of Pentagonal Cell

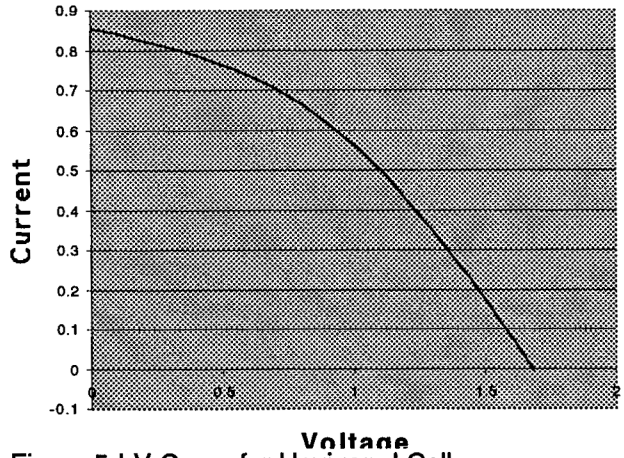

Figure 5 I-V Curve for Hexigonal Cell

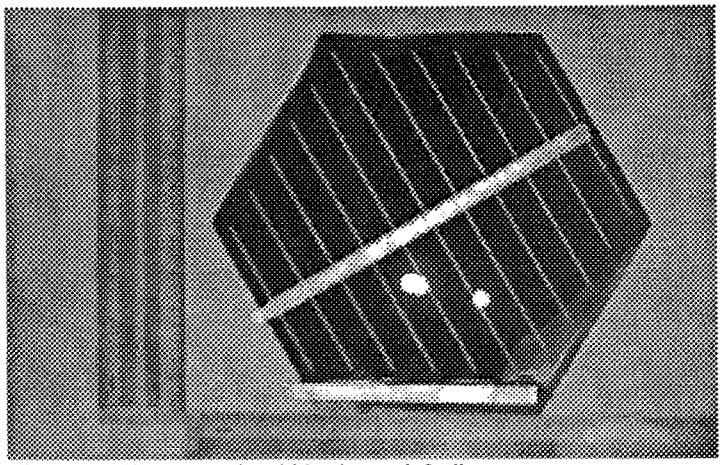
Figure 6 Photograph of Hexigonal Cell

production run.

Results of Preliminary Electrical Testing

As of this writing the cells electrical tests were performed on cells fabricated with the Printed Ink top contacts. These tests were performed using Aerospace Corporation's Spectrolab X-10 solar simulator, which provides an AM0 spectrum. Figures 1 through 6 provide photographs and I-V curves for each of the three sizes of cells produced.

Table 2 provides a comparison of the electrical performance for the three different size cells. As shown the measured efficiency of these cells is significantly less than the 5% capability of the Iowa Thin Film process. This can be attributed to the problems encountered in the vapor deposition phase of the processing caused by the substitution of the aluminum on the back of the polyimide. The problem caused a buildup of powder on the cell, which was visually evident on the pentagonal cell. The problem was not evident on the rectangular or hexagonal cell. The relatively high series resistance of the printed silver ink and thin aluminum back conductor has impacted cell performance.

However, when the performance of the large hexagon with an area of 358 cm^2 is compared with the smaller rectangular cell, which has an area of 79 cm^2, the performance is nearly the same. The difference observed might be explained by the difference in series resistance that the contacts have for the two different cells.

Table 2 Comparison of Electrical Performance of the Three Different Size Cells

	Rectangular Cell	Pentagonal Cell	Hexagonal Cell
Voc	1.52	1.36	1.68
Isc	0.220	0.516	0.853
Vmax	1.016	0.849	0.989
Imax	0.155	0.289	0.569
Pmax	0.158	0.246	0.563
Fill Factor	0.4709	0.348	0.392
Active Area cm^2	79	232	358
Efficiency	1.5%	0.8%	1.2%

This data also demonstrated that the basic process is capable of producing large area cells without sacrificing performance.

Results of Thermal Properties Measurements

Measurements of the thermal properties of a completed rectangular solar cell were made using a Solar Spectrum Reflectometer (Model SSR-ER) and an Emissometer (Model AE) both by Devices and Services Co., Dallas TX. The measured thermal asbortance for the front surface was 0.67 and the emmitance was 0.8. The asbortance of the back surface was measured to be 0.7 and the emittance was 0.76. These measurements confirm the design features incorporated into the thin film space solar cell and meet the requirement number 4.

Summary and Conclusions

Results to date for this ongoing project are encouraging. The first development production of the joint Iowa Thin Films/Aerospace Corporation Space Solar Cells meet almost all of the requirements defined as goals for this effort. The work completed demonstrates that the proper thermal properties for a space thin film solar cell can be designed into the basic materials from which the thin film solar arrays are fabricated. The roll to roll process implemented by Iowa Thin Films is capable of producing solar cells and arrays that can be of any geometric shape. The process is also capable of producing large area solar cells. The cells meet the requirements for flexibility and storage during launch. The finished cells are capable of being integrated into mechanical and or inflatable deployment structures. Verification of the durability and life of the cells produced in this project will be performed in FY 2000.

References

[1] E. J. Simburger, "PowerSphere Concept", The Aerospace Corporation, Proceedings of Government Microcircuit Applications Conference, 8-11 March 1999.

[2] Alonzo Prater, Edward J. Simburger, Dennis Smith, Peter J. Carian, and James Matsumoto, The Aerospace Corporation, "Power Management and Distribution Concept for Microsatellites and Nanosatellites", Proceedings of IECEC 1-5 August 1999.

[3] David G. Gilmore, Edward J. Simburger, Michael J. Meshishnek, David M. Scott, Dennis A. Smith, Alonzo Prater, James H. Matsumoto and Margot L. Wasz, The Aerospace Corporation, "Thermal Design Aspects of the PowerSphere Concept", Proceedings of Micro/Nano Technology for Space Applications Conference, 11-15, April 1999.

[4] S. Gua, J. Yang, A. Banerjee, P. Nath, J. Call, and T. Glatfelter, United Solar Systems Corp. and F.J. Boelens and G. Oomen Fokker Space B.V., "Low Cost and Lightweight Amorphous Silicon Alloy Solar Array for Space Applications", Proceeding of IECEC 1-5, August 1999.

[5] J. R. Srour, G .J. Vendura, Jr., D. H. Lo, C .M. C. Toporow, M. Dooley, and R. P. Nakano, TRW Space and Electronics Group and E. E. King, The Aerospace Corporation, "Damage Mechanisms in Radiation-Tolerant Amorphous Silicon Solar Cells", IEEE Transactions on Nuclear Science, December 1998.

[6] G. J. Vendura Jr., C. M. C. Toporow and M. A. Kruer, TRW Space and Technology Division, "Irradiation and Annealing of Amorphous Silicon Space Solar Cells", Proceedings of the Second World Conference on Photovoltaic Energy Conversion, Vienna Austria, July 1998.

[7] F. Jeffrey, D. Grimmer, S. Martins, M. Thomas, V. Dalal, M. Noack and H. Shanks, Lightweight, Flexible, Monolithic, "Thin-Film Amorphous Silicon Modules on Continuos Polymer Substrates", Int. J. Solar Energy, 1996, Vol. 18, pp.205-212.

TOWARDS A THIN FILM SILICON HETEROJUNCTION SOLAR CELL

Young Song, Elena Guliants and Wayne Anderson
State University of New York at Buffalo
Department of Electrical Engineering
217 Bonner Hall, Buffalo, NY14260

ABSTRACT

This project utilizes an a-Si:H/polycrystalline or microcrystalline Si concept as a low–cost, light-weight means of achieving photovoltaic power conversion. The base region is produced by a metal-induced growth (MIG) in which Si is sputtered onto a foreign substrate, first coated with 25 nm of Ni. Films thus far have reasonable electrical properties. The emitter region is deposited by electron cyclotron resonance CVD with the substrate illuminated during deposition to improve the properties of the a-Si:H. Theoretically, this design should achieve an efficiency of 16-18%, depending on the features.

INTRODUCTION

At the previous SPRAT Conference, we reported on the proposed design of a light-weight, thin-film, all Si heterojunction solar cell, based upon deposition of a-Si:H onto a thin film of microcrystalline Si (μc-Si) [1]. Computer modeling predicts a conversion efficiency of 16-18%. The lightweight and thinness are attractive for space applications. This paper reports on progress towards the goal.

Progress is being made on several fronts in the area of thin film crystalline Si photovoltaics. Researchers in Germany have introduced the "Micromorph" cell, in which they use very high frequency glow discharge (VHF-GD) to produce microcrystal hydrogenated Si (μc-Si:H) [2]. They report a 10.7% efficiency on an a-Si:H/μc-Si:H cell. Tanaka et. al. [3] reported an a-Si/poly-Si cell having a 9.2% efficiency. Miyamoto et.al. [4] reported a remote PECVD method to obtain poly-Si on glass. N. Beck et. al. [5] also utilized VHF-GD and different gas dilutions to achieve μc-Si:H with drift mobilities up to 3 cm^2/V-s. Very recently, ultrathin crystalline Si on glass was formed by CVD at 1000°C [6] or by laser crystallization of a-Si on plastic [7]. Our approach utilizes a thin Ni layer on a foreign substrate upon which Si is sputtered at a temperature of 500-600°C. The Ni forms a silicide which acts as an Ohmic contact while promoting a crystalline Si growth. We call this metal-induced growth (MIG).

Recent progress in a-Si:H-type cells was reported in the 26th IEEE Photovoltaics Specialists Conference proceedings. Triple junction cells show promise for manufacture [8]. Whereas many groups work on high frequency glow discharge, some work is done on low frequency glow discharge, which gives a high growth rate [10]. Hydrogen radical CVD purposely introduces hydrogen radicals at the growing surface to obtain high quality microcrystalline Si films [11]. Stability of a-Si:H continues to be a serious problem [12]. Both hot-wire [13] and ECR-CVD [14] are proposed as techniques to improve stability of a-Si:H. The problem then lies in producing a Si thin-film solar cell, which is stable, low-cost, and of acceptable efficiency. This requires: a low-cost, thin-film absorbing layer; a low-temperature, thin-film junction-forming technique; and suitable grid with A/R coating. Our approach utilizes ECR-CVD (which we call MECR) with a focus upon dilution of SiH_4 with He, H_2 and Ar, which might be called double (or multiple) dilution [14,15] modified by illuminating the substrate during deposition, which we call photon-assisted MECR or PAMECR. This approach gives much flexibility in establishing process variables. For example, excess H_2 produces microcrystalline Si (μc-Si) at significantly lower temperatures. Helium serves as a preferred carrier gas for silane compared to Ar, although a small percentage of Ar serves to improve the deposition rate. Photon assist offers other advantages to be reported herein.

The following will provide details of growing poly-Si by MIG, depositing a-Si:H by PAMECR and most recent performance of solar cells.

BASE REGION

Since losses in the base have always been a limiting factor for good solar cell performance we tried to devote special attention to the growth of polycrystalline silicon for the absorber layer. Recently, it has been shown that recrystallization of the pre-deposited amorphous silicon in the presence of some transitional metals successfully leads to uniform polycrystalline structure of the former [16,17,18]. Moreover, metal induced crystallization (MIC) dramatically decreased both time and temperature of annealing. Normally, this involved the deposition of a thin (5-50Å) Pd [17] or Ni [18] film on the surface of a-Si with subsequent furnace annealing. The driving force for the Si crystallization was assumed to be the formation of the Ni-silicide transition layer at the Si-Ni interface. Having only 0.4% lattice mismatch with silicon, cubic $NiSi_2$ provides a necessary prerequisite for Si epitaxial growth[16]. The migration of disilicide precipitates then results in the crystallization of the whole volume of the a-Si layer. In the present study, we performed silicon deposition onto Ni-coated substrates. The silicide phase forms first due to consuming Si atoms by Ni. Thus, the Si crystal formation and subsequent crystal growth occur immediately during the film deposition on the Ni-silicide prelayer.

EXPERIMENT

Thin, 5nm to 70nm, Ni films were thermally evaporated on oxidized Si wafers. The silicon films were deposited by DC Magnetron sputtering at a base pressure of $2x10^{-7}$ Torr. N-type Si targets with resistivity of 0.02 and 0.006 Ω-cm were chosen for this study. All runs were carried out at a fixed pressure of 1 mTorr of a 5%H_2/Ar mixture where Ar was used as a carrier gas and H_2 helped saturate dangling bonds at grain boundaries. DC Magnetron power was kept at 50W and the substrate temperature was varied in the 525-600°C range. The duration of the deposition was normally 1 hour and the deposition rate was calculated to be 0.6 μm/h. In order to investigate the dynamics of the MIG mechanism, the deposition was interrupted for several runs after 3, 6 and 12 minutes, respectively. The surface of the samples was analyzed using atomic force microscopy (AFM) and scanning electron microscopy (SEM). Crystallinity and the grain size were evaluated by means of X-ray diffraction (XRD) and Raman Spectroscopy. Finally, one sample was prepared for cross-sectional transmission electron microscopy (XTEM) for more detailed microstructure investigation. X-ray photoelectron spectroscopy (XPS) alongside with Auger electron spectroscopy (AES) depth profiles were taken for two sets of samples (deposited for 6min and 1hour (XPS) and 3min and 12min (AES), respectively). I-V characteristics helped to determine resistivity of poly-Si films with Yb Ohmic contacts. The RF conductivity method was utilized for carrier lifetime measurement at NREL. For Schottky diode fabrication, the samples were annealed at 700°C for 2 hours in the presence of forming gas. Pd was used to provide a Schottky contact to the film.

RESULTS

Cross-sectional TEM revealed columnar growth of polycrystalline silicon on the Ni-silicide prelayer. The most interesting observation was, as can be clearly seen in Figure 1, the fact that the Si – Ni-silicide interface had a well-distinguishable boundary which suggests that Ni-silicide precipitates do not migrate in the silicon film. Cross-sectional SEM study was in good agreement with TEM data revealing a columnar structure as well (Fig.2). The 0.5 μm diameter features on the surface of the samples may be whole grains or clusters of grains with smaller size. A series of samples were analyzed by means of AFM in order to determine the influence of the Ni prelayer thickness on maximum cluster size on the surface of the poly-Si film. Figure 3 shows that the Si film deposited on the 5nm thick Ni prelayer reveals features in the 0.25-0.3μm range while a 50nm thick Ni film resulted in 0.4-0.5μm diameter features. Statistical data collected for several sets of samples deposited at a temperature in the 525-600°C range indicates much stronger dependence of the grain size on the Ni film thickness than dependence on the temperature of deposition. Thus, maximum grain

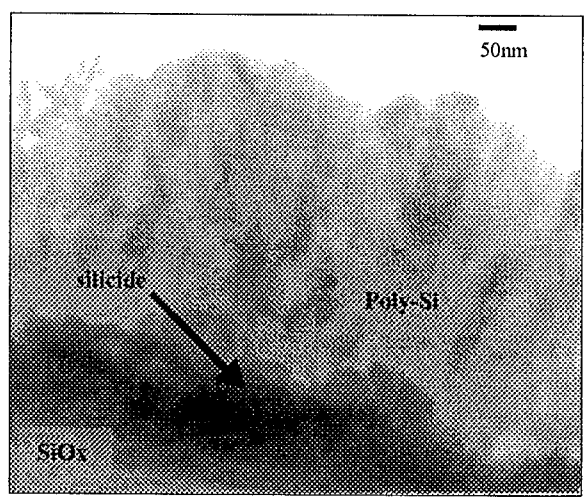

Fig.1. Cross-sectional TEM image of the sample deposited at 600°C on the 25 nm thick Ni prelayer.

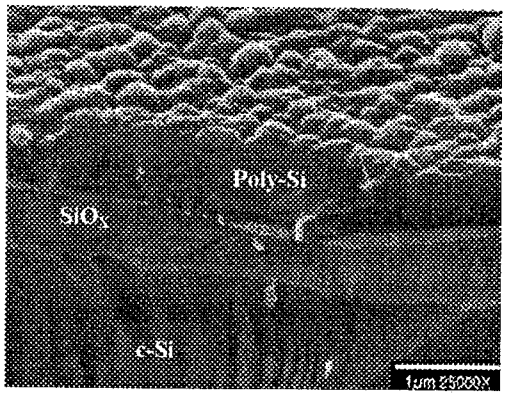

Fig.2. Cross-sectional SEM photo of the sample deposited onto a 15nm thick Ni film at 525°C.

size was observed for the Si films deposited on a 25-30nm thick Ni underlayer.

The XRD data confirmed the above described observation. The grain size calculated from the FWHM of corresponding Si crystalline peaks has the maximum value for the samples deposited on the Ni film with the thickness of 25nm. However, the grain size obtained from XRD analysis was much smaller (30-100nm) than the grain size shown by SEM and AFM which implies the existence of clusters of grains. Figure 4 shows the XRD spectra for three samples deposited during the same run at 525°C on 5nm, 25nm and 50nm thick Ni prelayer, respectively. The intensity of c-Si peaks corresponding to (111), (220) and (311) planes were corrected due to variation of the angle of incidence and, hence, the thickness of the sample available for the X-ray wave propagation. From Figure 4, the Si film on a 25nm thick Ni prelayer obviously exhibits a higher intensity of (111) and (220) peaks. Interestingly, the (220) orientation becomes preferred at a Ni thickness above 25-30nm as seen from Table I.

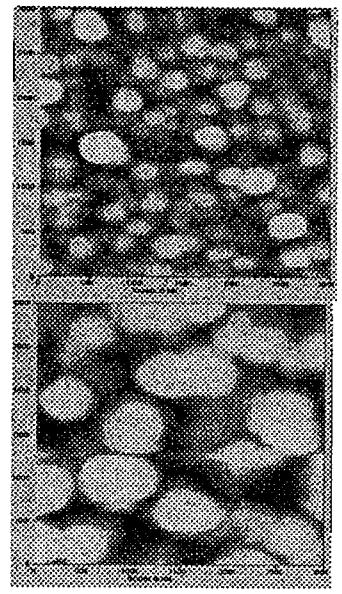

Fig. 3. AFM pictures of surface morphology for the samples deposited at 550°C on 5nm (top) and 50nm (bottom) thick Ni prelayer.

The maximum grain size of the samples deposited by sputtering from a higher resistivity target was found to be shifted towards the lower values of the Ni prelayer thickness. Figure 5 shows the Raman spectra of two samples deposited using 0.02 Ω-cm target. Thus, the target with 3.5 times higher resistivity provided largest grains for the Ni film with thickness in the 15-17nm range. The peak intensity was also improved for the sample deposited on a 15nm thick Ni film. Neither XRD nor Raman analysis indicated the presence of an amorphous phase.

The XPS depth profile obtained for the sample deposited for 6 minutes on a 25 nm thick Ni prelayer exhibited a rapid decrease of the Ni concentration away from the Ni-Si interface. The sample deposited for 1 hour also showed the presence of Ni in the 50-60nm region near the Ni-Si interface, while no Ni was detected in the bulk of the film. The preliminary analysis of the Ni-to-Si atomic concentration ratio indicated the NiSi stoichiometry. AES depth profile of a 30nm Si / 25nm Ni sample deposited for 3 minutes revealed the mixture of atomic Ni and Ni_2Si. No atomic Ni was found in a 120nm Si / 25nm Ni sample which implies the complete consumption of Ni by the silicide phase. We found instead that the composition of the silicide can be referred to as Ni_xSi, where $1<x<2$, which indicates the mixture of the Ni_2Si and NiSi phases.

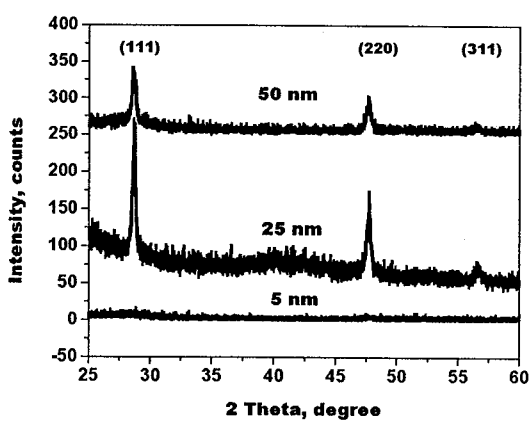

Fig.4. XRD spectra of poly-Si films deposited at 525°C on 5nm, 25nm and 50nm thick Ni prelayer, respectively.

Table I. Corrected peak intensity (a.u.) values for the samples deposited on 10,13,30,50 and 70nm, respectively, thick Ni film at 575°C for different planes.

	10 nm	13nm	30nm	50nm	70nm
(111)	38	50	54	32.5	30
(220)	45	45	56	52	54
(311)	28	28	37	35	18

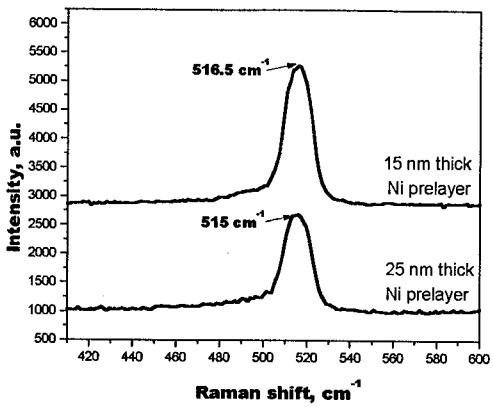

Fig.5. Raman spectra of Si films deposited at 550°C on 15nm and 25 nm thick Ni prelayer, respectively.

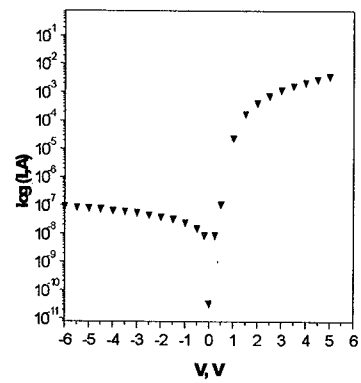

Fig.6. The I-V characteristics of the Schottky diode fabricated on an annealed Si film.

Electrical properties of metal induced grown poly-Si film were investigated by taking vertical I-V charactiristics. The resistivity was found to be in the 10^2-$10^3\Omega$-cm range and tends to decrease with the thickness of the Ni prelayer. Thus, a 20nm thick Ni prelayer resulted in a Si resistivity of $1x10^3\Omega$-cm while 50nm thick Ni film gave $5x10^2\Omega$-cm. The RF conductivity carrier lifetime measurement carried out on the poly-Si film surface resulted in 11μs. Finally, Schottky diodes fabricated on the Si film deposited at 525°C on a 25 thick Ni prelayer and subsequently annealed for 2 hours at 700°C in the presence of forming gas showed a forward-to-reverse current ratio of 10^5. This is shown in Figure 6.

EMITTER REGION

In this work, we have introduced a photon-assist (PA) process into the conventional ECRCVD for the purpose of further control of the hydrogen related profile in the film because the PA process during the film formation may modify the chemical reaction mechanisms in the growth zone. We investigated the effects of the PA process on the film's chemical structure, electro-optical and photovoltaic properties.

Together with the PA process, the insertion of a thin μc-Si buffer layer between a-Si:H and c-Si is also conducted for better solar cell performance, since the μc-Si buffer layer is expected to improve the interface quality. The influence of the μc-Si buffer layer on the solar cell parameters has been investigated by varying its thickness, in order to find the exact role of the buffer layer. After that, the optimal configuration of the heterojunction solar cell will be discussed.

EXPERIMENT

The a-Si:H film was deposited by microwave (2.45 GHz) ECRCVD, both with and without the PA process. For the PA process, a focused tungsten halogen light beam was used to illuminate the substrate during the film growth with intensity of 1 – 10 W/cm^2. The source gas was a 2% SiH_4/He mixture, while a minimum amount of Ar was used for plasma generation. All the a-Si:H depositions were performed without hydrogen dilution at a substrate temperature of 250 °C, a chamber pressure of 10 mTorr, an input power of 400 W, with a deposition rate of 70 – 80 Å/min. All samples were grown on either glass substrates for the measurement of electro-optical properties (conductivity, activation energy, carrier lifetime, and light absorption) or on HF-treated p-type (100) CZ c-Si for both Fourier transform infrared spectroscopy (FTIR) and a-Si:H/c-Si heterojunction solar cell fabrication. In the FTIR study, 5000 Å thick a-Si:H films were deposited, and for the measurement of electro-optical properties, the a-Si:H film thickness was fixed at 1000 Å. Photoconductivity and photovoltaic response tests were done under a 100 mW/cm^2 AM1.0 spectrum from a tungsten halogen lamp calibrated with a solar cell previously tested at NREL. Regarding the metallization for top contacts, a thermally evaporated Mg/Al double layer was used (100 Å/1000 Å for solar cells and 100 Å/500 Å for conductivity measurement). The carrier lifetime measurement of the a-Si:H film was done at NREL. The μc-Si buffer layer was grown with H_2 dilution (R_H = 0.33, where $R_H = H_2/(2\%\ SiH_4/He + H_2 + Ar)$) at a substrate temperature of 400 °C, a chamber pressure of 1 mTorr, and an input power of 350 W. Three different μc-

Si buffer layers (70 Å, 200 Å and 400 Å) were inserted between the a-Si (700 Å)/c-Si interface to examine the role of the buffer layer on photovoltaic properties.

RESULTS

Chemical structure

PA effects on the chemical bonding configuration in the a-Si:H film was investigated by FTIR. As seen in Figure 7, compared to the a-Si:H film deposited without PA, the film grown with PA shows a weaker peak at 2090 cm^{-1}, representing a lesser amount of dihydride phase (=Si-H_2) in the film. Since the dihydride bonding degrades the general semiconductor properties of a-Si:H, the film deposited with PA is expected to have improved properties. Meanwhile, both films show very comparable peak intensities at 2000 cm^{-1}, meaning that both films have a comparable amount of monohydride phase (≡Si-H). Since it was experimentally observed that there is no preferential reduction in the integrated band intensities near 2090 cm^{-1}, relative to the band near 2000 cm^{-1}, by increasing deposition or subsequent annealing temperature up to 350 °C [19], it could be said that the reduction of peak intensity at 2090 cm^{-1} alone in the PA processed film is not from the temperature effect but from the photon-related effect. Furthermore, it is generally agreed that the substrate temperature increase above 250 °C does not improve the quality of the a-Si:H film due to the increased possibility of dangling bond creation by the desorption of hydrogen molecules in the film.

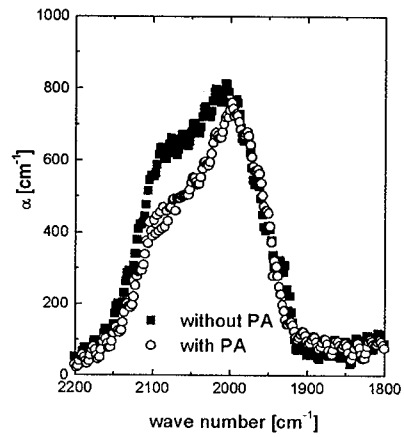

Fig. 7. FTIR spectra of the a-Si:H films deposited with and without PA.

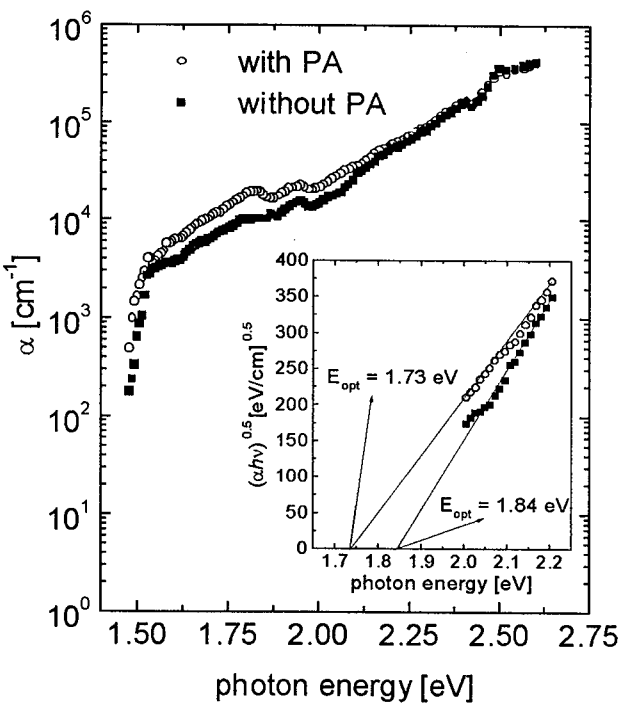

Fig. 8. Light absorption spectra of the a-Si:H films deposited with and without PA. The inset shows $(\alpha h\nu)^{0.5}$ vs. photon energy.

Consequently, the photons (wavelength of 300 – 700 nm) emitted from the tungsten halogen lamp in the PA process during the film growth may accelerate the decomposition of the dihydride phase in the growth zone, even at the same substrate temperature (250 °C). The smaller bonding energy between Si and H in the dihydride phase (~1.5 eV) than in the monohydride phase (~3.2 eV) is responsible for this result. The necessary energy for the decomposition of the dihydride phase is supplied by the recombination energy of excess electron-hole pairs, which are generated by the photon absorption. Since the recombination energy cannot exceed the film's energy gap (1.7 –1.8 eV), it would break weak and unstable Si-H bonds selectively, which is related to the dihydride phase. Moreover, the enhanced hydrogen removal capability of the PA process results in a relatively lower hydrogen content (approximately 20% less amount from the integrated areas under the curves) in the film deposited with PA. This lower hydrogen content in the PA processed film is related to less degradation after light-soaking than for the film deposited without PA [20].

Electro-optical Properties

As-deposited and light-soaked properties of a-Si:H processed with and without PA are compared in Table II. As seen in the table, PA processed a-Si:H films generally show better semiconductor characteristics, as expected from the FTIR result. The film deposited with PA reveals a higher photoconductivity ($\sigma_p \sim 10^{-4}$ S/cm) than that of the film

grown without PA (~ 10^{-5} S/cm), by a factor of about 10. On the other hand, both films have quite comparable dark conductivity (σ_d) values (order of 10^{-9} S/cm). The measured larger carrier lifetime (1.35 μsec) and smaller optical gap (E_{opt} = 1.73 eV)) of the PA processed film explains its superior photoconductivity. The activation energy (E_a) of the sample processed without PA undergoes a relatively large variation, from 0.72 to 0.81 eV, under the 3 month continuous exposure to light. In contrast, the E_a of the sample deposited with PA shows a relatively large initial value (0.94 eV) and then it reveals a slight change to 0.96 eV after the exposure. This result reflects the better stability of the film because there is a general agreement that the increase in E_a after light-soaking is mainly due to the introduction of light-induced metastable defects into

Table II. As-deposited and light-soaked properties of the a-Si:H films deposited with and without PA.

	As-deposited				After 3 month light soaking	
	Carrier lifetime [μsec]	σ_d/σ_p [S/cm]	E_a [eV]	E_{opt} [eV]	σ_d/σ_p [S/cm]	E_a [eV]
with PA	1.35	$8\times10^{-9}/1\times10^{-4}$	0.94	1.73	$9\times10^{-10}/6\times10^{-5}$	0.96
without PA	0.17	$3\times10^{-9}/1\times10^{-5}$	0.72	1.84	$8\times10^{-10}/6\times10^{-6}$	0.81

the gap of a-Si:H. This is believed to result in the displacement of the Fermi level from the conduction band edge. In addition, the influence of the PA process on the light absorption spectra is shown in Figure 8. From the spectra, it is observed that the film grown with PA has a larger light absorption coefficient (α) than the film deposited without PA, especially in the photon energy ($h\nu$) range of 1.5 eV– 2.3 eV.

Photovoltaic Properties

Table III. Photovoltaic properties of the heterojunction solar cells with and without a μc-Si buffer layer [(a)].

Sample	$t_{a\text{-}Si}$ [(b)] [Å]	PA	$t_{\mu c\text{-}Si}$ [(c)] [Å]	As-fabricated J_{SC} [mA/cm^2]	V_{OC} [V]	FF	η [%]	After 3 month exposure to light J_{SC} [mA/cm^2]	V_{OC} [V]	FF	η [%]
A45	250	no	-	25.37	0.51	0.47	6.08	24.89	0.50	0.46	5.72
A53	800	yes	-	28.60	0.55	0.58	9.12	28.16	0.55	0.57	8.83
MA8	700	yes	70	30.59	0.54	0.58	9.58	30.29	0.53	0.58	9.31
MA13	700	yes	200	31.81	0.51	0.61	9.89	31.72 (31.57	0.51 0.51	0.60 0.60	9.71 9.66)[(d)]
MA15	700	yes	400	29.78	0.43	0.64	8.19	29.36	0.43	0.63	7.95

[a] Without an antireflection coating. [b] a-Si:H thickness. [c] μc-Si buffer layer thickness.
[d] Solar cell parameters measured at NREL.

The photovoltaic properties of a-Si:H/c-Si heterojunction solar cells with and without the μc-Si buffer layer are illustrated in Table III. Considering the solar cells without a μc-Si layer, the a-Si:H layer thickness providing the highest efficiency (η) is quite different between the a-Si:H/c-Si heterojunction solar cells fabricated with and without PA. For the cell fabricated with PA (A53), the maximum efficiency was 9.1% at a thickness of 800 Å. On the other hand, the highest efficiency of 6.1% was observed at a thickness of 250 Å for the cell fabricated without PA (A45). The greatly improved carrier lifetime of the PA processed film translates to a greater permitted a-Si:H layer thickness. Furthermore, the PA processed cell exhibited a more stable efficiency (less than an average 4% degradation even after 3 month exposure to light) than the cell fabricated without PA (about 6% degradation observed) in spite of the thicker a-Si:H layer of the PA processed cell.

Table III also shows that the insertion of a μc-Si buffer layer into the PA processed a-Si:H/c-Si interface either improves or degrades the solar cell efficiency, depending on the buffer layer thickness. Compared to the cell without a μc-Si buffer layer (A53), the cells with the buffer layer generally show improved short circuit currents (J_{SC}) and fill factors (FF). The increased J_{SC} of the cells with a μc-Si buffer layer is possibly explained by both better photon absorption (i.e. more carrier generation by light) in the material, and improved carrier collection at the interface. The enhanced photo carrier generation could be from the enhanced absorption of lower energy photons (< 2.0 eV) in the μc-Si buffer layer, which has a smaller energy gap than a-Si:H. It is supported in Figure 9 by the improvement in red response of the cells with a μc-Si layer. However, it is seen that the solar cell with a 400 Å thick μc-Si layer (MA15) reduces the blue response, which is believed to degrade the J_{SC} value slightly. This is possibly from the elevated crystallinity of the whole emitter layer, leading to a weak light absorption in the layer. Meanwhile, the reduced barrier height at the hetero-interface from band gap grading in the solar cells with a μc-Si layer seems to improve the carrier collection at the interface.

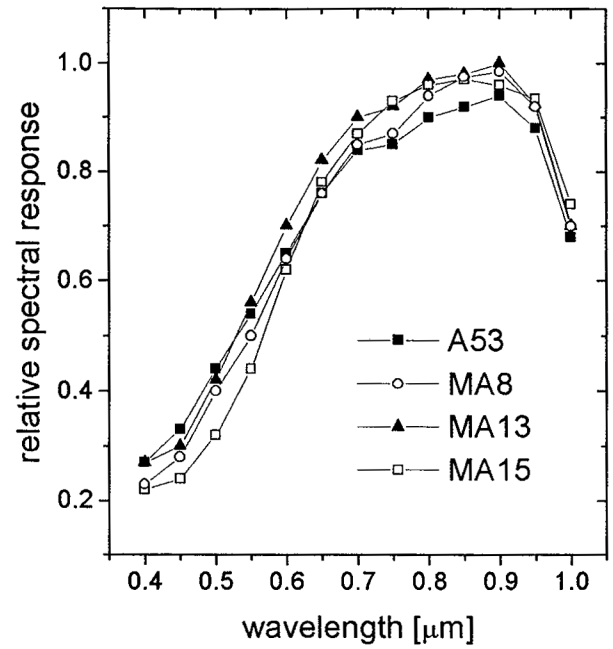

Fig. 9. Spectral responses of the heterojunction solar cells with and without μc-Si buffer layer.

However, the solar cells with a μc-Si buffer layer reveal smaller open circuit voltages (V_{OC}) as the μc-Si thickness increases. The degraded V_{OC} in the samples with buffer layer could be from the two possible origins; reduced energy gap of the window layer material due to its higher crystallinity, and increased defect density near the interface between thin film silicon and c-Si. Reasonably, the greatly reduced V_{OC} of the cell with a 400 Å μc-Si layer (MA15) should be from the higher defect density near the interface. It seems that the emitter layer with a μc-Si layer thicker than 200 Å suffers from the unpassivated dangling bonds at grain boundaries, even after the subsequent a-Si:H deposition, because hydrogen atoms in a-Si:H cannot easily diffuse through the thick μc-Si underlayer. On the other hand, the slightly decreased V_{OC} of the cell with a 200 Å thick μc-Si buffer layer (MA13) is thought to be from the energy gap grading effects rather than the interface defects because of the cell's high J_{SC} and FF values. In fact, this solar cell shows the highest efficiency (~ 10 %) of all cells.

DISCUSSION AND CONCLUSIONS

Heterojunction a-Si:H/polycrystalline or microcrystalline Si solar cells are theoretically a candidate for light-weight, 18% efficient solar cells. In this work, the base region is being developed by metal-induced growth, which produces a microcrystalline Si at a temperature of 525-625C. Ni, 25nm in thickness, is deposited on a suitable substrate and forms a silicide as the Si is sputtered from a Si target. The silicide leads to a microcrystalline Si film on top, with the boundary controlled by temperature, rate and amounts of Si or Ni. The films have reasonable electrical properties and have been used to fabricate Schottky diodes. Efforts will now be made to establish the doping conditions suitable for solar cell fabrication.

The emitter region is being explored using a microwave CVD technique with photon assist to increase stability of the usually unstable a-Si:H. Using the photon assist process, more stable cells have been made with a-Si:H/ p-type crystalline Si.

The improved stability is attributed to a lesser dihydride component as revealed by FTIR. Efficiency exceeding 10.5% can be made without use of an antireflection coating. The interface between a-Si:H and crystalline Si is still a problem but has been improved using a 20nm μc-Si layer between. Still, open circuit voltage and fill factor are below the desired value and must be improved. A new deposition system may produce even better films since it is turbo-pumped and has an in-situ mass spectrometer which should correlate deposition conditions, electrical properties and reaction species.

The base and emitter tasks will be combined to form the thin-film solar cell. Issues to be resolved include doping, the interface, A/R coating and thickness optimization to maximize efficiency. Figure 10 shows a possible final design.

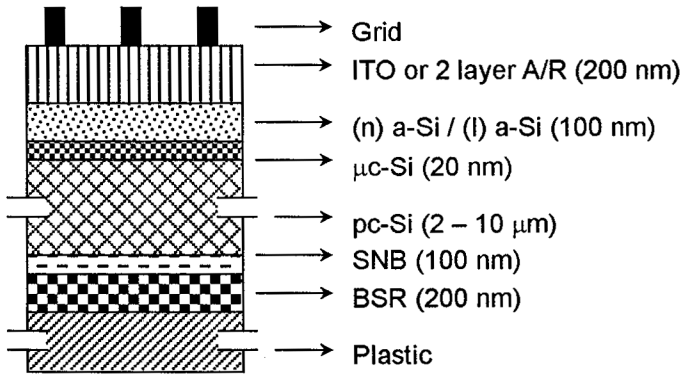

Fig. 10. Possible design of a completed thin film heterojunction solar cell

REFERENCES

1. W.A. Anderson, B. Jagannathan, and E. Klementieva, "Lightweight, Thin-film Si Heterojunction Solar Cells," Progress in Photovoltaics: Research and Applications, Vol. 5, pp. 433-441 (1997).
2. Meier, S. Dubail, R. Platz, P. Torres, U. Kroll, J.A. Anna Selvan, N. Pellaton Vaucher, ch. Hof. D. Fischer, H. Keppner, R. Fluckiger, A. Shah, V. Shklover, and K.D. Ufert, "Towards High-Efficiency Thin-Film Silicon Solar Cells with the "Micromorph" Concept," Preprint of the 9th PVSEC, Miyazaki, Nov. 11-15, 1996, Japan.
3. Tanaka, S. Tsuge, S. Kiyama, S. Tsuda and S. Nakano, "Fabrication of Polycrystalline Si Thin Film for Solar Cells," Materials Research Society (MRS) Fall Meeting, Boston, Dec. 2-6, 1996.
4. Miyamoto, A. Miida and I. Shimizu, "Epitaxy-Like Growth of Polycrystalline Si on the Seed Crystallites Grown on Glass," MRS Fall Meeting, Boston, Dec. 2-6, 1996.
5. Beck, P. Torres, J. Fric, Z. Remes, A. Poruba, H. Stuchlikova, A. Fejfar, N. Wyrsch, M. Vanecek, J. Kocka and A. Shah, "Optical and Electrical Properties of Undoped Microcrystalline Silicon Deposited by VHF-GD with Different Dilutions of Silane in Hydrogen," MRS Fall Meeting, Boston, Dec. 2-6, 1996.
6. R. Brendel, R.B. Bergmann, P. Lolgen, M. Wolf and J.H. Werner, "Ultrathin Crystalline Silicon Solar Cells on Glass Substrates," Appl. Phys. Lett., 70, 343-344, 1997.
7. P.M. Smith, P.G. Carey and T.W. Sigmon, "Excimer Laser Crystallization and Doping of Silicon Films on Plastic Substrates," Appl. Phys. Lett., 70, 390, 1997.
8. S. Guha, J. Yang, A. Banerjee, K. Hoffman, S. Sugiyama, and J. Call, "Triple-Junction Amorphous Silicon Alloy PV Manufacturing Plant of 5 MW Annual Capacity, Proc. 26th PVSC, Anaheim, CA, pp. 607-610, 1997.
9. K. Tabuchi, S. Fujikakke, H. Sato, S. Saito, A. Takano, T. Wada, T. Yoshida, Y. Ichikawa, H. Sakai and F. Natsume, "Improvement of Large-Area SCAF Structure A-Si Solar Cells with Plastic Film Substrate," Proc. 26th PVSC, Anaheim, CA, pp. 607-610, 1997.
10. B.G. Budaguan, A.Y. Sazonov, and A.A. Aivazov, "The Application of Low-Frequency Glow Discharge to High-Rate a-Si:H Deposition," Proc. 26th PVSC, Anaheim, CA, pp. 607-610, 1997.
11. L.-F. Lo, M. Hatta, N. Andoh, H. Nagayoshi, and K. Kamisako, "Preparation of High-Quality :c-Si:H Films By A Hydrogen-Radical CVD Method," Proc. 26th PVSC, Anaheim, CA, pp. 607-610, 1997.
12. D.E. Carlson, K. Rajan, and D. Bradley, "Irreversible Light-Induced Degradation in Amorphous Silicon Solar Cells," Proc. 26th PVSC, Anaheim, CA, pp. 607-610, 1997.
13. Y. Ziegler, S. Dubail, C. Hof, U. Kroll, and A. Shah, "High-Efficiency P-I-N Solar Cells with <I> Layer Deposited by Hot-Wire Technique," Proc. 26th PVSC, Anaheim, CA, pp. 607-610, 1997.

14. V.L. Dalal, T. Maxson, and K. Han, "Properties of a-Si:H and a-(SI GE):H Solar Cells Prepared Using ECR Deposition Techniques," Proc. 26th PVSC, Anaheim, CA, pp. 607-610, 1997.
15. B. Jagannathan, R.L. Wallace, W.A. Anderson, and R.N. Ahrenkeil, "Amorphous and Microcrystalline Silicon by ECR-CVD using Highly Dilute Silane Mixtures," Proc. 26th PVSC, Anaheim, CA, pp. 607-610, 1997.
16. C.Hayzelden and J.L.Batstone, "Silicide formation and silicide-mediated crystallization of nickel-implanted amorphous silicon thin films", J. Appl. Phys. 73, 8279, 1993.
17. S.W.Lee, B.-I.Lee, T.-K.Kim, and S.-K.Joo, "Pd_2Si-assisted crystallization of amorphous silicon thin films at low tempersture", J.Appl. Phys. 85, 7180, 1999.
18. Z.Jin, G.A.Bhat, M.Yeung, H.S.Kwok, and M.Wong, "Nickel induced crystallization of amorphous silicon thin films", J.Appl. Phys. 84, 194, 1998.
19. P. John, I. M. Odeh, M. J. Tricker, F. Riddoch, and J. I. B. Wilson, "Studies of the mechanism of the decomposition of hydrogenated a-Si films," Philos. Mag. B 42, 671, 1980.
20. H. Yamagishi. A. Hiroe, H. Nishio, K. Miki, K. Tsuge, and Y. Tawada, U. S. Patent No. 5264710, 1993.

CHEMICALLY DEPOSITED THIN-FILM SOLAR CELL MATERIALS

R. Raffaelle, W. Junek
Rochester Institute of Technology, Rochester, NY 14623

J. Gorse, T. Thompson
Baldwin-Wallace College, Berea, OH 44017

J. Harris, D. Hehemann
Kent State University, Kent, OH 44242

A. Hepp, G. Rybicki
NASA Glenn Research Center, Cleveland, OH 44135

Abstract

We have been working on the development of thin film photovoltaic solar cell materials that can be produced entirely by wet chemical methods on low-cost flexible substrates. P-type copper indium diselenide (CIS) absorber layers have been deposited via electrochemical deposition. Similar techniques have also allowed us to incorporate both Ga and S into the CIS structure, in order to increase its optical bandgap. The ability to deposit similar absorber layers with a variety of bandgaps is essential to our efforts to develop a multi-junction thin-film solar cell. Chemical bath deposition methods were used to deposit a cadmium sulfide (CdS) buffer layers on our CIS-based absorber layers. Window contacts were made to these CdS/CIS junctions by the electrodeposition of zinc oxide (ZnO). Structural and elemental determinations of the individual ZnO, CdS and CIS-based films via transmission spectroscopy, x-ray diffraction, x-ray photoelectron spectroscopy and energy dispersive spectroscopy will be presented. The electrical characterization of the resulting devices will be discussed.

1. Introduction

The development of light-weight and efficient photovoltaic solar cells for use in space power applications is of great interest to NASA. It is desirable that these cells should be flexible for easy deployment and control. The materials used in making these cells must also have a good tolerance to the types of radiation they will be exposed to in space. Thin-film solar cells based on copper indium diselenide or CIS have proven to be an excellent candidate for such applications.[1] Wet-chemical methods of producing photovoltaic thin films have also generated much interest. These methods are cost-effective, easily scalable, and can be used to deposit thin-films at low-temperatures on inexpensive flexible substrates.

We have been investigating the use of electrochemically deposited p-type $CuInSe_2$ (CIS) thin films for use as solar cell absorber layers. CIS is an excellent optical absorber with good electrical conductivity.[3] CIS has an optical bandgap of around 1.1 eV, which although not ideal, can be improved by the substitutional doping of Ga for In and/or S for Se.[4] The most efficient thin film solar cells developed to date employ $CuIn_{1-x}Ga_xSe_2$ (CIGS) absorber layers.[5] To produce flexible cells, we have focussed on the growth of CIS-based films on thin Mo foils, and Mo on Kapton.™

The most commonly used window materials for CIS-based solar cells are cadmium sulfide (CdS) and zinc oxide (ZnO) (see Figure 1). The CdS serves as a n-type buffer layer. CdS is well-lattice matched to CIS with a good optical transparency and optical bandgap of approximately 2.4 eV.[6] The CdS films are most commonly deposited using a chemical bath deposition technique.[7] Zinc oxide (ZnO) is a transparent conducting

oxide which serves as the top contact for the cell. ZnO has an optical bandgap of around 3.3 eV and conductivity as high as 200 $\Omega^{-1}cm^{-1}$.[8] Electrochemical deposition and chemical bath deposition techniques have both been previously used to deposit ZnO thin films.[9-10]

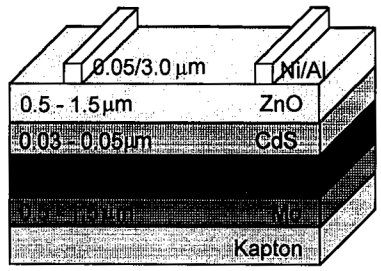

Figure 1. Typical thin-film photovoltaic solar cell.

2. Experimental Details

$CuInSe_2$ was electrochemically deposited on Mo foil, Mo coated Kapton, and indium tin oxide (ITO) coated glass from a solution containing 1 mM $CuSO_4$, 10 mM $In_2(SO_4)_3$, 5 mM SeO_2, 25 mM citric acid, and 10% ethanol by volume. The films were deposited at room temperature using a deposition potential of –1.2 V versus a saturated calomel electrode (SCE). The substrates were mounted in a rotating disk electrode and rotated at 500 r.p.m. The active electrode area had a radius of 1.27 cm. In order to deposit a 1 µm thick film, a deposition time of 600 s was used. The as-deposited films were then annealed in a flowing Argon atmosphere at 400 °C for 1 hour. Thiourea (5 mM) was added to the basic CIS solution as the sulfur source to deposit $CuIn(S,Se)_2$ films. To deposit $Cu(In,Ga)Se_2$, a $CuGa_2$ film was first electrodeposited at –1.8 V vs. SCE for 300 s from a 1 mM $Cu(SO_4)$, 20 mM $Ga_2(SO_4)_3$, and 5 M NaOH bath, before depositing the CIS. These resulting films were annealed at 600°C for 1 hour in flowing argon.

CdS buffer layers were grown on the CIS-based absorber layers using chemical bath deposition. The CIS-based films were immersed for 600 s in a 60 °C solution of 1mM Cd-acetate, 1 M NaOH, and 60 mM thiourea. The top contacts were made by electrochemical deposition of ZnO at –1.0 V vs. SCE for 300 s using a solution of 100 mM $Zn(NO_3)_2$ in deionized water held at 60 °C.

X-ray diffraction was performed on each of the deposited films associated with this study using a Phillips PW 3710 diffractometer. The surface morphology of the films were examined in a Hitachi S-4700 FE-SEM. Energy dispersive spectroscopy was also performed in the SEM using an EDAX DX prime system utilizing ZAF standardless correction. X-ray photoelectron spectroscopy was used in conjunction with argon ion ablation to depth profile the CIS deposited on Mo. Sensitivity factors based on the EDS results were used to quantify the measurements.

Transmission spectrophotometry was performed on the films deposited on ITO coated glass using a Perkin Elmer Lamba 19 spectrophotometer. This data was converted to absorption coefficients using the film thickness as determined by a Dektak II profilometer. The resulting absorption coefficients versus photon energy plots were used to determine the optical bandgaps of the films.

An Alessi four-point probe was used to monitor the conductivity of the different films deposited in this study. The four-point probe was also used to type the different semiconductors deposited via the Seebeck effect.

Current versus voltage measurements on the ZnO/CdS/CIS junctions were performed using a computer controlled Keithley 236 source/measure unit. Contacts were made to the device using silver paint and an Alessi Rel-2100 wafer probing station.

3. Results and Discussion

The SEM micrographs of the $CuInSe_2$ $CuIn(S,Se)_2$, and $CuInS_2$ films which were electrodeposited at –1.2 V vs. an SCE on Mo foil are shown in Figure 2. The samples show increasing roughness with sulfur incorporation. This behavior is most probably due to the volatility of the sulfur during the annealing process. The films were all conducting and p-type as determined by the polarity of the Seebeck voltage using a four-point probe.

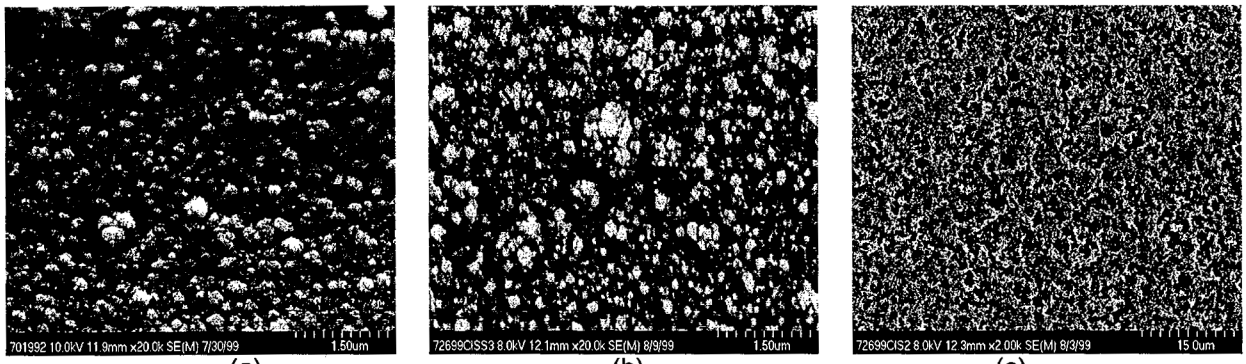

(a) (b) (c)

Figure 2. SEM micrographs of electrodeposited (a) $CuInSe_2$, (b) $CuIn(Se,S)_2$, (c) $CuInS_2$.

X-ray photoelectron spectroscopy (XPS), in conjunction with argon ion ablation, was used to depth profile a CIS on Mo film. Energy dispersive spectroscopy (EDS) was used to determine the bulk atomic ratios. These results were used to identify the sensitivity factors used in the XPS measurement. The EDS results showed that the CIS deposited at –1.2 V vs. SCE is copper rich ([Cu]=28%, [In]=22%, [Se]=50%). The XPS profile of the same film indicates that it had a uniform composition in the direction perpendicular to the substrate (see Figure 3). The results show a slight increase in the selenium concentration and a decrease in the copper concentration at the surface of the sample.

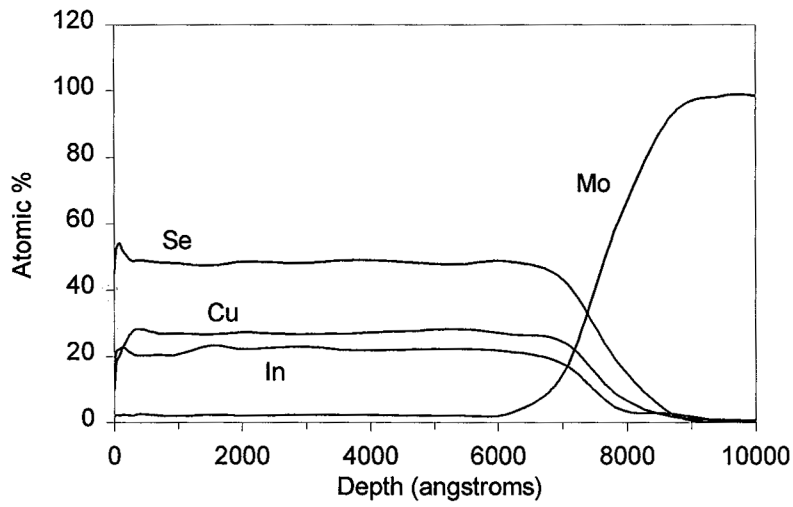

Figure 3. XPS depth profile of a CIS thin film deposited at –1.2 V vs. SCE for 600 s and annealed at 400 °C for 1 hour in flowing argon.

X-ray diffraction (XRD) of the CIS-based absorber films confirmed that they all had the basic chalcopyrite crystal structure. A shift is seen in the main Bragg peaks as either Ga or S is introduced into the CIS lattice. Figure 4 shows a comparison of the XRD pattern for a CIGS film to the reference patterns for $CuInSe_2$ and $CuIn_{0.5}Ga_{0.5}Se_2$. Figure 5 shows a comparison of the XRD pattern of a $CuIn(Se,S)_2$ film to the reference patterns of $CuInSe_2$, $CuIn(Se_{0.5},S_{0.5})_2$, and $CuInS_2$. These results indicate that both Ga and/or S are being incorporated into the basic CIS structure. XRD results also confirmed that the CdS films had a hexagonal crystal structure and the ZnO was in the zincite structure.

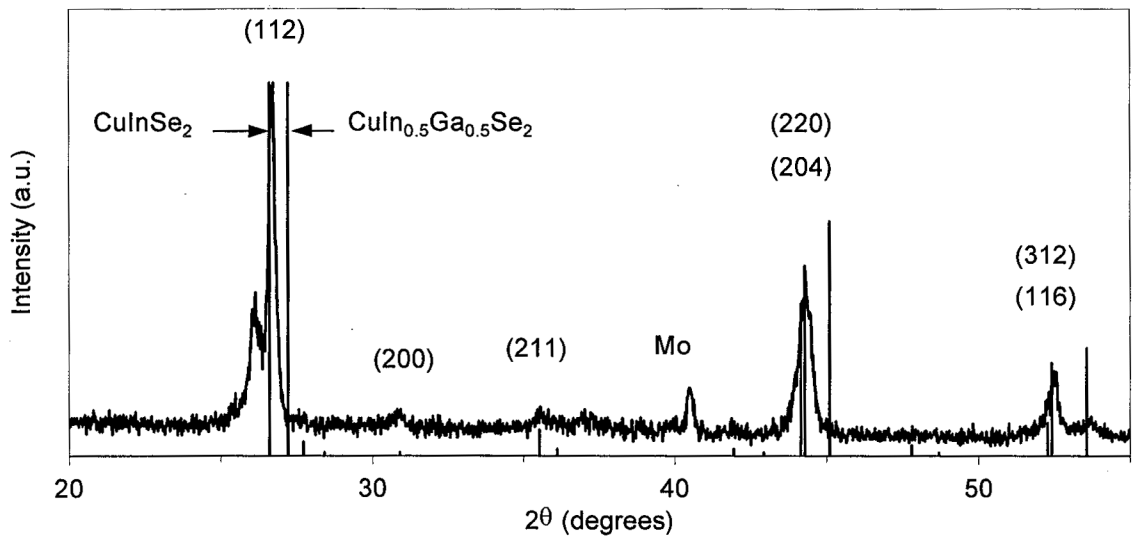

Figure 4. XRD pattern of Ga-doped CIS overlayed on $CuInSe_2$ and $CuIn_{0.5}Ga_{0.5}Se_2$ reference patterns.

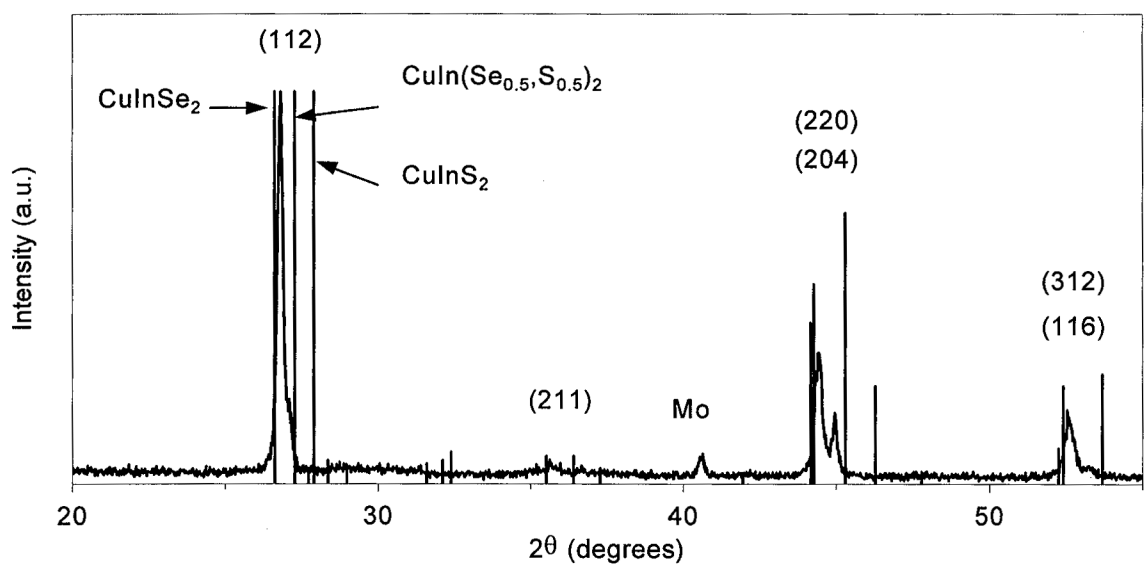

Figure 5. XRD pattern of S-doped CIS overlayed on $CuInSe_2$, $CuIn(Se_{0.5},S_{0.5})_2$, and $CuInS_2$ reference patterns.

We used optical transmisson spectroscopy to determine the optical bandgaps for the absorber and window films. The raw transmission data was coverted to absorption coefficients after film thickness was determined using a Dektak II profilometer. The absorption coeffcients were then used to determine the optical bandgaps, assuming the direct bandgap relation

$$\alpha = \frac{\left(E_g - h\upsilon\right)^{1/2}}{h\upsilon} \tag{1}$$

The CdS, ZnO, and CIS-based films deposited on ITO coated glass showed good linearity when plotted in accordance with Eq. 1, indicating that they are direct bandgap semiconductors. The optical bandgaps were determined from the x-intercepts of a least-squares fit to the linear portion of the curves (see Figure 6). The

values of 1.1 eV, 2.4 eV, and 3.3 eV for CIS, CdS, and ZnO, respectively are in good agreement with their accepted values.[4,6,8] A shift to larger values was also verified for S incorporation into $CuInSe_2$ (see Figure 7).

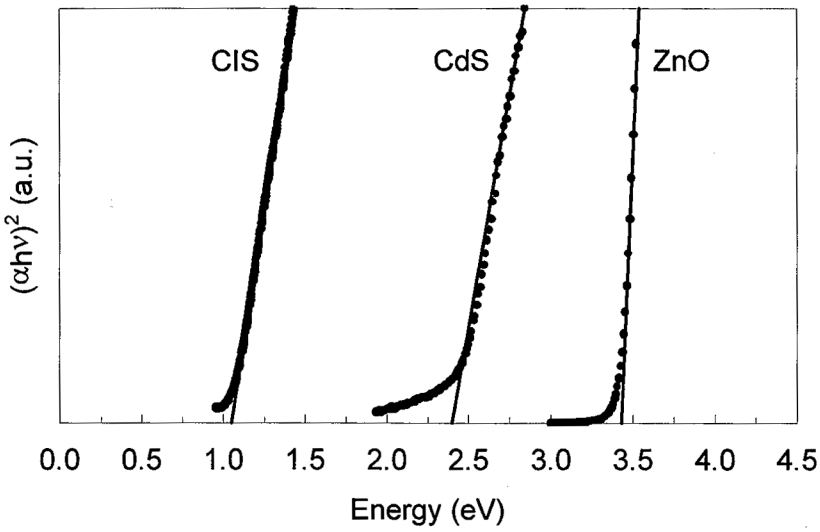

Figure 6. Optical bandgaps for $CuInSe_2$, CdS, and ZnO. The y-values have been normalized and plotted in arbitrary units in order to display the different materials on the same plot.

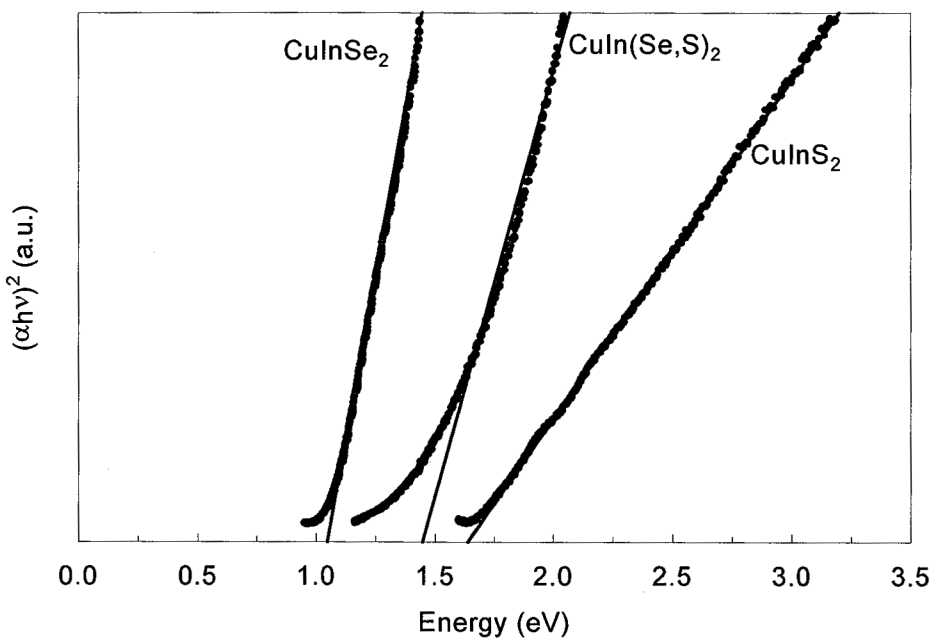

Figure 7. Optical bandgaps for $CuInSe_2$, $CuIn(Se,S)_2$, and $CuInS_2$. The y-values have been normalized and plotted in arbitrary units in order to display the different materials on the same plot.

The current versus voltage behavior of a device that consisted of electrodeposited ZnO on chemical bath deposited CdS, on electrodeposited $CuInSe_2$, on thin Mo foil, is shown in Figure 8. The device exhibited good rectification with a measurable short-circuit photo-current under ambient lighting. However, the device had an open-circuit voltage of only 220 mV and considerable reverse-bias leakage current. These results are most

likely attributable to point defects near the junction and/or grain boundary shunting. Improvement in the junction performance is being addressed by changes in the absorber stoichiometry and improved annealing conditions. The shallow slope of the forward-bias current versus voltage behavior indicates a significant series resistance. This resistance is probably a result of poor conductivity in the top contact. The top contact performance is being studied as a function of the deposition voltage and temperature of the ZnO. Improvement through the use of a post-deposition annealing of the ZnO is also being examined.

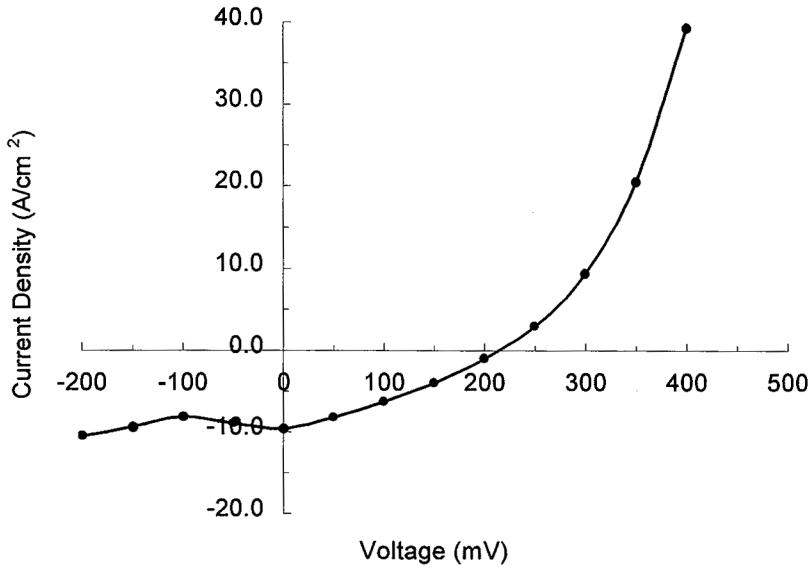

Figure 8. Current versus voltage characteristics of a ZnO/CdS/CIS solar cell under ambient light.

4. Conclusions

Compositionally uniform p-type $CuInSe_2$ thin films were deposited on inexpensive flexible substrates using low-temperature electrochemical deposition. X-ray diffraction analysis confirmed that it is possible to sustitutionally dope Ga and S for In and Se, repectively in $CuInSe_2$ thin films using electrochemical deposition. Optical spectroscopy verified that the incorporation of S into $CuInSe_2$ signifcantly increased the optical bandgap of the materials. Low-temperature electrochemical depostition and chemical bath deposition were used to deposit ZnO transparent conductive windows and CdS buffer layers, respectively onto p-type $CuInSe_2$. This combination of electrochemical and chemical bath deposition techniques were succesfully used to produce a working heterojunction thin-film photovoltaic solar cell.

5. References

[1] D.J. Flood, *Int'l Photovolt. Solar Energy Conf.*, **5**, Japan (1990) 551.
[2] C. Guillen and J. Herrero Sol. *Energy Mater. And Sol. Cells*, **43** (1996) 47.
[3] K. Zweibel, H.S. Ullal, and B. von Roedem, *25th IEEE Photovoltaic Specialists Conf.*, (IEEE, Washington, 1996) 159.
[4] H.W. Schock, *Solar Energy Materials and Solar Cells* **34** (1994) 19.
[5] J.R. Tuttle, M.A. Contreras, T.J. Gillispie, K.R. Ramanathan, A.L. Tenant, J. Keane, A.M. Gabor, and R, Noufi, *Prog. Photovoltaics* **3** (1995) 235.
[6] R.W. Birkmire, B.E. McCandless, W.N. Shafarman, and R.D. Varrin, *Proc. Of the 9th European Photovoltaic Solar Energy Conference*, Freiburg, Germany (Kluwer Academic Publishers, Dodrecht, 1991) 1415.
[7] B.R. Lanning and J.H. Armstrong, *Int. J. Solar Energy* **12** (1992) 247.
[8] J. Ma, F. Ji, H. Ma, S. Li, *Thin Solid Films* **279** (1996) 213.
[9] J. Lee and Y. Tak, *Mat. Res. Soc. Symp.* **495** (1998) 457.
[10] K. Ito and K. Nakamura, *Thin Solid Films* **286** (1996) 35.

$Cu(In,Ga)S_2$ THIN-FILM SOLAR CELLS PREPARED BY H_2S SULFURIZATION OF CuGa-In PRECURSOR[1]

Neelkanth G. Dhere, Shashank R. Kulkarni, Sanjay S. Chavan and Shantinath R. Ghongadi
Florida Solar Energy Center
Cocoa, FL 32922-5703

ABSTRATCT

Thin-film $CuInS_2$ solar cell is the leading candidate for space power because of bandgap near the optimum value for AM0 solar radiation outside the earth's atmosphere, excellent radiation hardness, and freedom from intrinsic degradation mechanisms unlike a-Si:H cells. Ultra-lightweight thin-film solar cells deposited on flexible polyimide plastic substrates such as Kapton®, Upilex® and Apical® have a potential for achieving specific power of 1000 W/kg, while the state-of-art specific power of the present day solar cells is 66 W/kg.

This paper describes the preparation of Cu-rich $CuIn_{1-x}Ga_xS_2$ (CIGS2) thin films and solar cells by a process of sulfurization of CuGa-In precursor similar to that being used for preparation of large-compact-grain $CuIn_{1-x}Ga_xSe_2$ thin films and efficient solar cells at FSEC PV Materials Lab. Copper-gallium and indium layers having Cu:(In+Ga) atomic proportion of 1.4:1 were deposited on unheated molybdenum-coated glass substrates by DC magnetron sputtering from CuGa(22%) and In targets. Well-adherent Cu-rich CIGS2 films were obtained by sulfurization in 1-4% hydrogen sulfide diluted in argon at temperatures ranging from 425-500° C for 30-60 minutes. Films tended to peel off when sulfurization was carried out for 60 min at 550° C. Because of indications of excessive indium loss at high (1300 sccm) argon flow rates and low Ar:H_2S (1%) gas proportion during sulfurization, possibly in form of volatile In_2S, H_2S gas concentration in argon was increased to 4% and argon flow rate was reduced to 650 sccm. CuGa/In intermixing and sulfur incorporation during sulfurization were promoted by adding intermediate 30 minute steps at 125° C and 325° C so as to avoid indium and gallium globule formation, instead of adding small traces of oxygen. $CuIn_{1-x}Ga_xS_2$ thin films were bluish, dark gray in color. Resistance measurement of CIGS2 films was used to verify if it was Cu-rich or Cu-poor. AES depth profile of unetched Cu-rich CIGS2 thin film showed segregation of excess copper at the surface possibly as a $Cu_{2-x}S$ layer. Excess $Cu_{2-x}S$ near the surface was etched away in dilute (10%) KCN solution for 3 minutes. Atomic proportions of Cu:In:Ga:S of typical Cu-poor CIGS2 films as measured by EMPA at 20 keV incident electron energy was 24.0:19.1:6.9:51.9, corresponding to formula $Cu_{0.92}In_{0.73}Ga_{0.27}Se_2$ thus very near the desired Cu content. A new intermediate chalcopyrite phase $CuIn_{0.7}Ga_{0.3}S_2$ was identified by X-ray diffraction in unetched and etched CIGS2 films. Peaks from a new In-rich phase, probably a new ordered vacancy compound (OVC) $Cu(In_{0.7}Ga_{0.3})_3S_5$, similar to the In-rich OVC phase $CuIn_3Se_5$, were also detected in XRD pattern from etched CIGS2 films. Scanning electron microscopy revealed large (2-2.5 μm) compact-grain morphology for films sulfurized at and above the temperatures of 450° C. Based on visual observations and results of material characterization, sulfurization parameters were optimized as follows: Ar:H_2S of proportion of 1:0.04 and argon flow rate of 650 sccm, 30 minutes each at 125° C and 325° C, and 60 minutes at maximum temperature of 475° C. Four or five, small solar cells were completed by deposition of CdS heterojunction partner layer by chemical-bath deposition, transparent-conducting ZnO/ZnO:Al window bilayer by RF sputtering and vacuum deposition of Ni/Al contact fingers through metal mask on several $CuIn_{1-x}Ga_xS_2$ thin films on Mo-coated 2.5 cmx2.5 cm glass substrates. All the cells showed PV conversion efficiency, η above 6%, most being over 7% (AM1.5, Total area). PV performance was uniform from one region to another, on the same substrate. AM1.5, total area, PV parameters of the best solar cell were as follows: V_{oc} = 705 mV, J_{sc} = 18.63 mA/cm^2, FF = 64.58%, and η = 8.48%, QE cutoff at 800 nm, equivalent to CIGS2 bandgap of 1.55 eV, showing an actual bandgap increase to the required optimum value for efficient AM0 PV conversion as a result of Ga incorporation.
1

[1] This work has been supported by the NASA Glenn Research Center at Lewis Field and the National Renewable Energy Laboratory

1. INTRODUCTION

Peter Glaser proposed the concept of solar power satellites (SPS) in 1968. In the earlier two studies carried out by NASA and DOE, the concept has been found to be scientifically and technologically feasible. The 1998 Space Solar Power (SSP) Concept Definition Study (CDS) has determined that SSP system performance goals could be accomplished through coordinated, strategic technology development efforts. Because of the estimated launch costs of low earth orbit (LEO) and geosynchronous-earth orbit (GEO) of $ 11,000/kg and $66,000/kg, specific power i.e. power per unit mass becomes very important [1]. 50 μm thick Si cells, without concentration, annealed with CO_2 lasers and monocrystalline 5 μm thick gallium arsenide, GaAs, solar cells on synthetic corundum substrates with x2 concentration were considered for SPS. Such a system would require thick single crystal substrates or wafers and interconnections for fabrication of interconnected strings. Integrally interconnected thin-film solar arrays would be free from both the constraints. Significant gains in spacecraft performance can be achieved at lower cost with ultra-lightweight, radiation-resistant, copper-indium sulfide, $CuInS_2$ polycrystalline-thin-film, flexible solar arrays having efficiencies comparable to current silicon solar cell arrays [1,2]. The bandgap of 1.53-1.55 eV of $CuInS_2$ is near the optimum value for an efficient conversion of AM0 solar radiation outside the earth's atmosphere. If necessary, it could also be increased slightly with the addition of small amount of gallium. High solar absorptances of $CuInS_2$ would allow the possibility of fabricating the cells with the absorber layer as thin as 1-2 μm. These cells do not suffer from intrinsic degradation mechanisms as is the case with a-Si:H cells. Copper chalcopyrites $CuIn_{1-x}Ga_x Se_{2-y}S_y$ have the highest radiation tolerances of all known materials. Ultra-light weight thin-film solar cells have a potential for achieving specific power of 1000 W/kg, while the state-of-art specific power of the present day solar cells is 66 W/kg. Higher efficiencies, freedom from intrinsic degradation, and high radiation resistance of $CuInS_2$ thin-film solar cells make them the leading candidate for this purpose.

Currently, copper-indium selenide and cadmium telluride are the leading absorber materials for terrestrial thin-film PV technology [3-10]. Small amounts of gallium and sulfur are added to copper-indium selenide for adjusting the bandgap. The efforts at NASA GRC over the last several years have focused on production of $CuInSe_2$, $CuInS_2$ and related materials through low-temperature methods [11-14]. Polycrystalline-thin-film solar cells of $CuIn_{1-x}Ga_x Se_2$ (CIGS), $CuInS_2$ and CdTe have already shown total-area PV conversion efficiencies of 18.8%, 11.1% (12.5% active area), and 15.8% at air mass 1.5 (AM 1.5) respectively. These are equivalent to conversion efficiencies in the space of ~15.2%, 9.0% and ~12.8% (AM0) respectively. There is considerable potential for enhancing the conversion efficiency of $CuInS_2$ thin-film solar cells. More importantly, thin-film solar cells can be produced economically because of the ease of coating large areas uniformly and reproducibly; and because of the incorporation of steps for monolithically integrated interconnections during the fabrication.

The objective of the present research is to develop ultra-lightweight, radiation-resistant, highly efficient, high specific power $CuIn_{1-x}Ga_xS_2$ (CIGS2) thin-film solar cells for space electric power. Small proportion of gallium is being incorporated so as to obtain benefits of improved adhesion, slightly higher bandgap, and incorporation of back-surface field as has been done with CIGS cells. Initially CIGS2 thin film solar cells are being fabricated on glass substrates. The main thrust is towards development of fundamental understanding and baseline processes rather than attaining the highest efficiencies.

1.1 Review of Previous Research

Scheer [15] has reviewed the surface and interface properties of Cu-chalcopyrite semiconductors and devices. A ternary phase diagram of copper-indium-sulfur system shows tie lines between Cu_2S and In_2S_3 as well as between InS and CuS pointing to possible pathways for the synthesis of $CuInS_2$. On the indium rich side, it shows the presence of $CuInS_2$ and $CuIn_5S_8$ ternary phases and the binary phase In_2S_3. On the copper-rich side, there are only the binary $Cu_{2-x}S$ phases besides the ternary phase $CuInS_2$ [16]. Migge [17] and Migge and Grzanna [18] have estimated free energies of the compounds In_6S_7, $In_{2.8}S_4$, $CuInS_2$, $CuIn_5S_8$, and $CuIn_2$ at 298 K and In_6S_7, $In_{417}S_{583}$, In_2S_3, $Cu_{951}In_{149}$, and $CuIn_5S_8$ at 723 K by thermochemical analysis of Cu-In-S system. The compound $CuInS_2$, is shown to equilibrate with most compounds of the system. Formation of $CuInS_2$ by sulfidization (sulfurization) of Cu-In alloy e.g. Cu_7In_3 with H_2S at 723 K by applying a ratio $pH_2S/pH_2 \approx 10^{-5}$ is predicted [18]. More interestingly, even in slightly In-rich film having cation ratio In/Cu+In of ~0.55, both the front and back surfaces are covered by $CuIn_3S_5$ phase showing that In-rich copper-indium sulfide phase segregates at the surfaces of $CuInS_2$ grains [19]. On the other hand, only the front surface shows the presence of copper sulfide even in highly Cu-rich copper-indium sulfide thin films [19]. Thus stoichiometric $CuInS_2$ thin films may be obtained by growing a Cu-rich film and etching away the excess copper sulfide at the surface. This fact has been used in the development of a tolerant two-step process by Klaer et al at the Hahn-Meitner Institute [20]. It consists of sulfurization of sputter deposited copper and indium layers on molybdenum-coated float glass

substrates, in vacuum-evaporated sulfur vapor at 550° C, to form a 2 μm thick copper-rich $CuInS_2$ thin film. Excess $Cu_{2-x}S$ secondary phase acting as a flux can assist in the formation of large grain $CuInS_2$ layer and then can segregate to the surface. It can be removed by etching in a KCN solution leaving behind a slightly copper-poor $CuInS_2$ layer. Solar cells are completed by chemical bath deposition of a thin CdS layer, sputter deposition of ZnO and evaporation of Al contact fingers. The best morphology and PV conversion efficiency of 11.1 % (AM1.5, total area, 12.5% active area) has been obtained at Cu/(Cu+In) ratio of 1.8 [20]. Comparison of $CuInS_2$ thin film growth by co-evaporation, sulfurization, and spray pyrolysis has indicated that CuS segregation at the surface is induced by excess S at the surface and is activated thermally [21]. Earlier, Ogawa et al [22] have prepared 10% (AM1.5) $CuInS_2$ thin-film solar cells by sulfurization of vacuum evaporated copper and indium layers in Argon/H_2S 5% mixture at 550° C.

Gosala et al [23] have found that roughness of coevaporated In-rich Cu-In precursor layers as determined by Rutherford Back Scattering (RBS) can be suppressed by cooling substrates to below room temperature while for Cu-rich precursor films, copper excess must be maintained above 1.4. Sulfurization was carried out in 3 % H_2S at 400° C. 3% solar cells were prepared with $CuInS_2$ thin films prepared from In-rich films deposited on cooled precursors. On the other hand, Cu-excesses over 1.8 led to deterioration of conversion efficiencies probably because KCN etching may not be removing excess copper sulfide completely leading to shunting paths. Miles et al [24] prepared $Cu_{11}In_9$ phase free of inhomogeneous secondary phases by deposition of ~1700 alternate Cu and In layers on Mo-coated glass substrates by magnetron sputtering. Precursor layers were placed face upwards either on strip heaters and excess sulfur was placed underneath at a distance of 10 cm or in a graphite box. Samples were heated after evacuating annealing chambers to 1.3 Pa and sealing. X-ray diffraction (XRD) and optical absorption spectroscopy analyses indicated formation of $CuInS_2$ films, free from binary phases, and with a direct bandgap of 1.45 eV. At annealing temperatures below 300° C, Cu and In binary compounds were detected showing an incomplete reaction. At FSEC PV Materials Lab, sputter-deposited Cu-In precursor layers have been intermixed to form single $Cu_{11}In_9$ phase by modest in-situ heating.

Watanabe et al [25] have sulfidized in Ar/H_2S 5%, stoichiometric and sulfur-deficient Cu-In-S layers sputtered respectively from Cu_2S and In_2S_3 mixed powder and $CuInS_x$ powder targets. Better crystallinity and cell properties (1.4%) were observed from $CuInS_2$ thin films prepared by annealing S-deficient amorphous Cu-In-S films. More recently, Watanabe and Matsui [26] deposited Cu-In-S precursors on rotating substrates by reactive sputtering from Cu and In targets in a H_2S/Ar mixture. $CuInS_2$ thin films were prepared by annealing in 5% H_2S/Ar at 550° C. Randomly oriented needlelike $CuIn_5S_8$ crystallites were observed in $CuInS_2$ thin films formed from precursors containing little S. Large grain, single phase $CuInS_2$ thin films and 6.3% cells were obtained without KCN treatment with Cu-In-S precursors having S/(Cu+In) ratio of 0.3. Grain size and uniformity deteriorated at much higher S/(Cu+In) ratios. Sulfur atoms probably restrain atomic migration thus eliminating indium aggregates on the film surface. However, above the optimum amount, sulfur seems to limit atomic migration excessively reducing grain size and complete intermixing. Ito and coworkers [27] have compared sulfurization of multiple (three) In_2S_3/Cu bilayers with that of metallic precursors. Adhesion of $CuInS_2$ thin films was found to improve when a small amount of gallium was deposited prior to the deposition of metallic precursors. Large (5 μm) grain $CuInS_2$ thin films were obtained with the gallium deposition, however, with rough morphology and segregation of islands of Cu_xS and InS_x phases on the surface. Films prepared using multiple In_2S_3/Cu bilayers were smooth and more homogeneous. Best typical efficiencies were Cu/In 10.4%, Ga-doped Cu/In 10.4%, In_2S_3/Cu 10.6%. Most of the improvement was due to an improvement in the fill factor [27]. Similar to CIGS cells, gallium incorporation has been found to increase the open circuit voltage and efficiencies of $CuInS_2$ cells, even though only small amount of gallium has been detected in the electrically active region near the surface [28]. Recent preliminary results of the growth of Cu-In-Se-S by selenization, sulfurization in H_2Se + H_2S (0.5%) in argon gas mixture at 350° to 450° C showed that a denser $CuInS_2$ films and 8% efficiency can be obtained by first reacting Cu-In layer at 350° C for 30 min followed by a 60 minute reaction at 450° C [29]. Indium segregation was avoided during experiments by adding minute amounts of oxygen ($O_2/H_2S+H_2Se=0.01$). Yukawa et al [30] have prepared $CuInS_2$ thin films by electrodeposition from an aqueous ternary bath. Well crystallized films were obtained by annealing in vacuum at 673 K without H_2S. Hepp and colleagues have prepared GaS, InS and $CuInS_2$ thin films by spray chemical vapor deposition using single-precursor sources [9-12].

Wet chemical oxidation of absorber surface have been found to result in considerable reduction of the reverse saturation current and the diode ideality factor thus improving $CuInS_2$ thin-film solar cell characteristics [31]. Sub-bandgap structure at 1.44 eV has been assigned to donor-acceptor transitions based on temperature dependence of photo- and electroreflectance analysis of CdS/$CuInS_2$ heterostructures [32]. A reasonable correlation has been found to exist between the electron-beam induced current and quantum efficiency of $CuInS_2$ solar cells [33]. Attempts have been made to improve the open circuit voltage of $CuInS_2$ thin-film solar cells by

modifying the grain boundaries and heterointerface by addition of ZnS and CdS [34]. $CuIn_{1-x}Ga_x Se_{2-y}S_y$ thin-film solar cells have been found to possess excellent radiation hardness [35].

Steps for monolithically integrated interconnections can be incorporated during the fabrication of thin-film solar cells. Monolithically integrated, flexible 10% (AM0) $CuInSe_2$ submodule has been fabricated on titanium foil [36]. Solar cell parameters under lunar conditions have been calculated by Dhere and Santiago [37].

CIGS thin-film solar cell technology has evolved considerably over the years [9,10]. On the other hand, considerable work must be performed on $CuInS_2$ thin-film solar cell technology. Especially fundamental understanding must be gained so as to attain the level of maturity comparable to that of CIGS. Because of the similarity between the processes for the synthesis of CIGS and $CuInS_2$ thin films and cell fabrication procedure, much can be learned from the CIGS solar cell technology. CIGS thin films with good crystallinity and smooth morphology having excellent efficiencies have been prepared by initial co-evaporation of indium, gallium and selenium followed by copper and selenium co-evaporation passing through a copper rich film and finishing off with indium, gallium and selenium co-evaporation to obtain an overall Cu-poor film. Contrera et al [38] have fabricated the champion (18.8%) cell by passing through an intermediate Cu-rich phase. However, this does not seem to be as critical for their process at 550° C. In another instance of CIGS thin films deposited by co-evaporation at 550° C, efficiencies of solar cells prepared using an uniform composition all along was higher (15.0%) compared to that (12.9%) prepared using intermediate Cu-excess [29]. However, for deposition at 400° C, uniform composition resulted in a lower (9.5%) efficiency than that (12.9%) obtained with intermediate Cu-excess.

Two-selenization process has been developed at FSEC PV Materials Lab for the deposition of large compact grain $CuIn_{1-x}Ga_xSe_2$ thin films and efficient solar cells [3-8]. It relies on the fluxing action of $Cu_{2-x}Se$ phase in copper-rich CIGS films obtained after the first selenization. Deposition of indium followed by the second selenization converts the entire film into a copper-poor CIGS film suitable for highly efficient solar cells. The excess $Cu_{2-x}Se$ phase is reconverted to CIGS rather than etching it away. Resultant CIGS thin films are considerably more adherent to Mo-coated glass substrates with initial Cu-rich phase [6,7]. A CuGa(22 at. %) alloy target was used to eliminate the problem of sputtering from liquid gallium target. Adhesion improved still further with gallium incorporation. Higher rates of temperature ramp-up to 550°C and a controlled cool-down to 300 °C under continued selenium evaporation helped in enhancing gallium content [5]. Solar cell efficiency of 9.02% was achieved with a $CuIn_{0.82}Ga_{0.18}Se_2$ thin film [4-5]. Addition of gallium and sulfur can raise the band gap of CIGS closer to the optimum value. In post-deposition selenized films, gallium has a tendency to diffuse towards the back contact. Ga incorporation near the back contact provides the back-surface field.

Woodcock et al [39] and Bruton et al [40] have carried out a cost analysis of terrestrial thin-film and c-Si solar cells for annual production level of 500 MW based on the procedure developed by Ugalde et al [41]. A similar study would be beneficial in the planning of manufacturing of space thin-film solar cells.

For space applications it would be necessary to deposit solar cells onto a thin plastic substrates. Thin plastic sheets of polyimides such as Kapton®, (DuPont), Apical® (Allied-Apical), and Upilex® (Ube Industries/ICI America), and uniaxially oriented fluoropolymer teflon are suitable substrates because they are lighter in weight, flexible, shatterproof, durable in UV radiation, and transparent to IR radiation. The polyimides Kapton® and Upilex® can maintain their properties even when heated continuously to temperatures of 270-290° C. Other properties need to be considered when selecting the specific product for coating applications. A square foot of 12.5 μm Upilex sheet weighs only 1.7 g. Polyimide Kapton® has been chosen as the primary material in flexible solar arrays on Space Station Freedom. Fluoropolymer tefzel is stable to 180° C, and is recommended for use as a cover sheet. Plastic cover sheets for radiation protection in space are not available at present. Thin films especially those of noble metals do not adhere well to inert substrates. Usually the sheets are treated with corona discharge to improve adhesion. The corona treatment may not be essential for deposition of films by sputter deposition because of the plasma ambient which provides ion bombardment. An undercoat of chromium, titanium-tungsten, etc have been used to improve the adhesion. Sputter-deposited back molybdenum contact is expected to adhere well to the polymer sheets. Polyimide sheets are readily attacked by atomic oxygen which is the predominant atmospheric species in low earth orbit (LEO). The energy of 3.3-5.5 eV of the atmospheric constituents impinging on the polyimide foils is sufficient to break chemical bonds and allow chemical reaction to occur. Polyimide Kapton sheets have been commercially coated with 650-1300 Å silicon oxide on both sides to minimize the damage by atomic oxygen. The silicon oxide coatings have also been helpful in minimizing the moisture attack. There are indications that handling and processing techniques may increase the number of defects in the coatings. Hence it is necessary to take adequate care during the processing to avoid too many large or continuous defects. Other dielectric coatings could also be used as protective buffer layers.

NASA has developed more transparent polyimide sheets. However, the yellow color of Kapton® will not pose a problem for substrate type $CuInS_2$ thin film solar cells. Times required to reduce the ultimate elongation

of Kapton® from from 70% to 1% by heating in air at 350° C, 400° C and 450° C are for six days, 12 hours and 2 hours respctively. It will last longer in inert ambient and in vacuum. Hence the processing temperatures and times must be minimized for fabrication of flexible ultra-lightweight thin-film solar cells on polyimide substrates.

2. EXPERIMENTAL TECHNIQUE

The two-selenization process developed at FSEC PV Materials Lab is being used routinely for preparation of large compact grain $CuIn_{1-x}Ga_xSe_2$ thin films and efficient solar cells. The second selenization is being replaced by sulfurization for the fabrication of $CuIn_{1-x}Ga_x Se_{2-y}S_y$ thin films. Using a similar process, approximately 40% Cu-rich $CuIn_{1-x}Ga_x S_2$ thin films were fabricated by sulfurization of CuGa/In layers on Mo-coated substrates, in H_2S/Ar mixtures. The process begins with deposition of ~1 μm thick molybdenum back contact layer on unheated soda-lime float-glass substrates by DC magnetron sputtering in a 47 cm diameter, 60 cm height stainless-steel bell jar pumped with a cryopump and a rotary vacuum pump. Some Mo coated glass substrates were obtained from Siemens Solar Industries. Copper-gallium CuGa(22%) and indium layers were also deposited by DC magnetron sputtering in the same cryopumped vacuum system. Thicknesses of the metallic precursors CuGa(22%) and In calculated so as to obtain an initially 40% cooper-rich CIGS film were as follows: CuGa(22 at.%) 5150 Å and In 3925 Å. The final thickness of the slightly copper-poor $Cu_{0.92}In_{1-x}Ga_xS_2$ layer was projected to be 2.5 μm. Initially the entire thickness (5150 Å) of CuGa(22%) was sputter-deposited on Mo-coated glass substrates followed by deposition of 3925 Å thick In layer. More recently, this has been modified so as to minimize the loss of indium, in the form volatile In_2S during the sulfurization, by covering it with a thin CuGa layer. The new sequence is shown in Figure 1. It consists of the deposition of 70% of CuGa (3605 Å), followed by 100% of In (3925 Å), and finally covered with the remainder 30% of CuGa (1545 Å).

Sulfurization was carried out in flowing argon:H_2S gas mixture. Samples were placed in a 5 cm outer diameter, 45 cm long alumina tube fitted with gas-tight end-caps and glass flow console. Alumina tube was placed in a 5 cm diameter, 30 cm long, single zone furnace. Argon and H_2S flow was measured with gas flow meters. Effluent gas was passed through 2 M KOH aqueous solution in four wash-bottles for scrubbing. For this purpose, two wash bottles were connected in each of two parallel branches to minimize pressure build-up. An initial empty wash bottle prevented inadvertent back-flow of scrubbing fluid. The entire set-up was housed in a fume hood. H_2S gas detector monitored the presence of hydrogen sulfide in the fume hood at parts per million (ppm) level. Care was taken to avoid atmospheric air and moisture contamination by sealing off the gas flow set-up in between experiments. System was primed by passing argon for 120 minutes at a rate of 1300 standard cubic centimeters per minute (sccm) and Ar:H_2S gas mixture for 30 minutes at the preset rate prior to initialization of sulfurization. The flow rate of 1300 sccm is approximately equivalent to the change of entire reaction volume once per minute. Sulfurization temperatures were varied over a range of 425-550° C. Sulfurization time was either 30 or 60 minutes at the maximum temperature. Initially the preset Ar:H_2S gas proportion was maintained at 1:0.01 and the preset argon gas flow rate was 1300 sccm. However, because of indications of excessive indium loss, the preset argon flow rate was reduced to 650 sccm while the preset Ar:H_2S gas proportion was increased to 1:0.04. In earlier selenization experiments, indium has been found to escape in the form of volatile In_2Se at low selenium vapor incidence rates. Argon to hydrogen sulfide gas flows were controlled independently to obtain the desired Ar:H_2S proportion. No oxygen was added to avoid indium and gallium globule formation. Instead, precursor intermixing and sulfur incorporation were promoted by maintaining metallic precursors for 30 minutes each and at 125° C and 325° C under the flow of Ar:H_2S gas mixture at the preset proportion and rate.

Materials properties of CIGS2 thin films were studied for optimizing the preparation parameters. Adhesive strength at the interface of Mo/metallic precursors and Mo\CIGS thin films was tested by a simple adhesive-tape peeling test. Formation of crystalline phases and morphology was studied by X-ray diffraction (XRD) and scanning electron microscopy (SEM). Composition was analyzed by wavelength-dispersive analysis of X-rays i.e. electron probe microanalysis (EMPA) and energy-dispersive analysis of X-rays (EDAX). Composition variation along the depth was analyzed by Auger electron spectroscopy (AES) in conjunction with sputter-etching. Near stoichiometric, slightly Cu-poor CIGS2 thin films were obtained by etching away excess $Cu_{2-x}S$ in 10% aqueous KCN solution for 3 minutes. Solar cells were completed by deposition of ~500 Å CdS heterojunction partner layer by chemical-bath deposition, transparent-conducting ZnO/ZnO:Al window bilayer by RF sputtering and vacuum deposition of Ni/Al contact fingers through metal mask on CIGS2 thin films on Mo-coated glass substrates (Fig. 2). Because of vacuum problems in an existing RF sputtering system, the cells completion and current-voltage IxV and quantum efficiency, QE measurements were carried out at the National Renewable Energy Laboratory (NREL) with the kind help of Dr. Kannan Ramanathan.

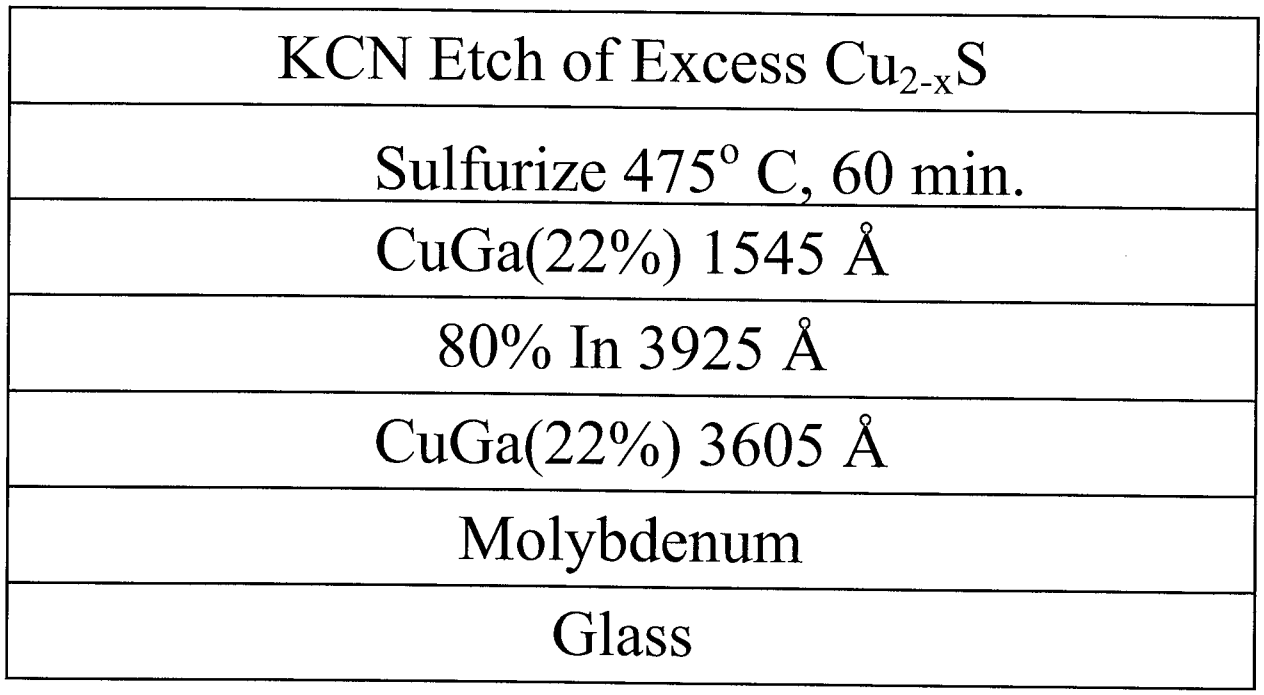

Figure 1. Preparation steps of 2.5 μm thick, nearly stoichiometric, slightly Cu-poor CIGS2 thin film.

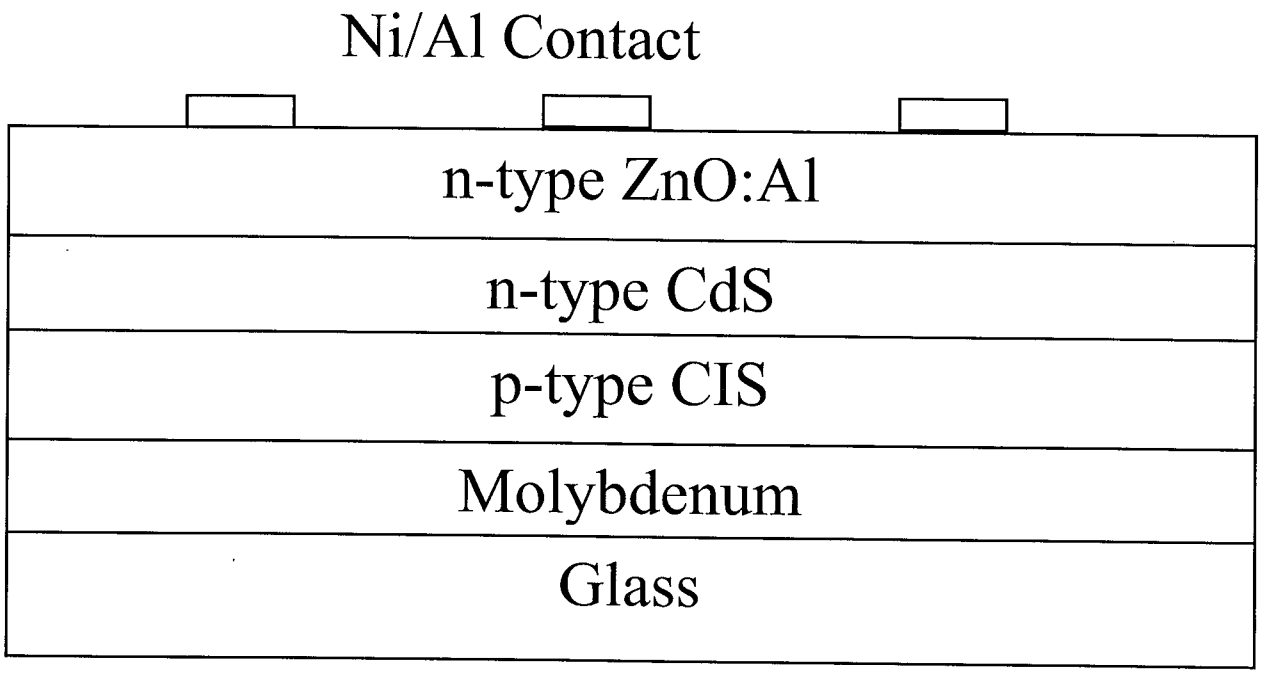

Figure 2. Layer sequence of CIGS2 thin film solar cell.

3. RESULTS AND DISCUSSION

Metallic precursors were found to remain on the molybdenum back contact layer, when a transparent adhesive tape was applied onto CuGa/In and CuGa/In/CuGa metallic precursors and peeled off, showing that they adhered well to the molybdenum back contact layer. There was spontaneous, partial peeling off of films after sulfurization for 60 minutes at substrate temperature of 550 °C. Well-adherent films were obtained for sulfurization at maximum temperatures in the range 425-500° C for 60 minutes, in 1-4% H_2S diluted in argon at argon flow rate of 650 sccm.

In case of sulfurization in Ar:H_2S(0.5%) mixture at high argon flow rate of 1300 sccm, sides and back of glass substrates and alumina carrier were found to be coated with semitransparent, brownish yellow film, while the CIGS2 film itself was semi-reflecting whitish gray. This indicated excessive indium loss possibly in the form In_2S. Earlier indium has been found to escape in the form of volatile In_2Se at low selenium vapor incidence rates. Bluish, dark gray $CuIn_{1-x}Ga_xS_2$ thin films were obtained when the sulfurization were carried out in Ar:H_2S(4%) mixture at argon flow rate of 650 sccm.

Composition analysis of Cu-rich and Cu-poor $CuIn_{1-x}Ga_xS_2$ thin films was carried out by EMPA at NREL by Amy Swatzlander Guest. Proportions of atomic concentrations of Cu:In:Ga:S of typical Cu-poor CIGS films was found to be 24.0:19.1:6.9:51.9 at incident electron energy of 20 keV. Thus EPMA composition of Cu-poor CIGS2 thin films seems to correspond to the formula $Cu_{0.92}In_{0.73}Ga_{0.27}Se_2$. This is very near the desired composition in terms of copper content. At incident electron energy of 10 keV, the proportion of gallium as compared to that of indium was lower. This is to be expected because of the lower depth of analytical volume at the lower electron energy and the tendency of gallium to diffuse towards the back contact. In typical Cu-rich CIGS2 films, proportion of atomic concentrations of Cu:In:Ga:S measured at 20 keV was 41.5:9.8:3.8:44.93. At 10 keV, the proportion of copper was still higher. This gives an indication of much higher than desired copper-excess Cu/In+Ga of 1.4-1.8. However, results of EDAX analysis of unetched and etched CIGS2 thin films prepared in the present study were compared with that of unetched and etched reference $CuInS_2$ thin films having copper excess Cu/In+Ga = 1.8 kindly provided by Dr. Roland Scheer at the Hahn-Meitner Institut, Cu-excesses were seen to be comparable.

In a manner similar to the practice with CIGS thin films, a simple resistance measurement test was routinely used to gauge whether the CIGS2 thin film is Cu-rich or Cu-poor. Low resistance (<500 ♦) of the films indicated the formation of copper-rich film whilst a high resistance (>100 k♦) indicated Cu-poor film.

AES analysis of the surfaces of unetched and etched CIGS2 samples showed the presence of S at 152 eV, C at 270 eV, In at 404 eV, O at 510 eV and Cu at 920 eV. Surface of etched CIGS2 sample showed AES peaks of S, C, In, O, Cu and a small Ga peak at 1070 eV. Oxygen and carbon AES peaks disappeared after sputter-etching approximately 500 Å of surface layer with an argon sputter gun. AES depth profile of unetched $CuIn_{1-x}Ga_xS_2$ thin film sample in Figure 3 shows the predominance of a copper-rich phase in an approximately 8500 Å thick surface layer. In this layer, copper excess as measure by ratio Cu/In+Ga of atomic concentration is in the range 4-14. Thus during the sulfurization of copper-rich precursor, the excess copper precipitates at the surface as a $Cu_{2-x}S$ layer. In a similar manner to the case with CIGS thin films, it would provide a fluxing action for improved morphology. Moreover, the remainder of the film is nearly stoichiometric CIGS2. This forms the basis of the process of etching away the excess copper phase in a dilute KCN solution, leaving behind a nearly stoichiometric $CuIn_{1-x}Ga_xS_2$ thin film. The presence of slightly copper-poor, nearly stoichiometric $CuIn_{1-x}Ga_xS_2$ thin film is confirmed by the AES depth profile of an etched CIGS thin film in Figure 4. Concentration increase of gallium towards the back molybdenum contact once again demonstrates the tendency of gallium to diffuse towards the Mo back contact possibly because of the residual stress at that interface. AES depth profiles also explain the increasing gallium concentration and decreasing copper concentration detected in EPMA analysis at higher incident electron energy.

Morphology of CIGS thin films was studied by scanning electron microscopy (SEM). An SEM image of an etched $CuIn_{1-x}Ga_xS_2$ thin film in Figure 5 shows the film to consist of compact, large-grain crystallites. The grain size is estimated at 2-2.5 m, i.e. comparable to the film thickness.

-2 type X-ray diffraction pattern of Cu-rich (unetched) $CuIn_{1-x}Ga_xS_2$ thin film obtained using Cu K X-rays is shown in Figure 6. At present JCPDS data of $CuIn_{1-x}Ga_xS_2$ phase having intermediate compositions between of $CuInS_2$ and $CuGaS_2$ is not available. It was verified that crystallographic parameters 'a' and 'c' of the intermediate chalcopyrite phases: $CuIn_{0.7}Ga_{0.3}Se_2$, $CuIn_{0.6}Ga_{0.4}Se_2$ and $CuIn_{0.5}Ga_{0.5}Se_2$ follow a linear variation between those of $CuInSe_2$ and $CuGaSe_2$. A similar linear extrapolation of 'a' and 'c' parameters between those of $CuInS_2$ and $CuGaS_2$ was employed for indexing the XRD peaks. The values of lattice spacing 'd' of crystallographic planes calculated from 2 positions of XRD peaks were found to fit crystallographic parameters of

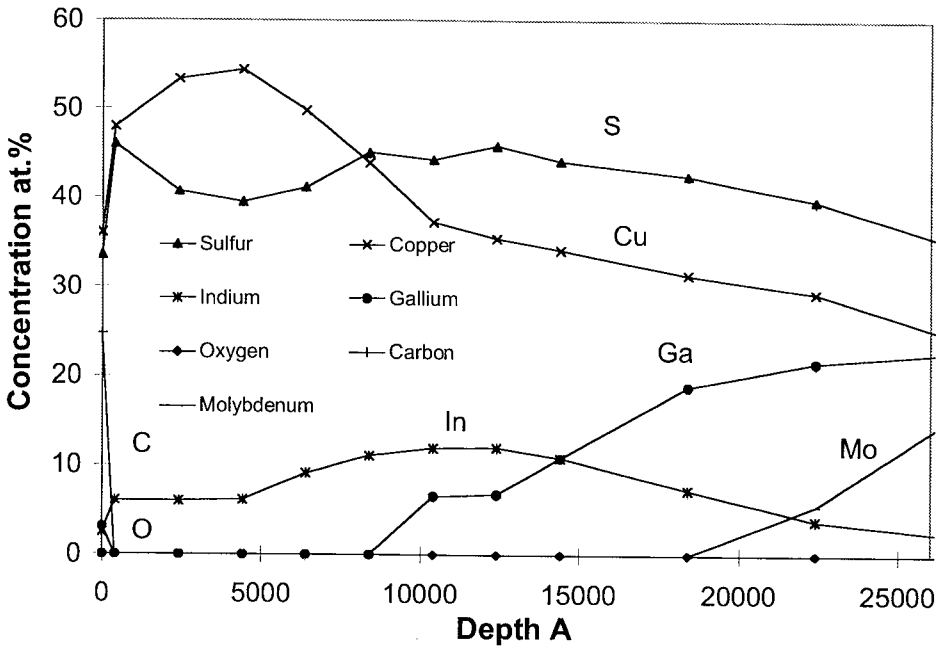

Figure 3. AES depth profile of unetched CIGS2 thin film showing a copper-rich surface layer.

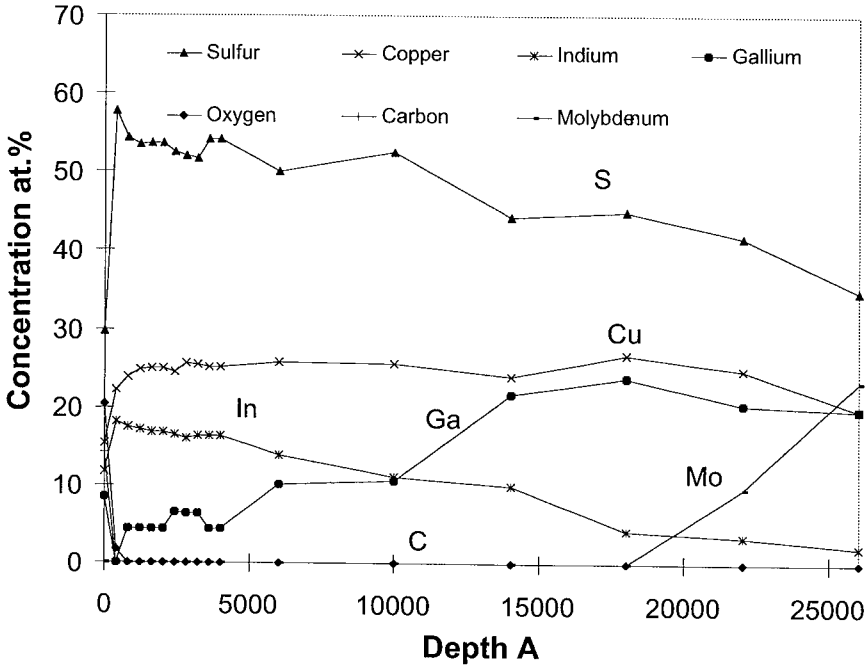

Figure 4. AES depth profile of a near stoichiometric, slightly Cu-poor, etched CIGS2 thin film.

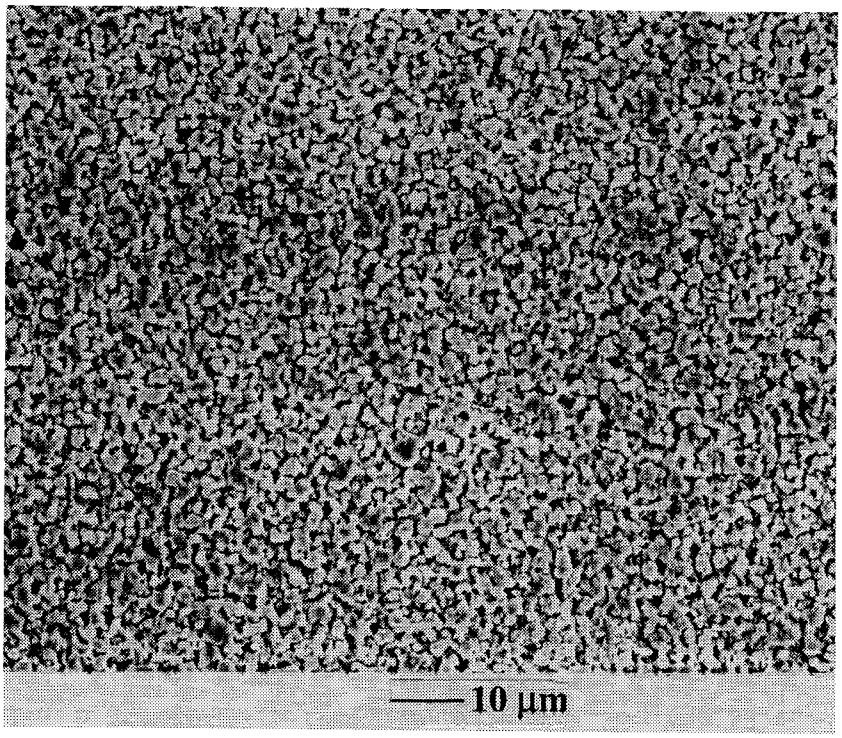

Figure 5. SEM image of a large (2-2.5 µm), compact-grain, etched CIGS2 thin film.

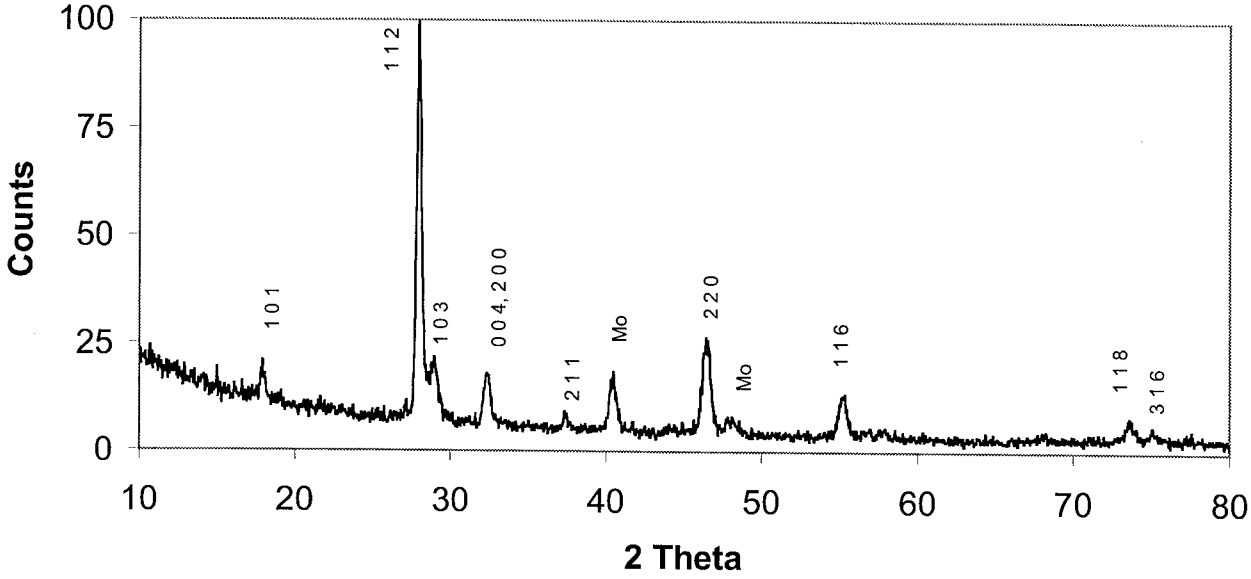

Figure 6. XRD pattern from an unetched, Cu-rich (Cu/In+Ga ≈ 1.4) CIGS2 thin film.

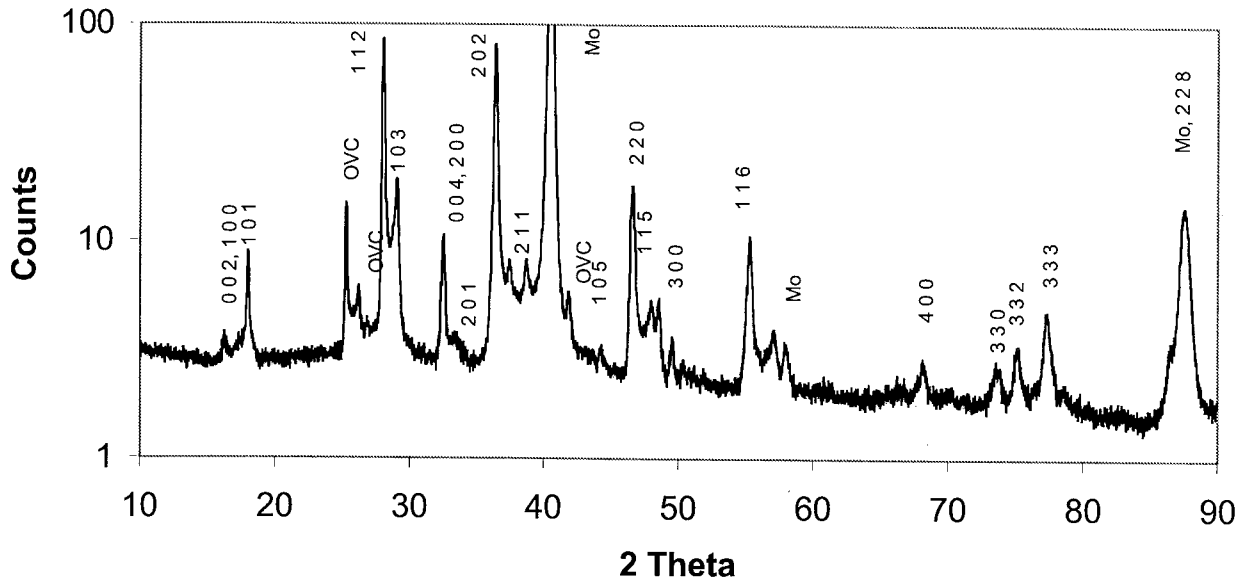

Figure 7. XRD pattern from a near stoichiometric, slightly Cu-poor, etched CIGS2 thin film.

a new chalcopyrite phase $CuIn_{0.7}Ga_{0.3}S_2$ with 'a' = 5.47 Å and 'c' = 10.94 Å. The crystallographic parameters are being refined further. Besides the XRD peaks of molybdenum, the following XRD peaks of the intermediate chalcopyrite phase were identified: 101, 112, 103, 004, 220, 116, and 316. As expected 112 peak is the strongest. X-ray diffraction pattern of Cu-poor (etched) $CuIn_{1-x}Ga_xS_2$ thin film obtained at NREL by Dr. Helio Moutinho is shown in Figure 7. In this case also the calculated lattice spacing 'd' of crystallographic planes again fit well with 'a' and 'c' parameters of the intermediate chalcopyrite phase $CuIn_{0.7}Ga_{0.3}S_2$. XRD peaks of molybdenum were stronger because of the lower thickness of the etched film. The following XRD peaks of the intermediate chalcopyrite phase were identified: 100, 002, 101, 110, 102, 11, 112, 103, 200, 004, 201, 210, 202, 211, 220, 213, 105, 220, 221, 115, 300, 116, 400, 330, 331, 332, 333, 228, and 424. Thus both the XRD patterns unequivocally show the formation of the new intermediate chalcopyrite phase $CuIn_{0.7}Ga_{0.3}S_2$. Three peaks that could not be attributed to either $CuIn_{0.7}Ga_{0.3}S_2$ or molybdenum were again found to arise from an indium-rich intermediate chalcopyrite phase having parameters of 'a' = 6.128 Å and 'c' = 12.257 Å. Possibly it may be a phase $Cu(In_{0.7}Ga_{0.3})_3S_5$. A similar indium-rich phase $CuIn_3Se_5$ has been found to exist at the surface of copper-indium selenide films and has been termed the ordered vacancy (OVC) phase [42]. It is n-type and hence forms a buried homojunction with the p-type CIGS films and is known to lead to high conversion efficiency of solar cells. In the XRD pattern in Figure 7, the following peaks of the chalcopyrite OVC phase $CuIn_{0.7}(Ga_{0.3})_3S_5$ were identified: 112, 103, and 220.

Based on visual observations and results of material characterization, sulfurization parameters were optimized as follows: Ar:H_2S of proportion of 1:0.04 and argon flow rate of 650 sccm, 30 minutes each at 125° C and 325° C, and 60 minutes at maximum temperature of 475° C. Most of the results presented above and in the following pertain to these conditions.

Solar cells were completed at NREL on five substrates. Each possessed an area covered with an etched, near stoichiometric, slightly Cu-poor CIGS2 thin film on Mo-coated glass substrate of 2.5 cm x 2.5 cm. Cell completion began with a deposition of ~500 Å CdS heterojunction partner layer by chemical-bath deposition. Afterwards, a transparent-conducting window bilayer consisting of a thin film of undoped ZnO and a thin film of zinc oxide doped with aluminum was deposited by RF sputtering. Finally Ni/Al contact fingers were deposited by vacuum evaporation through metal mask (Fig. 2). Three to five small cells were scribed on each substrates to

test for uniformity. Current versus voltage (IxV) characteristics were measured under simulated AM1.5 conditions at 25° C. All the devices showed photovoltaic activity with the minimum efficiency, □ of 6%, most having efficiency >7% (AM1.5, Total area). On the same substrate, the performance was uniform from one region to another. Open circuit voltage, V_{oc} ranged between 650-728 mV. Short circuit current density, J_{sc} was in the range 16.8-19.2 mA/cm^2 and the fill factor, FF ranged between 50-65%. The fill factor seemed to be limited by high series resistance. The devices are undergoing heat treatment at 200° C in air and are expected to improve. So far, PV parameters of the best cell were as follows: V_{oc} = 705 mV, J_{sc} = 18.63 mA/cm^2, FF = 64.58%, and □ = 8.48% (Figure 8). Quantum efficiency, QE measurement showed a maximum of 83% absolute external efficiency, with a reasonably flat response over the 550-730 nm range, and high wavelength i.e. absorber bandgap cutoff at 800 nm equivalent to CIGS2 bandgap of 1.55 eV. It is interesting to note that high wavelength cutoff of $CuInS_2$ thin films prepared with 80% Cu-excess at Hahn-Meitner Institut is ~825 nm equivalent to CIGS2 bandgap of 1.50 eV. Thus it can be seen that gallium incorporation has in fact increased the bandgap to the required optimum value for efficient AM0 PV conversion. After further photovoltaic characterization at NREL by IxV and under AM1.5 conditions, the solar cells will be brought to NASA Glenn Research Center for performance evaluation under AM0 conditions.

4. CONCLUSIONS

Well-adherent, nearly stoichiometric, slightly copper-poor, large (2-2.5 □m) compact grain, CIGS2 thin films approximately corresponding to formula $Cu_{0.92}In_{0.73}Ga_{0.27}Se_2$ were prepared on Mo-coated glass substrates by sulfurization of a 40% Cu-rich sputter-deposited stack of CuGa(22%)/In/CuGa(22%) metallic precursors in 4% H_2S diluted in argon, at argon flow rate of 650 sccm and maximum temperature of 475° C for 60 minutes, with intermediate 30 minute steps at 125° and 325° C, after etching away excess $Cu_{2-x}S$ near the surface in dilute (10%) KCN solution for 3 minutes. A new intermediate chalcopyrite phase $CuIn_{0.7}Ga_{0.3}S_2$ was identified by XRD in unetched and etched CIGS2 films. Peaks from a new In-rich phase, probably a new ordered vacancy compound $Cu(In_{0.7}Ga_{0.3})_3S_5$, were also detected in XRD pattern from etched CIGS2 films. Several $CuIn_{1-x}Ga_xS_2$ thin film solar cells with PV conversion efficiency exceeding 7% (AM1.5, Total area) were fabricated. The best AM1.5, total area, PV parameters were V_{oc} = 705 mV, J_{sc} = 18.63 mA/cm^2, FF = 64.58%, and □ = 8.48%, and QE cutoff at 800 nm, equivalent to CIGS2 bandgap of 1.55 eV, showing an actual bandgap increase to the required optimum value for efficient AM0 PV conversion as a result of Ga incorporation.

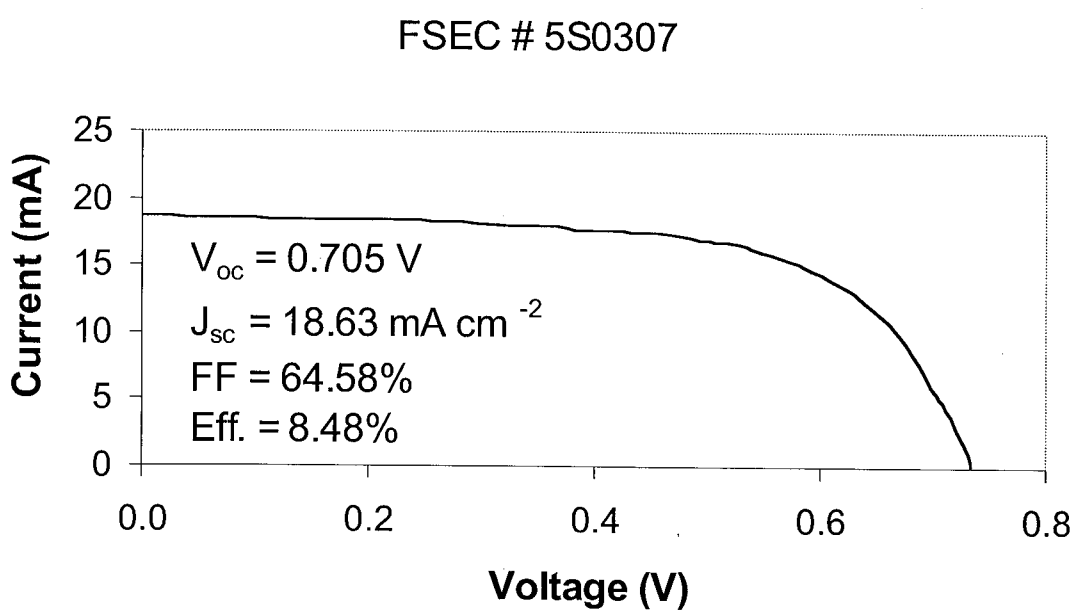

Figure 8. IxV characteristics of CIGS2 thin film solar cells under AM1.5 conditions.

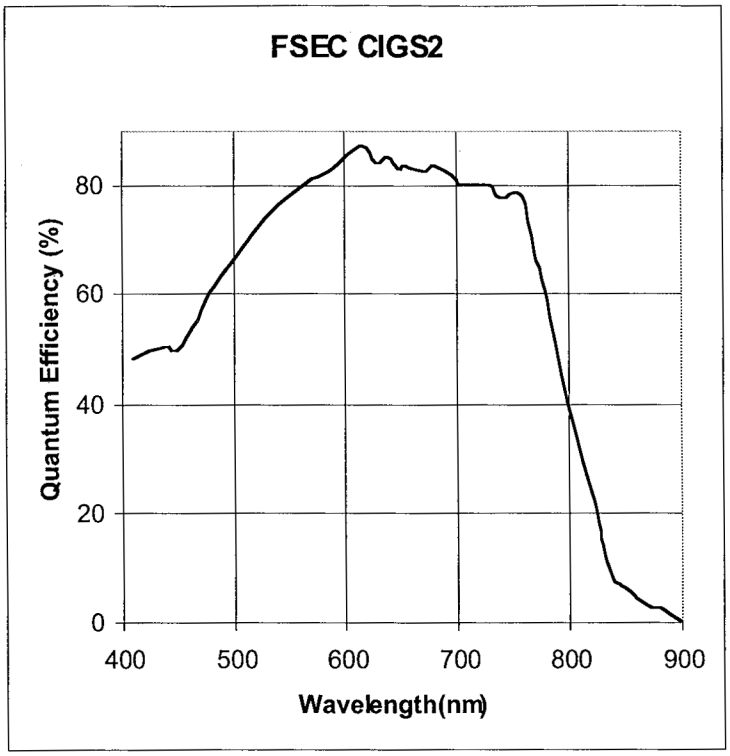

Figure 9. External quantum efficiency of CIGS2 thin film solar cells.

5. REFERENCES

1. S. G. Bailey and D. J. Flood, Prog. Photovolt. Res. Appl. **6**, (1998), 1-14.
2. D. J. Flood, Prog. Photovolt. Res. Appl. **6**, (1998), 187-192.
3. N. G. Dhere and K. W. Lynn, Proc. 2nd World Conf. Exhibit. Photovoltaic Solar Energy Conv. (WCEPVSEC), Vienna, (1998), 1125-1128.
4. N. G. Dhere and K. W. Lynn, Proc. 25th Photovoltaic Specialists' Conf. (PVSC), Washington, (1996), 897-900.
5. N. G. Dhere and K. W. Lynn, Solar Energy Mat. & Solar Cells, **41/42**, (1996), 271-279.
6. N. G. Dhere, S. Kuttath, and H. R. Moutinho, J. Vac. Sci. Technol. **A13**, (1995), 1078-1082.
7. N. G. Dhere, S. Kuttath, K. W. Lynn, R. W. Birkmire, and W. N. Shafarman, Proc. 1st WCEPVSEC, Hawaii, (1994), 190-193.
8. N. G. Dhere, D. L. Waterhouse, K. B. Sundaram, O. Melendez, N. R. Parikh, B. K. Patnaik, J. Mat. Sci.: Mat. in Electronics, **6**, (1995),52-59.
9. H. S. Ullal, K. Zweibel and B. von Roedern, 26th PVSC, Anaheim, CA, (1997), 301-305.
10. K. Ramanathan, R. N. Bhattacharya, J. Granata, J. Webb, D. Niles, M. Contreras, H. Wiesner, F. S. Hasoon and R. Noufi, 26th PVSC, Anaheim, CA, (1997), 319-322.
11. A.F. Hepp, M.T. Andras, S.G. Bailey, and S.A Duraj, Adv. Mater. for Optics and Elec. **1**, (1992), 99-103.
12. R.P. Raffaelle, H. Forsell, T. Potdevin, R. Friedfeld, J.G. Mantovani, S.G. Bailey, S.M. Hubbard, E.M. Gordon, and A.F. Hepp, Solar Energy Materials & Solar Cells, **57**, (1999), 167-178.
13. J.A. Hollingsworth, W.E. Buhro, and A.F. Hepp, Chemical Vapor Deposition **5**, (1999), 000-000.
14. J.A. Hollingsworth, W.E. Buhro, A.F. Hepp, D.O. Henderson, A. Ueda, P.P. Jenkins, and M.A. Stan, Solid State Electronics **43**, (1999), 000-000
15. R. Scheer, Trends in Vac. Sci. & Technol. **2**, (1997), 77-112.
16. Chr. Dzionk, M. Brüssler and H. Metzner, Nuclear Instr. & Methods in Phys. Res. **B63**, (1992), 231-235.

17. H. Migge, J. Mater. Res., **6**, (1991), 2381-2386.
18. H. Migge and J. Grzanna, J. Materials Res., **9**, (1994), 125-131.
19. R. Scheer and H. -J. Lewerenz, J. Vac. Sci. Technol. **A13**, (1995), 1924-1929.
20. J. Klaer, J. Bruns, R. Henninger, K. TΙΙpper, R. Klenk, K. Ellmer and D. Br⌂unig, 2nd WCEPVSEC, Vienna, (1998), 537-540.
21. R. Scheer, I. Luck, S. Hessler, H. Sehnert, and H. J. Lewerenz, 1st WCEPVSEC, Hawaii, (1994), 160- 163.
22. Y. Ogawa, S. Uenishi, K. Tohyama, and K. Ito, Solar Energy Mat. Solar Cells, **35**, (1994), 157.
23. M. Gossla, H. Metzner and H. -E. Mahnke, 2nd WCEPVSEC, Vienna, (1998), 593-596.
24. R. W. Miles, K. T. R. Reddy and I. Forbes, 2nd WCEPVSEC, Vienna, (1998), 496-499.
25. T. Watanabe, M. Matsui and K. Mori, Solar Energy Materials and Solar Cells, **35**, (1994), 239-245.
26. T. Watanabe and M. Matsui, Jpn. J. Appl. Phys., **35**, (1996), 1681-1684.
27. Y. Hashimoto, T. Ohashi, K. Shimoyama, K. Ichino and K. Ito, 2nd WCEPVSEC, Vienna, (1998), 589-592.
28. I. Hengel, R. Klenk, E. Garc☼a Villora and M. -Ch. Lux-Steiner, 2nd WCEPVSEC, Vienna, (1998), 545-548.
29. R. Birkmire and M. Engelmann, AIP Proc. NCPV Photovoltaics Program Review, (1998), 23-28.
30. T. Yukawa, K. Kuwabara and K. Koumoto, Thin Solid Films, **286**, (1996), 151-153.
31. M. Weber, R. Scheer and H. J. Lewerenz, 2nd WCEPVSEC, Vienna, (1998), 565-568.
32. R. Henninger, K. TΙΙpper, J. Bruns, J. Klaer and D. Br⌂unig, 2nd WCEPVSEC, Vienna, (1998), 561-564.
33. R. Scheer, M. Wilhelm, V. Nadenau, H. W. Schock and L. Stolt, 14th European PV Solar Energy Conf. (EPVSEC), Barcelona, (1997), 1299-1302.
34. D. Braunger, Th. D≈rr, D. Hariskos, Ch. KΙΙble, Th. Walter, N. Wieser and H. W. Schock, 25th PVSC, Washington, (1996), 1001-1004.
35. K. Weinert, G. Lippold, M. V. Yakushev, R. D. Tomlinson, R. Klenk and V. Nadenau, 2nd WCEPVSEC, Vienna, (1998), 3679-3682.
36. B. Basol and V. J. Kapur, 13th Space PV Res. Technol. (SPRAT) Conf., (1994), 101-106.
37. N. G. Dhere and J. V. Santiago, Proc. 12th Space Photovoltaic Research and Technology Conference (SPRAT XII), (1992), p. 298.
38. M. Contreras, B. Egaas, K. Ramanathan, J. Hiltner, F. Hasoon and R. Noufi, Progress in Photovoltaics, **7**, (1999), 311-316.
39. J. M. Woodcock, H. Schade, H. Maurus, B. Dimmler, J. Springer and A. Ricaud, 14th EPVSEC, Barcelona, (1997), 857-860.
40. T. M. Bruton, G. Luthardt, K-D Rasch, K. Roy, I. A. Dorrity, B. Garrard, L. Teale, J. Alonso, U. Ugalde, K. De Clerq, J. Nijs, J. Szlufcik, A. Rauber, W. Wettling and A. Vallera, 14th EPVSEC, Barcelona, (1997), 11-16.
41. Ugalde, J. Alonso, T. M. Bruton, J. M. Woodcock, K. Roy, and K. De Clerq, 14th EPVSEC, Barcelona, (1997), 897-900.
42. M. A. Contreras, H. Wiesner, R. Matson, J. Tuttle, K. Ramanathan, and R. Noufi, Mat. Res. Soc. Proc., **426**, (1996), 243-254.

INVESTIGATION OF THE CARBON ARC SOURCE AS AN AM0 SOLAR SIMULATOR FOR USE IN CHARACTERIZING MULTI-JUNCTION SOLAR CELLS[1]

Jianzeng Xu and James R. Woodyard
Wayne State University
Detroit, Michigan 48202

ABSTRACT

The operation of multi-junction solar cells used for production of space power is critically dependent on the spectral irradiance of the illuminating light source. Unlike single-junction cells where the spectral irradiance of the simulator and computational techniques may be used to optimized cell designs, optimization of multi-junction solar cell designs requires a solar simulator with a spectral irradiance that closely matches AM0. This is particularly true for multi-junction solar cells designed to be used in radiation environments as well as cells that experience photo-degradation under AM0. The carbon arc source is being investigated to determine its suitability as an AM0 solar simulator for the characterization of multi-junction solar cells. The spectral irradiance of readily available solid and cored carbon rods has been investigated. The spectral irradiance produced by the carbon rods used in these investigations is due to two mechanisms. One is spectral emission from atoms and molecules in the arc that originate from the gaseous atmosphere and the carbon rods. The other mechanism is thermal radiation from the high temperature carbon rods. The spectral irradiances for these two mechanisms are quantified and compared with the WRL AM0 spectrum.

INTRODUCTION

High efficiency two-terminal monolithic multi-junction solar cells are attractive for space applications because they can be designed to convert a larger fraction of AM0 irradiance into electrical power than single-junction cells. The design of multi-junction cells for space applications requires matching the optoelectronic properties of the junctions to the spectral irradiance of the AM0 spectrum. This is the case because the junctions are in series and optical injection and carrier collection in each junction must be critically balanced to optimize cell performance.

Multi-junction solar cells, unlike single junction cells, must be characterized under light-bias conditions with a light source having the spectral irradiance of the source to be used under power-generating conditions. Cells employed for space-power applications must therefore be characterized either using AM0 or a solar simulator that approximates AM0. Since true AM0 measurements can only be made in space, and access to space is limited and costly, there is a need to develop laboratory-based methods for characterizing multi-junction solar cells. The methods include measurements of current-voltage characteristics and quantum efficiencies, as well as determining the accuracy of the solar simulator spectral irradiance required for effective AM0 cell characterization. If laboratory-based AM0 measurements are going to be effectively employed in optimizing multi-junction solar cell designs and fabrication methodologies, the specifications of the spectral irradiance of solar simulators to be used in the characterization of virgin, photo-degraded and irradiated cells must be determined. The goal of this work is to evaluate the carbon arc source for use in the characterization of multi-junction solar cells and to determine the dependence of the accuracy of the spectral irradiance compared to AM0 for effective cell characterization.

---

[1] This work was supported under NASA Grant NAG3-2180.

DESCRIPTION OF CARBON ARC LIGHT SOURCE

Investigations in our laboratory of the carbon arc light source for use as an AM0 solar simulator were carried out with an Aschraft Super-High projection lamp house. The unit is typical of lamp houses used in movie film projectors prior to their replacement with high-pressure xenon arc discharge lamp in the late 1960's. The lamp house used in this work was made available by the Department of Public Works, Dearborn, Michigan. The National Electrical Carbon Company (NECC) in Fostoria, Ohio, was very helpful in providing a manual for the lamp house, showing us how to "burn" carbon rods, and transferring company reports on the development of carbon arc technology. The carbon rods used in these investigations were purchased from NECC.

A diagram of the lamp house is shown in Figure 1. The arc is maintained between two carbon rods; one is maintained at a positive polarity and the other is negative. The horizontal positive rod is rotated and fed into the arc at a rate of about 300 to 600 mm per hour. The negative carbon rod is not rotated; it is fed into the arc at an angle that is about 25 to 30 degrees below the horizontal axis of the positive rod. The feed rate of the negative rod is about one-third that of the positive rod. The rotation of the positive rod and the feed rate of both rods is accomplished with a drive assembly that includes a variable-speed DC motor, gear box and drive chains. The rod holders are designed for positive rods 10 to 11 mm in diameter and negative rods 9 mm in diameter. The positive and negative rods used in this work were about 510 and 230 mm in length, respectively, and the negative rods were copper cladded.

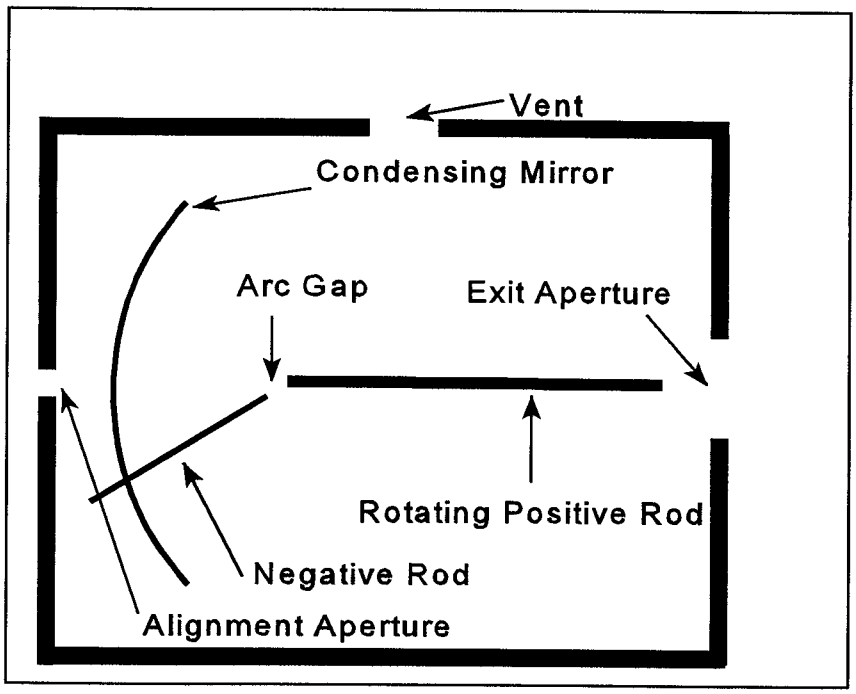

Figure 1. Diagram illustrating the optics of the carbon arc lamp house

Light is produced by sustaining an arc between the positive and negative carbon rods that is powered by a DC power supply. A model 330A/BP Miller welding power supply was used for the initial experiments. However, it was difficult to control the carbon arc current and voltage; the unit was subsequently replaced with a Miller Syncrowave 500 constant current power supply. The feed rate of the rods was controlled to maintain an arc gap of about 10 mm during the experiments. Electrical contact to the rotating positive rod is effectuated with water-cooled silver contact shoes located about 25 mm from the arc gap. Arc currents and voltages were typically 90 to 130 A at 40 to 90 VDC, respectively. The burn time for a positive rod was about one hour. The lamp house also had external mechanical controls for displacing the rod holders to strike the arc and to correct for variations in the feed rate of the rods in order to maintain a good burn. A good burn is one that produces the maximum constant light intensity with minimum arc instabilities. The lamp house was vented to an air handling system that discharged the arc gases to a stack on the roof of the research laboratory.

Figure 1 shows the lamp house with a condensing mirror that focuses the light from the carbon arc on the exit aperture of the lamp house. The mirror was removed from the lamp house to permit the light to pass through the alignment aperture for the spectral irradiance measurements. The modification was made to insure the spectral irradiance of the light produced by the carbon arc was not influenced by the optical properties of the condensing mirror. The spectral irradiance was measured with a computer-interfaced spectral radiometer [1]. The spectral radiometer employs an integrating sphere, order-sorting filters, 275 mm focal length f/3.8 monochromator and silicon photodetector. The spectral response of the photodetector limits the spectral irradiance measurements to the 350 to 1100 nm wavelength range. The wavelength scale of the monochromator was calibrated with a Hg(Ar) pencil light source. The intensity calibration was carried out with a FEL lamp traceable to NIST standards. The entrance port of the spectral radiometer was positioned on the axis of the positive rod and located opposite the alignment aperture

at a distance of 43.2 cm from the center of the carbon arc.

RESULTS

The spectral irradiance of NECC L-0106 and NECC TC-190 positive rods was investigated. The L-0106 positive rod has an outer carbon shell filled with a proprietary compound; the rod is referred to as a cored rod. The TC-190 positive rod is a high purity solid carbon rod and referred to as a pure carbon rod in this work. NECC L-1115 negative rods were used with the positive rods. The negative rods were solid carbon with a copper cladding.

The spectral radiometer was configured with 2 mm slits and measurements made in 10 nm steps; the resolution of the spectral radiometer was about 6 nm for the first set of experiments. The spectral irradiance of a cored carbon rod is shown in Figure 2. The current, voltage and power were unstable during the experiment and were about 100 A, 90 V and 9.0 kW, respectively. For comparison purposes, the spectral irradiance of the World Radiation Laboratory AM0 spectrum and the calculated spectral irradiance of a 6000 K blackbody are shown. The spectral irradiance of the 6000 K blackbody and cored carbon rod were normalized to the AM0 spectrum. The major deviation from the AM0 spectrum occurs in 300 to 440 nm region. The spectral irradiance of the carbon arc is greater than AM0 from 360 to 440 nm and less than AM0 in the 300 to 350 nm range. The existence of a peak at 390 nm, as well as the structure of the peak, suggest that spectral emission contributes to the spectrum. The measurements shown in Figure 2 were complicated by the instability of the arc due to the difficulty in controlling the arc current and voltage with the model 330A/BP Miller power supply. A more stable power supply, namely, a Miller Syncrowave 500 constant current power supply, was installed in the system.

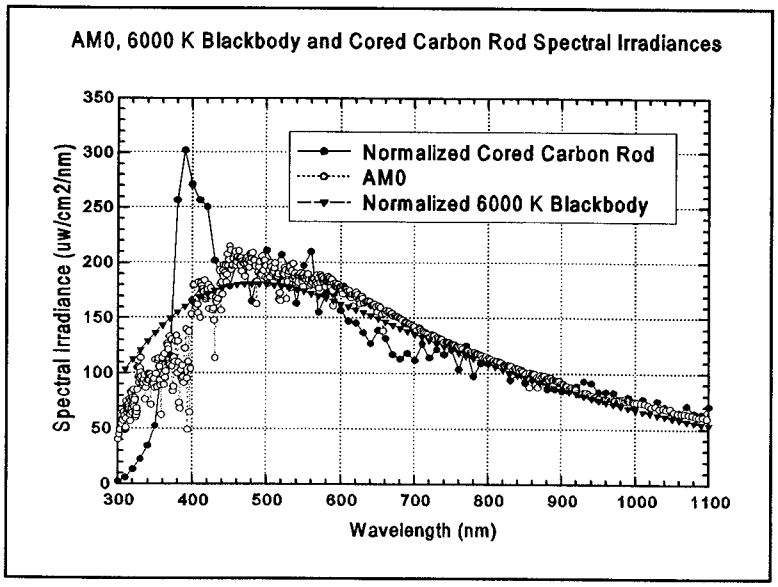

Figure 2. AM0 spectrum and the spectral irradiances of a 6000 K blackbody and cored carbon rod measured with 6.0 nm resolution

Investigations of the cored carbon rods were then carried out with 0.15 mm slits in the spectral radiometer and a resolution of about 0.5 nm. The wavelength was stepped in intervals of 0.25 nm. The measured spectral current is shown in Figure 3. The arc current, voltage and power were 105.6 ±1.2 A, 52 ± 4 V and 5.5 kW, respectively. The spectral current has a great deal of structure suggesting the spectrum contains a large number of emission lines.

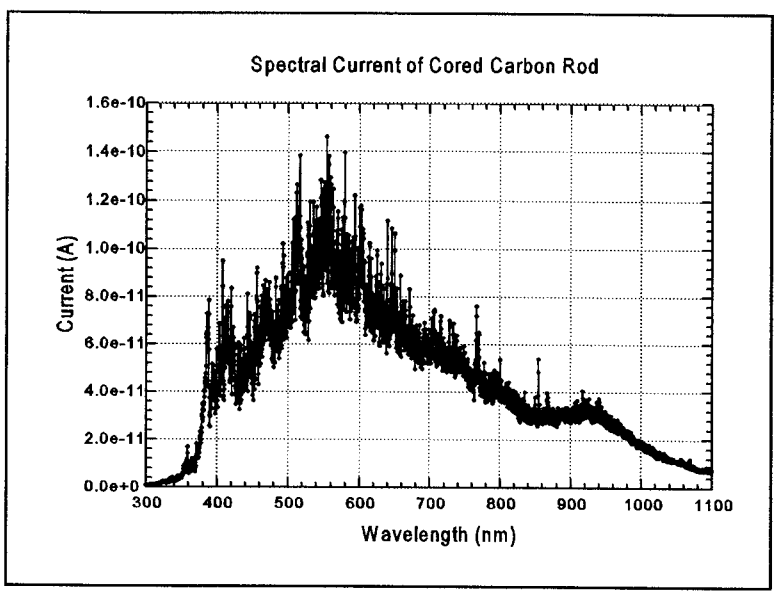

Figure 3. Spectral current of cored carbon rod measured with 0.5 nm resolution

The literature was reviewed to determine if the elements producing the spectral lines could be identified [2,3]. Several elements have emission lines in the wavelength range investigated. The cited references do not specify the measurement conditions under which the spectral lines were measured. Relative values are reported for the intensity of lines resulting from the numerous transitions

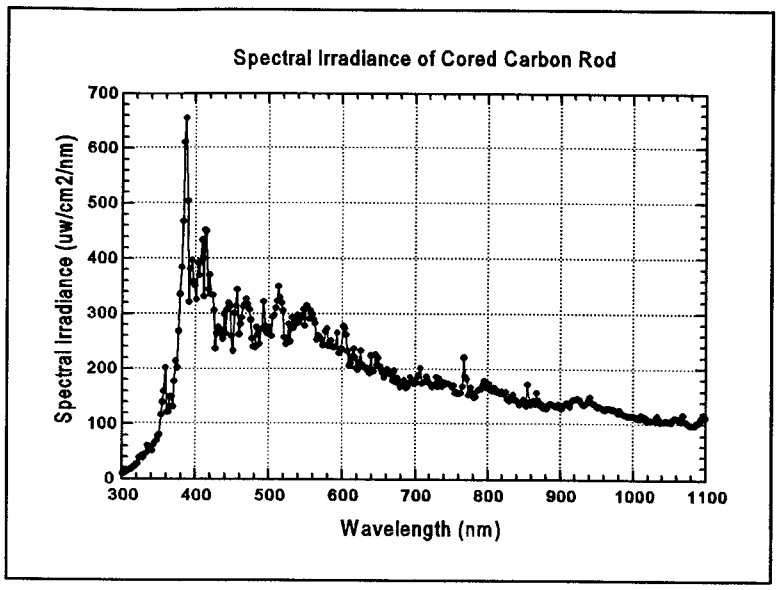

Figure 4. Spectral irradiance of cored carbon rod averaged over 2.0 nm intervals

that are possible in the various elements. At this time we are unable to identify most of the spectral lines in Figure 3.

The spectral irradiance was calculated from the spectral current using the calibration data for the spectral radiometer. The spectral radiometer was calibrated with a resolution of 2.0 nm, the resolution of the data supplied with the calibrated FEL lamp. However, the data in Figure 3 are the spectral current measured in 0.25 nm wavelength intervals. Instead of extrapolating the lamp calibration data to obtain the spectral irradiance in 0.25 nm wavelength intervals, the spectral irradiance was calculated in 2.0 nm intervals by averaging the spectral current over 2.0 nm intervals. The results are shown in Figure 4. The peaks in the 360 to 420 nm range of the spectral irradiance dominate at shorter wavelengths. The literature [4] suggests that these peaks are due to three vibrational bands of the cyanogen molecule, CN. According to the literature, the emission spectrum of these bands can be eliminated by burning the arc in a nitrogen-free atmosphere.

Figure 4 is instructive because the fine structure illustrated in Figure 3 is smoothed by the averaging calculations; only the structure at about 380 nm remains. It points to the role of the optoelectronic properties of a solar cell in determining the specifications of the spectral irradiance for an AM0 simulator. The rate of change of the optical absorption coefficient with respect to wavelength of the solar cell determines the importance of the fine structure in the simulator spectral irradiance. Should the rate of change of the optical absorption coefficient be small over the spectral range where emission lines dominate, then the fit of the averaged spectral power to AM0 over the wavelength range is the determining factor. The spectral-irradiance specifications of an AM0 solar simulator are therefore critically dependent on the wavelength dependence of the optical absorption coefficient of the materials used in the fabrication of multi-junction solar cells.

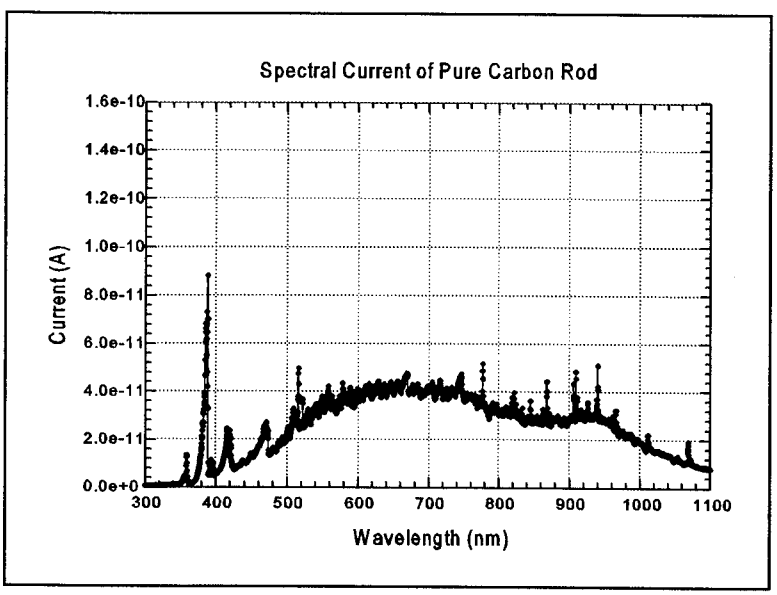

Figure 5. Spectral current of a pure carbon rod measured with a resolution of 0.5 nm

Pure carbon positive rods with 11 mm diameters were investigated to determine the role of the spectral emission of compounds in the cored carbon rods. It was reasoned that black body radiation of the carbon rods, and the emission spectrum of carbon atoms, would dominate the spectral irradiance if only carbon were in the arc. Figure 5 shows the spectral current measured with 0.15 mm slits, 0.25 nm steps and a resolution of about 0.5 nm. The arc current, voltage and power were 104.0 ± 0.4 A, 49 ± 1 V and 5.1 kW, respectively. Note that there is very little structure in the 400 to 800 nm range. A comparison of Figure 5 with Figure 3 suggests that the structure in the 400 to 800 nm range of Figure 3 is due to spectral emission from the compounds in the cored carbon rods.

The spectral current of the pure carbon rod in Figure 5 and the spectral radiometer calibration data were used to calculate the average spectral irradiance over 2.0 nm intervals. The results are shown in Figure 6.

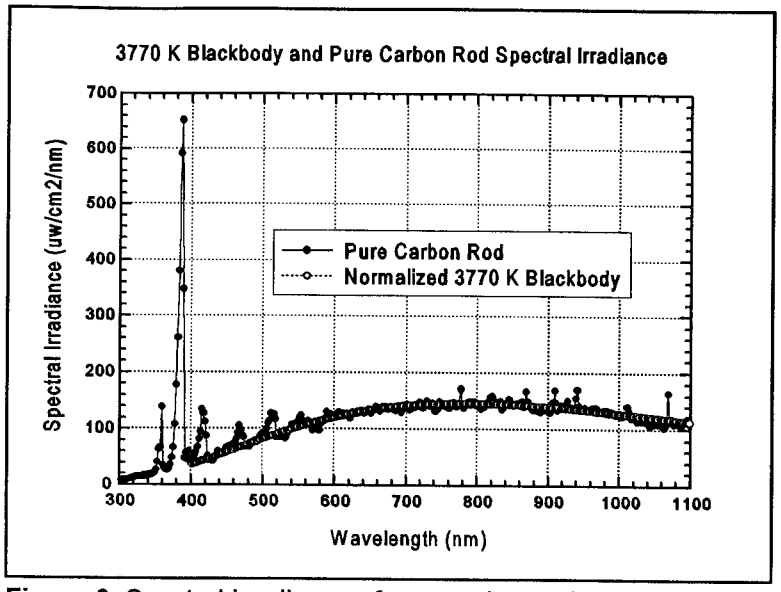

Figure 6. Spectral irradiance of pure carbon rod averaged over 2.0 nm intervals and spectral irradiance of normalized 3770 K blackbody

Comparison of Figure 6 with Figure 4 illustrates the relative power irradiated by an arc with cored carbon rods as compared to pure carbon rods.

A least-squared fit of the spectral irradiance of the pure carbon rod shown in Figure 6 to the spectral irradiance of blackbody at a given temperature was investigated. The spectral lines in shown in the figure were subtracted from the spectral irradiance of the pure carbon rod. The best fit to the data was obtained for a blackbody temperature of 3770 ± 10 K. The temperature compares favorable with the 3752 to 3825 K range of sublimation temperatures for carbon with various types of structures. This suggests that thermal radiation is the main mechanism for radiating power from an arc produced by burning pure carbon rods. The suggestion is is also confirmed by the fact that there is relatively little structure in the spectral current in Figure 5 as compared to Figure 3. The agreement of the spectral irradiance in the 900 to 1100 nm range of Figures 4 and 6 suggests that the cored carbon rods are at approximately the same temperature as the temperature of the pure carbons.

A comparison of the burn rate, input power and radiated power for the pure and cored carbon rods is presented in Table I. The radiated power was determined by numerical integration of the spectral irradiance in the 300 to 1100 nm wavelength range. The table shows that the burn rate of the cored rod is 2.1 times higher than the pure carbon rod; the arc input power is the same to within about 7% for the two types of rod. The radiated power is 93 mW/cm^2 for the pure carbon rod as compared to 150 mW/cm^2 for the cored carbon rod. The radiated power is 1.6 times higher for the cored carbon rods. The difference in the irradiated power for the two rod types, namely, 57 mW/cm^2, appears to be due to power radiated by atomic emission of the elements in the cored carbon rods. While the burn rate for the cored carbon rods is 2.1 times that of the pure carbon rods, it does not appear to be a determining factor in power radiated as long as the input power to the arc is approximately the same for the two types of carbon rods. The AM0 integrated power in the 300 to 1100 nm wavelength range is 99.8 mW/cm^2. Table I shows that 150 mW/cm^2. Is radiated by the cored carbon rods on a surface located at a distance of 43.2 cm from the arc. Therefore the intensity of the light radiated from the carbon arc in this spectral range is more that sufficient for AM0 simulation.

Table I

Rod	Dia. (mm)	Burn Rate (mm/hr)	Input Power (kW)	Radiated Power mW/cm^2
Cored	10	530	5.5	150
Pure	11	250	5.1	93

CONCLUSIONS

The investigations enabled us to quantify the mechanisms for radiation produced by a carbon arc. The best fit to the data was obtained for a blackbody temperature of 3770 ± 10 K. This compares favorable with the 3752 to 3825 K range of sublimation temperatures for carbon with various types of structures. The spectral irradiance produced by the carbon rods used in these investigations is due to two mechanisms. One is spectral emission from atoms and molecules in the arc that originate from the gaseous atmosphere and the carbon rods. The other mechanism is thermal radiation from the high temperature carbon rods. The spectral irradiances for these two mechanisms were quantified; the spectral irradiance from the carbon arc compares favorable with the WRL AM0 spectrum. Future work will include extending the wavelength measurement capability to 1800 nm and modifying the lamp house to permit investigations in inert gases in an effort to reduce the spectral irradiance in the 360 to 440 nm wavelength range.

REFERENCES

1. Laboratory Instrumentation and Techniques for Characterizing Multi-Junction Solar Cells, James R. Woodyard, Proceedings of the XIV Space Photovoltaic Research and Technology Conference 1995, NASA Conference Publication 10180, page 158.
2. Tables of Spectral Lines of Neutral and Ionized Atoms, A. R. Striganov and N. S. Sventitskii, IFI/Plenum Data Corporation, New York, 1968.
3. Tables of Spectral Lines, A. N. Zaidel, V. K. Prokofev, S. M. Raiskii, V. A. Slavnyi and E. Ya. Shreider, IFI/Plenum Data Corporation, New York, 1970.
4. L. H. Ahrens and S. R. Taylor. Spectrochemical Analysis. Reading, MA: Addison-Wesley Publishing Company, 1961, pages 66 and 172.

ELECTRICAL CHARACTERIZATION OF DEFECTS IN SiC SCHOTTKY BARRIERS

C. M. Schnabel and M. Tabib-Azar
Case Western Reserve University
Cleveland, Ohio 44106

R. P. Raffaelle
Rochester Institute of Technology
Rochester, New York 14623

H.B. Su and M. Dudley
SUNY at Stony Brook, Stony Brook, NY 11794

P. G. Neudeck and S. Bailey
NASA Glenn Research Center at Lewis Field
Cleveland, Ohio 44135

Abstract

We have been investigating the effects of screw dislocation and other structural defects on the electrical properties of SiC. SiC is a wide-bandgap semiconductor that is currently receiving much attention due to its favorable high temperature behavior and high electric field breakdown strength. Unfortunately, the current state-of–the-art crystal growth and device processing methods produce material with high defect densities, resulting in a limited commercial viability. In order to characterize these defects, we have been correlating the electrical behavior of Au on 6H-SiC Schottky barriers with other physical measurements. We have been able to related minority carrier recombination centers, identified by electron beam induced current (EBIC) measurements, to screw dislocations observed by synchrotron white-beam x-ray topography. These screw dislocations have also been correlated with growth pits on the SiC surface observed via the Nomarski imaging method and atomic force microscopy. We have characterized the electrical behavior of the Au on Sic Schottky barriers using current versus voltage and capacitance versus voltage measurements. The effects of the observed electronic defects on the electrical behavior of these devices will be discussed.

1. Introduction

The 6H-SiC polytype is a promising wide bandgap (E_g = 3.0 eV) semiconductor which is being developed for use in high-temperature, high-power, high-frequency, and high-radiation conditions.[1] The advantages of this material lie in its extremely large breakdown field strength, high thermal conductivity, good electron saturation drift velocity, and stable electrical performance at temperatures as high as 600 °C.[2] These properties have made SiC an ideal candidate for high-temperature electronics and high-power microwave devices. In addition, it has also generated interest in the space power community as a possible photovoltaic solar cell material for devices capable of operating within three solar radii of the sun.[3]

The processing techniques required to produce high-quality SiC wafers has undergone tremendous improvement since this material was first investigated for semiconductor applications. However, even the best SiC produced today still has a large density of crystallographic defects.[4] The most prominent of these defects being screw-dislocations and their hollow-core counterparts, micropipes.[5] These defects have been correlated with increased reverse leakage currents and soft reverse bias breakdown in SiC Schottky diodes.[6]

In order to better characterize these defects and understand their role in the electronic performance of SiC-based devices, Schottky barriers on 6H-SiC epilayers have been analyzed by a variety of electrical and structural characterization techniques. An effort has been made to correlate the structural defects, specifically screw dislocations, with electronic recombination centers.

The structural defects have been investigated using synchrotron white-beam X-ray topography. This technique produces a gray-scale image that identifies regions of stress within the crystalline lattice. Surface imperfections have also been examined using Nomarski microscopy and atomic force microscopy. Nomarski microscopy uses the interference of converging beams of light to be able to identified surface features and atomic step heights as small a 30 angstroms.[7] Atomic force microscopy is an ultra-low force profilometer capable of measuring height differences on the atomic scale.

The electronic recombination centers have been identified using electron-beam induced current (EBIC) measurements. EBIC is performed in an scanning electron microscope (SEM). In this technique, as the electron beam in the SEM is rastered across the Schottky barrier surface, the current induced in the device by the creation of electron-hole pairs at or near the boundary depletion width is measured.[8] The induced current is then plotted in gray-scale as a function of beam position. Areas in which there is significant carrier recombination and low induced current appear darker in the resulting image.

2. Experimental Details

The 6H-SiC samples were made at the NASA Glenn Research Center by growing a 3.5 μm thick homoepilayer on 3.5° off-axis n-type SiC wafers obtained from Cree Research. The samples were nitrogen doped to approximately 10^{16} cm^{-3} during epilayer growth. Immediately following a surface clean-up using a buffered HF etch and rinse, 40 nm thick gold contacts were electron beam evaporated and patterned into 0.9 mm square pads using lift-off photolithography.

The structural defects in the 6H-SiC were analyzed using synchrotron white-beam X-ray topography (SWBXT) at NSLS at Brookhaven National Lab. Surface defects were imaged using Nomarski microscopy and a Digital Instruments Nanoscope III atomic force microscope (AFM). The electrical behavior of the Schottky diodes was analyzed using current versus voltage and capacitance versus voltage measurements using a computer controlled Keithley 236 Source/Measure Unit and a Keithley 590 CV Analyzer. Electronic defects in the diodes were imaged using electron-beam induced current (EBIC) measurements performed in a Hitachi S-800 Field-Emission Scanning Electron Microscope (SEM).

3. Results and Discussion

The contrast in the SWBXT image shown in Figure 1a represents areas of stress in the crystalline lattice. The image shown was digitally re-scaled to remove the asymmetric distortion associated with the SWBXT technique. The white spots appearing in the image are indicative of screw dislocations. EBIC was performed on the same area that is shown in Figure 1a, after it was coated with gold (see Figure 1b). Many dark areas corresponding to recombination centers or electronic defects at or near the metal semiconductor junction can be seen. A mask of the screw dislocations identified in the SWBXT image in Figure 1a was overlaid on the EBIC image shown in Figure 1b (see Figure 2). It is evident from this result that the screw dislocations act as electronic recombination centers.

A Nomarski microscope was used to look at the surface imperfections on the same sample discussed above. The area was divided into 12 smaller sections from which to obtain the high resolution Nomarski images. These images were then combined to produce the image of the entire area as shown in Figure 3a. Overlaying the same screw dislocation mask used in Figure 2 (generated using the SWBXT image) on the Nomarski image shows that screw dislocations also result in growth pits (see Figure 2b). Surface particulates were found at the locations in which screw dislocations were present and no growth pits were recorded. It is believed that the particulates may have obscured the growth pits in those areas. The growth pits that correspond to screw dislocations have a characteristic shape, as seen in the Nomarski images. Atomic force microscopy was used to investigate the topography of the screw dislocation growth pits (see Figure 4).

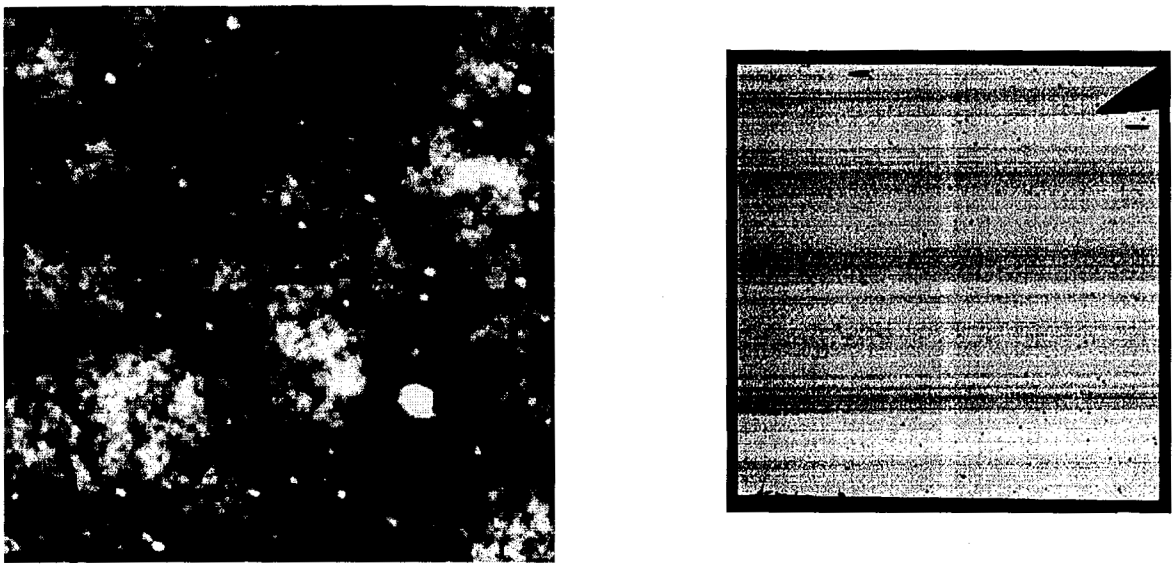

(a) (b)

Figure 1. a) SWBXT image showing stress in the crystal lattice. The light colored dots are indicative of screw dislocations, where the stress is high. b) EBIC image representing collected current as a function of postion. Dark spots indicate recombination centers in the epilayer.

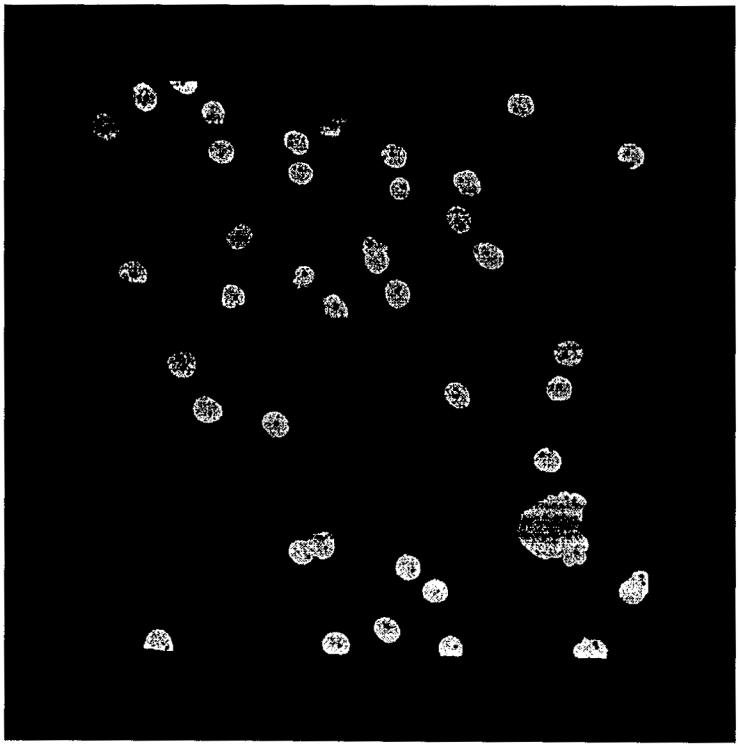

Figure 2. A Screw dislocation mask, from a SWBXT image, overlaid on an EBIC scan of a Au Schottky barrier placed on the same area. Dark spots in the EBIC scan correspond to electronic recombination centers and are found at each of the screw dislocations identified.

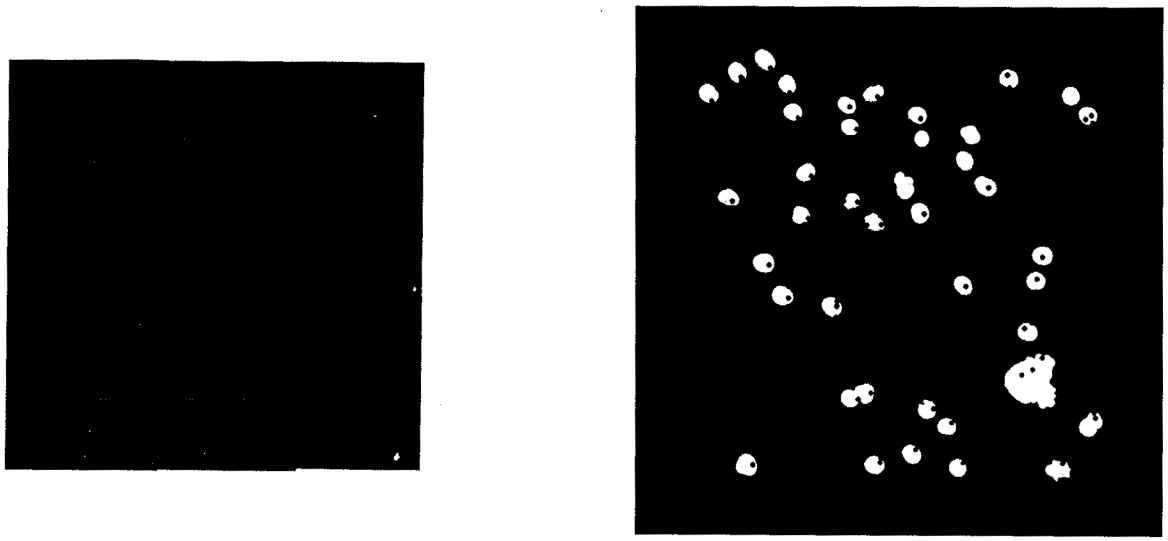

(A) (B)

Figure 3. a) Nomarski image of a die with locations of growth pits marked. b) A mask of screw dislocations from Figure 1a is overlaid onto the Nomarski image in a) revealing that screw dislocations are correlated with growth pits.

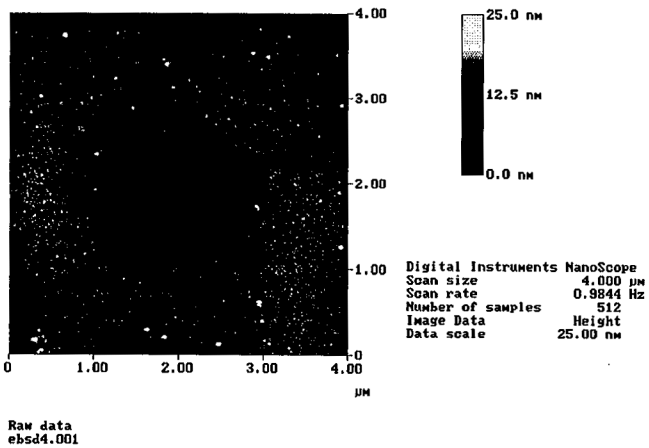

Figure 4. **An** AFM image of a growth pit that was identified as a screw dislocation in Figure 3b.

The current versus voltage scans of the Schottky barriers produced in this study showed good Shockley diode behavior (see Figure 5a). However, several of the diodes showed non-linear behavior in the Log current versus voltage forward bias scan (see Figure 5b). This behavior has previously been reported in SiC Schottky diodes by Defives et. al. and has been attributed to a dual barrier height model.[9] It is believed that junction defects give barrier height inhomogeneities which cause the causing the device characteristics to resemble two barriers in parallel. This behavior did not correlate to the position of the die on the sample surface. This behavior also did not correlate with the number or type of electrical or structural defects identified in this study. The barrier heights obtained from the current versus voltage behavior of the various dies were between 0.85 and 1.08 eV. The ideality factors for all the diodes measured were between 1.1 and 1.5. The reverse-bias analysis of these Schottky diodes showed a wide variety of breakdown types and voltages. The types range from very soft to

extremely hard and the voltages ranged from approximately 40 V to nearly 140 V. However, only a slight correlation between screw dislocation and premature breakdown was apparent.

Capacitance versus voltage measurements were performed on all the Schottky barriers to determine dopant densities as a function of position on the sample surface. The results were analyzed using a simple parallel-plate capacitor model.[10] These results were also used to investigate possible vertical dopant gradients within the epilayer. All of the dies showed excellent linearity in their inverse capacitance squared versus voltage behavior, indicating a homogenous vertical doping in the epilayer (see Figure 6). The carrier densities for 5 different dies spread out uniformly over the sample surface were all with a range of 1.12×10^{16} to 1.21×10^{16} cm^{-3}. These values are in good agreement with the anticipated doping density. The dies from which these values were obtained were randomly distributed across the sample surface and therefore did not indicate any transverse doping gradients across the sample. The barrier heights were found to be between 1.18 and 1.29 eV.

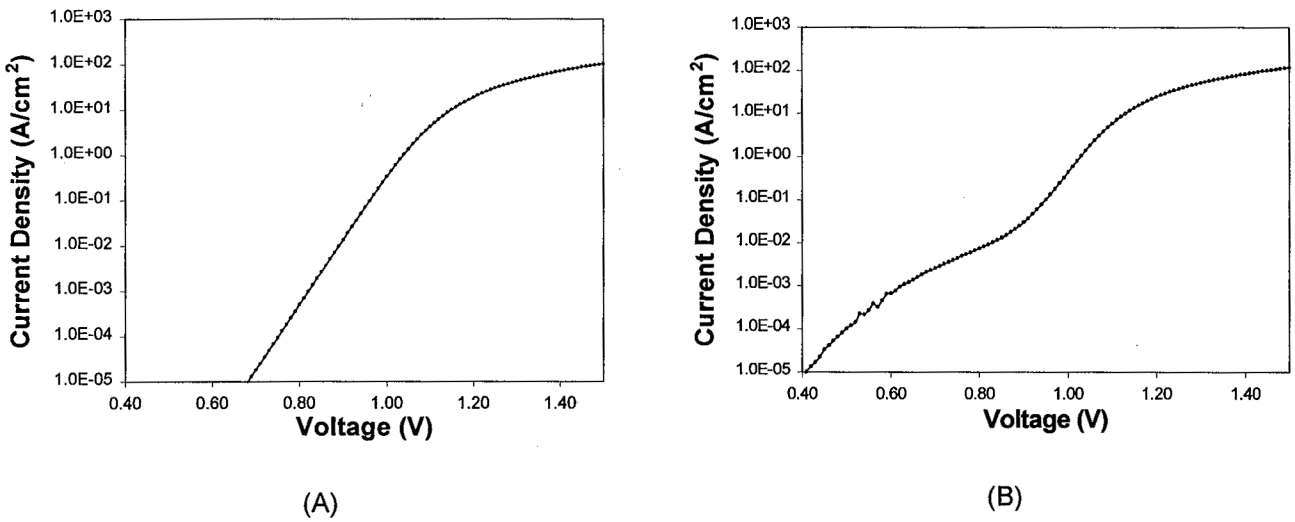

Figure 5. Current versus voltage characteristics of similar dies within the same area show both a) linear and b) non-linear characteristics.

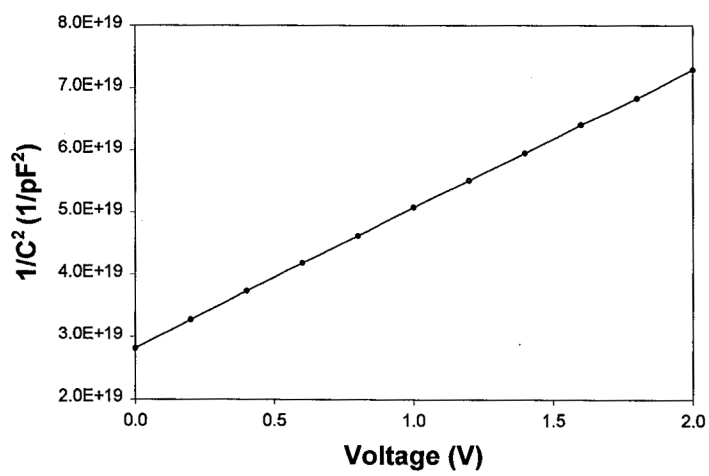

Figure 6. Capacitance versus voltage data reveals that the doping of the sample is 1.15×10^{16} cm^{-3}.

4. Conclusions

A positive correlation has been shown between screw dislocations, identified by sychrotron white-beam x-ray topography, and electronic recombination centers, identified by electron-beam induced current measurements of gold on 6H-SiC Schottky barriers. Nomarski microscopy was used to show that the aforementioned screw dislocations also result in growth pits on the semiconductor surface. The growth pits associated with screw dislocations have a characteristic shape that can be imaged with atomic force microscopy. Although the Schottky barriers analyzed by EBIC were shown to have numerous electronic defects, current versus voltage characterization showed that they still exhibited reasonable diode characteristics. Capacitance versus voltage measurements were used to determine a carrier density in the SiC on the order of 10^{16} cm^{-3}. Some of the diodes measured here did exhibit non-linear logarithmic current versus voltage behavior, as previously identified in 6H-SiC Schottky diodes. However, no correlation was seen between this behavior and the density of screw dislocations.

References

[1] P.G. Neudeck, *J. Electron. Mater.* **24**, 283 (1995).
[2] M. Bhatnagar and B.J. Baliga, *IEEE Trans. on Electron Devices* **40**, 645 (1993).
[3] D.A. Scheiman, G.A. Landis, and V.G. Weizer, *Space Technology and Applications International Forum*, AIP Proc. **453** (1999).
[4] P.G. Neudeck, W. Huang, and M. Dudley, in *Power Semiconductor Materials and Devices*, edited by S.J. Pearton, R.J. Shul, E. Wolfgang, F. Ren, and S. Tenconi (Materials Research Society, Warrendale, PA 1998), Vol. 483, pp. 285-384.
[5] P.G. Neudeck and J.A. Powell, *IEEE Electron Device Lett.* **15**, 63 (1994)
[6] P.G. Neudeck, W. Huang, and M. Dudley, *IEEE Trans. Electron Devices* **46**, 478 (1999).
[7] G. Nomarski, French Patents Nos. 1059124 and 1056361.
[8] D.K. Schroder, Semiconductor Material and Device Characterization (John Wiley & Sons, New York, NY 1990), pp.391-394.
[9] D. Defives, O. Noblanc, C. Dua, C. Brylinski, M. Barthula, V. Aubry-Fortuna, and F. Meyer, *IEEE Trans.on Electron Dev.* **46**, 449 (1999)
[10] S.M. Sze, *Physics of Semiconductor devices* (John Wiley & sons, New York, NY 1981), 2nd edition, pp.248-249.

INVESTIGATIONS TO CHARACTERIZE MULTI-JUNCTION SOLAR CELLS IN THE STRATOSPHERE USING LOW-COST BALLOON AND COMMUNICATION TECHNOLOGIES[1]

Glenroy A. Bowe, Qianghua Wang and James R. Woodyard, Wayne State University, Detroit, Michigan 48202
Richard R. Johnston, Lawrence Technological University, Southfield, Michigan 48075
William J. Brown, High Altitude Research Corporation, Huntsville, Alabama 35758

ABSTRACT

The use of current balloon, control and communication technologies to test multi-junction solar cells in the stratosphere to achieve near AM0 conditions has been investigated. The design criteria for the technologies are that they be reliable, low cost and readily available. Progress is reported on a program to design, launch, fly and retrieve payloads dedicated to testing multi-junction solar cells. The system investigated includes a state-of-the-art multi-junction solar cell and two-axis suntracker that weighs less than one pound. Data acquisition is carried out with programmable microcontrollers, A/D converters, digital I/O lines, AX.25 encoding and GPS, and VHF, UHF and HF transmitters. One flight has been carried with a 1000 gram extensible helium balloon and a payload that weighed under six pounds. During a flight that lasted about two hours, the balloon traveled to an altitude of 87,000 feet and data were downlinked. Th payload was retrieved about 40 miles from the launch site.

INTRODUCTION

Multi-junction solar cells are attractive for space-power generation. Triple-junction $GaInP_2$/GaAs/Ge cells with areas of 2x2 cm^2 have been fabricated by two companies with lot average efficiencies of 24.2 and 23.8% [1]. Programs are underway to reduce fabrication costs and increase cell area and efficiency. Cells with four junctions are currently under development. It is anticipated that progress in the next ten years will include cell designs with at least five junctions and efficiencies approaching 40%. In order to achieve these goals, it is necessary to have access to AM0 cell standards and testing under AM0 conditions. NASA is developing a solar cell test bed for the Space Station that includes a single axis tracer which will be used to test solar cells and calibrate cells. The first mission is projected for 2004.

The objective of this program is to investigate current balloon, control and communication technologies in an effort to develop a system that is reliable and low-cost, and readily accessible to the photovoltaic community for testing solar cells in the stratosphere where near AM0 conditions exist. After exploring several approaches, it was decided to pursue the technology developed by amateur radio groups. One of the amateur groups that flies balloons on a regular basis is the Edge of Space Sciences (EOSS) located in the Denver, Colorado area. The group maintains a Web site, http://www.eoss.org/, that lists seven other balloon groups; the site has an EOSS Handbook that is a beginner's guide to ballooning. One of the authors of this paper, William J. Brown, has flown several balloon flights, both as an amateur and professional; he handled the ballooning aspects of this project while the other authors focused on the design, construction and testing of the suntracker system.

SUNTRACKER DESCRIPTION

The suntracker is designed to point a solar cell at the sun as a balloon ascends and downlink data containing the cell short-circuit current, cell temperature and electronics module temperature. The suntacker is shown in Figure 1; it includes a two-axis tracker and electronics module that together weigh less than thirteen ounces. The two-axis tracker has a collimator and two motors that are supported 5.06" above the electronics module by a 0.25" aluminum rod. The collimator is made of 0.062" aluminum plate and assembled with 00-90 brass screws in order to minimize

---

1 This work was supported under NASA Grant NAG 3-2180.

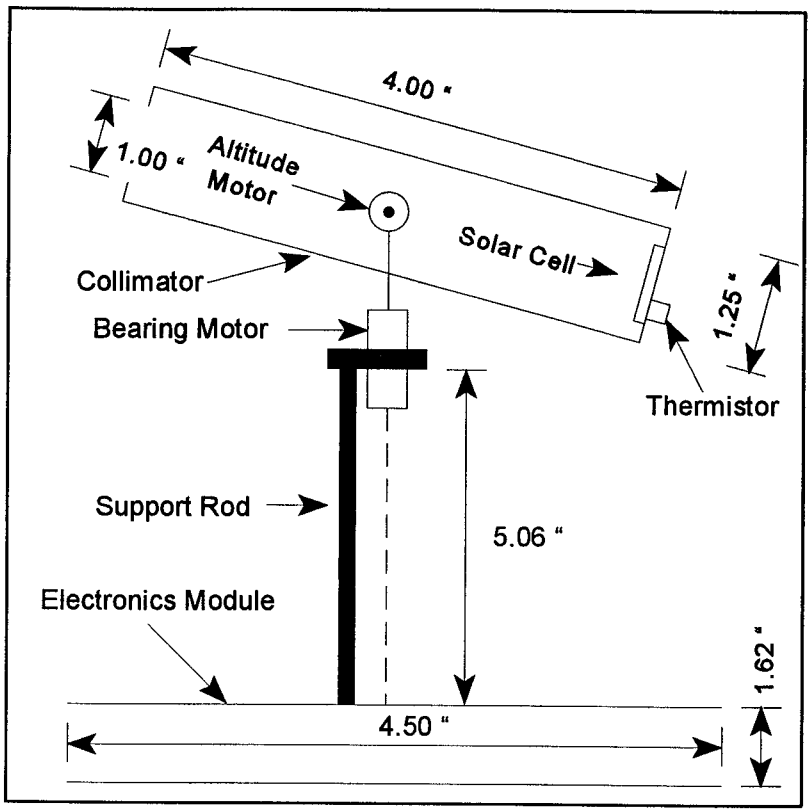

Figure 1. Diagram of suntracker

the weight. The dimensions of the collimator are 1.25"x1.25"x4.00"; the front aperture is 1.00"X1.00" and the cell area 0.79"x0.79". The design provides a plus or minus 3.0 ° collimation of the full intensity of the sun on the solar cell. Since the intensity of the sun varies as the cosine of the incident angle, the dimensions of the collimator insure the intensity of the sun varies less than 0.15% if the sun is tracked to plus or minus 3.0°. The full-width at half maximum is plus or minus 15° for the collimator. The dimensions of the collimator were selected to prevent light scattered from the balloon, earth, moon or clouds arriving at the solar cell. The solar cell was soldered on a copper plate that was affixed to the bottom of the collimator. A thermister was attached to the copper plate to measure the temperature of the solar cell. The collimator was painted with a flat black paint on the inside surfaces to minimize reflections of light. The exterior surfaces of the collimator, motors and support rod were also painted flat black to increase absorption of sun light for heating the suntracker and minimizing the effects of the low temperature environment at high altitudes.

The suntracker has two MicroMo series 1016 DC motors that point the collimator at the sun. Each motor assembly has a gearhead and magnetic encoder and weighs less than one ounce. The gearheads have a 256:1 reduction ratio enabling the motors and gearheads to deliver 13 oz-in torque. One motor controls the altitude angle of the collimator that ranges between 0° and 90°; the other motor controls the bearing angle between 0° and 360°. Each magnetic encoder produces two channels of square wave pulses in quadrature that are TTL/CMOS compatible; ten pulses are produced per revolution of the motor. The pulses are input to the electronic module to keep track of the position of the collimator.

The length and diameter of a motor assembly are 2.00" and 0.39", respectively. The altitude motor is supported by an aluminum bracket mounted on the shaft of the bearing motor. The shaft of the altitude motor is affixed to an aluminum collet that is attached to the collimator with four 1-72 screws. The collet is 0.25" thick and 0.50" in diameter, and the four 1-72 screws are equally spaced on a 0.31" circle . The bearing motor is held with a 0.25" aluminum bracket that is mounted on the aluminum rod and bolted to the top of the electronics module. All the aluminum parts were fabricated from 6061 aluminum stock. The specification for the temperature operating range of the motor assembly is -30 to 85 °C. Since temperatures as low as -60 °C can be expected at 40,000 feet, the grease in the gearheads was removed and replaced with light oil.

A challenging problem that had to be solved was transferring the electrical signals of the motors, encoders, solar cell and thermistor across the rotating interfaces of the two motors. Electrical slip rings are generally used for this purpose. However, available slip rings were too large and heavy for this application. The design that we adopted employed virtual stops and flexible wire. Virtual stops were effectuated using the pulses from the encoder, software and a microcontroller; the stops limited the altitude and bearing angles to 0° and 90° and 0° and 360° ranges, respectively. The wire that was used is a high-performance modified fluoropolymer-insulated wire with -65 to 200 °C specifications; it is a radiation-crosslinked, 28 AWG, 7 strands x 36 AWG, tin-coated copper wire manufactured by Raychem Corporation. The wire remained flexible during tests in a dry-ice acetone solution at -78 °C.

A diagram illustrating the suntracker telemetry and control system is shown in Figure 2. The signal from the solar cell is input to an operational amplifier. One of the outputs from the operational amplifiers is input to a MIM module that was purchased from Clement Engineering; it is a 1200-baud, AX.25, transmit terminal node controller (TNC) that can telemeter five analog and eight digital signals at user selectable intervals. The MIM module is slightly larger than a credit card and programmable via a serial port connected to a personal computer (PC). It draws less

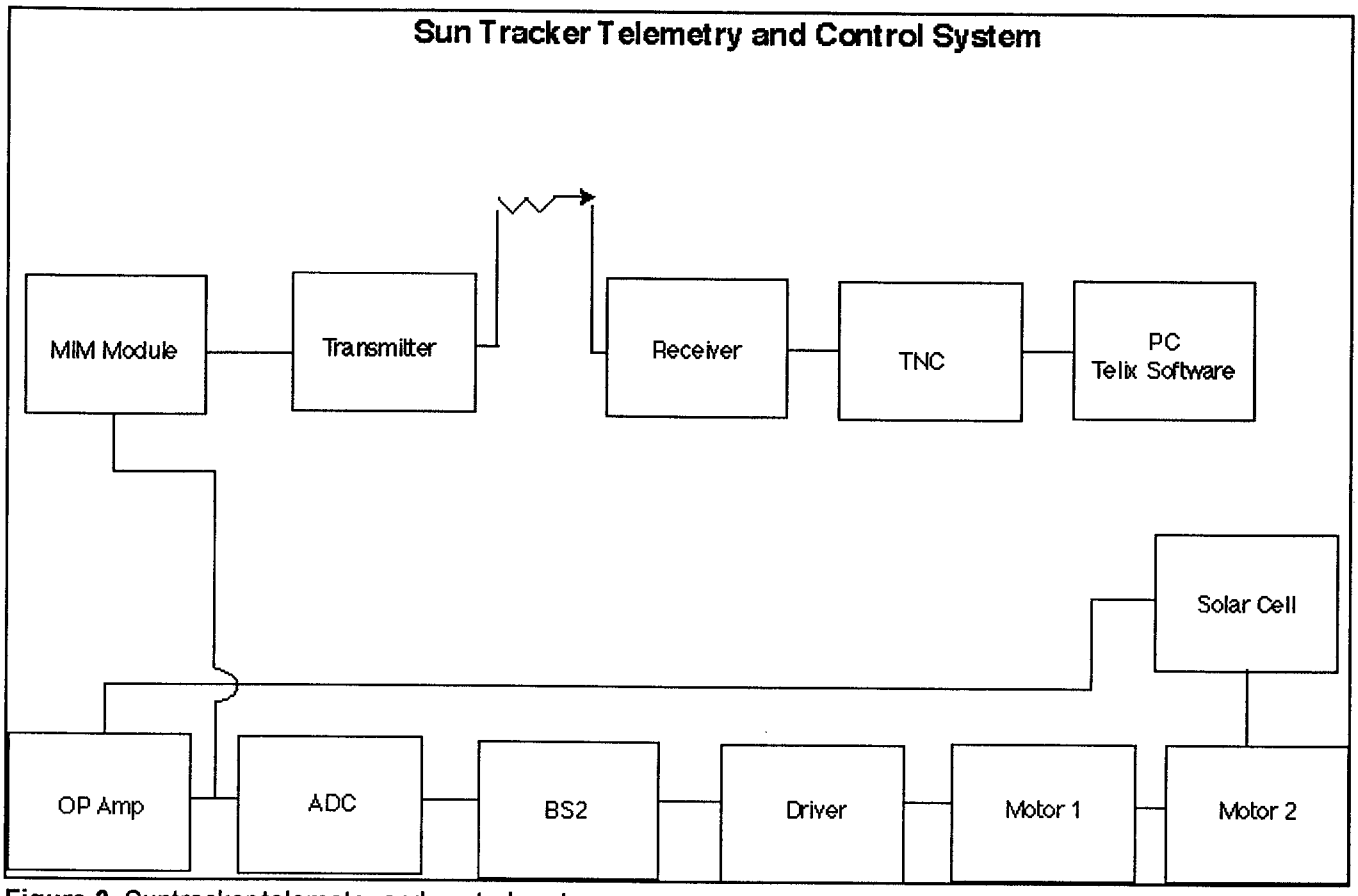

Figure 2. Suntracker telemetry and control system

than 15 mA and was powered during the flight by regulated 5.0 VDC from a battery pack. The unit was programmed to activate the push-to-talk function of the transmitter, and transmit data and a beacon message. The MIM module encodes data in the AX.25 format and inputs it to a credit-card size Alinco DJ-S11T 0.25 watt VHF transmitter. The transmitter power requirements are 9.0 V and 40 mA under quiescent conditions and 300 mA while transmitting. The data and beacon message from the MIM module are downlinked to a transmitter interfaced to a terminal node controller (TNC). The TNC translates the AX.25 code into ASCII text and outputs it to a serial port that is connected to a PC running Telix, a state-of-the-art communications software package. The data are saved in a PC file for analysis at a later time.

The signal from the solar cell is used to control the suntracker in order to produce a maximum in short-circuit current. The design specification is to control the suntracker in seeking the maximum in solar cell short-circuit current to better than 1 %. This is done with a controller consisting of an eight bit analog to digital converter (ADC) and a Parallax, Inc. Basic Stamp 2 microcontroller (BS2). Figure 2 shows the solar cell signal from the operational amplifier is input to the ADC that has a resolution of 0.39 % The digital signals from the ADC are input to the BS2 which is programmed to control the altitude and bearing DC motors. The BS2 is programed in PBASIC via a PC serial port. PBASIC instructions are executed by BS2 at a rate of over 10,000 per second. There are 16K of EEPROM space in 8 blocks of 2K Bytes each in BS2 for downloading up to 8 different PBASIC programs.

The suntracker was designed to be mounted on top of the payload and suspended about 50 feet below the balloon. It was expected that there would be instabilities in the motion of the balloon as it ascended. These instabilities will result in the instrument package rotating and oscillating like a pendulum. Some of the data available from balloon flights carried out by other groups show periods of rotation of the order of one revolution per minute. The period of oscillation for the pendulum for our system has been calculated to be about eight seconds. The design criterion for the suntracker system is that it be able to lock on an AM0 light source in about 10 seconds and track it with a response time of the order of one second. The pre-programmed minimum short-circuit current, PBASIC program and collimator dimensions were selected to enable the suntracker to discern the sun from light reflected from the balloon, earth, moon and clouds.

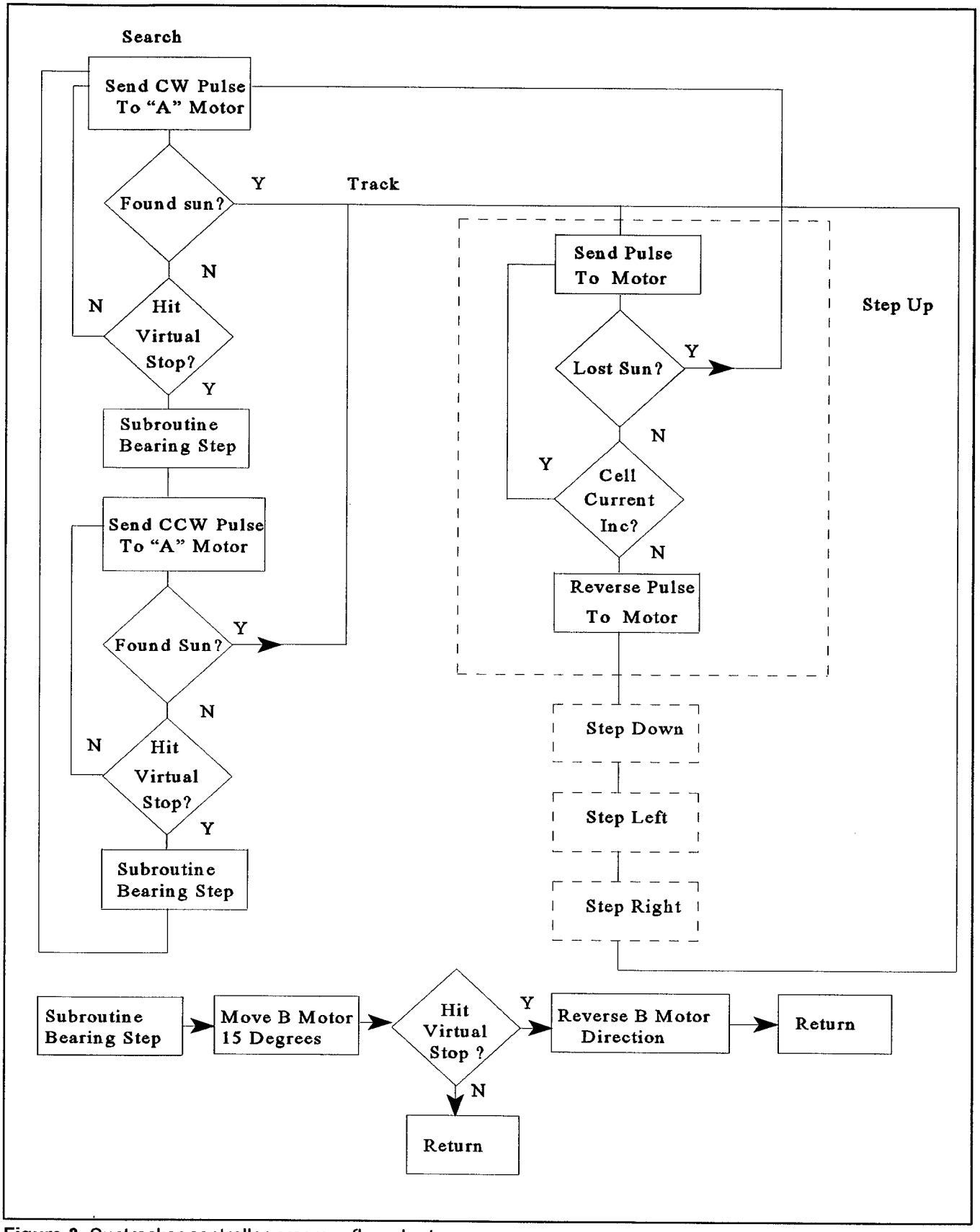

Figure 3. Suntracker controller program flow chart

The program algorithm for the suntracker is illustrated by the flow chart in Figure 3. The sun-tracking task has been divided into two sub-tasks: searching and tracking. In the search mode the collimator altitude is swept from zenith to horizon, the bearing is changed by about 15°, the collimator altitude is swept from horizon to zenith, the bearing is changed again by about 15°, and the process is repeated until the sun is located. The sun is located when the cell short-circuit current exceeds a predetermined threshold. In the tracking mode the controller takes a step up by increasing the altitude of the collimator by a few degrees. If this results in an increase in the cell current, another step up is taken. If the step up does not result in an increase in the cell current, the collimator is returned to its starting position, and a step down is taken. As long as a step produces an increase in the cell current, the step is repeated; when a step does not result in a cell current increase, the step is undone, and a step in the next direction is taken. The step order is up, down, left and right. If the cell current drops below a second predetermined threshold with any step, the controller has lost the sun, and the controller reverts to search mode. The virtual stops are produced by the controller continuously monitoring the pulses generated by the motor shaft encoders and calculating the altitude and bearing angles. The controller changes direction whenever an angle is equal to one of the range limits, i.e., 0° and 90° for the altitude angle and 0° and 360° for the bearing angle.

PAYLOAD DESCRIPTION

The payload included the suntracker, video system, GPS receiver, battery pack, beacon transmitter and antennas. The video system was included in the payload in order to monitor the operation of the suntracker and determine the stability of the payload during the flight. An ATV Research model BJ-3650WX color camera provided live video that was downlinked using a 1 watt UHF TV transmitter connected to an omnidirectional Little Wheel antenna manufactured by Olde Antenna Labs. A Motorola VP Oncore GPS receiver was used to determine longitude, latitude, heading, altitude and speed data. The GPS data were overlaid directly onto the live video with an Intuitive Circuits OSD-GPS video overlay circuit board. The electronics in the payload were powered by a battery pack that included 5 SAFT LX 3457 lithium D-cells with a 15 VDC output and 7.5 Ah capability. Lithium cells were used because they maintain high efficiencies in the -60 °C temperatures encountered in the upper atmosphere. The batteries have the capacity to supply power to the payload for a minimum of 6 hours. The beacon was a separate package with a transmitter and battery pack that was placed below the main package; it added redundancy to facilitate recovery of the payload in the event the main systems failed.

The payload, except for the collimator, solar cell, thermistor, motors and beacon, was encased in a 1.0" thick Styrofoam box to insulate the electronics from the low temperature environment during flight. The box was a rectangular parallelepiped with length=15", width=8" and height=20". The aluminum rod that supported the suntracker motors and collimator protruded through the top surface of the box. The video camera was mounted on top of the package and pointed at the suntracker. The weight of the payload weight was 5.5 pounds. The payload was attached to a Totex model TA-1000 latex meteorological balloon with a train that included three 0.020" Vectran shrouds and a four-foot diameter parachute.

The suntracker was flown without prior approval from any governmental entities. Payloads under 6 pounds may be flown by meeting the Federal Aviation Administration (FAA) requirement to file a verbal Notice to Airmen a few days in advance of the flight. Heavier payloads require FAA waivers and subsequent approval cycles which could take weeks of advance planning. UHF, VHF and HF amateur frequency bands were used for downlinking video, suntracker data and beacon signals. Since two of the authors (WLB and JRW) hold amateur radio licenses, prior approval of the Federal Communications Commission was not required.

FLIGHT RESULTS

There were 20 knot and higher gusting surface winds on the day of the launch. It was anticipated that the payload could be damaged during the launch due to the resulting relatively high horizontal balloon velocity. The balloon was inflated with helium to lift 13 pounds, considerably more lift than required for a 5.5 pound payload, in order to minimize the risk of damaging the payload. The 13 pounds lift resulted in a higher ascent rate at the cost of achieving the desired altitude of 110,000 feet. Signals were successfully received from the UHF, VHF and HF transmitters until just before launch. Minutes before launch the VHF signals ceased to be transmitted by the package. Because of the several delays that had already occurred, and the fact that the sun was moving to a lower altitude, it was decided to proceed with the launch. Liftoff occurred at 2:27 p.m. EDT on a farm located five miles southeast of Findlay, Ohio and the balloon ascended at a rate of about 1,300 feet/minute. The downlinked video signals from the UHF transmitter were used successfully to track the balloon throughout the flight. The video showed the payload was highly unstable. The suntracker operated throughout the ascent and locked on the sun only

occasionally because of the unstable motion of the payload. The balloon burst at an altitude of 87,000 feet and the package began the descent. At about 65,000 feet, as observed on the video, the collimator became entangled in the shroud lines and was pulled off the shaft of the altitude motor. The collimator dangled from the electrical wires during the descent. The wires subsequently broke and the collimator dropped from the payload.

Chase vehicles equipped with notebook PC's, direction finding equipment and video receivers were used in the recovery of the payload. The video receivers were used to receive and display GPS data that was input to the PC's. The PC's ran mapping software that displayed the location of the package on local maps. The payload parachuted into a corn field just northeast of Marion, Ohio 40 miles southeast from the launch site. The payload was retrieved some 15 minutes after landing with the aid of handheld direction finders; it was located about 150 feet from a paved road. The suntracker motors and video system were still operating. Aside from the fact that the suntracker collimator and solar cell were lost during descent, the payload was in excellent condition. Inspection of the suntracker showed that the collimator collet was missing from the shaft of the altitude motor. The collet probably deformed and came free of the motor shaft as a result of the forces on the collimator during entanglement in the shrouds lines.

Conclusions

The suntracker operated successfully as it ascended to 87,000 feet in the low temperature environment. It did not continuously track the sun throughout the ascent. The instability of the payload resulted in the suntracker system response time being too slow to track the sun continuously. If ground winds had been lighter the balloon could have been flown with less lift resulting in a lower ascent rate. The lower ascent rate would have resulted in a more stable payload with less horizontal spin and vertical oscillation. A more stable payload would have placed less demands on the suntracker system and it would have spent a larger fraction of the flight tracking the sun. Additionally, the payload would most likely have achieved an altitude in excess of 110,000 feet before balloon burst. Future efforts will be directed at designing an aerodynamically more stable payload; improving the reliability of the electronics; decreasing the response time of the suntracker system; and increasing the mechanical integrity of the suntracker.

REFERENCE

1. David N. Keener, Dean C. Marvin, David J. Brinker, Henry B. Curtis and P. Michael Price, Proceedings of the Twenty Sixth IEEE Photovoltaic Specialists Conference, 1997, page 787.

Photovoltaic Engineering Testbed On the International Space Station

Geoffrey A. Landis
David Scheiman
Ohio Aerospace Institute,
NASA Glenn Research Center mailstop 302-1,
Cleveland, OH 44135

Andrew Sexton, Richard Abramczyk, Joseph Francz, D. B.Johnson, Liu Yang,
Daniel Minjares, and James Myers
Dynacs, Inc.,
2001 Aerospace Parkway,
Brook Park, OH 44142

ABSTRACT

The Photovoltaic Engineering Testbed (PET) is a space-exposure test facility to fly on the International Space Station to calibrate, test, and qualify advanced solar cell types in the space environment. The purpose is to reduce the cost of validating new technologies and bringing them to spaceflight readiness by measuring them in the in-space environment. This paper will present the current status of the PET engineering development.

Introduction

The Photovoltaic Engineering Testbed (PET) is a space-exposure test facility to fly on the International Space Station to test advanced solar cell types in the space environment. The purpose is to reduce the cost of validating new technologies and bringing them to spaceflight readiness by measuring them in the in-space environment. The facility is scheduled to be launched on the Japanese Exposure Facility.

The facility will be used for three primary functions [1]:

1. AM0 solar cell calibration
2. space measurement
3. space qualification

Calibration is used to create a space-measured reference cell which can be used to calibrate the performance of cells on the ground, allowing ground measurements to be referenced to an actual space-flown standard of the same type. The most important purpose of the PET space calibration facility will be to allow routine measurements of performance parameters at true AM0, in actual space sunlight.

Measurement consists of measurements of the performance of cells in space, in particular measuring values of parameters which are sensitive to the space solar spectrum or environment, such as the temperature coefficient. The PET facility will measure full current-voltage curves at a range of temperatures.

Qualification consists of verifying that the performance of an interconnected solar-cell coupon does not degrade over time in the space environment.

Photovoltaic Engineering Testbed Design

The PET facility will be mounted on the Exposed Facility of the Japanese Experiment Module (JEM-EF). This location allows simplicity of exchange of samples. More details on the trade-off involved in selection of the PET location can be found in reference 2.

A conceptual drawing of the PET facility is shown in figures 1 and 2.

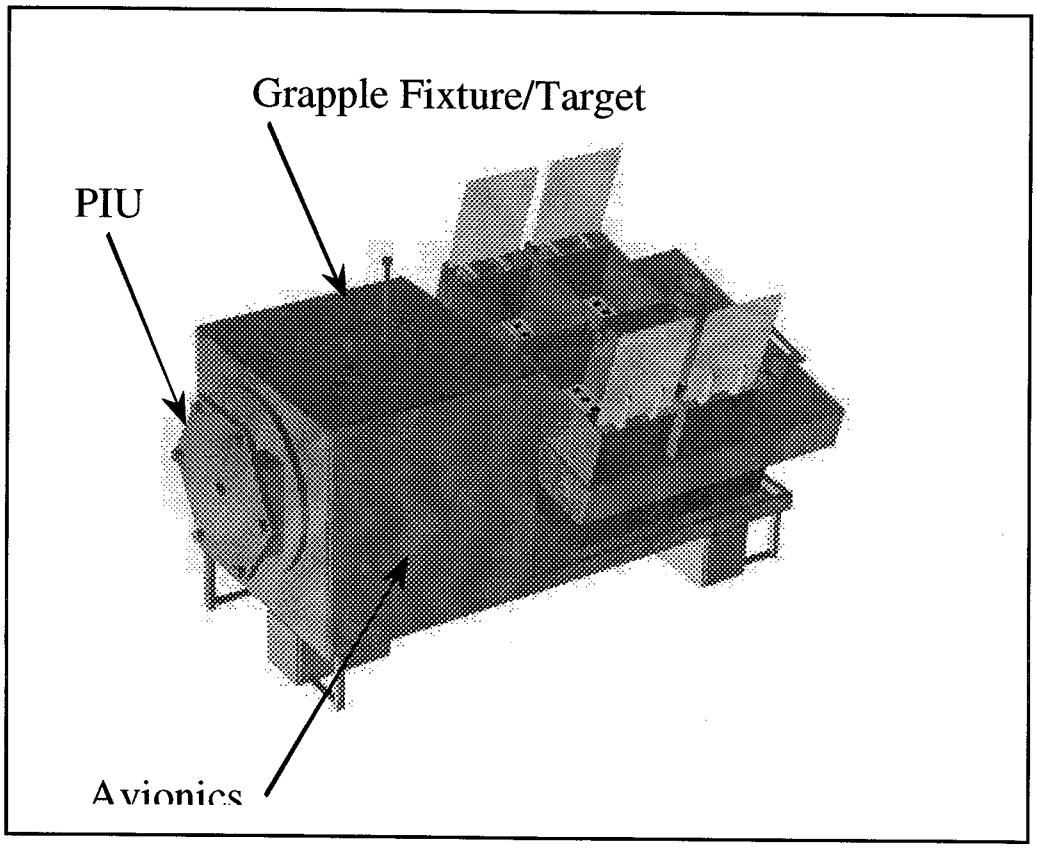

Figure 1:

PET facility. The hexagonal fixture on the end is the interface to the JEM (labeled PIU, or "Payload Interface Unit"), and the circular disk at the top is the robotic grapple fixture to remove or re-emplace the facility. The beta-axis tracking tray is shown with the four sample holders mounted and the exposure doors open to space. In this view, the zenith (space facing) direction is up, and the nadir (Earth-facing) direction down.

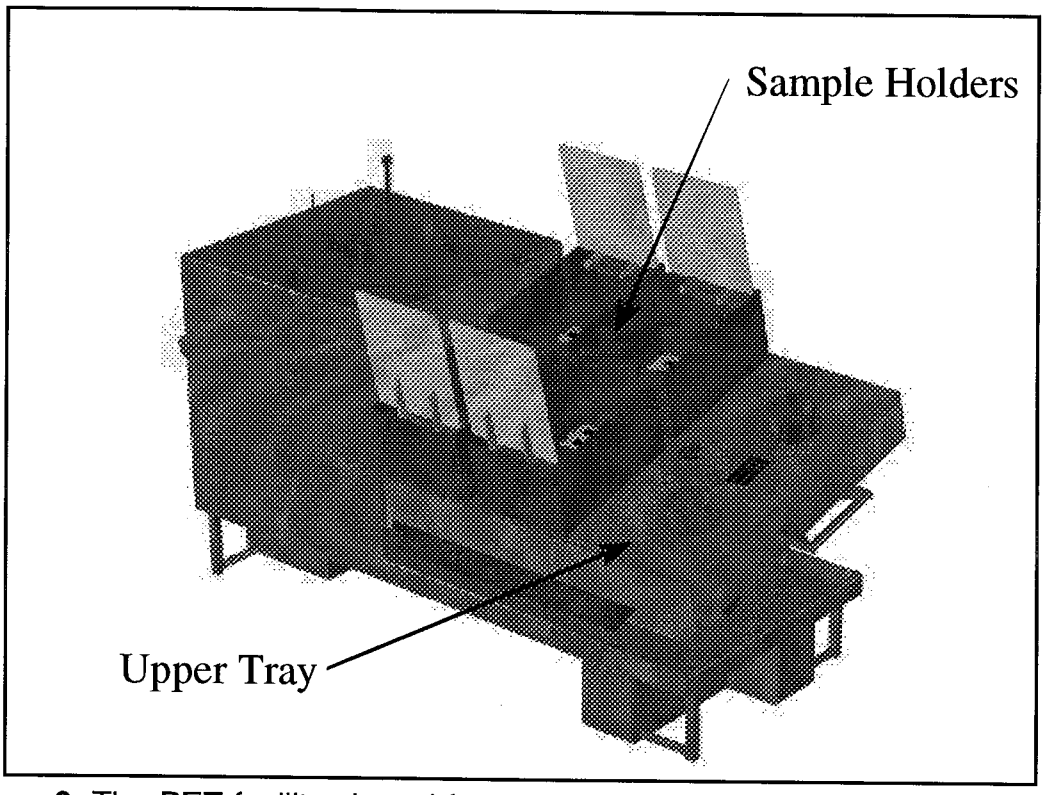

Figure 2. The PET facility viewed from the opposite angle.

The PET facility is designed for samples to be changed out regularly. Sample change-out is accomplished by the robotic manipulator, by removing the upper tray from the Beta tracking platform. This change-out process is shown in figure 3. The upper tray has four sample holders, which include electronics. New samples can be taken to the station on any resupply flight, and the actual exchange is done inside the pressurized facility, without requirement of extravehicular activity. Once new samples are placed on the upper tray, it is cycled through the airlock and re-emplaced on the PET tracking platform by the robotic manipulator.

Since solar cells on-orbit typically operate at temperatures between 45 and 100°C, characteristic of sun-facing surfaces in Earth orbit. The standard measurement temperature for solar cells is 28°C. This standard test temperature requires a temperature coefficient measurement to predict performance in space. The PET facility will measure performance of the cells by measuring current-voltage characteristics (I-V curves) under actual in-space operating conditions.

Finally, the qualification function of the testbed will be used to verify that the performance of an interconnected coupon does not degrade in the space environment, which is the final critical step leading to flight qualification and acceptance of a new technology. By doing flight exposure on the space station testbed, the qualified samples can be returned for examination after the test. This will give us the ability to diagnose failure mechanisms (if any), allowing a technology to be fine-tuned as required to pass performance specifications.

Although the PET facility was designed for testing photovoltaic cells and coupons, the versatile design can be used for space environment testing of any type of materials or electronic components of interest.

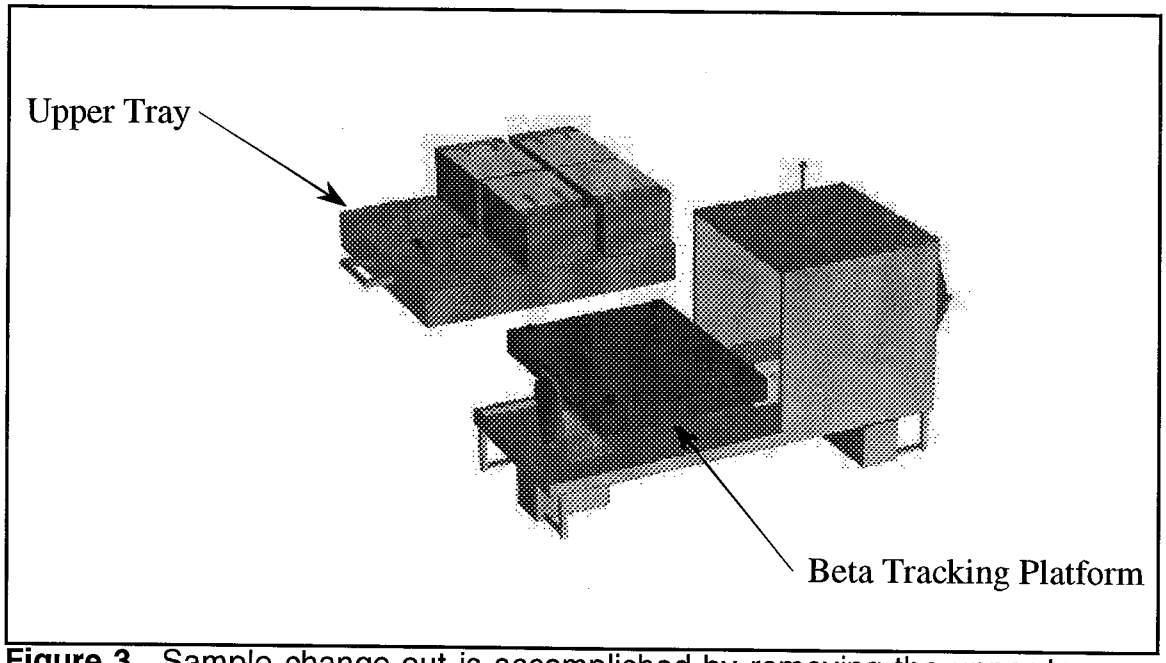

Figure 3. Sample change-out is accomplished by removing the upper tray from the Beta tracking platform. The upper tray has four sample holders, which include electronics.

Conclusions

The Photovoltaic Engineering Testbed will be a facility which will allow solar cell samples to be flown in space, calibrated, and then returned to Earth to serve as primary AM0 standards. The facility is designed to simplify sample change-out, to allow rapid testing of samples. It will produce full current-voltage curves at a range of temperatures, allowing measurement of temperature coefficient of all cell parameters in AM0 conditions. It will additionally be a facility which can be used for long-duration testing of cell exposure to the space environment.

References

1. G. Landis and S. Bailey, "Photovoltaic Engineering Testbed on the International Space Station," *2nd World Conference on Photovoltaic Energy Conversion, Vol. III,* Vienna, Austria, July 1998, pp. 3564-3567.
2. G. Landis, A. Sexton, R. Abramczyk, J. Francz, D. Johnson, L. Yang, D. Minjares, and J. Myers, "The Photovoltaic Engineering Testbed: Design Options and Trade-offs," *AIP Conference Proceedings Volume 504*, presented at Space Technology and Applications International Forum (STAIF-2000), Jan. 30 - Feb. 3, 2000, Albuquerque NM.

SILICON CARBIDE RADIOISOTOPE BATTERIES

George C. Rybicki
Photovoltaic Branch
NASA Glenn Research Center
Cleveland, Ohio 44135

ABSTRACT

The substantial radiation resistance and large bandgap of SiC semiconductor materials makes them an attractive candidate for application in a high efficiency, long life radioisotope battery. To evaluate their potential in this application, simulated batteries were constructed using SiC diodes and the alpha particle emitter Americium (^{241}Am) or the beta particle emitter Promethium (^{147}Pm). The ^{241}Am based battery showed high initial power output and an initial conversion efficiency of approximately 16%, but the power output decayed 52% in 500 hours due to radiation damage. In contrast the ^{147}Pm based battery showed a similar power output level and an initial conversion efficiency of approximately 0.6%, but no degradation was observed in 500 hours. However, the ^{147}Pm battery required approximately 1000 times the particle fluence as the ^{241}Am battery to achieve a similar power output. The advantages and disadvantages of each type of battery and suggestions for future improvements will be discussed.

INTRODUCTION

The maturation of new wide bandgap, highly radiation resistant semiconductor materials has made it worthwhile to revisit the topic of radioisotope batteries. SiC has a very desirable combination of properties for radioisotope battery design, including a large bandgap of 3 eV in the 6H polytype and a radiation induced atomic displacement threshold second only to diamond.(1) These attributes may make it possible to use an inexpensive radioisotopes to construct high efficiency, long lifetime radioisotope batteries. These batteries are potential power sources for applications where neither solar nor chemical battery power are feasible.

The operation of the SiC radioisotope battery is analogous to that of a solar cell except that high energy electrons or alpha particles are impinging on the cell rather than solar photons. Early radioisotope battery designs were based on beta emitting isotopes such as ^{147} Pm and silicon diodes. (2) However, their performance was limited by the leakage current in the low bandgap Si diodes and the poor radiation resistance of Si. (3) Highly radiation resistant SiC semiconductor materials and diodes with very low leakage currents may make large performance increases in radioisotope batteries possible.

Previous attempts to use alpha particle emitting isotopes to fabricate a radioisotope battery have been made. (4) In that work, SiC photodetector diodes were irradiated with 5.5 MeV alpha particles from the radioisotope ^{241}Am. This isotope is inexpensive, widely available, and has a long half life of 458 years. It was also desirable because the alpha particles have a limited range in the semiconductor and this gives a better chance of capturing the generated carriers. The initial performance of the alpha particle based battery was impressive, but the power output rapidly decayed due to the high rate of radiation damage in the SiC diode materials.

The advantages of SiC as an energy conversion material may still be realized in a betavoltaic energy conversion scheme. In this case, a beta radioisotope based SiC battery was constructed using the isotope ^{147}Pm. ^{147} Pm decays with the emission of high energy electrons, with an average energy of 62 KeV, and maximum energy of 225 KeV. Although the range of the beta particles is larger than that of the alpha particles, and thus the generated carriers may be harder to collect, the reduced radiation damage rate may make this design preferable.

EXPERIMENTAL

A simulated radioisotope battery was constructed by mounting a 2mm x 2mm SiC diode on a transistor header and placing it in a holder directly above the radioisotope source; this was a plated metal film source in the case of the ^{241}Am, and a Pm_2O_3 sealed disk source in the case of the ^{147}Pm. The diodes used in this study were SiC photodetector diodes obtained from the Cree Corporation in Durham, NC. Details of the structure and characteristics of the diodes are described elsewhere, (5) but briefly, they are composed of a p-type SiC substrate with an aluminum doped p-type epitaxial layer and nitrogen doped n-type emitter. The diodes were analyzed by the capacitance voltage technique before irradiation. A carrier concentration in the base of $(2.25 \pm 0.6) \times 10^{16}$ cm^{-3} was determined. The samples were then irradiated under vacuum with 5.5 MeV alpha particles using a 1.5 mCi ^{241}Am radioisotope source or with beta particles from a 30 mCi ^{147}Pm source. During the irradiation, the power output of the SiC cell was monitored as a function of time using an electrometer.

RESULTS

The power output in nanowatts as a function of time for the alpha and betavoltaic batteries are shown in Figure 1, Figure 2, and Table 1 below.

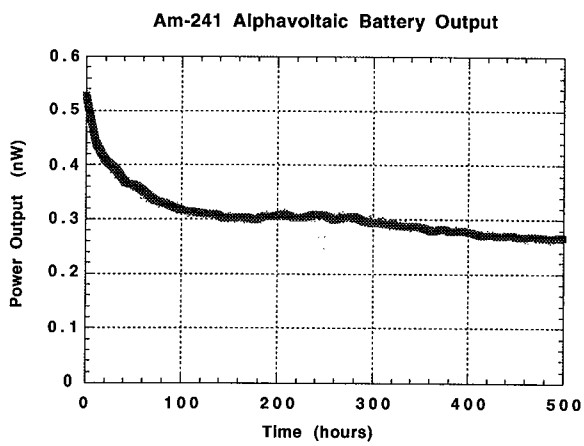

Figure 1. Alphavoltaic battery output

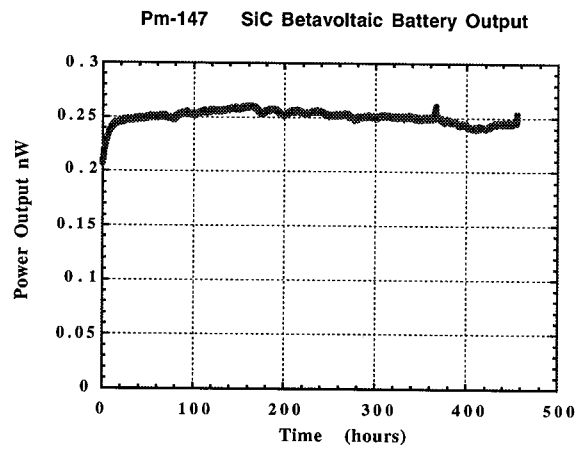

Figure 2. Betavoltaic battery output

Time (hours)	alpha battery power output	beta battery power output
0	0.527 nW	0.250 nW
100	0.321 nW	0.251 nW
200	0.304 nW	0.253 nW
300	0.298 nW	0.249 nW
400	0.276 nW	0.242 nW
500	0.259 nW	0.254 nW

Table I: Power output of alpha and betavoltaic batteries in nW as a function of time.

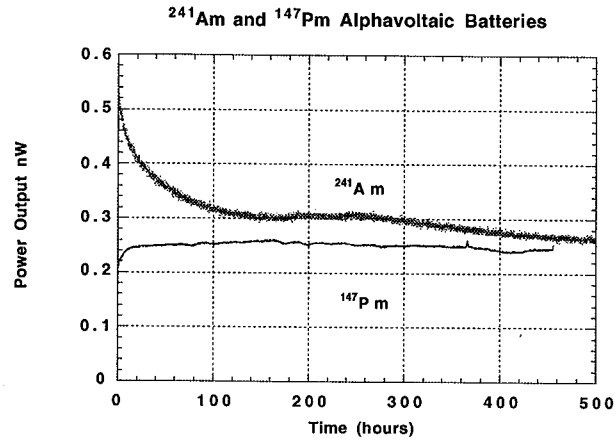

Figure 3. Output of Alphavoltaic and Betavoltaic batteries

The results clearly show that significant degradation occurs in the case of the alphavoltaic battery, but that essentially no degradation occurs in the case of the betavoltaic battery. The initial power output of the ^{241}AM battery degraded by 40% in the first 100 hours, 52% in the first 500 hours, and continued to decay at a lower rate, through 1000 hours and beyond. The comparative performance of the two batteries is illustrated more clearly in Figure 3. It is clear that the alphavoltaic battery had a higher initial power output, but after 100 hours the power output of the two batteries is comparable. However, the power output of the two cells should be considered in terms of the strengths of the isotope and their geometric configurations. The fluence at the sample surface was 6000 alpha particles per second per mm^2 , in the case of the alpha battery, and was 5.8 X 10^6 electrons per second per mm^2 in the case of the beta battery. The net result was that it took approximately 1000 times as much beta flux as alpha flux to generate a similar amount of power. Part of this is certainly due to the fact that the beta particles had much less energy than the 5.5 MeV alpha particles, (62 KeV on average and 225 KeV maximum). Based on the 62 KeV average energy, the beta particles had on 90 times less energy than the alpha particles, and would thus generate fewer electron hole pairs. The remaining difference, accounting for the required higher beta fluence, is likely related to the longer range and thus greater difficulty in collecting the electron hole pairs generated by the beta particles. The 5.5 MeV alpha particles have a range of approximately 28 μm in SiC, but the beta particles have a range of up to 300 μm. The diffusion length in SiC is only a few microns (6) so the longer particle range makes it more difficult to collect the energy of the beta particles.

The effect of the particle range on energy collection can be demonstrated by making an estimate of the power conversion efficiency of the two simulated batteries. A commonly used theoretical model predicts that the energy lost in the creation of an electron hole pair in an absorber by a charged particle is 2.8 E_g + 0.5 eV, or 8.9 eV in SiC. (3) Each alpha particle could thus generate 616,000 electron hole pairs and each beta particle, on average, 6965 electron hole pairs. At the measured fluxes in these experiments, this would result in the generation of 1.48 x 10^{10} carriers per second or 2.4 nA in the case of the alphavoltaic battery and 1.6 x 10^{11} carriers per second, and 25.8 nA in the case of the betavoltaic battery. The actual collected currents were 0.382 nA in the case of the alphavoltaic battery, or a 16% conversion efficiency, and 0.148 nA in the case of the betavoltaic battery, or 0.6% conversion efficiency. In this case the advantage of the alphavoltaic approach is clear.

In a previous study, the degradation of the power output of the simulated alphavoltaic battery was correlated with radiation damage in the diodes, and specifically to the introduction of deep levels in the SiC diodes. (4) The introduction rate of these defects was also measured under both 1 MeV electron irradiation and 5.5 MeV alpha particle irradiation. Of course, the introduction rate of defects during electron irradiation was much lower than that in the case of alpha particle irradiation; a defect introduction rate 5700 times lower was measured for the 1 MeV electrons. If the collision stopping power of 1 MeV electrons is compared to 62 KeV and 225 KeV electrons, the production of defects by the lower energy electrons might be expected to be lower still.

The degradation of battery output under electron irradiation is not observed here, probably as a result of a combination of effects. First, it would require several thousand times as much fluence under beta particle irradiation as alpha particle irradiation to generate a equivalent number of defects. Another factor that may contribute is that the minimum energy required to displace an atom in SiC, at 21.8 eV, is higher than in almost any other material, and results in a displacement threshold of 108 KeV in SiC (1). The electron energy spectra for the beta decay of ^{147}Pm has an average energy of 62 KeV, which is below the threshold energy for lattice damage in SiC. For these reasons, no power output degradation was observed in the betavoltaic battery, and in the absence of any apparent degradation in power output, no studies were made of deep levels introduced by the ^{147}Pm irradiation.

The implications of these results is that similar power outputs can be obtained using alpha particle emitters or properly selected beta particle emitters in the construction of semiconductor based radioisotope batteries. The advantage of the higher energy, shorter range alpha particles is reduced by the higher rate of radiation damage they cause. Several attempts were made to reduce the rate of radiation damage in the alpha particle based radioisotope battery, for example thicker emitters, larger surface area diodes and junction edge protection were all investigated. Unfortunately none of these approaches significantly reduced the radiation damage rate. (4)

Several other avenues may still be available for the improvement of these radioisotope batteries. For example, lower energy alpha emitters and higher and lower energy beta emitters should be investigated. For the isotope selected, both the energy of the decay product and the half life must be considered. A very long half life results in a low specific activity and an impractical amount of radioisotope material would be required. A very short half life would make the battery impractical to use before its output decayed. Alpha isotopes are suggested that had reasonable half lives and alpha energies significantly less than 5.5 MeV. Beta isotopes were suggested that had an average decay energy of less 108 KeV. A table of candidate isotopes is presented below.

Material	Half Life (yrs)	Alpha Energy (MeV)	Beta energy (KeV)
^{148}Gd	74.6	3.183	
^{63}Ni	100		66 max, 17.1 avg
^{14}C	5730		156 max 49.5 avg
^{60}Co	5.27		317 max 95 avg
^{99}Tc	21300		293 max 85 avg
^{241}Am	432	5.49	
^{147}Pm	2.63		225 max 62 avg

Table 2: Potentially useful isotopes for radioisotope batteries

Although there are hundreds of available radioisotopes, few are suitable for these applications. Even the use of those isotopes thought to be suitable may be complicated by radiation hazards as in ^{60}Co, or high cost and limited availability as in ^{63}Ni. The use of ^{148}Gd in the alpha battery may look promising as it is a lower energy alpha emitter than ^{241}Am, but the alpha particle energy still far exceeds the damage threshold in SiC. In the case of other potential beta emitting isotopes, ^{60}Co looks nearly ideal but its use might be complicated by the strong gamma emission associated with its decay. Isotopes such as ^{204}Tl have been suggested, but they have an average electron energy higher than the damage threshold in SiC. Others such as tritium or ^{14}C have energies less than that of ^{147}Pm and would produce less electron hole pairs. However, low energy beta emitting isotopes may have some potential, as they could result in higher conversion efficiencies due to the shorter range of the electrons in the diode material.

Conclusions

Both alpha and beta particle emitting radioisotopes can be used to construct semiconductor based radioisotope batteries. The alpha based design shows high efficiency and power output, but a shorter lifetime due to the severe radiation damage caused by the alpha particle irradiation. The beta particle based design, on the other hand, showed lower efficiency but no degradation over time. The beta design could probably be loaded with more isotopes to compensate for its lower efficiency, but no easy solution appears to be available for the radiation damage problem with the alpha based design. Additionally, experiments with low energy, short range beta emitters may result in a more efficient, higher output betavoltaic battery design.

References

1.) A.Barry, B.Lehmann, D. Fritsch and D. Braunig, *IEEE Trans. on Nucl. Sci.*,**38**, 1111 (1991).

2.) H.Flicker, J. Loferski, and T. Elleman, *IEEE Trans.On Electron Devices*, **ED-11**, 2 (1964).

3.) L.Olsen, *Proc. of the 12th Space Photovoltaic Research and Technology Conference*, Cleveland, Ohio, October 1992, p. 256

4.) G.C. Rybicki, C.V Aburto and R. Uribe, SiC Alphavoltaic Battery, *Proceedings of the 25 th. IEEE Photovoltaics Specialist Conference*, Washington, DC, May 13-17, 1996, p.93-96.

5.) D. Brown, E. Downey, M. Ghezzo, J. Kretchmer, R. Saia, Y. Liu, J. Edmond, G. Gati, J. Pimbley and W. Schneider, *IEEE Trans. On Electron Devices.*,**40**, 325 (1993).

6.) S.M. Hubbard, M. Tabib-Azar, S.G. Bailey, G. Rybicki, P. Neudeck, R.P. Raffaelle, Effect of Crystal Defects on the Minority Carrier Diffusion Lengths in 6H SiC, 26th IEEE PVSC (IEEE, New York, 1997)

HIGH QUALITY GAAS GROWTH BY MBE ON SI USING GESI BUFFERS AND PROSPECTS FOR SPACE PHOTOVOLTAICS[1]

J.A. Carlin and S.A. Ringel
The Ohio State University
Dept. of Electrical Engineering
Columbus, OH 43210

E.A. Fitzgerald
Massachusetts Institute of Technology
Dept. of Materials Science & Engineering
Cambridge, MA 02139

M. Bulsara
Amberwave, LLC
Windham, NH
03087

ABSTRACT

III-V solar cells on Si substrates are of interest for space photovoltaics since this would combine high performance space cells with a strong, lightweight and inexpensive substrate. However, the primary obstacles blocking III-V/Si cells from achieving high performance to date have been fundamental materials incompatibilities, namely the 4% lattice mismatch between GaAs and Si, and the large mismatch in thermal expansion coefficient. In this paper, we report on the molecular beam epitaxial (MBE) growth and properties of GaAs layers and single junction GaAs cells on Si wafers which utilize compositionally graded GeSi intermediate buffers grown by ultra-high vacuum chemical vapor deposition (UHVCVD) to mitigate the large lattice mismatch between GaAs and Si. GaAs cell structures were found to incorporate a threading dislocation density of 0.9 – 1.5 $x10^6$ cm^{-2}, identical to the underlying relaxed Ge cap of the graded buffer, via a combination of transmission electron microscopy, electron beam induced current, and etch pit density measurements. AlGaAs/GaAs double heterostructures were grown on the GeSi/Si substrates for time-resolved photoluminescence measurements, which revealed a bulk GaAs minority carrier lifetime in excess of 10 ns, the highest lifetime ever reported for GaAs on Si. A series of growths were performed to assess the impact of a GaAs buffer layer that is typically grown on the Ge surface prior to growth of active device layers. We found that both the high lifetimes and low interface recombination velocities are maintained even after reducing the GaAs buffer to a thickness of only 0.1 μm. Secondary ion mass spectroscopy studies revealed that there is negligible cross diffusion of Ga, As and Ge at the III-V/Ge interface, identical to our earlier findings for GaAs grown on Ge wafers using MBE. This indicates that there is no need for a buffer to "bury" regions of high autodoping, and that either pn or np configuration cells are easily accommodated by these substrates. Preliminary diodes and single junction AlGaAs heteroface cells were grown and fabricated on the Ge/GeSi/Si substrates for the first time. Diodes fabricated on GaAs, Ge and Ge/GeSi/Si substrates show nearly identical I-V characteristics in both forward and reverse bias regions. External quantum efficiencies of AlGaAs/GaAs cell structures grown on Ge/GeSi/Si and Ge substrates demonstrated nearly identical photoresponse, which indicates that high lifetimes, diffusion lengths and efficient minority carrier collection is maintained after complete cell processing.

1. INTRODUCTION

The ability to achieve high efficiency and reliable space solar cells on lightweight, strong and inexpensive substrates is of great interest for virtually every satellite mission. For III-V space photovoltaics, this has led to the development of various types of III-V cells on Ge wafers, since Ge offers certain advantages in strength and cost over GaAs substrates while providing a lattice constant that closely matches that of GaAs. Nevertheless, from purely a substrate perspective, Ge is not ideal, especially when compared with Si, which is far cheaper, readily available in large areas, substantially stronger, and possesses a larger thermal conductivity. However, as is the

[1] Supported by NASA Glenn Research Center under grant NAG3-1461, and by a NASA GSRP fellowship (JAC)

case for many otherwise desirable combinations of substrates and epitaxial semiconductors, there exists a large mismatch in lattice constant (4% for GaAs/Si) that negates the advantage of the substrate by generating large densities of defects in the active device layers unless methods to control and reduce the density of mismatch-related defects are implemented. Numerous efforts have been made to deal with the mismatch during epitaxial growth, including thermally-cycled growth of the III-V intermediate layers, compositionally-graded III-V graded buffers, strained buffer layers, etc., and each has been successful in reducing the density of threading dislocations from ~ 10^{10} cm^{-2} for direct epitaxy of GaAs on Si, to ~ 10^{7} cm^{-2} for the various defect control approaches.[1-5] However, at this dislocation density minority carrier lifetimes in the range of ~ 1-3 ns have been demonstrated, which are not high enough to generate efficient III-V solar cells. An alternative approach is to engineer the lattice constant of the Si substrate surface itself prior to III-V epitaxy, rather than dealing with the mismatch within the III-V regions alone. The Ge_xSi_{1-x} compositional alloy system is well-suited for this application since by slowly increasing the Ge content (x) during growth of a Ge_xSi_{1-x} epitaxial layer on Si, the lattice constant can be increased from that of Si to Ge, which provides a close lattice match for subsequent GaAs-based device growth. Of course this requires that the compositionally graded buffer layer is strain-relaxed so that the Ge surface lattice constant is matched to GaAs, and that the threading dislocations generated from relaxing the 4% misfit between Ge and Si are maintained to a minimum concentration in the Ge cap of this "virtual" Ge substrate. Recent work by Fitzgerald and co-workers has demonstrated that low threading dislocation densities (TDD) in relaxed Ge layers grown on compositionally-graded Ge_xSi_{1-x} buffers on Si are achievable.[6] Record-low TDD values of ~ < $2x10^{6}$ cm^{-2} were achieved, as confirmed using plan-view and cross section transmission electron microscopy (TEM), electron beam induced current (EBIC) and etch pit density (EPD) measurements. As a result, these "virtual" Ge substrates are appealing for not only photovoltaic substrate applications, but also for integration of III-V optoelectronics with Si in general, since the residual TDD value in the substrate is already an order of magnitude lower than that observed for III-V layers grown on Si using III-V epitaxy-based dislocation control methods. At these TDD values, minority carrier lifetimes on the order of 10 ns can be expected, which can be translated into very respectable GaAs cell efficiencies. However, III-V epilayer growth and cell processing on $Ge/Ge_xSi_{1-x}/Si$ wafers may not behave identically to III-V cell fabrication on Ge wafers, and issues such as the impact of residual dislocation density, thermal expansion mismatch, surface morphology, etc., on III-V overlayer quality all must be considered. In this paper, we present a growth, characterization and preliminary device study of GaAs and AlGaAs/GaAs layers and cell structures grown by molecular beam epitaxy (MBE) on graded $Ge/Ge_xSi_{1-x}/Si$ substrate wafers. Note that for the remainder of the paper, the graded Ge_xSi_{1-x} buffer will be denoted by GeSi.

2. EXPERIMENTAL

III-V layers and AlGaAs/GaAs p on n single junction cell structures were grown by solid source MBE on Ge/GeSi/Si substrates. The Ge/GeSi growth was done by ultra high vacuum chemical vapor deposition. The composition of the GeSi buffer was increased during growth by step-grading from x = 0 (pure Si) to x = 1 (pure Ge) at an average rate of 10% Ge/μm. Details of the GeSi graded buffer growth have been described in previous work.[6] A combination of plan-view and cross sectional transmission electron microscopy (TEM), electron beam induced current (EBIC), and etch pit density (EPD) measurements were used to confirm an average TDD = 0.9 – $2x10^{6}$ cm^{-2} within the relaxed Ge cap layer for a number of growth runs. For all III-V growths, the MBE chamber background pressure was in the high 10^{-11} torr range. Substrate temperatures were measured by infrared pyrometry except for temperatures below 450 °C for which substrate thermocouple readings are reported. In all cases, the substrates were (001) oriented with a 6° offcut toward the in-plane [110] direction. Substrate cleaning was found to be an important issue and here all substrates were cleaned in organic solvents, followed by a UV-ozone treatment before loading into the growth chamber.[7] Prior to MBE growth, surface oxides were removed by a 20 minute, 640 °C anneal, after which a thin Ge epitaxial layer was deposited onto the substrates, followed by GaAs epitaxy that was initiated using a 10 monolayer migration enhanced epitaxy (MEE) nucleation step. Two types of basic structures were grown, AlGaAs/GaAs/AlGaAs double heterostructures to facilitate minority carrier lifetime measurements by time resolved photoluminescence (TRPL), and p on n AlGaAs/GaAs heteroface cell structures. For either structure, we chose to vary the thickness of a GaAs buffer layer grown on top of the Ge prior to growth of the active III-V layers, from 0.1 μm - 1.0 μm, in order to assess the electronic quality of the III-V layers as a function of their proximity to the Ge/GeSi/Si surface. This is important from the viewpoint of reducing thermal expansion stress effects. The DH structure used for all minority carrier lifetime measurements is as follows: a GaAs layer doped at $n=1.1x10^{17}$ cm^{-3} of variable thickness (d = 0.5, 1.0, or 1.5 μm) sandwiched between $Al_{0.3-}$

$Ga_{0.7}As$ layers of 50 nm and 20 nm thicknesses for the surface and buried barrier layers, respectively. Room temperature TRPL was used to measure the transient lifetime of the 870 nm GaAs band-to-band luminescence peak, the details of which have been described in earlier work.[8]. The bulk minority carrier lifetime (τ_p) and AlGaAs/GaAs interface recombination velocity (S) of each sample set was extracted from the net TRPL decay time (τ_{TRPL}) using

$$1/\tau_{TRPL} = 1/\tau_p + 2S/d \quad (1)$$

where d is the DH GaAs layer thickness. Cell structures were fully processed (without anti-reflection coatings), and were evaluated by dark and light I-V measurements, and by spectral response measurements. Identical cell and diode structures were grown on Ge/GeSi/Si, Ge and GaAs wafers to directly compare device characteristics as a function of substrate choice. To facilitate these measurements, Au-Cr and Au-Sb were used for front (p-type) and back (n-type) ohmic contacts, respectively. Finally, atomic diffusion of Ga, As and Ge across the heterovalent GaAs/Ge interfaces of DH and cell structures grown on the Ge/GeSi/Si substrates was investigated using secondary ion mass spectroscopy (SIMS).

3. RESULTS AND DISCUSSION

3.1. Structural Properties, Minority Carrier Lifetime and the Effect of GaAs Buffer Layer Thickness

Figure 1 shows a representative cross-sectional TEM image of an MBE-grown AlGaAs/GaAs heterostructure grown on a Ge/GeSi/Si substrate. At this scale, no threading dislocations are observable. Using a combination of lower magnification EBIC, plan-view TEM and EPD measurements, the III-V layers were found to contain a TDD = $0.9\text{-}1.5\times10^6$ cm^{-2}, identical to the underlying Ge cap of the GeSi/Si substrate. This indicates that the GaAs/Ge interface is behaving as would be expected for an "ideal" low-mismatched interface (the misfit between GaAs and Ge is ~ 0.17%) that generates only a very low density of new dislocations. Moreover, we did not detect any APB's or indication of APD disorder, consistent with our earlier results of an in-depth investigation of APD disorder in GaAs on Ge and is relation to GaAs growth nucleation conditions.[9] This is indicative of the successful transfer of our optimum GaAs growth and nucleation process on Ge wafers to Ge/GeSi/Si wafers. It is interesting to note that while the compositionally graded GeSi buffer results in the well-known crosshatched surface morphology characteristic of low TDD, high quality graded buffers, this did not have an effect on the structural quality of the III-V overlayers.

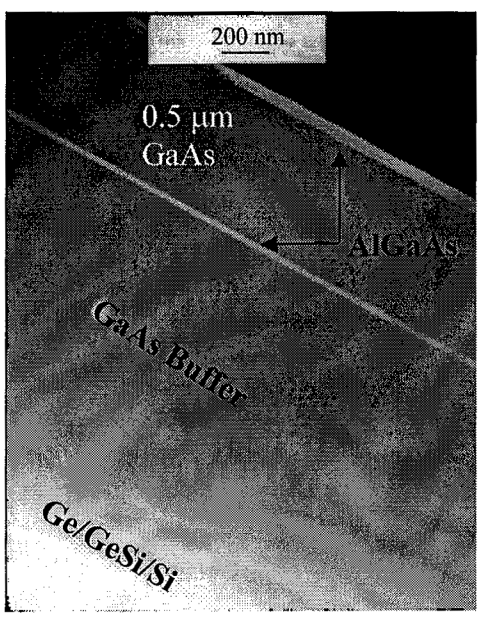

Figure 1. Cross section TEM micrograph of MBE-grown AlGaAs/GaAs/AlGaAs DH structure on Ge/GeSi/Si.

Note from figure 1 that a 1 μm thick GaAs buffer layer is present beneath the AlGaAs/GaAs/AlGaAs DH structure. For GaAs cells on Ge, a passive GaAs buffer layer grown on the Ge surface is often included to bury defects such as APB's emanating from the polar/nonpolar GaAs/Ge interface and to bury potential autodoping problems well below the active device regions. However, a critical aspect for successful, large area GaAs on Si device integration is the minimization of possible thermal stress-induced cracks resulting from thermal expansion coefficient mismatches. Thus it is imperative to reduce the thickness of GaAs (or Ge) buffer layers to a minimal amount. To investigate how the GaAs material quality varied with GaAs buffer layer thickness, a series of DH structures were grown on Ge/GeSi/Si substrates that incorporated a range of GaAs buffer layers from 0.1 – 1 μm in thickness. TRPL measurements indicated that there is no degradation of the minority carrier lifetime as a function of the GaAs buffer thickness. Indeed, figure 2 shows a comparison of the net TRPL decay curves for d = 1.5 μm DH structures grown on Ge/GeSi/Si having GaAs buffers of

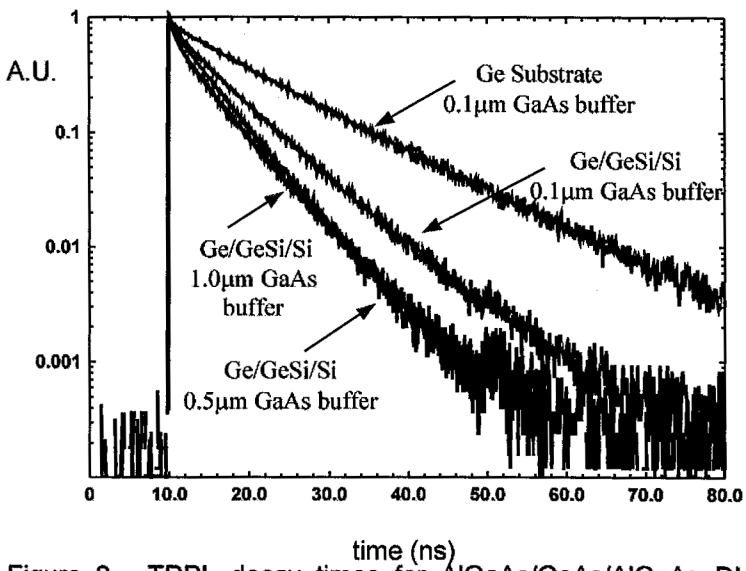

Figure 2. TRPL decay times for AlGaAs/GaAs/AlGaAs DH structures grown on Ge/GeSi as a function of GaAs buffer thickness as indicated. Meaurements were done at 300 K.

1.0, 0.5 and 0.1 μm in thickness. Also shown, for comparison, is the TRPL decay for the same DH structure grown on a Ge wafer. First looking at the 1.0 and 0.5 μm GaAs buffer results, we observe no change in the TRPL decay time. A full analysis of the former resulted in a bulk minority carrier lifetime for n-type GaAs of 7.7 ns and an interface recombination velocity (S) of 3,900 cm/s, by TRPL measurements applied to a range of DH GaAs thicknesses following eq. (1).[8] Note that for these particular structures, the Ge surface was chemically etched prior to III-V epitaxy. The recombination velocity was found to be very sensitive to substrate cleaning prior to III-V growth, and subsequent improvements (inclusion of UV-ozone exposure) resulted in a reduction in S to ~ 1,800 – 2,200 cm/s, independent of GaAs buffer thickness.

The TRPL results for the 0.1 μm thick GaAs buffer are even more encouraging as seen by the longer decay time in figure 2. The net PL decay time of 8.2 ns for this sample translates into a bulk minority carrier lifetime of 10.5 ns. This is calculated by using a value of 2,000 cm/s for S, which we consistently obtain independent of GaAs buffer thickness for all UV-ozone treated Ge/GeSi/Si surfaces (note from eq. 1 that a higher value for S will result in an even higher value for the minority carrier lifetime). These lifetime values are the highest bulk GaAs minority carrier lifetimes ever reported for GaAs grown on a Si substrate, and indicate that the GaAs buffer can safely be reduced to an almost negligible thickness of 0.1 μm with no degradation of either carrier lifetime or interface recombination velocity. The variations in our lifetimes from ~ 8 – 10 ns result from continued optimization of both the GaAs nucleation procedure and defect control in the Ge/GeSi/Si substrates. It should be noted that at these TDD values, the lifetime is a strong function of TDD, hence minor improvements in the TDD for the Ge/GeSi/Si substrates translates directly into higher lifetime values. This point is evident from figure 3 which shows a range of lifetime values measured on our samples as a function of TDD in the substrate, plotted along with the theoretical dependence of minority carrier lifetime on TDD as calculated by Yamaguchi.[2] As seen, our data correlates well with the calculated values. The small scatter observed in the data is most likely due to uncertainties in measuring TDD with high accuracy, since it is very difficult to count and separate individual threading dislocations at these low TDD values, which is further clouded by the presence of small dislocation pileups from which it is difficult to discern individual threads. In comparison to other reports, the highest previous lifetimes for GaAs on Si using other methods of defect control are on the order of ~ 1-3 ns.[1-5] From figure 3 it is clear that our current lifetime values are approaching the lifetime plateau below a TDD of ~ mid 10^5 cm^{-2} range, but even at 10 ns, high efficiency GaAs cells should be possible. Note that a lifetime value is also shown for GaAs grown on Ge as a point of reference, and that all TRPL data reported here were obtained from DH structures that were uniformly doped n-type to 1.1×10^{17} cm^{-3}.

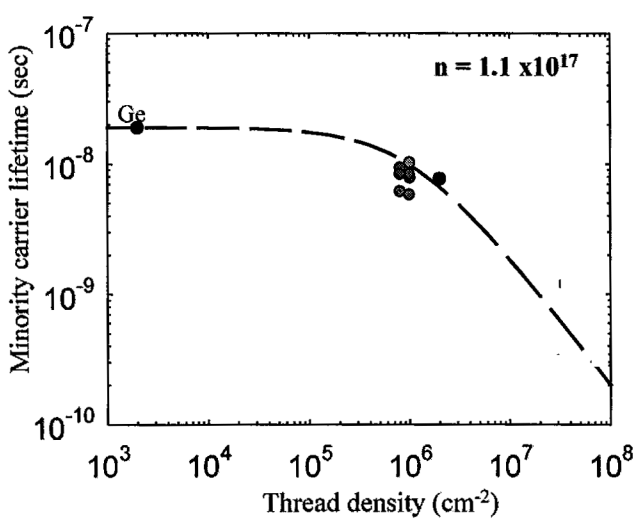

Figure 3. Bulk minority carrier lifetimes measured from a set of AlGaAs/GaAs/AlGaAs DH structures by TRPL plotted with the theoretically expected lifetime dependence on threading dislocation density. [after 2]

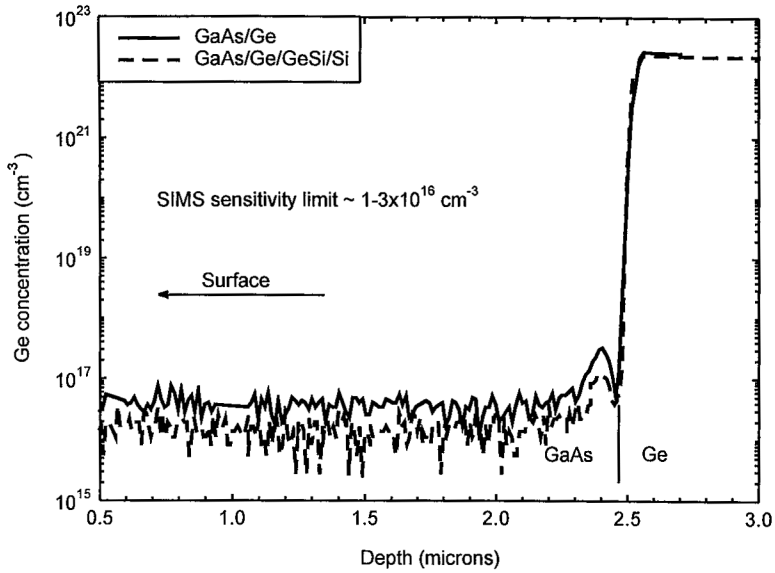

Figure 4(a). Ge SIMS profiles in GaAs grown on Ge/GeSi/Si and Ge substrates.

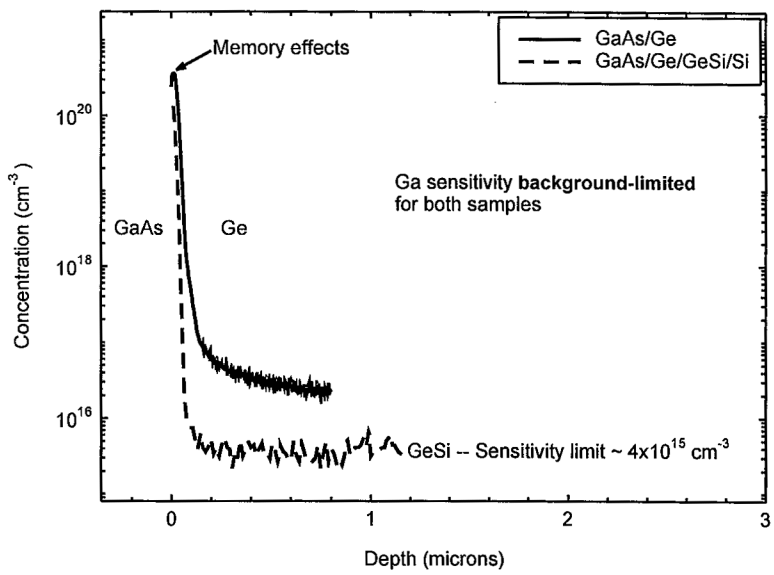

Figure 4(b). SIMS profiles showing negligible Ga penetration into the Ge/GeSi/Si and Ge substrates after 2.5 μm of GaAs MBE growth on each substrate.

3.2. GaAs/Ge Interface Diffusion for MBE-Grown GaAs on Ge/GeSi/Si Substrates

While the electronic quality (i.e. lifetime and diffusion length) of the GaAs material grown on the Ge/GeSi/Si buffer is perhaps the most important aspect for photovoltaic performance, it is also necessary to determine whether the minimal 0.1 μm GaAs buffer discussed above is appropriate from the viewpoint of autodoping. This is an important issue for GaAs grown on a Ge terminated substrate since the high growth temperatures of conventional epitaxy (especially MOCVD) can cause cross diffusion of As, Ga and Ge at the GaAs/Ge interface, generating high background doping over many microns, and even type conversion. In previous work on GaAs growth on Ge wafers by MBE, we demonstrated the successful minimization of such diffusion to negligible levels using an optimum interface nucleation procedure, which includes a low temperature MEE nucleation step, that is maintained even after complete cell growth and processing under typical conditions.[9-11] Here, we repeat these experiments for GaAs grown on Ge/GeSi/Si substrates to investigate whether the residual TDD or the presence of the crosshatch morphology has an effect on atomic diffusion at the GaAs/Ge interface.

Figures 4a, 4b and 4c show the SIMS atomic concentration profiles obtained for Ge in GaAs, Ga in Ge, and As in Ge, for a 2 μm thick GaAs layer grown on the Ge/GeSi/Si substrates. For comparison, SIMS profiles are also shown for GaAs grown on Ge wafers under identical growth conditions. In all cases, GaAs growth was initiated by the MEE step and the 2.5 μm thick GaAs layer was grown at a substrate temperature of 620 C. As can be seen from figure 4, there is negligible diffusion across the interface boundary for all cases on either substrate. It is interesting to note that while the profiles for Ge in GaAs and Ga in Ge appear to be identical for either substrate (the only difference in figures 4a and 4b between the substrates is the lower detection limit for the SIMS measurements made on the GaAs/Ge/GeSi/Si structures), there is actually less As diffusion into the Ge cap of the GeSi/Si substrate than for the Ge wafer. The reason for this is not known and warrants additional investigation. These are very encouraging results since they confirm that the 0.1 μm GaAs buffer is more than sufficient to protect an overlying III-V cell from diffusion and autodoping effects. Moreover, the lack of detectable Ga or As diffusion into the Ge/GeSi/Si substrate indicates that complete control of the subsequent cell polarity (p on n versus n on p) is possible.

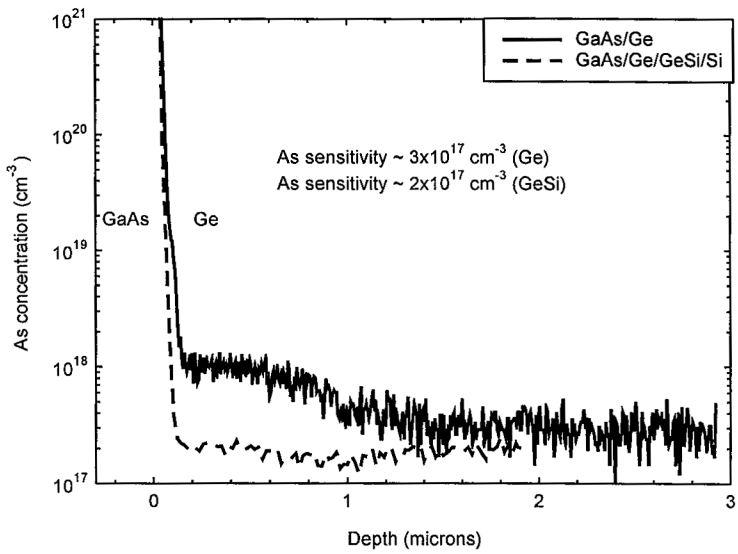

Figure 4(c). SIMS profiles showing minimal As penetration into the Ge/GeSi/Si and Ge substrates after 2.5 μm of GaAs MBE growth on each substrate.

3.3. GaAs Diode and Preliminary Solar Cell Characteristics on Ge/GeSi/Si

P^+n AlGaAs/GaAs heteroface cell structures were grown on the Ge/GeSi/Si substrates, and were fabricated into test diodes and solar cells for preliminary device analysis. All devices were grown using a 0.1 μm GaAs buffer as discussed above. Identical structures were also grown on both GaAs and Ge substrates in order to obtain a preliminary comparison of device characteristics as a function of substrate material and mismatch. Figure 5 shows forward and reverse bias dark I-V characteristics for 1 mm diameter diodes on each substrate. As seen, the I-V curves are almost identical, with turn-on voltages of ~ 1 V for all cases, and identical reverse leakage currents out to at least –2 volts. The most noticeable difference between the diodes is a slightly increased series resistance in forward bias for GaAs/Ge and GaAs/Ge/GeSi/Si as compared to the GaAs/GaAs diode. We attribute this to a higher back contact resistance for our ohmic contact process to the group IV substrates. The identical turn-on voltages and reverse leakage currents are significant, since this is where any negative effect of the residual TDD for the Ge/GeSi/Si substrates would be expected to manifest itself in the form of a shunt path that would lower the diode turn on voltage and increase the reverse leakage current. The fact that with a TDD = 1×10^6 cm^{-2} , the 1 mm diameter diode covers ~ 7,800 threading dislocations and yet these diodes yield very similar characteristics to the GaAs/Ge and GaAs/GaAs diodes, suggest that shunt currents in a completed, properly processed GaAs cell on Ge/GeSi/Si should not be significantly impacted by threading dislocations at our current threading dislocation density. We have recently begun to fabricate GaAs solar cells on Ge and Ge/GeSi/Si substrates. Figure 6 shows a comparison of the external quantum efficiency (EQE) responses of our first cells fabricated on Ge/GeSi/Si substrates, along with an EQE curve for a GaAs cell grown on a Ge wafer. At this time, no anti-reflection coatings were applied and the AlGaAs window layer (85% Al) was conservatively thick at 50 nm. The comparison indicates that the carrier collection efficiency is virtually identical for GaAs cells on either substrate. Hence, the high lifetime observed in the GaAs DH structures discussed earlier is replicated in the cell growth and maintained during the entire cell fabrication process. This is even more significant if one considers that only a 0.1 μm GaAs buffer was used between the cell layers and the substrate, demonstrating the robustness of our interface nucleation and MBE growth procedures. At this time, we have not yet completed a final cell with an optimum fabrication process. However, at the current

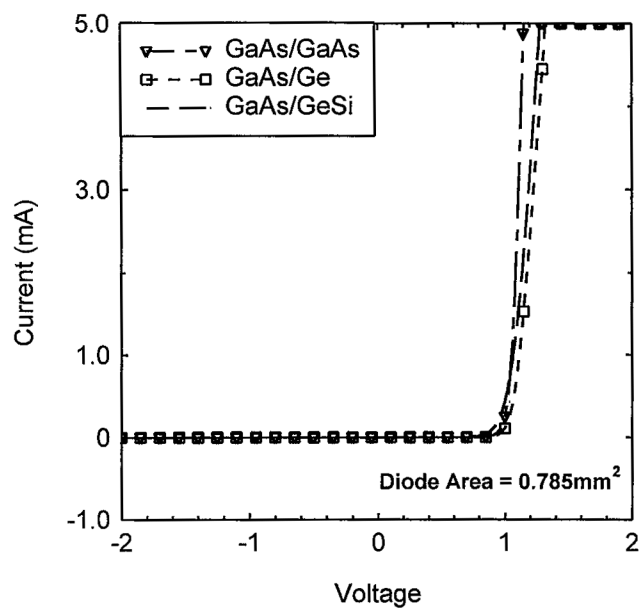

Figure 5. Comparison of dark I-V characteristics for AlGaAs/GaAs test diodes grown on GaAs, Ge and Ge/GeSi/Si substrates.

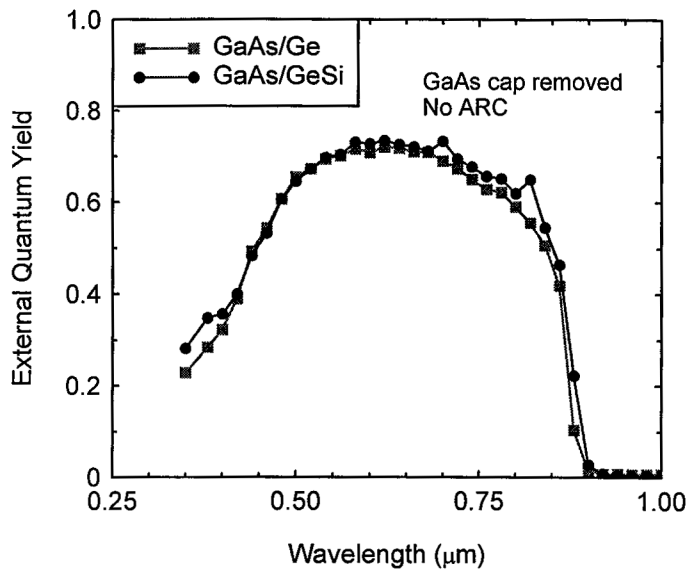

Figure 6. External quantum efficiency measurements for single junction GaAs cells grown on Ge and Ge/GeSi/Si substrates indicating the similar minority carrier collection efficiency for each.

stage of processing our first cells, an AM0 Jsc = 24.0 mA/cm^2 with a Voc = 0.95 V has been achieved prior to the application of an anti-reflection coating. This compares favorably to a completed ~ 20% AM0 MBE-grown GaAs single junction cell on Ge, which at the same stage of processing, yielded a Jsc = 24.5 mA/cm^2 and a Voc = 0.99 V.

4. Conclusions

The material and device properties of GaAs grown on low defect density Ge/GeSi/Si substrates were investigated for potential applications in space III-V solar cell technology. Record high minority carrier lifetimes in excess of 10 ns were demonstrated for GaAs on Si, which resulted from the combined use of high quality graded GeSi buffer layers coupled with careful GaAs/Ge interface nucleation. It was shown that the high material quality was maintained for GaAs buffer layer thickness as low as 0.1 μm. Moreover, the MBE nucleation conditions resulted in a negligibly small atomic interdiffusion at the GaAs/Ge interface that was at or below the SIMS detection limits on either side of the interface. The material results translated into excellent device characteristics, with nearly identical dark I-V characteristics being obtained for GaAs diodes grown on GaAs, Ge and Ge/GeSi/Si substrates in both forward and reverse bias regimes. Preliminary cell results are extremely promising, with virtually identical EQE responses for GaAs cells grown on Ge and Ge/GeSi/Si substrates that indicates long diffusion lengths and high collection efficiencies are maintained in the GaAs cell, even to within 0.1 μm of the Ge/GeSi/Si substrate. These results hold great promise for future demonstration of high efficiency III-V cells on Si via heteroepitaxy and group IV graded buffer technology.

5. References

1. T. Soga, M. Kawai, K. Otsuka, T. Jimbo, and M. Umeno, Proc. 2nd World Conf. on Photovoltaic Solar Energy Conversion, 3733 (1998).
2. M. Yamaguchi, J. Mater. Res. **6**, 376 (1991).
3. R.K. Ahrenkiel, M.M. Al-Jassim, B. Keyes, D. Dunlavy, K.M. Jones, S.M. Vernon, and T.M. Dixon, J. Electrochem. Soc. **137**, 996 (1990).
4. R. Venkatasubramanian, M.L. Timmons, J.B. Posthill, B.M. Keyes, and R.K. Ahrenkiel, J. Cryst. Growth **107**, 489 (1991).
5. A. Freundlich, M. Leroux, J.C. Grenet, A. Leycuras, G. Neu, and C. Verie, Proc. 8th Eur. Comm. Photovoltaic Solar Energy Conf., 1522 (1988).
6. M.T. Currie, S.B. Samavedam, T.A. Langdo, C.W. Leitz and E.A. Fitzgerald, Appl. Phys. Lett. 72, 1718 (1998).
7. J.A. Carlin, J.J. Boeckl, S.A. Ringel, C.W. Leitz, M.T. Currie, E.A. Fitzgerald and B.M. Keyes, conf. rec., Elecron. Mat. Conf. Santa Barbara, CA (1999).
8. R.M. Sieg, J.A. Carlin, J.J. Boeckl, S.A. Ringel, M.T. Currie, S.M. Ting, T.A. Langdo, G. Taraschi, E.A. Fitzgerald and B.M. Keyes, Appl. Phys. Lett. 73, 3111 (1998).
9. R.M. Sieg, S.A. Ringel, S.M. Ting, E.A. Fitzgerald and R.N. Sacks, J. Electron. Mater. 27, 900 (1998).
10. R.M. Sieg, S.A. Ringel, S.M. Ting and E.A. Fitzgerald, Proc. 26th IEEE Photovolt. Spec. Conf., 793 (1997).
11. R.M. Sieg, S.A. Ringel, S.M. Ting, S.B. Samavedam, M. Currie, T.A. Langdo and E.A. Fitzgerald, J. Vac. Sci. Technol. B16, 1471 (1998).

n/p/n Tunnel Junction InGaAs Monolithic Interconnected Module (MIM)

David M. Wilt
NASA Glenn Research Center
Cleveland, OH

Christopher S. Murray
Bechtel Bettis Inc.
West Mifflin, PA

Navid S. Fatemi
Emcore Inc.
Albuquerque, NM

Victor Weizer
Essential Research, Inc.
Cleveland, OH

Abstract

The Monolithic Interconnected Module (MIM), originally introduced at the First NREL thermophotovoltaic (TPV) conference, consists of low-bandgap indium gallium arsenide (InGaAs) photovoltaic devices, series interconnected on a common semi-insulating indium phosphide (InP) substrate. An infrared reflector is deposited on the back surface of the substrate to reflect photons, which were not absorbed in the first pass through the structure. The single largest optical loss in the current device occurs in the heavily doped p-type emitter. A new MIM design (pat. pend.) has been developed which flips the polarity of the conventional MIM cell (i.e., n/p rather than p/n), eliminating the need for the high conductivity p-type emitter. The p-type base of the cell is connected to the n-type lateral conduction layer through a thin InGaAs tunnel junction. 0.58 eV and 0.74 eV InGaAs devices have demonstrated reflectances above 90% for wavelengths beyond the bandgap (> 95% for unprocessed structures). Electrical measurements indicate minimal voltage drops across the tunnel junction (< 3 mV/junction under 1200K-blackbody illumination) and fill factors that are above 70% at current densities (J_{sc}) above 8 A/cm^2 for the 0.74eV devices.

Introduction

In thermophotovoltaic (TPV) energy conversion, a radiator is heated to incandescence and a photovoltaic device is placed in view of the radiator to convert the radiant energy into electrical energy. Research in TPV has been renewed recently due to the development of new radiator, filter and photovoltaic cell technologies [1]. Most current efforts in TPV research have concentrated on using front surface spectral control elements such as selective emitters (radiators) [2] or greybody radiators combined with plasma, dielectric or dipole filters [3,4] in order to improve system efficiency. The front-surface spectral control approach generally produces systems with lower power densities (W/cm^2).

A different approach involves the use of rear-surface spectral controls. Using this technique, the entire radiant output from the radiator is incident upon the photovoltaic (PV) device, thereby providing higher output power densities. Photons that the PV device is unable to convert pass through the cell structure and reflect off of a rear reflector back to the radiator for recuperation. Researchers have developed TPV cells that utilize low-doped substrates and reflective rear contacts to provide photon recuperation [5,6].

A Monolithic Interconnected Module, or MIM, TPV cell design, originated at NASA Lewis Research Center [3], takes a different approach to rear surface spectral control. The device consists of series-connected indium gallium arsenide (InGaAs) devices on a common, semi-insulating indium phosphide (InP) substrate. An infrared reflector is deposited on the rear surface of the InP substrate to reflect photons back toward the front surface of the cell. This provides a second pass opportunity for photons capable of being converted by the cell. In addition, long wavelength photons are returned to the radiator for "recuperation", improving the system efficiency.

The MIM design offers several advantages. Firstly, small series-connected cells provide high voltages and low currents, reducing I^2R losses. In addition, the small size of the cells permits an array to be comprised of series/parallel strings rather than a single series-connected string of larger cells. This should improve the reliability of the TPV module since the failure of a single cell would not debilitate the entire array. Also, the cell size and distribution may be easily adjusted to minimize the losses associated with radiator non-uniformity (i.e., variation in view factor, temperature, etc.).

The MIM design maximizes output power density since losses associated with front-surface spectral controls are eliminated. The lack of front surface spectral control represents a significant simplification of TPV system design and thermal management, as there are no filters to cool. In addition, the rear surface of the device is not electrically active, therefore the cell may be directly bonded to the substrate/heat sink without concern for electrical isolation. This greatly simplifies the array design and improves the thermal control of the cells. Lastly, photons that are weakly absorbed have the possibility of multiple passes through the cell structure. This feature is particularly important for lattice-mismatched devices, where poor minority carrier diffusion length can be partially offset by making the cell thin, forcing the carrier generation to occur closer to the p/n junction.

Although the MIM design has many beneficial attributes, there are limitations. The optical efficiency of the conventional MIM design [7] and interdigitated MIM design, developed by NREL [8], suffer from free carrier absorption losses in the heavily doped p-type InGaAs emitter. The trade off between optical and electrical losses forces a balance of emitter thickness and doping level. To date, most devices have utilized heavily doped ($>1x10^{19}$ cm^{-3}) emitters of approximately 0.1μm in thickness. This layer accounts for the majority of the optical losses in the MIM for unprocessed structures. Recent Monte Carlo photonic modeling, being presented at this conference [9], suggests that the processing techniques used can also have a significant affect on the amount of photons that can be recuperated at the radiator. Four areas of particular concern are the specular/diffuse reflectance of the BSR, light trapping due to surface features (i.e., isolation trenches), the reflectance of the electrical metallization at the metal semiconductor interface, and IR absorption in the anti-reflective coatings.

Cell Description

In order to optimize the optical efficiency of the MIM device, it is desirable to minimize the thickness of heavily doped p-type material. P-type material has exhibited ~20x higher free carrier absorption compared to similarly doped n-type InGaAs. Converting the photovoltaic device polarity from p on n (p/n) to n/p allows the use of n-type material for the emitter. In addition to reducing the optical losses, majority carriers in the n-type emitter have approximately 25x higher mobility than p-type material, leading to lower resistive and grid shadowing losses.

It is also desirable to use n-type material for the lateral conductor layer (LCL) in order to minimize electrical and optical losses. This layer conducts the collected carriers to the interconnect (in the case of the conventional MIM design) or to the closest back contact (in the case of the interdigitated MIM). The use of p-type material for this layer imposes significant optical and electrical losses. Therefore, we employ a thin InGaAs tunnel junction (TJ) to connect the p-type base to the n-type LCL. The complete device structure for 0.74eV InGaAs is shown in Figure 1. For use in lattice-mismatched InGaAs, a suitable buffer layer would be inserted between the substrate and the active device. The use of the n/p/n TJ MIM structure is applicable to both the conventional and interdigitated MIM configurations.

Tunnel Junction Development

Successful development of the tunnel junction (TJ) MIM requires the development of a thin, high conductance tunnel junction. Test TJ devices were fabricated using a low-pressure Organo-Metallic Vapor Phase Epitaxy (OMVPE) reactor. Tunnel junction structures were produced using both 0.74 eV and 0.60 eV InGaAs. 150 μm diameter test diodes were fabricated for characterization with TJ layer thickness' from 200Å to 1 μm. Figure 2 shows the I-V characteristic of a 0.74 eV InGaAs tunnel junction with 0.5 μm layers. The TJ demonstrated

excellent resistivity (R_{max} = 3.7x10^{-4} ohm-cm^2) and current carrying capability (J_p = 1900 A/cm^2). Tunnel junctions fabricated from 0.6 eV InGaAs also demonstrated excellent I-V characteristics (J_p = 700 A/cm^2, R_{max} = 5.6x10^{-4} ohm-cm^2). Perfect 0.6 eV devices (QE = 1) fabricated using these tunnel junctions could expect to lose 2.4 mV/junction under a 1200K blackbody illumination (view factor = 1).

0.1 µm n++ InGaAs	Contact Layer
0.1 µm n+ InP	Front Window
0.3 µm n+ InGaAs	Emitter
1.5 µm p InGaAs	Base
0.1 µm p+ InP	Back Window
500Å p++ InGaAs	Tunnel Junction
500Å n++ InGaAs	
0.1 µm n+ InP	Etch Stop
1.0 µm n++ InGaAs	Lateral Conduction Layer
InP:Fe	Substrate

Figure 1 - Test structure for 0.74 eV InGaAs n/p/n TJ MIM (conventional).

Next, tunnel junction test structures were grown with the appropriate over-layer thickness of InGaAs. This was done so that the effects of an extended temperature soak on dopant distribution within the tunnel junction were appropriately considered. Three test n/p 0.74 eV cell structures were fabricated and tested. Two of them n/p/n structures that had tunnel junctions with layer thickness of 1000Å and 500Å. The third was a control structure, which had the same n/p cell layers, but deposited on a p-type substrate. The I-V tests of these structures were identical, indicating that the tunnel junction was not negatively impacting the device operation.

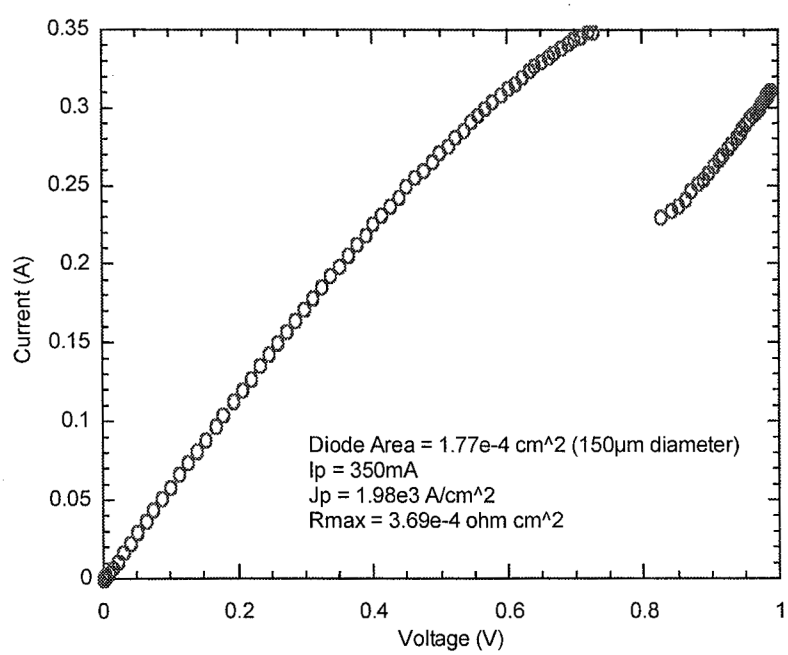

Figure 2 - I-V characteristic of tunnel junction fabricated from 0.74 eV InGaAs.

0.74 eV n/p/n MIM Characterization

Verification of the n/p/n cell concept was accomplished by fabricating the test device structure shown in figure 1. Figure 3 shows the variation of fill factor with current density for this structure compared to several conventional p/n structures. The n/p/n device was processed using our standard contact design for p/n MIM devices. All of the devices had the same LCL thickness and doping level. The differences in FF can be attributed to variations in the emitter type, doping level and thickness.

Measurements were taken in a flash simulator with the cell at room temperature. As shown in the data, there is very little reduction in FF as the current density is increased for the n/p/n device, whereas the p/n structures all show significant degradation with increasing intensity. For operation of this device under a 1200K radiator, it is expected that the current density would not exceed 0.9 A/cm^2. Thus, there is ample opportunity to reduce layer thickness', doping levels and grid coverage without sacrificing electrical performance. This optimization was not performed because the bandgap of this device is too high for the illumination source of interest.

Figure 4 shows the reflectance measurements for an n/p/n device structure (NAS468 - not a processed device) similar to that shown in Figure 1. The principle differences are a reduction in the thickness of the tunnel junction layers from 500 Å to 100 Å, and a reduction in the LCL thickness from 1.0 μm to 0.15 μm. There is also a reduction in the doping level of the LCL from 3x10^{19} cm^{-3} to the low 10^{18} cm^{-3} range. This structure is suitable for fabrication into an interdigitated MIM device.

For comparison, a conventional p/n MIM structure reflectance is also plotted (NAS445). There are two features of significance in this figure, the elimination of the plasma absorption peaks at approximately 6 μm and 9 μm and the increase in reflectance in the short wavelength region. The elimination of the plasma peaks can be attributed to the interdigitated cell design with it's lower doped LCL. This feature is not specific to the n/p/n design. The increase in the short wavelength reflectance from ~0.88 to ~0.95 is a direct result of the elimination of the heavily doped p-type emitter through the n/p/n design.

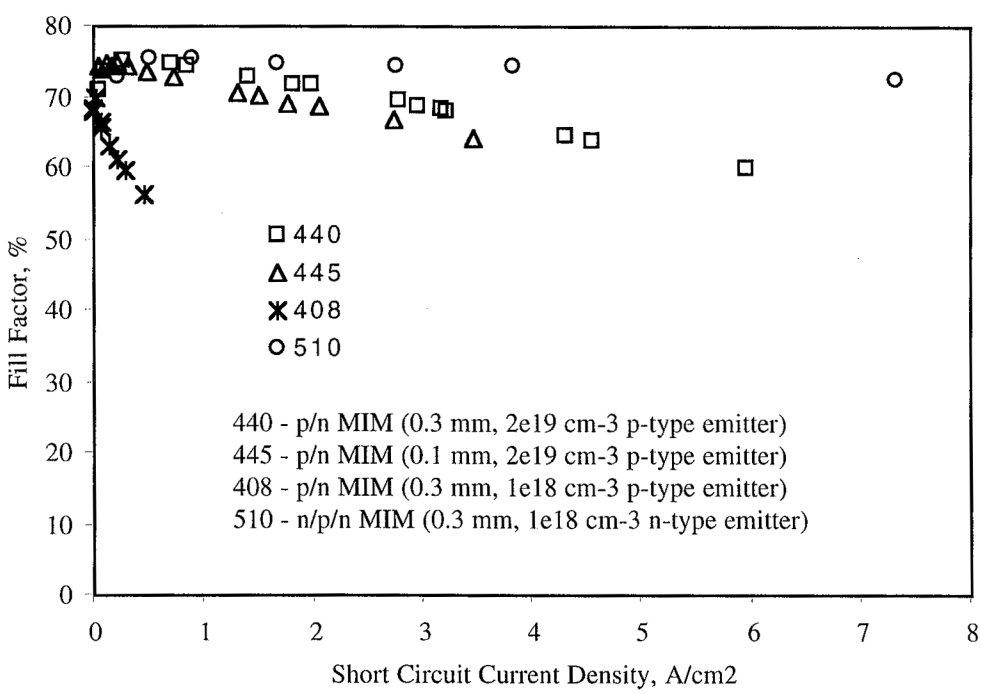

Figure 3 - Variation in fill factor with current density for the n/p/n 0.74 eV MIM with the architecture shown in Figure 1.

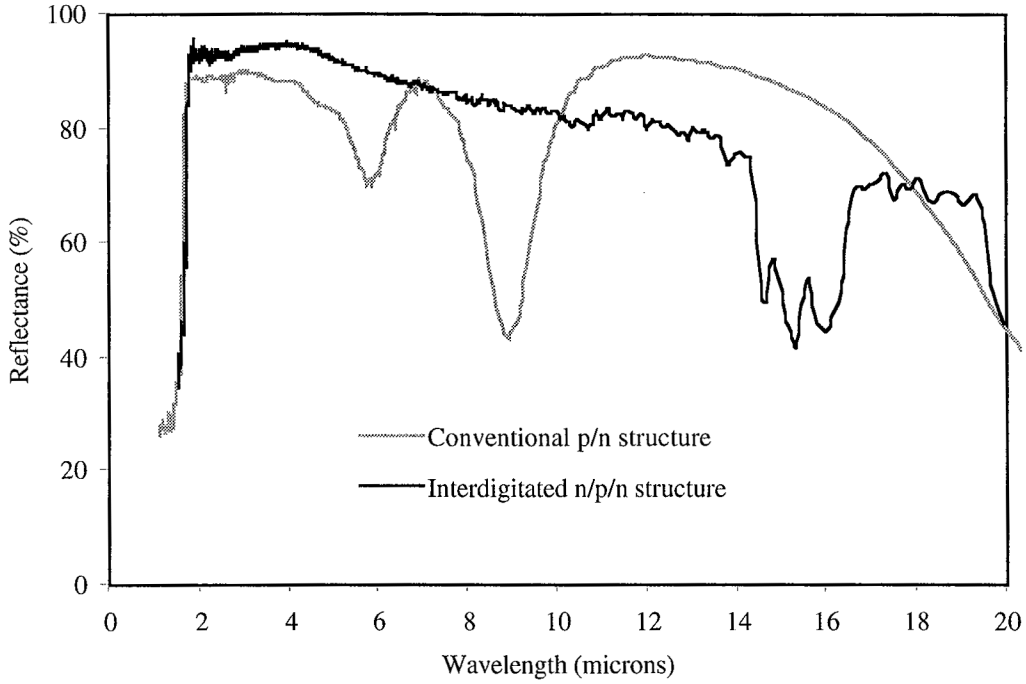

Figure 4. Reflectance comparison of conventional p/n and interdigitated n/p/n structures.

Table 1 lists the short circuit current density, FF, spectral utilization (Fu) and the product of FF and Fu for the five (5) devices previously described under a variety of blackbody temperatures. The spectral utilization is a ratio of the useful energy absorbed in the emitter and base divided by the total energy absorbed. Also shown is the change in the FF*Fu product compared to the n/p/n interdigitated device design. The FF*Fu product captures both the electrical efficiency and optical efficiency of the MIM device in a single, evenly weighted factor. The p/n conventional MIM devices all show significantly lower combined efficiency, particularly at the lower emitter temperatures. The difference between the conventional and interdigitated n/p/n MIM is smaller, particularly at the higher temperature emitters.

0.6 eV n/p/n Cell Development

As was stated previously, the goal of this development effort is to develop a low bandgap MIM device suitable for operation with a low temperature radiator. After demonstration of the 0.74 eV n/p/n device, efforts shifted to development of 0.6 eV and lower bandgap n/p/n structures. These device structures, being lattice mismatched to the InP substrate, use a proprietary buffer layer which has demonstrated reverse saturation current densities of $<4\times10^{-7}$ A/cm^2 in p/n 0.6 eV MIMs.

Several test structures have been fabricated, both conventional and interdigitated n/p/n MIM designs. These devices have utilized 200Å tunnel junction layers. The data from these structures indicates that resistance in the thin tunnel junction does not limit the FF. A typical interdigitated n/p/n design is shown in Figure 5.

MIM	Trad °F	Jsc A/cm^2	FF	Fu	Fu*FF	% Change Relative to 468
440, 0.3 _m, 2x10 ^{19} p-type emitter p/n MIM	1750	0.68	0.746	0.197	0.147	-97%
	2250	2.85	0.69	0.389	0.268	-65%
	2500	4.65	0.63	0.472	0.297	-64%
445, 0.1 _m, 2x10 ^{19} p-type emitter p/n MIM	1750	0.68	0.731	0.232	0.17	-71%
	2250	2.85	0.67	0.443	0.297	-49%
	2500	4.65	0.6	0.526	0.316	-54%
408, 0.3 _m, 1x10 ^{18} p-type emitter p/n MIM	1750	0.68	0.5	0.272	0.136	-13%
	2250	2.85	-	0.499	-	
	2500	4.65	-	0.583	-	
510, 0.3 _m, 1x10 ^{18} n-type emitter n/p/n MIM	1750	0.68	0.754	0.296	0.223	-30%
	2250	2.85	0.744	0.508	0.378	-17%
	2500	4.65	0.740	0.584	0.432	-13%
468, 0.1 _m, 1x10 ^{18} n-type emitter n/p/n MIM	1750	0.68	0.754	0.384	0.29	-
	2250	2.85	0.744	0.596	0.443	-
	2500	4.65	0.740	0.660	0.488	-

Table 1 - Summary of Fill Factor and Spectral Utilization Data for 0.74 eV p/n and n/p/n MIMs.

Figure 6 compares the reflectance test data from a 0.58 eV n/p/n structure, as grown material (as shown in Figure 5), to a processed cell from the same material. The cell includes a dual layer anti-reflective (AR) coating (ZnS/MgF) and Cr/Au contact metallization. The structure has a gold BSR layer only. The data demonstrates a reduction in the reflectance of the cell beyond the InGaAs bandedge. This difference is due to several factors. The Cr adhesion layer for the front surface metallization reduces the reflectance in the 2-4 μm region. Overlying that is an absorption peak near 3 μm associated with water absorbed in the AR coating. The difference in reflectance shrinks to insignificant levels by approximately 7 μm.

0.1µm n++ InGaAs	Contact Layer
500Å n+ InPAs	Front Window
0.3µm n+ InGaAs	Emitter
3.0µm p InGaAs	Base
500Å p+ InPAs	Back Window
200Å p++ InGaAs	Tunnel Junction
200Å n++ InGaAs	
500Å n+ InPAs	Etch Stop
0.3µm n+ InGaAs	Lateral Conduction Layer
InPAs	Buffer Layer
InP:Fe	Substrate

Figure 5 - low bandgap (< 0.74 eV) n/p/n interdigitated MIM test structure

Figure 7 shows the external quantum efficiency for the 0.58 eV n/p/n interdigitated MIM device described above. The device has a dual layer AR coating and Au back surface reflector. This data is from the first attempt at producing this device. Continued development is expected to improve this encouraging start.

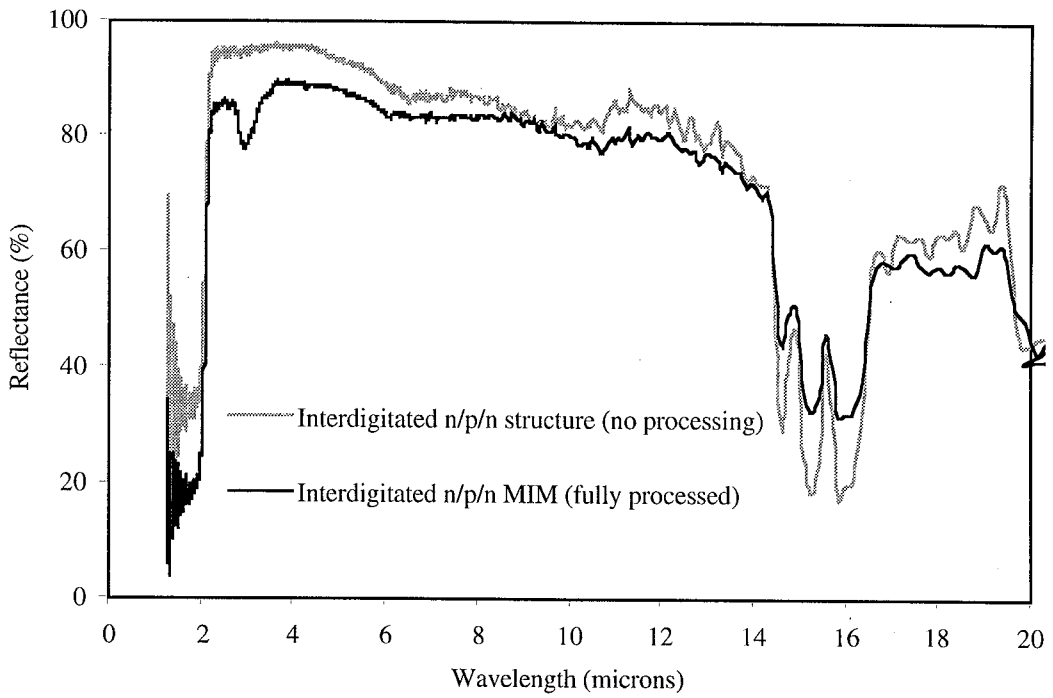

Figure 6 - Comparison of 0.58 eV Cell and Structure Reflectance.

Conclusion

A new tunnel junction MIM design has been described (pat. pend.) which offers the potential for higher power density and efficiency compared to p/n conventional or interdigitated MIM devices. Both 0.74eV conventional and 0.58eV interdigitated n/p/n MIM devices have been demonstrated with encouraging results. The 0.58eV and 0.74 eV InGaAs devices have demonstrated reflectance's above 90% for wavelengths beyond the bandgap (> 95% for unprocessed structures).

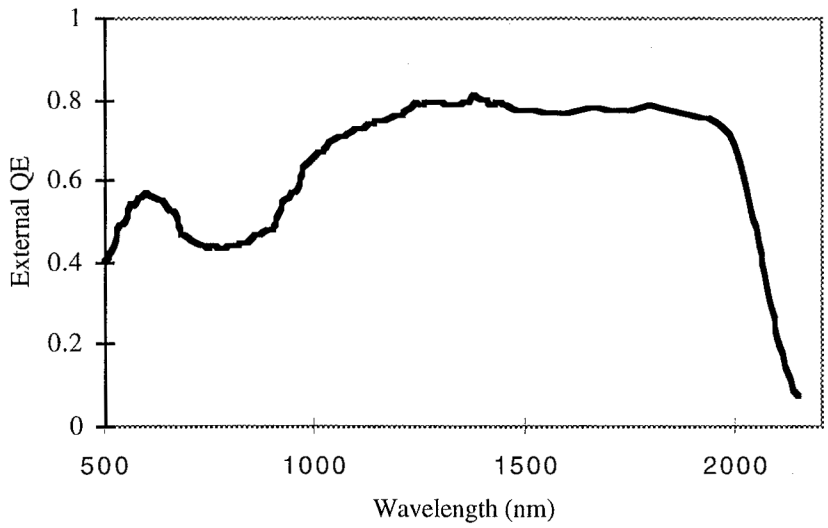

Figure 7 - External QE of 0.58 eV n/p/n Interdigitated MIM

Electrical measurements indicate minimal voltage drops across the tunnel junction (< 3 mV/junction under 1200K-blackbody illumination) and fill factors that are above 70% out to current densities (J_{sc}) above 8 A/cm^2 for 0.74eV devices. The emphasis now shifts to optimizing the devices through reduction in tunnel junction layer thickness' (currently at 200 angstroms), active cell region optimization, grid design and new processing strategies. Care must be exercised in designing a fabrication process since these processes can seriously degrade the optical efficiency of the completed MIM device.

References

1) Proc. First NREL Conf. On TPV Generation of Electricity, AIP 321, 1994.
2) D.L. Chubb, "Reappraisal of Solid Selective Emitters," Proc. 21st IEEE Photovoltaic Specialists Conference, pp. 1326-1342, 1990.
3) D.M. Wilt, et al., "InGaAs PV Device Development for TPV Power Systems," 1st NREL Conf. On TPV Gen. Of Elect, pp. 210, AIP 321, 1994.
4) W.E. Horne, et al., "IR Filters for TPV Convertor Modules", Proc. 2nd NREL Conf. On TPV Gen. Of Elect, pp. 35, AIP 358, 1995.
5) G.W. Charache, et al., "Thermophotovoltaic Devices Utilizing Back Surface Reflector for Spectral Control," Proc. 2nd NREL Conf. On TPV Gen. Of Elect, pp. 191, AIP 358, 1995.
6) P.A. Iles and C.L. Chu, "TPV Cells with High BSR," Proc. 2nd NREL Conf. On TPV Gen. Of Elect, pp. 361, AIP 358, 1995.
7) D.M. Wilt, et al., "Electrical and Optical Performance Characteristics of 0.74eV p/n InGaAs Monolithic Interconnected Modules," Proc. 3rd NREL Conf. On TPV Gen. Of Elect, pp. 237, AIP 401, 1997.
8) J.S. Ward, et al., "A Novel Design for Monolithically Interconnected Modules (MIMs) for Thermophotovoltaic

Power Conversion," Proc. 3rd NREL Conf. On TPV Gen. Of Elect, pp. 227, AIP 401, 1997.
9) C.T. Ballinger, et al., "Monte Carlo Analysis of a MIMs Device with a Back Surface Reflector," Proc. 4th NREL Conf. On TPV Gen. Of Elect, AIP, 1998.

NOVEL PASSIVATING/ANTIREFLECTIVE COATINGS FOR SPACE SOLAR CELLS.

Mircea Faur*, Maria Faur*, S.G. Bailey**, D.J. Flood**, H.M. Faur*, C.G. Mateescu*, S.A. Alterovitz**, D. Scheiman***, P. P. Jenkins***, D.J.Brinker**, J.D. Warner**, and D.R. Wheeler**

*SPECMAT, Inc., c/o NASA GRC, 27390 Lusandra Circle, North Olmsted OH 44070
Phone: 216-433-2293; Fax: 216-433-6106; E-mail: MFaur@specmat.com

**NASA Glenn Research Center, 21000 Brookpark Rd., Cleveland OH 44135

***Ohio Aerospace Institute, Brookpark, OH 44142

ABSTRACT

We are developing a novel process to grow passivating/antireflective (AR) coatings for terrestrial and space solar cells. Our approach involves a Room Temperature Wet Chemical Growth (RTWCG) process, which was pioneered, and is under development at SPECMAT, Inc., under a Reimbursable Space Act Agreement with NASA Glenn Research Center.

The RTWCG passivating/AR coatings with graded index of refraction are applied in one easy step on finished (bare) cells. The RTWCG coatings grown on planar, textured and porous Si, as well as on poly-Si, $CuInSe_2$, and III-V substrates, show excellent uniformity irrespective of surface topography, crystal orientation, size and shape.

In this paper we present some preliminary results of the RTWCG coatings on Si and III-V substrates that show very good potential for use as a passivation/AR coating for space solar cell applications. Compared to coatings grown using conventional techniques, the RTWCG coatings have the potential to reduce reflection losses and improve current collection near the illuminated surface of space solar cells, while reducing the fabrication costs.

1. INTRODUCTION

The main reasons for low current collection efficiency near the illuminated surface for many conventional planar and textured terrestrial and space solar cells are: increased reflection, and damaged AR coating/emitter interface.

The anti-reflection (AR) coating is one of the most important part of a solar cell design. It allows a substantial reduction in the amount of reflected light [e.g. 1,2]. A proper single layer AR coating (e.g. MgF_2, SiO_2, SiO, TiO_2 and Ta_2O_5) can reduce reflection to about 10%, averaged over the 0.4 μm to 1.1 μm wavelength range. A double layer AR coating can reduce reflection to 3 - 5% on the average. For uncoated Si cells, a textured front surface, e.g. regularly spaced pyramids or porous silicon (PS), can lower the reflection coefficient to 12 - 18%. For textured surfaces with well designed single or double layer AR coatings, such as ZnS/MgF_2,TiO_2/MgF_2, and TiO_2/Al_2O_3 [3, 4] the reflection is on average down to 2 – 5%. Due to the difficulty of depositing uniform AR coatings on textured surfaces, especially on fine pyramid-coated surfaces, some cell manufacturers are choosing not to use any AR coating. The penalty they pay is up to 10% loss in efficiency along with surface stability problems.

Depositing/growing uniform AR coatings on PS is even more difficult using conventional techniques due to the nanometer-sized features of the PS structure: uniform, stable coatings have yet to be produced.

For simple cell structures, conventional AR coating layers are deposited directly onto the emitter surface usually by physical vapor deposition and spin-on techniques. This approach destroys the stoichiometry at the cell's front surface which by increasing the scattering at the grain boundaries, decreases the AR coating/semiconductor interface transparency and introduces additional defects at the emitter/AR coating interface. For Si cells the above problems can be partially addressed by using a combination of a thin passivating oxide (e.g. SiO_2, SiN_x) and a single or double layer AR coating. Using this approach contributed, for example, to the improvement of the PERL one sun terrestrial Si solar cells efficiency, at the University of South Wales [5] and at SunPower [6], to about 24% (AM 1.5, 25°C), and 20.3% (AM0), respectively.

This approach has been proposed for III-V solar cells as well. For instance, for InP solar cells we suggested a three layer AR coating structure, namely $In(PO_3)_3/ZnS/MgF_2$ [7]. In this case the thin $In(PO_3)_3$ layer (about 10 nm thick) is grown by chemical oxidation of the emitter surface. Its role is to passivate the surface, and to prevent damage to the emitter surface during the evaporation of the second layer. Technological difficulties due to insufficient development and probable cost constraints, have prevented the use of the three layer AR coating structures for both commercial terrestrial and space solar cells.

We are proposing a novel RTWCG technique to grow a passivation/AR coating with graded index of refraction on terrestrial and space solar cells. The RTWCG process of SiO-based coatings was pioneered [8], and is under development at SPECMAT, Inc., under a Reimbursable Space Act Agreement with NASA GRC.

At the 2nd World PVSEC Conference we demonstrated the effectiveness of using the RTWCG technique to grow stable passivating oxide layers on planar silicon cell surfaces [9]. In this paper, we demonstrate the potential of using this simple-to-apply RTWCG process to grow cost effective passivating/AR coatings for space solar cell applications. The next sections will provide some preliminary results on the use of RTWCG coatings for Si and GaAs solar cells.

2. RESULTS AND DISCUSSION

2.1 RTWCG Process

SPECMAT's approach involves a Room Temperature Wet Chemical Growth (RTWCG) process of SiOX thin films on large area silicon (Si) substrates. The composition of the RTWCG oxide layers is $Si_xO_yX_z$, (SiOX) where x is from 0.9 to 1.1, y is from 0.9 to 1.9 and z is from 0.01 to 0.2. X is usually carbon (C), and nitrogen (N) of various concentrations depending on the redox system being used [8].

To date, most of the work has been concentrated on the growth and characterization of SiOX coatings on Si. However, the RTWCG process has also been tried in order to grow dielectric coatings on other than Si substrates such as GaAs, GaP, AlGaAs, and $CuInSe_2$ thin films. These latter coatings aren't however fully characterized yet.

The SPECMAT proprietary, patent pending process comprises soaking the substrates into the growth solution. The process utilizes a mixture of inexpensive liquid precursors along with homogeneous

catalysts that increase the growth rate. Non-invasive acidic or alkaline solutions are added to the growth system in order to adjust the pH.

The composition of the RTWCG coatings and their growth rate is dependent on a number of factors such as the nature of the precursors and additives, pH, the catalyst, and to a lesser extent on the type of the substrate (crystalline orientation, and doping type). The RTWCG rate of SiOX coatings on single crystal Si surfaces is from 2 nm/minute to up to 64 nm/minute, depending on the composition of the liquid-phase growth system.

2.2 Surface Passivation

2.2.1 Si Surfaces

Without any need for post-growth annealing, the RTWCG process produces SiOX coatings that are chemically stable and passivate well the Si surfaces. However, both the chemical stability and passivating properties of these SiOX coatings depend on their chemical composition which is in turn dependent on the chemical system being used.

Within our work, the best candidate for surface passivation is the Si-O-C-N coating grown in the BS:B19 chemical system. An example of an XPS profile of a RTWCG Si-O-C-N coating is shown in Fig.1. The relatively large surface C concentration and the relatively large N interface concentration explain the excellent chemical stability, and good surface passivation capability of this oxide.

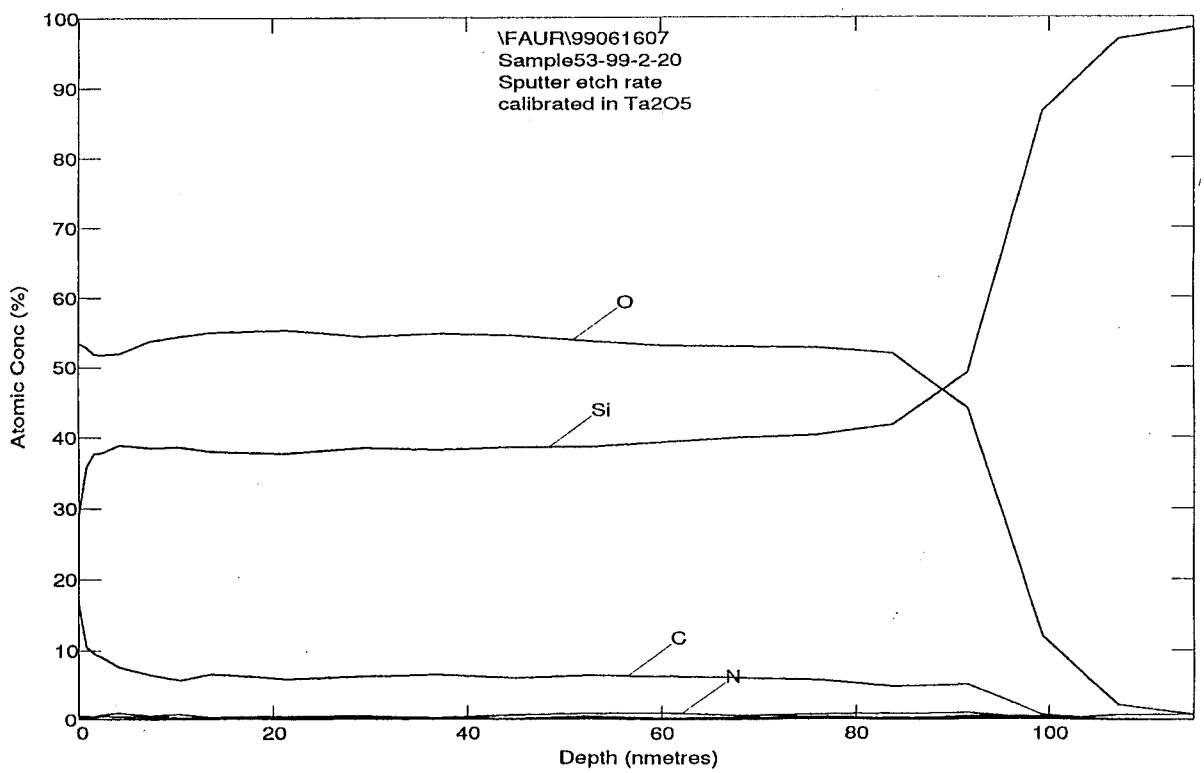

Fig. 1 XPS depth profile of a RTWCG Si-O-C-N coating (about 110 nm thick), grown on p-type Si in the BS:B19 chemical system. Growth time:3 minutes.

No in-depth investigation of the RTWCG SiOX/Si interface has been performed thus far. However, the good passivating properties of the RTWCG Si-O-C-N coatings on Si substrates are suggested by an analysis of coated devices, e.g. the improvements in the performance parameters of VMJ Si cells, as can be seen in paragraph 2.4.2.

2.2.2 GaAs Surfaces

Very uniform RTWCG coatings have been grown on both n- and p-type GaAs substrates in several chemical systems. These coatings haven't been fully characterized yet. In order to show the potential of these as-grown coatings for surface passivation of GaAs, we present some recent room temperature photoluminescence (PL) data acquired on 5 n-GaAs samples, prior to and after the growth of RTWCG coatings. The peak intensity of the PL spectra are compared in Fig.2. The coatings were grown in five different chemical systems. For consistency, the growth time (2 to 10 minutes) has been adjusted such that the oxide thickness has about the same thickness, as estimated from our calibrated color code (e.g. about 100 nm - dark blue). The data for two of the coatings, 115-99-2, and 116-99-5, show that the PLI increases noticeably compared to the uncoated surfaces. This data show that the room temperature oxide can be grown without damaging the GaAs surface and may provide some electronic surface passivation of the GaAs surface.

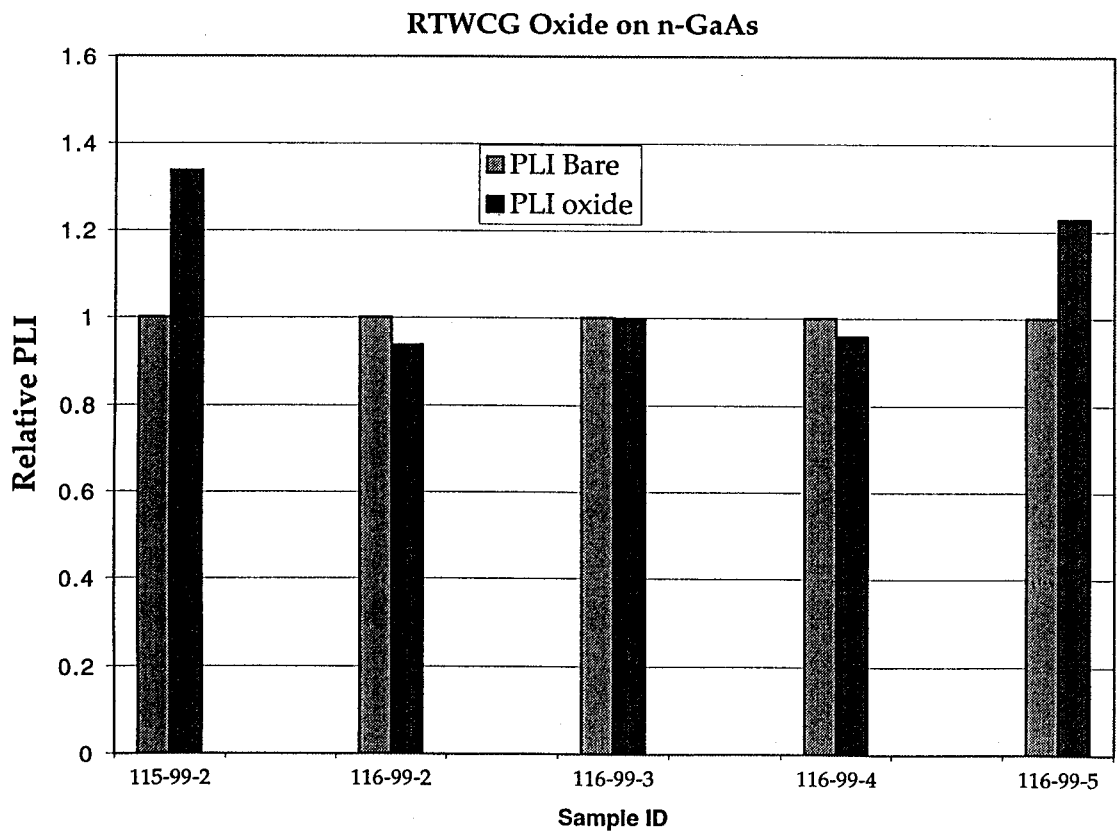

Fig. 2. Relative PLI of RTWCG coated vs. bare surfaces for coatings grown on n-GaAs substrates in five chemical systems.

2.3 Optical Properties of RTWCG Coatings

2.3.1 Reflectance

Low reflectivity coatings require a multi-layered structure that has an increasing index of refraction relative to the depth of the coating layer to the underlying Si surface. We have previously demonstrated that on Si substrates, by varying the chemistry of the chemical system it is possible to grow Si-O-X AR coatings with graded "n" [9]. Ellipsometric analysis of various RTWCG SiO-based coatings have shown that the index of refraction for the C-rich top layer is smaller than that of SiO_2; it is between that of SiO_2 and SiO for the mid-layer, and between that of SiO and that of the underlying Si substrate for the Si-rich interfacial layer.

2.3.1.1 Si substrates

For bare Si, the loss of incident light amounts to about 42% at long wavelengths (1.1 μm), has a minimum of 37% at 1 μm and rises to about 54% at short wavelengths (0.4 μm) (see Fig. 3-a). A proper single layer AR coating can reduce the reflection to about 10%, averaged over this wavelength range, and a double layer AR coating can reduce it to around 3% on the average. The RTWCG Si-O-C-N coating in Fig.3-b, grown in similar conditions as the coating in Fig.2, has a reflectivity of below 1.8% from 600 nm to 950 nm and below 3.3% on the average from 400 nm to 1100 nm.

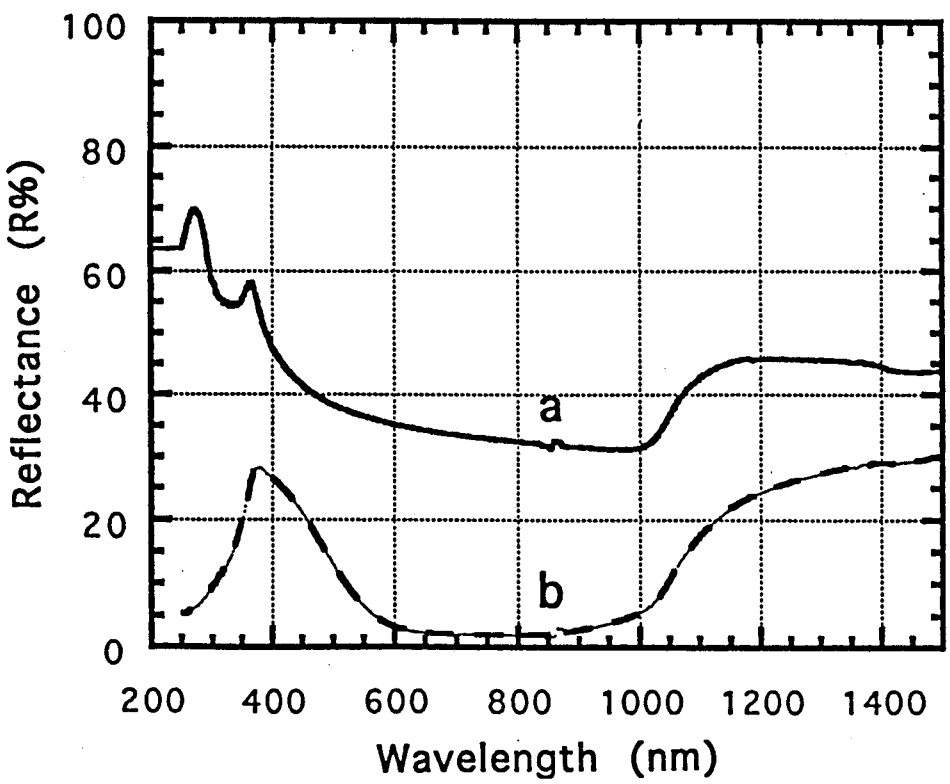

Fig. 3 Reflectivity of: (a) bare and (b) RTWCG Si-O-C-N (about 0.1 μm thick) coated p-Si wafer.

Recent work was directed toward increasing the reflectivity of the unusable red part of the solar spectrum, while maintaining the low reflectivity in the visible. The first good results, such as shown in Fig. 4, show an increase in red reflectivity to over 60%. However, an increase in the red reflectivity also increases the blue reflectivity. More work is still necessary to find a way of increasing the red reflectivity while maintaining the visible reflectivity and lowering the blue reflectivity.

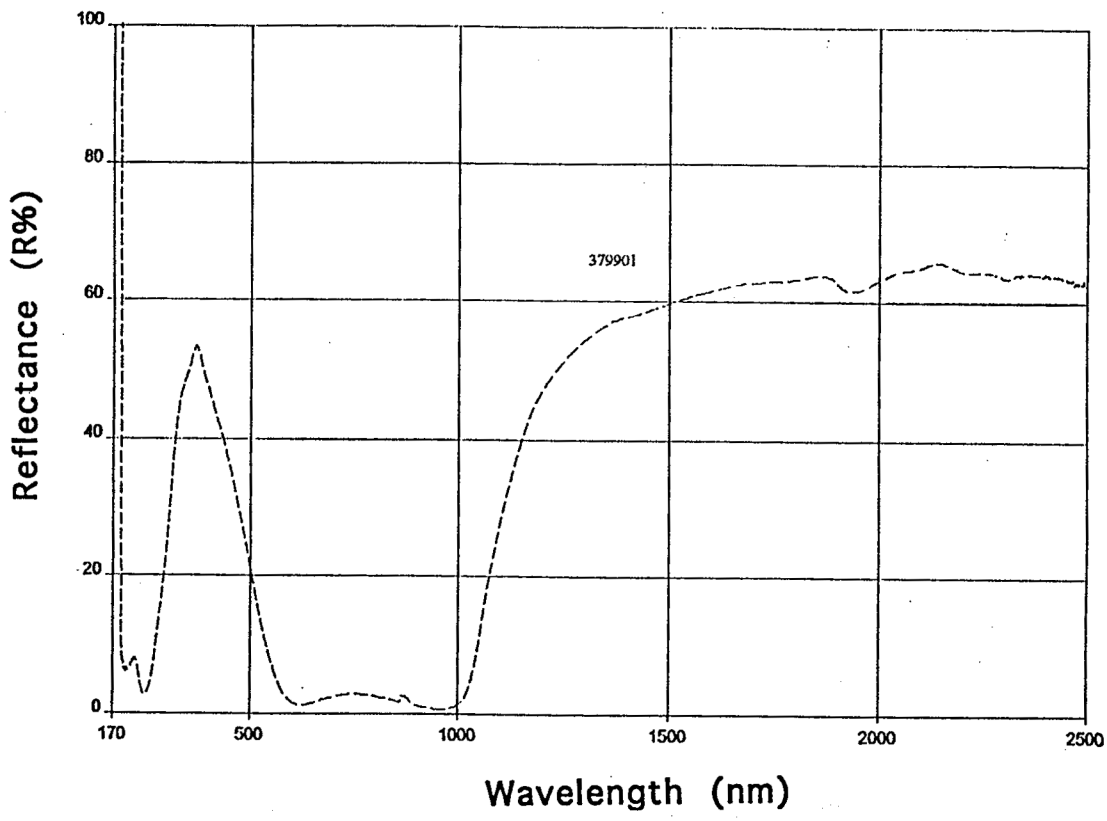

Fig. 4 Reflectivity of a RTWCG Si-O-C-N (about 120 nm thick) coated p-Si wafer.

2.3.1.2 GaAs Substrates

As mentioned above, the work on RTWCG dielectric coatings on GaAs has only recently been started. The chemical system hasn't yet been optimized either for the passivating nor for the optical properties of the oxide. The reflectivity plots of the five n-GaAs RTWCG coated substrates as compared to the reflectivity of a bare substrate in Fig. 2 are shown in Fig 5. As seen, the 115-99-2 and 116-99-5 coatings might qualify the RTWCG oxide for the dual use as a passivation/AR coating for GaAs. Still more work is necessary to further decrease the reflectivity of the RTWCG coated GaAs, while increasing its passivation capabilities.

2.3.2 Transmittance

Qualitative Transmittance studies of the RTWCG coatings have thus far been conducted only on Si-O-C-N coatings grown on Si substrates. The transparency of these coatings was qualitatively evaluated from the values of the extinction coefficient (k) derived from ellipsometric measurements in

the 400 nm to 800 nm wavelengths range. Si-O-C-N coatings similar to those in Fig.3 have "k" values that are at least 3 times lower than that of a thermal SiO_2 of a similar thickness (about 100 nm) grown in dry oxygen at 1000°C on a similar Si substrate.

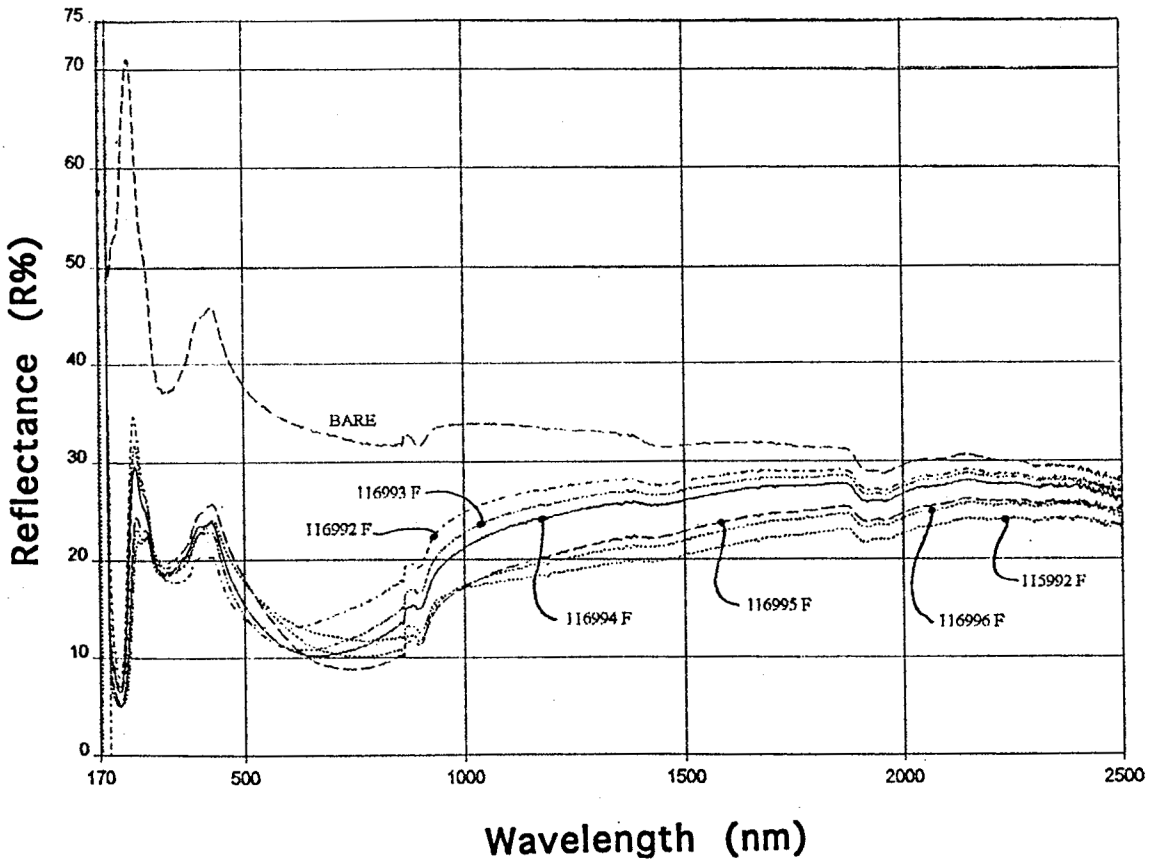

Fig. 5 Reflectivity plots of RTWCG coated and bare n-GaAs samples in Fig. 2.

2.4 Si Solar Cells

2.4.1 Planar n/p Si Solar Cells

For our preliminary study we used several dozen readily available planar 2x2 cm^2 n/p Si solar cells with an AM0, 25°C efficiency of about 7% (bare cells). RTWCG Si-O-C-N coatings were grown in 3 to 5 minutes using several chemical systems. The performance parameters were measured under AM0, 25°C conditions at NASA GRC prior to and after the coatings. A selection of the performance parameters can be found in Table 1. After the RTWCG SiOX coating, the only treatment the cells received prior to the AM0 measurements was a DI water rinse and followed by N_2 drying.

The increase of AM0 efficiency of coated relative to bare cells was from 32% to up to 37.3%. For these cells the gain in efficiency was mostly due to corresponding gains in I_{SC}, with little or no change in V_{OC} or FF values. The explanation might have to do with the fact that the surfaces of the 15 year old planar cells could not be properly cleaned prior to growing the Si-O-C-N coating, without removing some or all front grid fingers. For instance, a one minute dip in 5% HF solution started to remove some of the front grid fingers. To avoid this, prior to the AM0 measurements, the front surfaces

of the bare cells were only cleaned with organics, followed by a few seconds dip into a 2% HF bath. This surface treatment may have left some contaminated native oxide on the surface. This might explain the apparent lack of surface passivation provided by the Si-O-C-N coating. The same coating applied to the surfaces of a Si VMJ cell which was properly cleaned prior to the oxide growth, clearly passivated well the Si surfaces. In any event, although the passivating quality of this room temperature Si-O-C-N coating is certainly not yet as good as those of CVD grown Si_3N_4 or thermal SiO_2 thin films, for which sensitive gains in V_{oc} have been reported, the optical properties of this simple to apply coating is as good or better than those of conventional two layer AR coatings.

Table 1. AM0, 25°C performance parameters of selected 2x2 cm^2 n/p Si cells prior to (bare) and after RTWCG of Si-O-C-N coatings. Growth time: 3 to 5 minutes; Oxide thickness: 95 to 120 nm; No annealing.

Cell	Bare Cell				Coat. Cell				
	I_{sc} (mA)	V_{oc} (mV)	FF (%)	η (%)	I_{sc} (mA)	V_{oc} (mV)	FF (%)	η (%)	(η,ox-η,bare)/η,bare (%)
Cox 12	89.2	583.9	75.2	7.16	118.9	579.5	75.0	9.45	32.0
Cox 27	88.0	573.1	70.4	6.49	117.2	572.7	71.8	8.81	35.7
Cox 23	88.3	570.9	68.7	6.33	119.9	571.0	69.5	8.69	37.3
Cox 12	After 16 months in air in a chemistry laboratory environment				121.8	573.7	72.6	9.27	
Cox 23					119.8	566.6	67.2	8.35	

In Table 1 are also shown the AM0 performances of two of the cells, Cox 12 and Cox 23, after being stored in air in a chemistry laboratory for about 16 months. As can be seen, there are no significant differences in the I_{sc}, while the small drop in V_{oc} and FF are to be expected due to humidity and contaminants adsorbed on the surfaces.

2.4.2 VMJ Si Solar Cells.

For this preliminary experiment some early Vertical MultiJunction (VMJ) Si solar cells [10] were provided to us by PhotoVolt, Inc. The biggest contributor to efficiency loss in the Si VMJ cell structure is the fact that its illuminated surfaces, back surfaces, and two edge surfaces uncovered by metallization are high recombination surfaces with exposed junctions that are difficult to passivate. Also, traditional AR coatings are difficult to form on these cells because of temperature constraints and because of their configuration with the four exposed surfaces.

The RTWCG process grows SiOX coatings simultaneously on the four exposed surfaces. The performances on both sides of a Si VMJ cell were measured by PhotoVolt, Inc. after cleaning and etching the bare "PV4-14-x" cell. The performances were measured after growing a RTWCG Si-O-C-N coating for three minutes, and subsequently for additional 0.5 minutes each, during the second and third growth.

After the initial 3 minutes growth the thickness of the Si-O-C-N oxide was evaluated from the color code at about 100 nm. The second and third growth each successively added about 15 nm to the thickness. After each growth, the only treatment the cell received was a rinsing in DI water and nitrogen drying.

After the measurements, following the second growth, the cell was measured again after two minutes under light. This slightly increased the cell performance parameters is due to a partial removal of humidity from the cell surfaces. The drop in performances after the third growth is consistent with reflectivity plots, such as in Figs. 2 and 3, which were acquired on Si-O-C-N coated Si surfaces with an oxide of about 110 nm thick. After the third growth, annealing the cell for 10 minutes in air increased all performance parameters noticeably. However, after a subsequent overnight annealing under similar conditions as above, no further change in the cell parameters was noticed. The short time illumination and the annealing experiments, might indicate the fact that the Si-O-C-N oxide is only hydrated at the surface. The aproximately 15 hour annealing in air at 100°C gives a qualitative indication of the good stability of this room temperature oxide.

Table 2. Performance parameters of a bare and RTWCG Si-O-C-N coated VMJ Si concentrator cell (PV4 –14 -x). PhotoVolt, Inc. performed the initial etching and surface cleaning of the bare cell surfaces, as well as the performance parameter measurements.

		Etched and Cleaned	1st Growth 3 min	2nd Growth		3rd Growth	
				Additional ½ min Growth	After 2 min Under Light	Additional ½ min Growth	10 min Annealing In Air At 100* C
Side 1	V_{oc} (V)	8.786	9.883	9.641	9.659	9.239	9.272
	I_{sc} (mA)	0.17	0.34	0.30	0.31	0.26	0.33
	FF	.5365	0.6073	0.579	0.579	0.5575	0.5570
	P_p (mW)	0.779	2.022	1.66	1.712	1.321	1.699
Side 2	V_{oc} (V)	8.699	9.672	9.951	9.909	9.363	9.575
	I_{sc} (mA)	0.15	0.30	0.33	0.35	0.28	0.35
	FF	.5139	0.5934	0.6005	0.6029	0.5660	0.5775
	P_p (mW)	0.672	1.741	1.989	2.095	1.494	1.919

Note that the V_{OC} and FF values for the VMJ cells increase significantly after the coating. These values, and the large increase in Isc, after coating, cannot be explained simply by a reduction of optical-type losses. They offer a clear indication that surface passivation plays an essential role in increasing the maximum power (Pp) as much as three fold compared to that recorded for the bare cell.

3. CONCLUSIONS

In summary, our results show that using the novel RTWCG process of SiOX coatings, has the potential of improving the efficiency and stability of space Si solar cells. The process can lower the cost of conventional passivating/AR coating structures, and simplify the Si or GaAs solar cell structures. The

RTWCG process is very attractive for a one-step growth of surface passivation/AR coatings on Si and III-V solar cells because these coatings:

- passivate the surfaces;
- their reflectivity is equal to or lower than that of well designed double layers AR coatings;
- are transparent in the spectrum of interest;
- are physically hard, and non-straining on the substrate;
- should have good stability with respect to factors such as heat, humidity, prolonged exposure to UV light, and resistant to high fluences of energetic electrons and protons.

The RTWCG process for growing SiO-based coatings, once fully developed, should be an attractive alternative to conventional passivation/AR coating techniques for the Si, GaAs and other space solar cell manufacturers because the novel process:

- eliminates several concomitant photoresist, etching and surface passivation steps, thus reducing cell fabrication costs;
- after the RTWCG process, the contacts are readily solderable since the coating is not covering the metallization;
- the growth process should be applicable to any surface, irrespective of surface topography, crystal orientation, size and shape;
- has high output due to large growth rates;
- has reduced capital and materials costs;

References

[1] B.O. Seraphin and A.B. Meinel, "Optical Properties of Solids, North -Holland, Amsterdam, 1974.

[2] A. Lique, "Solar Cells and Optics for Photovoltaics," Adam Hilger ed., Bristol-Philadelphia, 1989.

[3] B.L. Sopori and R.A. Prior, "Design of Antireflective Coatings for Textured Silicon Solar Cells," Solar Cells 8, 1983, p.249.

[4] Mircea Faur, Maria Faur, S.G. Bailey, D.J. Flood, D.J. Brinker, D.R. Wheeler, S.A. Alterovitz, D. Scheiman, G. Mateescu, J. Faulk, C Goradia, and M. Goradia, "Front Surface Engineering of High Efficiency Si Solar Cells and Ge TPV Cells," 26th IEEE PVSC, 1997, Anaheim, CA, p.847.

[5] J. Zhao, A. Wang, E. Abbaspour-Sani, F. Yun, M. A. Green, and D.L. King, "Improved Efficiency Silicon Solar Cell Module," IEEE Electron Devices Letters, 18, p. 48, 1997.

[6] G.T. Crotty, P.J. Verlinden, M. Cudzinovic, R.M. Swanson and R.A. Crane, "18.3% Efficient Silicon Solar Cells for Space Applications," 26th IEEE PVSC, 1997, Anaheim, CA, p.1035.

[7] Mircea Faur, Maria Faur, S.G. Bailey, D.J. Flood, D.J. Brinker, S.A. Alterovitz, D.R. Wheeler, G. Mateescu, C. Goradia, and M. Goradia, "Passivating Window/First Layer AR Coating for Space Solar Cells," 15th SPRAT Conference, 1997, Cleveland, Ohio.

[8] Maria Faur, Mircea Faur, D.J. Flood, S.G. Bailey, and H.M. Faur, "Room Temperature Wet Chemical Growth Process of SiO Based Oxides on Silicon," Patent Pending, February 1998.

[9] Maria Faur, Mircea Faur, S.G. Bailey, D.J. Flood, D.J. Brinker, H.M. Faur, S.A. Alterovitz, D.R. Wheeler, and D.L. Boyd, "Room Temperature Wet Chemical Growth of Passivating/Antireflection Coatings for Si-Based Solar Cells," 2nd World Conference and Exhibition on Photovoltaic Energy Conversion, 1998, Vienna, Austria, p. 1574

[10] B.L. Sater, "Recent Results on High Intensity Silicon VMJ Cell," Proc. at the American Solar Energy Conference, Minnesota, July 15-20, 1995.

ADVANCED FLEXIBLE SOLAR ARRAY PROGRAM [1,2]

Peter V. Meyers and Leon Fabick
ITN Energy Systems
Wheat Ridge, CO 80033

Kitt C. Reinhardt
Air Force Research Laboratory
Kirtland AFB, NM 87117-5773

William N. Shafarman
Institute of Energy Conversion
University of Delaware
Newark, DE 19716

1 OVERVIEW

Increased specific power (W/kg) solar arrays are needed for next-generation military and commercial spacecraft to enable greater payload mass and power budgets, and possibly more satellites per launch. Researchers from ITN Energy Systems (ITN), Global Solar Energy (GSE) and the Institute of Energy Conversion (IEC), with support from the Air Force Research Laboratory (AFRL), are developing polycrystalline thin-film multijunction photovoltaic (PV) modules for space power applications under the Advanced Flexible Solar Array (AFSA) program. Complementary support is provided by the Advanced Technology Program for Premium Power directed toward tandem PV devices. Two-terminal, two-junction tandem PV cells deposited onto lightweight flexible substrates have good potential to achieve PV blanket efficiency of 15% (AM0) and specific power greater than 1000 W/kg. Combined with ITN's innovative solar array pantograph deployment / support structure, the specific power goal for the flexible thin-film solar array under development is 150 W/kg.

2 NEED FOR HIGH SPECIFIC POWER – APPLICATIONS

Spacecraft today have greater power requirements than ever before. More and more electrical energy is needed to run increasingly complicated and diversified military and commercial satellites that are assigned longer and more complex missions in space. Demands include increased power on orbit with lower power system mass and cost. Increased power system efficiency results in reduced power system mass which is important for increasing satellite payload mass and power budgets. Thin-film solar photovoltaic technology has recently enabled the design of next-generation ultra-lightweight satellite solar arrays that promise to be lighter and cheaper than state-of-the-art (SOTA) rigid solar arrays by a factor of 3X and 10X, respectively. Ultra-lightweight, flexible, low-cost solar

[1] Partially funded by contract F29601-98-C0220 (AFRL/Space Vehicles Directorate) and cooperative agreement 70NANB8H4070 (ATP/NIST).

[2] Additional research contributors to this work include Scot Albright, Don Morgan, Lawrence Woods, Robert Wendt, Scott Wiedeman and Jeff Britt of Global Solar Energy (GSE), Tucson, AZ and Greg Kleen of ITN,.

array blankets can be used in a variety of space solar array structure configurations. Possible military satellites that will benefit from the increased specific power and reduced cost of thin-film solar arrays include the Air Force Research Laboratory's TechSat 21 smallsat constellation program for low-earth-orbit space-based radar, and the Air Force Space-Based Infra-Red System (SBIRS-Low) satellite program. Possible commercial applications for the flexible thin-film solar arrays include telecommunications satellites being developed by Teledesic and Matra Marconi. Terrestrial applications include satellite earth telecommunications stations; personal communications cellular (PCS) microcell sites, and distributed remote power for portions of the world not connected to the utility grid.

Flexible thin-film PV (TFPV) has several important advantages over conventional rigid crystalline solar cells for use in space. Crystalline silicon solar cells have proven themselves to be efficient and reliable, however, compared to the potential of TFPV, crystalline silicon-based arrays are heavy, expensive, and subject to space radiation damage. Multijunction III-V-based crystalline solar cells such as the 3-junction $GaInP_2$/GaAs/Ge cell design have demonstrated AM0 efficiencies of ~30%, however, they are even heavier and more expensive than silicon cells. The specific power goal for next-generation flexible TFPV-based solar arrays is 150-200 W/kg compared to ~70 W/kg for today's rigid solar arrays using 22-25% efficient III-V solar cells. The cost goal for the flexible TFPV solar arrays is $100-200/W compared to greater than $1000/W for today's crystalline-based solar arrays.

In addition, high-efficiency multijunction TFPV will have a significant "dual use" impact on the terrestrial PV market. Dollars per watt ($/W) costs of multijunction TFPV are expected to be similar to competing single-junction TFPV modules, but the increased conversion efficiency of the multijunction devices will reduce total system costs by reducing the required panel collection area (number of PV modules) for constant power. Demand for terrrestrial photovoltaics is growing – PV system sales for the first half of 1999 were 25% greater than for the same period in 1998 (when annual sales exceeded 150 MW). Increased market volume is due in part to lower prices; wholesale prices for large modules in large quantities are falling toward $3/W. Nonetheless, PV market growth is constrained by costs, weight and rigidity of existing PV technology – all of which constraints will be reduced by TFPV.

3 Technical Approach

3.1 Monolithic Tandem PV Cells

Multijunction devices consist of layers of PV absorbers wherein each absorber is tuned to a certain portion of the incident solar spectrum. As shown schematically in Figure 1 the top cell absorbs the higher energy photons and converts them to electrical power in the same way as would a single junction device. In the case of a multijunction device, however, long wavelength (sub-bandgap) light transmitted by the top cell is converted to electrical power by the bottom cell which has a narrow bandgap absorber layer. Proper choice of the bandgaps of the upper and lower semiconductor absorber layers produces device conversion efficiency of the multijunction device which is greater than could be achieved with a single absorber device.

As shown in Figure 1, two terminal devices are constrained by the fact that the electrical current must be the same in the top and bottom cells. Optimization of two terminal device efficiency requires that both cells have the same optimum current density. Mismatch of the optimum current density between top and bottom cells leads to significantly reduced efficiency, thus cell design - including selection of appropriate bandgaps - is critical to achieving high efficiency in two terminal devices. In operation, however, monolithically interconnected two terminal multijunctions behave as a single power source and therefore are compatible with existing, single-junction electrical load circuitry.

Although multijunction tandem cells based on single crystalline materials are well known, lightweight, flexible, two-terminal, thin film, polycrystalline multijunction PV devices have not been developed. AFSA's goal is to develop 15% efficient polycrystalline Cu-chalcopyrite alloy - based monolithic two terminal tandem photovoltaic modules on lightweight, flexible polyimide substrates. AFSA addresses the limitations of existing technology by:

- use of multijunctions to increase efficiency over state-of-the-art single junction thin film PV
- replacing bulky (~100-500 μm) crystalline materials with thin (~5-10 μm) polycrystalline films
- replacing piece-by-piece wire interconnection with monolithic integration
- replacing fragile single crystals with flexible thin films
- use of high throughput manufacturing techniques to reduce costs

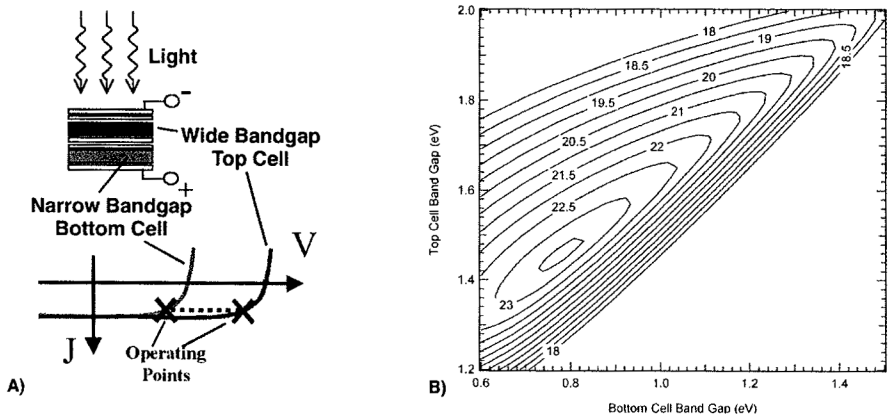

Figure 1 **Schematic representation of A) two terminal multijunction device and B) calculated AM0 power conversion efficiency as a function of the top and bottom cell energy band gaps. Device operation is constrained in that both cells in the two terminal multijunction devices must have the same current.**

As displayed in Figure 2, AFSA's proposed structure builds upon the single junction CIGS PV technology presently employed at GSE, thereby giving AFSA researchers unique insights into the technical issues involved in the manufacture of polycrystalline thin film PV on flexible web. Nonetheless, development of the proposed device is much more than a simple scale-up of existing technology. Technical objectives that must be achieved include demonstration of:

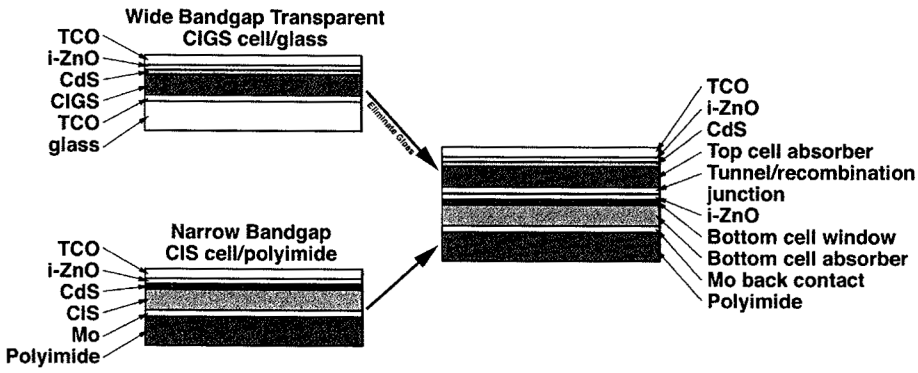

Figure 2 **AFSA's proposed two terminal monolithic tandem PV device structure. GSE currently produces single junction CIGS cells on a polyimide web in a manufacturing environment.**

- advanced wide bandgap and narrow bandgap Cu-chalcopyrite alloy absorber PV devices
- a transparent recombination / tunnel junction between the top and bottom cells, and
- processing which does not compromise the efficiency of either cell.

AFSA is a high risk, high payoff program. Achievement of program goals will result in significant advances over SOTA specific power coupled with significant reductions in array costs. AFSA has a goal of >1000 W/kg for PV blanket specific power. ITN is working with AFRL to develop a lightweight deployment / PV blanket support structure which is expected to result in a total array specific power greater than 150 W/kg.

3.2 Polycrystalline Cu-chalcopyrite thin films

ITN's approach is to employ Cu-chalcopyrites – $CuInSe_2$ and its alloys - as absorbers in both the wide bandgap top cell and the narrow bandgap bottom cell. As listed in Table 1, Cu-chalcopyrite alloys of In, Ga, Al, S and Se span the range of bandgaps from 1.04 to 3.5 eV. Furthermore, alloys of Cu-chalcopyrite compounds are generally single phase materials with bandgaps that depend monotonically on composition. An example showing the dependence of bandgap on alloy composition for the In, Ga, S and Se Cu-chalcopyrite system is displayed in Figure 3.

Table 1 Bandgaps of some copper chalcogenide semiconductors.

Copper Chalcogenide	Direct Bandgap (eV)
$CuInSe_2$	1.04
$CuGaSe_2$	1.70
$CuAlSe_2$	2.70
$CuInS_2$	1.55
$CuGaS_2$	2.42
$CuAlS_2$	3.50

AFSA's approach is to control absorber composition – and therefore bandgap – by co-evaporation with control of elemental fluxes in a steady state reactor which deposits film onto a moving web as shown schematically in Figure 4. ITN and GSE have developed and are continuing development of intelligent manufacturing technology[3] which utilizes advanced sensor technology combined with scientific models to achieve controlled film composition and electrical / optical properties of copper indium gallium diselenide films deposited onto 1000 ft polyimide web in a manufacturing environment at GSE's plant in Tucson. Intelligent manufacturing techniques will be required to achieve the precise control of bandgap necessary for fabrication and manufacturing of high efficiency monolithic tandem PV devices.

3.3 Major Technical Challenges

3.3.1 Development of high-efficiency wide bandgap (>1.6 eV) top cell with >85% sub-bandgap optical transmission

In order to achieve a high-efficiency, transparent top cell absorber, AFSA is exploring a wide range of Cu-chalcopyrite alloys. Earlier work with high-Ga $Cu(In,Ga)Se_2$ alloys[4] indicates that minority carrier diffusion length for alloys with Ga/[Ga+In] ratio >0.5 (Eg 1.3 eV) is significantly less than is observed with lower Ga-content alloys. AFSA is therefore exploring alternatives to high-Ga alloys. For example, other metals substituted for In result in a wider bandgap Cu-chalcopyrite alloys than would substitution of an equal molar concentration of Ga. As the high Ga substitution level itself may be partially responsible for the low minority carrier diffusion length, other alloys may result in a higher efficiency, wide bandgap cell.

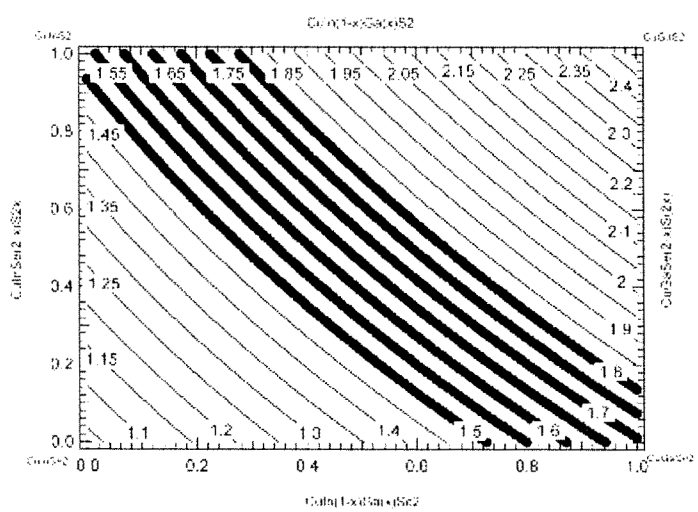

Figure 3 Bandgap of copper chalcopyrite alloys of In, Ga, S and Se. Compositions suitable for wide bandgap top cells are indicated by red.

---

[3] Work supported in part through "Vapor Phase Manufacturing of Flexible Thin-Film CIS Photovoltaics", DARPA agreement No. MDA972-95-3-0036

[4] J.E. Phillips and W.N. Shafarman, Proc. NCPV PV Prog. Rev., AIP Conf. Proc. 462, (1998) pp120-125.

4

As seen in Figure 3, substitution of sulfur for selenium in $Cu(In,Ga)(S,Se)_2$ alloys also enables fabrication of wide bandgap absorber layers with low Ga content. More generally, all sulfur chalcogenides have wider bandgaps than their selenium counterparts and researchers have begun to investigate use of sulfur to modify the bandgap of single junction PV devices. Experimentally sulfur has a higher vapor pressure than selenium's and options for appropriate modifications of existing thin film Cu-chalcopyrite deposition and processing conditions are underway.

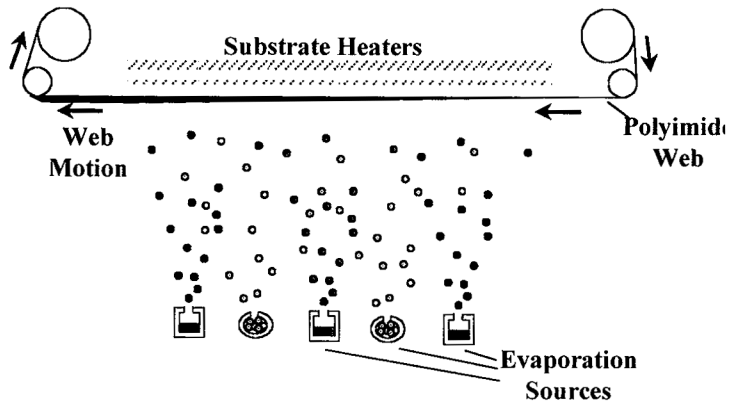

Figure 4 **Schematic representation of co-evaporation of copper chalocopyrite film onto a continuous web. Film composition is established through control of the flux of the individual elements.**

3.3.2 Development of a low-loss, optically transparent tunnel / recombination junction between the top and bottom cells

High efficiency tandem junctions require a low resistivity, transparent, chemically stable recombination junction to make the electrical and optical connection between the window layer of the narrow bandgap bottom cell and the absorber of the wide bandgap top cell. Specifically the interfacial layer must:

- have low electrical resistance,
- be optically transparent, and
- provide a chemical barrier to prevent interdiffusion or chemical reaction between the window layer below and the wide bandgap absorber above.

Electrically, the transparent layer does not need high conductivity because there will be no lateral current and the layer can be made sufficiently thin so that through-film resistance is negligible. However the junction must provide a low resistance tunnel / recombination path which enables holes from the valence band of the top cell absorber to combine with electrons from the conduction band of the bottom cell window. Note that the carriers combining across the interfacial layers are the majority carriers on their respective sides of the junction. Also note that, unlike recombination of photogenerated minority carriers, electron-hole recombination across the recombination junction is associated with a current flow through the junction.

Crystalline monolithic multijunction devices employ tunnel junctions. Tunnel junctions are formed by heavily doping the p-type and n-type crystals in the vicinity of the metallurgical interface between them. By making these layers degenerate, the depletion width in both crystals is thin enough for carriers to tunnel from one side to the other with minimal voltage drop. Heavy doping increases the sub-bandgap optical absorption of the materials, but in crystalline materials the junction can be made sufficiently thin that optical absorption is minimal. Thin, heavily doped layers are not practical in polycrystalline thin films, however, due in large measure to the high atomic diffusion coefficient that exists at grain boundaries.

An alternative approach suitable for polycrystalline films to providing the shorting path between the two cells is utilized in multijunction amorphous silicon solar cells. In this case the charge transport mechanism is by tunnel / recombination between nearly iso-energetic mid-gap states in a thin layer between two cells. The requirements for a good recombination junction are that it be thin, transparent, and with a high density of mid-gap defect states to provide recombination sites.

Chemical stability is another important feature of material utilized in the recombination / tunnel junction. Mo is the material of choice for single junction back contacts to polycrystalline Cu-chalcopyrite films in large part because Mo- a refractory metal - withstands the elevated temperature and Se-ambient associated with deposition of the Cu-chalcopyrite. Se_2 gas and other Se compounds are known to react strongly with most metals at temperatures above ~ 400°C. Oxides, including transparent conducting oxides (TCO's) are chemically inert relative to most metals and have the electrical and optical properties required of low resistance contacts. As shown below, AFSA researchers have shown that indium tin oxide (ITO) serves as a low resistance, transparent back contact to 1.2 eV $Cu(In,Ga)Se_2$. At this point, however, low resistance contacts have not been demonstrated to wider bandgap Cu-chalcopyrite alloys.

3.3.3 Development of an efficient and durable narrow bandgap bottom cell which withstands the deposition ambient of the wide bandgap top cell

Existing thin film CIS-alloy PV *devices* degrade dramatically when heated to temperatures far below those existing in the CIS-alloy *film* deposition ambient. Fabrication of a wide bandgap CIS-alloy top cell onto a narrow bandgap bottom cell requires that new device structures or fabrication processes be developed which enable retention of the electrical and optical properties of the bottom cell under conditions which are compatible with the fabrication of a high efficiency top cell.

Although heat and vacuum induced degradation of CIS-alloy PV devices have been confirmed, the mechanisms responsible for this degradation have not been established. Possible degradation mechanisms include: degradation of minority carrier diffusion length in the CIGS absorber; interdiffusion of the window and absorber layers resulting in reduced barrier height and/or increased interfacial carrier recombination; increased resistance at the CIGS/back contact; and solid-gas reactions which change the material properties of the CIGS absorber layer. Identification and quantification of the heat/vacuum-induced degradation mechanisms will suggest further strategies for minimization of this effect and could lead to design and fabrication of a durable narrow bandgap bottom cell that will be stable during the subsequent fabrication of the wide bandgap top cell.

An alternative approach is to develop processing procedures for fabrication of the wide bandgap top cell which do not result in degradation of the bottom cell. Approaches consistent with this strategy include 1) use of Na in the top cell CIS-alloy growth ambient and 2) use of techniques such as plasma assisted deposition which add non-thermal energy to atoms on the growing surface.

3.4 AFSA Status

3.4.1 Wide bandgap deposition system

Wide bandgap top cell development centers on development of equipment and procedures to deposit and characterize wide bandgap Cu-chalcopyrite alloys. AFSA researchers at ITN and GSE have designed and built a wide bandgap deposition system, as seen in Figure 5, which is capable of depositing copper chalocopyrite alloys onto both moving web and moving rigid glass substrates. AFSA researchers, including those at IEC, are developing equipment and procedures for deposition of wide bandgap Cu-chalcopyrite alloys. Steady progress is being made, although devices fabricated to this point have been fabricated with $Cu(In,Ga)Se_2$ absorber layers.

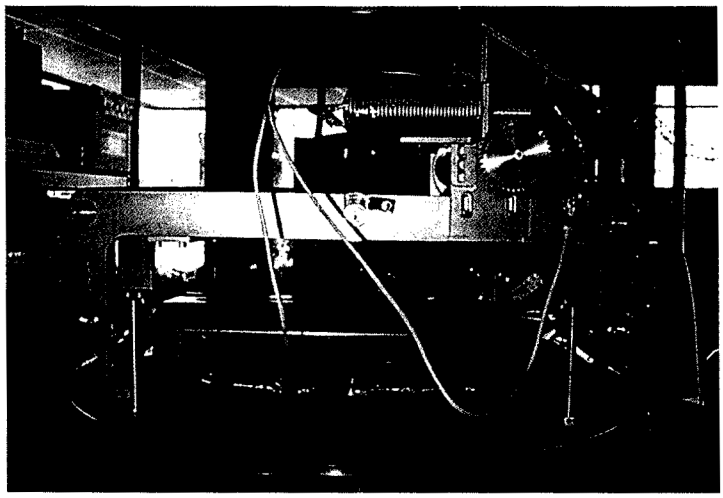

Figure 5 Wide bandgap deposition system with web drive.

6

3.4.2 Transparent back contact

Researchers at IEC have demonstrated that ITO makes a low resistance back contact to low bandgap (Eg ~ 1.2 eV) $Cu(In,Ga)Se_2$ devices. As can be seen in the data displayed in Figure 6A and listed in Table 2, open circuit voltage (Voc) and short circuit current density (Jsc) of the device on ITO is essentially the same as that on Mo. Although the lower fill factor (FF) of the ITO back contact device is at least in part related to the higher sheet resistance of the ITO compared to the Mo, studies with higher Ga-content films suggest that additional mechanisms may be involved. Mechanisms that could affect the Cu-chalcopyrite / TCO contact include chemical or physical factors which affect nucleation or growth of the absorber films or which affect the defect chemistry – and therefore the electrical properties - of the chalcopyrite back contact. As shown in Figure 6B, sub-bandgap optical transmission needs to be greatly improved in order to fully realize the benefits of multijunction PV devices.

Table 2 Device parameters of devices whose I-V and optical data are shown in Figure 6.

Substrate/ Back contact	Voc (V)	Jsc (mA/cm^2)	FF (%)	AM1.5G Efficiency (%)
Mo/glass	0.587	31.4	67.7	12.5
ITO/glass	0.585	32.0	58.4	10.9

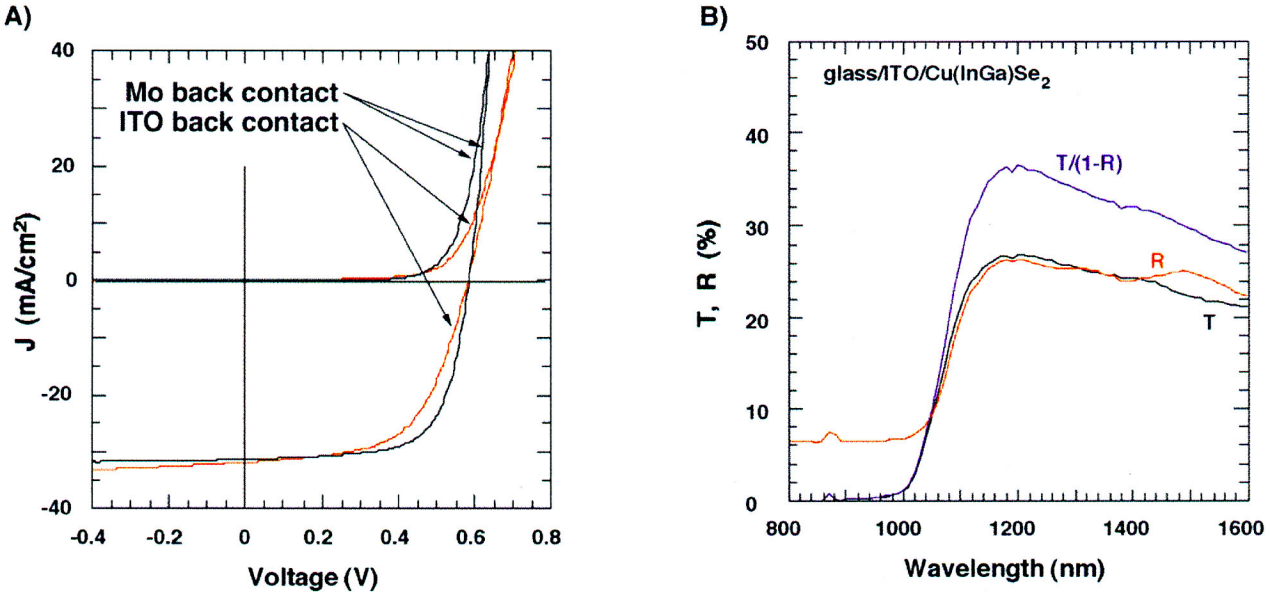

Figure 6 A) I-V and B) optical transmission and reflection data from CIGS devices deposited on Mo/glass and ITO/glass substrates during AFSA Phase I. Device I-V parameters are listed in Table 2.

3.4.3 Bottom cell durability

Preliminary studies of $Cu(In,Ga)Se_2$ devices subjected to conditions simulating deposition of wide bandgap chalcopyrite alloys - 350°C for 30 minutes in vacuum / Se-deposition ambient – display low Jsc, Voc and FF. Analysis of I-V and quantum efficiency data suggests that a reverse diode junction is formed at the back (Mo) electrode. Studies are in progress to discover the mechanisms responsible for this behavior. There is some evidence that this stress-induced degradation is at least partially reversible by heat treating in air, but further studies are required.

4 SUMMARY

AFSA is a high risk / high payoff program designed both to dramatically increase the specific power of satellite arrays by a factor of 2 – 3 X and to reduce array costs by about a factor ~10 X over present values. AFSA's technical approach is to deposit monolithic tandem thin film copper chalcopyrite PV devices onto lightweight flexible substrates. No fundamental technical barriers to achievement of program goals are believed to exist, but significant technical challenges remain. Progress is being made in addressing the three key technical areas: 1) high-efficiency, transparent wide bandgap top cell, 2) low-loss, transparent recombination / tunnel junction between cells and 3) durable bottom cell.

MARS ORBITER SAMPLE RETURN POWER DESIGN

N. Mardesich, S. Dawson

Jet Propulsion Laboratory
California Institute of Technology
Pasadena, California 91109-8099

Introduction:

Mars has greatly intrigued scientists and the general public for many years because, of all the planets, its environment is most like Earth's. Many scientists believe that Mars once had running water, although surface water is gone today. The planet is very cold with a very thin atmosphere consisting mainly of CO_2 . Mariner 4, 6 and 7 explored the planet in flybys in the 1960s and by the orbiting Mariner 9 in 1971. NASA then mounted the ambitious Viking mission, which launched two orbiters and two landers to the planet in 1975. The landers found ambiguous evidence of life. Mars Pathfinder landed on the planet on July 4, 1997, delivering a mobile robot rover that demonstrated exploration of the local surface environment.. Mars Global Surveyor is creating a highest-resolution map of the planet surface. These prior and current mission to Mars have paved the way for a complex Mars Sample Return mission planned for 2003 and 2005. Returning surface samples form Mars will necessitates retrieval of material from Mars orbit. Sample mass and orbit are restricted to the launch capability of the Mars Ascent Vehicle. A small sample canister having a mass less than 4 kg and diameter of less than 16cm will spend from three to seven in a 600 km orbit waiting for retrieval by second spacecraft consisting of an orbiter equipped with a sample canister retrieval system, and a Earth Entry Vehicle. To allow rapid detection of the on-orbit canister, rendezvous, and collection of the samples, the canister will have a tracking beacon powered by a surface mounted solar array.

The canister must communicate using RF transmission with the recovery vehicle that will be coming in 2006 or 2009 to retrieve the canister. This paper considers the aspect and conclusion that went into the design of the power system that achieves the maximum power with the minimum risk. The power output for the spherical orbiting canister was modeled and plotted in various views of the orbit by the Satellite Orbit Analysis Program (SOAP).

Description:

The spherical orbiting canister has a limited area for power generation, less than 40%, on the surface, due to the restrictions for lid sealing and canister albedo. The solar cells will be arranged in serial circuits and mounted into facets cut into the spherical canister. This was done in order to maximize power generation from each serial circuit at any view angle to the sun. The serial circuits will be diode protected and connected in parallel. The minimum power will be produced when the spherical canister lid is facing the sun and the cells have a 71 degree view of the sun. An additional 20% of the power can also be generated by the cells facing Mars, due to the albedo. The spherical canister will be operating below -26 degrees Celsius and needs to produce a minimum voltage of 3.3 volts. Silicon solar cells were selected as the best option since six silicon triangles would be the best fit onto a circle defined by the facet cut into the spherical surface. Each radiation hardened silicon cell can produce its peak power of .55 volts at -26 degrees Celsius after 10E14 e/cm^2 exposure. Figure 1

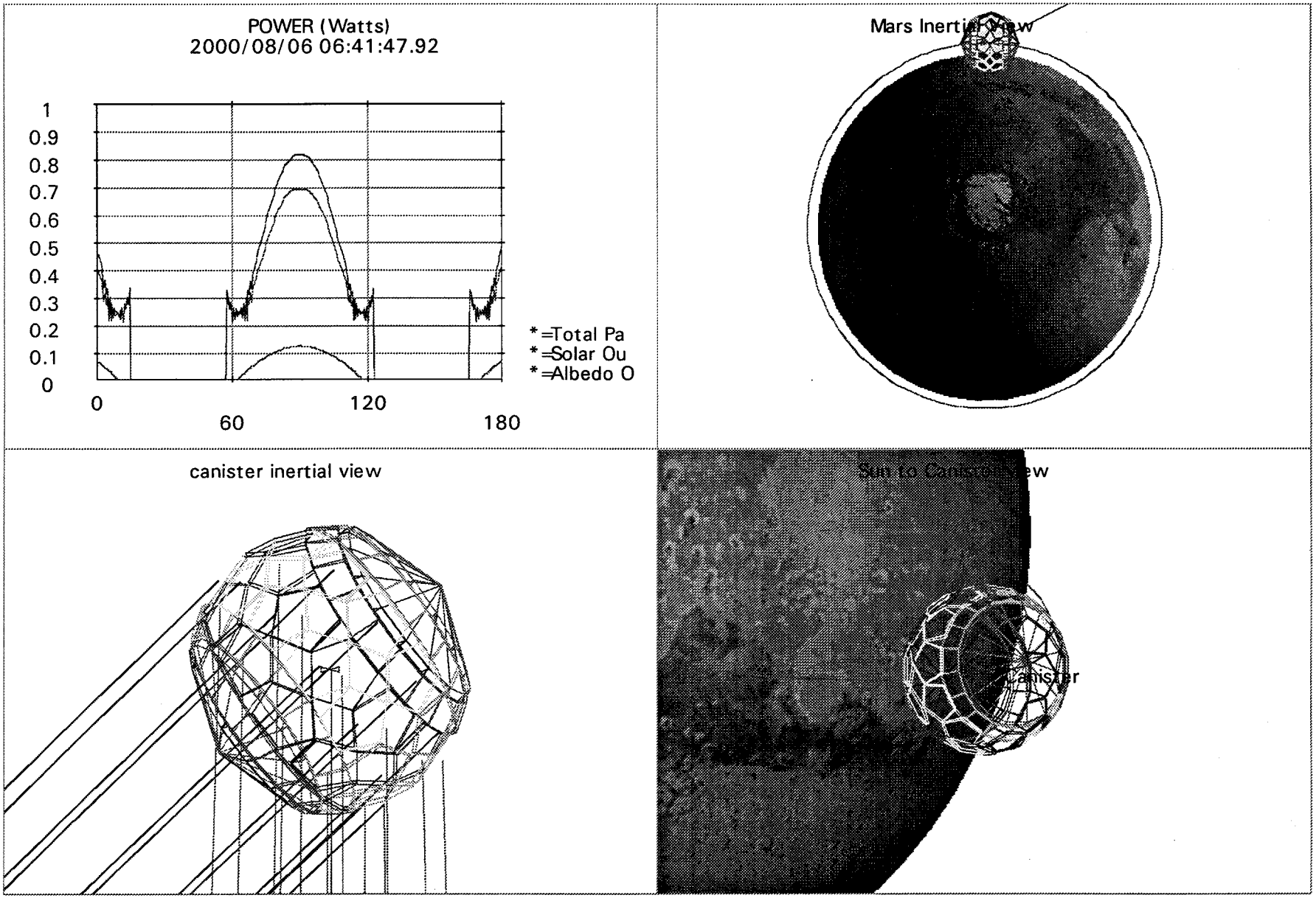

Figure 1. SOAP generated simulation of canister orbiting Mars
Courtesy of Robert Carnright JPL

shows a plot generated by SOAP, of the power produced by the rotating spherical canister as it orbits Mars. The first quad illustrates the power in Watts as it moves in and out of eclipse, second quad illustrates the Mars inertial view of the canister in the 600 km orbit, the third quad illustrates the canisters inertial view indicating the direction of sun and albedo flux, and quad four illustrates the Sun to canister view while in orbit.

The requirements and geometry for a solar array on a sphere are unique and place special constraints on the design. These requirements include 1) accommodating a lid for sample loading into the canister, surface area was restricted from use on the Northern pole of the spherical canister. 2) minimal cell surface coverage (maximum cell efficiency), less than 40%, for the recovery vehicle to locate the canister by optical techniques. 3) a RF tracking beacon which operates during 50% of MARS orbit time on any spin axis, which requires optimum circuit placement of the solar cells onto the spherical canister.

The optimum configuration would have been a 4.5 volt round cell, but in the real world we compromised with six triangular silicon cells connected in series to form a hexagon. These hexagon circuits would be mounted onto a flat facet cut into the spherical canister, Figure 2. The surface flats are required in order to maximize power, the surface of the cells connected in series must be at the same angle relative to the sun. The flat facets intersect each other to allow twelve circuits, evenly spaced just North and twelve circuits South of the equator of the spherical canister. Connecting these circuits in parallel allows sufficient power to operate the transmitter at minimum solar exposure, with the Northern pole of the canister facing the sun. Additional power, as much as 20%, is also generated by the circuits facing MARS due to albedo of MARS.

15.5 cm Diameter Canister

Top side

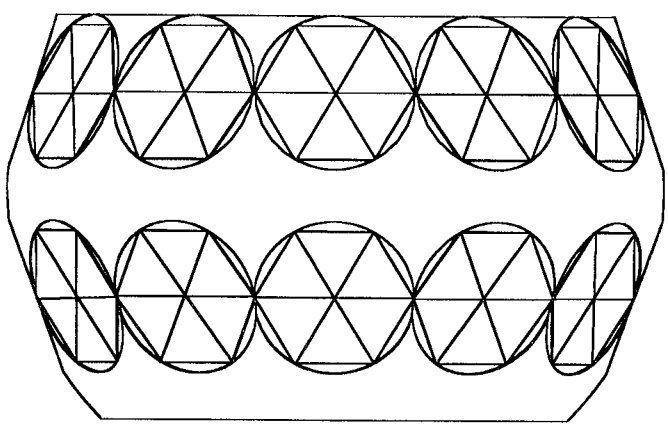

Figure 2

Performance:

It is planned to use thin (50 micron) high efficiency (19%) silicon solar cells with 7.5 micron filters. At Beginning of life (BOL) AM0 28 degree Celsius the six triangular cells connected in series can achieve a maximum power of 244 mW with light normal to the surface, or in orbit about Mars at -26 degree Celsius we expect 117 mW from each circuit. With 12 circuits mounted on each hemisphere we expect an illumination from the sun to be 3.9 to 6.3 circuits which will produce 460 to 737 mW. Additional power of 280 mW also will be generated by the cells facing Mars by the reflection of the Sun off Mars.

The addition of the circuits to the surface of the canister is expected to add less than 120 grams to the weight. The weight is an important factor to consider since this canister must be launched from the surface of Mars and every additional gram of payload requires additional fuel that must be transported to Mars at a high cost.

Summation:

Returning samples from Mars is an ambiguous program for NASA and will add to the exploration and knowledge of our solar system. Teams efforts such as Mars Sample Return are what dreams are made of.

PROGRESS OF THE MARS ARRAY TECHNOLOGY EXPERIMENT (MATE) ON THE 2001 LANDER

David A. Scheiman, Cosmo Baraona*, Dave Wilt*, Phil Jenkins, Michael Krasowski*, Lawrence Greer*, John Lekki*, Daniel Spina*, and Geoff Landis
Ohio Aerospace Institute
Cleveland, Ohio, 44142
*NASA Glenn Research Center
Cleveland, Ohio,44135

ABSTRACT

NASA is planning missions to Mars every two years until 2010, these missions will rely on solar power. Sunlight on the surface of Mars is altered by airborne dust and fluctuates from day to day. The MATE flight experiment was designed to evaluate solar cell performance and will fly on the Mars 2001 Surveyor Lander as part of the Mars In-Situ Propellant Production Precursor (MIP) package. MATE will measure several solar cell technologies and characterize the Martian environment's solar power. This will be done by measuring full IV curves on solar cells, direct and global insolation, temperature, and spectral content. The Lander is is scheduled to launch in April 2001 and arrive on Mars in January of 2002. The site location has not been identified but will be near the equator, is a powered landing, and is baselined for90 sols. The intent of this paper is to provide a brief overview of the MATE experiment and progress to date. The MATE Development Unit (DU) hardware has been built and has completed testing, work is beginning in the Qualification Unit which will start testing later this year, Flight Hardware is to be delivered next spring .

1. INTRODUCTION

This flight experiment is one of five experiments that make up the MIP package. MIP is designed to demonstrate the conversion of atmosphere CO_2 into propellant (O_2), which can be used to return to earth. One of the most important resources required to produce propellant on Mars is energy. Power is required for all phases of propellant production, from the initial collection and compression of atmospheric carbon dioxide to the liquification and storage of the cryogenic propellants produced. In many propellant production systems, the power system is the single largest and most massive component.

The four other experiments on MIP are; Mars Atmosphere Acquisition and Compression (MAAC), Oxygen Generating System (OGS), Mars Thermal Environment Radiator Characterization (MTERC), and Dust Accumulation and Removal Technology (DART). The MIP experiment control and main structure is being built and operated by NASA Johnson Space Center, as is OGS. MAAC and MTERC are being built at the NASA Jet Propulsion Laboratory, and DART is being built at NASA Glenn Research Center as well. The MATE and DART experiments share a 26 cm. x 24 cm. honeycomb substrate.

2. MATE DESCRIPTION

MATE is Mars Array Technology Experiment and its primary goal is to determine the optimum solar cell type for future missions. To do this it will measure the performance of solar cells, the solar spectrum, solar insolation, and temperature. MATE has several components and electronics, they are:

10 solar cells (5 pairs) Note: 9 on DU

2 solar cell strings

2 radiometers, direct and global
6 temperature sensors
1 dual spectrometer, 300 –1700 nm

2.1 Component Description

Each component is described briefly. Figure 1 shows a layout of the MATE DU experiment, the outlines represent components under the plate and the empty space is for the DART experiment which shares the same plate. The Qualification and Flight units will have slightly different component locations and configurations. This experiment has no moving parts. The diagram in figure 2 shows the general concept of the experiment and its interfaces.

MATE has a dedicated 4" x 6" circuit board in the MIP warm electronics box (WEB). This board is instructed what test scenario to perform and can run IV curves, sense temperatures, read insolations, run the spectrometers, then sorts the data, repeats any measurements, and sends the data back to MIP, which it sends to the Lander. The Lander stores the data until it is ready to be transmitted to an orbitting satellite and then back to Earth.

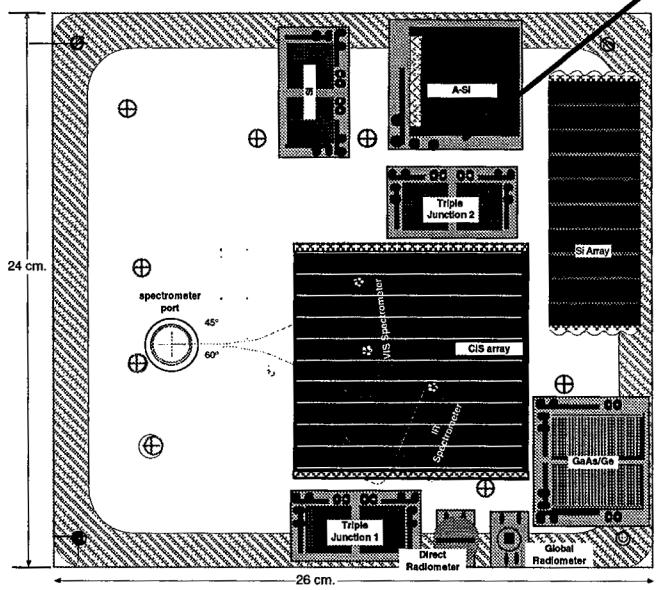

Figure 0: MATE DU Layout

Solar Cells (10): The solar cells will be made from a variety of materials and sizes. There are 5 pairs of different cell types. The space available, 80 mA maximum current, and 6 V maximum voltage limit the sizes of the cells. Cell selection was based on state-of-the-art viable cell technologies which will be suitable for the Mars environment. The cell types selected include; high efficiency Si from Sharp, Amorphous Si form United Solar Systems, two types of GaInP/GaAs/Ge triple junction cells from Spectrolab and Tecstar (these are p/n and n/p designs), and GaAs/Ge from Tecstar which are similar to those used on pathfinder [1,2].

Cells must perform at a lower temperature intensity then is common to most space cells [3]. The solar intensity on Mars is approximately one third of earth's AM0 or 45 mW/cm^2. Preliminary spectral data from Mars pathfinder and Viking have shown that the sunlight on Mars varies with dust content and tends to scatter the red part of the spectrum.

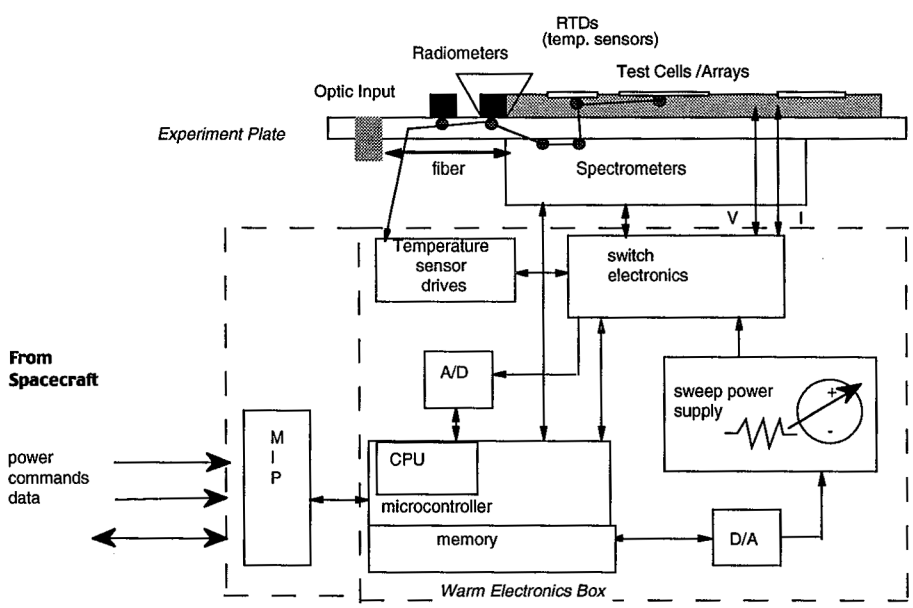

Figure 2 : Functional Diagram

Studies show that large area roll out thin film arrays prove very useful for many Mars missions. Thin films include CIS and Amorphous Si, both of which are being considered in the space community. Mobile manned missions will require large portable arrays that can be easily moved.

Solar Cell Strings (2): Two series strings will be flown on this mission. One string will be standard solar cells; the other will be a thin film. These strings are intended to test new technology as well as identify any problems with array designs. A string of Si cells from Sunpower and a CIS string from Global Solar are planned. Both of these strings demonstrate new unproven space technologies, the Si string has interdigitated front and back contacts, the CIS string contains fully integrated processing for cells and interconnects.

Radiometers (2): The radiometers are thermocpile devices that contain 20 thin film thermocouple junctions.. They are in an Argon filled TO-5 can with a Sapphire window and carbon black absorber as shown Figure 3. These devices generate a voltage proportional to the solar intensity and are 1-10 mV at Mars with a -.4%/°C temperature correction. They are being made by Dexter Research and have typically been used for measuring laser power.

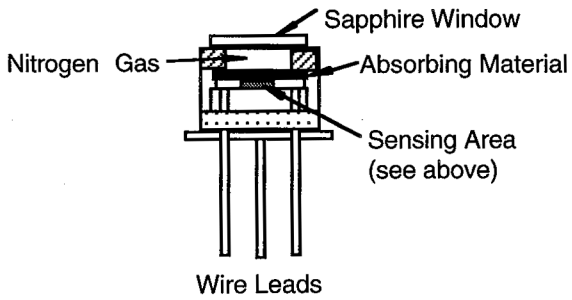

Figure 3 : Radiometer Design

There are two radiometers, one measuring global and the other measuring direct radiation or solar insolation. The global measurement is done with a radiometer that has approximately 130° field of view. This field of view is considered adequate based on the limitations of the device and the expected amount of scattered light. A second radiometer will have a cylindrical shell placed over it with baffles and a slit; this will measure direct radiation with the sun overhead. The direct radiometer can only be read when the sun is directly over the slit, this will consist of a timed measurement in 20 second intervals for 20 minutes around its optimum sun sensing. A precision landing allows for proper orientation of the slit prior to launch (within 15°).

Temperature Sensors (6): Six temperature sensors from Wahl will be scattered around the MATE experiment, two will be attached to the radiometers, two will be on the photodiode arrays of the spectrometers, and the rest will be under solar cells. The temperature sensors are platinum devices known as RTD (resistance temperature dependence). They have a well-characterized linear change in resistance with temperature (.385 %/°C) and a 0° C resistance of 1000 Ω. They are in a small ceramic case with two wires. Measurement accuracy will be 1 degree C. The temperature will be measured using a 3-wire technique and constant 100 μA current source.

Dual Spectrometer (2): The dual spectrometer consists of an input optic and two spectrometers, both having optical fiber inputs. This will span the solar spectrum from .3μm to 1.7 μm with a nominal resolution of 10 nm. This range was selected based on the bandwidth of solar cells and the AM0 spectrum, covering 86% of the total energy.

The input optic converts incident radiation into a diffuse light source. It consists of a tube, thin diffusing element made of Spectralon, a folding prism, and a fiber output. Light enters this diffusing element and is scattered uniformly and therefore each fiber will see the same amount of light. This diffuser extends the capability to look at the sky at any time of the day. Figure 4 shows a sketch of the input optics and figure 7 shows the

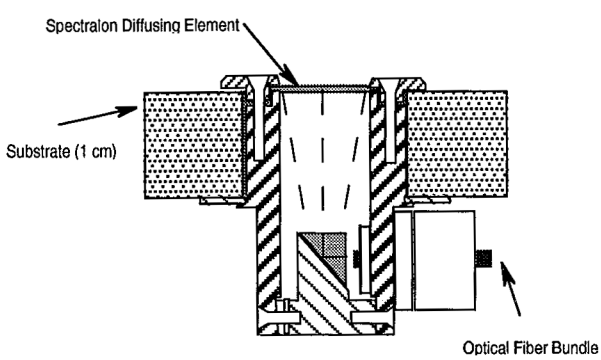

Figure 4: Spectrometer Input Optic Design

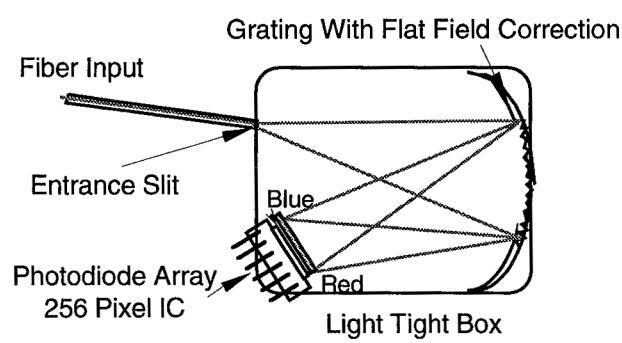

Figure 5: Fixed Grating Spectrometer

individual components.

The spectrometers are two separate devices with the same basic design except for the wavelength range they are designed for. Traditional spectrometers have used a rotating grating with a single detector, measurements for each wavelength range had to be made sequentially by turning the grating and reading the detector. These spectrometers have a fixed grating with multiple detectors where the entire spectral range is read simultaneously (figure 5). The multiple detectors are a photodiode array (PDA), each of these spectrometers has a PDA with 256 elements or detectors. These are very compact devices, but have a fixed resolution based on the detector response, grating, slit size, pixel size, and number of pixels. One spectrometer is made by Zeiss and has a Si PDA (Hamamatsu) covering 300-1100 nm, and the other is made by Control Development with an InGaAs PDA (Sensors Unlimitied) covering 900-1700 nm.

The sensitivity of the spectrometers is adjusted by one of two ways, by a gain adjustment or a change in the integration time. These spectrometers will have a fixed gain amplifier with a variable integration time to optimize the signal for the A/D. With the gain fixed, the integration time is proportional to the signal level and can be divided out to compare readings over different days. The resolution of this spectrometer is much higher then any current or planned measurements and should be able to resolve many narrow absorption bands over a wide range of environmental conditions [4,5].

Electronics : The operation of the electronics is based on an 8-bit CPU, session programmed into ROM which is dumped into RAM, and an 8-bit D/A and A/D. There are 65 wires that connect to the experiment and 25 wires that connect to the MIP Main Controller Board. The board is a multi-layer 4" x 6" and gets ±15V from MIP and has a 5V regulator on board. All of the A/D is converted using optimized 8-bit setup which guarantees <1% resolution over the range being measured. All of the data is passed to MIP as it is generated in a 256 byte packet system.

2.2 MATE specifications

The MATE/DART plate is 24 cm. x 26 cm and rests on the top horizontal surface of MIP. MATE is 500 cm^2 and will be operated from a single 4 x 6" electronics board in the MIP Warm Electronics Box. It requires 7.5 W of power and operates for less then 1 minute per session. The board will receive power and instructions from the MIP main controller board and transfer data for storage to MIP. The MIP main controller board will store data and transmit data to the lander. The total mass of MATE including the electronics is 510 g.

3. MATE Operation

The MATE operation currently has five different measurement scenarios, a sixth will be added for the flight unit, and a seventh is a ground test. Three of the measurement scenarios are identical and only vary by the time(s) of day, a fourth scenario is for the direct radiometer, and the fifth is a health check. MATE is scheduled to run once per day at solar noon, once per hour throughout the day one day per week, and once per week at night. MATE is operated 19 times per week unless power limitations or Lander priorities prevent it.

The three operation scenarios will measure full IV curves on all cells and strings, the radiometers, temperatures, and spectrometers. This sequence will run about 1 minute, use 7.5 W nominally, and take about 60 Kbits of data. All of the data will be in 8-bit format with the A/D scaled to optimize resolution. An IV curve will have 256 points and clearly identify open circuit voltage, short circuit current, and maximum power. The temperature will be within 1 degree C. Solar Insolation will be a converted voltage and temperature measurement The spectrometers will first be reset, read once to adjust the A/D scaling, and then read a second time. The

The direct radiometer measurement can only be done when the sun is passing over the slit. The radiometer will be measured every 20 seconds over a 20 minute interval centered around solar noon. A plot of this data will result in a peak measurement under direct illumination. Comparison of the other data is necessary to interpolate the direct insolation. Health checks will consist of a quick scan of all the instruments and cells. Data will be cell open and shirt circuit conditions, temperatures, and radiometer data.

A sixth session will be added to measure the spectral effectt of the dust directly. This will be coordinated with the DART Material Adherence Experiment (MAE) which has a moving glass window. MATE and DART experiments will be operated simultaneously and do not share any common communication so timing is critical to obtain this data. Dust will accumulate on the MAE window which can be rotated over the spectrometer input

optics. Taking the spectrum with and without the dust laden window and subtracting the two spectrums will result in a spectrum of just the effect of the dust.

4. DESIGN COMMENTS

The DU Unit has been built and has completed all testing and is shown in Figure 6. This unit included all the components of MATE except with lower fidelity, alternate but representative cell types were used. The testing included functional test, communication protocol, Mars chamber thermal tests (hot, cold, and nominal sols at 6 torr), cruise in hard vacuum, vibration, electromagnetic interference, and pyroshock.. All tests were considered successful with two mechanical failures during vibration and pyroshock. The conical slit resting on the direct radiometer caused a lead wire to break on the temperature sensor during vibration and the InGaAs PDA pulled away from the optic during pyroshock. Both of these failures have been resolved with design modifications which will be implemented in the qualification and flight hardware.

The flight unit will differ from the DU with some minor design modifications. The locations of the components will be changed to improve the field of view for many of the solar cells, all the high components to one side, and allowing for shorter wire runs on the top plate. The direct radiometer will be cylindrical and have additional baffling to improve its response. The dual spectrometer input optics will be raised slightly to rest just under the MAE window when it is opened to avoid stray light and it will have a light pie feed inside the optics. MIP is located in close proximity to the Additional changes include the use of ferrite beads and mesh to reduce EMI. MIP

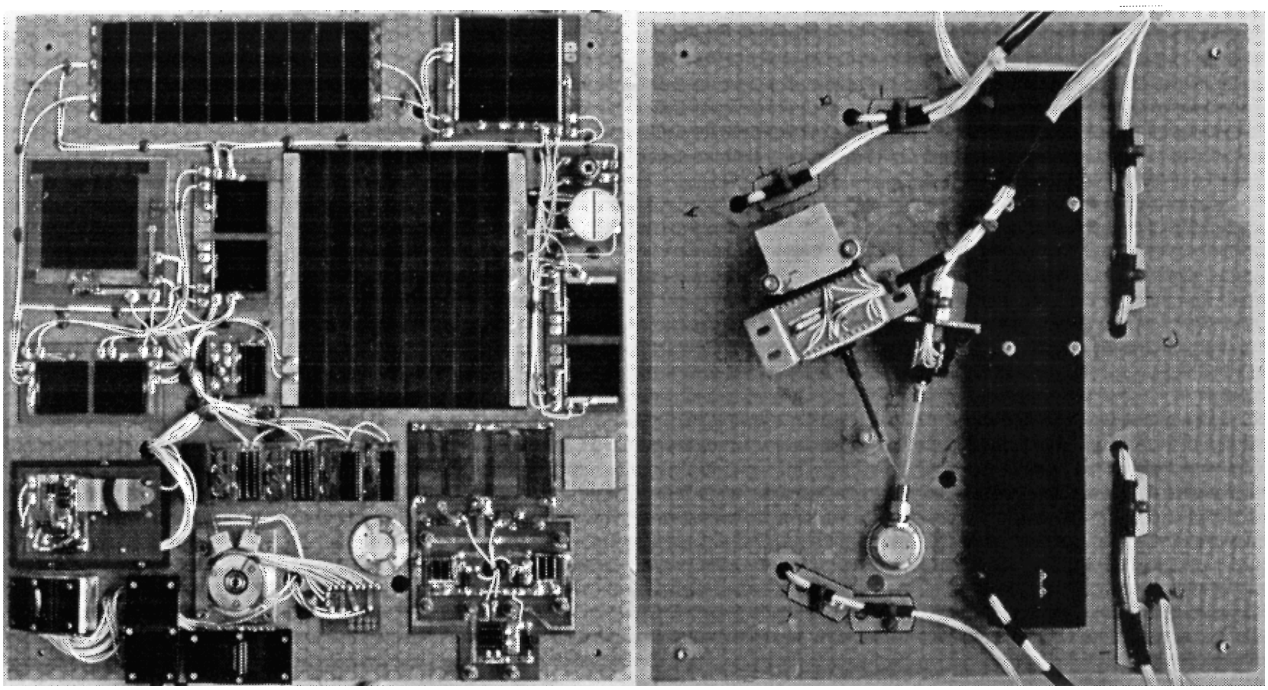

Figure 6 : MATE/DART DU (top and bottom views)

5. CONCLUSIONS

Both MATE and DART are ready toi proceed toi the Qual and Flight hardware build with confidence in the survivability of their experiments. The data obtained form MATE will be both beneficial in assessing the performance of solar cells and arrays on Mars as well as characterizing the Mars environmnet for modelling of future solar cell materials. The mission is baselined for 90 days depending on site location and power. MATE main objectives .are to:

- Measure solar cell performance in-situ
- Evaluate different types of solar cells

- Study long term effects of the Martian environment, particularly dust, on solar cells [6].
- Characterize the Martian environment by measuring the spectral content, solar insolation, and cell temperature

The MATE experiment is teamed up with the DART experiment [7]. With these two experiments, many of the concerns related to providing solar power on Mars will be studied.

Successful operation of the MATE experiment is dependent on several factors. Complete calibration of the radiometers, spectrometerrs, and temperature sensors will be performed on the flight hardware. One important test condition is a dust free baseline measurement on the surface of Mars. MIP will have a dust cover which will be opened after the landing dust has settled and the rover and pan cam have been deployed. A second issue is the field of view of the solar cells and sensors; Lander equipment may shadow some of the experiment. The orientation and location of the Lander will be known; the site and the location of the sun must be identified. These are critical elements in interpreting the data. The DART experiment also contains a sun sensor which will locate the sun and help to determine the optimum times to measure the direct radiometer. These two elements will aid in data analysis and measurement timing.

6. REFERENCES

More information can be found on the NASA Glenn Research Center PVSE branch web page at http://powerweb.lerc.nasa.gov/pvsee/publications/wcpec2/mate2001.html or NASA JPL Mars Missions web page at http://mars.jpl.nasa.gov/2001/lander/index.html

[1] G.A. Landis, "Solar Cell Selection for Mars," 2nd World Conference on Photovoltaic Energy Conversion, Vienna, Austria, July 1998

[2] G.A. Landis and J. Appelbaum, "Design Considerations for Mars PV Power Systems," *Proceedings of the 21st IEEE Photovoltaic Specialists Conference, Vol. 2,* pp. 1263-1270, May 1990.

[3] D. Scheiman, P. Jenkins, D. Brinker, and J. Appelbaum," Low-Intensity, Low-Temperature (LILT) Measurements and Coefficients on New Photovotaic Structures." Progress in Photovoltaics, Vol. 4, pp. 117-127 (1996)

[4] G.A. Landis, "Dust Obscuration of Mars Photovoltaic Arrays," *Acta Astronautica, Vol. 38, No.* 11. pp. 885-891 (1996). Presented as paper IAF-94-380, 45th International Astronautical Federation Congress, Jerusalem, Oct. 9-14 1994.

[5] E.A. Guiness, C.E. Leff and R.E. Arvidson, "Two Mars Years of Surface Changes Seen at the Viking Landing Sites," *J. Geophys. Res, Vol 87,* B12, pp. 10051-10058 (1982).

[6] G.A. Landis and P. Jenkins, "Dust on Mars: Materials Adherence Experiment Results from Mars Pathfinder," *Proceedings of the 26th IEEE Photovoltaic Specialists Conference,* Anaheim CA, pp. 865-869, Sept. 29-Oct. 3 1997.

[7] G.A. Landis, P. Jenkins, C. Baraona, D. Wilt, M. Krasowski, and L.Greer, "Dust Accumulation and Removal Technology (DART) Experiment on Mars 2001 Lander," 2nd World Conference on Photovoltaic Energy Conversion, Vienna, Austria, July 1998

PROGRESS OF THE DUST ACCUMULATION AND REMOVAL TECHNOLOGY EXPERIMENT (DART) FOR THE MARS 2001 LANDER

Phillip Jenkins*, Geoffrey A. Landis*, David Wilt†, Michael Krasowski†, Lawrence Greer†, Cosmo Baraona† and David Scheiman*
* Ohio Aerospace Institute, Cleveland, Ohio 44142
† NASA Glenn Research Center, Cleveland, Ohio 44135

ABSTRACT

Dust deposition could be a significant problem for photovoltaic array operation for long duration missions on the surface of Mars. Measurements made by Pathfinder showed 0.3 percent loss of solar array performance per day due to dust obscuration. We have designed an experiment package, "DART," which is part of the Mars ISPP Precursor (MIP) package, to fly on the Mars-2001 Surveyor Lander. This mission, to launch in April 2001, will arrive on Mars in January 2002. The DART experiment is designed to quantify dust deposition from the Mars atmosphere, measure the properties of settled dust, measure the effect of dust deposition on array performance, and test several methods of clearing dust from solar cells.

INTRODUCTION

The Mars Pathfinder lander and its rover, Sojourner, demonstrated that it is possible to operate a mission on the surface of Mars entirely on solar power [1]. Future missions even more ambitious in scope will require higher power levels and will operate for longer duration on Mars.

Large amounts of dust are raised into the atmosphere of Mars during dust-storms. Atmospheric dust consists of relatively small (micron scale) particles, suspended at altitudes of up to 20 km. The effect of this suspended dust on the insolation reaching the surface of Mars has been calculated by several researchers [2,3].

This dust settles out the atmosphere onto any horizontal surface. Atmospheric dust settling can be visible from Earth in the form of albedo variations visible when dust covers surface rocks after large dust storms. Both the Pathfinder lander and the Sojourner rover measured a progressive loss of solar array power due to deposited dust. The most accurate measurement, by the MAE experiment on the rover, measured an obscuration of the solar arrays due to dust deposition at a rate of 0.3% per day over the first 4 weeks of the mission [4]. This is potentially the major lifetime-limiting factor for a solar-power system on any Mars mission which is required to last for longer than 100 days, unless a technique is developed to periodically remove the dust or prevent settled dust from coating the array.

Atmospheric dust deposition can be considered to consist of two components: the settling of dust after global dust storms, and the settling of the ordinary atmospheric dust always present in the atmosphere [5]. A third component is the dust raised during spacecraft landing or by human or robotic operations on the surface. The worst-case scenario is that the lander must operate during the settling phase of a global dust storm.

Dust obscuration can be catastrophic for a long mission, unless dust removal is effected. It will be necessary to have a means to remove dust if a long-duration stay on the surface is to be achieved. Preferably, the dust removal should require little or no EVA activity by astronauts, since, even for a human mission, a Mars propellant plant will probably be operated as an unmanned vehicle launched two years before the piloted launch. A technique that requires no moving parts and is as simple as just pressing a button would be most desirable. A survey of dust removal techniques on Mars is given by Landis [6].

The utility of dust removal technique on Mars may depend on the detailed properties of the surface dust, including composition, binding strength, particle size distribution, native charge, and surface chemical state. These properties cannot be adequately simulated in an Earth environment, but must be tested with actual Mars dust. It would also be desirable to demonstrate operation in the actual environment, with the temperature, UV radiation, and dry, low-pressure mixed-gas atmosphere (CO_2 plus secondary components of N_2, and Ar) of Mars.

MARS ISPP PRECURSOR (MIP)

The Mars ISPP Precursor (MIP) package is a set of experiments designed to demonstrate on Mars the component technologies required to produce oxygen from Martian atmosphere. The experiment package is scheduled to fly on the Mars-2001 Surveyor lander, to launch in April of 2001. The five experiments comprising MIP will demonstrate production of power by advanced solar-cell technologies, acquisition and compression of carbon dioxide from the Martian atmosphere, conversion of the compressed atmosphere to oxygen by zirconia electrolysis, radiation of waste heat from the compression process to the night sky, and methods of mitigation of the effects of dust on solar arrays. The package will also make measurements of the Mars environment which will be of engineering use and scientific interest.

The Dust Accumulation and Removal Technology (DART) experiment is one of the five experiments of the MIP package. DART will gather engineering data about the deposition rate and properties of the dust and demonstrate the removal of dust. By improving knowledge of the operating conditions of solar cells on Mars, the uncertainty in power output for future Mars missions can be reduced.

A companion experiment, the Mars Array Technology Experiment, will test the operation of different solar cell types on the Mars-2001 Surveyor lander [7].

DART SENSORS

The DART experiment consists of five different instruments shown in schematic in figure 1. The first three listed below support the characterization of Mars dust. The last two instruments are experiments designed to mitigate dust build up on solar cells. During development of DART, silicon solar cells and GaInP cells [8] were used. For flight, either single junction GaAs or GaInP solar cells supplied by Spectrolab are used.

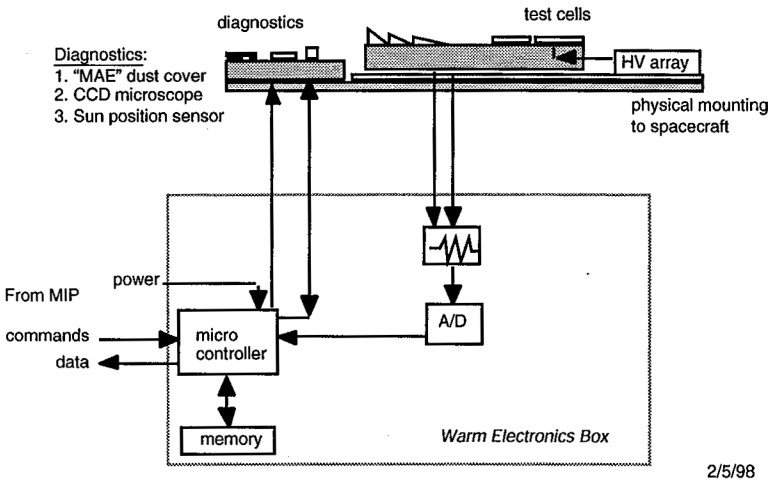

Figure 1: DART experiment package block diagram

Material Adherence Experiment (MAE)

The MAE dust coverage monitor is a device to measure how much dust settling has occurred on the spacecraft. The method of measuring dust is identical to that flown on Pathfinder: dust settles on a transparent plate, and a solar cell measures the intensity of the sunlight through the settling plate. By command, the settling plate can be rotated away from the cell, and the solar cell measured again. This results in a direct measurement of the optical obscuration [9]. By incorporating three solar cells under the settling plate, we can observe the effect of dust coverage in three spectral bands of interest.

The MAE dust coverage monitor is comprised of the following elements:

1. Transparent plate for dust settling
2. Rotary mechanism to move plate
3. A GaInP solar cell, GaAs filtered bottom cell and a single junction GaAs cell.
4. Resistors to measure photodiode current
5. Sensor element to detect position of rotation

Dust Microscope

The microscope measures the amount and properties of settled dust. It will give the rate of dust deposition, the particle size distribution, the particle opacity, and will image the shape of the larger particles. Since detailed information about dust properties is required to design dust mitigation strategies, this is probably the single most important instrument on the DART package.

The microscope is comprised of the following elements:

1. Settling plate. A transparent, horizontal, glass plate. Dust settling from the atmosphere will land on this plate, which will hold it at a fixed focus distance from the objective.
2. Objective lens. A lens system which magnifies the image of the front surface of the plate. We are anticipating use of a 40x objective, to resolve particles down to roughly half-micron diameter.
3. Turning prism. The turning prism bends the light path by 90 degrees to allow us to mount the microscope horizontally beneath the plate.
4. Focal plane array. The microscope focal plane uses a FUGA-15D active-pixel array.
5. Short-pass filter ("blue filter").
6. Illuminator. A light-emitting diode which illuminates the dust particles.
7. Control electronics
8. Structure. A structural frame holds the components in optical alignment and also excludes stray light.

The microscope is shown schematically in Figure 2.

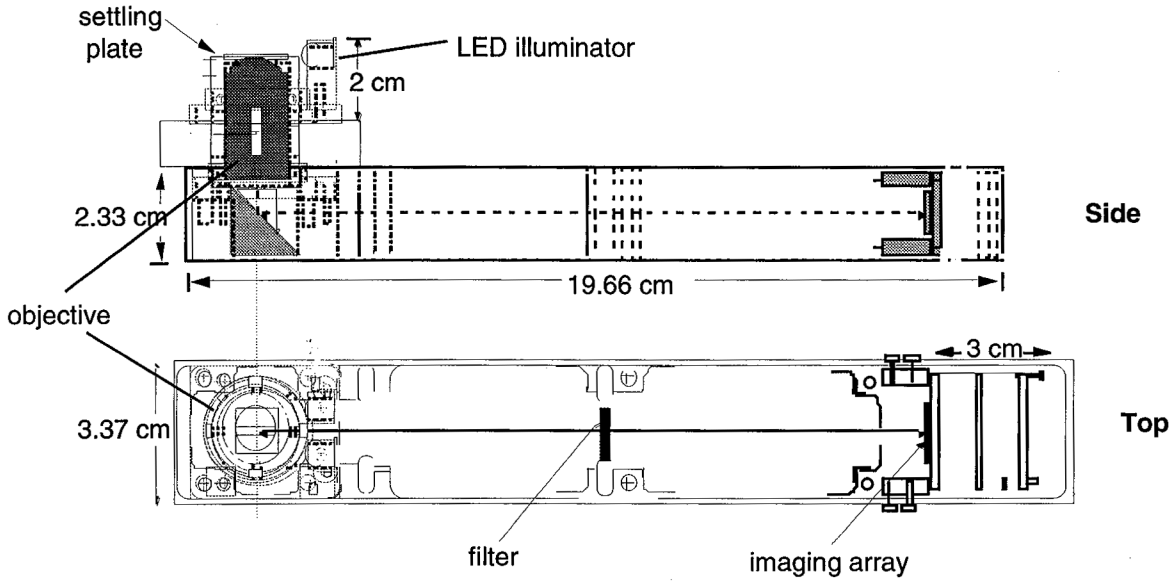

Figure 2: Schematic of microscope to image settled dust. Top: view from the side. Bottom: view from top

Sun position sensor

The sun position sensors locate where the sun is relative to the solar panel. We also intend to use this measurement to obtain a measure of the optical depth of the atmospheric dust (τ). The sun sensors are designed to measure sun position when the sun is within 45 degrees of zenith. A third element measures sun elevation at lower sun angles.

The sun position sensor is comprised of three each of the following elements, oriented orthogonally:

1. 512 element linear photodiode array
2. Neutral density filter
3. Cylindrical lens
4. Mounting and stray-light shield

Tilted cells

First, we will test whether the dust will deposit onto tilted surfaces. Use of a tilted solar array may be the simplest

solution to the dust accumulation problem. The Pathfinder experiment measured only dust accumulation on a horizontal surface. Measurements of the camera window on the Viking lander showed no dust adhering to the vertical surface. Observations of the thermal shell of the Viking landers seemed to show that dust also did not build up on the tilted surfaces. Unfortunately, this observation is anecdotal, and no quantitative measurement of accumulation has been made. Due to this observation, we have decided that a high priority is to verify the conjecture that tilted solar cells do not accumulate dust, and to get an indication of what angle is required to avoid dust coverage.

The following elements comprise the tilted cell measurement:

1. Single junction GaAs Solar cells tilted at 30°, 45°, and 60°, plus a control (horizontal) cell
1a. Solar cell tilted at 30°es with low friction, diamond- like carbon coating
2. Horizon mask
3. Resistors to measure current

Electrostatic Dust Mitigation

An electrostatic dust removal method will be tested. Electrostatic dust removal is a possible means of dust mitigation with the advantage of requiring no moving parts. Since the Martian dust is most likely charged (due to triboelectric charging and photoionization), a continuous electrostatic charge may prevent dust from settling on solar cells. A high-voltage vertical junction photovoltaic array [10] will provide an electrostatic potential continuously to the test cell (during daylight operation). The electric field strength in the neighborhood of the cells will be approximately 100 Volts/cm.

Three solar cells will be tested, one with positive potential, one with negative potential, and one solar cell to test whether a transverse electric field can sweep dust away from the cell before it accumulates. Figure 3 shows the electrical schematic. In each case, a wire at a "ground" reference is used as the second electrode.

The following elements comprise the electrostatic dust mitigation measurement:

1. Three GaAs solar cells, each fitted with a transparent, conductive, cover glass
2. Four vertical multi-junction cells wired to yield ±80V
3. Wires suspended above and to one side of the cells to establish the direction of the electric field.
4. Resistors to measure solar cell current and monitor the high voltage array

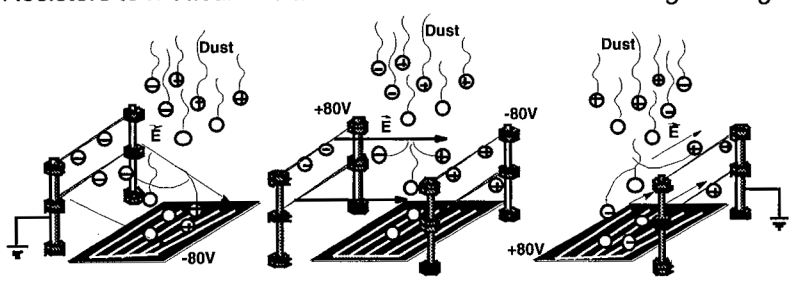

Figure 3: Schematic of electrostatic dust removal.

STATUS

The DART experiment on the Mars-2001 Surveyor Lander mission will measure the deposition rate and properties of Martian dust, and will test two methods for mitigating the effect of dust accumulation on solar arrays. At this time, the Qualification hardware is being built and Flight hardware is scheduled for March 2000 delivery.

REFERENCES

further information can be found on the NASA Lewis PV branch web page, http://powerweb.lerc.nasa.gov/pv

[1] R. Ewell and D.R. Burger, "Solar Array Model Corrections from Mars Pathfinder Lander Data," *Proceedings of the 26th IEEE Photovoltaic Specialists Conference,* pp. 1019-1022, Sept.-Oct. 1997.

[2] R. Haberle, C.P. McKay, O. Gwynne, D. Atkinson, G.A. Landis, R. Zurek, J. Pollack and J. Appelbaum, "Atmospheric Effects on the Utility of Solar Power on Mars," *Resources of Near Earth Space,* pp. 799-818, U. Arizona Press Space Science Series (1993).

[3] G.A. Landis and J. Appelbaum, "Design Considerations for Mars PV Power Systems," *Proceedings of the 21st IEEE Photovoltaic Specialists Conference, Vol. 2,* pp. 1263-1270, May 1990.

[4] G.A. Landis and P. Jenkins, "Dust on Mars: Materials Adherence Experiment Results from Mars Pathfinder," *Proceedings of the 26th IEEE Photovoltaic Specialists Conference,* Anaheim CA, pp. 865-869, Sept. 29-Oct. 3 1997.

[5] G.A. Landis, "Dust Obscuration of Mars Photovoltaic Arrays," *Acta Astronautica , Vol. 38,* No. 11. pp. 885-891 (1996). Presented as paper IAF-94-380, 45th International Astronautical Federation Congress, Jerusalem, Oct. 9-14 1994.

[6] G.A. Landis, "Mars Dust Removal Technology," *Journal of Propulsion and Power,Vol. 14*, No. 1, pp. 126-128, Jan. 1998; paper IECEC-97345.

[7] D. Scheiman, C. Baraona, D. Wilt, G. Landis and P. Jenkins, "Mars Array Technology Experiment (MATE) for 2001 Lander," 2nd World Conference on Photovoltaic Energy Conversion, Vienna, Austria, July 1998.

[8] The authors wish to thank Dr. Sarah Kurtz for supplying GaInP cells during development of the DART experiment.

[9] P. Jenkins, G. Landis, and L. Oberle, "Materials Adherence Experiment: Technology," paper IECEC-97339, *Proc. 32nd Intersociety Energy Conversion Engineering Conf., Vol. 1*, 728-731, July 27-Aug. 1 1997, Honolulu HI.

[10] B.L. Sater, "Vertical Multijunction Cells for Thermophotovoltaic Conversion," *First NREL Conf. on Thermophotovoltaic Generation of Electricity, AIP Conference Proceedings 321,* pp. 165-176 (1994).

REPORT OF THE WORKSHOP ON NEXT-GENERATION SPACE PV: THIN FILMS

R.P. Raffaelle
NASA Glenn Research Center at Lewis Field, Cleveland, OH 44135

A workshop on the future use of thin-film photovoltaic devices in space power was convened at the 16th Space Photovoltaic Research and Technology Conference held at the NASA Glenn Research Center in Cleveland, OH. This workshop began by addressing three questions pertaining to future use of thin film devices for space power systems. What follows is a summary of the discussion that transpired.

1. What are the leading impediments or technological challenges to be overcome with regard to the use of thin-film PV in space?

Higher efficiency large-area cells need to be developed. Efficiencies need to exceed approximately 13% before thin-films could realistically displace silicon cells. Thin film technology has many wonderful attributes (e.g., radiation tolerance, power to weight ratio, flexibility, etc.). There would be a tremendous market for high-efficiency light-weight non-degradable cells. Unfortunately, the space power community has yet to realistically evaluate this perceived potential.

Two separate sets of issues must be considered for space implementation:
1) Systems level issues, 2) Device level issues.

Systems level
A complete systems study is necessary to match power level versus size, mission time, array type, and thermal management requirements. Just because one could make a inexpensive thin-film array the size of a football field does not mean it would be useful. There are serious deployment and control issues that would have to be considered in the design stage. It is also not clear at this point if the good attributes such as the radiation tolerance are scalable.

In large-area cell development, the use of a light-weight flexible substrate such as Mo on Kapton or suitable polyimide is essential. However, the CIS processing temperatures are still to high. Either a higher temperature substrate material or lower processing temperatures must be developed.

Device Level
The is more to do to achieve higher efficiency thin-film cell than just adjusting the bandgaps. Questions such as: Why are CIS polycrystalline thin films are nearly as good as their single crystals counterparts? Can all this be explained with Zunger et. al.'s defect pairing mechanism? What is happening at the grain boundaries? What is the real nature of the so-called buried junction between the CdS and CIS? The limiting factors at the junction level need to be identified and addressed.

Many feel that the possibility of a multi-junction CIS – CIGS cell may work. However, a efficient top-cell is the biggest hurdle. As Ga or S is introduced to increase the bandgap or CIS, device performance and efficiencies degrade.

2. What is the status of organic based cells? Will they have a role in space PV, if so when?

Stability is a big problem. Difficult to produce a n-type materials that will not degrade. Absorption is still very low. However, if tunnel junctions could be made, you could stack say 10 to 20 junctions and still have a light-weight device.

3. What about an integrated PV/Li battery array – up and down sides?

People are already investigating the implementation of batteries in the honeycomb arrays etc. Thin film battery performance in space environments needs to be studied (temperature, radiation, etc.) Thermal management issues are still in question. These devices must operate in eclipse at very low temperatures, where batteries perform poorly.

A request was made to the conference organizers. As a result of this workshop, the participants would like to see a space thin-film PV workgroup established that could share information and ideas. They would also like to see a development of a space thin-film PV roadmap for the development of this technology. This would at a minimum get people thinking about and possibility working on the current impediments to the realization thin-film PV for space.

After the individual workshop was concluded, a joint meeting of all the SPRAT participants was held. Brief reports from the various workshops were made and comments were solicited from the entire group. What follows is a summary of the points of discussion.

Discussion Points

A multi-junction CIS-based cell with the ability to eclipse the 20% efficiency should be achievable with current materials. A CdTe top cell looks like a good possibility for a multi-junction thin-film cell with CIS.

Several people felt that development of thin-films space arrays has enormous potential, however it will never be realized unless a the government or a cell manufacturer is willing to invest the type of money necessary to develop the proposed materials. However, it was noted that NREL has invested multi-million dollars in CIS development. However, the development of cells for space has different problems that are not likely to be addressed by the terrestrial community. Although AM 1.5 testing on thin films has taken place, the AM 0 needs to be performed. Good numbers for temperature coefficients need to be measured. Questions pertaining to degradation and materials performance under space conditions need to be answered. Space qualification needs to be addressed.

Low efficiency cells although light do not necessarily give high power to weight in practice, for array weight scales with area. The larger the array, the more energy that must be expended to deploy the array and control the spacecraft. Also, as arrays size increases, more weight is required in the deployment mechanism. Air Force Research Labs and JPL are both working on new array technologies for light-weight blankets.

Space qualified arrays need much more inspection and tracability; this is a major organizational cost. Are the manufacturers willing to do this? Not likely since it is a long-term investment in a market which can be very volatile and unpredictable. Space areas need a total system engineering approach. This is not likely to happen until the development of a thin-film array becomes an enabling technology for a specific mission.

Cost is a perceived advantage for thin film cells. Terrestrial cell manufacturers claim manufacturing costs of under $2.00/watt presently and lower costs in the future. However, it is not clear if lower cell manufacturing costs translate into lower array costs, since much of the space array cost is due to space qualification requirements, that may be much higher than the actual manufacturing cost. However, one of the cost advantages of thin films comes in the integral interconnection of large-area blankets, which could translate directly into reduced costs for space arrays.

Since cost is such a critical point regarding the development of thin-film arrays, the question of what is the actual cost of a current PV array was posed.

> One cost example: A 500 watt array, cost at the panel level, not including substrate cost or deployment mechanism, came in at $1200/watt. The same array substituting 21.5% GaAs cells came to $1000/watt (no NRE cost). 60% of this cost is quoted as touch labor.
>
> For comparison, JPL noted a cost of $1000/watt for a Si array of similar size, but costs can be five to six thousand dollars/watt, depending on engineering, for some arrays. This depends often on testing costs, which can be high for non-standard arrays.
>
> For comparison, Goddard noted that the EOS-AM array, based on the JPL APSA design, had a final cost of $10,000/watt ($50,000 for a 5kW power system) at the completed array level (including structure and mechanisms). This price is unusually high, but shows that in some cases array costs can be extremely high.

It was pointed out that the same impediments to the development of GaAs cells, concentrator cells, and multi-junction cells for space are now being discussed with regard thin film cells. And on this note, the discussion on Next-generation Thin Film Space PV was concluded.

Predicting Environmental Interactions - SPRAT Workshop

The following questions were posed to the workshop participants. The answers received in and after the workshop are given below:

1. What environmental interactions predictive tools do you presently use?

A. Spacecraft Charging Tools:

i. 1984 NASA/JPL Spacecraft Charging Guidelines, at http://powerweb.lerc.nasa.gov/pvsee/publications/geo-guide.html

ii. NASCAP/GEO - Systems Division, Maxwell Technologies*

iii. NASCAP/LEO - Systems Division, Maxwell Technologies*

iv. EWB 5.0 - Systems Division, Maxwell Technologies*, not yet available, *also contains integrated tools for other environments*

v. On-line Spacecraft Charging Guidelines - Preliminary, Systems Division, Maxwell Technologies, at http://see.msfc.nasa.gov/see/ee/model_charging.html

B. Solar Activity Models:

i. MSFC Solar Activity Model, at http://www.ssl.msfc.nasa.gov/ssl/pad/solar/sunspots.html

ii. Solar Flare Models:

a. J. Feynmann and S. Gabriel - JPL (AIAA Paper 90-0292)

b. E. Stassinopoulos - GSFC (NASA TM-X-72573)

c. M. Xapsos, G.P. Summers, P. Shapiro, E.A. Burke - NRL, (IEEE Trans. Nuc. Sci. 1996, 43, 2772-2777)

d. ESP - MSFC at http://see.msfc.nasa.gov/see/ire/model_esp.html

C. Radiation Belt Environments and Radiation Damage Models

i. Spacerad at http://spacerad.com

ii. SAVANT, generalized NIEL rad. damage code for solar cells, in development by NASA Glenn PVSEE Branch

iii. SPENVIS at http://www.spenvis.oma.be/spenvis

iv. EQFLUX in the JPL Solar Cell Radiation Handbook, JPL Publ. 82-69 (1982)

v. CREME 96 (NRL) at http://crsp3.nrl.navy.mil/creme96/

*Dr. Gary Jongeward, 8888 Balboa Ave., San Diego CA 92123

2. For current spacecraft, what new tools need to be developed?

It was generally agreed that a fully integrated NIEL EOL radiation damage tool was desirable. This may be taken care of by continued development of SAVANT. EWB 5.0 was considered to be desirable for contamination calculations, including contamination from ion thrusters, etc. Since there is so much disagreement on the "correct" solar event model to use, it was felt that a "standard" solar event model should be developed. In addition, models of cosmic rays and heavy ions, and of UV, micrometeoroid, contamination, and AO darkening of spacecraft materials should be developed, based on laboratory test data. In addition, test results are needed for theory development, for example, NIEL coefficients must be found for multijunction cells, etc. Finally, we need better error estimation in our models, so one will know to what degree their results are believable.

The Working Group considered the following two questions together:

3. What new environmental factors and operating regimes need to be considered for new environments (dusty plasmas, Paschen regime, planetary magnetospheres, etc.)?

4. For what new environmental regimes (Moon, Mars, IP space, planetary orbits, etc.) should guidelines be developed?

The Working Group asked for improved distribution of the MSFC SEE Program monographs on environmental interactions. They may be found on-line at http://see.msfc.nasa.gov/see/srp.html. In addition, NASA should publish overview papers calling out new issues for new space environments and giving rough guidelines for how to deal with them. NASA should also publish standards for consideration in developing spacecraft specifications for new environments. One of the new environments mentioned in the meeting was Paschen discharge on the surface of Mars and within spacecraft interiors. Finally, spacecraft manufacturers were called upon to use zero-based spacecraft specifications, using reliability-based models for entire circuits, not just individual solar cells.

5. What should NASA's role be in developing design guidelines and/or predictive tools?

It was generally agreed that NASA's traditional role should be continued - of publishing guidelines and approved methodologies, validating and recommending predictive methods, and maintaining databases and doing experiments to complete databases on the behavior of space solar cells, arrays, and spacecraft materials in the space environment. NASA should also do testing of solar cell performance, and plasma testing when appropriate. In addition, NASA should perform flight experiments when possible to validate and qualify performance of solar cells, etc., in space, and publicize the models that are produced as a result. Finally, NASA should cooperate with ESA, NASDA, etc. to fulfill the goals of the entire community.

Dr. Dale C. Ferguson
Working Group Chairman

REPORT DOCUMENTATION PAGE

Form Approved
OMB No. 0704-0188

Public reporting burden for this collection of information is estimated to average 1 hour per response, including the time for reviewing instructions, searching existing data sources, gathering and maintaining the data needed, and completing and reviewing the collection of information. Send comments regarding this burden estimate or any other aspect of this collection of information, including suggestions for reducing this burden, to Washington Headquarters Services, Directorate for Information Operations and Reports, 1215 Jefferson Davis Highway, Suite 1204, Arlington, VA 22202-4302, and to the Office of Management and Budget, Paperwork Reduction Project (0704-0188), Washington, DC 20503.

1. AGENCY USE ONLY (*Leave blank*)

2. REPORT DATE
May 2005

3. REPORT TYPE AND DATES COVERED
Conference Publication

4. TITLE AND SUBTITLE
16th Space Photovoltaic Research and Technology Conference

5. FUNDING NUMBERS
WU–755–A4–02–00

6. AUTHOR(S)
Sheila Bailey, editor

7. PERFORMING ORGANIZATION NAME(S) AND ADDRESS(ES)
National Aeronautics and Space Administration
John H. Glenn Research Center at Lewis Field
Cleveland, Ohio 44135–3191

8. PERFORMING ORGANIZATION REPORT NUMBER
E–12676–1

9. SPONSORING/MONITORING AGENCY NAME(S) AND ADDRESS(ES)
National Aeronautics and Space Administration
Washington, DC 20546–0001

10. SPONSORING/MONITORING AGENCY REPORT NUMBER
NASA CP—2001-210747-REV1

11. SUPPLEMENTARY NOTES
This revised report supersedes the original report. Proceedings of a conference held at Ohio Aerospace Institute and sponsored by NASA Glenn Research Center, Brook Park, Ohio, August 31–September 2, 1999. Responsible person, Sheila Bailey, organization code RPV, 216–433–2228.

12a. DISTRIBUTION/AVAILABILITY STATEMENT
Unclassified - Unlimited
Subject Categories: 20, 18, 33, and 93 Distribution: Nonstandard
Available electronically at http://gltrs.grc.nasa.gov
This publication is available from the NASA Center for AeroSpace Information, 301–621–0390.

12b. DISTRIBUTION CODE

13. ABSTRACT ***(Maximum 200 words)***

The purpose of the SPRAT conference is to bring members of the space solar cell community together in a relatively informal conference setting to discuss the recent developments in solar cell technology and to discuss the future directions of the field. The conference is sponsored by the Photovoltaic and Space Environmental Effects Branch at the NASA Glenn Research Center.

14. SUBJECT TERMS
Solar cell; Photovoltaic; GaAs; Space radiation; Plasma; GaInP; Solar array; Mars; Thin film

15. NUMBER OF PAGES
269

16. PRICE CODE

17. SECURITY CLASSIFICATION OF REPORT	18. SECURITY CLASSIFICATION OF THIS PAGE	19. SECURITY CLASSIFICATION OF ABSTRACT	20. LIMITATION OF ABSTRACT
Unclassified	Unclassified	Unclassified	